Evaluation of variations in gross primary production over terrestrial ecosystem using remote sensing technique

（リモートセンシング技術を用いた陸域生態系における GPP 変化の評価に関する研究）

北海道大学　大学院農学院

共生基盤学専攻　博士後期課程

孫　仲益

Contents

Abstract

The terrestrial Gross Primary Production (GPP), which is defined as the amount of carbon uptake by vegetation through photosynthesis at the ecosystem scale, is the first step of atmospheric carbon dioxide (CO_2) entering the biosphere. Through GPP, which plays a pivotal role in the global carbon balance and almost all ecosystem processes, terrestrial ecosystem can partly mitigate global warming and offset the increasing CO_2 emissions. Therefore, it is of pivotal scientific significance to precisely measure terrestrial ecosystem GPP. However, directly measuring GPP at the global scale is impossible; to accurately quantify the spatiotemporal patterns of GPP, considerable efforts have been made to develop physiological process models as tools to understand terrestrial carbon mechanisms and fluxes at the global scale and to hindcast historical situations and predict future changes.

For the past ten years, remote sensing (RS)-based models have been widely used with the development of space technology because compared with process-oriented ecosystem models that entail a complex combination of model parameterizations, RS-based approaches are relatively simpler and more efficient for exploring dynamic changes in GPP and their spatiotemporal variations at the macroscale.Considerable and substantial efforts have been made to validate, regulate and contrast the models at flux tower sites, specific ecosystems and regional scales. However, the optimal model that is suitable for estimating GPP across different ecosystems and a wide range of enviro-climatic conditions has not been identified and designed, and the discrepancies associated with the spatial distributions of the environmental controls that influence the GPP variation simulated by different models are highly significant. Nonetheless, these studies have concluded that it is necessary and important to study and understand model sensitivity to indicators before designing and modifying GPP estimation models. Simultaneously, it is also important and necessary to accurately describe the changes of GPP in different regions to quantitatively evaluate how environmental factors influence GPP. Furthermore, a deeper understanding of how GPP has responded to past climate change, land cover change and rising atmospheric CO_2 concentration will provide insight into how the carbon cycle will change under future CO_2 and climate conditions.

In this study, I firstly used twelve models to estimate the global GPP over the past fifteen years and tested the performance by comparing them with eddy covariance (EC) flux tower measurements. Second, I utilized the models considering CO_2 fertilization effect to analyze the individual effect of environmental factors and the interactions through a series of factorial estimations around the global terrestrial ecosystems, and zoned the categories of GPP variations according to seasonal and dimensional characteristics using an unsupervised classifier, and then analyzed the GPP trend and its attribution spatially. Thirdly, the model ensemble was tested for their apparent sensitivities to climatic variability and rising atmospheric CO_2 concentration. Then, the values calculated via the flux tower measurements and Free-Air CO_2 enrichment (FACE) experiments were used to test the sensitivity of the modeled GPP to individual changes in climatic variables and CO_2. Finally, I combined the results obtained from this study with the design concept, structure, and parameters of each model to comprehensively analyze individual sensitivity.

This thesis is made up of six chapters. In Chapter 1, I made a brief introduction of the thesis, which mainly included the research background, research aim and research content. In the last part, Chapter 6, I summarized the theoretical and practical innovations in this study. Based on that, I eventually proposed how to conduct future researches. Chapter 2 to Chapter 5 are the main research content and the specific as follows.

Chapter 2: RS-based models play a significant role in estimating and monitoring terrestrial ecosystem GPP. Several RS-based GPP models have been developed using different criteria, yet the sensitivities to environmental factors vary among models; thus, the comparison of model sensitivity is necessary for analyzing and interpreting results and for choosing suitable models. In this part, we evaluated and compared the GPP estimated by 12 RS-based GPP models and benchmarked these estimates against the GPP measured at flux tower sites which longer than 12 years as well as the results estimated by dynamic global vegetation models (DGVM). The comparison among models and the comparison of models against observations helps document their strengths and weaknesses under current conditions and can also identify heuristic constraints about their applicable conditions and scopes. There is no model showing an isolated estimation in the spatial distribution, seasonal variation and interannual variation of GPP. Vegetation indices (VI) and light use efficiency (LUE) models, relatively simpler form and fewer parameters, can perform as well as complex physiological process models on GPP estimating. All the models show the similar distribution the largest annual GPP occur in the tropics where the model estimates more than 3300 gC m^{-2} $year^{-1}$, with a lower amplitude responding the alternation of wetter and drier seasons. But the maximum monthly GPP in tropical forest is exceeded by forest in the temperature zone in June with closing to 400 gC m^{-2} $month^{-1}$. The monthly global GPP estimates are low during the northern hemisphere's winter and high during its summer. Regarding on the trend of GPP, the models with inputting atmospheric CO_2 concentration data show more significantly.

Chapter 3: Quantitative estimation of the spatial pattern of the GPP trends and its drivers is one of the key issues in global change research. In Chapter 3, I applied the Carbon Fixation (CFix) model to estimate the net effect of each factor on GPP trends from 1982-2015, used an unsupervised classifier to group similar GPP trend behaviors, and analyzed the responses of GPP to changes in climatic, atmospheric and environmental drivers. According to the characteristics of the monthly GPP trends and the patterns of growing season, I presented nine categories that could belong to two groups (increasing in amplitude and extending the length of the growing season), as aids in interpreting large-scale behavior. Land-cover change (LCC), rising CO_2 concentration, temperature and water conditions changes have the overall effect of increasing GPP (positive) of the entire world, contrary to radiation change effects. The global average contributions of LCC, CO_2 concentration, temperature, radiation and water on the GPP trend are 4.57 %, 65.73 %, 13.07 %, -7.24 % and 11.74 %, respectively. The elevated atmospheric CO_2 concentration has had the greatest impact on the global GPP trend; however, LCC and climatic factors changes have had a greater impact on GPP in terms of a specific location or regional rather than globally. The sum of the GPP trends from each factor is smaller than the trend obtained when all of the factors are varied together, indicating positive interactions among factors. The effects of climatic factors trends on GPP can be positive or negative in different regions, in general: regionally, the GPP changes at middle and high latitudes are likely to be driven by increases in temperature and radiation; at lower latitudes, the GPP changes are likely dominated by shifts in water conditions; at high altitudes, the GPP changes are probably caused by changes in temperature and water conditions.

Chapter 4: Due to the increasing atmospheric CO_2 levels quantitative estimation of the GPP and its variations at spatial scales are critical issues for quantifying the feedbacks of ecosystems to climate change. This chapter applied the improved daily Boreal Ecosystem Productivity Simulator (BEPS) model to estimate the global GPP from 2000 to 2015, compared the estimated GPP with the flux tower measurements and other GPP products to verify the estimation accuracy and analyze the CO_2 fertilization effect, and conducted spatial analysis on the effects of the spatiotemporal distribution of the CO_2 concentration on the estimation of GPP. At the same time, however, the effects of the spatiotemporal variability in the atmospheric CO_2

concentrations on GPP estimations are challenging with respect to the terrestrial ecosystem due to land cover component characteristics and difficulties associated with measuring CO_2 concentrations over large spatial areas. The development of remote sensing offers a means to routinely monitor CO_2 concentrations both spatially and temporally from space. To introduce continuous spatial CO_2 data as an indicator for the estimation of the terrestrial biosphere GPP, I designed a new algorithm to evaluate the CO_2 fertilization effect which used the decoupling coefficients to evaluate the canopy CO_2 concentrations, photosynthetic biochemical models to calculate the photosynthetic rate, and Big-leaf model to scale up to a global scale. The results of the both two models showed that the estimates could capture the magnitude, amplitude, distribution and variation in GPP well compared with the flux tower measurements and the other GPP products. Thus, the method proposed in this study utilizing continuous spatial CO_2 data to estimate the GPP is practicable and feasible. In general, the terrestrial GPP increased as the atmospheric CO_2 concentrations increased; however, the CO_2 fertilization effect varied based on time and location and was constrained by climatic conditions. The increases in the lower latitudes were more significant than those in the middle and higher latitudes, and there were seasonal variation characteristics in the middle and higher latitudes. Not considering the CO_2 fertilization effect would underestimate the global GPP and its trend; additionally, not considering the spatiotemporal distribution of the CO_2 concentration would overestimate the global annual GPP, to put it more specifically, the estimate would overestimate the GPP in the lower latitudes and underestimate those in the middle and high latitudes; Regarding the monthly GPP estimates, using the annual averages caused the GPP estimates of the Northern Hemisphere to be overestimated during the first half of the year, while those during the second half of the year were underestimated; the GPP estimates for the Southern Hemisphere were underestimated each month. However, using monthly averages caused the GPP estimates for the Northern Hemisphere to be overestimated in summer and underestimated in spring and autumn, which are opposite to the estimates for the Southern Hemisphere. These results will increase the understanding of the variations in carbon flux under future climate change, especially under the conditions of changing atmospheric CO_2 concentration.

Chapter 5: The sensitivities to environmental factors vary among the RS-based models used in Chapter 1, and the comparison of model sensitivity is necessary for analyzing and interpreting results and for choosing suitable models. In this chapter, I globally evaluated and compared the sensitivities of 12 RS-based models (2 process-, 4 VI-, 5 LUE-, and 1 machine-learning (ML)-based model) and benchmarked them against GPP responses to climatic factors measured at flux sites and to elevated CO_2 concentrations measured at FACE experiment sites. The results demonstrated that the models with relatively high sensitivity to increasing atmospheric CO_2 concentrations showed a higher increasing GPP trend. The fundamental difference in the CO_2 effect in the models' algorithm either considers the effect of CO_2 through changes in greenness indices (nine models) or introduces the influences on photosynthesis (three models). The overall effects of temperature and radiation, in terms of both magnitude and sign, vary among the models, while the models respond relatively consistently to variations in precipitation. Spatially, the larger differences among model sensitivity to climatic factors occur in the tropics; at high latitudes, models have a consistent and obvious positive response to variations in temperature and radiation, and precipitation significantly enhances the GPP in mid-latitudes. Compared with the results calculated by flux-site measurements, the model performance differed substantially among different sites. However, the sensitivities of most models are basically within the confidence interval of the flux-site results. In general, the comparison revealed that models differed substantially in the effect of environmental regulations, particularly CO_2 fertilization and water stress, on GPP, and none of the models

showed performed consistently better across the different ecosystems and under the various external conditions.

This thesis evaluated the spatiotemporal pattern of variation and distribution of global terrestrial GPP and compared the estimates from different prevalent RS-based models. Moreover, I explored effective methods to introduce the spatial continuous atmospheric CO_2 concentration data into global terrestrial GPP estimations. In addition, I designed a new algorithm and combined with the models which consider the CO_2 fertilization effect to comprehensively analyze the effect of environmental factors change on global terrestrial ecosystems. All these will help us to understand the mechanism of terrestrial ecosystem GPP changing, which is very important for us to take certain measures or make relative policies to improve our living environment.

Chapter 1 General introduction

1.1 Introduction

The main objectives of this research are to investigate the spatiotemporal pattern of variation and distribution of global terrestrial GPP using RS algorithms, to introduce the satellite spatial continuous atmospheric CO_2 concentration data into GPP estimation, to analyze the contributions of environmental factors, especially the CO_2 fertilization effect, and to attempt to explain the possible factors influence GPP under different considering in each model. The chapter introduces the thesis structure: (a) the research background; (b) the datasets and models applied in this thesis and (c) the outline of the chapters.

1.2 Background

1.2.1 Terrestrial ecosystem GPP and its importance

Terrestrial GPP, which is defined as the amount of carbon uptake by vegetation through photosynthesis at the ecosystem scale (Beer et al., 2010), is the first step of atmospheric CO_2 entering the biosphere (Hilker et al., 2008; Beer et al., 2010; Zhang et al., 2017). As reported, the increase in atmospheric CO_2 on Earth is the major cause of global climate change (Stocke et al., 2013; IPCC, 2013), and over the past century, the CO_2 accumulation rate has continuously increased with the amount of CO_2 released due to landcover changes and fossil fuel combustion (Le Quéré et al., 2016). Through GPP, which constitutes the largest global land carbon flux (Zhao and Running, 2010; Beer et al., 2010) and plays a pivotal role in almost all ecosystem processes, terrestrial ecosystems can partially mitigate global warming and offset the increasing concentration of atmospheric CO_2 (Ballantyne et al., 2012). In recent decades, approximately 1.2 PgC $year^{-1}$ has been sequestered by terrestrial ecosystems as the net result of the impact of the changing climate and rising CO_2 on ecosystem productivity (CO_2-climate driven flux) and deforestation, harvesting and secondary forest regrowth (LCC flux) (Haverd et al., 2017). It is a key area in climate change research (Hilker et al., 2008; Beer et al., 2010). And, therefore, the accurate estimation of the GPP of terrestrial vegetation is critical for understanding ecosystem carbon cycling and its feedbacks to global change (Liu et al., 2016; Zhang et al., 2017). GPP is the starting point of the terrestrial carbon biogeochemical cycle (Raupach et al., 2008) and, thus, serves as the gateway for the energy and carbon that are required for almost all ecosystem processes (Gilmanov et al., 2003). The patterns of the variation and distribution of GPP in terrestrial ecosystems show large spatial variability due to interactions between the biological characteristics of plants and external environmental factors (e.g., rising CO_2 concentration, land-cover change, and climatic variables) (Beer et al., 2010; Anav et al., 2015). There is, thus, a need to better understand the mechanisms that control the terrestrial GPP to provide an accurate GPP estimations and the dynamic changes in the carbon fluxes between the biosphere and atmosphere to help quantify the potential changes resulting from global climate change (Poulter et al., 2014; Li et al., 2016). However, their contributions are highly uncertain. Furthermore, a deeper understanding of how GPP has responded to past climate change, LCC and rising CO_2 concentration will provide insight into how the carbon cycle will change under future CO_2 and climate conditions (Poulter et al., 2014; Huang et al., 2015; Li et al., 2016).

1.2.2 GPP estimation and RS-based GPP models

However, directly measuring GPP at the global scale is impossible (Ma et al., 2015); to accurately quantify the spatiotemporal patterns of GPP, considerable efforts have been made to develop terrestrial ecosystem models (Dury et al., 2011; Tian et al., 2015; Best et al., 2011;

Bondeau et al., 2007; Traore et al., 2014; Zeng et al., 2005; Ito et al., 2002) as tools to understand terrestrial carbon mechanisms and fluxes at the global scale and to hindcast historical situations and predict future changes (Cramer et al., 1999; Piao et al., 2009; Keenan et al., 2016) and predict future changes (Friedlingstein et al., 2006; Smith et al., 2016). In addition, inverse models that use atmospheric transport models and atmospheric CO_2 concentrations or isotopes (Bousquet et al., 1999; Reichstein et al., 2003; Welp et al., 2011) were also widely used to investigate the biosphere carbon flux. The discrepancies associated with the spatial distribution of environmental controls on GPP variation simulated by different models are considerable (Anav et al., 2015; Beer et al., 2010). Estimation models vary widely in terms of academic foundations and original purposes but can be grouped into the following three major categories (Cramer et al., 1999): prescribed vegetation structure-based models, physiological and ecological process models, and satellite-based models. For the past ten years, RS-based models have been widely used (Liu et al., 1997; Zhang et al., 2018; Ryu et al., 2011; Jiang et al., 2016; Verstraeten et al., 2006; Sun et al., 2018b; Potter et al., 1993; Yuan et al., 2007; Xiao et al., 2004; Running and Zhao 2015; Gitelson et al., 2006; Sims et al., 2008; Wu et al., 2010; Liu et al., 2014; Jung et al., 2011) with the development of space technology because compared with process-oriented ecosystem models that entail a complex combination of model parameterizations (Piao et al., 2013; Peng et al., 2015; Bonan and Doney 2018), RS-based approaches are relatively simpler and more efficient for exploring dynamic changes in GPP and their spatiotemporal variations at the macroscale (Pasetto et al.,2018; Song et al.,2013;Yuan et al., 2007 2014; Sun et al., 2018b). It is also easier to overcome the shortcomings of some process-oriented models, including the nutrient limiting effects on vegetation growth (Ollinger and Smith 2005; Song et al., 2013; Reich et al., 2006 2014), the influences from agricultural management (Lobell et al., 2003) and extreme emergency events (Lentile et al., 2006; Sun et al., 2018b), and the uncertainties involved in modeling the phenology of vegetation (Rawlins et al., 2015; Song et al, 2013; Xiao et al., 2004; Piao et al., 2007). Additionally, RS is a kind of comprehensive and representative way to obtain information (Liang et al., 2018). The prevalent algorithms requiring that RS data be inputted to estimate GPP could be categorized into the following groups (Song et al., 2013): (a) VI-based: empirical estimation from spectral vegetation indices (Li et al., 2013; Liu et al., 2014; Gitelson et al., 2006; Sims et al., 2008; Wu et al., 2010); (b) LUE-based: models that are based on LUE theory (Potter et al., 1993; Verstraeten et al., 1994 2006; Yuan et al., 2007; Running and Zhao 2015; Xiao et al., 2004); (c) process-based: models that are based on biophysical processes of plant photosynthesis (Ryu et al., 2011; Jiang et al., 2016; Liu et al., 1997; Zhang et al., 2018); and (d) ML-based: machine learning models that require RS data to train the model (Jung et al., 2011; Liu et al., 2016; Wei et al., 2017).

1.2.3 Main factors influencing terrestrial GPP and CO_2 fertilization effect

The increases in atmospheric CO_2 concentration that have occurred since the industrial revolution are expected to cause a CO_2 fertilization effect (Canadell et al., 2007), where photosynthesis is enhanced by the increase in CO_2 (Farquhar 1997). Additionally, many scholars (van Oijen et al., 2004; McMurtrie et al., 2008; Yang et al., 2016) have determined that the increasing atmospheric CO_2 concentration affects GPP, and numerous studies (Sun et al., 2018a; Norby et al., 2005; Ainsworth and Long 2005) have been conducted to improve our understanding on how plants and ecosystems respond to the elevated CO_2 levels. The large-scale FACE experiment showed that forest ecosystems were more responsive than were other functional types; specifically, C4 species showed little response to elevated CO_2 concentrations (Ainsworth and Long 2005). The response of plants to elevated CO_2 would be greater in dry, high-nitrogen conditions (McMurtrie et al., 2008); additionally, the CO_2 fertilization caused by the enhanced foliage cover across the global warm and arid environments is significant

(Donohue et al., 2013), resulting in increased photosynthesis area and improved GPP to a certain degree. At the same time, the climatic factors and their interactions (Chang et al., 2016) with the soil resources (Reich et al., 2014) and nitrogen level (Luo et al., 2004 2006; Donohue et al., 2013) would also constrain CO_2 fertilization to enhance GPP (Anav et al., 2015). Models that do not consider the CO_2 fertilization module may serve as a source of uncertainty in the estimation of GPP (Anav et al., 2015). In tropical ecosystems, CO_2 fertilization could explain as much as 100 % of the biospheric carbon sink (Ciais et al., 2004), with large uncertainties (bias: ± 68.42 %) (Howard 2005). Additionally, CO_2 fertilization could explain 50% of the Siberian and 10 % of the European sinks (Canadell et al., 2007). Therefore, including the atmospheric CO_2 concentration in the global GPP estimation should be a research priority (Liu et al., 2016).

However, few studies have incorporated the global-scale atmospheric CO_2 concentration into GPP estimates, or the studies have assumed that the CO_2 concentrations and variations are spatially and temporally uniform around the globe. Theoretically, CO_2, which is chemically inert, is generally well mixed globally (Eby et al., 2009), but it actually presents large temporal and spatial characteristics (Miles et al., 2012; Sun et al., 2016). According to the most recent global maps (Dec. 2016) of near surface air CO_2 concentrations from the Japan Meteorological Agency (JMA), the differences in the spatial distribution of atmospheric CO_2 concentrations could be greater than 40 ppm; furthermore, the concentrations are highest in South China (> 436 ppm) and lowest in Uruguay (< 396 ppm) (http:// ds.data.jma.go.jp /ghg /kanshi /CO_2map/ CO_2pmapp lot_alt_e.html), and these values mirror the increase in atmospheric CO_2 concentrations over the past 20 years (i.e., from 365.55 ppm in 1998 to 404.98 ppm in 2017). The spatial variation in the atmospheric CO_2 concentrations for the entire year of 2016 could reach approximately 50 ppm (lowest: 388 ppm in Canada during July), which is equivalent to the change in the global average mean annual CO_2 concentration from 1990 (353.96 ppm) to the present. In addition, the seasonal characteristics of the atmospheric CO_2 concentration have previously been reported at the local and regional scales (Davis et al., 2003; Miles et al., 2012; Liu et al., 2016). For example, the measurement of the atmospheric boundary layer of the CO_2 concentration from the North American Carbon Program's Mid Continent Intensive (MCI) from 2007 to 2009 showed that the seasonal CO_2 amplitude was five times larger than was the tropospheric background (Miles et al., 2012; Liu et al., 2016). The spatiotemporal characteristics of the atmospheric CO_2 concentrations affect the GPP, both intra- and inter-annually. Models that do not consider CO_2 fertilization modules might be a source of uncertainty (Anav et al., 2015) in estimating GPP. In a sensitivity analysis in which CO_2 was elevated by 200 ppm, there was a 5 % to 25 % increase in the modeled annual GPP (Wang et al., 2014), and, when the current atmospheric CO_2 concentrations were doubled, most types of ecosystems showed a 10 ~ 25 % ± 2 % increase in the net primary production (Norby et al., 2005; Luo et al., 2006). With increases in the atmospheric CO_2 concentration, seasonal CO_2 variations, resulting from photosynthesis and respiration, have substantially increased in amplitude over the last 50 years, particularly in high latitude regions north of 45°N, where the amplitude increased by approximately 50 % (Monroe 2013). The spatiotemporal characteristics of atmospheric CO_2 concentrations affect the GPP, both intra- and inter- annually; therefore, the spatial distribution of CO_2 concentrations should be considered factor that affect the GPP.

Almost no studies, however, have yet identified and compared the global discrepancy among model sensitivity to external enviro-climatic variability, and even fewer studies have analyzed the effect of CO_2 fertilization that is implied in RS models (De Kauwe et al., 2016; Smith et al., 2016; Sun et al., 2018ab; Liu et al., 2016; Verstraeten et al., 1994; Ryu et al., 2011, Jiang et al., 2016; Liu et al., 1997, Zhang et al., 2018), which is likely attributed to the fact that the effect from CO_2 in models is more concealed than are the influences from enviro-climatic

factors (Sun et al., 2018a; Ahlstrom et al., 2015). VI-based models assume that CO_2 affects GPP solely through changes in the greenness index (Wylie et al., 2003; Piao et al., 2007; Thomas et al., 2016; Watham et al., 2017; Sun et al., 2018b); ML- and LUE-based models assume that CO_2 affects GPP solely through changes in the fAPAR (fractional absorbed photosynthetically active radiation) (De Kauwe et al., 2016). However, both of the abovementioned indicators are closely related to leaf area (Cheng et al., 2017; Donohue et al., 2013), which is used as an input in process-based models; furthermore, process-based models incorporate some greenness indices and the modules that represent the photosynthetic rate that is affected by the CO_2 concentration (Jiang et al., 2016; Zhang et al., 2018). Models are typically developed based on specific assumptions, and they consider the different processes and complexities involved in the control of vegetation production (Garbulsky et al., 2010; Rossini et al., 2012; Yuan et al., 2014; Ardo et al., 2015); therefore, to make RS-based GPP estimations more robust, it is necessary to conduct a rigorous comparison using consistent validation datasets and driving variables (Wu et al., 2010 2017; Zhang et al., 2016).

1.3 Aims and data resource

The main objective of this research is to investigate the spatiotemporal pattern of variation and distribution of global terrestrial GPP. This requires various RS-based GPP models to explore the feature of the changing terrestrial ecosystem, understand the mechanism of the changing process, and determine the uncertainty of each approach. To achieve this objective, remote sensing data combining with climatic data and ground-measured data have been used to drive models, identify external influences and environmental change, and analyze the effects of environmental factors on terrestrial GPP changing. The more specific objectives are outlined below:

i. To examine the spatiotemporal distribution of terrestrial GPP.

ii. To investigate the contributions of each external factor to the variation in GPP

iii. To analyze the CO_2 fertilization effect on terrestrial GPP

iv. To compare and evaluate the sensitivity of RS-based models to the variation in environmental conditions

In this study, mainly six kinds of datasets have been used, RS-based vegetation indices, climatic datasets, soil property and land coverage datasets, atmospheric CO_2 concentration dataset, and ground-measured data.

1.3.1 Vegetation indices data

In this thesis, except for leaf area index (LAI), all the other VIs (e.g., normalized difference vegetation index (NDVI), enhanced vegetation index (EVI), clumping index (CI) and land surface water index (LSWI)) were calculated by using Moderate Resolution Imaging Spectroradiometer (MODIS) Bidirectional reflectance distribution function (BRDF)/Albedo Product MCD43. The LAI derived from GlobMap LAI v3 (8-day, 0.08°) (Liu et al., 2012) were employed in this study. In GlobMap LAI v3 dataset was generated by inputting MOD09A1 (MODIS land surface reflectance) (2001~2016) and advanced very high-resolution radiometer (AVHRR) NDVI (1981~2000) on the basis of GLOBCARBON LAI algorithm (Deng et al., 2006). In order to fusion two inputs well, the data series of AVHRR NDVI (Tucker et al., 2005) and the MODIS LAI during the overlapping period (2000~2006) were used to establish the fusion relationship pixel-by-pixel. Then, using the relationship re-estimate the AVHRR LAI values (Liu et al., 2012). In comparison of the previous version, v3 considers the clumping effect, and has been widely used for long-term global vegetation condition monitoring and detection (Piao et al., 2006; Beck et al., 2011; Wu et al., 2015; Liang et al., 2015). In this thesis, I considered the daily LAI values to be the same as the 8-day LAI, in which the day belonged to the period of products and resampled it to 0.5° × 0.5° spatial resolution by linear method. It should be noted that in Chapter 3 and Chapter 4, when the study period is longer than the available period of MODIS products, we also used the NDVI product from the above dataset. The BRDF, albedo and nadir surface reflectance of each pixel of the global land surface is inverted by the continuous land observations, which is multi-date, multi-angular, cloud-free, atmospherically corrected. And then according to the quality, observation coverage and the interval of interesting date in the nearest revisit cycle, the daily product weights are determined. Additionally, the necessary parameters used to drive the RossThick-LiSparse kernel functions (i.e., isotropic, volume and surface scattering) are estimated utilizing a kernel-driven semi-empirical BRDF model (Wanner et al., 1995 1997; Lucht et al., 2000; Schaaf et al., 2002 2011).

The calculation of clumping index requires characterization of the directional anisotropy of Earth surface reflectance. The calculation of clumping index requires characterization of the directional anisotropy of land surface reflectance which is also provided the products of the white-sky and black-sky (at local solar noon) albedo computations for user convenience. A complete set of quality control flags accompanies each product and should be utilized by the user.

1.3.2 Climate data

For the global estimation of GPP, I used the input datasets of climate from the Modern-Era Retrospective analysis for Research and Applications, Version 2 (MERRA-2) (Rienecker et al., 2011), which provides data beginning in 1980 at a resolution of 0.5° latitude × 0.625° longitude. MERRA-2 is the first long-term global reanalysis to assimilate space-based observations of aerosols and represent their interactions with other physical processes in the climate system. In comparison of MERRA-1, there are some advances made in the assimilation system which allow modern hyperspectral radiance and microwave observations to be assimilated. More information on the MERRA dataset is available from National Aeronautics and Space Administration (NASA) Goddard Earth Sciences (GES) Data and Information Services Center (DISC)/ Modeling/ Data Holding (http:// disc.gsfc.nasa.gov/daac-bin/DataHoldings.pl). The uncertainties of various meteorological factors at the global scale have been validated and evaluated by using surface metrological datasets (Rienecker et al., 2011; Li et al., 2013). The daily climate data including air temperature (Ta), specific humidity (SH), dew point temperature (TD) and wind speed (WS) were at 2 meters height, while air pressure (PS), land surface temperature (LST) and precipitation (Pre) were at surface level. We calculated the relative humidity (RH) and vapor pressure deficit (VPD) using SH, Ta and TD according to Henderson and Gornitz (1984) daily. In addition, PAR (Photosynthetically active radiation), Latent heat flux (LH or λH) and sensible heat flux(H) were also daily data. For BESS, the inputted radiation data should to be the corresponding data at the local time when the satellites overpassed, therefore, I applied the hourly PAR_{Diff} (downwelling PAR diffuse flux), PAR_{Dir} (downwelling PAR beam flux), NIR_{Diff} (downwelling NIR diffuse flux) and NIR_{Dir} (downwelling NIR beam flux) and then linearly interpolated them to get the corresponding data which during satellites overpass. All data were linearly interpolated and resampled to a spatial resolution of 0.5° × 0.5°. In order to compare the effects of inputting data on GPP estimation, we also used some other climatic datasets, we introduced these datasets in the corresponding chapter detailly.

1.3.3 Soil moisture and property data

There are two models (Boreal Ecosystem Productivity Simulator (BEPS) and CFix) who have a module calculating the water limitations on the photosynthetic rate by considering the stomatal regulating factor from the soil moisture deficits were used in this thesis. Therefore, in order to drive the two models, the soil water content and soil moisture characteristics are indispensable. In the present, we obtained the soil moisture characteristics, including wilting point (WP) and field water holding capacity (FC), from the Global Gridded Surfaces of Selected Soil Characteristics (IGBP-DIS) dataset (Global Soil Data Task, 2014). It is a global product generated at a resolution of 5×5 arc-minutes by the Soil Data System (SDS) which generates soil information and maps for geographic regions at user-selected soil depths and resolutions. Regarding soil moisture (SM), National Oceanic and Atmospheric Administration/Earth System Research Laboratory (NOAA/ESRL) Physical Sciences Division (PSD) run multiple land surface models to get a model-calculated Climate Prediction Center (CPC) soil moisture (SM) dataset v2 (van den Dool et al., 2003), since globally measuring the SM is impossible,

this dataset is to be the most suitable datasets because it provides global monthly data from 1948 to 2017 and consisted of a file containing the averaged SM water height equivalents at a spatial resolution of 0.5°×0.5°. The two datasets represent the SM and characteristics in different depth of soil, thus, we used the field capacity maps derived from IGBP-DIS and converted the data to the values at a soil depth of 1.6 m, which is the same as that used for the CPC-SM. We conducted the model at the daily step, therefore, the inputs of SM for each day during the study period ,2000 - 2014, were replaced by the monthly soil condition of which the day is located in. Finally, the data were resampled to the 0.5° × 0.5° spatial resolution by linear method.

1.3.4 Atmospheric CO_2 concentration data

Three datasets of the atmospheric CO_2 concentration were used to normalize the CO_2 fertilization factor in the thesis; one is the global monthly continuous spatial CO_2 concentration data from 2000 to 2015, Carbon Tracker (CT) 2016, which is an open product of NOAA's Earth System Research Laboratory that uses data from the NOAA ESRL greenhouse gas observational network and collaborating institutions (Peters et al., 2007), released on Feb 17th, 2017. In CT2016, land biosphere, wildfire, fossil fuel emissions, atmospheric transport and other factors are data-assimilated to produce the estimates of surface fluxes and atmospheric CO_2 mole fractions (https:// www. esrl. noaa. gov /gmd/ ccgg/ carbontracker/ index.php). The other is globally averaged surface monthly mean CO_2 data from 1982 to 1999 obtained from NOAA/ ESRL (www. esrl. noaa. gov /gmd/ ccgg/ trends/). A global average is constructed by first fitting a smoothed curve as a function of time to each site, after which the smoothed value for each site is plotted as a function of the latitude for 48 equal time steps per year. A global average is calculated from the latitude plot at each time step (Masarie 1995). In addition, in order to introduce the satellite spatial continuous atmospheric CO_2 concentration data into GPP estimation, I also used the global monthly continuous spatial CO_2 concentration data in 2014, which were captured by (Greenhouse gases observing satellite) GOSAT (http://www.gosat.nies.go.jp/en/), the world's first spacecraft to measure the concentrations of CO_2 from space. The production is GOSAT Fourier Transform Spectrometer (FTS) L2 CO_2 column amount SWIR (Short Wavelength InfraRed), which was used to calculate the atmospheric CO_2 concentration, and the FTS SWIR L2 CO_2 column abundance products (denoted XCO_2, in ppm), which contain column-averaged mixed volume ratios of CO_2 (Guo et al., 2012). The relative accuracy of the Level 2 data is 0.3 % ~ 1.0 % (1 ~ 4 ppm) for CO_2 (Butz et al., 2011), and the data form is a point set with a circle footprint with a diameter of approximately 10.5 km at nadir; nevertheless, the number of data points significantly surpasses that currently obtained from ground monitoring stations, which is below 200. The spatial continuous CO_2 concentration data were resampled to the 0.5° × 0.5° spatial resolution by linear method.

1.3.5 Land cover change datasets

The land cover map from 1982 to 1991 was acquired from the Global Land Cover Facility (GLCF): AVHRR Global Land Cover Classification (http:// glcf. umd. edu/ data/ landcover/). The images from the AVHRR satellites between 1981 and 1994 were utilized and analyzed to distinguish 14 land cover classes (Hansen et al., 1998). Three spatial scales are available in this product (1, 8 km and 1°), and we selected the highest resolution of 1 km. The other is the European Space Agency (ESA) Climate Change Initiative (CCI) Land Cover (LC) dataset (https://www.esa-landcover-cci.org/), a 300 m annual global land cover time series from 1992 to 2015. These 24 annual global land cover maps were produced by state-of-the-art reprocessing of the full archives of five different satellite missions that provided daily observations of the

Earth. CCI-LC provides information for 22 classes of dominant land cover types defined using the Land Cover Classification System (LCCS), which was found to be compatible with the Plant Functional Types (PFTs) used in the climate models (CCI-LC URD Phase I). Detailed information on the CCI-LC is available on the CCI-Viewer (http:// maps. elie. ucl. ac. be/CCI/viewer/). For the non-long-term series research, in order to keep the consistency, we used the landcover classification was obtained from the MODIS Land Cover Type product (MCD12C1), which provides information on 17 classes of dominant land cover types defined by the IGBP (Friedl et al., 2010). MCD12C1 is a product that aggregates a higher spatial resolution (500 m) of land coverage by selecting the dominant land cover types within the lower spatial resolution grids (Duveiller and Cescatti 2016). C3 and C4 species have different responses to light, temperature, CO_2, and nitrogen; additionally, they differ in physiological functions, such as stomatal conductance and isotope fractionation. Therefore, in this thesis, I overlaid the C4 vegetation percentage map with the landcover dataset to obtain the landcover component map.The C4 vegetation percentage map I obtained, which was determined from datasets that described the continuous distribution of plant growth forms, climate classifications, fraction of a grid cell covered in cropland, and national crop type harvest area statistics (Still et al., 2009), was one of the products from the International Satellite Land Surface Climatology Project (ISLSCP) Initiative II and had a spatial resolution of 1° × 1°.The land cover data need to be crossed with the grids analyzed in this study at a 0.5° spatial resolution; all 300 m and 1 km pixels falling in the 0.5° cells were used to calculate the proportion of the dominant land cover type.

1.3.6 *In situ* measurements

Not only GPP data but also the local meteorological data used in this study were obtained from the FluxNet 2015 dataset (http://www.fluxdata.org), which is a valuable source of GPP estimates based on EC measurements performed across the global network of flux towers. Briefly, at each tower site, the EC method is applied to quantify the fluxes of scalars and energy between the biosphere and atmosphere. The regional network and FluxData teams standardize the data format, perform uniform data quality checks, and produce value-added products using highly vetted gap-filling and flux partitioning. These data are assessed for quality and are gap-filled. In addition, value-added products, such as the GPP, are produced, and daily, monthly and annual sums, or averages, are computed (Agarwal et al., 2010). The current dataset includes over 1,500 site-years of data from 212 sites, covering variable time periods spanning from 1991 to 2016, depending on the site. In this study, we only used the sites in the period from 2000 to 2014. These flux sites cover most of the major biomes (DNF (deciduous needleleaf forest), ENF (evergreen needleleaf forest), CRO (croplands), DBF (deciduous broadleaf forest), EBF (evergreen broadleaf forest), GRA (grasslands), MF (mixed forest), OSH (open shrublands), CSH (closed shrublands), WET (wetlands), SAV (savannas), and WSA (woody savanna)), representing a total of 1,095 observed years from 160 tower sites.

1.4 Thesis contents

This thesis consists of six chapters, covering four main topics: an introduction of the thesis (Chapter 1), estimation on GPP of global terrestrial ecosystem (Chapter 2), the effect of external factors on terrestrial GPP (Chapter 3), the CO_2 fertilization effect on terrestrial GPP (Chapter 4), sensitivity of RS-based GPP models to environmental variation (Chapter 5), and final conclusions (Chapter 6). The schematic framework for this research is shown in Figure 1.1.

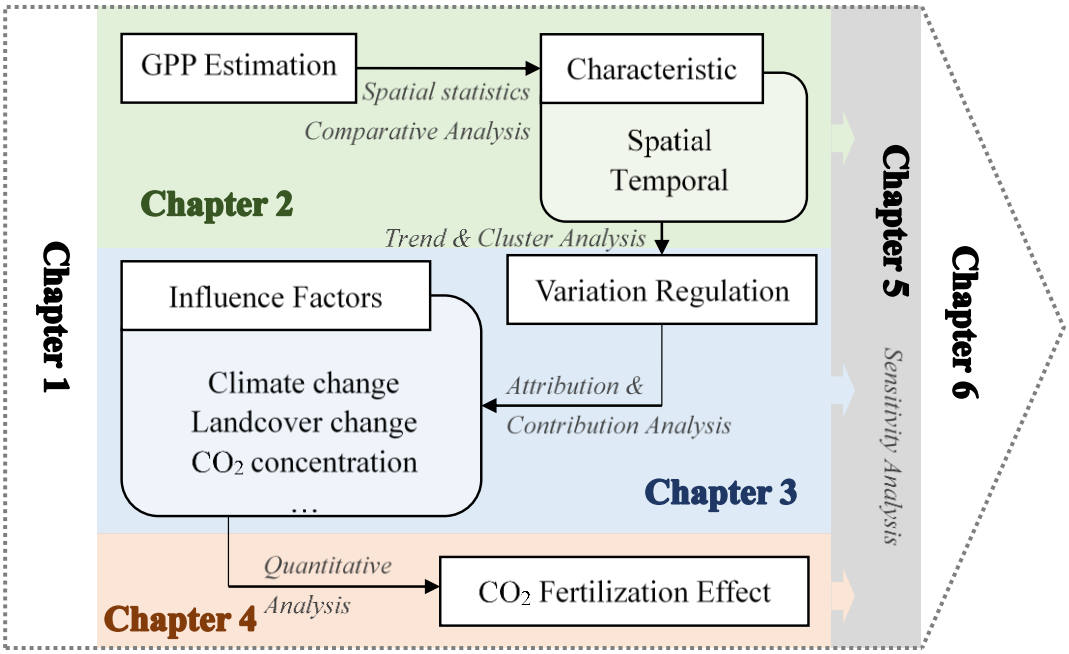

Figure 1.1 A schematic flow of the research organization.

References

Agarwal, D.A.; Humphrey, M.; Beekwilder, N.F.; Jackson, K.R.; Goode, M.M.; van Ingen, C. A data-centered collaboration portal to support global carbon-flux analysis. *Concurr Comp-Pract E* **2010**, *22*, 2323-2334.

Ahlstrom, A.; Raupach, M.R.; Schurgers, G.; Smith, B.; Arneth, A.; Jung, M.; Reichstein, M.; Canadell, J.G.; Friedlingstein, P.; Jain, A.K., et al. The dominant role of semi-arid ecosystems in the trend and variability of the land CO2 sink. *Science* **2015**, *348*, 895-899.

Ainsworth, E.A.; Long, S.P. What have we learned from 15 years of free-air CO2 enrichment (FACE)? A meta-analytic review of the responses of photosynthesis, canopy properties and plant production to rising CO2. *New Phytol* **2005**, *165*, 351-371.

Anav, A.; Friedlingstein, P.; Beer, C.; Ciais, P.; Harper, A.; Jones, C.; Murray-Tortarolo, G.; Papale, D.; Parazoo, N.C.; Peylin, P., et al. Spatiotemporal patterns of terrestrial gross primary production: A review. *Reviews of Geophysics* **2015**, *53*, 785-818.

Ardo, J. Comparison between remote sensing and a dynamic vegetation model for estimating terrestrial primary production of Africa. *Carbon Balance Manag* **2015**, *10*, 8.

Ballantyne, A.P.; Alden, C.B.; Miller, J.B.; Tans, P.P.; White, J.W. Increase in observed net carbon dioxide uptake by land and oceans during the past 50 years. *Nature* **2012**, *488*, 70-72.

Beck, H.E.; McVicar, T.R.; van Dijk, A.I.; Schellekens, J.; de Jeu, R.A.; Bruijnzeel, L.A. Global evaluation of four AVHRR–NDVI data sets: Intercomparison and assessment against Landsat imagery. *Remote Sensing of Environment* **2011**, *115*, 2547-2563.

Beer, C.; Reichstein, M.; Tomelleri, E.; Ciais, P.; Jung, M.; Carvalhais, N.; Rodenbeck, C.; Arain, M.A.; Baldocchi, D.; Bonan, G.B., et al. Terrestrial gross carbon dioxide uptake: global distribution and covariation with climate. *Science* **2010**, *329*, 834-838.

Best, M.J.; Pryor, M.; Clark, D.B.; Rooney, G.G.; Essery, R.L.H.; Menard, C.B.; Edwards, J.M.; Hendry, M.A.; Porson, A.; Gedney, N., et al. The Joint UK Land Environment Simulator (JULES), model description - Part 1: Energy and water fluxes. *Geoscientific Model Development* **2011**, *4*, 677-699.

Bonan, G.B.; Doney, S.C. Climate, ecosystems, and planetary futures: The challenge to predict life in Earth system models. *Science* **2018**, *359*, eaam8328.

Bondeau, A.; Smith, P.C.; Zaehle, S.; Schaphoff, S.; Lucht, W.; Cramer, W.; Gerten, D.; Lotze-Campen, H.; Muller, C.; Reichstein, M., et al. Modelling the role of agriculture for the 20th century global terrestrial carbon balance. *Global Change Biology* **2007**, *13*, 679-706.

Bousquet, P.; Peylin, P.; Ciais, P.; Ramonet, M.; Monfray, P. Inverse modeling of annual atmospheric CO2 sources and sinks: 2. Sensitivity study. *Journal of Geophysical Research: Atmospheres* **1999**, *104*, 26179-26193.

Butz, A.; Guerlet, S.; Hasekamp, O.; Schepers, D.; Galli, A.; Aben, I.; Frankenberg, C.; Hartmann, J.M.; Tran, H.; Kuze, A., et al. Toward accurate CO2 and CH4 observations from GOSAT. *Geophysical Research Letters* **2011**, *38*.

Canadell, J.G.; Kirschbaum, M.U.; Kurz, W.A.; Sanz, M.-J.; Schlamadinger, B.; Yamagata, Y. Factoring out natural and indirect human effects on terrestrial carbon sources and sinks. *environmental science & policy* **2007**, *10*, 370-384.

Chang, J.; Ciais, P.; Viovy, N.; Vuichard, N.; Herrero, M.; Havlík, P.; Wang, X.; Sultan, B.; Soussana, J.F. Effect of climate change, CO2 trends, nitrogen addition, and land-cover and management intensity changes on the carbon balance of European grasslands. *Global change biology* **2016**, *22*, 338-350.

Cheng, L.; Zhang, L.; Wang, Y.-P.; Canadell, J.G.; Chiew, F.H.; Beringer, J.; Li, L.; Miralles, D.G.; Piao, S.; Zhang, Y. Recent increases in terrestrial carbon uptake at little cost to the water cycle. *Nature communications* **2017**, *8*, 110.

Ciais, P.; Janssens, I.; Shvidenko, A.; Wirth, C.; Malhi, Y.; Grace, J.; Schulze, E.-D.; Herman, M.; Phillips, O.; Dolman, H. The potential for rising CO2 to account for the observed uptake of carbon by tropical, temperate, and boreal forest biomes. *The Carbon Balance of Forest Biomes* **2004**, 109-149.

Cramer, W.; Kicklighter, D.W.; Bondeau, A.; Moore, B.; Churkina, G.; Nemry, B.; Ruimy, A.; Schloss, A.L.; Intercompariso, P.P.N.M. Comparing global models of terrestrial net primary productivity (NPP): overview and key results. *Global Change Biology* **1999**, *5*, 1-15.

Davis, K.J.; Bakwin, P.S.; Yi, C.; Berger, B.W.; Zhao, C.; Teclaw, R.M.; Isebrands, J. The annual cycles of CO2 and H2O exchange over a northern mixed forest as observed from a very tall tower. *Global Change Biology* **2003**, *9*, 1278-1293.

De Kauwe, M.G.; Keenan, T.F.; Medlyn, B.E.; Prentice, I.C.; Terrer, C. Satellite based estimates underestimate the effect of CO 2 fertilization on net primary productivity. *Nature Climate Change* **2016**, *6*, 892.

Deng, F.; Chen, J.M.; Plummer, S.; Chen, M.; Pisek, J. Algorithm for global leaf area index retrieval using satellite imagery. *IEEE Transactions on Geoscience and Remote Sensing* **2006**, *44*, 2219-2229.

Donohue, R.J.; Roderick, M.L.; McVicar, T.R.; Farquhar, G.D. Impact of CO2 fertilization on maximum foliage cover across the globe's warm, arid environments. *Geophysical Research Letters* **2013**, *40*, 3031-3035.

Dury, M.; Hambuckers, A.; Warnant, P.; Henrot, A.; Favre, E.; Ouberdous, M.; François, L. Responses of European forest ecosystems to 21 (st) century climate: assessing changes in interannual variability and fire intensity. *iForest: Biogeosciences and Forestry* **2011**, *4*, 82-99.

Duveiller, G.; Cescatti, A. Spatially downscaling sun-induced chlorophyll fluorescence leads to an improved temporal correlation with gross primary productivity. *Remote Sensing of Environment* **2016**, *182*, 72-89.

Eby, M.; Zickfeld, K.; Montenegro, A.; Archer, D.; Meissner, K.; Weaver, A. Lifetime of anthropogenic climate change: millennial time scales of potential CO2 and surface temperature perturbations. *Journal of Climate* **2009**, *22*, 2501-2511.

Farquhar, G.D. Carbon dioxide and vegetation. *Science* **1997**, *278*, 1411-1411.

Friedl, M.A.; Sulla-Menashe, D.; Tan, B.; Schneider, A.; Ramankutty, N.; Sibley, A.; Huang, X. MODIS Collection 5 global land cover: Algorithm refinements and characterization of new datasets. *Remote sensing of Environment* **2010**, *114*, 168-182.

Friedlingstein, P.; Cox, P.; Betts, R.; Bopp, L.; von Bloh, W.; Brovkin, V.; Cadule, P.; Doney, S.; Eby, M.; Fung, I. Climate–carbon cycle feedback analysis: results from the C4MIP model intercomparison. *Journal of climate* **2006**, *19*, 3337-3353.

Garbulsky, M.F.; Peñuelas, J.; Papale, D.; Ardö, J.; Goulden, M.L.; Kiely, G.; Richardson, A.D.; Rotenberg, E.; Veenendaal, E.M.; Filella, I. Patterns and controls of the variability of radiation use efficiency and primary productivity across terrestrial ecosystems. *Global Ecology and Biogeography* **2010**, *19*, 253-267.

Gilmanov, T.G.; Verma, S.B.; Sims, P.L.; Meyers, T.P.; Bradford, J.A.; Burba, G.G.; Suyker, A.E. Gross primary production and light response parameters of four Southern Plains ecosystems estimated using long-term CO2-flux tower measurements. *Global Biogeochemical Cycles* **2003**, *17*, n/a-n/a.

Gitelson, A.A.; Vina, A.; Verma, S.B.; Rundquist, D.C.; Arkebauer, T.J.; Keydan, G.; Leavitt, B.; Ciganda, V.; Burba, G.G.; Suyker, A.E. Relationship between gross primary production and

chlorophyll content in crops: Implications for the synoptic monitoring of vegetation productivity. *J Geophys Res-Atmos* **2006**, *111*.

Guo, M.; Wang, X.; Li, J.; Yi, K.; Zhong, G.; Tani, H. Assessment of global carbon dioxide concentration using MODIS and GOSAT data. *Sensors* **2012**, *12*, 16368-16389.

Hansen, M.C.; Potapov, P.V.; Moore, R.; Hancher, M.; Turubanova, S.A.; Tyukavina, A.; Thau, D.; Stehman, S.V.; Goetz, S.J.; Loveland, T.R., et al. High-resolution global maps of 21st-century forest cover change. *Science* **2013**, *342*, 850-853.

Haverd, V.; Smith, B.; Nieradzik, L.; Briggs, P.; Canadell, J. A novel assessment of the role of land-use and land-cover change in the global carbon cycle, using a new Dynamic Global Vegetation Model version of the CABLE land surface model. In Proceedings of EGU General Assembly Conference Abstracts; p. 13881.

Henderson-Sellers, A.; Gornitz, V. Possible climatic impacts of land cover transformations, with particular emphasis on tropical deforestation. *Climatic Change* **1984**, *6*, 231-257.

Hilker, T.; Coops, N.C.; Wulder, M.A.; Black, T.A.; Guy, R.D. The use of remote sensing in light use efficiency based models of gross primary production: A review of current status and future requirements. *Science Of the Total Environment* **2008**, *404*, 411-423.

Howard Griffith, P.J. The Carbon Balance of Forest Biomes. *Taylor & Francis* **2005**, *57*, 232-233.

Huang, M.; Piao, S.; Sun, Y.; Ciais, P.; Cheng, L.; Mao, J.; Poulter, B.; Shi, X.; Zeng, Z.; Wang, Y. Change in terrestrial ecosystem water-use efficiency over the last three decades. *Glob Chang Biol* **2015**, *21*, 2366-2378.

Ito, A.; Oikawa, T. A simulation model of the carbon cycle in land ecosystems (Sim-CYCLE): a description based on dry-matter production theory and plot-scale validation. *Ecological Modelling* **2002**, *151*, 143-176.

Jiang, C.; Ryu, Y. Multi-scale evaluation of global gross primary productivity and evapotranspiration products derived from Breathing Earth System Simulator (BESS). *Remote Sensing of Environment* **2016**, *186*, 528-547.

Jung, M.; Reichstein, M.; Margolis, H.A.; Cescatti, A.; Richardson, A.D.; Arain, M.A.; Arneth, A.; Bernhofer, C.; Bonal, D.; Chen, J.Q., et al. Global patterns of land-atmosphere fluxes of carbon dioxide, latent heat, and sensible heat derived from eddy covariance, satellite, and meteorological observations. *J Geophys Res-Biogeo* **2011**, *116*.

Keenan, T.F.; Prentice, I.C.; Canadell, J.G.; Williams, C.A.; Wang, H.; Raupach, M.; Collatz, G.J. Recent pause in the growth rate of atmospheric CO 2 due to enhanced terrestrial carbon uptake. *Nature communications* **2016**, *7*, 13428.

Le Quéré, C.; Andrew, R.; Friedlingstein, P.; Sitch, S.; Pongratz, J.; Manning, A.; Korsbakken, J.; Peters, G. Global carbon budget 2016 Earth System Science Data. **2016**.

Lentile, L.B.; Holden, Z.A.; Smith, A.M.; Falkowski, M.J.; Hudak, A.T.; Morgan, P.; Lewis, S.A.; Gessler, P.E.; Benson, N.C. Remote sensing techniques to assess active fire characteristics and post-fire effects. *International Journal of Wildland Fire* **2006**, *15*, 319-345.

Li, F.; Wang, X.; Zhao, J.; Zhang, X.; Zhao, Q. A method for estimating the gross primary production of alpine meadows using MODIS and climate data in China. *International journal of remote sensing* **2013**, *34*, 8280-8300.

Li, X.; Zhu, Z.; Zeng, H.; Piao, S. Estimation of gross primary production in China (1982–2010) with multiple ecosystem models. *Ecological modelling* **2016**, *324*, 33-44.

Liang, S.; Goldberg, M.D.; Xiong, X.; Butler, J.J.; Crawford, M.M.; Chen, J.M.; Shi, J.; Loboda, T.V.; Zheng, Q.; Walsh, S.J. *Comprehensive Remote Sensing: Terrestrial Ecosystems*; Elsevier: 2018.

Liang, W.; Yang, Y.; Fan, D.; Guan, H.; Zhang, T.; Long, D.; Zhou, Y.; Bai, D. Analysis of spatial and temporal patterns of net primary production and their climate controls in China from 1982 to 2010. *Agricultural and Forest Meteorology* **2015**, *204*, 22-36.

Liu, J.; Chen, J.; Cihlar, J.; Park, W. A process-based boreal ecosystem productivity simulator using remote sensing inputs. *Remote sensing of environment* **1997**, *62*, 158-175.

Liu, S.; Zhuang, Q.; He, Y.; Noormets, A.; Chen, J.; Gu, L. Evaluating atmospheric CO 2 effects on gross primary productivity and net ecosystem exchanges of terrestrial ecosystems in the conterminous United States using the AmeriFlux data and an artificial neural network approach. *Agricultural and forest meteorology* **2016**, *220*, 38-49.

Liu, Y.; Liu, R.; Chen, J.M. Retrospective retrieval of long-term consistent global leaf area index (1981–2011) from combined AVHRR and MODIS data. *Journal of Geophysical Research: Biogeosciences* **2012**, *117*.

Liu Z, W.L., Wang S. Comparison of different GPP models in China using MODIS image and ChinaFLUX data. *Remote Sensing* **2014**, *6*, 10215.

Lucht, W.; Schaaf, C.B.; Strahler, A.H. An algorithm for the retrieval of albedo from space using semiempirical BRDF models. *IEEE Transactions on Geoscience and Remote Sensing* **2000**, *38*, 977-998.

Luo, Y.; Hui, D.; Zhang, D. Elevated CO2 stimulates net accumulations of carbon and nitrogen in land ecosystems: a meta-analysis. *Ecology* **2006**, *87*, 53-63.

Luo, Y.; Su, B.; Currie, W.S.; Dukes, J.S.; Finzi, A.C.; Hartwig, U.; Hungate, B.; McMurtrie, R.E.; Oren, R.; Parton, W.J., et al. Progressive nitrogen limitation of ecosystem responses to rising atmospheric carbon dioxide. *Bioscience* **2004**, *54*, 731-739.

Ma, J.; Yan, X.; Dong, W.; Chou, J. Gross primary production of global forest ecosystems has been overestimated. *Scientific reports* **2015**, *5*, 10820.

Masarie, K.A.; Tans, P.P. Extension and Integration of Atmospheric Carbon-Dioxide Data into a Globally Consistent Measurement Record. *J Geophys Res-Atmos* **1995**, *100*, 11593-11610.

McMurtrie, R.E.; Norby, R.J.; Medlyn, B.E.; Dewar, R.C.; Pepper, D.A.; Reich, P.B.; Barton, C.V. Why is plant-growth response to elevated CO2 amplified when water is limiting, but reduced when nitrogen is limiting? A growth-optimisation hypothesis. *Functional Plant Biology* **2008**, *35*, 521-534.

Miles, N.L.; Richardson, S.J.; Davis, K.J.; Lauvaux, T.; Andrews, A.E.; West, T.O.; Bandaru, V.; Crosson, E.R. Large amplitude spatial and temporal gradients in atmospheric boundary layer CO2mole fractions detected with a tower-based network in the US upper Midwest. *Journal of Geophysical Research: Biogeosciences* **2012**, *117*.

Monroe, R. Seasonal CO2 Amplitude is Growing as More is Added to the Atmosphere. *https://scripps.ucsd.edu/news/13139* **2013**.

Norby, R.J.; DeLucia, E.H.; Gielen, B.; Calfapietra, C.; Giardina, C.P.; King, J.S.; Ledford, J.; McCarthy, H.R.; Moore, D.J.P.; Ceulemans, R., et al. Forest response to elevated CO2 is conserved across a broad range of productivity. *Proceedings of the National Academy of Sciences of the United States of America* **2005**, *102*, 18052-18056.

Ollinger, S.V.; Smith, M.-L. Net primary production and canopy nitrogen in a temperate forest landscape: an analysis using imaging spectroscopy, modeling and field data. *Ecosystems* **2005**, *8*, 760-778.

Pasetto, D.; Arenas-Castro, S.; Bustamante, J.; Casagrandi, R.; Chrysoulakis, N.; Cord, A.F.; Dittrich, A.; Domingo-Marimon, C.; Serafy, G.; Karnieli, A., et al. Integration of satellite remote sensing data in ecosystem modelling at local scales: Practices and trends. *Methods In Ecology And Evolution* **2018**, *9*, 1810-1821.

Peng, S.; Ciais, P.; Chevallier, F.; Peylin, P.; Cadule, P.; Sitch, S.; Piao, S.; Ahlström, A.; Huntingford, C.; Levy, P., et al. Benchmarking the seasonal cycle of CO2fluxes simulated by terrestrial ecosystem models. *Global Biogeochemical Cycles* **2015**, *29*, 46-64.

Peters, W.; Jacobson, A.R.; Sweeney, C.; Andrews, A.E.; Conway, T.J.; Masarie, K.; Miller, J.B.; Bruhwiler, L.M.; Petron, G.; Hirsch, A.I., et al. An atmospheric perspective on North American carbon dioxide exchange: CarbonTracker. *Proc Natl Acad Sci U S A* **2007**, *104*, 18925-18930.

Piao, S.; Ciais, P.; Friedlingstein, P.; de Noblet-Ducoudré, N.; Cadule, P.; Viovy, N.; Wang, T. Spatiotemporal patterns of terrestrial carbon cycle during the 20th century. *Global Biogeochemical Cycles* **2009**, *23*, n/a-n/a.

Piao, S.; Fang, J.; Zhou, L.; Ciais, P.; Zhu, B. Variations in satellite-derived phenology in China's temperate vegetation. *Global Change Biology* **2006**, *12*, 672-685.

Piao, S.; Friedlingstein, P.; Ciais, P.; Viovy, N.; Demarty, J. Growing season extension and its impact on terrestrial carbon cycle in the Northern Hemisphere over the past 2 decades. *Global Biogeochemical Cycles* **2007**, *21*, n/a-n/a.

Piao, S.; Sitch, S.; Ciais, P.; Friedlingstein, P.; Peylin, P.; Wang, X.; Ahlstrom, A.; Anav, A.; Canadell, J.G.; Cong, N., et al. Evaluation of terrestrial carbon cycle models for their response to climate variability and to CO2 trends. *Glob Chang Biol* **2013**, *19*, 2117-2132.

Potter, C.S.; Randerson, J.T.; Field, C.B.; Matson, P.A.; Vitousek, P.M.; Mooney, H.A.; Klooster, S.A. Terrestrial ecosystem production: a process model based on global satellite and surface data. *Global Biogeochemical Cycles* **1993**, *7*, 811-841.

Poulter, B.; Frank, D.; Ciais, P.; Myneni, R.B.; Andela, N.; Bi, J.; Broquet, G.; Canadell, J.G.; Chevallier, F.; Liu, Y.Y., et al. Contribution of semi-arid ecosystems to interannual variability of the global carbon cycle. *Nature* **2014**, *509*, 600-603.

Raupach, M.; Canadell, J.; Quéré, C.L. Anthropogenic and biophysical contributions to increasing atmospheric CO 2 growth rate and airborne fraction. *Biogeosciences* **2008**, *5*, 1601-1613.

Rawlins, M.A.; McGuire, A.D.; Kimball, J.S.; Dass, P.; Lawrence, D.; Burke, E.; Chen, X.; Delire, C.; Koven, C.; MacDougall, A., et al. Assessment of model estimates of land-atmosphere CO2 exchange across Northern Eurasia. *Biogeosciences* **2015**, *12*, 4385-4405.

Reich, P.B.; Hobbie, S.E.; Lee, T.; Ellsworth, D.S.; West, J.B.; Tilman, D.; Knops, J.M.; Naeem, S.; Trost, J. Nitrogen limitation constrains sustainability of ecosystem response to CO 2. *Nature* **2006**, *440*, 922.

Reich, P.B.; Hobbie, S.E.; Lee, T.D. Plant growth enhancement by elevated CO 2 eliminated by joint water and nitrogen limitation. *Nature Geoscience* **2014**, *7*, 920.

Reichstein, M.; Tenhunen, J.; Roupsard, O.; Ourcival, J.M.; Rambal, S.; Miglietta, F.; Peressotti, A.; Pecchiari, M.; Tirone, G.; Valentini, R. Inverse modeling of seasonal drought effects on canopy CO2/H2O exchange in three Mediterranean ecosystems. *Journal of Geophysical Research: Atmospheres* **2003**, *108*.

Rienecker, M.M.; Suarez, M.J.; Gelaro, R.; Todling, R.; Bacmeister, J.; Liu, E.; Bosilovich, M.G.; Schubert, S.D.; Takacs, L.; Kim, G.K., et al. MERRA: NASA's Modern-Era Retrospective Analysis for Research and Applications. *Journal Of Climate* **2011**, *24*, 3624-3648.

Rossini, M.; Cogliati, S.; Meroni, M.; Migliavacca, M.; Galvagno, M.; Busetto, L.; Cremonese, E.; Julitta, T.; Siniscalco, C.; Morra di Cella, U. Remote sensing-based estimation of gross primary production in a subalpine grassland. *Biogeosciences* **2012**, *9*, 2565-2584.

Running, S.W., and Maosheng Zhao. Daily GPP and annual NPP (MOD17A2/A3) products NASA Earth Observing System MODIS land algorithm. **2015**.

Ryu, Y.; Baldocchi, D.D.; Kobayashi, H.; van Ingen, C.; Li, J.; Black, T.A.; Beringer, J.; Van Gorsel, E.; Knohl, A.; Law, B.E. Integration of MODIS land and atmosphere products with a coupled-

process model to estimate gross primary productivity and evapotranspiration from 1 km to global scales. *Global Biogeochemical Cycles* **2011**, *25*.

Schaaf, C.; Liu, J.; Gao, F.; Strahler, A.H. MODIS albedo and reflectance anisotropy products from Aqua and Terra. *Land Remote Sensing and Global Environmental Change: NASA's Earth Observing System and the Science of ASTER and MODIS* **2011**, *11*, 549-561.

Schaaf, C.B.; Gao, F.; Strahler, A.H.; Lucht, W.; Li, X.W.; Tsang, T.; Strugnell, N.C.; Zhang, X.Y.; Jin, Y.F.; Muller, J.P., et al. First operational BRDF, albedo nadir reflectance products from MODIS. *Remote Sensing Of Environment* **2002**, *83*, 135-148.

Sims D A, R.A.F., Cordova V D. A new model of gross primary productivity for North American ecosystems based solely on the enhanced vegetation index and land surface temperature from MODIS. *Remote Sensing of Environment* **2008**, *112*.

Smith, W.K.; Reed, S.C.; Cleveland, C.C.; Ballantyne, A.P.; Anderegg, W.R.; Wieder, W.R.; Liu, Y.Y.; Running, S.W. Large divergence of satellite and Earth system model estimates of global terrestrial CO 2 fertilization. *Nature Climate Change* **2016**, *6*, 306.

Song, C.; Dannenberg, M.P.; Hwang, T. Optical remote sensing of terrestrial ecosystem primary productivity. *Progress in Physical Geography* **2013**, *37*, 834-854.

Still, C.J.; Berry, J.A.; Collatz, G.J.; DeFries, R.S. Global distribution of C3 and C4 vegetation: carbon cycle implications. *Global Biogeochemical Cycles* **2003**, *17*, 6-1-6-14.

Stocker, T.F.; Qin, D.; Plattner, G.; Tignor, M.; Allen, S.; Boschung, J.; Nauels, A.; Xia, Y.; Bex, V.; Midgley, P. Contribution of working group I to the fifth assessment report of the intergovernmental panel on climate change. *Climate change 2013: the physical science basis* **2013**.

Sun, Z.; Wang, X.; Tani, H.; Zhong, G.; Yin, S. Spatial Distribution of CO2 Concentration over South America during ENSO Episodes by Using GOSAT Data. *American Journal of Climate Change* **2016**, *5*, 77.

Sun, Z.; Wang, X.; Yamamoto, H.; Tani, H.; Zhong, G.; Yin, S. An attempt to introduce atmospheric CO 2 concentration data to estimate the gross primary production by the terrestrial biosphere and analyze its effects. *Ecological Indicators* **2018**, *84*, 218-234.

Sun, Z.Y.; Wang, X.F.; Yamamoto, H.; Tani, H.; Zhong, G.S.; Yin, S. An attempt to introduce atmospheric CO2 concentration data to estimate the gross primary production by the terrestrial biosphere and analyze its effects. *Ecological Indicators* **2018**, *84*, 218-234.

Sun, Z.Y.; Wang, X.F.; Yamamoto, H.; Tani, H.; Zhong, G.S.; Yin, S.; Guo, E.L. Spatial pattern of GPP variations in terrestrial ecosystems and its drivers: Climatic factors, CO2 concentration and land-cover change, 1982-2015. *Ecological Informatics* **2018**, *46*, 156-165.

Task, G.S.D. Global soil data products CD-ROM contents (IGBP-DIS). *ORNL DAAC* **2014**.

Thomas, R.T.; Prentice, L.C.; Graven, H.; Ciais, P.; Fisher, J.B.; Hayes, D.J.; Huang, M.Y.; Huntzinger, D.N.; Ito, A.; Jain, A., et al. Increased light-use efficiency in northern terrestrial ecosystems indicated by CO2 and greening observations. *Geophysical Research Letters* **2016**, *43*, 11339-11349.

Tian, H.; Chen, G.; Lu, C.; Xu, X.; Hayes, D.J.; Ren, W.; Pan, S.; Huntzinger, D.N.; Wofsy, S.C. North American terrestrial CO 2 uptake largely offset by CH 4 and N 2 O emissions: toward a full accounting of the greenhouse gas budget. *Climatic Change* **2015**, *129*, 413-426.

Traore, A.K.; Ciais, P.; Vuichard, N.; Poulter, B.; Viovy, N.; Guimberteau, M.; Jung, M.; Myneni, R.; Fisher, J.B. Evaluation of the ORCHIDEE ecosystem model over Africa against 25 years of satellite-based water and carbon measurements. *Journal of Geophysical Research: Biogeosciences* **2014**, *119*, 1554-1575.

Tucker, C.J.; Pinzon, J.E.; Brown, M.E.; Slayback, D.A.; Pak, E.W.; Mahoney, R.; Vermote, E.F.; El Saleous, N. An extended AVHRR 8-km NDVI dataset compatible with MODIS and SPOT vegetation NDVI data. *International Journal of Remote Sensing* **2005**, *26*, 4485-4498.

Van den Dool, H.; Huang, J.; Fan, Y. Performance and analysis of the constructed analogue method applied to US soil moisture over 1981–2001. *Journal of Geophysical Research: Atmospheres* **2003**, *108*.

Van Oijen, M.; Dreccer, M.; Firsching, K.-H.; Schnieders, B. Simple equations for dynamic models of the effects of CO2 and O3 on light-use efficiency and growth of crops. *Ecological Modelling* **2004**, *179*, 39-60.

Veroustraete, F. On the Use of a Simple Deciduous Forest Model for the Interpretation of Climate-Change Effects at the Level of Carbon Dynamics. *Ecological Modelling* **1994**, *75*, 221-237.

Verstraeten, W.W.; Veroustraete, F.; Feyen, J. On temperature and water limitation of net ecosystem productivity: Implementation in the C-Fix model. *Ecological Modelling* **2006**, *199*, 4-22.

Wang, H.; Prentice, I.C.; Davis, T.W. Biophsyical constraints on gross primary production by the terrestrial biosphere. *Biogeosciences* **2014**, *11*, 5987-6001.

Wanner, W.; Li, X.; Strahler, A. On the derivation of kernels for kernel-driven models of bidirectional reflectance. *Journal of Geophysical Research: Atmospheres* **1995**, *100*, 21077-21089.

Wanner, W.; Strahler, A.; Hu, B.; Lewis, P.; Muller, J.P.; Li, X.; Schaaf, C.; Barnsley, M. Global retrieval of bidirectional reflectance and albedo over land from EOS MODIS and MISR data: Theory and algorithm. *Journal of Geophysical Research: Atmospheres* **1997**, *102*, 17143-17161.

Watham, T.; Patel, N.; Kushwaha, S.; Dadhwal, V.; Kumar, A.S. Evaluation of remote-sensing-based models of gross primary productivity over Indian sal forest using flux tower and MODIS satellite data. *International journal of remote sensing* **2017**, *38*, 5069-5090.

Wei, S.; Yi, C.; Fang, W.; Hendrey, G. A global study of GPP focusing on light-use efficiency in a random forest regression model. *Ecosphere* **2017**, *8*, e01724.

Welp, L.R.; Keeling, R.F.; Meijer, H.A.; Bollenbacher, A.F.; Piper, S.C.; Yoshimura, K.; Francey, R.J.; Allison, C.E.; Wahlen, M. Interannual variability in the oxygen isotopes of atmospheric CO2 driven by El Nino. *Nature* **2011**, *477*, 579-582.

Wu, C.; Munger, J.W.; Niu, Z.; Kuang, D. Comparison of multiple models for estimating gross primary production using MODIS and eddy covariance data in Harvard Forest. *Remote Sensing of Environment* **2010**, *114*, 2925-2939.

Wu, D.; Zhao, X.; Liang, S.; Zhou, T.; Huang, K.; Tang, B.; Zhao, W. Time-lag effects of global vegetation responses to climate change. *Global change biology* **2015**, *21*, 3520-3531.

Wu, Z.; Ahlström, A.; Smith, B.; Ardö, J.; Eklundh, L.; Fensholt, R.; Lehsten, V. Climate data induced uncertainty in model-based estimations of terrestrial primary productivity. *Environmental Research Letters* **2017**, *12*, 064013.

Wylie, B.K.; Johnson, D.A.; Laca, E.; Saliendra, N.Z.; Gilmanov, T.G.; Reed, B.C.; Tieszen, L.L.; Worstell, B.B. Calibration of remotely sensed, coarse resolution NDVI to CO2 fluxes in a sagebrush–steppe ecosystem. *Remote Sensing of Environment* **2003**, *85*, 243-255.

Xiao, X.; Zhang, Q.; Braswell, B.; Urbanski, S.; Boles, S.; Wofsy, S.; Moore, B.; Ojima, D. Modeling gross primary production of temperate deciduous broadleaf forest using satellite images and climate data. *Remote Sensing of Environment* **2004**, *91*, 256-270.

Yang, S.H.; Xu, J.Z.; Liu, X.Y.; Zhang, J.G.; Wang, Y.J. Variations of carbon dioxide exchange in paddy field ecosystem under water-saving irrigation in Southeast China. *Agricultural Water Management* **2016**, *166*, 42-52.

Yuan, W.; Cai, W.; Liu, S.; Dong, W.; Chen, J.; Arain, M.A.; Blanken, P.D.; Cescatti, A.; Wohlfahrt, G.; Georgiadis, T. Vegetation-specific model parameters are not required for estimating gross primary production. *Ecological modelling* **2014**, *292*, 1-10.

Yuan, W.P.; Liu, S.; Zhou, G.S.; Zhou, G.Y.; Tieszen, L.L.; Baldocchi, D.; Bernhofer, C.; Gholz, H.; Goldstein, A.H.; Goulden, M.L., et al. Deriving a light use efficiency model from eddy covariance flux data for predicting daily gross primary production across biomes. *Agricultural and Forest Meteorology* **2007**, *143*, 189-207.

Zeng, N.; Mariotti, A.; Wetzel, P. Terrestrial mechanisms of interannual CO2 variability. *Global biogeochemical cycles* **2005**, *19*.

Zhang, S.; Zhang, J.; Bai, Y.; Koju, U.A.; Igbawua, T.; Chang, Q.; Zhang, D.; Yao, F. Evaluation and improvement of the daily boreal ecosystem productivity simulator in simulating gross primary productivity at 41 flux sites across Europe. *Ecological Modelling* **2018**, *368*, 205-232.

Zhang, Y.; Xiao, X.; Wu, X.; Zhou, S.; Zhang, G.; Qin, Y.; Dong, J. A global moderate resolution dataset of gross primary production of vegetation for 2000–2016. *Scientific Data* **2017**, *4*, 170165.

Zhang, Y.; Zhu, Z.; Liu, Z.; Zeng, Z.; Ciais, P.; Huang, M.; Liu, Y.; Piao, S. Seasonal and interannual changes in vegetation activity of tropical forests in Southeast Asia. *Agricultural and Forest Meteorology* **2016**, *224*, 1-10.

Zhao, M.; Running, S.W. Drought-induced reduction in global terrestrial net primary production from 2000 through 2009. *Science* **2010**, *329*, 940-943.

Chapter 2 Estimation on GPP of global terrestrial ecosystem using multi-model

2.1 Introduction

Terrestrial GPP is defined as the amount of carbon uptake by vegetation through photosynthesis at the ecosystem scale, is the first step of atmospheric CO_2 entering the biosphere (Hilker et al., 2008; Beer et al., 2010; Zhang et al., 2017). Through GPP, which plays a pivotal role in the global carbon balance and almost all ecosystem processes, terrestrial ecosystems can partly mitigate global warming and offset increasing CO_2 emissions (Ballantyne et al., 2012). Therefore, it is of pivotal scientific significance to precisely measure terrestrial ecosystem GPP.

However, directly measuring GPP at the global scale is impossible (Ma et al., 2015); to accurately quantify the spatiotemporal patterns of GPP, considerable efforts have been made to develop physiological process models (Dury et al.,2011; Tian et al., 2015; Best et al., 2011; Bondeau et al., 2007; Traore et al., 2014; Zeng et al., 2005; Ito et al., 2002) as tools to understand terrestrial carbon mechanisms and fluxes at the global scale and to hindcast historical situations and predict future changes (Cramer et al., 1999; Piao et al., 2009; Keenan et al., 2016) and predict future changes (Friedlingstein et al., 2006; Smith et al., 2016). For the past ten years, RS-based models have been widely used (Liu et al., 1997; Zhang et al., 2018; Ryu et al., 2011; Jiang et al., 2016; Verstraeten et al., 2006; Sun et al., 2018b; Potter et al., 1993; Yuan et al., 2007; Xiao et al., 2004; Running and Zhao 2015; Gitelson et al., 2006; Sims et al., 2008; Wu et al., 2010; Liu et al., 2014; Jung et al., 2011) with the development of space technology because compared with process-oriented ecosystem models that entail a complex combination of model parameterizations (Piao et al., 2013; Peng et al., 2015; Bonan and Doney 2018), RS-based approaches are relatively simpler and more efficient for exploring dynamic changes in GPP and their spatiotemporal variations at the macroscale (Pasetto et al.,2018;Song et al.,2013;Yuan et al., 2007 2014; Sun et al., 2018b). It is also easier to overcome the shortcomings of some process-oriented models, including the nutrient limiting effects on vegetation growth (Ollinger and Smith 2005; Song et al.,2013; Reich et al., 2006 2014), the influences from agricultural management (Lobell et al., 2003) and extreme emergency events (Lentile et al., 2006; Sun et al., 2018b), and the uncertainties involved in modeling the phenology of vegetation (Rawlins et al., 2015; Song et al, 2013; Xiao et al., 2004; Piao et al., 2007). Additionally, RS is a kind of comprehensive and representative way to obtain information (Liang et al., 2018).

This chapter is the basis for the next three chapters of research. In this chapter, I evaluated and compared the GPPs estimated by 12 RS-based GPP models and benchmarked these estimates against the GPP measured at flux tower sites who have longer than 12 years available measurements. And then I compared the model output of GPP with the average of six DGVMs from ISIMIP2 (The Inter-Sectoral Impact Model Intercomparison Project, Phase II) (Chang et al., 2017). Because the DGVM average is not the true GPP value, we only utilized this value as an intermediate benchmarking reference to compare the difference in the global distributions among models. The comparison among models mainly includes globally averaged multi-year annual GPP estimates, the global spatial distribution of GPP estimates, the trend of GPP estimates and the characteristics of seasonal cycle and so on.

2.2 Materials and methods

2.2.1 Data

2.2.1.1 Flux sites data

In this chapter, one of the objects is evaluating the trend of GPP, therefore, the relatively long-term data are more useful. On the basis of that, I only selected the towers which have the available observation longer than 12 years from FluxNet 2015 dataset, in a total of 33 flux sites, 457 site-years, including 11 ENF sites, 2 EBF sites, 6 DBF sites, 4 MF sites, 3 GRA sites, 1 WSA site, 1 SAV site, 4 CRO sites and 1 WET site. The locations and general information for each site are listed in Table 5.3. The measurements of flux GPP in the 33 sites retrieved from the Fluxnet 2015 dataset were used to verify of the GPP estimations of each model. The measurements of flux GPP that was employed in this study was the mean value of GPP_DT_VUT_REF and GPP_NT_VUT_REF. These were respectively estimated using the daytime and nighttime partitioning method (Lasslop et al., 2010) and the variable ustar threshold method. And for analyzing the sensitivities of GPP to climatic factors, we selected the available towers which have been measured as the same period as the models ran, in a total of 17. For running models at site-scale, among the meteorological inputs, daily temperature, shortwave and longwave radiation, pressure, VPD, ambient CO_2 concentration and wind speed, were retrieved from the measurements from the flux sites. Missing data from tower observations were not included in this study.

2.2.1.2 Atmospheric CO_2 concentration data

The ambient CO_2 concentration is necessary for driving the BESS, BEPS and CFix to estimate GPPs, and also for analyzing the responses of GPPs to the increasing atmospheric CO_2 concentration. CT2016 contains global daily continuous spatial CO_2 concentration data from 2000 to 2015 by 2°×3°, was selected by the present study rather than using the CO_2 concentration data from satellite observing because the available timeseries of carbon observation is not enough, only from 2009 when the GOSAT launched. Additionally, CT2016 is an open product of NOAA/ESRL that uses data from the greenhouse gas observational network and collaborating institutions (Peters et al., 2007). In CT2016, the land biosphere, wildfire, fossil fuel emissions, atmospheric transport and other factors were data-assimilated to produce the estimates of surface fluxes and atmospheric CO_2 mole fractions (https: //www.esrl.noaa.gov /gmd /ccgg /carbontracker /index.php). The spatial continuous CO_2 concentration data were resampled to the 0.5° × 0.5° spatial resolution by linear method.

2.2.1.3 Soil moisture and property data

In BEPS and CFix there has a module calculating the water limitations on the photosynthetic rate by considering the stomatal regulating factor from the soil moisture deficits. Therefore, in order to drive these two models, the soil water content and soil moisture characteristics are indispensable. In the present, I obtained the soil moisture characteristics, including WP and FC, from IGBP-DIS dataset (Global Soil Data Task, 2014). It is a global product generated at a resolution of 5×5 arc-minutes by the SDS which generates soil information and maps for geographic regions at user-selected soil depths and resolutions. Regarding SM, NOAA/ESRL PSD run multiple land surface models to get a model-calculated CPC SM dataset v2 (van den Dool et al, 2003), since globally measuring the SM is impossible, this dataset is to be the most suitable datasets because it provides global monthly data from 1948 to 2017 and consisted of a file containing the averaged SM water height equivalents at a spatial resolution of 0.5°×0.5°. The two datasets represent the SM and characteristics in

different depth of soil, thus, I used the field capacity maps derived from IGBP-DIS and converted the data to the values at a soil depth of 1.6 m, which is the same as that used for the CPC-SM. I conducted the model at the daily step, therefore, the inputs of SM for each day during the study period, 2000 - 2014, were replaced by the monthly soil condition of which the day is located in. Finally, the data were resampled to the 0.5° × 0.5° spatial resolution by linear method.

2.2.1.4 GlobMap LAI

The leaf area index (LAI) derived from GlobMap LAI v3 (8-day, 0.08°) (Liu et al., 2012) were employed in this study. In GlobMap LAI v3 dataset was generated by inputting MOD09A1 (MODIS land surface reflectance) (2001-2016) and AVHRR NDVI (1981~2000) on the basis of GLOBCARBON LAI algorithm (Deng et al., 2006). In order to fusion two inputs well, the data series of AVHRR NDVI (Tucker et al., 2005) and the MODIS LAI during the overlapping period (2000~2006) were used to establish the fusion relationship pixel-by-pixel. Then, using the relationship re-estimate the AVHRR LAI values (Liu et al., 2012). In comparison of the previous version, v3 considers the clumping effect, and has been widely used for long-term global vegetation condition monitoring and detection (Piao et al., 2006; Beck et al., 2011; Wu et al., 2015; Liang et al., 2015). In this study, we considered the daily LAI values to be the same as the 8-day LAI, in which the day belonged to the period of products and resampled it to 0.5° × 0.5° spatial resolution by linear method.

2.2.1.5 Climate data

For the global estimation of GPP, I used the input datasets of climate from the MERRA-2 (Rienecker et al., 2011), which provides data beginning in 1980 at a resolution of 0.5° latitude × 0.625° longitude. MERRA-2 is the first long-term global reanalysis to assimilate space-based observations of aerosols and represent their interactions with other physical processes in the climate system. In comparison of MERRA-1, there are some advances made in the assimilation system which allow modern hyperspectral radiance and microwave observations to be assimilated. More information on the MERRA dataset is available from NASA GES DISC/ Modeling/ Data Holding (http:// disc.gsfc.nasa.gov/daac-bin/DataHoldings.pl). The uncertainties of various meteorological factors at the global scale have been validated and evaluated by using surface metrological datasets (Rienecker et al., 2011; Li et al., 2013). The daily climate data including Ta, S), TD and WS were at 2 meters height, while PS, LST and Pre were at surface level. We calculated the RH and VPD using SH, Ta and TD according to Henderson and Gornitz (1984) daily. In addition, PAR, LH and λH, and H were also daily data. For BESS, the inputted radiation data should to be the corresponding data at the local time when the satellites overpassed, therefore, we applied the hourly PAR_{Diff}, PAR_{Dir}, NIR_{Diff} and NIR_{Dir} and then linearly interpolated them to get the corresponding data which during satellites overpass. All data were linearly interpolated and resampled to a spatial resolution of 0.5° × 0.5°.

2.2.1.6 Satellite data

In this study, all the satellite data were derived from MODIS (Terra and Aqua) in a total of three products, including Land Cover product (MCD12C1 and MCD12Q2), Evapotranspiration product (MOD16A2), and Bidirectional Reflectance Distribution Function and Albedo product (MCD43C2, MCD43C3 and MCD43C4). MODIS as a sensor has become an indispensable source of earth observation at global scale since it was launched (Yebra et al., 2013).

MCD12Q2 is MODIS Global Vegetation Phenology product, providing the estimates of the timing of vegetation phenology globally at a spatial resolution of 500m × 500m. It identifies phenophase transition dates (onset greenness increase, onset greenness maximum, onset greenness decreases and onset greenness minimum) based on logistic functions fit to time series of EVI, which gets the date similar to that using the approach in VPM basing on an EVI seasonal threshold. Thus, for large-scale application of VPM across the whole globe in this study, MCD12Q2 dates can be used directly (Yuan et al., 2014). And it was interpolated and resampled to a spatial resolution of 0.5° × 0.5° by using majority method.

MCD12C1 is Land Cover Type product, providing a spatially aggregated (0.05° × 0.05°) and re-projected version of the tiled data product and having the information on 17 classes of dominant land cover types defined by the IGBP (Friedl et al., 2010). In addition, the responses of different species to light, temperature, CO_2 concentration are different since the physiological functions, such as stomatal conductance and isotope fractionation, are different. Therefore, we overlaid the MCD12C1 with the C4 vegetation percentage map which was one of the products from ISLSCP Initiative II with a spatial resolution of 1°×1° to obtain the landcover component map. Then we aggregated this map by selecting the dominant land cover types within the lower spatial resolution grids, 0.5° × 0.5° (Duveiller and Cescatti 2016).

MOD16A2, Evapotranspiration/Latent Heat Flux product, is an 8-day temporal granularity composite product produced at a spatial resolution of 500m × 500m (Running et al., 2017). We used two layers of evapotranspiration (ET) and potential ET (PET) from this product to calculate the limiting factor of water condition to drive CASA model. It is generated by Penman-Monteith equation inputting daily meteorological reanalysis data along with MODIS remotely sensed data products. Thanks to the quality control layer in this product, only the pixel with level equal to or better than good were used to aggregate a 0.5° × 0.5° spatial data by mean values. Additionally, in this study, we considered the daily ET and PET values to be the same as the 8-day values, in which the day belonged to the period of products.

MCD43C2, BRDF / Albedo Snow-free Quality Parameters, is produced daily global 0.05° grid, using all high quality observations acquired by two satellites, providing the three snow free model weighting parameters (isotropic, volumetric and geometric) used for band 1 (red, 620-670nm) and band 2 (NIR (Near Infrared) 841-876 nm) to calculate the NDHD (normalized difference between hotspot and darkspot) using the RossThickLiSparse-Reciprocal model (Roujean et al., 1992; Lucht et al., 2000; Wanner et al., 1995) in this study. I aggregated the 0.05 spatial resolution of NDHD to a 0.5 spatial resolution by using the mean values of the pixels which belonged to the coarse grid, only the high-quality pixels included. Then we according to the method proposed by He and Fang (2016) and Chen et al. (2005) which has been validated in multi-scale and multi-ecosystems estimated the global clumping index (He and Fang 2016).

MCD43C3 (Schaaf and wang 2015a) provides 0.05° × 0.05°daily both directional hemispherical reflectance (black sky albedo) and bihemispherical reflectance (white sky albedo) for each of the MODIS band 1-7 and the visible (vis), nir, and shortwave bands with Albedo Quality layers. Four datasets of the product, the black/white sky vis/nir albedo, were inputted into BESS canopy radiative modules. And it was resampled to a spatial resolution of 0.5° × 0.5°.

MCD43C4 (Schaaf and wang 2015b), Nadir BRDF-Adjusted Reflectance, is computed for each band at the local solar noon zenith angle in order to make the reflectance stable by removing the view angle effects from the directional reflectance. The spatial and temporal resolution of MCD43C4 are the same as MCD43C2 and MCD43C3. In this study, we used band

1(red 620-670 nm), 2 (NIR 841-876 nm), 3 (blue 459-479 nm) and 6 (SWIR 1628-1652nm) of MCD43C4 to compute three VIs (NDVI, EVI, LSWI) used to driven GPP estimating models.

For MCD43C2, MCD43C3 and MCD43C4, we used the same method to conduct the gap-filling and resample. Firstly, we identified the mandatory QA bit index of pixels classified belongs to 0 (best quality, 100% with full inversions) and 1 (good quality, 75 % or more with best full inversions and 90% or more with full inversions) as the high-quality pixels. Secondly for each day, we calculated the mean values of the high-quality pixels which belonged to the same 0.5° × 0.5° grid to resample and fill the resulted grid. If unfilled 0.5° grid exists, we used the multiyear mean value (at least three years of high-quality data exist in the same date) of the corresponding original 0.05° pixels to fill the data gap for specific date (Fang et al., 2008; Ryu et al., 2011) and conduct the second step again. If there is still a vacancy value, the mean value of the same PFT in the same date will be used as the filling value.

Sun-induced chlorophyll fluorescence (SIF) datasets from GOME (Global Ozone Monitoring Experiment)-2: The latest version (v26) of the monthly SIF data retrieved from the GOME-2 instrument onboard the MetOp-A satellite (channel 4 with ~0.5-nm spectral resolution and wavelengths between 734 and 758 nm) used in this study is the one proposed by Joiner et al. (2013) and is available to the public from the NASA Aura Validation Data Center (http://avdc.gsfc.nasa.gov/). The nominal ground pixel lengths at nadir are approximately 40 km in the along-track and 80 km in the across-track directions (40 km × 40 km from 15 July 2003) (Joiner et al., 2014). GOME-2 SIF data are quality filtered (e.g., heavily cloud-contaminated data are removed) and are aggregated into monthly means in 0.5° × 0.5° grids. Details of the effects of cloud on fluorescence measurements and the use of an effective cloud fraction to filter and quality control the products can be found in previous studies (Joiner et al. 2013; Joiner et al., 2014) the details of the effects of cloud on fluorescence measurements and using an effective cloud fraction to filter and quality control on products can be found. In comparison with other RS approaches, SIF data derived from GOME-2 meet the requirements of the study, in comparison, the GOSAT measurements have low spatial sampling, the SCIAMACHY results have low signal levels that are spectrally far from the fluorescence peak (Joiner et al., 2013), and the OCO-2 (Orbiting Carbon Observatory-2) results do not have sufficient time series data. GOME-2 provides the highest fidelity satellite fluorescence data set currently available; the data have estimated errors of 0.1–0.4 $mW/m^2/nm/sr$ (Joiner et al., 2014). In this study, I used GOME-2 SIF data for the period from 2007 to 2014.

2.2.2 Models

2.2.2.1 BEPS (Boreal Ecosystem Productivity Simulator)

BEPS was originally developed to manage and monitor the natural resources of forest ecosystem by Canada Center for Remote Sensing (Liu et al., 1997). BEPS is process-based and RS data driven model using stomatal conductance as the physiological regulator module to couple the carbon and water cycles (Chen et al., 1999; Bunkei et al., 2002). One of the main advantages in BEPS is combining LAI with "two-leaf" model to simulate the photosynthesis process of shaded and sunlit leaf (Erbs et al., 1982; Norman 1982; Chen et al., 1999), respectively, then scaling the instant photosynthetic capabilities up to the canopy, as:

$$GPP = A_{\text{canopy}} \times Daylength \times Factor_{GPP} \quad \text{Eq-2.1}$$

$$A_{\text{canopy}} = A_{sun}\text{LAI}_{\text{sun}} + A_{shade}\text{LAI}_{\text{shade}} \quad \text{Eq-2.2}$$

$$\text{LAI}_{\text{sun}} = 2\cos(1 - \exp(-0.5\Omega\text{LAI}/\cos\theta)) \quad \text{Eq-2.3}$$

$$\text{LAI}_{shade} = \text{LAI} - \text{LAI}_{sun} \quad \text{Eq-2.4}$$

$$\theta = \frac{1}{2}\left[\frac{1}{2}\left(\frac{\pi}{2} + \theta_{\text{noon}}\right) + \theta_{noon}\right] = \frac{\pi}{8} + \frac{3}{4}\theta_{noon} \quad \text{Eq-2.5}$$

$$\theta_{noon} = \frac{\pi}{180}\left[latitude - 23.5 \times \sin(Julianday - 81) \times \frac{2\pi}{365}\right] \quad \text{Eq-2.6}$$

where *Datlength* is the day of length in second, $Factor_{\text{GPP}}$ converts GPP unit into gC m^{-2} day^{-1}. A_{canopy} is the total assimilation rate of canopy, the subscripts '$_{\text{sun}}$' and '$_{\text{shade}}$' denote the sunlit and shaded components of photosynthesis and LAI, respectively. θ is the solar zenith angle, Ω is the clumping index, we obtained the values through the relationships between NDHD and clumping index (CI) across PFTs (Chen et al., 2005; He et al., 2012). θ_{noon} is the solar zenith angle at noon.

For calculating sunlit leaf irradiance and shaded lead irradiance:

$$\frac{S_{dif}}{S_g} = \begin{cases} 0.943 + 0.734R - 4.9R^2 + 1.796R^3 + 2.058R^4 & R < 0.8 \\ 0.13 & R \geq 0.8 \end{cases} \quad \text{Eq-2.7}$$

$$R = S_g / S_0 \cos\theta \quad \text{Eq-2.8}$$

$$S_{sun} = S_{dir}(\cos\alpha/\cos\theta) + S_{shade} \quad \text{Eq-2.9}$$

$$S_{shade} = (S_{dif} - S_{dif,under}) / LAI + 0.07\Omega S_{dir} \times (1.1 - 0.1LAI) \times e^{-\cos\theta} \quad \text{Eq-2.10}$$

$$S_{dif,under} = S_{dif} \times \exp(-0.5\Omega LAI / (0.537 + 0.025LAI)) \quad \text{Eq-2.11}$$

where S_0 is the solar constant of 1367 W m^{-2}, S_g is the total solar radiation in W m^{-2}. α is mean leaf-sun angle, 60° for a canopy with spherical leaf angle distribution (Chen et al., 1999). $S_{dif,under}$ is diffuse radiation under the plant canopy, S_{dif} and S_{dir} denote diffuse and direct radiation above the canopy, respectively.

For estimating A_{canopy}, in this study, I used the improved BEPS daily (iBEPSd) (Zhang et al., 2018), which has two key processes to estimate carbon assimilation rate. The first process is stomatal conductance (the conductance to CO_2 through the pathway from the atmosphere outside of leaf boundary layer), which is calculated according to Jarvis (Jarvis 1976) model:

$$g \approx 10^6 g_s / R_{gas}(\mathrm{T}_a + 273) \quad \text{Eq-2.12}$$

$$g_s = g_{s\max} f(\mathrm{PPFD}) f(\mathrm{T_a}) f(\mathrm{VPD}) f(\mathrm{LWP}) \quad \text{Eq-2.13}$$

$$f(\mathrm{PPFD}) = \mathrm{PPFD} \times \mathrm{PPFD}_{cof} / (1 + (\mathrm{PPFD} \times \mathrm{PPFD}_{cof})) \quad \text{Eq-2.14}$$

$$f(\mathrm{T_a}) = \begin{cases} 0 & \mathrm{T_a} > \mathrm{T_{max}}, \mathrm{T_a} < \mathrm{T_{min}} \\ \log(\mathrm{T_a}+1)/\log(\mathrm{T_{opt}}+1) & \mathrm{T_{min}} \le T_a < T_{opt} \\ \cos(\pi(\mathrm{T_a}-\mathrm{T_{opt}})/2(\mathrm{T_{max}}-\mathrm{T_{opt}})) & \mathrm{T_{opt}} \le \mathrm{T_a} \le \mathrm{T_{max}} \end{cases} \quad \text{Eq-2.15}$$

$$f(\mathrm{VPD}) = \begin{cases} 1 & \mathrm{VPD} < 0.2 \\ (3-\mathrm{VPD})/2.8 & 0.2 \le \mathrm{VPD} < 3 \\ 0.001 & \mathrm{VPD} \ge 3 \end{cases} \quad \text{Eq-2.16}$$

$$f(\mathrm{LWP}) = (\mathrm{LWP}_{close} - \mathrm{LWP}) / (\mathrm{LWP}_{close} - \mathrm{LWP}_{open}) \quad \text{Eq-2.17}$$

$$\mathrm{LWP} = 0.2 / (\mathrm{Soil}_{water} / \mathrm{Soil}_{cap}) \quad \text{Eq-2.18}$$

where g_s is the stomatal conductance (m s^{-1}) and $g_{s\max}$ is the maximum stomatal conductance to CO_2 (m s^{-1}). f(PPFD), f(T_a), f(VPD) and f(LWP) are the reductions described by photosynthesis photon flux density (PPFD), air temperature (T_a), vapor pressure deficit (VPD) and leaf water potential (LWP), respectively (Liu et al., 1997). $PPFD_{cof}$ is the coefficient in a relationship between g_s and PPFD (a constant of 0.01). Soil_{water} and Soil_{cap} are the soil moisture content and field capacity, respectively. T_{max} and T_{min} and T_{opt} represent the maximum temperature, the minimum temperature and the optimal temperature for photosynthesis.

The second key process is the maximum carboxylation rate (V_m), and in the iBEPSd V_m can be represented as the following equations:

$$V_m = V_{m,25} 2.4^{(\mathrm{T_a}-25)/10} f(\mathrm{T}_a) f(\mathrm{N}) f(\mathrm{NDVI}) \quad \text{Eq-2.19}$$

$$f(\mathrm{N}) = \mathrm{N} / \mathrm{N}_m \quad \text{Eq-2.20}$$

$$f(\mathrm{T}_a) = 1/(1+\exp((-220000+710(\mathrm{T}_a+273))/(R_{gas}(\mathrm{T}_a+273)))) \quad \text{Eq-2.21}$$

$$f(\mathrm{NDVI}) = \begin{cases} 0.01 & \mathrm{NDVI} \le \mathrm{NDVI}_{min} \\ ((\mathrm{NDVI} - \mathrm{NDVI}_{min})/(\mathrm{NDVI}_{max} - \mathrm{NDVI}_{min}))^2 & \mathrm{NDVI}_{min} < \mathrm{NDVI} < \mathrm{NDVI}_{max} \\ 1 & \mathrm{NDVI} \ge \mathrm{NDVI}_{max} \end{cases} \quad \text{Eq-2.22}$$

$$J = J_{max}\mathrm{PPFD}/\left(2.1J_{max} + \mathrm{PPFD}\right) \quad \text{Eq-2.23}$$

$$J_{max} = 29.1 + 1.64V_m \quad \text{Eq-2.24}$$

where $V_{m,25}$ is the maximum carboxylation rate at 25 ℃ in μmol m^{-2} s^{-1}. $f(T_a)$, f(N) and f(NDVI) denote the air temperature constrain, nitrogen constrain and NDVI constrain factors, respectively. R_{gas} is the molar gar constant (8.3143 m^3 Pa mol^{-1} K^{-1}). N is the leaf nitrogen content, and N_m is the maximum nitrogen content (Chen et al., 1999). We considered f(NDVI) as the constrain of chlorophyll content of leaf. NDVI is the time series value, $NDVI_{max}$ is the 95% percentile of the NDVI time series at one pixel (Zhang et al., 2018), and $NDVI_{min}$ was referenced from the same land surface parameterization as $V_{m,25}$ (Sellers et al., 1996). J_{max} is the light-saturated rate of electron in μmol m^{-2} s^{-1}, PPFD is the photosynthetically active flux density (μmol m^{-2} s^{-1}). The parameters used in BEPS for each PFTs are shown in Table 2.1.

2.2.2.2 BESS (Breathing Earth System Simulator)

BESS is a biophysical model with six key modules that include: evapotranspiration, two-leaf canopy conductance and temperature, maximum carboxylation rate, canopy photosynthesis, canopy radiative transfer, and atmospheric radiative transfer, which are important to drive this process-based approach (Ryu et al., 2011; Jiang et al., 2016). In order to be consistent with the input data of other models, in this study we used MERRA-2 data to get the near-infrared radiation and shortwave radiation for the beam and diffuse components at the top of canopy instead of using atmospheric radiative transfer module. To compute the absorbed radiation for sunlit and shaded canopy from that at the top of canopy, a "two-leaf" and "two-stream" (De Pury and Farquhar, 1977; Ryu et al., 2011) canopy radiative transfer module are used, which can calculate the net radiation (Ryu et al., 2008), absorbed longwave radiation (Wang and Leuning 1998), absorbed NIR (Goudriaan 1977) and APAR for sunlit and shade leaves. For estimating GPP of sunlit and shade canopy, an iterative carbon-water-coupled procedure which incorporated quadratic Penman-Monteith equations (Paw U and Gao 1988), FvCB photosynthesis process (Farquhar et al., 1980; Collatz et al., 1992) and a two-leaf longwave transfer models (Kowalczyk et al., 2006), and inputs clear-sky emissivity, air specific heat and VPD which calculated from the climatic data (e.g., temperature, pressure and humidity). Additionally, through this iterative procedure BESS solve the problem of calculating the intermediate variables (e.g., leaf temperature, intercellular CO_2 concentration and aerodynamic resistance). BESS formulates a PFT dependent look-up table (LUT) on the basis of TRY leaf trait database (Kattge et al., 2009) to quantify the plants' parameters (e.g., the maximum leaf carboxylation at 25℃), and then upscale them from the leaf-level to canopy level. The last step is that upscale the instantaneous GPP to daily estimation by a cosine function (Ryu et al., 2012). Since the high complexity of BESS, please refer to Ryu (2011) and Jiang (2016) for details. The parameters used in BEPS for each PFTs are shown in Table 2.1.

2.2.2.3 CFix (Carbon Fixation Model)

CFix is a parametric LUE model with a strong prognostic capability that is driven by plant-related, meteorological, climatic, and hydrological data to estimate carbon mass fluxes in terrestrial ecosystems (Veroustraete et al., 2006) from local (Veroustraete et al., 2002 2004; Yuan et al., 2014a) and regional (Maselli et al., 2009; Chiesi et al., 2011; Yan et al., 2016) to

global scales (Yuan et al., 2014b; Ma et al., 2015). CFix not only relies on the parameterization of fAPAR that is derived from RS-NDVI and downscale factors of environmental stresses to estimate GPP, which are the same as other LUE models, but also has a module of carbon fertilization effects caused by increases in the atmospheric CO_2 concentration, which is considered to be the major reason for global warming. CFix can use inputs averaged over different time periods (most commonly 10-day to monthly periods) and is conceptually simple and generally applicable (Chiesi et al., 2011). For a given geographic coordinate (x, y), GPP is calculated as (Veroustraete et al., 2006):

$$\mathrm{GPP} = \mathrm{PAR} \times \mathrm{fAPAR} \times \varepsilon_{wl} \times T_s \times S_{CO_2} \qquad \text{Eq-2.25}$$

where PAR is the incident photosynthetically active radiation, fAPAR is the fractional absorbed PAR, ε_{wl} is the LUE with water stress, T_s is the temperature dependency factor, and S_{CO2} is the carbon fertilization factor due to the rising atmospheric CO_2 concentration levels. The details of calculations of the parameters can be found in Table 2.2.

2.2.2.4 CASA (Carnegie-Ames-Stanford Approach)

CASA is a classic light use efficiency model that directly translates radiation into NPP (Potter et al., 1993) rather than GPP. The CASA model driven by five variables: NDVI, PAR, T_a, ET and PET.

$$\mathrm{GPP}=\alpha \times \mathrm{NPP}=\alpha \times \mathrm{PAR} \times \mathrm{fAPAR} \times \varepsilon_{\max} \times T_{\mathrm{scaled1}} \times T_{\mathrm{scaled2}} \times \mathrm{W_{ssm}} \qquad \text{Eq-2.26}$$

where $\varepsilon_{\max}$ is the potential light use efficiency without environmental limitation, α is the approximate conversion of 0.5 between NPP and GPP (Waring et al., 1998; Yuan et al., 2014). W_{ssm} (from 0.5 for extreme drought to 1 for fully humid) is the downward-regulation scalar for the effect of soil moisture using actual ET and PET as:

$$\mathrm{W_{ssm}}=0.5+0.5\times\frac{\mathrm{ET}}{\mathrm{PET}} \qquad \text{Eq-2.27}$$

T_{scaled1} and T_{scaled2} are down-regulation scalars for the effect of temperature on LUE of vegetation. T_{scaled1} reflects the limitation of biochemical effect on photosynthesis due to the low or high temperature while T_{scaled2} represents the decline trends of photosynthesis rate displaced from the optimum temperature.

$$T_{\mathrm{scaled1}}=0.8+0.02\times \mathrm{T}_{opt}-0.005\times \mathrm{T}_{opt}{}^{2} \qquad \text{Eq-2.28}$$

$$T_{\mathrm{scaled2}}=1.1919\Big/\left[1+\mathrm{e}^{0.2\times\left(\mathrm{T}_{\mathrm{opt}}-10-\mathrm{T}\right)}\right]\Big/\left[1+\mathrm{e}^{0.3\times\left(-\mathrm{T}_{\mathrm{opt}}-10+\mathrm{T}\right)}\right] \qquad \text{Eq-2.29}$$

and in Eq-2.26 the fAPAR is computed by a linear relationship with simple ratio (SR),

$$\mathrm{fAPAR}=\min\left[\frac{SR-SR_{\min}}{SR_{\max}-SR_{\min}},0.95\right] \qquad \text{Eq-2.30}$$

$$\mathrm{SR}=\left(1+\mathrm{NDVI}\right)\Big/\left(1-\mathrm{NDVI}\right) \qquad \text{Eq-2.31}$$

where SR_{min} represents for unvegetated land areas and is set for 1.08. SR_{max} is considered as the value in clear-sky which has been corrected for effects of the canopy architecture and cloud contamination (Yuan et al., 2014). The parameters used in CASA for each PFTs are shown in Table 2.2.

2.2.2.5 EC-LUE (Eddy Covariance Light Use Efficiency model)

The EC-LUE model, belonging to LUE model, developed by Yuan et al. (2007) is driven by inputting NDVI, PAR, T_a and Bowen ratio. Comparing with other LUE models, the most characteristic is the assumption that the realized LUE calculated from a biome-independent invariant potential LUE, is only limited by the most limiting factor between air temperature and moisture according to Liebig's Law.

$$\mathrm{GPP}=\mathrm{PAR}\times\mathrm{fAPAR}\times\varepsilon_{\max}\times\min(T_{\mathrm{scaled}},W_{\mathrm{SEF}}) \quad \text{Eq-2.32}$$

$$\mathrm{fAPAR}=1.24\times\mathrm{NDVI}-0.168 \quad \text{Eq-2.33}$$

$$T_{\mathrm{scaled}}=\frac{\left(\mathrm{T}-\mathrm{T}_{\min}\right)\times\left(\mathrm{T}-\mathrm{T}_{\max}\right)}{\left(\mathrm{T}-\mathrm{T}_{\min}\right)\times\left(\mathrm{T}-\mathrm{T}_{\max}\right)-\left(\mathrm{T}-\mathrm{T}_{opt}\right)^2} \quad \text{Eq-2.34}$$

$$\mathrm{W}_{\mathrm{SEF}}=\lambda\mathrm{E}/\mathrm{R}_{\mathrm{n}} \quad \text{Eq-2.35}$$

T_{scaled} is the temperature downward-scalar calculated using the equation designed for the terrestrial ecosystem model (TEM) (Raich et al., 1991). R_n is net radiation. The parameters used in EC-LUE for each PFTs are shown in Table 2.2.

2.2.2.6 VPM (Vegetation Photosynthesis Model)

The VPM developed by Xiao et al. (2004) is based on temperature, land surface moisture condition and leaf phenology. VPM assumes that the leaves and canopies are composed of photosynthetic parts and non-photosynthetically active parts. Based on that conceptual assumption, VPM introduces the P_{scaled} as the scalar for the effect of partitioning of leaf morphology, leaf age and growth history on fAPAR, as:

$$\mathrm{GPP}=\mathrm{PAR}\times\mathrm{fAPAR}\times\varepsilon_{\max}\times T_{\mathrm{scaled}}\times W_{\mathrm{SLSWI}}\times P_{\mathrm{scaled}} \quad \text{Eq-2.36}$$

where fAPAR is calculated by a linear function of EVI, and the coefficient set equal to 1 (Xiao et al., 2004). T_{scaled} is computed using the same Equation as shown at Eq-2.34. W_{SLSWL} represents the scalar for the effect of water limitation as:

$$W_{\mathrm{SLSWI}}=\left(1+\mathrm{LSWI}\right)/\left(1+\mathrm{LSWI}_{\max}\right) \quad \text{Eq-2.37}$$

where LSWI is land surface water index, utilized not only for capturing the effects of water stress but also for calculating the limiting of phenology on photosynthesis. $\mathrm{LSWI}_{\max}$ is the maximum LSWI within the plant growing season.

$$\mathrm{LSWI}=\left(\rho\mathrm{NIR}-\rho\mathrm{SWIR}\right)/\left(\rho\mathrm{NIR}+\rho\mathrm{SWIR}\right) \quad \text{Eq-2.38}$$

where ρNIR and ρSWIR represent the spectral reflectance in near infrared and short-wavelength infrared range, respectively.

P_{scaled} is used to account for the effect of leaf phenology on photosynthesis at canopy level, and it was dependent upon leaf longevity. For a canopy during one growing season, P_{scaled} was set to 1 after leaf full expansion, and during bud burst to leaf full expansion was calculated as:

$$P_{\text{scaled}} = (1 + \text{LSWI})/2 \qquad \text{Eq-2.39}$$

The parameters used in VPM for each PFTs are shown in Table 2.2.

2.2.2.7 MODIS GPP algorithm

In this study, we used MODIS GPP products MOD17 which generated using LUE approach as (Running and Zhao 2015):

$$\text{GPP} = \varepsilon_{\max} \times W_{\text{VPDscaled}} \times T_{\text{minscaled}} \times \text{fAPAR} \times \text{PAR} \qquad \text{Eq-2.40}$$

where $W_{VPDscaled}$ is the downward-scalar that reduces the potential LUE when the water condition is low enough to inhibit photosynthesis. $T_{minscaled}$ is the downward-scalar for the effect of low temperature on plant function. They are simple linear ramp functions of daily lowest temperature (T_{min}) and VPD (Eq-2.41, Eq-2.42) which obtained from the GMAO/NASA datasets. And εmax is the maximum radiation conversion efficiency in the optimum environmental conditions, obtained on the basis on of MOD12Q1, according to which a biome-properties-look-up-table was established for each grid. fAPAR is also the MODIS products, MOD15.

$$T_{\min scaled} = \begin{cases} 0 & \text{T min} \le \text{T min}_{\min} \\ (\text{T min} - \text{T min}_{\min})/(\text{T min}_{\max} - \text{T min}_{\min}) & \text{T min}_{\min} < \text{T min} < \text{T min}_{\max} \\ 1 & \text{T min} \ge \text{T min}_{\max} \end{cases} \qquad \text{Eq-2.41}$$

$$W_{\text{VPDscaled}} = \begin{cases} 1 & \text{VPD} \le \text{VPD}_{\min} \\ (\text{VPD}_{\min} - \text{VPD})/(\text{VPD}_{\max} - \text{VPD}_{\min}) & \text{VPD}_{\min} < \text{VPD} < \text{VPD}_{\max} \\ 0 & \text{VPD} \ge \text{VPD}_{\max} \end{cases} \qquad \text{Eq-2.42}$$

$Tmin_{min}$ and $Tmin_{max}$ represent the minimum and maximum daily lowest temperature at which ε=0 (at any VPD) and ε= ε_{max} (for optimal VPD) for one pixel, respectively. And VPD_{min} and VPD_{max} are the daytime average VPD at which ε=0 (at any Tmin) and ε= ε_{max} (for optimal Tmin), respectively. The parameters used in MODIS for each PFTs are shown in Table 2.2.

2.2.2.8 GR (Greenness-Radiation Model)

GR is a vegetation index type model driven by EVI and radiation (Gitelson et al., 2006). The model was original designed to study the relationship between GPP with chlorophyll content in crop ecosystem (Gitelson et al., 2006), but also calibrated and applied successfully in various ecosystems in North American continent (Wu et al., 2011). The EVI is used as the proxy for the chlorophyll content to upscale the GR model to regional and global scale (Liu et al., 2014). The model uses the following equations to estimate vegetation GPP:

$$GPP = m \times EVI \times PAR \quad \text{Eq-2.43}$$

where m is an empirical coefficient with the unit of gC MJ^{-1} day^{-1} in this study, EVI and PAR are the same as above. The parameters used in GR for each PFTs are shown in Table 2.2.

2.2.2.9 TG (Temperature-Greenness Model)

TG model was original developed to simulate 8-day vegetation GPP (Sims et al., 2008), which is driven by only two satellite-based variables obtained from MODIS: LST and EVI. In contrast to other models, the independence of climate variables makes TG an entirely RS-based model (Li et al., 2013). The conceptual formula is simple, but it performed well in various ecosystems in North America continent (Sims et al., 2008; Wu et al., 2011).

$$GPP = m \times EVI_{scaled} \times LST_{scaled} \quad \text{Eq-2.44}$$

where, m is a conversion coefficient with the unit of gC m^{-2} day^{-1} in this study, and EVI_{scaled} is given by:

$$EVI_{scaled} = EVI - EVI_{base} \quad \text{Eq-2.45}$$

according to the study of Sims et al. (2008), EVI will decline to a value of approximately 0.1 at a GPP of zero, therefore, EVI_{base} is set to 0.1. LST_{scaled} is defined as the minimum of two linear functions which are based on the determination of optimum temperature for GPP.

$$LST_{scaled} = \min\left[\frac{LST}{LST_{opt}}, 1 + 0.05 \times (LST_{opt} - LST)\right] \quad \text{Eq-2.46}$$

In addition, when LST_{scaled} lower than 0, it will be set to 0. In this study, we identified LST_{opt} for one pixel when the NDVI which as a proxy for plant physiological state get optimum level that larger than the 95% percentile of the NDVI time series. The parameters used in TG for each PFTs are shown in Table 2.2.

2.2.2.10 VI (Vegetation Indices Model)

VI model relies heavily on the VI-based approach, with inputs EVI and temperature, developed by Wu et al. (2010a) for crop ecosystems. Wu et al. (2010b) calibrated and successfully applied it in forest ecosystems. In VI model, EVI is incorporated as the proxies for both LUE and fAPAR (Li et at., 2013).

$$GPP = m \times EVI^2 \times PAR \quad \text{Eq-2.47}$$

where m is a conversion coefficient with the unit of gC MJ^{-1} day^{-1} in this study and the other inputs are the same as above. The parameters used in VI for each PFTs are shown in Table 2.2.

2.2.2.11 AVM (Alpine Vegetation Model)

AVM is a vegetation index model that utilizes satellite measurements to estimate GPP (Li et al., 2013). It was originally developed for estimating the GPP in alpine meadow ecosystems

since the air temperature is the dominated factor which limits plants growth in the ecosystem. And Liu et al. (2014) calibrated and successfully applied it in cropland, grassland, and various forest ecosystems in China. Since the temperature is closely correlated with other environmental variables (e.g., VPD, PAR, SM) (Li et al., 2013), and EVI can be adopted to explain the variance in FPAR, the AVM follows Eq-2.48:

$$GPP = m \times EVI_{scaled} \times T_{scaled} \quad \text{Eq-2.48}$$

where m is a conversion coefficient, EVI_{scaled} is calculated by the same approach as that in TG, and EVI_{base} is set to be 0.15. When EVI is less than EVI_{base}, EVI_{scaled} is set as zero. T_{scaled} is calculated as:

$$T_{scaled} = (T - T_{min}) / (T_{max} - T_{min}) \quad \text{Eq-2.49}$$

where T is the daily average air temperature, when it is less than T_{min}, T_{scaled} is set as zero. T_{max} and T_{min} are the biological maximum and minimum temperature during the growing season, respectively. The parameters used in AVM for each PFTs are shown in Table 2.2.

2.2.2.12 MTE (Multi-Tree Ensemble)

MTE is based on machine learning algorithms, employed by Jung et al. (2011), upscaling the GPP from in situ scale to the global scale. They forced 25 individual model trees for each biosphere-atmosphere flux using gridded inputs. The variables used to train the MTE are in total of 29, divided into four categories: climate, vegetation structure, meteorology and vegetation status. Among them the proxies of vegetation status and meteorology, temperature, precipitation, fAPAR and potential APAR, are at monthly resolution, the rest of driven data are static or yearly or monthly but static over years (Jung et al., 2011). Since it is based on direct eddy-covariance flux tower measurements of GPP and is thus considered close to the truth where the flux tower density is high (Beer et al., 2010; Frankenberg et al., 2011). However, under the circumstances that without considering the uncertainties of measurements of eddy covariance fluxes, of global climatic driven factors, of the unbalance of distribution of samples as well as the uncertainty sources from satellite observations, the uncertainty of the MTE GPP is relatively small, at about ± 5 % (Jung et al., 2011).

2.2.2.13 SIF_GPP model

Recently studies (Frankenberg et al. 2011; Guanter et al. 2012 2014; Joiner et al. 2013; Joiner et al. 2011) conducted using state-of-the-art methods have suggested that the spatial and temporal patterns of satellite-derived SIF data are highly correlated with those of GPP. Under appropriate conditions where light is moderate or high or environmental stress exists, SIF is strictly proportional to GPP (Van der Tol, Verhoef and Rosema 2009; Flexas et al. 2000; Lee et al. 2015). In particular, Frankenberg et al. (2011) found that “global space-borne observations of solar-induced chlorophyll exhibit a strong linear correlation with GPP and that the fluorencence emission even without any additional climatic or model information has the same or better predictive skill in estimating GPP as those derived from traditional remotelt sensed vegetation indices using ancillary data and model assumptions”. To quantify the spatial agreement between the observation-based GPP and satellite fluoresecnce, we also estimated the GPP-SIF and discussed the advantages and disadvantages of this method. A simple regression model was used to investigate the SIF-GPP relationship. Monthly SIF and GPP data were averaged over the observation period from 2007 to 2014 for each month to minimize the

uncertainties resulting from different spatial resolutions. Since the SIF-GPP relationship is biome-specific (Guanter et al., 2012), we established regression models for each PFT obtained from the MODIS land cover products to estimate GPP.

In this study, I only used the most spatially homogeneous sites in the period from 2007 to 2014, shown in Table 2.3. The most spatially homogeneous refers to the following: for a site to be selected for the study, the dominant vegetation cover type at the flux site must represent more than 65 % of the GOME-2 pixel area, and the standard deviation of the NDVI must be less than 0.1. These flux sites cover most of the major biomes (DNF, ENF, CRO, DBF, EBF, GRA, MF, OSH, SAV, WSA), representing a total of 231 observed years.

Table 2.1 List of parameters used in BESS and BEPS for each PFTs.

	δ_{PAR}[1]	δ_{NIR}[2]	ρ_{sP}[3]	ρ_{sN}[4]	N_{ratio}[5]	V_{m25}[6]				
						Equatorial[7]	Arid[7]	Warm temperate[7]	Snow[7]	Polar[7]
ENF	0.120	0.45	0.11	0.23	0.70	63[a]	150[b]	63[a]	63[a]	63[a]
EBF	0.150	0.70	0.11	0.23	0.50	83[c]	41[a]	62[a]	62[a]	62[a]
DNF	0.120	0.45	0.11	0.23	0.70	57[a]	57[a]	57[a]	60[d]	60[d]
DBF	0.150	0.70	0.11	0.23	0.65	66[a]	66[a]	96[a]	96[a]	96[a]
MF	0.120	0.55	0.11	0.23	0.70	75	54	79	79	79
CSH	0.175	0.83	0.11	0.23	0.70	62[a]	110[b]	72[b,e]	58[e]	58[e]
OSH	0.150	0.70	0.25	0.42	0.70	62[a]	110[b]	72[b,e]	58[e]	58[e]
WSA	0.100	0.62	0.25	0.42	0.70	99[b]	120[a]	120[a]	120[a]	120[a]
SAV	0.100	0.62	0.25	0.42	0.70	99[b]	120[a]	120[a]	120[a]	120[a]
GRA	0.175	0.83	0.25	0.42	0.80	90[e]	90[e]	78[a]	142[a]	142[a]
WET	0.175	0.83	0.11	0.23	0.70	90[e]	90[e]	78[a]	142[a]	142[a]
CRO	0.175	0.83	0.11	0.15	0.95	101[a]	101[a]	101[a]	101[a]	101[a]

[1]leaf scattering coefficient for PAR, derived from Sellers et al. (1996) except for WSA, SAV (Asner et al., 1998);
[2]leaf scattering coefficient for NIR, derived from Sellers et al. (1996) except for WSA, SAV (Asner et al., 1998);
[3]Soil reflectance for PAR, derived from Sellers et al. (1996) except for WSA, SAV and OSH (Asner et al., 1998; Roberts et al., 1993);
[4]Soil reflectance for NIR, derived from Sellers et al. (1996) except for WSA, SAV and OSH (Asner et al., 1998; Roberts et al., 1993);
[5]Nitrogen constrain factor, derived from Liu et al. (1997);
[6]Maximum carboxylation rate at 25 °C: [a]Jiang and Ryu 2016; [b]Ryu et al. 2011; [c]Walker et al. 2014; [d]Pan et al. 2015; [e]Zhang et al. 2012;
[7]The main climates of Koppen-Geiger climate classification, derived from Kottek et al. (2006).

Table 2.2 Key parameter values for LUE and VI models.

PFTs	For all[a] (°C)		ε_{max}[b] (gC m^{-2} MJ^{-1}day^{-1} APAR)					ε_{min}[c]	LST_{opt}[d]	m[e] (gC m^{-2} day^{-1})			
	T_{max}	T_{opt}	VPM	EC-LUE	CASA	C-Fix	MODIS	C-Fix	TG	TG	VI	GR	AVM
ENF	45	20	2.27	1.85	0.85	1.94	0.962	1.09	27.98	57.42	0.277	0.0873	121.09
EBF	48	28	2.33	1.70	0.87	1.85	1.268	1.33	25.00	18.91	0.149	0.0761	33.01
DNF	40	20	2.22	1.71	1.22	1.86	1.086	1.09	12.11	24.24	0.190	0.0655	66.32
DBF	40	20	2.38	1.68	1.04	1.92	1.165	1.27	17.32	21.52	0.112	0.0519	33.66
MF	48	19	2.27	1.72	0.89	1.78	1.051	1.16	19.89	27.03	0.177	0.0716	68.38
CSH	48	25	1.78	1.45	0.62	1.89	1.281	0.55	26.70	21.57	0.178	0.0449	59.92
OSH	48	31	1.78	1.45	0.62	1.89	0.841	0.55	11.96	38.93	0.289	0.0653	136.13
WSA	48	24	2.38	1.68	0.89	1.86	1.239	1.09	27.17	22.92	0.174	0.0675	48.84
SAV	48	30	2.38	1.68	0.89	1.86	1.206	1.09	27.15	20.53	0.161	0.0609	44.25
GRA	48	27	2.04	1.59	0.78	1.86	0.860	1.14	17.68	32.98	0.224	0.0634	80.48
WET	40	20	2.19	1.65	0.95	1.81	-	1.14	17.12	36.33	0.256	0.0858	67.97
CRO	48	21	2.38	1.68	0.89	1.86	1.044	1.09	27.04	24.71	0.164	0.0590	46.00

[a]T_{max} and T_{opt} are the biological maximum and minimum temperature during the growing season for all models, derived from Zhang et al. (2017), except for CFix and EC-LUE (T_{max} = 40 and T_{opt} = 21 for all PFTs) (Yuan et al., 2014);

[b]The potential light use efficiency without environmental limitations, derived from Yuan et al. (2014), which is based on the measurements of ecosystem carbon fluxes from 168 globally distributed sites in a range of vegetation types. Parameters of MODIS are derived from Running and Zhao (2015).

[c]The minimum light use efficiency with extreme environmental stress in CFix model, derived from Yuan et al. (2014).

[d]I identified LST_{opt} as the average value of the LSTs which the corresponding NDVI is larger than the 95% percentile of the NDVI time series calculated in this study.

[e]The conversion coefficient, in this study I obtained this value by using the MTE GPP of 2000.

Table 2.3 Details of the sites used in this study. σ NDVI is the standard deviation of NDVI within the GOME-2 pixel. MAX LC represents the fraction of a GOME-2 grid cell covered by the dominant plant. PFT is the plant functional type.

Site ID	COUNTRY	σ NDVI	Max LC (%)	Latitude (°)	Longitude (°)	Data period	PFT
RU-SkP	Russia	0.0113	65.00%	62.2550	129.1680	2012 - 2014	DNF
CZ-BK1	Czech Republic	0.0677	66.67%	49.5047	18.5411	2007 - 2014	ENF
DE-Lkb	Germany	0.0510	80.00%	49.0996	13.3047	2009 - 2013	ENF
DE-Wet	Germany	0.0842	85.00%	50.4535	11.4575	2007 - 2008	ENF
FI-Hyy	Finland	0.0534	80.00%	61.8475	24.2950	2007 - 2014	ENF
FI-Kns	Finland	0.0393	65.00%	60.6468	24.3562	2007 - 2008	ENF
RU-Fyo	Russia	0.0580	100.00%	56.4615	32.9221	2007 - 2014	ENF
US-Blo	United States	0.0669	85.00%	38.8953	-120.6328	2007	ENF
US-Me6	United States	0.0999	75.00%	44.3233	-121.6078	2010 - 2014	ENF
BE-Lon	Belgium	0.0285	94.74%	50.5516	4.7461	2007 - 2014	CRO
DE-Geb	Germany	0.0374	90.00%	51.1001	10.9143	2007 - 2010	CRO
DE-Kli	Germany	0.0944	95.00%	50.8929	13.5225	2007 - 2014	CRO
FR-AUR	France	0.0282	100.00%	43.5496	1.1061	2008 - 2010	CRO
FR-Lam	France	0.0280	100.00%	43.4965	1.2379	2007 - 2010	CRO
IT-BCi	Italy	0.0507	90.91%	40.5238	14.9574	2007 - 2010	CRO
IT-Cas	Italy	0.0357	100.00%	45.0700	8.7175	2007 - 2010	CRO
IT-Ro3	Italy	0.0456	100.00%	42.3754	11.9154	2008 - 2013	CRO
UA-Pet	Ukraine	0.0866	93.33%	46.4561	30.3361	2008 - 2011	CRO
US-Lin	United States	0.0580	100.00%	36.3566	-119.8423	2009 - 2010	CRO
US-Ne1	United States	0.0252	100.00%	41.1651	-96.4766	2007 - 2012	CRO
US-Ne3	United States	0.0273	100.00%	41.1797	-96.4397	2007 - 2012	CRO
US-WCr	United States	0.0296	94.74%	45.8059	-90.0799	2011 - 2014	DBF
US-Ha1	United States	0.0483	100.00%	42.5378	-72.1715	2007 - 2012	DBF
AU-Cum	Australia	0.0211	100.00%	-33.6133	150.7225	2012 - 2013	EBF
AU-Tum	Australia	0.0263	98.36%	-35.6566	148.1517	2007 - 2013	EBF
GF-Guy	French Guiana	0.0353	100.00%	5.2788	-52.9249	2007 - 2014	EBF
GH-Ank	Ghana	0.0350	95.00%	5.2685	-2.6942	2011 - 2014	EBF
MY-PSO	Malaysia	0.0443	98.17%	2.9730	102.3062	2007 - 2009	EBF
CN-Cng	China	0.0131	75.00%	44.5934	123.5092	2007 - 2010	GRA
CN-Du2	China	0.0286	100.00%	42.0467	116.2836	2007 - 2008	GRA
DE-Gri	Germany	0.0837	100.00%	50.9495	13.5125	2007 - 2014	GRA
FR-Lq2	France	0.0237	84.21%	45.6392	2.7370	2007 - 2010	GRA
UK-AMo	United Kingdom	0.0616	88.24%	55.7917	-3.2389	2007 - 2010	GRA
US-AR1	United States	0.0286	100.00%	36.4267	-99.4200	2009 - 2012	GRA
US-AR2	United States	0.0283	100.00%	36.6358	-99.5975	2009 - 2012	GRA
BE-Vie	Belgium	0.0368	84.62%	50.3051	5.9981	2007 - 2014	MF
CA-Gro	Canada	0.0497	100.00%	48.2167	-82.1556	2007 - 2014	MF
US-PFa	United States	0.0452	100.00%	45.9459	-90.2723	2007 - 2014	MF
US-SRC	United States	0.0446	66.67%	31.9083	-110.8395	2008 - 2014	OSH
US-Whs	United States	0.0302	100.00%	31.7438	-110.0522	2007 - 2014	OSH
AU-DaS	Australia	0.0343	100.00%	-14.1593	131.3881	2008 - 2013	SAV
AU-Dry	Australia	0.0307	100.00%	-15.2588	132.3706	2008 - 2013	SAV
ES-Lma	Spain	0.0540	68.42%	39.9415	-5.7734	2007 - 2011	SAV
ZA-Kru	South Africa	0.0359	100.00%	-25.0197	31.4969	2007 - 2013	SAV
AU-Ade	Australia	0.0629	100.00%	-13.0769	131.1178	2007 - 2009	WSA

2.3 Results and discussions

The original spatial resolution and the available spatial range of the datasets used to drive each model are different, although they are nominally global in scale; when the models run in global mode, these estimates must be scaled based on the land area to estimate a global total value; however, this scaling causes a difference of several PgC year^{-1} for the global total GPP (Avan et al., 2015). To remove this issue in our subsequent analysis, for the results presented here, we calculated the average estimates of grids in common according to the global moderate resolution dataset of GPP (Zhang et al., 2017) to estimate the total global GPP for each model.

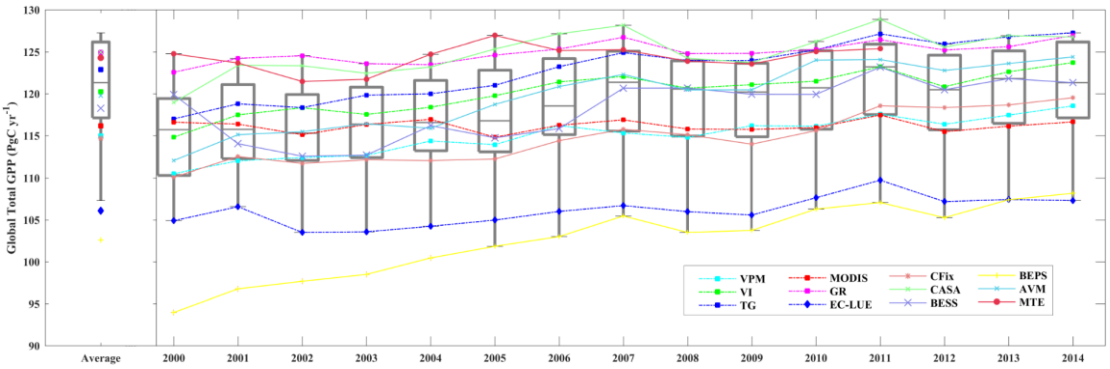

Figure 2.1 Global total annual GPP estimation of each model during 2000-2014.

Over the period of 2000~2014, the estimations of the 12 models diverged in terms of total global GPP, ranging from approximately 102.6 (BEPS) to 124.9 (GR) PgC year^{-1}, with a standard deviation of 7.2 PgC year^{-1} (Figure 2.1).

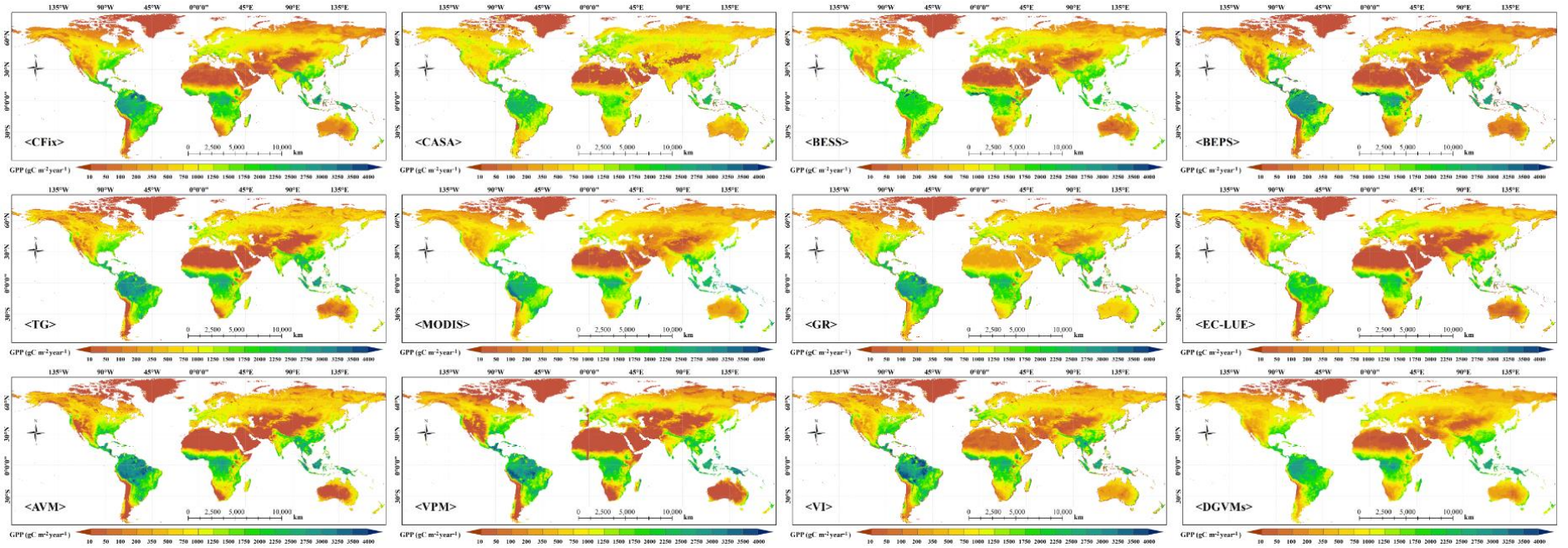

Figure 2.2 Comparison of the annual averaged GPP estimations among different models from 2000 to 2014.

However, the global spatial patterns from the 12 models agreed reasonably well (Figure 2.5), although differences were definited in some areas (Figure 2.2).

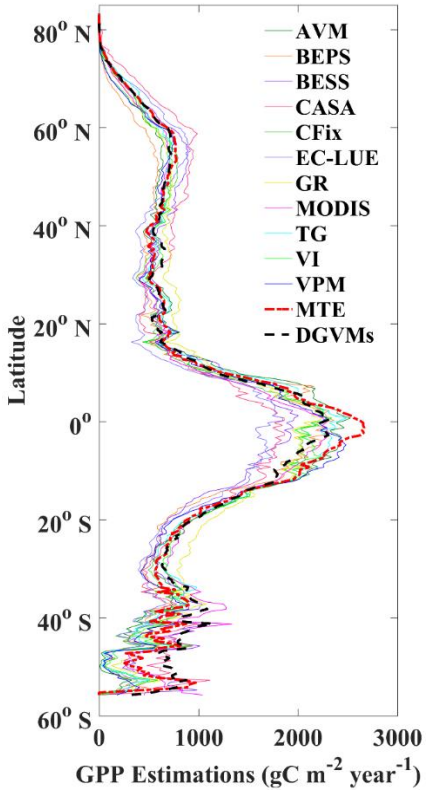

Figure 2.3 The latitudinal distribution of annual averaged GPP estimation of each model during the period of 2000-2014.

Specifically, there was good agreement in mid-high latitudes in the Northern Hemisphere, and relatively large differences in magnitude were found in the Tropics (Figure 2.3).

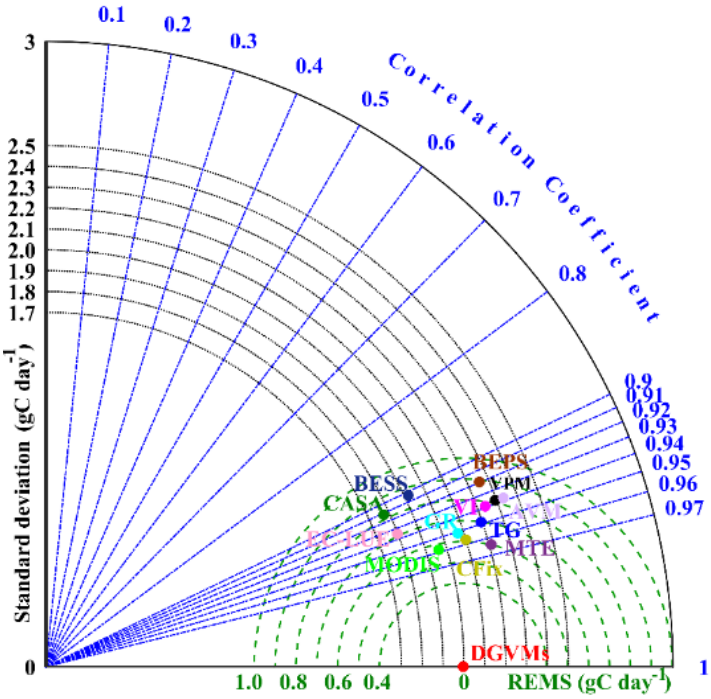

Figure 2.4 Comparison between the spatial distribution of the RS-based GPPs with that of DGVM's average.

To verify the relative spatial distribution of the estimates from each model, I also used the mean global GPP estimation from 7 DGVMs (i.e., CARAIB (CARbon Assimilation In the Biosphere), DLEM (Dynamic Land Ecosystem Model), JULES (the Joint UK Land Environment Simulator), LPJml (Lund-Potsdam-Jena managed Land), ORCHIDEE (Organising Carbon and Hydrology In Dynamic Ecosystems), VEGAS (VEgetation-Global Atmosphere-Soil Model) and VISIT (Vegetation Integrative Simulator for Trace Gases)) of ISIMIP2 to compare the values with those estimates. The DGVM average is not the true value, but running these DGVMs is not necessary to input the RS-based data; therefore, I used the average as the benchmark and intermediate reference to compare the performances between RS-based models.

The results showed that the GPP estimates of the 12 models were highly consistent with the DGVM average (Figure 2.4), with the correlation coefficient (R) ranging from 0.88 (BESS) to 0.95 (CFix) (Figure 2.5); these results mean that these RS-based models have a comparable ability to capture the spatial variations in GPP, at least at the same level as the DGVM.

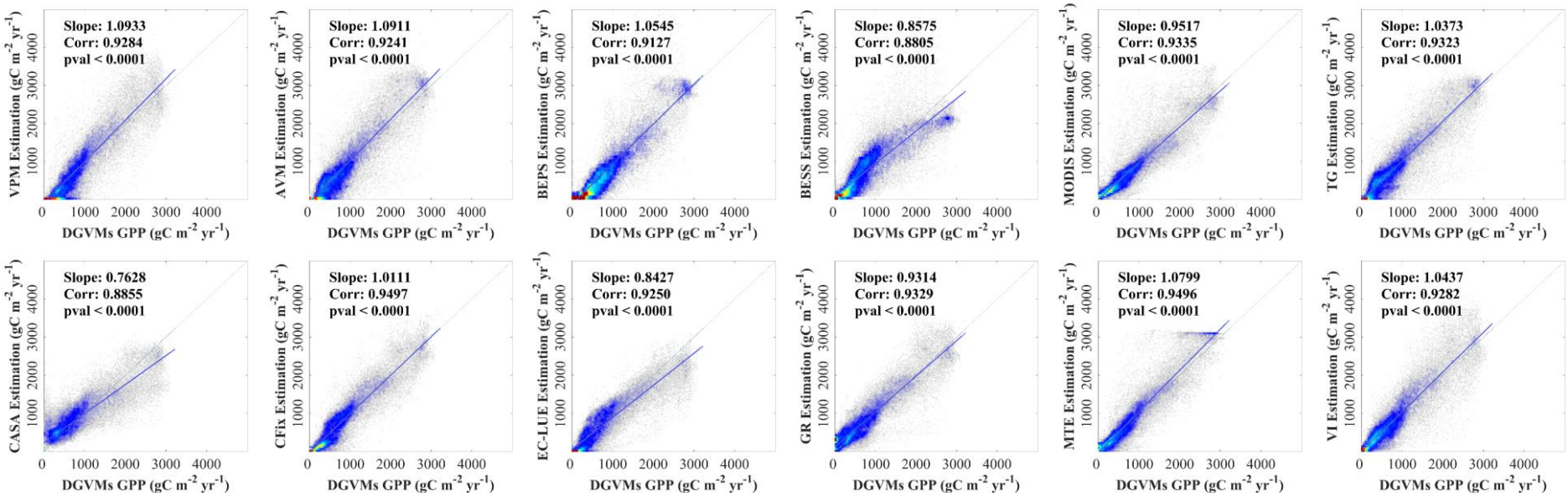

Figure 2.5 Annual averaged GPP comparison against DGVMs for different models.

However, the above results should be treated with caution because a small total difference can mask compensation of biases, which has been illustrated in the cumulative frequency distribution of GPP (Figure 2.6). As shown in Figure 2.6, the grids of global GPP, which are larger than 2000 gC m^{-2} $year^{-1}$, as estimated by BESS, CASA and EC-LUE, are few, while the other nine models show that at least 10 % of the global grids have GPP larger than 2200 gC m^{-2} $year^{-1}$. In addition, I also compared the estimates of 12 models at the site-scale (Figure S1).

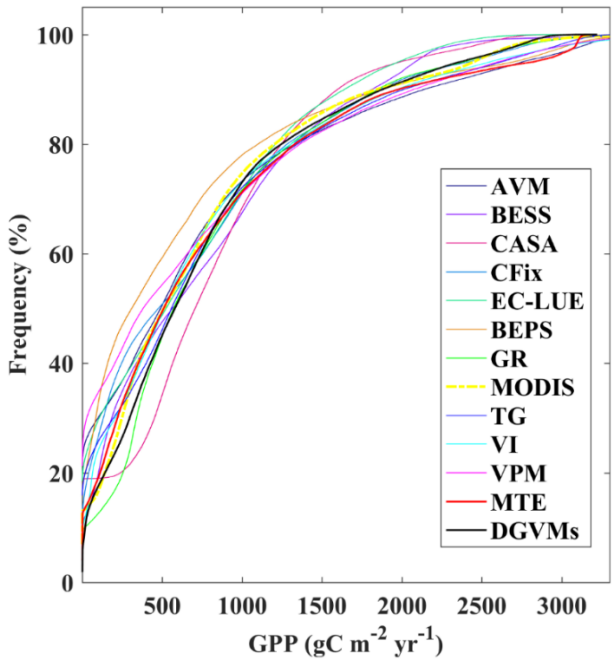

Figure 2.6 Cumulative frequency distribution for averaged GPP at each 0.5° × 0.5° pixel over global land estimated by each model during 2000-2014.

The performances of the 12 models varied among the sites (Figure S1), but generally, all the models basically captured the magnitudes of the daily GPP variations and the seasonal cycles (Figure 2.7).

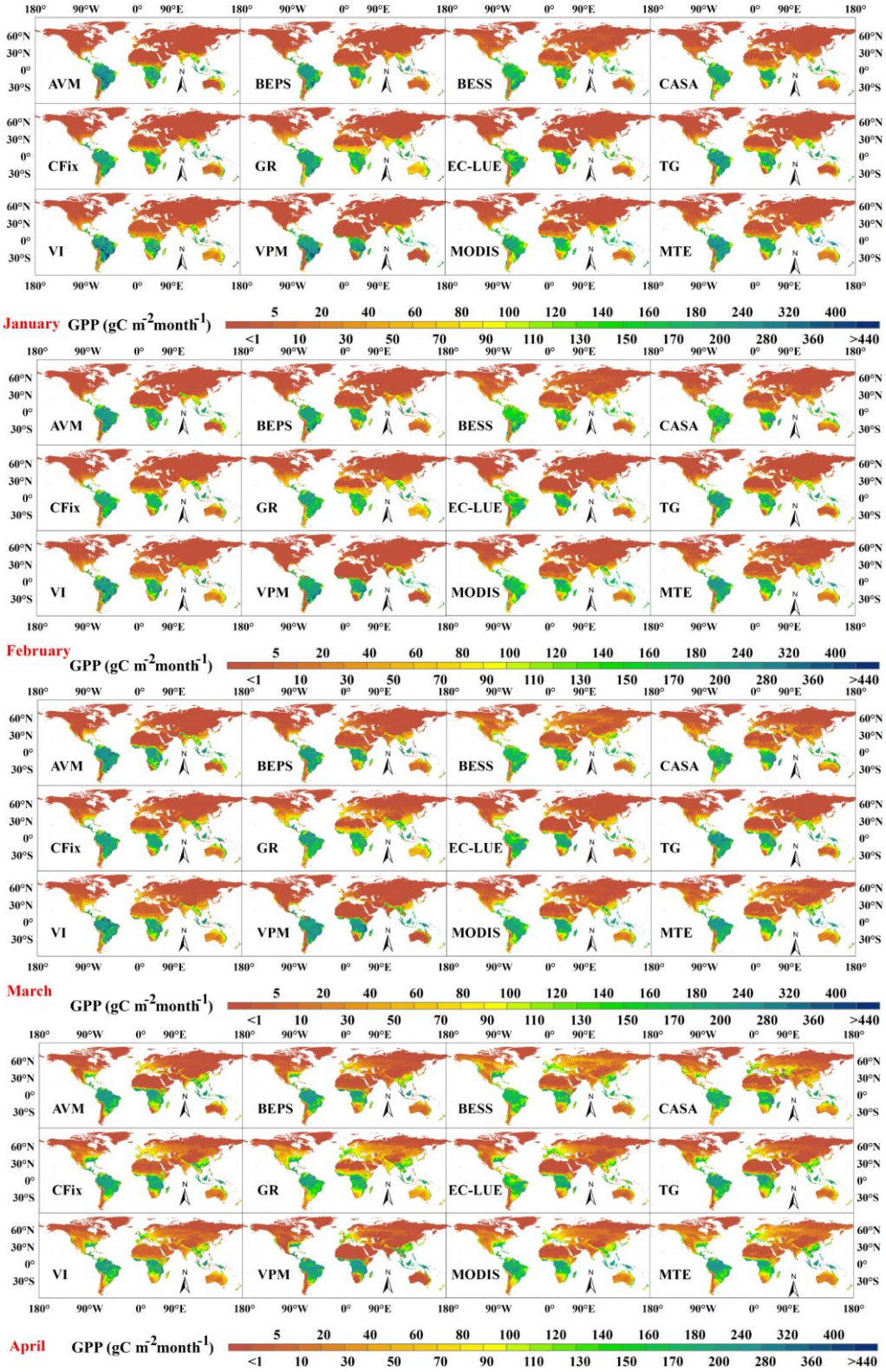

Figure 2.7-a Monthly global GPP estimation by each model.

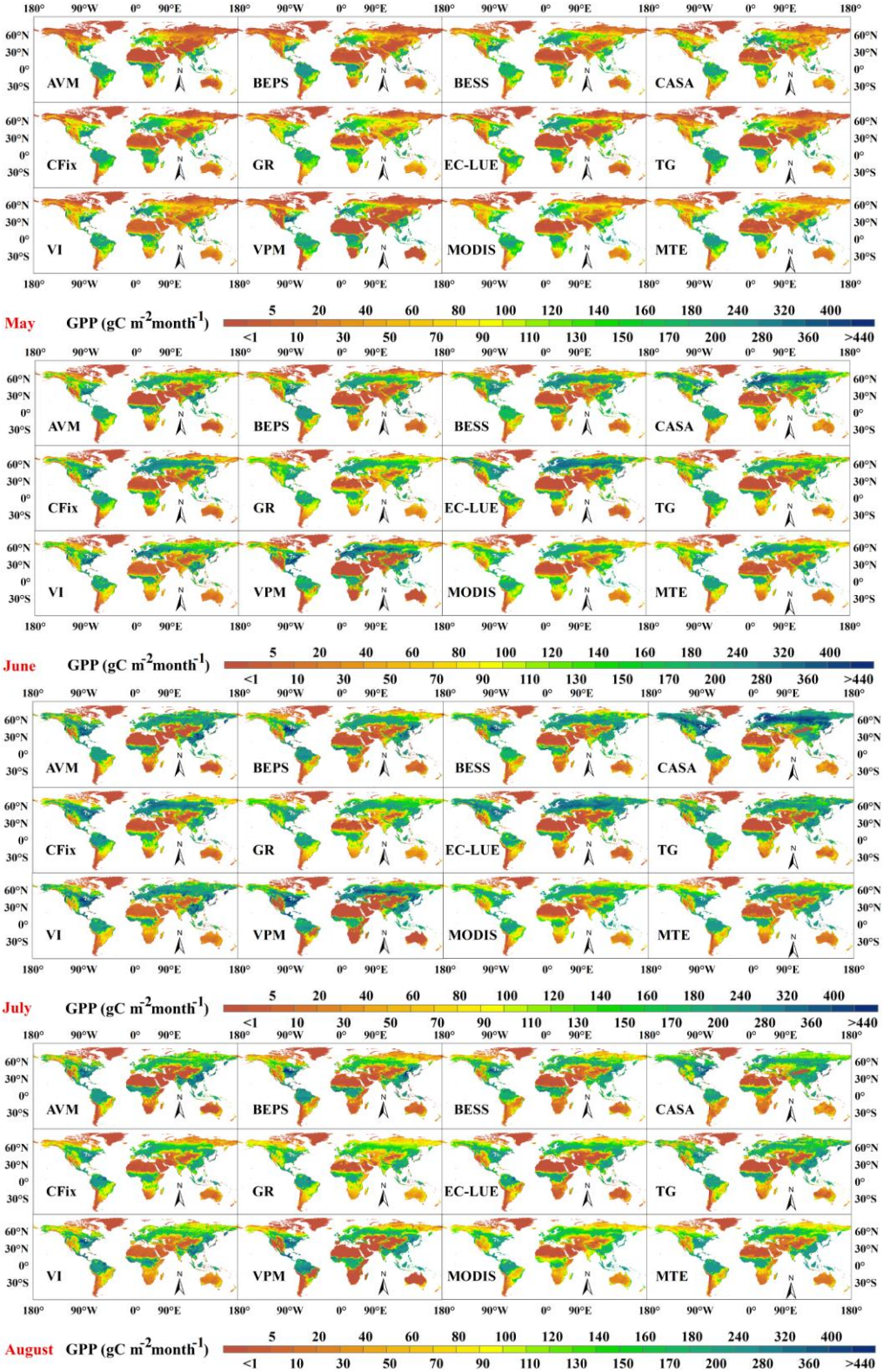

Figure 2.7-b Monthly global GPP estimation by each model.

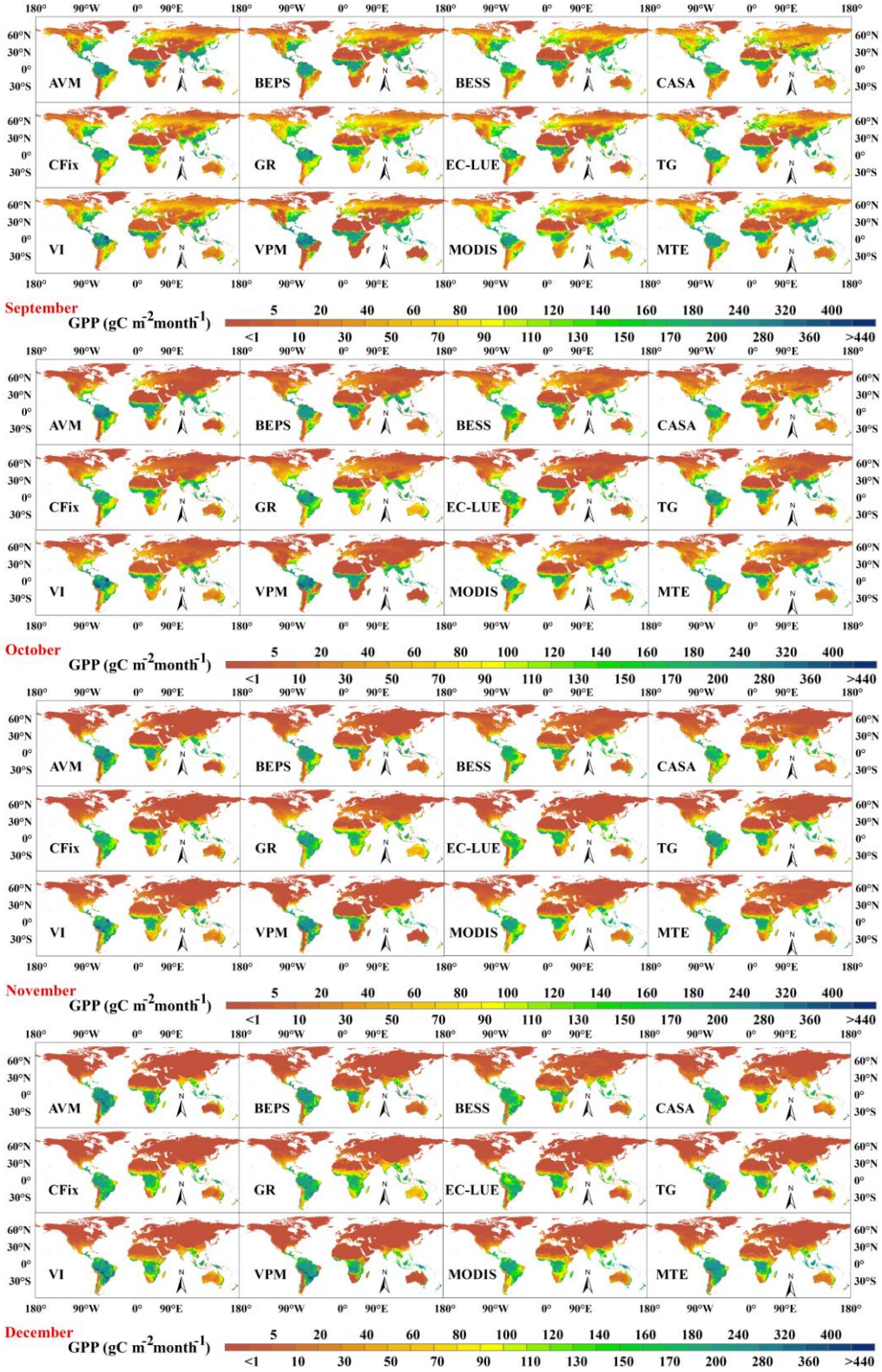

Figure 2.7-c Monthly global GPP estimation by each model.

For the mean seasonal cycle of GPP at the global scale, all models showed similar variations, with only CASA having a sharper transition during the boreal summer (Figure S8).

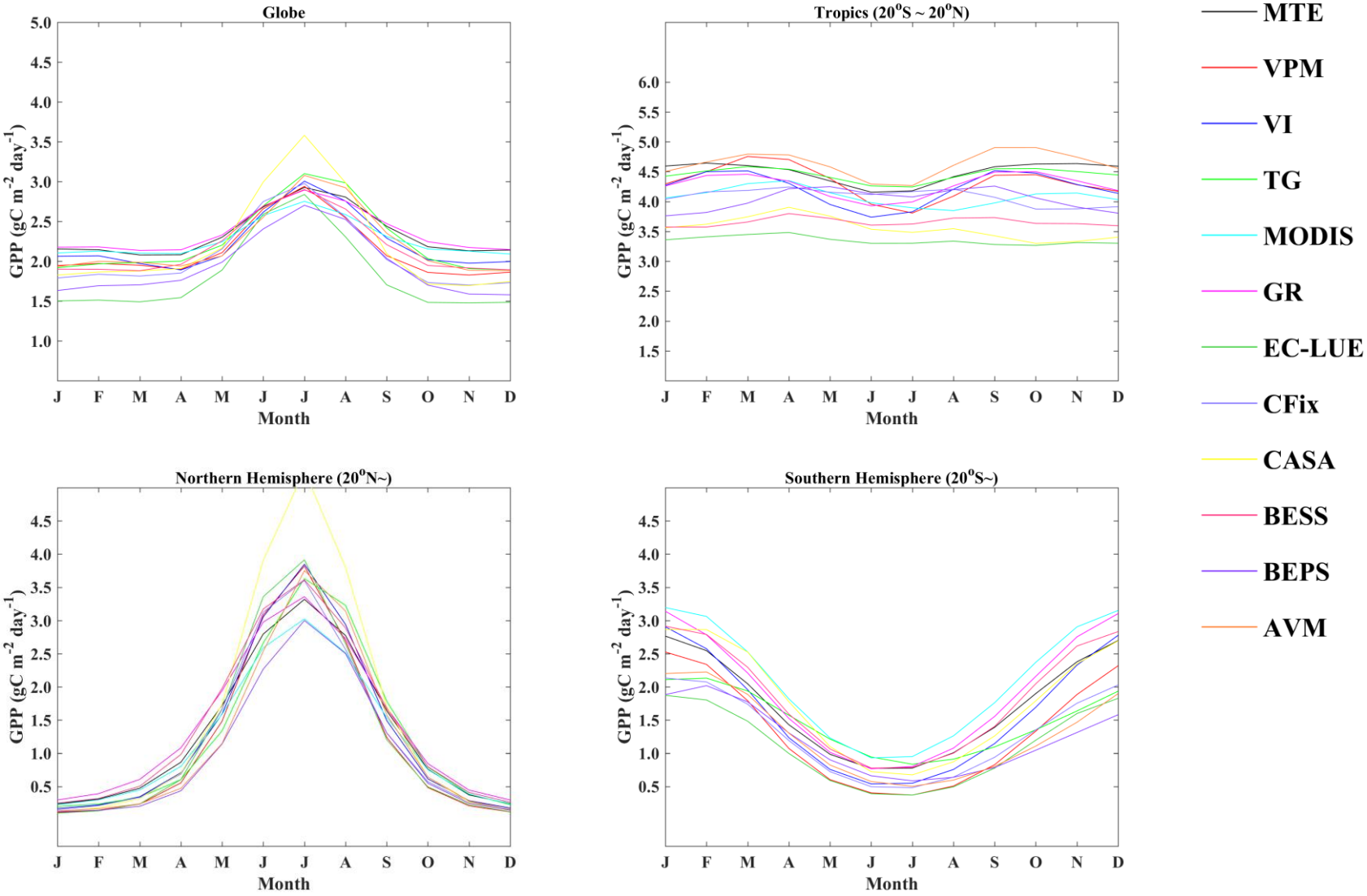

Figure 2.8 Comparison of seasonal variations in GPP among the different models.

Given the anti-phase of GPP between hemispheres, I also investigated the seasonal cycle of GPP over three subdomains (Figure 2.8): in the Northern Hemisphere (~20°N), characterized by a strong seasonality, all models estimated the small values during the boreal winter and the large values during the boreal summer, with R above 0.9; in the Southern Hemisphere (~20°S), characterized by an opposite seasonality to that of the Northern Hemisphere but with weaker amplitudes. All models showed similar seasonal variations, and among them, the minimum R of 0.86 appeared between BEPS and GR. Remarkable differences were found in the tropical regions (20°N~20°S), where the R between models was low or even negative (Figure 2.8); additionally, the tropical areas were characterized by low seasonality. In this study, I used the detrended GPP anomalies to evaluate the interannual GPP variations among different models (Figure 2.9). The interannual GPP variations of VI, VPM, TG, GR, BEPS, AVM and CASA showed a significant similar pattern with the R above 0.7, while that of the other models showed a moderate (or lower) correlation. No model showed an isolated result, and any model had a medium (or above) correlation with at least three other models. Among them, BESS showed a relatively independent performance but had the strongest correlation with MTE.

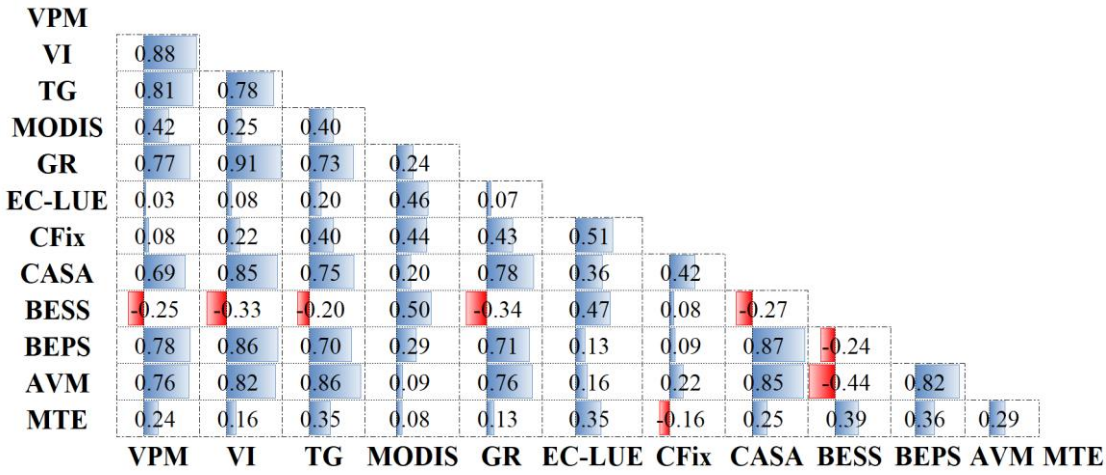

Figure 2.9 The correlation matrixes display correlation coefficient in pairs among detrended GPP anomalies estimated by the different models during 2000-2014.

The linear GPP trends over 2000-2014 were computed for each model using linear regression analysis (Figure 2.10). All the models estimated the increasing trend of GPP. The strongest trends were found in BEPS (0.888), AVM (0.807), TG (0.741), CFix (0.652) and BESS (0.654) (PgC year^{-1}), and the driving factors of these models led me to hypothesize that the positive responses of plants to both increasing atmospheric CO_2 concentration and temperature were the main reasons for the increasing GPP. This hypothesis is further discussed in the next section. Conversely, MTE and MODIS estimated the lowest GPP trends.

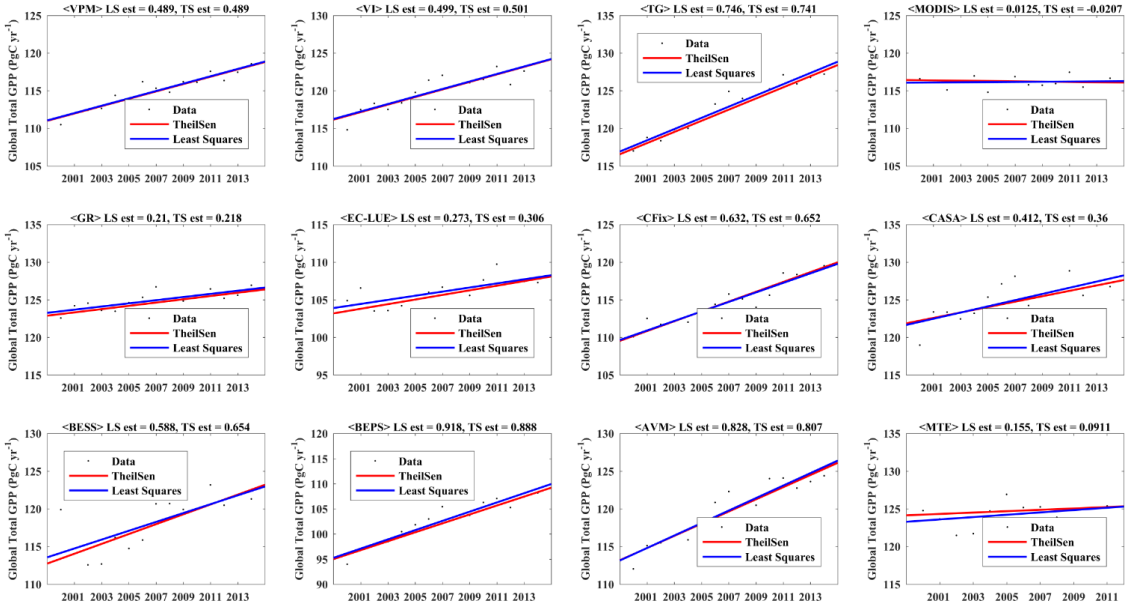

Figure 2.10 Long-term trends of GPP estimations by different models.

2.3.1 Discussion on SIF_GPP model

2.3.1.1 Estimation and distribution of GPP

I used GPP data from 45 eddy flux sites that comprised the Fluxnet 2015 dataset (Table 2.3). I extracted SIF data based on the coordinates of each EC tower site and averaged these to calculate the monthly means to minimize uncertainties arising from the different spatial scales of the SIF and GPP data (Guanter et al. 2014). A simple regression model was used to investigate the correlation between SIF and GPP. The scatter plots and regression lines between SIF and GPP are presented in Figure 2.11 for the PFTs. Collectively, there were no significant systematic errors in the model predictions shown in Table 2.4. Individually, the coefficients of correlation varied from 0.61 (ENF) to 0.96 (DBF), all of which were statistically significant at $p<0.001$ except for DNF ($p=0.0012$). Since the relationships for each vegetation type were stronger or strong, I used the relationships to scale GPP from the tower footprint to the global scale. To avoid signal contamination from urban or ocean areas, nearby pixels that fulfilled the homogeneity criteria were also extracted for six sites (shown in Figure 2.12).

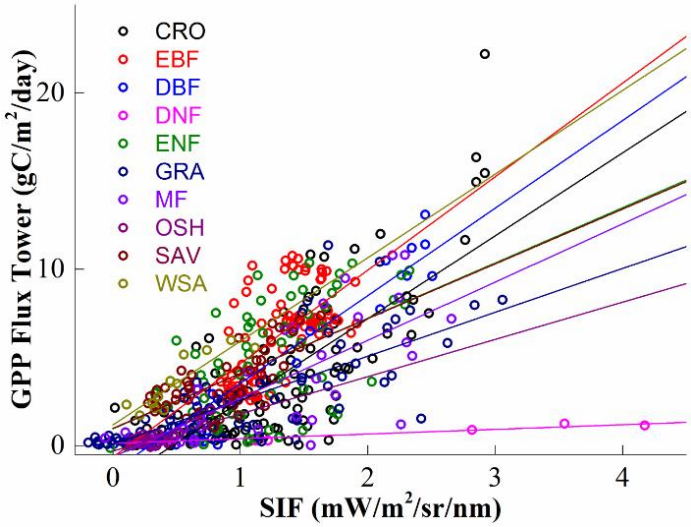

Figure 2.11 Relationship between monthly mean SIF obtained from GOME-2 and monthly mean GPP obtained from the Fluxnet 2015 dataset.

Table 2.4 Regression models between GPP and SIF for different ecosystems. Number is the number of samples used to calculate the relationship. Pearson's r is the Pearson correlation coefficient. Adj. R^2 is the adjusted R^2 value, i.e., the coefficient of determination.

	CRO	EBF	DBF	DNF	ENF	GRA	MF	OSH	SAV	WSA
Number	117	84	24	7	74	88	36	24	48	12
Pearson's r	0.7647	0.6187	0.9620	0.9479	0.6092	0.7745	0.7462	0.7567	0.7041	0.8890
Adj. R^2	0.5812	0.3753	0.9221	0.8782	0.3624	0.5952	0.5438	0.5531	0.4848	0.7693
p-value	0.0000	0.0000	0.0000	0.0012	0.0000	0.0000	0.0000	0.0000	0.0000	0.0001
Slope	4.7014	5.3008	4.9665	3.4092	3.1346	2.4879	3.3035	2.1095	3.1091	4.7411
Intercept	-2.1979	-0.6465	-1.4246	-0.2623	0.9582	0.0986	-0.6319	-0.3030	0.9837	1.1815

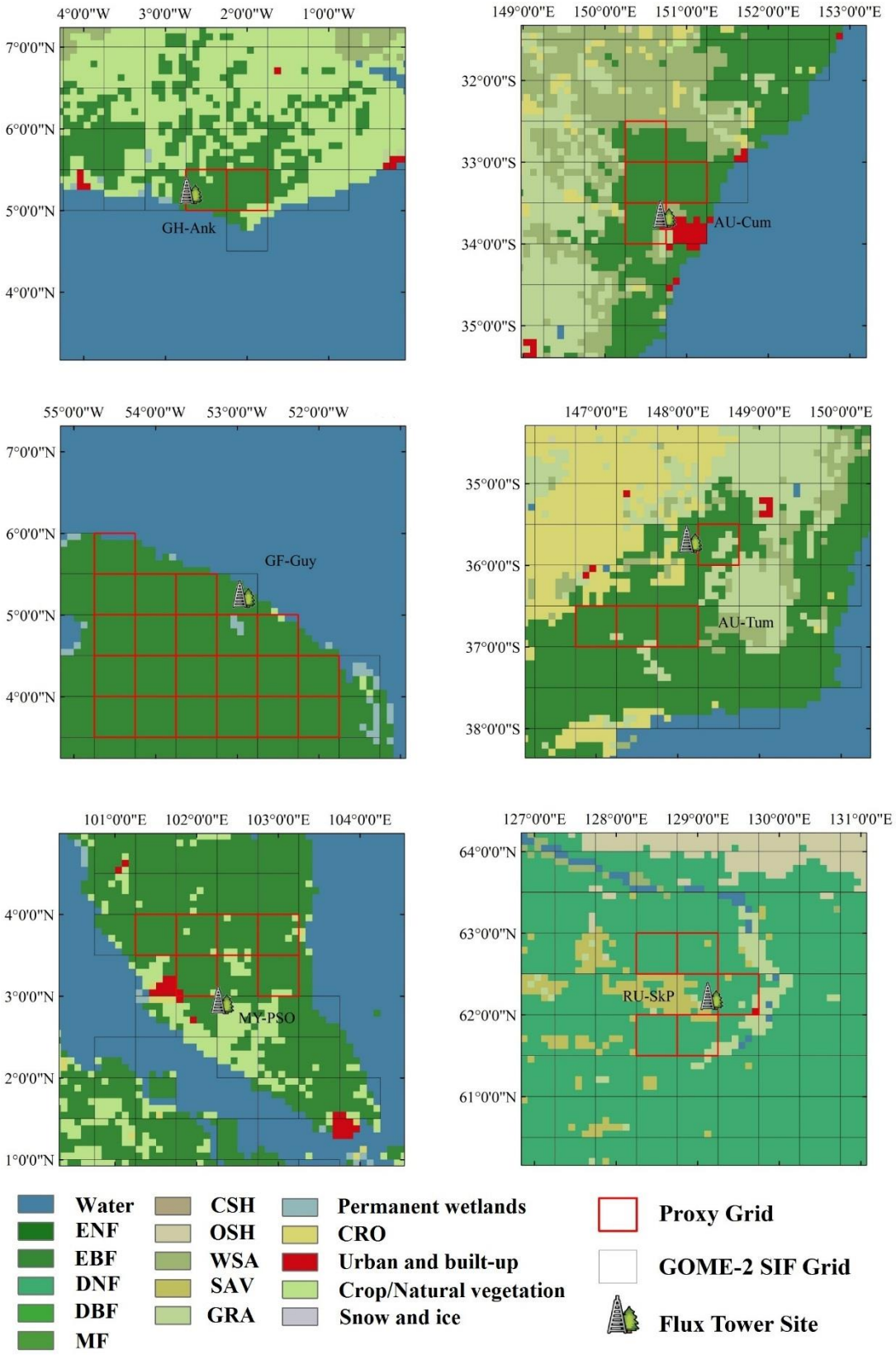

Figure 2.12 The selection of nearby grids to represent the impacted sites (sea effects: GH-Ank, AU-Cum, GF-Guy, MY-PSO; urban effects: AU-Cum, MY-PSO; vegetation effects: RU-SkP; South Atlantic Anomaly effects: GF-Guy).

Figure 2.13 shows the spatial distribution of multi-annual average GPP estimated in this study from 2007 to 2014. The figure shows that the highest GPP is found in the rainforest in the Intertropical Convergence Zone (ITCZ) (e.g., the Amazon Rainforest, Congo Rainforest, and Indonesia), with estimates of over 3000 g C m^{-2} $year^{-1}$, followed by monsoon subtropical regions (e.g., southeastern Asia, Central America), with values that exceed 2000 g C m^{-2} $year^{-1}$, and humid temperate regions in eastern North America and western and central Europe, with GPP values of approximately 1500 g C m^{-2} $year^{-1}$. Low GPP values occur in regions with adverse conditions, such as high-altitude regions (e.g., Tibetan Plateau), high latitude areas (e.g., northern Canada, North Russia), those characterized by short growing seasons due to low temperature, and dry areas (e.g., Sahara, Taklamakan, Arabian deserts) which are limited by water availability.

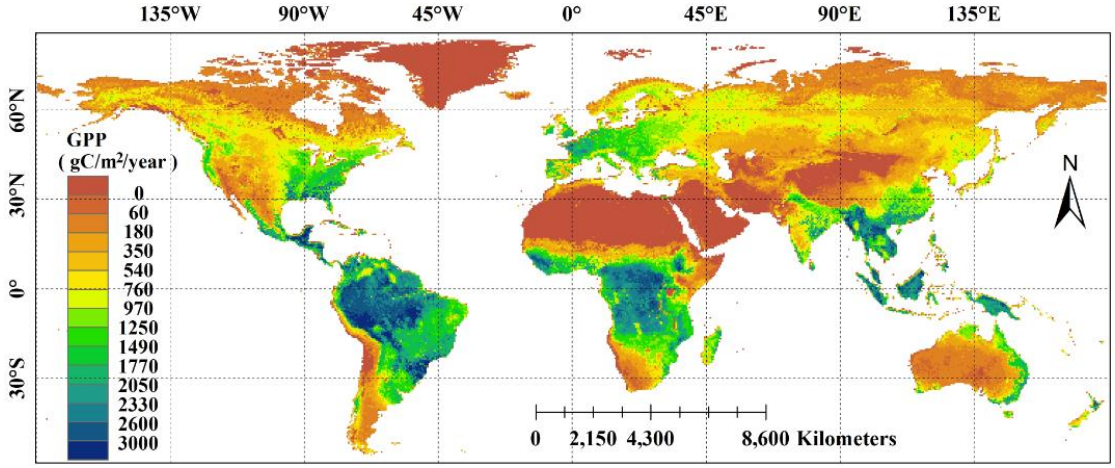

Figure 2.13 Global spatial distribution of estimated annual GPP.

Figure 2.14 shows considerable seasonal variations, especially in the Northern Hemisphere, with high GPP estimates in summer and low values during winter. The GPP in tropical rainforest areas is relatively high throughout the year, and changes in values correspond to seasonal changes, i.e., wet and dry seasons. However, in summer, the maximum monthly GPP of temperate forests exceeds that of tropical forests.

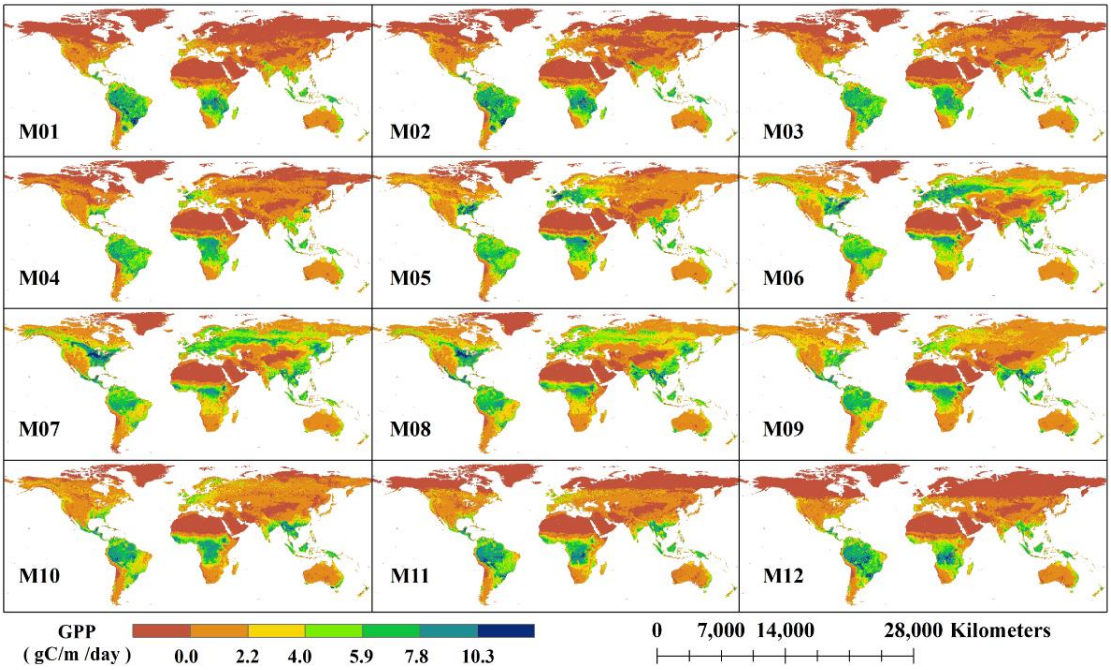

Figure 2.14 Global spatial distribution of estimated monthly GPP (M: Month (i.e., M06: June)).

Collectively, the spatial patterns of multi-annual average GPP and monthly GPP are consistent with those of numerous other models (Figure 2.7). The estimated GPP correctly captured the patterns at the global scale. For example, the GPP patterns over North America show considerable East-West differences, boreal forests exhibit a typical longitudinal gradient in Northern Eurasia and GPP decreases eastward as a consequence of increasing continental climatic patterns, and South America lies mainly in a tropical climate zone with relatively high GPP except for the Andes in western South America. Since light intensity, illumination time, and temperature considerably affect photosynthesis, monthly GPP latitudinal variations that follow solar insolation and temperature variations are evident at the global scale.

2.3.1.2 Accuracy assessment of GPP estimates

In this part, I estimated a series of monthly global GPP at a spatial resolution of 0.5°, which is larger than the footprint size of ground-based observations. Hence, I relied on the model and other remotely sensed data for a comparison on the global scale. As a benchmark, I compared the estimates against the MTE model GPP from 2007 to 2011 (Jung et al., 2011) because it is based on direct EC flux tower measurements of GPP and is thus considered close to the truth where the flux tower density is high (Beer et al., 2010; Frankenberg et al., 2011). MODIS GPP products from 2007 to 2016 were also used because MODIS products have been widely known and used (Turner et al., 2006; Zhao and Running, 2010; Frankenberg et al., 2011). For the annual GPP, I found a strong linear spatial correlation between the estimated GPP with model-based and remotely sensed GPP data shown in Figure 2.15 The estimated GPPs are highly consistent with MTE and MODIS products; thus, the estimated GPP in the present study can be used in GPP estimations.

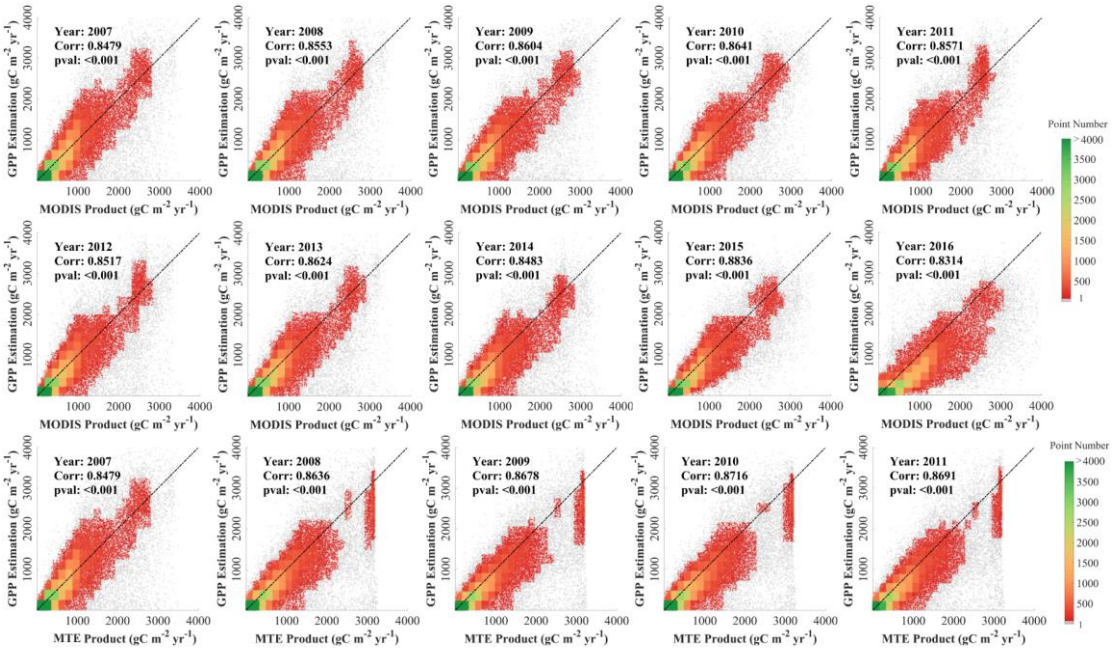

Figure 2.15 Accuracy assessment of GPP by comparing with MODIS and MTE GPPs.

2.3.1.3 Uncertainties of SIF_GPP model

Although estimating GPP is not the focus in the thesis, it is worthwhile to further analyze the limitations of GPP_{SIF} (the estimates of GPP based on SIF) to provide information on the uncertainties. Here, I discussed the sources of uncertainties in GPP_{SIF} at a global scale from the aspects of input data and methods.

For the Fluxnet 2015 dataset, although the GPP recorded at the flux towers was treated in this study as "observed", these data include the advantages, disadvantages and assumptions of the original net ecosystem exchange (NEE) observations. Uncertainties in the GPP derived from flux tower measurements have been calculated by (Schaefer et al., 2012). Due to the lack of surface energy balance closure, the threshold used to filter ecosystem respiration under stable conditions, the hypothesis that the entire system temperature is equal to air temperature and the factors that control ecosystem respiration such as soil moisture have not been included in the partitioning algorithm, which may result in errors in the observed GPP. The complete set of uncertainties includes i) contributions from random errors, which account for the greatest contribution, ~50% (winter) and ~90% (summer) of total uncertainties, ii) friction velocity uncertainties and iii) partitioning uncertainties, which depend on the variance generated by the different partitioning algorithms (Desai et al., 2008). I discarded values that were less than or equal to zero. Consequently, many sites were not included for the calculation of the GPP-SIF relationship.

With respect to the GOME-2 SIF data, it has been explicitly reported that the v26 products have undergone only limited validation (Yang et al., 2015). Due to instrumental (e.g., instruments degrade significantly during their lifetime (Joiner et al., 2016)) and algorithmic effects, temporal variations may not be recommended for long-term analysis. Clouds and aerosol are present in nearly every single observation despite the following: various filters have been applied to the monthly average products to reduce the shielding effects of cloud contamination and aerosols, a relatively large footprint of approximately 40 km × 80 km (40 km × 40 km after 15 July 2003) was used, and cloud fractions have been reduced to 30%. At high latitudes, owing to very high solar zenith angles (>70°), fluorescence will be slightly

positive or negative, resulting in very large uncertainties. According to Joiner et al. (2013), GOME-2 errors are generally higher over South America compared with other areas due to the South Atlantic Anomaly (SAA). Nevertheless, given the objectives of this study, the GOME-2 SIF dataset is the most appropriate choice among the SIF datasets.

Most of the flux towers used in this study are located in the Northern Hemisphere, especially Europe and North America (Table 2.3); therefore, there are large uncertainties for regions that are poorly covered by a limited number of flux sites (e.g., tropical areas, Siberia, South America). In order to avoid signal contamination from ocean, desert or urban areas, we extracted SIF data from a nearby pixel or used average values of nearby pixels fulfilling the homogeneity criteria (Guanter et al., 2014). For example, the GF-Guy site was established near the Atlantic Ocean; thus, the SIF grid in which the site is located is not pure EBF; rather, it is a combination of sea water and EBF (Figure 2.12). I selected the closest valid pixels within a region of 7 × 7 pixels (smaller than $5.5^{o} \times 5.5^{o}$) (Duveiller and Cescatti 2016), to calculate the averages to represent the SIF values for the GF-Guy site. Although this method can reduce signal contamination, imperfect points may result in other uncertainties. Even though the PFTs are the same, the different spatial scales of the SIF retrievals and the flux tower data may result in a mixed signal sampled within the GOME-2 footprint. For example, the PFT of the site, US-Ne3, is croplands, but both soybean and corn fields exist in one GOME-2 grid, so the SIF signal is mixed. To reduce this type of uncertainty, I used the averages for each month to calculate the relationship between GPP and SIF. While I calculated the relationship between GPP and SIF according to the PFTs, relationships with the same PFT exhibited large differences, e.g., both corn (C4 species) and soybean (C3 species) are crops, but their relationships are different, and estimations will result in uncertainties. In addition, different correction parameters between GPP and SIF for different sites or pixels of the same PFT also increase the uncertainty. Several hypotheses must be formulated to estimate GPP from the linear relationship with SIF. For example, the sampling time of GOME-2 is approximately 9:30 am local time, and under the light intensities at this time, I assumed that a linear relationship between SIF and GPP would be valid for each ecosystem. However, I do not know whether every sampling period satisfies the hypotheses. This is also one source of uncertainty. The SIF data showed a significantly ($p < 0.01$) positive correlation with GPP in all ecosystems. Among the relationships between SIF and GPP for each PFT, only ENF and EBF did not exhibit strong correlations; the correlation coefficients were 0.61 and 0.62, respectively. The moderate correlation with ENF can be explained by the different spatial scales of the footprints of GOME-2 and the flux tower: the PFT in the Fluxnet 2015 dataset is ENF, whereas the land cover product indicated that a large component is MF. I selected the flux sites by using homogeneity criteria, while for the forest ecosystems, MF was not subjected to the heterogeneity calculation because the number of valid flux sites was too small to perform the statistical analysis. Therefore, there were a large number of mixed MF signals in the pixels in which the ENF flux towers were located, e.g., the ENF sites such as FI-Hyy, RU-Fyo, CA-BK1, DE-Wet and De-Lkb had high proportions of MF. The moderate correlation of EBF can be explained by cloud contamination. EBF consists mainly of rainforests distributed in tropical regions characterized by high levels of cloud cover.

2.4 Conclusions

RS-based models play a significant role in estimating and monitoring terrestrial ecosystem GPP. Several RS-based GPP models have been developed using different criteria, yet the sensitivities to environmental factors vary among models; thus, the comparison of model sensitivity is necessary for analyzing and interpreting results and for choosing suitable models. In this part, we evaluated and compared the GPP estimated by 12 RS-based GPP models and benchmarked these estimates against the GPP measured at flux tower sites which longer than 12 years as well as the results estimated by dynamic global vegetation models (DGVM). The comparison among models and the comparison of models against observations helps document their strengths and weaknesses under current conditions and can also identify heuristic constraints about their applicable conditions and scopes. There is no model showing an isolated estimation in the spatial distribution, seasonal variation and interannual variation of GPP. Vegetation indices (VI) and light use efficiency (LUE) models, relatively simpler form and fewer parameters, can perform as well as complex physiological process models on GPP estimating. And we detailed described, discussed and explained the distinctions among the models and its reasons in Chapter 5. All the models show the similar distribution the largest annual GPP occur in the tropics where the model estimates more than 3300 gC m^{-2} $year^{-1}$, with a lower amplitude responding the alternation of wetter and drier seasons. But the maximum monthly GPP in tropical forest is exceeded by forest in the temperature zone in June with closing to 400 gC m^{-2} $month^{-1}$. The monthly global GPP estimates are low during the northern hemisphere's winter and high during its summer. Regarding on the trend of GPP, the models with inputting atmospheric CO_2 concentration data show more significantly.

References

Asner, G.P.; Wessman, C.A.; Archer, S. Scale dependence of absorption of photosynthetically active radiation in terrestrial ecosystems. *Ecological Applications* **1998**, *8*, 1003-1021.

Ballantyne, A.P.; Alden, C.B.; Miller, J.B.; Tans, P.P.; White, J.W. Increase in observed net carbon dioxide uptake by land and oceans during the past 50 years. *Nature* **2012**, *488*, 70-72.

Beck, P.S.; Goetz, S.J. Satellite observations of high northern latitude vegetation productivity changes between 1982 and 2008: ecological variability and regional differences. *Environmental Research Letters* **2011**, *6*, 045501.

Beer, C.; Reichstein, M.; Tomelleri, E.; Ciais, P.; Jung, M.; Carvalhais, N.; Rodenbeck, C.; Arain, M.A.; Baldocchi, D.; Bonan, G.B., et al. Terrestrial gross carbon dioxide uptake: global distribution and covariation with climate. *Science* **2010**, *329*, 834-838.

Beerling, D.J. Gas valves, forests and global change: a commentary on Jarvis (1976) 'The interpretation of the variations in leaf water potential and stomatal conductance found in canopies in the field'. *Philos T R Soc B* **2015**, *370*.

Best, M.J.; Pryor, M.; Clark, D.B.; Rooney, G.G.; Essery, R.L.H.; Menard, C.B.; Edwards, J.M.; Hendry, M.A.; Porson, A.; Gedney, N., et al. The Joint UK Land Environment Simulator (JULES), model description - Part 1: Energy and water fluxes. *Geoscientific Model Development* **2011**, *4*, 677-699.

Bonan, G.B.; Doney, S.C. Climate, ecosystems, and planetary futures: The challenge to predict life in Earth system models. *Science* **2018**, *359*.

Bondeau, A.; Smith, P.C.; Zaehle, S.; Schaphoff, S.; Lucht, W.; Cramer, W.; Gerten, D.; Lotze-Campen, H.; Muller, C.; Reichstein, M., et al. Modelling the role of agriculture for the 20th century global terrestrial carbon balance. *Global Change Biology* **2007**, *13*, 679-706.

Chang, J.F.; Ciais, P.; Wang, X.H.; Piao, S.L.; Asrar, G.; Betts, R.; Chevallier, F.; Dury, M.; Francois, L.; Frieler, K., et al. Benchmarking carbon fluxes of the ISIMIP2a biome models. *Environmental Research Letters* **2017**, *12*.

Chen, J.; Liu, J.; Cihlar, J.; Goulden, M. Daily canopy photosynthesis model through temporal and spatial scaling for remote sensing applications. *Ecological modelling* **1999**, *124*, 99-119.

Chen, J.M.; Menges, C.H.; Leblanc, S.G. Global mapping of foliage clumping index using multi-angular satellite data. *Remote Sensing Of Environment* **2005**, *97*, 447-457.

Chiesi, M.; Fibbi, L.; Genesio, L.; Gioli, B.; Magno, R.; Maselli, F.; Moriondo, M.; Vaccari, F.P. Integration of ground and satellite data to model Mediterranean forest processes. *International Journal of Applied Earth Observation and Geoinformation* **2011**, *13*, 504-515.

Collatz, G.J.; Ribas-Carbo, M.; Berry, J.A. Coupled Photosynthesis-Stomatal Conductance Model for Leaves of C4 Plants. *Aust J Plant Physiol* **1992**, *19*, 519-538.

Cramer, W.; Kicklighter, D.W.; Bondeau, A.; Moore, B.; Churkina, G.; Nemry, B.; Ruimy, A.; Schloss, A.L.; Intercompariso, P.P.N.M. Comparing global models of terrestrial net primary productivity (NPP): overview and key results. *Global Change Biology* **1999**, *5*, 1-15.

Deng, F.; Chen, J.M.; Plummer, S.; Chen, M.; Pisek, J. Algorithm for global leaf area index retrieval using satellite imagery. *IEEE Transactions on Geoscience and Remote Sensing* **2006**, *44*, 2219-2229.

Desai, A.R.; Richardson, A.D.; Moffat, A.M.; Kattge, J.; Hollinger, D.Y.; Barr, A.; Falge, E.; Noormets, A.; Papale, D.; Reichstein, M., et al. Cross-site evaluation of eddy covariance GPP and RE decomposition techniques. *Agricultural And Forest Meteorology* **2008**, *148*, 821-838.

Dury, M.; Hambuckers, A.; Warnant, P.; Henrot, A.; Favre, E.; Ouberdous, M.; François, L. Responses of European forest ecosystems to 21 (st) century climate: assessing changes in interannual variability and fire intensity. *iForest: Biogeosciences and Forestry* **2011**, *4*, 82-99.

Duveiller, G.; Cescatti, A. Spatially downscaling sun-induced chlorophyll fluorescence leads to an improved temporal correlation with gross primary productivity. *Remote Sensing of Environment* **2016**, *182*, 72-89.

Erbs, D.G.; Klein, S.A.; Duffie, J.A. Estimation Of the Diffuse-Radiation Fraction for Hourly, Daily And Monthly-Average Global Radiation. *Sol Energy* **1982**, *28*, 293-302.

Fang, H.L.; Liang, S.L.; Townshend, J.R.; Dickinson, R.E. Spatially and temporally continuous LAI data sets based on an integrated filtering method: Examples from North America. *Remote Sensing Of Environment* **2008**, *112*, 75-93.

Farquhar, G.v.; von Caemmerer, S.v.; Berry, J. A biochemical model of photosynthetic CO2 assimilation in leaves of C3 species. *Planta* **1980**, *149*, 78-90.

Flexas, J.; Briantais, J.-M.; Cerovic, Z.; Medrano, H.; Moya, I. Steady-state and maximum chlorophyll fluorescence responses to water stress in grapevine leaves: a new remote sensing system. *Remote Sensing of Environment* **2000**, *73*, 283-297.

Frankenberg, C.; Fisher, J.B.; Worden, J.; Badgley, G.; Saatchi, S.S.; Lee, J.E.; Toon, G.C.; Butz, A.; Jung, M.; Kuze, A., et al. New global observations of the terrestrial carbon cycle from GOSAT: Patterns of plant fluorescence with gross primary productivity. *Geophysical Research Letters* **2011**, *38*.

Friedl, M.A.; Sulla-Menashe, D.; Tan, B.; Schneider, A.; Ramankutty, N.; Sibley, A.; Huang, X.M. MODIS Collection 5 global land cover: Algorithm refinements and characterization of new datasets. *Remote Sensing Of Environment* **2010**, *114*, 168-182.

Friedlingstein, P.; Cox, P.; Betts, R.; Bopp, L.; von Bloh, W.; Brovkin, V.; Cadule, P.; Doney, S.; Eby, M.; Fung, I. Climate–carbon cycle feedback analysis: results from the C4MIP model intercomparison. *Journal of climate* **2006**, *19*, 3337-3353.

Gitelson, A.A.; Vina, A.; Verma, S.B.; Rundquist, D.C.; Arkebauer, T.J.; Keydan, G.; Leavitt, B.; Ciganda, V.; Burba, G.G.; Suyker, A.E. Relationship between gross primary production and chlorophyll content in crops: Implications for the synoptic monitoring of vegetation productivity. *J Geophys Res-Atmos* **2006**, *111*.

Goudriaan, J. Crop micrometeorology: a simulation study. Pudoc, 1977.

Guanter, L.; Frankenberg, C.; Dudhia, A.; Lewis, P.E.; Gómez-Dans, J.; Kuze, A.; Suto, H.; Grainger, R.G. Retrieval and global assessment of terrestrial chlorophyll fluorescence from GOSAT space measurements. *Remote Sensing of Environment* **2012**, *121*, 236-251.

Guanter, L.; Zhang, Y.; Jung, M.; Joiner, J.; Voigt, M.; Berry, J.A.; Frankenberg, C.; Huete, A.R.; Zarco-Tejada, P.; Lee, J.E., et al. Global and time-resolved monitoring of crop photosynthesis with chlorophyll fluorescence. *Proc Natl Acad Sci U S A* **2014**, *111*, E1327-1333.

He, L.M.; Chen, J.M.; Pisek, J.; Schaaf, C.B.; Strahler, A.H. Global clumping index map derived from the MODIS BRDF product. *Remote Sensing Of Environment* **2012**, *119*, 118-130.

Henderson-Sellers, A.; Gornitz, V. Possible climatic impacts of land cover transformations, with particular emphasis on tropical deforestation. *Climatic Change* **1984**, *6*, 231-257.

Hilker, T.; Coops, N.C.; Wulder, M.A.; Black, T.A.; Guy, R.D. The use of remote sensing in light use efficiency based models of gross primary production: A review of current status and future requirements. *Science Of the Total Environment* **2008**, *404*, 411-423.

Ito, A.; Oikawa, T. A simulation model of the carbon cycle in land ecosystems (Sim-CYCLE): a description based on dry-matter production theory and plot-scale validation. *Ecological Modelling* **2002**, *151*, 143-176.

Jarvis, P. The interpretation of the variations in leaf water potential and stomatal conductance found in canopies in the field. *Phil. Trans. R. Soc. Lond. B* **1976**, *273*, 593-610.

Jiang, C.; Ryu, Y. Multi-scale evaluation of global gross primary productivity and evapotranspiration products derived from Breathing Earth System Simulator (BESS). *Remote Sensing Of Environment* **2016**, *186*, 528-547.

Joiner, J.; Guanter, L.; Lindstrot, R.; Voigt, M.; Vasilkov, A.P.; Middleton, E.M.; Huemmrich, K.F.; Yoshida, Y.; Frankenberg, C. Global monitoring of terrestrial chlorophyll fluorescence from moderate-spectral-resolution near-infrared satellite measurements: methodology, simulations, and application to GOME-2. *Atmospheric Measurement Techniques* **2013**, *6*, 2803-2823.

Joiner, J.; Yoshida, Y.; Guanter, L.; Middleton, E.M. New methods for the retrieval of chlorophyll red fluorescence from hyperspectral satellite instruments: simulations and application to GOME-2 and SCIAMACHY. *Atmospheric Measurement Techniques* **2016**, *9*, 3939-3967, doi:10.5194/amt-9-3939-2016.

Joiner, J.; Yoshida, Y.; Vasilkov, A.; Schaefer, K.; Jung, M.; Guanter, L.; Zhang, Y.; Garrity, S.; Middleton, E.M.; Huemmrich, K.F., et al. The seasonal cycle of satellite chlorophyll fluorescence observations and its relationship to vegetation phenology and ecosystem atmosphere carbon exchange. *Remote Sensing Of Environment* **2014**, *152*, 375-391.

Joiner, J.; Yoshida, Y.; Vasilkov, A.P.; Yoshida, Y.; Corp, L.A.; Middleton, E.M. First observations of global and seasonal terrestrial chlorophyll fluorescence from space. *Biogeosciences* **2011**, *8*.

Jung, M.; Reichstein, M.; Margolis, H.A.; Cescatti, A.; Richardson, A.D.; Arain, M.A.; Arneth, A.; Bernhofer, C.; Bonal, D.; Chen, J. Global patterns of land-atmosphere fluxes of carbon dioxide, latent heat, and sensible heat derived from eddy covariance, satellite, and meteorological observations. *Journal of Geophysical Research: Biogeosciences* **2011**, *116*.

Kattge, J.; DÍAz, S.; Lavorel, S.; Prentice, I.C.; Leadley, P.; BÖNisch, G.; Garnier, E.; Westoby, M.; Reich, P.B.; Wright, I.J., et al. TRY - a global database of plant traits. *Global Change Biology* **2011**, *17*, 2905-2935

Keenan, T.F.; Prentice, I.C.; Canadell, J.G.; Williams, C.A.; Wang, H.; Raupach, M.; Collatz, G.J. Recent pause in the growth rate of atmospheric CO 2 due to enhanced terrestrial carbon uptake. *Nature communications* **2016**, *7*, 13428.

Kottek, M.; Grieser, J.; Beck, C.; Rudolf, B.; Rubel, F. World map of the Köppen-Geiger climate classification updated. *Meteorologische Zeitschrift* **2006**, *15*, 259-263.

Kowalczyk, E.; Wang, Y.; Law, R.; Davies, H.; McGregor, J.; Abramowitz, G. The CSIRO Atmosphere Biosphere Land Exchange (CABLE) model for use in climate models and as an offline model. *CSIRO Marine and Atmospheric Research Paper* **2006**, *13*, 42.

Lasslop, G.; Reichstein, M.; Papale, D.; Richardson, A.D.; Arneth, A.; Barr, A.; Stoy, P.; Wohlfahrt, G. Separation of net ecosystem exchange into assimilation and respiration using a light response curve approach: critical issues and global evaluation. *Global Change Biology* **2010**, *16*, 187-208.

Lee, J.E.; Berry, J.A.; Tol, C.; Yang, X.; Guanter, L.; Damm, A.; Baker, I.; Frankenberg, C. Simulations of chlorophyll fluorescence incorporated into the Community Land Model version 4. *Global change biology* **2015**, *21*, 3469-3477.

Lentile, L.B.; Holden, Z.A.; Smith, A.M.; Falkowski, M.J.; Hudak, A.T.; Morgan, P.; Lewis, S.A.; Gessler, P.E.; Benson, N.C. Remote sensing techniques to assess active fire characteristics and post-fire effects. *International Journal of Wildland Fire* **2006**, *15*, 319-345.

Li, F.; Wang, X.F.; Zhao, J.; Zhang, X.Q.; Zhao, Q.J. A method for estimating the gross primary production of alpine meadows using MODIS and climate data in China. *International Journal Of Remote Sensing* **2013**, *34*, 8280-8300.

Liang, S.; Goldberg, M.D.; Xiong, X.; Butler, J.J.; Crawford, M.M.; Chen, J.M.; Shi, J.; Loboda, T.V.; Zheng, Q.; Walsh, S.J. *Comprehensive Remote Sensing: Terrestrial Ecosystems*; Elsevier: 2018.

Liang, W.; Yang, Y.; Fan, D.; Guan, H.; Zhang, T.; Long, D.; Zhou, Y.; Bai, D. Analysis of spatial and temporal patterns of net primary production and their climate controls in China from 1982 to 2010. *Agricultural and Forest Meteorology* **2015**, *204*, 22-36.

Liu, J.; Chen, J.M.; Cihlar, J.; Park, W.M. A process-based boreal ecosystem productivity simulator using remote sensing inputs. *Remote Sensing Of Environment* **1997**, *62*, 158-175.

Liu, Y.; Liu, R.; Chen, J.M. Retrospective retrieval of long-term consistent global leaf area index (1981–2011) from combined AVHRR and MODIS data. *Journal of Geophysical Research: Biogeosciences* **2012**, *117*.

Liu Z, W.L., Wang S. Comparison of different GPP models in China using MODIS image and ChinaFLUX data. *Remote Sensing* **2014**, *6*, 10215.

Lobell, D.B.; Asner, G.P.; Ortiz-Monasterio, J.I.; Benning, T.L. Remote sensing of regional crop production in the Yaqui Valley, Mexico: estimates and uncertainties. *Agriculture, Ecosystems & Environment* **2003**, *94*, 205-220.

Lucht, W.; Schaaf, C.B.; Strahler, A.H. An algorithm for the retrieval of albedo from space using semiempirical BRDF models. *IEEE Transactions on Geoscience and Remote Sensing* **2000**, *38*, 977-998.

Ma, J.; Yan, X.; Dong, W.; Chou, J. Gross primary production of global forest ecosystems has been overestimated. *Scientific reports* **2015**, *5*, 10820.

Matsushita, B.; Tamura, M. Integrating remotely sensed data with an ecosystem model to estimate net primary productivity in East Asia. *Remote Sensing Of Environment* **2002**, *81*, 58-66.

Myneni, R.; Williams, D. On the relationship between FAPAR and NDVI. *Remote Sensing of Environment* **1994**, *49*, 200-211.

Norman, J.M. Simulation of microclimates. *Biometeorology in integrated pest management* **1982**, 65-99.

Ollinger, S.V.; Smith, M.-L. Net primary production and canopy nitrogen in a temperate forest landscape: an analysis using imaging spectroscopy, modeling and field data. *Ecosystems* **2005**, *8*, 760-778.

Pan, S.F.; Tian, H.Q.; Dangal, S.R.S.; Ouyang, Z.Y.; Lu, C.Q.; Yang, J.; Tao, B.; Ren, W.; Banger, K.; Yang, Q.C., et al. Impacts of climate variability and extremes on global net primary production in the first decade of the 21st century. *Journal Of Geographical Sciences* **2015**, *25*, 1027-1044.

Pasetto, D.; Arenas-Castro, S.; Bustamante, J.; Casagrandi, R.; Chrysoulakis, N.; Cord, A.F.; Dittrich, A.; Domingo-Marimon, C.; Serafy, G.; Karnieli, A., et al. Integration of satellite remote sensing data in ecosystem modelling at local scales: Practices and trends. *Methods In Ecology And Evolution* **2018**, *9*, 1810-1821.

Paw, K.T.; Gao, W.G. Applications Of Solutions To Non-Linear Energy Budget Equations. *Agricultural And Forest Meteorology* **1988**, *43*, 121-145.

Peng, S.; Ciais, P.; Chevallier, F.; Peylin, P.; Cadule, P.; Sitch, S.; Piao, S.; Ahlström, A.; Huntingford, C.; Levy, P., et al. Benchmarking the seasonal cycle of CO2fluxes simulated by terrestrial ecosystem models. *Global Biogeochemical Cycles* **2015**, *29*, 46-64.

Piao, S.; Fang, J.; Zhou, L.; Ciais, P.; Zhu, B. Variations in satellite-derived phenology in China's temperate vegetation. *Global change biology* **2006**, *12*, 672-685.

Piao, S.; Sitch, S.; Ciais, P.; Friedlingstein, P.; Peylin, P.; Wang, X.; Ahlstrom, A.; Anav, A.; Canadell, J.G.; Cong, N., et al. Evaluation of terrestrial carbon cycle models for their response to climate variability and to CO2 trends. *Glob Chang Biol* **2013**, *19*, 2117-2132.

Potter, C.S.; Randerson, J.T.; Field, C.B.; Matson, P.A.; Vitousek, P.M.; Mooney, H.A.; Klooster, S.A. Terrestrial ecosystem production: a process model based on global satellite and surface data. *Global Biogeochemical Cycles* **1993**, *7*, 811-841.

Pury, D.d.; Farquhar, G. Simple scaling of photosynthesis from leaves to canopies without the errors of big-leaf models. *Plant, cell & environment* **1997**, *20*, 537-557.

Raich, J.; Rastetter, E.; Melillo, J.; Kicklighter, D.; Steudler, P.; Peterson, B.; Grace, A.; Moore, B.; Vorosmarty, C. Potential net primary productivity in South America: application of a global model. *Ecological Applications* **1991**, *1*, 399-429.

Rawlins, M.A.; McGuire, A.D.; Kimball, J.S.; Dass, P.; Lawrence, D.; Burke, E.; Chen, X.; Delire, C.; Koven, C.; MacDougall, A., et al. Assessment of model estimates of land-atmosphere CO2 exchange across Northern Eurasia. *Biogeosciences* **2015**, *12*, 4385-4405.

Reich, P.B.; Hobbie, S.E.; Lee, T.D. Plant growth enhancement by elevated CO2 eliminated by joint water and nitrogen limitation. *Nature Geoscience* **2014**, *7*, 920.

Rienecker, M.M.; Suarez, M.J.; Gelaro, R.; Todling, R.; Bacmeister, J.; Liu, E.; Bosilovich, M.G.; Schubert, S.D.; Takacs, L.; Kim, G.K., et al. MERRA: NASA's Modern-Era Retrospective Analysis for Research and Applications. *Journal Of Climate* **2011**, *24*, 3624-3648.

Roberts, D.A.; Smith, M.O.; Adams, J.B. Green Vegetation, Nonphotosynthetic Vegetation, And Soils In Aviris Data. *Remote Sensing Of Environment* **1993**, *44*, 255-269.

Roujean, J.L.; Leroy, M.; Deschamps, P.Y. A bidirectional reflectance model of the Earth's surface for the correction of remote sensing data. *Journal of Geophysical Research: Atmospheres* **1992**, *97*, 20455-20468.

Running, S.W.; Mu, Q.; Zhao, M.; Moreno, A. Modis Global Terrestrial Evapotranspiration (ET) Product (NASA MOD16A2/A3) NASA Earth Observing System Modis Land Algorithm. *NASA: Washington, DC, USA* **2017**.

Running, S.W.; Zhao, M. Daily GPP and annual NPP (MOD17A2/A3) products NASA Earth Observing System MODIS land algorithm. *MOD17 User's Guide* **2015**.

Ryu, Y.; Baldocchi, D.D.; Black, T.A.; Detto, M.; Law, B.E.; Leuning, R.; Miyata, A.; Reichstein, M.; Vargas, R.; Ammann, C., et al. On the temporal upscaling of evapotranspiration from instantaneous remote sensing measurements to 8-day mean daily-sums. *Agricultural And Forest Meteorology* **2012**, *152*, 212-222.

Ryu, Y.; Baldocchi, D.D.; Kobayashi, H.; van Ingen, C.; Li, J.; Black, T.A.; Beringer, J.; Van Gorsel, E.; Knohl, A.; Law, B.E. Integration of MODIS land and atmosphere products with a coupled-process model to estimate gross primary productivity and evapotranspiration from 1 km to global scales. *Global Biogeochemical Cycles* **2011**, *25*.

Ryu, Y.; Kang, S.; Moon, S.K.; Kim, J. Evaluation of land surface radiation balance derived from moderate resolution imaging spectroradiometer (MODIS) over complex terrain and heterogeneous landscape on clear sky days. *Agricultural And Forest Meteorology* **2008**, *148*, 1538-1552.

Schaaf, C.; Wang, Z. MCD43C3 MODIS/Terra+ Aqua BRDF/Albedo Albedo Daily L3 Global 0.05 Deg CMG V006. In *Technical Report*, NASA EOSDIS Land Processes DAAC: 2015.

Schaaf, C.; Wang, Z. MCD43C3 MODIS/Terra+ Aqua BRDF/Albedo Albedo Daily L3 Global 0.05 Deg CMG V006, NASA EOSDIS Land Processes DAAC. 2015.

Schaefer, K.; Schwalm, C.R.; Williams, C.; Arain, M.A.; Barr, A.; Chen, J.M.; Davis, K.J.; Dimitrov, D.; Hilton, T.W.; Hollinger, D.Y., et al. A model-data comparison of gross primary productivity: Results from the North American Carbon Program site synthesis. *J Geophys Res-Biogeo* **2012**, *117*.

Sellers, P.J.; Tucker, C.J.; Collatz, G.J.; Los, S.O.; Justice, C.O.; Dazlich, D.A.; Randall, D.A. A revised land surface parameterization (SiB2) for atmospheric GCMs. Part II: The generation of global fields of terrestrial biophysical parameters from satellite data. *Journal of climate* **1996**, *9*, 706-737.

Sims D A, R.A.F., Cordova V D. A new model of gross primary productivity for North American ecosystems based solely on the enhanced vegetation index and land surface temperature from MODIS. *Remote Sensing of Environment* **2008**, *112*.

Smith, W.K.; Reed, S.C.; Cleveland, C.C.; Ballantyne, A.P.; Anderegg, W.R.; Wieder, W.R.; Liu, Y.Y.; Running, S.W. Large divergence of satellite and Earth system model estimates of global terrestrial CO 2 fertilization. *Nature Climate Change* **2016**, *6*, 306.

Song, C.H.; Dannenberg, M.P.; Hwang, T. Optical remote sensing of terrestrial ecosystem primary productivity. *Progress In Physical Geography* **2013**, *37*, 834-854.

Sun, Z.Y.; Wang, X.F.; Yamamoto, H.; Tani, H.; Zhong, G.S.; Yin, S.; Guo, E.L. Spatial pattern of GPP variations in terrestrial ecosystems and its drivers: Climatic factors, CO2 concentration and land-cover change, 1982-2015. *Ecological Informatics* **2018**, *46*, 156-165.

Task, G.S.D. Global soil data products CD-ROM contents (IGBP-DIS). *ORNL DAAC* **2014**.

Tian, H.; Chen, G.; Lu, C.; Xu, X.; Hayes, D.J.; Ren, W.; Pan, S.; Huntzinger, D.N.; Wofsy, S.C. North American terrestrial CO 2 uptake largely offset by CH 4 and N 2 O emissions: toward a full accounting of the greenhouse gas budget. *Climatic Change* **2015**, *129*, 413-426.

Traore, A.K.; Ciais, P.; Vuichard, N.; Poulter, B.; Viovy, N.; Guimberteau, M.; Jung, M.; Myneni, R.; Fisher, J.B. Evaluation of the ORCHIDEE ecosystem model over Africa against 25 years of satellite-based water and carbon measurements. *Journal of Geophysical Research: Biogeosciences* **2014**, *119*.

Tucker, C.J.; Pinzon, J.E.; Brown, M.E.; Slayback, D.A.; Pak, E.W.; Mahoney, R.; Vermote, E.F.; El Saleous, N. An extended AVHRR 8-km NDVI dataset compatible with MODIS and SPOT vegetation NDVI data. *International Journal of Remote Sensing* **2005**, *26*, 4485-4498.

Van den Dool, H.; Huang, J.; Fan, Y. Performance and analysis of the constructed analogue method applied to US soil moisture over 1981–2001. *Journal of Geophysical Research: Atmospheres* **2003**, *108*.

Van der Tol, C.; Verhoef, W.; Rosema, A. A model for chlorophyll fluorescence and photosynthesis at leaf scale. *Agricultural and forest meteorology* **2009**, *149*, 96-105.

Veroustraete, F. On the use of a simple deciduous forest model for the interpretation of climate change effects at the level of carbon dynamics. *Ecological modelling* **1994**, *75*, 221-237.

Veroustraete, F.; Sabbe, H.; Eerens, H. Estimation of carbon mass fluxes over Europe using the C-Fix model and Euroflux data. *Remote Sensing of Environment* **2002**, *83*, 376-399.

Verstraeten, W.W.; Veroustraete, F.; Feyen, J. On temperature and water limitation of net ecosystem productivity: Implementation in the C-Fix model. *Ecological Modelling* **2006**, *199*, 4-22.

Walker, A.P., I. Aranda, A.P. Beckerman, H. Bown, L.A. Cernusak, Q.L. Dang, T.F. Domingues, L. Gu, S. Guo, Q. Han, J. Kattge, M. Kubiske, D. Manter, E. Merilo, G.F. Midgley, A. Porte, J.C. Scales, D. Tissue, T. Turnbull, C. Warren, G. Wohlfahrt, F.I. Woodward, and S.D. Wullschleger. **2014**. A Global Data Set of Leaf Photosynthetic Rates, Leaf N and P, and Specific Leaf Area. ORNL DAAC, Oak Ridge, Tennessee, USA. https://doi.org/10.3334/ORNLDAAC/1224.

Wang, K.-Y. Canopy CO2 exchange of Scots pine and its seasonal variation after four-year exposure to elevated CO2 and temperature. *Agricultural and Forest Meteorology* **1996**, *82*, 1-27.

Wang, Y.P.; Leuning, R. A two-leaf model for canopy conductance, photosynthesis and partitioning of available energy I: Model description and comparison with a multi-layered model. *Agricultural And Forest Meteorology* **1998**, *91*, 89-111.

Wanner, W.; Li, X.; Strahler, A. On the derivation of kernels for kernel-driven models of bidirectional reflectance. *Journal of Geophysical Research: Atmospheres* **1995**, *100*, 21077-21089.

Waring, R.H.; Landsberg, J.J.; Williams, M. Net primary production of forests: a constant fraction of gross primary production? *Tree Physiology* **1998**, *18*, 129-134.

Wei, S.S.; Fang, H.L. Estimation of canopy clumping index from MISR and MODIS sensors using the normalized difference hotspot and darkspot (NDHD) method: The influence of BRDF models and solar zenith angle. *Remote Sensing Of Environment* **2016**, *187*, 476-491.

Wu, C.; Chen, J.M.; Huang, N. Predicting gross primary production from the enhanced vegetation index and photosynthetically active radiation: Evaluation and calibration. *Remote Sensing of Environment* **2011**, *115*, 3424-3435.

Wu, C.Y.; Han, X.Z.; Ni, J.S.; Niu, Z.; Huang, W.J. Estimation of gross primary production in wheat from in situ measurements. *International Journal Of Applied Earth Observation And Geoinformation* **2010**, *12*, 183-189.

Wu, C.Y.; Munger, J.W.; Niu, Z.; Kuang, D. Comparison of multiple models for estimating gross primary production using MODIS and eddy covariance data in Harvard Forest. *Remote Sensing Of Environment* **2010**, *114*, 2925-2939.

Wu, D.; Zhao, X.; Liang, S.; Zhou, T.; Huang, K.; Tang, B.; Zhao, W. Time-lag effects of global vegetation responses to climate change. *Global change biology* **2015**, *21*, 3520-3531.

Xiao, X.; Zhang, Q.; Braswell, B.; Urbanski, S.; Boles, S.; Wofsy, S.; Moore, B.; Ojima, D. Modeling gross primary production of temperate deciduous broadleaf forest using satellite images and climate data. *Remote Sensing of Environment* **2004**, *91*, 256-270.

Yang, X.; Tang, J.W.; Mustard, J.F.; Lee, J.E.; Rossini, M.; Joiner, J.; Munger, J.W.; Kornfeld, A.; Richardson, A.D. Solar-induced chlorophyll fluorescence that correlates with canopy photosynthesis on diurnal and seasonal scales in a temperate deciduous forest. *Geophysical Research Letters* **2015**, *42*, 2977-2987.

Yebra, M.; Van Dijk, A.; Leuning, R.; Huete, A.; Guerschman, J.P. Evaluation of optical remote sensing to estimate actual evapotranspiration and canopy conductance. *Remote Sensing Of Environment* **2013**, *129*, 250-261.

Yuan, W.; Cai, W.; Liu, S.; Dong, W.; Chen, J.; Arain, M.A.; Blanken, P.D.; Cescatti, A.; Wohlfahrt, G.; Georgiadis, T., et al. Vegetation-specific model parameters are not required for estimating gross primary production. *Ecological Modelling* **2014**, *292*, 1-10.

Yuan, W.; Cai, W.; Xia, J.; Chen, J.; Liu, S.; Dong, W.; Merbold, L.; Law, B.; Arain, A.; Beringer, J., et al. Global comparison of light use efficiency models for simulating terrestrial vegetation gross primary production based on the LaThuile database. *Agricultural and Forest Meteorology* **2014**, *192-193*, 108-120.

Yuan, W.P.; Liu, S.; Zhou, G.S.; Zhou, G.Y.; Tieszen, L.L.; Baldocchi, D.; Bernhofer, C.; Gholz, H.; Goldstein, A.H.; Goulden, M.L., et al. Deriving a light use efficiency model from eddy covariance flux data for predicting daily gross primary production across biomes. *Agricultural and Forest Meteorology* **2007**, *143*, 189-207.

Yuan, W.P.; Liu, S.; Zhou, G.S.; Zhou, G.Y.; Tieszen, L.L.; Baldocchi, D.; Bernhofer, C.; Gholz, H.; Goldstein, A.H.; Goulden, M.L., et al. Deriving a light use efficiency model from eddy covariance flux data for predicting daily gross primary production across biomes. *Agricultural And Forest Meteorology* **2007**, *143*, 189-207.

Zeng, N.; Mariotti, A.; Wetzel, P. Terrestrial mechanisms of interannual CO2 variability. *Global biogeochemical cycles* **2005**, *19*.

Zhang, F.; Chen, J.M.; Chen, J.; Gough, C.M.; Martin, T.A.; Dragoni, D. Evaluating spatial and temporal patterns of MODIS GPP over the conterminous U.S. against flux measurements and a process model. *Remote Sensing of Environment* **2012**, *124*, 717-729.

Zhang, S.; Zhang, J.; Bai, Y.; Koju, U.A.; Igbawua, T.; Chang, Q.; Zhang, D.; Yao, F. Evaluation and improvement of the daily boreal ecosystem productivity simulator in simulating gross primary productivity at 41 flux sites across Europe. *Ecological Modelling* **2018**, *368*, 205-232.

Zhang, Y.; Xiao, X.; Wu, X.; Zhou, S.; Zhang, G.; Qin, Y.; Dong, J. A global moderate resolution dataset of gross primary production of vegetation for 2000–2016. *Scientific Data* **2017**, *4*, 170165.

Zimmer, C. Earth's Oxygen: A Mystery Easy to Take for Granted. *New York Times* **2013**.

Chapter 3 Analysis on long-term trends of variations in GPP

Quantitative estimation of spatial pattern of GPP trends and its drivers plays a crucial role in global change research. This chapter applied CFix model to estimate the net effect of each factor on GPP trends of 1982~2015, used an unsupervised classifier to group similar GPP trend behaviors, and analyzed the responses of GPP to changes in climatic, atmospheric and environmental drivers. According to the features of monthly GPP trends and the patterns of growing season, I presented nine categories as aids in interpreting large-scale behavior. LCC, rising CO_2, temperature and water conditions changes have the positive overall effect on GPP over the entire world, contrary to radiation change effects. The global average contributions of LCC, CO_2, temperature, radiation and water on GPP trend are 4.57 %, 65.73 %, 13.07 %, -7.24 % and 11.74 %, respectively. LCC and climatic factors changes have had a greater impact on GPP in terms of a specific location or regional rather than globally, and the interactions between factors are positive on GPP. The effects of climatic factors trends on GPP in different locations can be opposite, in general: regionally, GPP changes at middle and high latitudes are likely dominated by rises in radiation and temperature; at lower latitudes, GPP changes are likely to be driven by shifts in water conditions; at high altitudes, GPP changes are probably caused by changes in temperature and water conditions. These results will increase the understanding of the variations of carbon flux under future CO_2, LCC and climate conditions.

3.1 Introduction

Terrestrial GPP is the amount of CO_2 fixed as organic compounds by vegetation through photosynthesis at the ecosystem scale (Beer et al., 2010); GPP plays a pivotal role in the global carbon balance and almost all ecosystem processes (Gilmanov et al., 2003). The patterns of the variation and distribution of GPP in terrestrial ecosystems show large spatial variability due to interactions between the biological characteristics of plants and external environmental factors (e.g., rising CO_2 concentration, land-cover change, and climatic variables) (Beer et al., 2010; Anav et al., 2015). In recent decades, approximately 1.2 PgC $year^{-1}$ has been sequestered by terrestrial ecosystems as the net result of the impact of the changing climate and rising CO_2 on ecosystem productivity (CO_2-climate driven flux) and deforestation, harvesting and secondary forest regrowth (LCC flux) (Haverd et al., 2017). However, their contributions are highly uncertain. Therefore, it is important and necessary to accurately describe the changes of GPP in different regions and to quantitatively evaluate how environmental factors influence GPP. Furthermore, a deeper understanding of how GPP has responded to past climate change, LCC and rising CO_2 concentration will provide insight into how the carbon cycle will change under future CO_2 and climate conditions (Poulter et al., 2014; Huang et al., 2015; Li et al., 2016).

However, directly measuring GPP at the global scale is infeasible (Ma et al., 2015), and the discrepancies associated with the spatial distribution of environmental controls on GPP variation simulated by different models are considerable (Anav et al., 2015; Beer et al., 2010). In recent years, with the development of space technology, satellite-based LUE models have been widely used because they rely on simple algorithms to estimate the macroscale terrestrial GPP (Yuan et al., 2014b). In this study, the CFix model (Verstraeten et al., 2006) was selected to perform a series of factorial estimations to explore the drivers' net effect on GPP because in CFix, a CO_2 fertilization factor exists that differs from other LUE models, and we can directly introduce the effect of the atmospheric CO_2 concentration, which is considered one of the main causes of global warming (Bazzaz 1990; Gillett et al., 2013).

Many studies have been performed, and various models and approaches, from individual sites to global scales, have been developed and used to examine climate factors that affect GPP

(Nemani et al., 2003; Beer et al., 2007 2010; de Jong et al., 2013; Anav et al., 2015; Liang et al., 2015). Simultaneously, that CO_2 concentration effect on GPP has also been found by many scholars (Farquhar 1997; Norby et al., 2005; Luo et al., 2006; Yang et al., 2016; Sun et al., 2018), and numerous studies (van Oijen et al., 2004; Ainsworth and Long, 2005; Yang et al., 2016) have been conducted to reveal how ecosystems respond to elevated CO_2 levels, although the magnitude and the spatial distribution of the influence remain unclear. Moreover, it is an indisputable fact that large-scale land-cover changes have taken place over the past few decades (Lambin et al., 2001; Hansen et al., 2013), and large-scale estimates of terrestrial carbon fluxes are highly dependent on the land cover (Quaife et al., 2008). However, studies that combined climate change, LCC, rising CO_2 concentration and their interactions into the effects on the pattern and trend of GPP are few.

In this chapter, I first used the CFix model to estimate the global monthly GPP over the past 34 years and tested the performance by comparing it with MTE GPP and MODIS products. Second, I analyzed the individual effect of each factor and the interactions through a series of factorial estimations around the world. Third, I zoned the categories of GPP variations according to seasonal and dimensional characteristics using an unsupervised classifier. Finally, I analyzed the GPP trend and its attribution spatially. The overarching goals of this chapter are to (globally during the period of 1982~2015) investigate the spatial distribution and magnitude of GPP trend; separate the contributions of climate factors, the rising CO_2 concentration, LCC and their interactions on the pattern of GPP trends spatially and quantitatively; and explain how the possible factors influence GPP in different regions.

3.2 Materials and methods

3.2.1 Materials

Table 3.1 Overview of the datasets used in this chapter.

Data used to estimate GPP	Datasets /products	Period	Resolution	Data source / acquisition
NDVI	GIMMS-3g	1982-2015	8 km×8 km	NOAA AVHRR
Land-cover classification	UMD Land-cover Classification	1981-1994	1 km×1 km	GLCF
	CCI-LC	1992-2015	300 m×300 m	ESA
Atmospheric CO_2 concentration	CO_2 records	1982-1999	global	NOAA ESRL
	CT2016	2000-2015	2° latitude × 3° longitude	
Photosynthetically active radiation Air temperature Sensible heat flux Latent heat flux	MERRA	1980-2015	0.5° latitude × 0.6° longitude	NASA GES DISC
Soil moisture	CPC-SM v2	1980-2015	0.5°×0.5°	NOAA ESRL PSD
Wilting point & field capacity	IGBP-DIS	1950-1996	0.5°×0.5°	NASA ORNL DAAC

3.2.1.1 Climate data

For the global estimation of GPP, I used input datasets of sensible heat flux, latent heat flux, Ta and PAR from MERRA (Rienecker et al., 2011), which is a NASA reanalysis for the satellite era based on the main new version of the Goddard Earth Observing System Data Assimilation System Version 5 (GEOS-5) to produce an estimate of global climatic conditions at a resolution of 0.5° latitude × 0.6° longitude. More information on the MERRA dataset is available from NASA GES DISC/ Modeling/ Data Holding (http:// disc.gsfc.nasa.gov/daac-bin/DataHoldings.pl). The uncertainties of various meteorological factors at the global scale have been validated and evaluated by using surface metrological datasets (Rienecker et al., 2011; Li et al., 2013).

3.2.1.2 Vegetation indices data

The VI I used in this study, NDVI dataset, is Global Inventory Modelling and Mapping Studies (GIMMS)-3g (Tucker et al., 2005), which spanned 1982 to 2015 at a spatial resolution of 8×8 km^2 and a 15-day interval and was acquired from NOAA-AVHRR (Advanced Very High-Resolution Radiometer). The dataset provides the only continuous and longest time series of approximately three decades that has been continually assessed and validated, and it has been widely used for long-term global vegetation condition monitoring and detecting (Piao et al., 2006; Wu et al., 2015; Liang et al., 2015). We conducted the biweekly data composite with pixels using the maximum value composite (MVC) method (Holben 1986) to generate a

monthly temporal scale NDVI dataset to calculate fAPAR (Myneni and Williams 1994) for running the CFix model.

3.2.1.3 Land cover data

The land cover map from 1982 to 1991 was acquired from the GLCF: AVHRR Global Land Cover Classification (http://glcf.umd.edu/data/landcover/). The images from the AVHRR satellites between 1981 and 1994 were utilized and analyzed to distinguish 14 land cover classes (Hansen et al., 1998). Three spatial scales are available in this product (1, 8 km and 1°), and we selected the highest resolution of 1 km. The other is the ESA CCI-LC dataset (https://www.esa-landcover-cci.org/), a 300m annual global land cover time series from 1992 to 2015. These 24 annual global land cover maps were produced by state-of-the-art reprocessing of the full archives of five different satellite missions that provided daily observations of the Earth. CCI-LC provides information for 22 classes of dominant land cover types defined using the Land Cover Classification System (LCCS), which was found to be compatible with the PFTs used in the climate models (CCI-LC URD Phase I). Detailed information on the CCI-LC is available on the CCI-Viewer (http://maps.elie.ucl.ac.be/CCI/viewer/). The land cover data need to be crossed with the grids analyzed in this study at a 0.5° spatial resolution; all 300-m and 1-km pixels falling in the 0.5° cells were used to calculate the proportion of the dominant land cover type.

3.2.1.4 Atmospheric CO_2 concentration data

Two datasets of the atmospheric CO_2 concentration were used to normalize the CO_2 fertilization factor in the present study; one is the global monthly continuous spatial CO_2 concentration data from 2000 to 2015, CT2016, which is an open product of NOAA's Earth System Research Laboratory that uses data from the NOAA ESRL greenhouse gas observational network and collaborating institutions (Peters et al., 2007), released on Feb 17th, 2017. In CT2016, land biosphere, wildfire, fossil fuel emissions, atmospheric transport and other factors are data-assimilated to produce the estimates of surface fluxes and atmospheric CO_2 mole fractions (https://www.esrl.noaa.gov/gmd/ccgg/carbontracker/index.php). The other is globally averaged surface monthly mean CO_2 data from 1982 to 1999 obtained from NOAA/ESRL (www.esrl.noaa.gov/gmd/ccgg/trends/). A global average is constructed by first fitting a smoothed curve as a function of time to each site, after which the smoothed value for each site is plotted as a function of the latitude for 48 equal time steps per year. A global average is calculated from the latitude plot at each time step (Masarie 1995). The spatial continuous CO_2 concentration data were resampled to the 0.5°×0.5° spatial resolution by linear method.

3.2.1.5 Soil property data

The CPC SM dataset v2 (van den Dool et al., 2003) provided by the NOAA/OAR/ESRL PSD (http://www.esrl.noaa.gov/psd/) and the IGBP-DIS dataset (Global Soil Data Task, 2014) (http://www.daac.ornl.gov) were used in this study to calculate the water limitation on LUE by considering the stomatal regulating factor from soil moisture deficits. Since globally measuring soil moisture is impossible, we used the model-calculated CPC-SM dataset, which provides global monthly data from 1948 to 2017 consists of a file containing the averaged soil moisture water height equivalents at a spatial resolution of 0.5°×0.5°. On the other hand, IGBP-DIS dataset is a global product generated at a resolution of 5×5 arc-minutes by the SDS, which generates soil information and maps for geographic regions at user-selected soil depths and resolutions. I used the wilting point and field capacity maps derived from this dataset and

converted the data to the values at a soil depth of 1.6 m, the same as CPC-SM. The data were resampled to the 0.5°×0.5° spatial resolution by linear method.

3.2.2 Model description

CFix is a parametric LUE model with a strong prognostic capability that is driven by plant-related, meteorological, climatic, and hydrological data to estimate carbon mass fluxes in terrestrial ecosystems (Veroustraete et al., 2006) from local (Veroustraete et al., 2002 2004; Yuan et al., 2014a) and regional (Maselli et al., 2009; Chiesi et al., 2011; Yan et al., 2016) to global scales (Yuan et al., 2014b; Ma et al., 2015). Comparing with other LUE models, CFix has a module of carbon fertilization effects caused by increases in the atmospheric CO_2 concentration, which is considered to be the major reason for global warming. CFix can use inputs averaged over different time periods (most commonly 10-day to monthly periods) and is conceptually simple and generally applicable (Chiesi et al., 2011). For a given geographic coordinate (x, y), GPP is calculated as (Veroustraete et al., 2006):

$$\mathrm{GPP} = \mathrm{PAR} \times \mathrm{fAPAR} \times \varepsilon_{wl} \times T_s \times S_{CO_2} \quad \text{Eq-3.1}$$

fAPAR is the fraction of absorbed photosynthetic active radiation (PAR) (0,1). Myneni and Williams (1994) used a set of empirical constants to establish a linear equation to describe the relationship between fPAR and NDVI:

$$\mathrm{fAPAR} = 0.8624 \times \mathrm{NDVI} + 0.0814 \quad \text{Eq-3.2}$$

ε_{wl} is the LUE by considering the impact of water limitation. Veroustraete (2006) combined the soil moisture deficit and vapor pressure deficit to calculate a linearly water limited LUE delimited between ε_{max} and ε_{min}:

$$\varepsilon_{wl} = \varepsilon_{min} + (a \times F_s + b \times F_a) \times (\varepsilon_{max} - \varepsilon_{min}) \quad \text{Eq-3.3}$$

where ε_{max} and ε_{min} are the maximum and minimum LUE, respectively, which are biome-dependent invariant. I used the values from Yuan (2014), which is based on the measurements of ecosystem carbon fluxes from 168 globally distributed sites in a range of vegetation types. a and b are the empirical coefficients in the weighting of water limitations in LUE originating from soil and air according to Veroustraete (2006) (a=0.5, b=0.5). F_s and F_a are stomatal regulating factors from soil and air, which are simulated by SM and evaporative fraction (EF), respectively:

$$F_s = 1 - \mathrm{a_1} \times \exp[\mathrm{a_2} \times (\mathrm{FC} - \mathrm{SM}) \times (\mathrm{FC} - \mathrm{WP})^{-1}] \quad \text{Eq-3.4}$$

$$F_a = \mathrm{b_1} \times \exp(\mathrm{b_2} \times \mathrm{EF}) \quad \text{Eq-3.5}$$

$$\mathrm{EF} = \lambda\mathrm{E} \times (\lambda\mathrm{E} + \mathrm{H})^{-1} \quad \text{Eq-3.6}$$

where a_1 (0.5), a_2 (0.5), b_1 (0.1) and b_2 (2.88) are empirical coefficients in the stomatal regulating factor relation (Veroustraete et al., 2006). SM is the volumetric moisture content, FC and WP are the volumetric moisture content at the field capacity and wilting point. λE is the latent heat flux, and H is the sensible heat flux.

The temperature dependency factor was defined by Wang (1996) as:

$$T_s = \frac{\exp\left[C_l - \Delta H_{a,p} \times (R_g \times T)^{-1}\right]}{1 - exp\left[(\Delta S \times T - \Delta H_{d,p}) \times (R_g \times T)^{-1}\right]} \quad \text{Eq-3.7}$$

where R_g, $H_{d,p}$, $H_{a,p}$, S and C_l in the temperature dependency factor equation are 8.31 J K^{-1} mol^{-1}, 211 kJ mol^{-1}, 52.75 kJ mol^{-1}, 704.98 J K^{-1} mol^{-1} and 21.77, according to Veroustraete (2002).

S_{CO_2} is defined by Veroustraete (1994) (0,+∞), due to CO_2 concentration levels above the reference level enhancing the carbon assimilation rate, as follows.

$$S_{CO_2} = \frac{[CO_2] - [O_2] \times (2s)^{-1}}{[CO_2]^{ref} - [O_2] \times (2s)^{-1}} \times \frac{K_m \times \left(1 + [O_2] \times {K_0}^{-1}\right) + [CO_2]^{ref}}{K_m \times \left(1 + [O_2] \times {K_0}^{-1}\right) + [CO_2]} \quad \text{Eq-3.8}$$

where the parameters of s, K_m, K_o, $[CO_2]^{ref}$ are 2550, 948, and 30 and the CO_2 mixing ratio for the reference year is 1833 (281ppm). $[CO_2]$ is the atmospheric CO_2 concentration (for 1982~1999, we used the global averaged monthly mean value; for 2000~2015, we used the spatial continuous monthly grid data). In this study, $[O_2]$ was set to 209,500 ppm according to Zimmer (2013). The datasets used in this study to calculate these parameters are shown in Table 3.1.

3.2.3 Attribution method of GPP trends

Five drivers were considered for their impact on estimated GPP trends: i) rising global CO_2 concentration, ii) land-cover change and changes in iii) solar radiation, iv) temperature and v) water conditions. These five drivers were prescribed in the CFix model and the sources are introduced in Table 3.1. To assess the contribution of each of the five factors and possible interactions between them, we conducted a series of CFix factorial estimates where one driver remains fixed while the others vary during the period of 1982~2015. The estimation protocol is shown in Table 3.2.

Table 3.2 Illustration of the estimation protocol and the five factors used as input data for factorial estimates.

Factorial estimates	Water forcing	Temperature forcing	Radiation forcing	CO_2 level increasing	Land-cover change
$GPP_{Control}$	1982-2015	1982-2015	1982-2015	1982-2015	1982-2015
GPP_{Water}	1980-1984	1982-2015	1982-2015	1982-2015	1982-2015
$GPP_{Temperature}$	1982-2015	**1980-1984**	1982-2015	1982-2015	1982-2015
$GPP_{Radiation}$	1982-2015	1982-2015	**1980-1984**	1982-2015	1982-2015
$GPPCO_2$	1982-2015	1982-2015	1982-2015	**1982**	1982-2015
GPP_{LCC}	1982-2015	1982-2015	1982-2015	1982-2015	**1982**

The estimation with all factors varying defines the $GPP_{Control}$. In each factorial estimate, the selected factor is held to the fixed value as the gray background in Table 3.2, while all other factors vary as the group of $GPP_{Control}$. In the case of "constant water, temperature and radiation",

to eliminate the particularity of one year, we used the averaged values of five years from 1980 to 1984.

The individual contribution of each factor is defined as the difference, δX (X represents the individual factor), between GPP trends from each corresponding estimation and that of $GPP_{control}$ ($Trend_{control}$), in which all factors are varied (Chang et al., 2016). Since the factors influence each other, in this study, the nonlinear interaction as a residual is defined as δResidual:

$$\delta\text{Residual} = \text{Trend}_{control} - \sum_{i=1}^{n} \text{Trend}_{X_i} \quad \text{Eq-3.9}$$

where n is the number of factors and $Trend_{Xi}$ denotes the linear trend of Factorial X_i.

3.2.4 Study process

Figure 3.1 shows the logical process of this study. First, due to the different spatial resolutions of global datasets, all grid data were resampled by mean values or dominated indicators to a 0.5° × 0.5° spatial resolution. Second, all data were inputted into CFix to estimate the $GPP_{Control}$. I used two widely used GPP products to test the accuracy of the estimated GPP. If the accuracy of the estimates were acceptable, the factorial estimates would be calculated to obtain the estimates of $GPP_{FactorX}$. Based on the attribution method of the GPP trend, I can obtain the spatial distributions of the individual effect of each factor. I can better know the spatial and seasonal patterns of GPP variations through the monthly trend information, therefore, the GPP trend for each month of the year was calculated (e.g., the monthly GPP trends of all 34 Decembers were averaged to obtain a December trend). After spatially calculating, I got the map that shows the annual cycle of monthly GPP trends. I then calculated the monthly GPP mean values of 34 years from January to December for each pixel. Therefore, we can obtain information on the vegetation average growing situation in one year to represent the annual cycle of growing season. The two annual cycles revealed the month of one year when GPP increases or decreases at a given location were caused by changes in the GPP amplitude or the growing season length (Hicke et al., 2002); and I draw the description figure following Hicke et al. (2002) as Figure 3.2. I used this characteristic as the index of vegetation growth changes in the cluster classification to obtain the spatial distribution of the GPP change types. Finally, according to the spatial distribution of each factor monthly trends, net effects and GPP change types, we will more clearly understand the spatial patterns and the drivers of GPP variations.

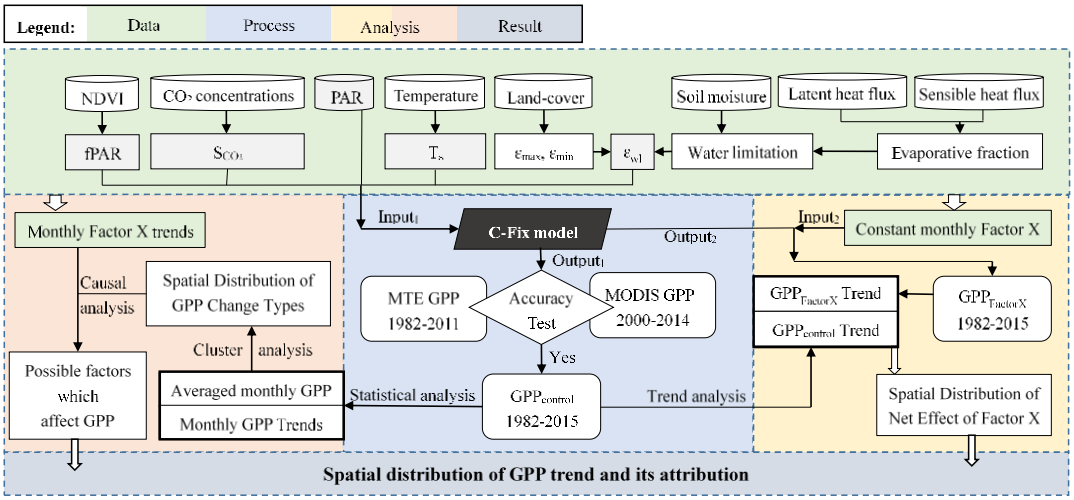

Figure 3.1 Study flowchart.

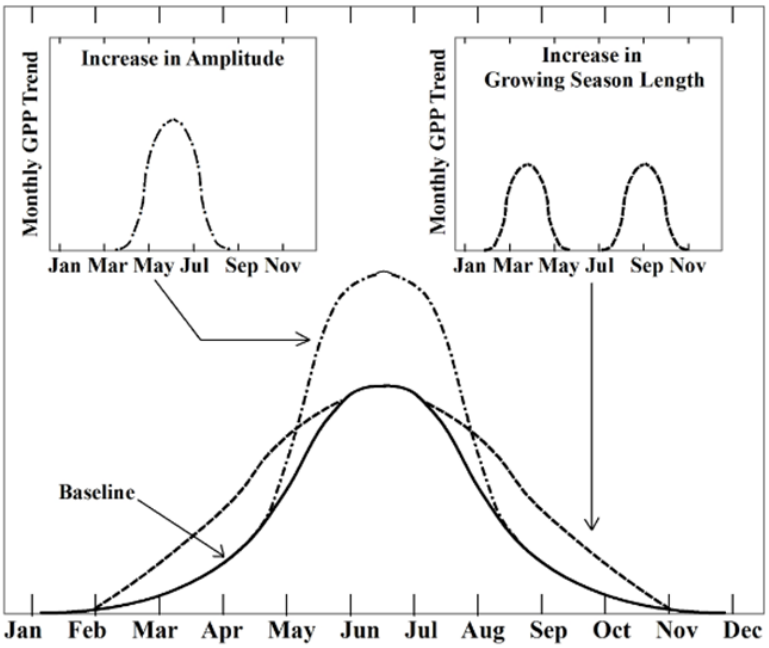

Figure 3.2 Schematic showing monthly trends in GPP in response to an increase in the amplitude if the GPP annual cycle (dashed-dotted curve) and an increase in the length of the growing season (dashed curve) occurred from a baseline GPP annual cycle (solid curve).

3.3 Results

3.3.1 Accuracy assessment of estimated GPP

In this chapter, I estimated a relative long-term series global GPP at a spatial resolution of 0.5°, which is larger than the footprint size of ground-based observations. Hence, I relied on the model and other remotely sensed data for a comparison on the global scale. As a benchmark, I compared the estimates against the MTE model GPP from 1982 to 2011 (Jung et al., 2011) because it is based on direct eddy-covariance flux tower measurements of GPP and is thus considered close to the truth where the flux tower density is high (Beer et al., 2010; Frankenberg et al., 2011). MODIS GPP products from 2000 to 2014 were also used because MODIS products have been widely known and used (Turner et al., 2006b; Zhao and Running, 2010; Frankenberg et al., 2011). As well as the results from process-based models (Table 3.4) of 1982-2010 from the ISIMIP2a (Reyer et al., 2017; Chang et al., 2017) were selected to test the accuracy of estimated GPP. For the annual GPP, I found a strong linear spatial correlation between the estimated GPP with process-based models, MTE and remotely sensed GPP values, most notably with MTE_GL GPP (averaged r=0.9269, averaged slope=1.0977), followed by MTE_MR GPP (averaged r=0.9266, averaged slope=1.1008) and MODIS GPP (averaged r=0.9205, averaged slope=1.3089) (Table 3.3). The performs of the comparing with the results from different process-based models were different (Table 3.3), but all show a strong correlation. Compared with the results of multiple models, the spatial correlation coefficient could reach 0.8377 with the slope of 1.0159. I found that the estimated GPPs are highly consistent with MTE GPP and MODIS products; thus, the estimated GPP in the present study can be used in subsequent analyses.

Table 3.3 The parameters of linear regression lines of GPP comparisons.

	GSWP3		PGMFD		WATCH	
	Slope	**R**	**Slope**	**R**	**Slope**	**R**
CARAIB	1.0268	0.8544	1.0451	0.8619	1.0422	0.8590
DLEM	1.0188	0.8241	1.0055	0.8290	1.0542	0.8266
JULES-B1	0.7151	0.7565	0.7005	0.7633	-	-
LPJml	1.1017	0.8500	1.0843	0.8475	1.1225	0.8399
ORCHIDEE	0.9963	0.8727	0.9452	0.8785	1.0201	0.8766
VEGAS	-	-	1.2797	0.8720	1.2984	0.8792
VISIT	0.8661	0.8051	0.9571	0.8195	1.0231	0.8012

models: Climate dataset: G- GSWP3; P- PGMFD v.2 (Princeton); W- WATCH (WFD).
The GPP datasets used in this chapter were obtained from The Inter-Sectoral Impact Model Intercomparison Project (ISIMIP2a) (https://www.isimip.org/).

Table 3.4 The parameters of linear regression lines of GPP comparisons (p_value < 0.0001).

Year	MTE_GL GPP		MTE_MR GPP		MODIS GPP	
	Correlation coefficient	Slope	Correlation coefficient	Slope	Correlation coefficient	Slope
Average	**0.9269**	**1.0977**	**0.9266**	**1.1008**	**0.9205**	**1.3089**
1982	0.9267	0.9909	0.9267	0.9943	-	-
1983	0.9107	0.9540	0.9108	0.9567	-	-
1984	0.9270	1.0000	0.9265	1.0038	-	-
1985	0.9317	1.0443	0.9311	1.0477	-	-
1986	0.9293	1.0529	0.9285	1.0561	-	-
1987	0.9196	1.0137	0.9192	1.0164	-	-
1988	0.9251	1.0266	0.9247	1.0294	-	-
1989	0.9293	1.0761	0.9291	1.0795	-	-
1990	0.9241	1.0620	0.9243	1.0664	-	-
1991	0.9221	1.0314	0.9224	1.0348	-	-
1992	0.9238	1.0382	0.9230	1.0414	-	-
1993	0.9266	1.0637	0.9262	1.0678	-	-
1994	0.9235	1.0761	0.9228	1.0789	-	-
1995	0.9291	1.0857	0.9284	1.0886	-	-
1996	0.9271	1.0955	0.9265	1.0983	-	-
1997	0.9241	1.0829	0.9265	1.0983	-	-
1998	0.9153	1.0645	0.9155	1.0656	-	-
1999	0.9320	1.0993	0.9321	1.1029	-	-
2000	0.9325	1.1324	0.9324	1.1355	0.9242	1.2429
2001	0.9312	1.1501	0.9313	1.1525	0.9239	1.2634
2002	0.9269	1.1553	0.9264	1.1578	0.9178	1.2603
2003	0.9281	1.1635	0.9264	1.1578	0.9201	1.2630
2004	0.9308	1.1522	0.9303	1.1543	0.9189	1.2650
2005	0.9290	1.1321	0.9285	1.1340	0.9162	1.2856
2006	0.9325	1.1807	0.9322	1.1833	0.9206	1.3155
2007	0.9319	1.1927	0.9319	1.1958	0.9222	1.3232
2008	0.9299	1.1983	0.9296	1.2019	0.9225	1.3246
2009	0.9302	1.2000	0.9294	1.2029	0.9170	1.3268
2010	0.9274	1.1915	0.9273	1.1931	0.9229	1.3631
2011	0.9280	1.2254	0.9278	1.2287	0.9200	1.3602
2012	-	-	-	-	0.9218	1.3179
2013	-	-	-	-	0.9201	1.3623
2014	-	-	-	-	0.9188	1.3603

3.3.2 GPP trends

3.3.2.1 Contributions of different factors to GPP trends

For the global terrestrial ecosystems, the overall effect of all the five factors considered is positive (Table 3.5). The key result is that the increases in the atmospheric CO_2 concentration make the largest contribution to the globally averaged GPP trend. The changes in water conditions and temperature caused comparable but lower GPP positive trends. The changes in solar radiation caused the whole effect of decreasing GPP. Although the change in GPP attributed to land-cover change is positive around the world, the regional maximum negative effect also occurred due to land-cover changes. That the sum of the effects of each factor on GPP trends is 0.0795 gC m^{-2} $year^{-1}$ smaller than the overall GPP trend attributed to all factors indicates that the interactions between each factor are positive.

Table 3.5 Trends in GPP globally during the period 1982-2015 and the effects of the factors on the trend.

Factors	Average effect*	Max effect*	Min effect*	Standard deviation*	Globally averaged contribution%	Positive effect fraction%
Overall effect	0.6560	7.6213	-4.9341	0.7811	100.00	75.76
Temperature	0.0857	5.8234	-4.4056	0.5412	13.07	73.16
Water	0.0770	3.6817	-2.3074	0.2944	11.74	42.68
Radiation	-0.0475	1.5470	-3.2759	0.3480	-7.24	35.74
CO_2 concentration	0.4312	2.7181	-0.0027	0.5088	65.73	57.74
LCC	0.0300	3.7428	-6.1646	0.2244	4.57	63.08
Residual	0.0795	2.1355	-2.5261	0.2115	12.13	46.23

3.3.2.2 Spatial distribution of the GPP trend and its attribution

The spatial distribution of annual GPP trend in the period of 1982~2015 is shown in Figure 3.3. The contribution of different factors in different areas vary considerably (Figure 3.4). The figure shows that the largest increases in GPP are found in the southern parts of the Amazon rainforest with increases of 5 gC m^{-2} $year^{-1}$, where the changes in temperature and water conditions play the major roles in causing the increasing GPP trends (Figure 3.4). Positive GPP trends greater than 3 gC m^{-2} $year^{-1}$ were found in the ITCZ except for Congo rainforest, which has the largest decreases in GPP with values that exceed -2 gC m^{-2} $year^{-1}$, where the changes in water conditions and the enhanced interactions play the most important roles in explaining those GPP trends. Followed by humid temperature regions in eastern North America, western and central Europe and eastern China, with an increment of approximately 2.5 gC m^{-2} $year^{-1}$ is found, and solar radiation and temperature have positive effects on GPP trends. Not all regions show the positive GPP trends, I also found negative GPP trends in the Borbolima Plateau, Diamantine Plateau, Pampas grassland, Cordillera Mountains, Australian desert and the areas east of Caspian Sea. And relatively concentrated are the trends of the Congo Basin which were attributed to the effect of the changes in temperature and water conditions.

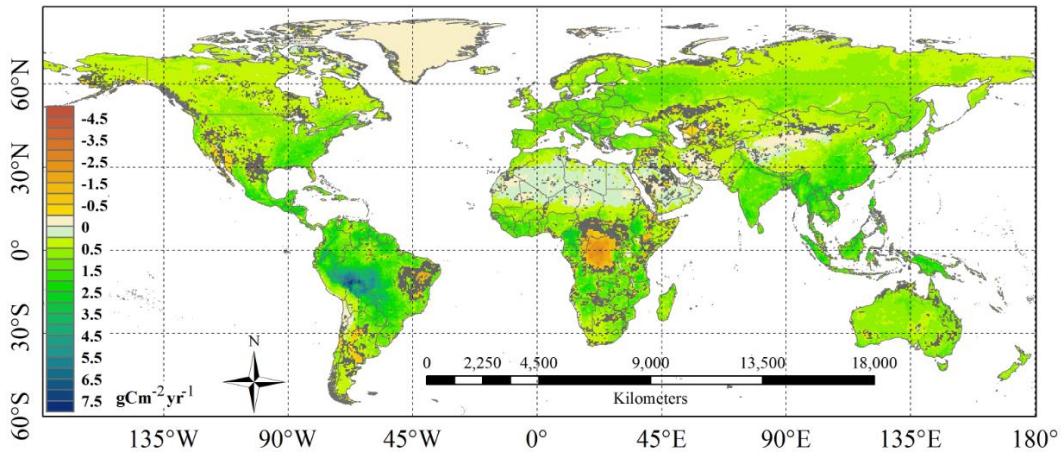

Figure 3.3 The spatial distribution of linear trends in GPP during the period 1982-2015. The pixels that are not satisfied at p_value < 0.1 are drawn in gray.

The changes in the atmospheric CO_2 concentration make almost no negative contribution to the pattern of the GPP trend globally. Significant positive GPP trend effects of land-cover changes were found in regions such as high latitudes, mid-latitudes inland areas, high altitude areas and some barren vegetation areas. In contrast, in many areas, especially the dry forest of South America and eastern Africa and the Eurasian rainforest, the land-cover change shows a decreasing GPP effect. Regarding contributions of climatic factors (temperature, water, and radiation), regionally, climate change can have either a positive or a negative effect on GPP trends. In addition, the interactions among different factors also have regional characteristics.

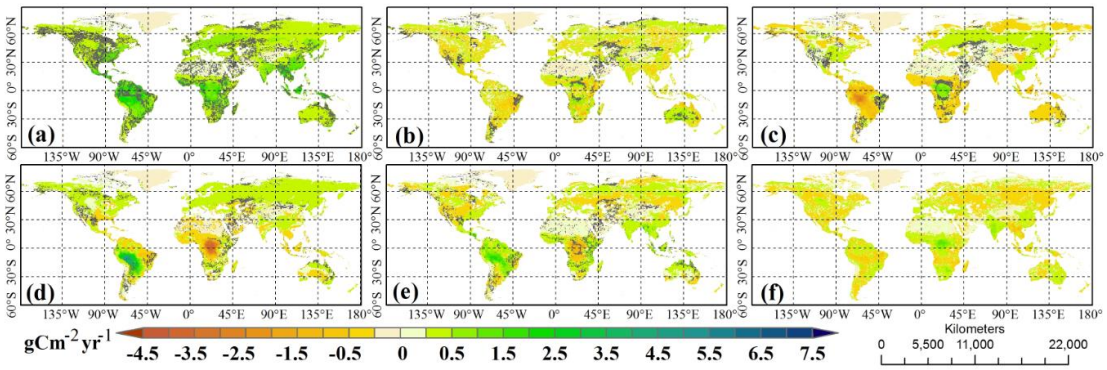

Figure 3.4 Spatial distribution of the trends in GPP due to (a) increases in atmospheric CO_2 concentration, (b) land-cover change, (c) solar radiation changes, (d) temperature changes, (e) changes in water conditions, and (f) their nonlinear interactions or non-attributed. The pixels ((a) to (e)) that are not satisfied at p_value < 0.1 are drawn in gray.

3.3.2.3 Spatial Distribution of GPP trend in each month of a year

All drivers considered in this study have the overall effect of increasing GPP for each month for the whole terrestrial ecosystems (Units: gC m^{-2} $year^{-1}$; Jan: 0.3918; Feb: 0.3818; Mar: 0.3999; Apr: 0.5234; May: 0.6968; Jun: 1.0340; Jul: 1.0418; Aug: 0.8255; Sep: 0.6338; Oct: 0.4390; Nov: 0.3869; Dec: 0.3680). Figure 3.5 shows considerable seasonal variations, especially in the Northern Hemisphere, with larger increases in later spring and summer and low increases or decreases in earlier spring and autumn. Regarding the ITCZ regions, GPP

trends in Amazon and Asian rainforests are continuously increasing throughout the year; on the contrary, the GPP trends in the Congo rainforest is reduced. The GPP trends in Southern South America, southern Africa and Australia also have seasonal change characteristics. The GPP trends in two regions, southern Amazon and Congo Basin, have trends that reflect the most significant changes more obviously following the subsolar point from the equator moving northward. The GPP trends correctly captured patterns at the global scale, such as the trends over North America showing considerable East-West differences and a typical longitudinal gradient in Northern Eurasia.

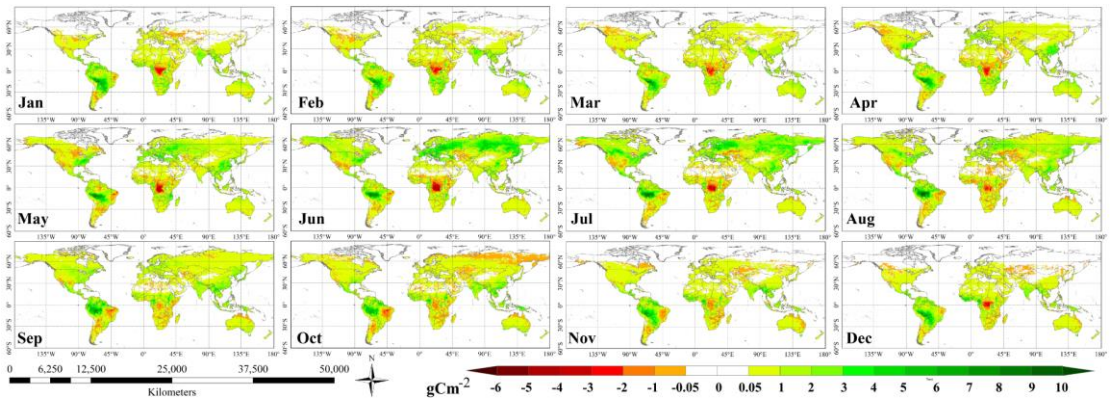

Figure 3.5 The monthly spatial distributions of linear trends in GPP during the period 1982-2015.

3.3.2.4 GPP trend category zoning

To further investigate the seasonal dynamics and varying patterns of GPP during the period of 1982~2015, we classified the monthly GPP and monthly GPP trends to group locations with similar behaviors. This isolated regions that had lengthening growing seasons, for example, or had increased GPP in the rapid growth stage (RGS). We used the average monthly GPP in the classification as an index of the vegetation growth stage. The monthly GPP and GPP trends were first normalized to allow these variables to be used together in the classification (Hicke et al., 2002).

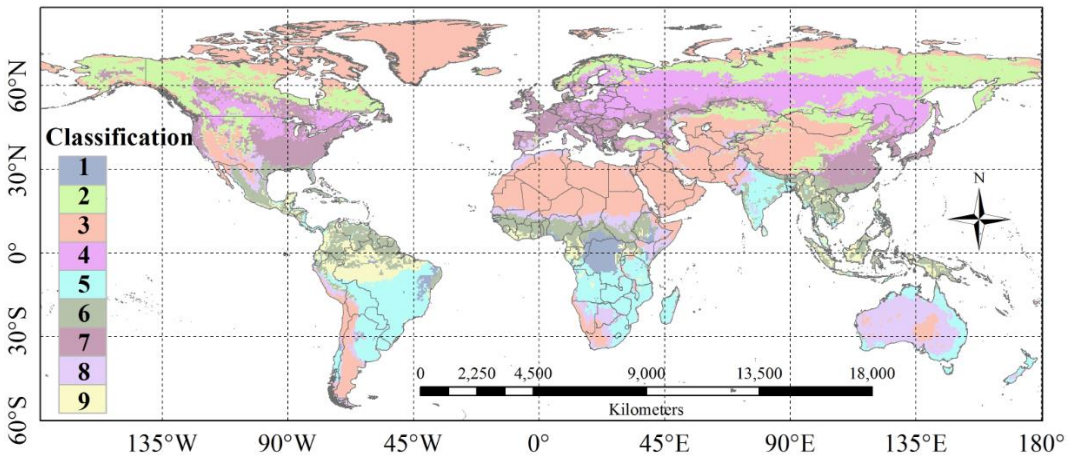

Figure 3.6 The spatial distribution of classes on variations in GPP during the period 1982-2015.

Nine general categories (Figure 3.6) resulted from using a k-means (Hartigan, 1975) classifier according to the statistical characteristics information of GPP variations. Here, I focus these results on the large-scale patterns that occurred. Because specifying fewer groups obscured some information in the analysis, and although the classification assigns each pixel to a group and we present the class mean information (Figure 3.7), I have to admit that the circumstance that a pixel may not behave in a manner close to the class mean exists. This categorization is necessarily approximate; I used the groups as an aid to explain the large-scale behavior of GPP variations: Class 1: Mainly in the African rainforest, GPP trends are negative, especially in July between two RGSs; the first RGS ends early and the second RGS has a delayed start; Class 2: Mainly in high latitudes and high altitudes, GPP trends are positive, and the main reason for the increasing GPP is the changes in the amplitude. Class 3: Mainly in polar and barren areas, there are low or almost no GPP in these areas, and the increases or decreases are almost equal to 0; Class 4: Mainly in cool temperate zones, GPP trends are positive, and the RGS has an early lengthening trend. However, the changes in the amplitude play a more important role. In Class 5, Mainly in equatorial, winter dry climate zones, the GPP trends are positive throughout the growing season; and the increasing trend in the early period is less than that in the middle and later periods. The RGS has a trend of delayed ends; Class 6: Mainly in equatorial, fully humid climate zones, the GPP trends were positive throughout the growing season, and the end of the RGS has a slightly delayed trend. In Class 7: Mainly in warm temperate zones, the curve of the GPP trends are similar to a bimodal curve, and the trend of lengthening in growing season is obvious; Class 8: Mainly distributed in desert areas, the vegetation has two RGSs, and the increment in the first RGS is larger than that in the second RGS; Class 9: Mainly distributed in the fully humid zones of Amazon rainforest, the GPP is stable at a high level throughout the year, and the RGS extends backwards.

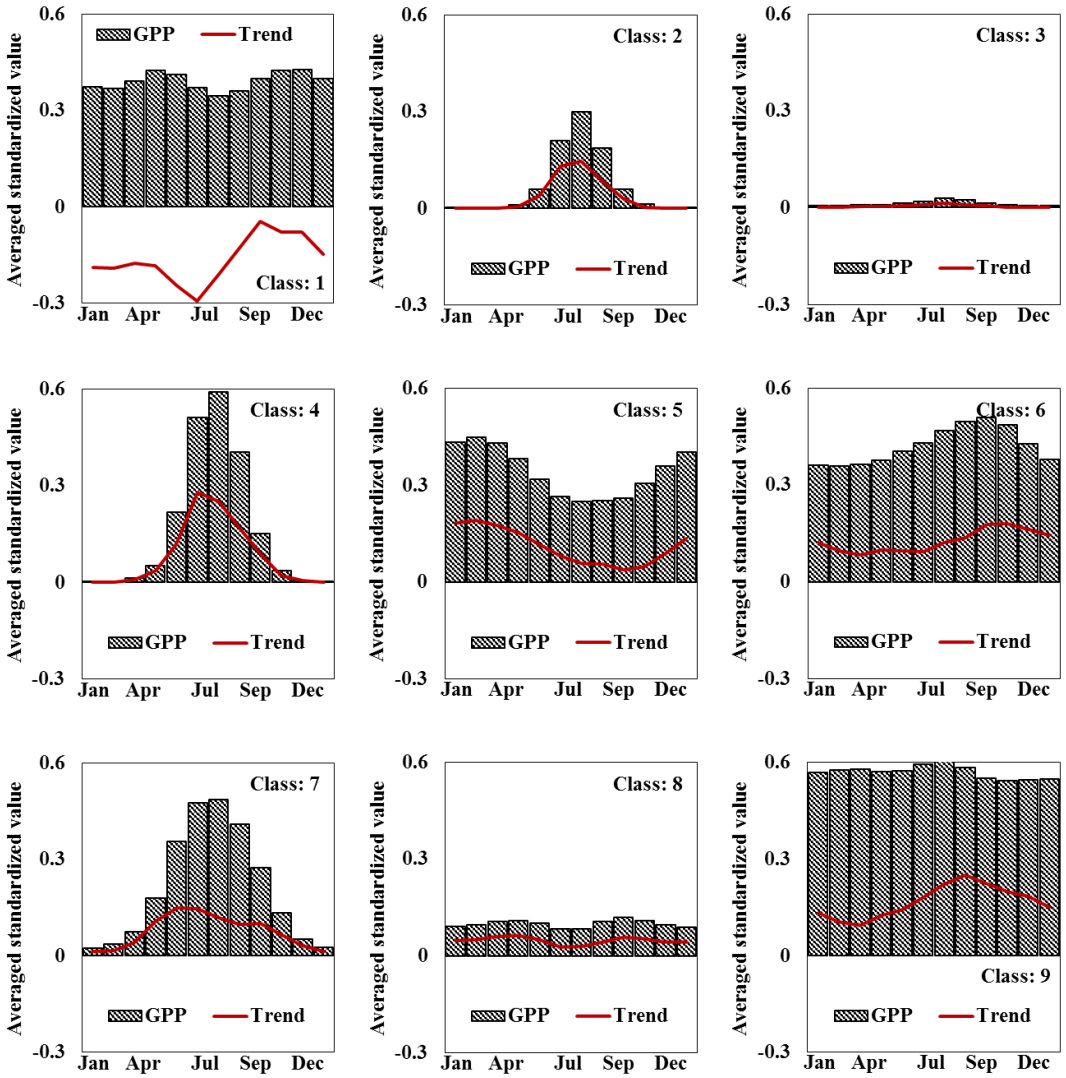

Figure 3.7 Characteristics of the annual cycle of the growing season distribution and GPP trends associated with each class.

3.4 Discussions

3.4.1 Increases in atmospheric CO_2 concentration

In this chapter, the contribution of the rising CO_2 concentration on the globally averaged GPP trend is the largest proportion. However, I cannot conclude that the effect of the increasing CO_2 concentration on GPP variations is more important than the changes in other factors. The main reason is that the increases in the CO_2 concentration occurred in a globally synchronous manner, while the global averaged effects of the other factors are neutralized because the attributions can be positive or negative in different locations (Figure 3.7). An elevated atmospheric CO_2 concentration enhances vegetation photosynthesis and has indirect effects on increasing water use efficiency (Donohue et al., 2013; Fensholt et al., 2012), and in this chapter, I can see that the regions with a relatively larger increasing GPP trend also had better water condition trends (e.g., Asian rainforest, Amazon rainforest, eastern Africa, and large areas in the middle-high latitudes in the Northern Hemisphere). In my estimation, the rising CO_2 concentration causes an average of a 2.63% increase around the globe over 34 years which falls within the range of a sensitivity analysis on GPP affected by increasing CO_2 (Wang et al. 2014). Models that do not consider CO_2 fertilization modules might be a source of uncertainty (Anav et al. 2015) in estimating GPP, and elevated atmospheric CO_2 concentration is one of the main reasons for global climate change. Therefore, I used the CFix model, which has a carbon fertilization module instead of other LUE models such as the CASA (Potter et al., 1993), CFlux (Turner et al., 2006a) VPM (Xiao et al., 2004), VPRM (Mahadevan et al., 2008), EC-LUC (Yuan et al., 2007) and MODIS-GPP algorithms (Running et al., 2000). I used the MTE GPP and MODIS product to compare our estimated GPP and found that we estimated a higher GPP than the MTE GPP and MODIS product. The relationship with MODIS GPP is consistent with previous studies (Heinsch et al., 2006; Avan et al., 2015), which reported that the products are smaller than the GPP observed at many flux tower sites. The growth rate of the slopes of the estimated GPP on the MODIS product shows a significant correlation with the trend of rising CO_2 concentrations with a correlation coefficient of 0.9290 (Figure 3.8). This finding can better illustrate that without considering carbon, fertilization is the main reason for the lower values in MODIS product. Regarding the comparison with MTE GPP, my estimates are larger than MTE GPP, with an average slope of 1.1985 from 1982 to 2011, with the trend of following the rising CO_2 concentration. This result is almost the same as the finding by Piao (2013), who used 10 process-based terrestrial biosphere models used for the IPCC Fifth Assessment Report compared to MTE GPP, and the models were found to produce a higher GPP than MTE with a trend of 1.1271 from 1982 to 2008. Therefore, my estimates can successfully reflect the effect of elevated CO_2 concentration on GPP during the period of 1982-2015.

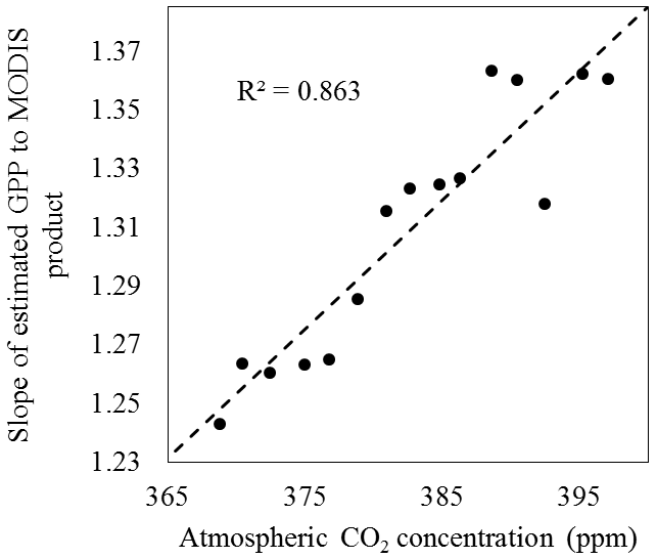

Figure 3.8 Relationship between the slopes of the estimated GPP to MODIS product and atmospheric CO_2 concentration.

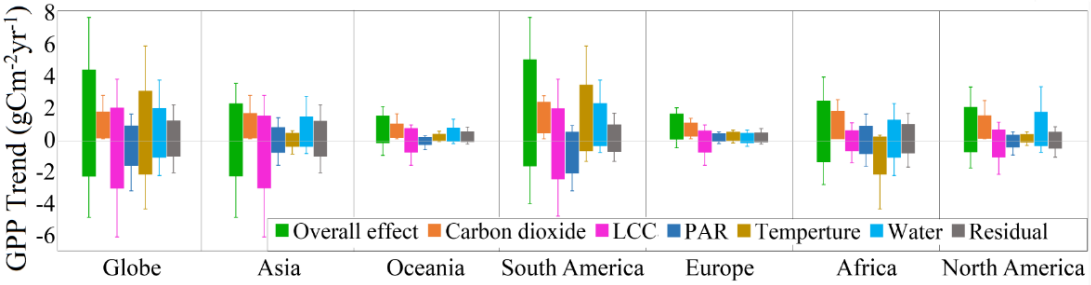

Figure 3.9 The range of contributions of GPP to different factors globally and on each continent (The bottom of the box is the lower quartile, and the top is the upper quartile. The whiskers extend to the maximum and minimum values).

3.4.2 Effects of LCC

For the globe, the greatest negative impact on the GPP trend is from LCC, which has a direct effect on PFTs (Chen et al., 2006). These negative effect areas are concentrated in South America (especially Brazil, Argentina, Bolivia and Paraguay), Eurasian rainforests (especially Indonesia), and tropical dry forests in Africa (especially Ethiopia), all of which had the highest rate of forest loss (Lepers et al., 2005; Hansen et al., 2017). In addition, the rates of forest loss were relative lower in the temperate climate zones of North America and Europe, where the LCC also had a relatively lower negative effect on GPP. In Europe and Oceania, the latitudinal span is not as great as on other continents; therefore, the range of the effects of radiation, water and temperature are relatively consistent, and the most significant spatial difference effect is from LCC (Figure 3.9).

3.4.3 Effects of climatic factors on GPP

The changes in the temperature and water over the past 34 years are estimated to cause increases in GPP around the world as a whole, which is contrary to the results caused by changes in radiation. However, the effect of these factor trends can be positive or negative in different

regions. To further investigate the possible climate drivers that cause the seasonal dynamics and varying patterns of GPP during the period of 1982-2015, we analyzed the monthly trends for each factor (Figure S2-S5) and summarized the distribution of the regions where GPP has varied due to different possible drivers.

The productivity of vegetation in tropical dry zone is weak; climate change induces a slight trend in GPP in those regions. The GPP trends in tropical wet zones (i.e. Indonesian- Malaysian rainforest, Latin America) are positive because their dominant factor, water conditions, have become increasingly suitable for vegetation growth, which is also suitable for the high altitudes in Africa. In cool temperate moist zones, the positive trend is the result from the early growing season lengthening caused by radiation shifts and plant growth enhancement caused by temperature and radiation changes. With respect to cool temperate dry zones, the positive effects of the temperature and radiation during the rapid growth stage are the main drivers causing increases in the amplitude of vegetation growth. For most warm temperate dry zones, the changes of the GPP are dominated by radiation; hydrothermal conditions in the regions are almost unchanged during the growing season (from May to September). Conversely, radiation and water conditions together led to an increasing GPP trend in warm temperate moist zones, where water condition changes enhance the plant growth magnitudes and radiation lengthens the growing season. Additionally, in tropical moist zones, the evapotranspiration is reduced by the decreasing temperature; simultaneously, the water conditions become more suitable for plant growth. Therefore, the GPP trends are positive. Moreover, in South America, the growing season length has been extended by increased radiation in the later period of the rapid growth stage. In boreal moist zones, radiation and hydrothermal conditions in the growing season jointly promote vegetation growth. Regarding polar moist zones, in September, the rapid growth stage has an early end due to the declining radiation, but the water conditions and temperature elevating the GPP magnitude during the growing season result in a positive effect. For Congo Basin and Brazilian Highlands where following by increasing temperatures and decreasing water the monthly GPP decreased mostly. The Congo rainforest has some continental climate characteristics, where water is the dominant factor inducing the trend in GPP. Water conditions become more unsuitable; although radiation became more abundant, it is accompanied by increasing temperatures and evapotranspiration, ultimately inducing a negative trend in GPP. Additionally, in South Central Australia, three factors contribute to the conditions: water conditions dominate the GPP changes, including the magnitudes and growing season length; radiation increased during the later growth period; and temperatures became more suitable during the growing season.

Combined with terrain and location, I can generally and summarily conclude that radiation and temperature are relatively sufficient for vegetation in lower latitudes since solar irradiation occurs twice a year. Therefore, water conditions have become the dominant climatic factor affecting GPP trends. In addition, adequate water conditions are associated with decreasing radiation due to cloud cover and reducing temperature due to evaporation. Hence, the trends of GPP in lower latitudes are also affected by radiation and temperature synergistically, while in the middle and high latitudes, the main climatic factors affecting GPP trends are temperature and radiation, which have improved the demand for suitable conditions during the growing season and explains much of the increasing GPP trends in temperature and radiation variability in the northern regions of North America and Eurasia. Additionally, in high altitude regions, since the hydrothermal conditions are further from the ideal situation, temperature and water conditions are the main climatic factors in GPP trends in these regions.

3.5 Conclusions

In this chapter, I estimated the global monthly GPP at a 0.5° × 0.5° spatial resolution during the period of 1982~2015, analyzed the effects of drivers on GPP trend and zoned the categories of GPP variation.

The five factors considered in this chapter resulted in an overall positive effect on the GPP trend but with different spatial patterns, magnitudes, and mechanisms. Globally, increases in GPP occurred in over 75 % of the areas; the interactions between factors were positive, and the increases in atmospheric CO_2 concentration had the greatest contribution on global increasing GPP. However, regionally, the LCC and climatic factors appear play more important roles in GPP changes.

Larger areas in the lower latitudes showed increases in the amplitude of the GPP annual cycle which dominated by shifts in water conditions; in contrast, in the middle latitudes GPP expressed not only the amplitude changes but also a lengthened rapid growth stage during the early period which were likely to be driven by increases in temperature and radiation; in large areas of the Southern Hemisphere, GPP increased in both the early and later period of the growing season, resulting in a lengthening growing season. However, at high altitudes, the changes in GPP were probably caused by the changes in the temperature and water conditions.

The CO_2 fertilization effect was explicitly expressed in this study by comparisons with MTE and MODIS GPP. By contrast, the effect of nutrition cannot be quantified from our study since any resulting changes were implicit in the satellite-observed NDVI and were not explicitly modeled. Many studies show that nutrient availability strongly constrains vegetation growth through water availability, the CO_2 assimilation rate and other factors (Reich et al., 2014; Wieder et al., 2015). The potential effects of nutrient limitation should be considered in estimates of the terrestrial GPP in future studies.

In summary, I found a wide range of GPP trends, both spatially and seasonally. It appears that CO_2, LCC and climatic factors together played a role in global terrestrial GPP changes.

References

Ainsworth, E.A.; Long, S.P. What have we learned from 15 years of free-air CO2 enrichment (FACE)? A meta-analytic review of the responses of photosynthesis, canopy properties and plant production to rising CO2. *New Phytol* **2005**, *165*, 351-371.

Anav, A.; Friedlingstein, P.; Beer, C.; Ciais, P.; Harper, A.; Jones, C.; Murray-Tortarolo, G.; Papale, D.; Parazoo, N.C.; Peylin, P., et al. Spatiotemporal patterns of terrestrial gross primary production: A review. *Reviews of Geophysics* **2015**, *53*, 785-818.

Bazzaz, F.A. The Response Of Natural Ecosystems To the Rising Global Co2 Levels. *Annual Review Of Ecology And Systematics* **1990**, *21*, 167-196.

Beer, C.; Reichstein, M.; Ciais, P.; Farquhar, G.D.; Papale, D. Mean annual GPP of Europe derived from its water balance. *Geophysical Research Letters* **2007**, *34*.

Beer, C.; Reichstein, M.; Tomelleri, E.; Ciais, P.; Jung, M.; Carvalhais, N.; Rodenbeck, C.; Arain, M.A.; Baldocchi, D.; Bonan, G.B., et al. Terrestrial gross carbon dioxide uptake: global distribution and covariation with climate. *Science* **2010**, *329*, 834-838.

CCI-LC URD Phase I. Land Cover Climate Change Initiative - User Requirements Document. Issue 2.2.Date 23.02.**2011**.

Chang, J.; Ciais, P.; Viovy, N.; Vuichard, N.; Herrero, M.; Havlík, P.; Wang, X.; Sultan, B.; Soussana, J.F. Effect of climate change, CO2 trends, nitrogen addition, and land-cover and management intensity changes on the carbon balance of European grasslands. *Global change biology* **2016**, *22*, 338-350.

Chen, H.; Tian, H.Q.; Liu, M.L.; Melillo, J.; Pan, S.F.; Zhang, C. Effect of land-cover change on terrestrial carbon dynamics in the southern United States. *Journal Of* Environmental *Quality* **2006**, *35*, 1533-1547.

Chiesi, M.; Fibbi, L.; Genesio, L.; Gioli, B.; Magno, R.; Maselli, F.; Moriondo, M.; Vaccari, F.P. Integration of ground and satellite data to model Mediterranean forest processes. *International Journal of Applied Earth Observation and Geoinformation* **2011**, *13*, 504-515.

Conway, D.; Persechino, A.; Ardoin-Bardin, S.; Hamandawana, H.; Dieulin, C.; Mahé, G. Rainfall and water resources variability in sub-Saharan Africa during the twentieth century. *Journal of Hydrometeorology* **2009**, *10*, 41-59.

de Jong, R.; Schaepman, M.E.; Furrer, R.; de Bruin, S.; Verburg, P.H. Spatial relationship between climatologies and changes in global vegetation activity. *Glob Chang Biol* **2013**, *19*, 1953-1964.

Donohue, R.J.; Roderick, M.L.; McVicar, T.R.; Farquhar, G.D. Impact of CO2 fertilization on maximum foliage cover across the globe's warm, arid environments. *Geophysical Research Letters* **2013**, *40*, 3031-3035.

Farquhar, G.D. Carbon dioxide and vegetation. *Science* **1997**, *278*, 1411-1411.

Fensholt, R.; Langanke, T.; Rasmussen, K.; Reenberg, A.; Prince, S.D.; Tucker, C.; Scholes, R.J.; Le, Q.B.; Bondeau, A.; Eastman, R. Greenness in semi-arid areas across the globe 1981–2007—an Earth Observing Satellite based analysis of trends and drivers. *Remote sensing of environment* **2012**, *121*, 144-158.

Frankenberg, C.; Fisher, J.B.; Worden, J.; Badgley, G.; Saatchi, S.S.; Lee, J.E.; Toon, G.C.; Butz, A.; Jung, M.; Kuze, A., et al. New global observations of the terrestrial carbon cycle from GOSAT: Patterns of plant fluorescence with gross primary productivity. *Geophysical Research Letters* **2011**, *38*.

Gibbs, H.K.; Ruesch, A.S.; Achard, F.; Clayton, M.K.; Holmgren, P.; Ramankutty, N.; Foley, J.A. Tropical forests were the primary sources of new agricultural land in the 1980s and 1990s. *Proceedings of the National Academy of Sciences* **2010**, *107*, 16732-16737.

Gillett, N.P.; Arora, V.K.; Matthews, D.; Allen, M.R. Constraining the ratio of global warming to cumulative CO2 emissions using CMIP5 simulations. *Journal of Climate* **2013**, *26*, 6844-6858.

Gilmanov, T.G.; Verma, S.B.; Sims, P.L.; Meyers, T.P.; Bradford, J.A.; Burba, G.G.; Suyker, A.E. Gross primary production and light response parameters of four Southern Plains ecosystems estimated using long-term CO2-flux tower measurements. *Global Biogeochemical Cycles* **2003**, *17*, n/a-n/a.

Hansen, M.; DeFries, R.; Townshend, J.R.; Sohlberg, R. UMD global land cover classification, 1 kilometer, 1.0. *Department of Geography, University of Maryland, College Park, Maryland* **1981**, *1994*, 1998.

Hansen, M.C.; Potapov, P.V.; Moore, R.; Hancher, M.; Turubanova, S.A.; Tyukavina, A.; Thau, D.; Stehman, S.V.; Goetz, S.J.; Loveland, T.R., et al. High-resolution global maps of 21st-century forest cover change. *Science* **2013**, *342*.

Hartigan, J. The K-means algorithm. *Clustering algorithms* **1975**, *4*.

Haverd, V.; Smith, B.; Nieradzik, L.; Briggs, P.; Canadell, J. A novel assessment of the role of land-use and land-cover change in the global carbon cycle, using a new Dynamic Global Vegetation Model version of the CABLE land surface model. In Proceedings of EGU General Assembly Conference Abstracts; p. 13881.

Heinsch, F.A.; Zhao, M.; Running, S.W.; Kimball, J.S.; Nemani, R.R.; Davis, K.J.; Bolstad, P.V.; Cook, B.D.; Desai, A.R.; Ricciuto, D.M. Evaluation of remote sensing based terrestrial productivity from MODIS using regional tower eddy flux network observations. *IEEE Transactions on Geoscience and Remote Sensing* **2006**, *44*, 1908-1925.

Hicke, J.A.; Asner, G.P.; Randerson, J.T.; Tucker, C.; Los, S.; Birdsey, R.; Jenkins, J.C.; Field, C. Trends in North American net primary productivity derived from satellite observations, 1982–1998. *Global Biogeochemical Cycles* **2002**, *16*.

Holben, B.N. Characteristics of Maximum-Value Composite Images from Temporal Avhrr Data. *International Journal of Remote Sensing* **1986**, *7*, 1417-1434.

Huang, M.; Piao, S.; Sun, Y.; Ciais, P.; Cheng, L.; Mao, J.; Poulter, B.; Shi, X.; Zeng, Z.; Wang, Y. Change in terrestrial ecosystem water-use efficiency over the last three decades. *Glob Chang Biol* **2015**, *21*, 2366-2378.

Jepson, W. A disappearing biome? Reconsidering land-cover change in the Brazilian savanna. *The* Geographical *Journal* **2005**, *171*, 99-111.

Jung, M.; Reichstein, M.; Margolis, H.A.; Cescatti, A.; Richardson, A.D.; Arain, M.A.; Arneth, A.; Bernhofer, C.; Bonal, D.; Chen, J.Q., et al. Global patterns of land-atmosphere fluxes of carbon dioxide, latent heat, and sensible heat derived from eddy covariance, satellite, and meteorological observations. *J Geophys Res-Biogeo* **2011**, *116*.

Lambin, E.F.; Turner, B.L.; Geist, H.J.; Agbola, S.B.; Angelsen, A.; Bruce, J.W.; Coomes, O.T.; Dirzo, R.; Fischer, G.; Folke, C. The causes of land-use and land-cover change: moving beyond the myths. *Global environmental change* **2001**, *11*, 261-269.

Lepers, E.; Lambin, E.F.; Janetos, A.C.; DeFries, R.; Achard, F.; Ramankutty, N.; Scholes, R.J. A synthesis of information on rapid land-cover change for the period 1981–2000. *AIBS Bulletin* **2005**, *55*, 115-124.

Li, X.; Liang, S.; Yu, G.; Yuan, W.; Cheng, X.; Xia, J.; Zhao, T.; Feng, J.; Ma, Z.; Ma, M. Estimation of gross primary production over the terrestrial ecosystems in China. *Ecological Modelling* **2013**, *261*, 80-92.

Li, X.; Zhu, Z.; Zeng, H.; Piao, S. Estimation of gross primary production in China (1982–2010) with multiple ecosystem models. *Ecological modelling* **2016**, *324*, 33-44.

Liang, W.; Yang, Y.; Fan, D.; Guan, H.; Zhang, T.; Long, D.; Zhou, Y.; Bai, D. Analysis of spatial and temporal patterns of net primary production and their climate controls in China from 1982 to 2010. *Agricultural and Forest Meteorology* **2015**, *204*, 22-36.

Luo, Y.; Hui, D.; Zhang, D. Elevated CO2 stimulates net accumulations of carbon and nitrogen in land ecosystems: a meta-analysis. *Ecology* **2006**, *87*, 53-63.

Ma, J.; Yan, X.; Dong, W.; Chou, J. Gross primary production of global forest ecosystems has been overestimated. Scientific *reports* **2015**, *5*, 10820.

Mahadevan, P.; Wofsy, S.C.; Matross, D.M.; Xiao, X.; Dunn, A.L.; Lin, J.C.; Gerbig, C.; Munger, J.W.; Chow, V.Y.; Gottlieb, E.W. A satellite-based biosphere parameterization for net ecosystem CO2 exchange: Vegetation Photosynthesis and Respiration Model (VPRM). *Global Biogeochemical Cycles* **2008**, *22*.

Masarie, K.A.; Tans, P.P. Extension and Integration of Atmospheric Carbon-Dioxide Data into a Globally Consistent Measurement Record. *J Geophys Res-Atmos* **1995**, *100*, 11593-11610.

Maselli, F.; Papale, D.; Puletti, N.; Chirici, G.; Corona, P. Combining remote sensing and ancillary data to monitor the gross productivity of water-limited forest ecosystems. *Remote Sensing of Environment* 2009, *113*, 657-667.

Myneni, R.; Williams, D. On the relationship between FAPAR and NDVI. *Remote Sensing of Environment* 1994, *49*, 200-211.

Nemani, R.R.; Keeling, C.D.; Hashimoto, H.; Jolly, W.M.; Piper, S.C.; Tucker, C.J.; Myneni, R.B.; Running, S.W. Climate-driven increases in global terrestrial net primary production from 1982 to 1999. *Science* **2003**, *300*, 1560-1563.

Norby, R.J.; DeLucia, E.H.; Gielen, B.; Calfapietra, C.; Giardina, C.P.; King, J.S.; Ledford, J.; McCarthy, H.R.; Moore, D.J.; Ceulemans, R. Forest response to elevated CO2 is conserved across a broad range of productivity. *Proceedings of the National Academy of Sciences of the United States of America* **2005**, *102*, 18052-18056.

Peters, W.; Jacobson, A.R.; Sweeney, C.; Andrews, A.E.; Conway, T.J.; Masarie, K.; Miller, J.B.; Bruhwiler, L.M.; Petron, G.; Hirsch, A.I., et al. An atmospheric perspective on North American carbon dioxide exchange: CarbonTracker. *Proc Natl Acad Sci U S A* **2007**, *104*, 18925-18930.

Piao, S.; Fang, J.; Zhou, L.; Ciais, P.; Zhu, B. Variations in satellite-derived phenology in China's temperate vegetation. *Global Change Biology* **2006**, *12*, 672-685.

Piao, S.; Sitch, S.; Ciais, P.; Friedlingstein, P.; Peylin, P.; Wang, X.; Ahlstrom, A.; Anav, A.; Canadell, J.G.; Cong, N., et al. Evaluation of terrestrial carbon cycle models for their response to climate variability and to CO2 trends. *Glob Chang Biol* **2013**, *19*, 2117-2132.

Potter, C.S.; Randerson, J.T.; Field, C.B.; Matson, P.A.; Vitousek, P.M.; Mooney, H.A.; Klooster, S.A. Terrestrial ecosystem production: a process model based on global satellite and surface data. *Global Biogeochemical Cycles* **1993**, *7*, 811-841.

Poulter, B.; Frank, D.; Ciais, P.; Myneni, R.B.; Andela, N.; Bi, J.; Broquet, G.; Canadell, J.G.; Chevallier, F.; Liu, Y.Y., et al. Contribution of semi-arid ecosystems to interannual variability of the global carbon cycle. *Nature* **2014**, *509*, 600-603.

Quaife, T.; Quegan, S.; Disney, M.; Lewis, P.; Lomas, M.; Woodward, F.I. Impact of land cover uncertainties on estimates of biospheric carbon fluxes. *Global Biogeochemical Cycles* **2008**, *22*.

Reich, P.B.; Hobbie, S.E.; Lee, T.D. Plant growth enhancement by elevated CO2 eliminated by joint water and nitrogen limitation. *Nature Geoscience* **2014**, *7*, 920-924.

Reyer, Christopher; Asrar, Gassem; Betts, Richard; Chang, Jinfeng; Chen, Min; Ciais, Philippe; Dury, Marie; Francois, Louis; Henrot, Alexandra; Hickler, Thomas; Ito, Akihiko; Jacquemin, Ingrid; Nishina, Kazuya; Mishurov, Mikhail; Morfopoulos, Catherine; Munhoven, Guy; Ostberg, Sebastian; Pan, Shufen; Rafique, Rashid; Schaphoff, Sibyll; Steinkamp, Jörg; Tian, Hanqin; Ren,

Wei; Yang, Jia; Zeng, Ning; Zhao, Fang; Büchner, Matthias, ISIMIP2a Simulation Data from Biomes Sector. GFZ Data Services, **2017**.

Rienecker, M.M.; Suarez, M.J.; Gelaro, R.; Todling, R.; Bacmeister, J.; Liu, E.; Bosilovich, M.G.; Schubert, S.D.; Takacs, L.; Kim, G.-K. MERRA: NASA's modern-era retrospective analysis for research and applications. *Journal of climate* **2011**, *24*, 3624-3648.

Running, S.W.; Thornton, P.E.; Nemani, R.; Glassy, J.M. Global terrestrial gross and net primary productivity from the Earth Observing System. *Methods in ecosystem science* **2000**, *3*, 44-45.

Sun, Z.Y.; Wang, X.F.; Yamamoto, H.; Tani, H.; Zhong, G.S.; Yin, S. An attempt to introduce atmospheric CO2 concentration data to estimate the gross primary production by the terrestrial biosphere and analyze its effects. *Ecological Indicators* **2018**, *84*, 218-234.

Task, G.S.D. Global soil data products CD-ROM contents (IGBP-DIS). *ORNL DAAC* **2014**.

Tucker, C.J.; Pinzon, J.E.; Brown, M.E.; Slayback, D.A.; Pak, E.W.; Mahoney, R.; Vermote, E.F.; El Saleous, N. An extended AVHRR 8-km NDVI dataset compatible with MODIS and SPOT vegetation NDVI data. *International Journal of Remote Sensing* **2005**, *26*, 4485-4498.

Turner, D.; Ritts, W.; Styles, J.; Yang, Z.; Cohen, W.; Law, B.; Thornton, P. A diagnostic carbon flux model to monitor the effects of disturbance and interannual variation in climate on regional NEP. *Tellus B* **2006**, *58*, 476-490.

Turner, D.P.; Ritts, W.D.; Cohen, W.B.; Gower, S.T.; Running, S.W.; Zhao, M.; Costa, M.H.; Kirschbaum, A.A.; Ham, J.M.; Saleska, S.R. Evaluation of MODIS NPP and GPP products across multiple biomes. *Remote Sensing of Environment* **2006**, *102*, 282-292.

Van den Dool, H.; Huang, J.; Fan, Y. Performance and analysis of the constructed analogue method applied to US soil moisture over 1981–2001. *Journal of Geophysical Research: Atmospheres* **2003**, *108*.

Veroustraete, F.; Sabbe, H.; Eerens, H. Estimation of carbon mass fluxes over Europe using the C-Fix model and Euroflux data. *Remote Sensing of Environment* **2002**, *83*, 376-399.

Veroustraete, F.; Sabbe, H.; Rasse, D.P.; Bertels, L. Carbon mass fluxes of forests in Belgium determined with low resolution optical sensors. *International Journal of Remote Sensing* **2004**, *25*, 769-792.

Verstraeten, W.W.; Veroustraete, F.; Feyen, J. On temperature and water limitation of net ecosystem productivity: Implementation in the C-Fix model. *Ecological Modelling* **2006**, *199*, 4-22.

Wang, H.; Prentice, I.C.; Davis, T.W. Biophsyical constraints on gross primary production by the terrestrial biosphere. *Biogeosciences* **2014**, *11*, 5987-6001.

Wang, K.-Y. Canopy CO2 exchange of Scots pine and its seasonal variation after four-year exposure to elevated CO2 and temperature. *Agricultural and Forest Meteorology* **1996**, *82*, 1-27.

Wieder, W.R.; Cleveland, C.C.; Smith, W.K.; Todd-Brown, K. Future productivity and carbon storage limited by terrestrial nutrient availability. *Nature Geoscience* **2015**, *8*, 441.

Wu, D.; Zhao, X.; Liang, S.; Zhou, T.; Huang, K.; Tang, B.; Zhao, W. Time-lag effects of global vegetation responses to climate change. *Glob Chang Biol* **2015**, *21*, 3520-3531.

Xiao, X.; Zhang, Q.; Braswell, B.; Urbanski, S.; Boles, S.; Wofsy, S.; Moore, B.; Ojima, D. Modeling gross primary production of temperate deciduous broadleaf forest using satellite images and climate data. *Remote Sensing of Environment* **2004**, *91*, 256-270.

Yan, H.M.; Zhan, J.Y.; Yang, H.C.; Zhang, F.; Wang, G.F.; He, W.J. Long time-series spatiotemporal variations of NPP and water use efficiency in the lower Heihe River Basin with serious water scarcity. *Phys Chem Earth* **2016**, *96*, 41-49.

Yang, S.H.; Xu, J.Z.; Liu, X.Y.; Zhang, J.G.; Wang, Y.J. Variations of carbon dioxide exchange in paddy field ecosystem under water-saving irrigation in Southeast China. *Agricultural Water Management* **2016**, *166*, 42-52.

Yuan, W.; Cai, W.; Liu, S.; Dong, W.; Chen, J.; Arain, M.A.; Blanken, P.D.; Cescatti, A.; Wohlfahrt, G.; Georgiadis, T., et al. Vegetation-specific model parameters are not required for estimating gross primary production. *Ecological Modelling* **2014**, *292*, 1-10.

Yuan, W.; Cai, W.; Xia, J.; Chen, J.; Liu, S.; Dong, W.; Merbold, L.; Law, B.; Arain, A.; Beringer, J., et al. Global comparison of light use efficiency models for simulating terrestrial vegetation gross primary production based on the LaThuile database. *Agricultural and Forest Meteorology* **2014**, *192-193*, 108-120.

Yuan, W.P.; Liu, S.; Zhou, G.S.; Zhou, G.Y.; Tieszen, L.L.; Baldocchi, D.; Bernhofer, C.; Gholz, H.; Goldstein, A.H.; Goulden, M.L., et al. Deriving a light use efficiency model from eddy covariance flux data for predicting daily gross primary production across biomes. *Agricultural And Forest Meteorology* **2007**, *143*, 189-207.

Zhao, M.S.; Running, S.W. Drought-Induced Reduction in Global Terrestrial Net Primary Production from 2000 Through 2009. *Science* **2010**, *329*, 940-943.

Zimmer, C. Earth's Oxygen: A Mystery Easy to Take for Granted. *New York Times* **2013**.

Chapter 4 Investigation on effect of CO_2 fertilization on GPP

Quantitative estimations of the GPP and its variations at spatial scales are important issues with future significance due to the increasing atmospheric CO_2 levels. However, the effects of the spatiotemporal variability in the atmospheric CO_2 concentrations on GPP estimations are challenging with respect to the terrestrial ecosystem due to land cover component characteristics and difficulties associated with measuring CO_2 concentrations over large spatial areas. The development of remote sensing offers a means to routinely monitor CO_2 concentrations both spatially and temporally from space. Therefore, this chapter firstly applied the improved daily BEPS model to estimate the global GPP from 2000 to 2015, compared the estimated GPP with the flux tower measurements and other GPP products to verify the estimation accuracy and analyze the CO_2 fertilization effect, and conducted spatial analysis on the effects of the spatiotemporal distribution of the CO_2 concentration on the estimation of GPP. And then, to introduce continuous spatial CO_2 data as an indicator for the estimation of the terrestrial biosphere GPP, I used the decoupling coefficients to evaluate the canopy CO_2 concentrations, photosynthetic biochemical models to calculate the photosynthetic rate, and big-leaf model to scale up to a global scale. the method proposed in this study utilizing continuous spatial CO_2 data to estimate the GPP is practicable and feasible.

4.1 Introduction

The terrestrial GPP, which is defined as the amount of carbon uptake by vegetation through photosynthesis at the ecosystem scale, is a key area in climate change research (Hilker et al., 2008, Beer et al., 2010). The GPP through photosynthesis by terrestrial ecosystems constitutes the largest global land carbon flux (Zhao and Running, 2010; Beer et al., 2010; Zhu et al., 2016), affects the land-atmosphere CO_2 exchange and is important for regulating atmospheric CO_2 concentrations (Li et al., 2016). As reported, the increase in atmospheric CO_2 on Earth is the major cause of global climate change (Hartmann et al., 2013; IPCC AR5), and over the past century, the CO_2 accumulation rate has continuously increased with the amount of CO_2 released due to landcover changes and fossil fuel combustion (Le Quéré et al., 2016). GPP is the starting point of the terrestrial carbon biogeochemical cycle (Raupach et al., 2008) and, thus, serves as the gateway for the energy and carbon that are required for almost all ecosystem processes (Gilmanov et al., 2003). Therefore, the GPP is an important biophysical parameter for any ecosystem that plays a key role in the spatiotemporal dynamics of CO_2 (Ahongshangbam et al., 2016). At the global scale, direct measurements of the GPP do not exist (Anav et al., 2015); therefore, GPP estimation has become a key issue for scientists quantifying global carbon cycles (Canadell et al., 2000; Gitelson et al., 2006). There is, thus, a need to better understand the mechanisms that control the terrestrial GPP to provide an accurate GPP estimations and the dynamic changes in the carbon fluxes between the biosphere and atmosphere to help quantify the potential changes resulting from global climate change (Poulter et al., 2014; Li et al., 2016).

However, directly measuring GPP at the global scale is infeasible (Ma et al. 2015); rather, the global terrestrial GPP has been estimated using inverse models that use atmospheric transport models and atmospheric CO_2 concentrations or CO_2 isotopes (Bousquet et al., 1999; Reichstein et al., 2003; Welp et al., 2011), physiological and ecological process models (Schaefer et al., 2012; Beer et al., 2010; Anav et al., 2015) and RS estimates (Joiner et al., 2011; Frankenberg et al., 2011; Guanter et al., 2014; Yuan et al., 2014). In recent years, with the development of space technology, satellite-based models, particularly LUE models, have been widely used to estimate the GPP on regional and global scales (Yuan et al., 2014). However, for

most RS-based models, CO_2, which is the raw material needed for photosynthesis and the main cause of global warming, is rarely considered as a primary parameter (Wang et al., 2014).

The increases in atmospheric CO_2 concentration that have occurred since the industrial revolution are expected to cause a CO_2 fertilization effect (Canadell et al., 2007), where photosynthesis is enhanced by the increase in CO_2 (Farquhar 1997). Additionally, many scholars (van Oijen et al., 2004; McMurtrie et al., 2008; Yang et al., 2016) have determined that the increasing atmospheric CO_2 concentration affects GPP, and numerous studies (Sun et al., 2018; Norby et al., 2005; Ainsworth and Long 2005) have been conducted to improve our understanding on how plants and ecosystems respond to the elevated CO_2 levels. The large-scale FACE showed that forest ecosystems were more responsive than were other functional types; specifically, C4 species showed little response to elevated CO_2 concentrations (Ainsworth and Long 2005). The response of plants to elevated CO_2 would be greater in dry, high-nitrogen conditions (McMurtrie et al., 2008); additionally, the CO_2 fertilization caused by the enhanced foliage cover across the global warm and arid environments is significant (Donohue et al., 2013), resulting in increased photosynthesis area and improved GPP to a certain degree. At the same time, the climatic factors and their interactions (Chang et al., 2016) with the soil resources (Reich et al., 2014) and nitrogen level (Luo et al., 2004 2006; Donohue et al., 2013) would also constrain CO_2 fertilization to enhance GPP (Anav et al., 2015). Theoretically, CO_2, which is chemically inert, is generally well-mixed globally (Eby et al., 2009), but it presents temporal and spatial characteristics (Miles et al, 2012; Sun et al., 2016). However, few studies have incorporated the global-scale atmospheric CO_2 concentration into GPP estimates, or the studies have assumed that the CO_2 concentrations and variations are spatially and temporally uniform around the globe. According to the most recent global maps (Dec. 2016) of near surface air CO_2 concentrations from the Japan Meteorological Agency, the differences in the spatial distribution of atmospheric CO_2 concentrations could be greater than 40 ppm; furthermore, the concentrations are highest in South China (> 436 ppm) and lowest in Uruguay (< 396 ppm) (http:// ds.data.jma.go.jp / ghg / kanshi /CO_2map /CO_2pmapplot_alt_e. html), and these values mirror the increase in atmospheric CO_2 concentrations over the past 20 years (i.e., from 365.55 ppm in 1998 to 404.98 ppm in 2017). The spatial variation in the atmospheric CO_2 concentrations for the entire year of 2016 could reach approximately 50 ppm (lowest: 388 ppm in Canada during July), which is equivalent to the change in the global average mean annual CO_2 concentration from 1990 (353.96 ppm) to the present. In addition, the seasonal characteristics of the atmospheric CO_2 concentration have previously been reported at the local and regional scales (Davis et al., 2003; Miles et al., 2012; Liu et al., 2016). For example, the measurement of the atmospheric boundary layer of the CO_2 concentration from the North American Carbon Program's Mid Continent Intensive (MCI) from 2007 to 2009 showed that the seasonal CO_2 amplitude was five times larger than was the tropospheric background (Miles et al., 2012; Liu et al., 2016). Although numerous studies have demonstrated that increasing atmospheric CO_2 levels can influence the terrestrial GPP, the magnitude and the spatial distribution of the influence remain unclear. Models that do not consider the CO_2 fertilization module may serve as a source of uncertainty in the estimation of GPP (Anav et al., 2015). In tropical ecosystems, CO_2 fertilization could explain as much as 100% of the biospheric carbon sink (Ciais et al., 2004), with large uncertainties (bias: ± 68.42 %) (Howard 2005). Additionally, CO_2 fertilization could explain 50% of the Siberian and 10% of the European sinks (Canadell et al., 2007). In a sensitivity analysis in which CO_2 was elevated by 200 ppm, there was a 5 % to 25 % increase in the modeled annual GPP (Wang et al., 2014), and, when the current atmospheric CO_2 concentrations were doubled, most types of ecosystems showed a 10 ~ 25 %±2 % increase in the net primary production (Norby et al., 2005; Luo et al., 2006). With increases in the atmospheric CO_2 concentration, seasonal CO_2 variations, resulting

from photosynthesis and respiration, have substantially increased in amplitude over the last 50 years, particularly in high latitude regions north of 45°N, where the amplitude increased by approximately 50 % (Monroe 2013). Therefore, including the atmospheric CO_2 concentration in the global GPP estimation should be a research priority (Liu et al., 2016). The spatiotemporal characteristics of the atmospheric CO_2 concentrations affect the GPP, both intra- and inter-annually; therefore, the spatiotemporal distribution of the CO_2 concentrations should be considered as a factor in the estimation of GPP (Liu et al., 2016; Sun et al., 2018).

Global-scale models rarely use spatial CO_2 data, which may be due to difficulties related to the observation of global variations in CO_2 because the direct sampling of gasses requires great effort and cost (Sun et al., 2016). However, launching satellites to collect CO_2 data can solve this issue quite well. Since the launching of GOSAT, OCO-2 and other satellites, obtaining global CO_2 concentrations data has been possible (Oguma et al., 2011; Reuter et al., 2010).

Therefore, in this chapter, I used the BEPS (Chen et al., 1999), which is an RS-based process model based on the FvCB photosynthesis model (Farquhar et al., 1980), that considers the atmospheric CO_2 concentration data to estimate the GPP. Despite its namesake, BEPS can be used to simulate vegetation GPP for the entire global terrestrial ecosystem (Chen et al., 2012). In addition, in contrast with other ecological process-based models, BEPS proposes an algorithm to solve the spatiotemporal scaling conversion problem that occurs when using RS data to successfully drive the ecological process model (Chen et al., 1999); furthermore, BEPS works in combination with the multiple-layer canopy transfer model to describe the structure of the canopy, thereby eliminating the limitation of overestimations that occur when using actual solar radiation data (Matsushita et al., 2004). Considering the advantages of BEPS and because I mainly focused on the effects of the spatial distribution of the atmospheric CO_2 concentration on the GPP simulation, we selected the BEPSd (Zhang et al., 2018).

Firstly, I integrated the global-scale spatial continuous atmospheric CO_2 concentration data into the improved BEPSd (iBEPSd) model to estimate the daily GPP from 2000 to 2015; additionally, I utilized EC flux tower measurements to verify the accuracy of the model. Then, I analyzed the CO_2 fertilization effect by comparing the GPP products from the MTE, the MODIS and the VPM, which do not include the CO_2 fertilization module. Furthermore, this chapter considered that there are a few studies using global scale satellite-based CO_2 concentrations data to estimate the GPP and attempted to apply satellite-based CO_2 concentrations data to global GPP estimations, thus extending the range of satellite-based CO_2 applications, increasing the sources of CO_2 indicators, determining the effects of the spatiotemporal variations in atmospheric CO_2 concentrations on the spatial and temporal distributions of the GPP, and understanding the response of the GPP variation to the elevated atmospheric CO_2 concentrations. To achieve the objective of incorporating CO_2 concentration constraints into estimates of the terrestrial GPP, I calculated photosynthesis using a land surface model of leaf- and canopy-level photosynthesis based on Farquhar et al. (1980)'s measurement of C3 species and Collatz et al. (1992)'s measurement of C4 species at a photosynthesis model scale for the canopy level (Sellers et al., 1996a b). I utilized MODIS land products; GOSAT global CO_2 distribution data; MERRA global reanalysis climate data; and NACP (North American Carbon Program) Model Driver Data, which are supported by the canopy transmittance model and other methods, and relies on the assumptions that the realized photosynthetic rate, which is calculated from the biome-dependent invariant potential photosynthetic rate, is controlled by sucrose synthesis, Rubisco, light hitting canopy leaves, and upper- and lower-layer leaves that are only controlled by light (whichever is most limiting) to estimate the terrestrial GPP. Using the year 2014 as a case study, the GPP was estimated, and the accuracy of the estimates was assessed using by the GPP estimates from the Fluxnet 2015

dataset. Finally, I conducted an analysis on the GPP estimations from different atmospheric CO_2 concentration data forms to determine the influences of the seasonal and spatial variations and the distribution of atmospheric CO_2 concentration on the GPP estimates.

4.2 Data and methods

4.2.1 Data

4.2.1.1 Flux sites data

BEPS is a mature model for estimating the process in ecosystem, therefore, only sixty flux sites, including 9 ENF sites, 3 EBF sites, 1 DNF site, 13 DBF sites, 3 MF sites, 11 GRA sites, 6 CRO sites, 5 OSH sites, 4 WSA sites, 2 SAV sites and 3 WET sites, were used for assessing BEPS. A total of 395 site-years was available. The locations and general information for each site are listed in the Table 4.1. Among the meteorological inputs of iBEPSd, the daily temperature, radiation, VPD and C_a were retrieved from the measurements from the flux sites. Missing data from tower observations were not included in this study. The estimated GPP values were validated using the flux GPP at the 60 flux sites retrieved from the Fluxnet 2015 dataset. The available flux GPP that was employed in this study was the mean value of GPP_DT_VUT_REF and GPP_NT_VUT_REF. These were respectively estimated using the daytime and nighttime partitioning method (Lasslop et al., 2010) and the variable ustar threshold method. It is best to use as many sites as possible for new model accuracy assessment, therefore, all the sites in the period from 2000 to 2014 were used in the second step, representing a total of 1,095 observed years from 160 tower sites.

Table 4.1 The list of the flux tower sites used in this study.

No.	Site	PFT	Latitude	Longitude	Years
1	CA-TPD	DBF	42.64	-80.56	2012-2014
2	GF-Guy	EBF	5.28	-52.92	2004-2014
3	RU-SkP	DNF	62.26	129.17	2012-2014
4	US-AR2	GRA	36.64	-99.60	2009-2012
5	US-ARM	CRO	36.61	-97.49	2003-2012
6	US-Ha1	DBF	42.54	-72.17	2000-2012
7	US-IB2	GRA	41.84	-88.24	2004-2011
8	US-Ne3	CRO	41.18	-96.44	2001-2013
9	US-Oho	DBF	41.55	-83.84	2004-2013
10	US-SRC	OSH	31.91	-110.84	2004-2010
11	US-SRM	WSA	31.82	-110.87	2004-2010
12	US-Syv	MF	46.24	-89.35	2004-2007,2012-2013
13	US-Ton	WSA	38.43	-120.97	2004-2013
14	US-UMB	DBF	45.56	-84.71	2004-2013
15	US-UMd	DBF	45.56	-84.70	2004-2011
16	US-WCr	DBF	45.81	-90.08	2000-2006,2011-2014
17	US-Whs	OSH	31.74	-110.05	2007-2014
18	US-Wi3	DBF	46.63	-91.10	2002, 2004
19	US-Wi9	ENF	46.62	-91.08	2002-2003
20	CN-Cng	GRA	44.59	123.51	2007-2010
21	CA-TP1	ENF	42.66	-80.56	2003-2014
22	CA-SF3	OSH	54.09	-106.01	2002-2006
23	CA-SF2	ENF	54.25	-105.88	2001-2005
24	CA-SF1	ENF	54.49	-105.82	2003-2006
25	CA-Qfo	ENF	49.69	-74.34	2003-2010
26	CA-NS7	OSH	56.64	-99.95	2002-2005
27	CA-NS6	OSH	55.92	-98.96	2002-2005
28	CA-NS4	ENF	55.91	-98.38	2003-2005
29	AU-TUM	EBF	-35.66	148.15	2001-2013
30	AU-RDF	WSA	-14.56	132.48	2011-2012
31	AU-Fog	WET	-12.55	131.31	2006-2008
32	AU-Dry	SAV	-15.26	132.37	2008-2014
33	AU-DaS	SAV	-14.16	131.39	2008-2014
34	AU-Ade	WSA	-13.08	131.12	2007-2009
35	AU-ASM	ENF	-22.28	133.25	2010-2013
36	AU-DaP	GRA	-14.06	131.32	2008-2014
37	US-Ne1	CRO	41.17	-96.48	2001-2012
38	US-MMS	DBF	39.32	-86.41	2000-2014
39	US-Me6	ENF	44.32	-121.61	2010-2014
40	US-Los	WET	46.08	-89.98	2001-2008,2010,2014
41	US-ARM	CRO	36.61	-97.49	2003-2012
42	US-AR1	GRA	36.43	-99.42	2009-2012
43	RU-Ha1	GRA	54.73	90.00	2002-2004
44	JP-SMF	MF	35.26	137.08	2002-2006
45	JP-MBF	DBF	44.39	142.32	2004, 2005
46	IT-PT1	DBF	45.20	9.06	2002-2004

47	IT-CA3	DBF	42.38	12.02	2012-2013
48	IT-CA1	DBF	42.38	12.03	2011-2014
49	FR-Pue	EBF	43.74	3.60	2000-2013
50	FI-Jok	CRO	60.90	23.51	2002-2003
51	DK-Eng	GRA	55.69	12.19	2005-2007
52	DE-Lkb	ENF	49.10	13.30	2009-2013
53	CZ-BK2	GRA	49.49	18.54	2006-2011
54	CN-Du2	GRA	42.05	116.28	2008
55	ZM-Mon	DBF	-15.44	23.25	2007-2009
56	US-WPT	WET	41.46	-83.00	2011-2013
57	US-Wkg	GRA	31.74	-109.94	2004-2014
58	US-SRG	GRA	31.79	-110.83	2008-2014
59	US-PFa	MF	45.95	-90.27	2000-2014
60	US-Ne2	CRO	41.16	-96.47	2001-2012

4.2.1.2 CO_2 concentration data

The atmospheric CO_2 concentration data used to drive the BEPS model that estimated the GPP and analyzed the CO_2 fertilization effect in the present study was CT2016, which contains global daily continuous spatial CO_2 concentration data from 2000 to 2015; additionally, CT2016 is an open product of NOAA/ESRL that uses data from the greenhouse gas observational network and collaborating institutions (Peters et al., 2007) that was released on Feb 17th, 2017. In CT2016, the land biosphere, wildfire, fossil fuel emissions, atmospheric transport and other factors were data-assimilated to produce the estimates of surface fluxes and atmospheric CO_2 mole fractions.

The leaf-internal CO_2 concentration (C_i) can be estimated from C_a (ppm), which has been proposed to be equal to the canopy CO_2 concentration. Many scholars have performed many studies on the ratio of the intercellular to ambient CO_2 concentration, and the C_i/C_a ratio is similar in all species (Morison et al., 1983). Many studies (Morison et al., 1983; Van et al., 2004) found that the C_i/C_a ratio is associated with vapor pressure, temperature, etc.; when various pressures approximate environment conditions, the ratio is a constant for a species, generally approximately 0.7 for C3 species and 0.3 for C4 species (Wong et al.,1979a b; Caemmerer and Evans,1991). Therefore, in this part, I calculate the internal CO_2 concentration by $C_i = 0.7 \times C_a$ for C3, and $C_i = 0.3 \times C_a$ for C4. In addition, the canopy CO_2 concentration was calculated from the atmospheric CO_2 concentration using the decoupling coefficient, which indicates the degree of canopy decoupling from the bulk air (Jarvis and McNaughton 1986). A completely smooth surface has a decoupling coefficient of 1.0, and a canopy in which the air is identical to that in the atmosphere has a decoupling coefficient of zero (Chapin III et al., 2011). According to Jarvis et al. (1986) and Jones (1992), the decoupling coefficients of diverse PFTs in this study are approximately 0.1 for ENF and DNF; 0.2 for EBF, DBF and MF; 0.8 for GRA; 0.5 for SAV, WSA, CRO, CSH, OSH and WET, and 0 for BAR.

Two types of atmospheric CO_2 concentration data were used to analyze the CO_2 fertilization effect; one type is the global monthly continuous spatial CO_2 concentration data in 2014, which were captured by GOSAT (http://www.gosat.nies.go.jp/en/), the world's first spacecraft to measure the concentrations of CO_2 from space. The production is GOSAT FTS L2 CO_2 column amount SWIR, which was used to calculate the atmospheric CO_2 concentration,

and the FTS SWIR L2 CO_2 column abundance products (denoted XCO_2, in ppm), which contain column-averaged mixed volume ratios of CO_2 (Guo et al., 2012). The relative accuracy of the Level 2 data is 0.3 % ~ 1.0 % (1 ~ 4 ppm) for CO_2 (Butz et al., 2011), and the data form is a point set with a circle footprint with a diameter of approximately 10.5 km at nadir; nevertheless, the number of data points significantly surpasses that currently obtained from ground monitoring stations, which is below 200. The other type is globally averaged surface CO_2 data, including globally averaged surface monthly mean data in 2000 and 2014 and globally averaged surface annual mean data (Ed Dlugokencky and Pieter Tans, 2017) obtained from NOAA/ESRL (www.esrl.noaa.gov /gmd/ccgg/trends/). A global average is constructed by first fitting a smoothed curve as a function of time to each site, and then, the smoothed value for each site is plotted as a function of the latitude for 48 equal time steps per year. A global average is calculated from the latitude plot at each time step (Masarie 1995). I used different types of CO_2 concentration data to analyze the effect of CO_2 concentrations on the GPP estimates.

4.2.1.3 Climatic data

For the global estimation of GPP using BEPS, I used the input datasets of Ra, Ta, and RH from the National Centers for Environmental Prediction (NCEP), Department of Energy (DOE) Reanalysis 2 (NECPR2), which uses a state-of-the-art analysis/forecast system to perform data assimilation using data from 1979 to the previous year at a spatial resolution of 2.5° × 2.5° (Kanamitsu et al., 2002). The daily Ta and Ra were from surface data, while the RH was pressure level data at 1000 hPa. We calculated the VPD using RH and Ta. All data were linearly interpolated and resampled to a spatial resolution of 0.5° × 0.5°. Regarding introducing satellite CO_2 concentration into GPP estimation, because the driving variables.

4.2.1.4 Land cover component map

The land cover component is an important factor for global primary productivity estimates. If the vegetation covers are different, the photosynthetic capacity will be different. In addition, photosynthesis rate estimation models of C3 species are different from those for C4 species; thus, it is necessary to know the spatial distributions of the C3 and C4 species. Therefore, a global land component map was drawn by overlaying the global C3/C4 maps and the land cover data to estimate the global GPP. I obtained current global grassland C3 and C4 maps from the NACP model driver data using the Spatial Data Access Tool (SDAT) (http://webmap.ornl.gov/wcsdown/). This dataset provides environmental data that have been standardized and aggregated for use as input in carbon cycle models at global scales, and the relative fraction of C3 (*f*C3) and C4 (*f*C4) grasses can be obtained (Wei et al., 2014). Because C4 plants are largely confined to an herbaceous growth form (Still et al., 2003), *f*C4 was considered the relative fraction of the C4 species in this chapter. The driver data were used in 22 terrestrial biosphere models to perform baseline and sensitivity simulations. For driving BEPS, the C4 vegetation percentage map I also obtained, which was determined from datasets that described the continuous distribution of plant growth forms, climate classifications, fraction of a grid cell covered in cropland, and national crop type harvest area statistics (Still et al., 2009), was one of the products from the ISLSCP Initiative II and had a spatial resolution of 1°×1°. The land cover classification was obtained from the MCD12C1, which provides information regarding 17 classes of dominant land cover types defined by the IGBP, including 11 natural vegetation classes, three human-altered classes, and three non-vegetated classes (Friedl et al., 2010). MCD12C1 is a product that aggregates a higher spatial resolution (500 m) land coverage by selecting the dominant land cover types within lower spatial resolution grids (Duveiller and Cescatti 2016). However, the MCD12C1 product was unavailable in 2014; thus, the 2012 data were used instead.

4.2.1.5 Soil moisture and property data

The CPC-SM dataset v2 (van den Dool et al, 2003) provided by NOAA/ESRL Physical PSD and IGBP-DIS dataset (Global Soil Data Task, 2014) were used in this study to calculate the water limitations on the photosynthetic rate by considering the stomatal regulating factor from the soil moisture deficits. Since globally measuring the SM is impossible, I used the model-calculated CPC-SM dataset, which provided global monthly data from 1948 to 2017 and consisted of a file containing the averaged SM water height equivalents at a spatial resolution of 0.5° × 0.5°. On the other hand, the IGBP-DIS dataset is a global product generated at a resolution of 5 × 5 arc-minutes by the SDS, which generates soil information and maps for geographic regions at user-selected soil depths and resolutions. I used the field capacity maps derived from this dataset and converted the data to the values at a soil depth of 1.6 m, which is the same as that used for the CPC-SM.

4.2.1.6 Other GPP products

Multiple GPP products are currently available based on different methods, but their performances vary substantially when validated against GPP estimates from EC data (Zhang et al., 2017; Ma et al., 2015). In addition to verifying the estimates at tower sites, I compared the estimated GPP with the other GPP products. As a benchmark, I compared the estimates against the GPP values from the MTE model from 2000 to 2011 (Jung et al., 2011) because the MTE model is based on direct eddy covariance flux tower measurements of GPP and is thus considered close to the truth where the flux tower density is high (Beer et al., 2010; Frankenberg et al., 2011). The MODIS GPP products from 2000 to 2014 were also used because MODIS products have been widely known and used (Turner et al., 2006; Zhao and Running, 2010; Frankenberg et al., 2011). In addition, I also selected one RS-based VPM GPP product, which is based on an improved LUE theory, a state-of-the-art VI gap-filling and smoothing algorithm and a separate treatment for C3/C4 photosynthesis pathways (Zhang et al., 2017). Since the three datasets calculated GPP without considering the CO_2 fertilization effect, I also conducted CO_2 effect analysis by converting those products to monthly and yearly temporal resolutions.

4.2.1.7 Vegetation indices data

LAI and fAPAR depend on the canopy structure, vegetation element optical properties, atmospheric conditions, and angular configuration. LAI is a dimensionless variable that is defined as the total one-sided area of green leaves in a vegetation canopy relative to a unit of ground area. Since leaves are photosynthetic organs, LAI was used to calculate the photosynthesis area. fAPAR is directly related to the primary productivity function of photosynthesis and, therefore, is used to estimate the assimilation of CO_2 in vegetation. MCD 15A3 is the level-4 combined (Terra and Aqua) MODIS global LAI and fAPAR products composited every 4 days at a 1 km resolution. I calculated the data from the same month to obtain averaged monthly values to develop the model which introduces satellite CO_2 concentration data into GPP estimation. For driving BEPS, vegetation indices (VIs), including NDVI from GIMMS-3g.v1 (15 days, 8 km) and LAI from the GlobMap LAI v3 (8 days, 0.08°)(Zhu et al., 2013), were employed in this study. GlobMap LAI v3 was made of a combination of AVHRR LAI (1981~2000) and MODIS LAI (2001~2016). The MODIS LAI series was generated from MODIS land surface reflectance data (MOD09A1) based on the GLOBCARBON LAI algorithm (Deng et al., 2006). The relationships between the AVHRR observations (GIMMS NDVI) (Tucker et al., 2005) and the MODIS LAI were established pixel-by-pixel using two data series during an overlapping period (2000~2006). Then, the AVHRR LAI was back-estimated to 1981 using historical AVHRR observations based on these pixel-

level relationships (Liu et al., 2012). GIMMS-3g.v1 provides the only continuous and the longest time series (of approximately three decades) that has been continually assessed and validated, and it has been widely used for long-term global vegetation condition monitoring and detection (Piao et al., 2006; Beck et al., 2011; Wu et al., 2015; Liang et al., 2015). In this chapter, I considered the daily VI values to be the same as the biweekly NDVI and the weekly LAI, in which the day belonged to the period of products.

4.2.2 Study process

4.2.2.1 Study process of BEPS

The logical workflow of this part is shown in Figure 4.1 and the data are listed in Table 4.2. The global data with different spatial resolutions were resampled to a spatial resolution of 0.5° × 0.5° and inputted into a collaborative spatial dataset. The climate, CO_2 concentration and soil water data were resampled by using the linear interpolation method, and the RS data and landcover map were resampled using the mean values and the dominant indicators, respectively. The C3/C4 fractional map was overlaid with the landcover map to determine the land component in each pixel, meaning that the V_m of each pixel could be calculated; finally, based on the NDVI and temperature limitation, I calculated the actual V_m. Sunlit leaves and shaded leaves were separated by using the two-leaf model according to the location of the pixel, the Julian day, the LAI values and the canopy clumping index of each PFT, which is the same as in the BEPS model (Chen et al., 1999). All parameters used in this study were the same as those used in the BEPSd model unless otherwise specified. Daytime duration was calculated by using the location of the pixel and the Julian day. The direct and diffuse irradiances were calculated by using the computationally efficient estimation methodology developed by Chen (1999) for driving BEPS. Finally, after calculating the aforementioned variables and combining the data with the ambient constraints, including the limitation of SM, temperature, CO_2 concentration, radiation and VPD, the daily GPP of each pixel was estimated using the iBEPSd model. I verified the estimated GPP at both the site and the global scale; I compared the results with the measurements from 60 flux tower sites, the other RS GPP products, including MODIS and VPM, and the MTE modeled GPP products. At the same time, I conducted the CO_2 fertilization effect analysis by comparing the estimated GPP with the other global-scale GPP products. If the accuracy of the estimated GPP was acceptable, then the inputted CO_2 concentration data were changed to the globally averaged monthly and annual mean CO_2 concentrations to analyze the effects of not considering the annual temporal variability and the spatial distribution of the atmospheric CO_2 concentrations around the globe on the estimation of GPP.

Table 4.2 Overview of the datasets used to drive iBEPSd.

Data Source	Dataset	Derived variables	Temporal resolution	Reference URL
GLOBMAP LAI	LAI Version 3	LAI	8-day	doi:10.1029/2012JG002084
CPC Soil Moisture	Soil Moisture	Soil Water	Monthly	https://www.esrl.noaa.gov/psd/data/gridded/data.cpcsoil.html
IGBP-DIS	Global Gridded Soil Characteristics	Soil Capacity	Invariant	doi:10.3334/ORNLDAAC/1004
ISLSCP II	C4 Vegetation Percentage	C3/C4 Fraction	Invariant	https://daac.ornl.gov/cgi-bin/dsviewer.pl?ds_id=932
NCEP/DOE Reanalysis 2	Air Temperature	Temperature	Daily	https://www.esrl.noaa.gov/psd/data/gridded/data.ncep.reanalysis2.html
	Downward Solar Radiation Flux	Radiation	Daily	
	Relative Humidity	Relative Humidity	Daily	http://www.esrl.noaa.gov/psd/data/gridded/data.ncep.reanalysis.html
FluxNet	FLUXNET2015 Dataset	GPP	Daily, Monthly	http://fluxnet.fluxdata.org/data/fluxnet2015-dataset/
Scientific DATA	VPM-Monthly_HD	GPP	Monthly	DOI: 10 .1038 /sdata.2017 .165
MTE	MTE-GPP	GPP	Monthly	https://www.bgc-jena.mpg.de/geodb/projects/Reg2.php
MODIS	MOD17A2	GPP	8-day	https://lpdaac.usgs.gov/dataset_discovery/modis
	MCD12Q1	LandCover	Annual	
Carbon Tacker	CT2016	CO_2 Concentration	Daily	http://carbontracker.noaa.gov
GIMMS	NDVI3g.v1	NDVI	Half monthly	https://ecocast.arc.nasa.gov/

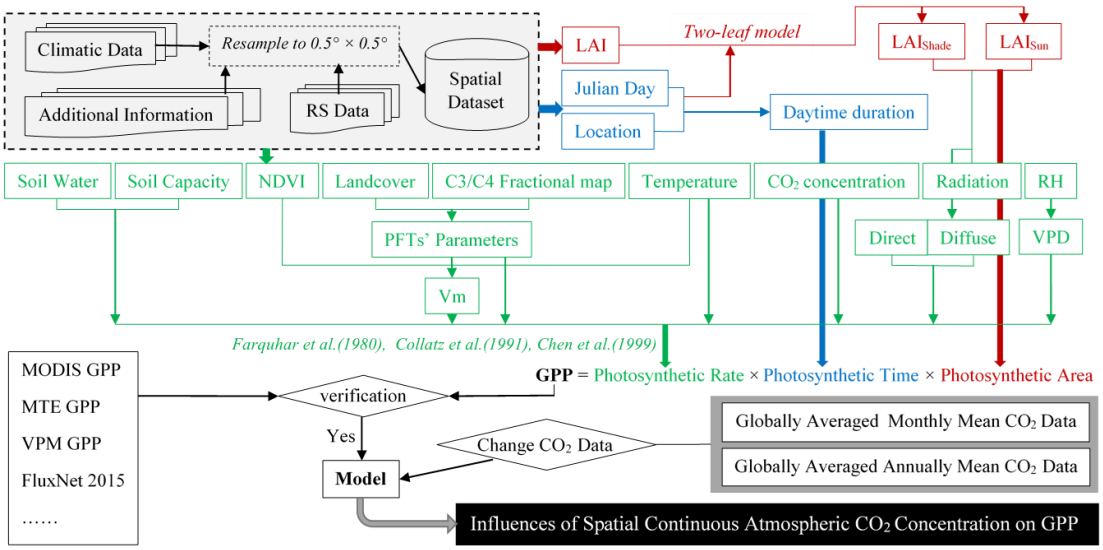

Figure 4.1 The logical flowchart for indentifing CO_2 fertilization effect by iBEPSd.

4.2.2.2 Methods for model developing

The photosynthetic rate of the canopy leaf (P_{rate}) is usually expressed as the rate of CO_2 assimilation (A). According to previous studies (Farquhar et al., 1980 1982; Kirschbaum and Farquhar 1984; Collatz et al., 1991; Sellers et al., 1996a b), we know that A is described as the minimum of the three limiting rates, which are functions that describe the assimilation rate as being limited by the photosynthetic enzyme system (Rubisco-limited); the amount of PAR captured by the leaves (light-limited); and the capacity of the leaf to export or utilize the products of photosynthesis (sucrose synthesis-limited). A is estimated as follows:

$$A \approx \min(J_e, J_s, J_c) \quad \text{Eq-4.1}$$

where J_e, J_s and J_c are separate rate expressions for the photosynthetic CO_2 assimilation rate in terms of different rate-limiting steps in the photosynthesis process (J_e, light-limiting; J_s, sucrose synthesis-limiting; J_c, Rubisco-limiting) (μmol m^{-2} s^{-1}).

J_e describes the response of photosynthesis to PAR as follows:

$$J_e = \varphi_0 \times \tilde{a} \times \text{PAR} \times \text{FAPAR} \times (C_i - \Gamma^*)/(C_i + 2 \times \Gamma^*) \quad \text{,for C3} \quad \text{Eq-4.2}$$

$$J_e = \varphi_0 \times \tilde{a} \times \text{PAR} \times \text{FAPAR} \quad \text{, for C4} \quad \text{Eq-4.3}$$

where φ_0 is the intrinsic quantum efficiency of photosynthesis (mol mol^{-1}, C3: 0.08, C4: 0.05), $\tilde{a}$ is the leaf absorbance (dimensionless, C3: 0.86, C4: 0.80), PAR is the incident photosynthetically active radiation quantum unit (μmol m^{-2} s^{-1}), and fAPAR is the fractional absorbed PAR (dimensionless). C_i is the leaf internal CO_2 concentration (mlCO_2 m^{-3}), and Γ^* is the CO_2 compensation point (mlCO_2 m^{-3}).

The sucrose synthesis-limited rate of assimilation, J_s, is given by:

$$J_s = V_m/2 \quad \text{, for C3} \quad \text{Eq-4.4}$$

$$J_s = 2 \times 10^4 \times C_i \times V_m/\text{P, for C4} \quad \text{Eq-4.5}$$

where V_m is the maximum catalytic capacity of Rubisco (μmol m^{-2} s^{-1}), and P is the atmospheric pressure (hPa).

The third limiting rate is Rubisco-limited rate, J_c, which is calculated by:

$$J_c = V_m \times (C_i - \Gamma^*)/(C_i + K_C \times (1 + [O_2]/K_O)), \text{ for C3} \quad \text{Eq-4.6}$$

$$J_c = V_m \quad \text{, for C4} \quad \text{Eq-4.7}$$

where $[O_2]$ is the atmospheric O_2 concentration (20.95 %), K_C is the Michaelis-Menten Constant for CO_2 (ppm), and K_O is the inhibition constant of O_2 (%).

Γ^* can be calculated by:

$$\Gamma^* = 0.5 \times f_{K_O K_C} \times [O_2] \times K_C/K_O \quad \text{Eq-4.8}$$

where f_{KcKo} is the ratio of the turnover of oxygenase and carboxylase (dimensionless, 0.21), and K_O and K_C can be modeled as follows:

$$K_C = K_{C,25} \times \exp(1/298 - 1/(T + 273.15) \times E_{KC}/8.314) \quad \text{Eq-4.9}$$

$$K_O = K_{O,25} \times \exp(1/298 - 1/(T + 273.15) \times E_{KO}/8.314) \quad \text{Eq-4.10}$$

where 8.314 is the universal gas constant (J $K^{-1}mol^{-1}$), $K_{C,25}$ is the Michaelis-Menten constant for CO_2 at 25℃ (460 ppm), and $K_{O,25}$ is the Inhibition Constant of O_2 at 25℃ (%, C3: 33, C4: 34). T is the average photoperiod-temperature (℃) that is approximately equal to T_{air} in this

study. E_{KO} and E_{KC} are the activation energy for K_C and K_O, respectively. The V_m for the different land cover components is referenced from a revised land surface parameterization established by Sellers (1996b).

The low-temperature inhibition of photosynthesis is calculated by weighting T_{air}. If T_{air} is below 0℃, the weight value is 0; if $0 < T_{air} < 10$, the weight value = $T_{air}/10$ (Wang et al., 2014).

There are mainly three types of canopy-leaf models to estimate the canopy photosynthetic rate from the single leaf photosynthetic rate. The first type considers the canopy to be a large leaf (Lloyd et al., 1995) that is suitable for measuring the CO_2 flux using the EC method. The second type integrates the photosynthetic rate from the top layer leaves to the bottom layer leaves according to Beer law, which is based on the hypothesis that the photosynthetic rate in the leaf in the canopy is proportional to the intensity of the light. The third type is the sun/shade model, which was presented by de Pury and Farquhar (1997) and considers both direct light and scattered light. In this chapter, I used the second method, the canopy photosynthetic rate, which can be calculated by:

$$A_{\text{canopy}} = \int_0^{\text{LAI}_{max}} A d\text{LAI} = A_{max} \frac{1 - \exp(-k \times \text{LAI})}{k} \qquad \text{Eq-4.11}$$

where A_{canopy} is the canopy photosynthetic rate, A_{max} is the photosynthetic rate of the top leaf calculated by Eq-4.1, LAI_{max} is the maximum leaf area index of the canopy, and k is the light extinction coefficient (0.41 (Monteith and Moss 1997; Norby et al., 2003), dimensionless).

4.2.2.3 Study process of new model

First, I defined some symbols in this paty to facilitate the comprehension of this part. GPP_{2000} denotes the estimated GPP under the atmospheric CO_2 concentration conditions in 2000 using globally averaged monthly mean data, and the climatic conditions are the same as those in 2014. Tower GPP is the GPP data from the Fluxnet 2015 dataset $GPP_{2014}^{\text{monthly mean global } CO_2}$, $GPP_{2014}^{\text{annual mean global } CO_2}$ and $GPP_{2014}^{\text{monthly spatial } CO_2}$ represent the estimated GPPs in 2014 using globally averaged monthly mean CO_2 data, globally averaged annual mean CO_2 data and continuous spatial monthly CO_2 data, respectively.

The data are listed in Table 4.3 and are described in greater detail below. Four types of data were used in this part, including RS data and reanalysis climate data from NASA and the Japan Aerospace Exploration Agency (JAXA), observation data from NOAA and GPP data from the Fluxnet 2015 Dataset. The RS data and climatic data were mainly used to estimate the terrestrial GPP, and the Fluxnet 2015 Dataset was used to evaluate the estimated results.

Table 4.3 Overview of the datasets used to develop model. P_{area}, P_{rate} and P_{period} are the photosynthetic area, photosynthetic rate and photosynthetic period, respectively.

Surface parameter measured	Datasets / products	Resolution	Data source / acquisition	Function effect
Leaf area index (LAI)				Estimating P_{area}
Fractional absorbed photosynthetically active radiation (FPAR)	MODIS MCD 15A3	Global 1 km×1 km	NASA MODIS	Calculating P_{rate}
Land cover classification	MODIS MCD 12C1	Global 0.05°×0.05°	NASA MODIS	Acquiring land cover component maps to calculate P_{rate}
Global C3 and C4 fractional maps	NACP Model Driver Data	Global 0.5°×0.5°	NASA ORNL DAAC	
Photosynthetically active radiation (PAR) Atmospheric pressure Air temperature at 10 m	MERRA	Global 0.5°latitude × 0.6° longitude	GES DISC	Calculating PAR photon flux density and calculating P_{rate}
Sunshine duration	MCDW	≈ 2000 stations	NOAA PSD	Estimating P_{period}
Column-averaged mixed volume ratios of CO_2	GOSAT FTS L2	Global ≈ 10.5 km×10.5 km	JAXA	Estimating leaf-internal CO_2 concentration to calculate P_{rate}

The global datasets have different spatial resolutions; thus, I created a spatial dataset to establish concordance among the spatial resolutions of all the data, which includes the RS data, climate grid data, underlying surface observed data, and so on. The observed data from over 2000 stations were interpolated using the Kriging method to convert to raster data, and then, all the raster data were resampled by mean values to a 0.5° × 0.5° spatial resolution. According to the definition of the GPP, the GPP is generally the amount of the fixation of organic carbon through photosynthesis by vegetation. Therefore, a conceptual formula was proposed for estimating the terrestrial GPP as the product of the photosynthetic rate, photosynthetic duration and photosynthetic area. In this part, I utilized the Eq-4.1 to calculate the photosynthetic rate. But due to the vertical structure of the plants, the light intensity and PAR absorption of canopy leaves, upper-layer leaves, and lower-layer leaves are different. Thus, in addition to the canopy leaves, the extinction effects of the vertical structure of the plants were considered in the calculation of the photosynthetic CO_2 assimilation rate, which was calculated using the canopy transmittance as supported by the big-leaf model (Eq-4.11) used in this model. Generally, without light, there will be no photosynthesis, and the rate of photosynthesis increases as the light intensity increases, except for in cases limited by other factors, such as temperature, water and CO_2. Therefore, sunshine hours are defined as the photosynthetic duration, which is the maximum lasting time for solar radiation. The leaf is the place for vegetation to proceed with photosynthesis, and without leaves, there will no photosynthesis; therefore, LAI was considered the photosynthetic area of one-unit area. Based on the logical flow chart shown in Figure 4.2, the global GPP can be estimated. Then, the GPP estimates are compared with the GPP data from the Fluxnet 2015 dataset; if the discrepancy is great, the calculation attempt explained above is infeasible. However, if the distribution of the GPP estimates is consistent with that from the Fluxnet dataset, the attempt to use atmospheric CO_2 concentration data in the estimation of the

GPP is feasible. Then, the inputted CO_2 concentration data were changed to analyze the effects of CO_2 concentrations on the GPP estimation. The input of the CO_2 concentration data includes the globally averaged monthly mean data from 2000, the globally averaged monthly mean data from 2014 and the globally averaged annual mean data for 2014, which are used for estimating GPP_{2000}, $GPP_{2014}^{\text{monthly mean global } CO_2}$ and $GPP_{2014}^{\text{annual mean global } CO_2}$, respectively. Finally, the most important step is comparing the multifarious GPP estimates as follows: by comparing GPP_{2000} vs. $GPP_{2014}^{\text{monthly mean global } CO_2}$, the response of the global GPP estimates to the elevated atmospheric CO2 concentrations between 2000 and 2014 can be found; by comparing $GPP_{2014}^{\text{monthly spatial } CO_2}$ vs. $GPP_{2014}^{\text{monthly mean global } CO_2}$, the effects, which without considering atmospheric CO_2 concentration spatial distribution on global GPP estimates can be expressed; and by comparing $GPP_{2014}^{\text{monthly spatial } CO_2}$ vs. $GPP_{2014}^{\text{annual mean global } CO_2}$, the spatiotemporal biases in the GPP estimates, which without considering the annual temporal variability and the spatial distribution of atmospheric CO_2 concentrations around the globe can be represented.

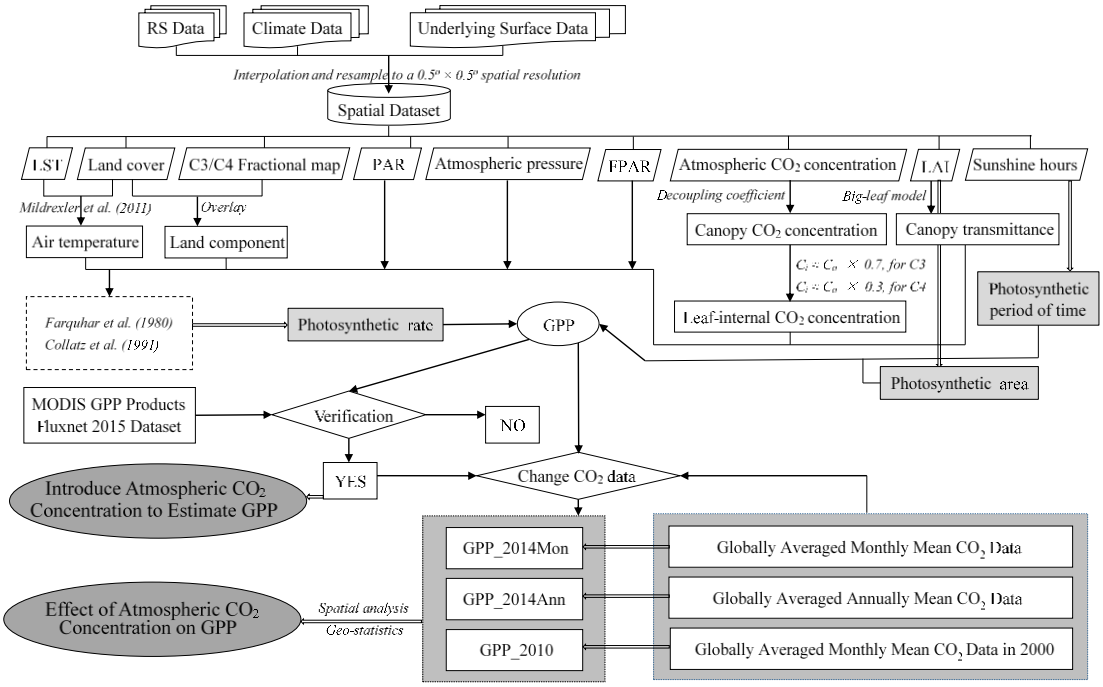

Figure 4.2 The logical flow chart for detecting the CO_2 effects.

4.3 Results and discussions

4.3.1 BEPS estimation

First, I define some symbols in this section to facilitate the description of the results: GPPspaCO_2 denotes the estimated GPP under the daily spatial continuous atmospheric CO_2 concentration; GPPannCO_2 and GPPmonCO_2 represent the estimated GPP using the globally averaged annual and monthly mean CO_2 concentrations, respectively. The two estimates were used to explain the effect of the spatial distribution of CO_2 concentrations on the estimation of GPP. For $GPP_{2000}CO_2$, the daily value of the spatial continuous atmospheric CO_2 concentration in the year 2000 was simply employed for every year of the inputted data. In this simulation, I ignored the inter-annual variability and development of the atmospheric CO_2 concentration.

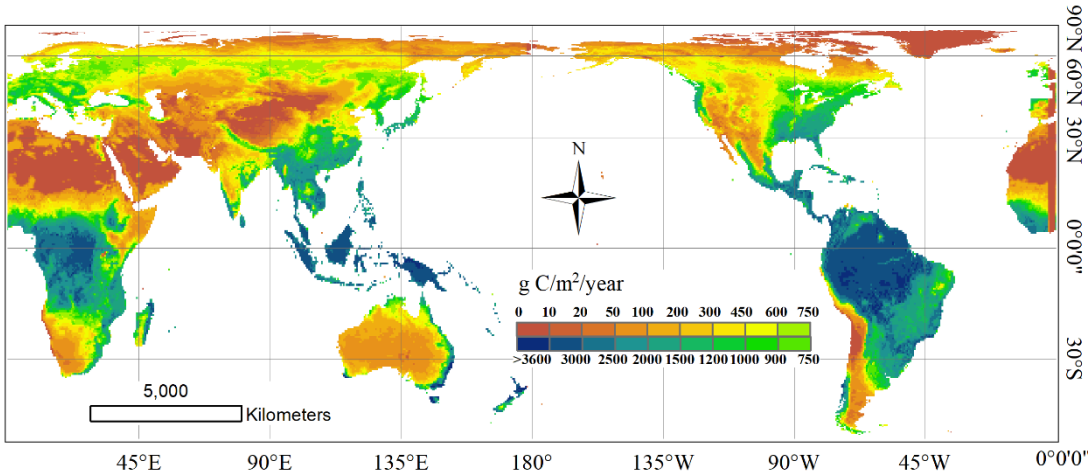

Figure 4.3. Global spatial distribution of the annual mean GPP for 2000-2015.

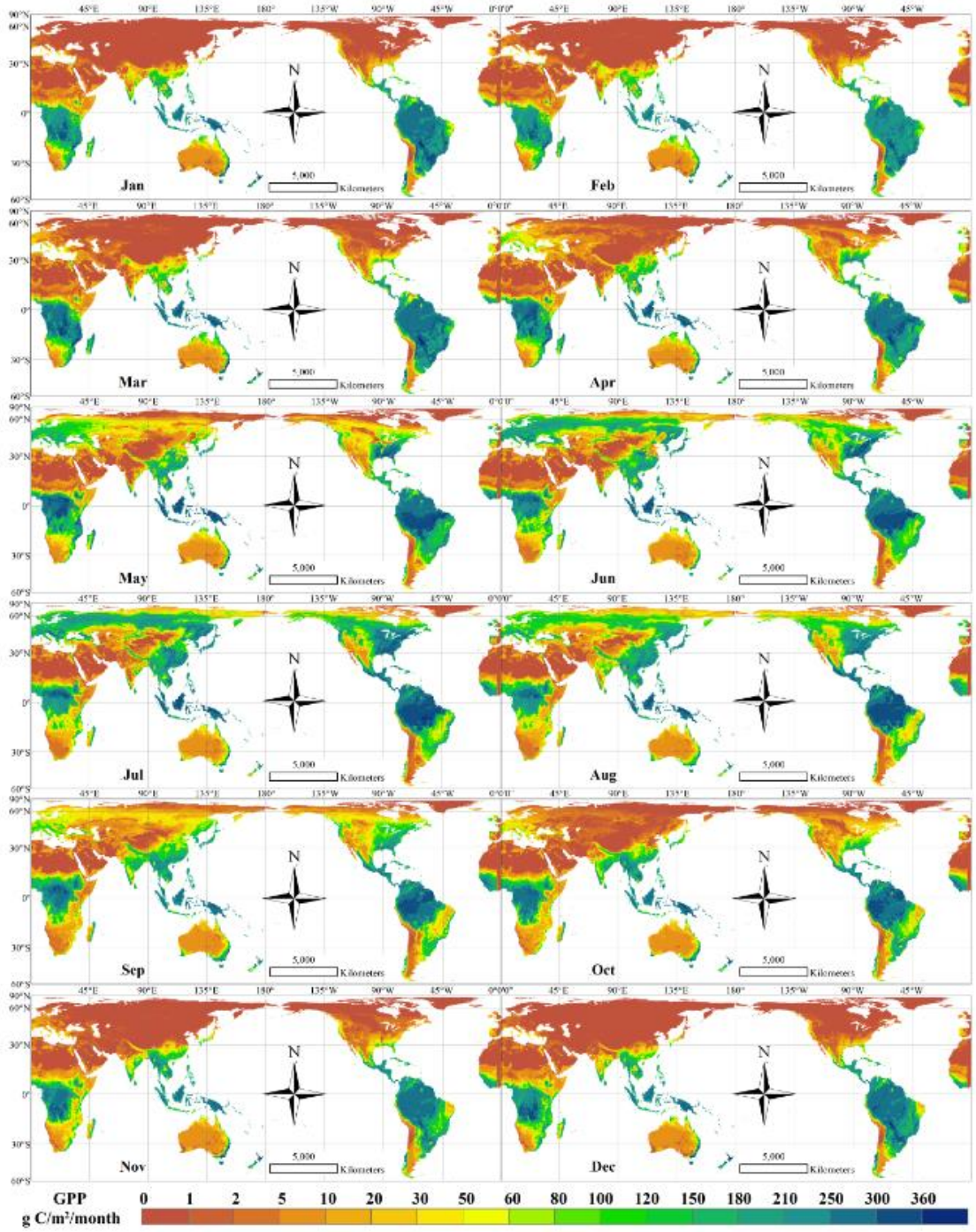

Figure 4.4 Global spatial distribution of the monthly mean GPP for 2000-2015.

4.3.1.1 Accuracy assessment of GPP estimates

I evaluated the accuracy of the estimated GPP in this section at the site scale and global scale (Figure 4.3 and Figure 4.4). At the site scale, I showed the performance of the iBEPSd by validating with the flux tower GPP, as shown in Figure 4.5. The overall accuracy of the estimated GPP was relatively high, with a determination coefficient (R^2) of 0.7546, a low root mean square error (RMSE) of 2.0494 gC m^{-2} day^{-1} and a slope of 1.0074. For the individual biome types, the estimated GPP was underestimated in needleleaf forests (~30 % and 24 % for DNF and ENF, respectively) and slightly overestimated in savanna types. For other biome types, the estimated GPP did not show a systematic bias, and the accuracy of the estimates in the EBF,

DBF, MF, GRA and CRO ecosystems were relatively higher, in which the biases were less than ±10 %. A complete list of the used sites is available in Table 4.1. As there was only one DNF site (RU-SkP), the number of flux tower sites for DNF was slightly less, and the fraction of this grid cell covered by the dominant plant was 65 %, which indicated that the spatial homogeneity was low. Therefore, the underestimation in the DNF ecosystem may be partly due to the decline in the LAI and NDVI when the RS data were resampled as the mean values and because of the different spatial footprint size between this study and the flux tower measurements. The correlation coefficient (R) between the estimates and the EC flux tower GPP ranged from 0.6705 in WSA to 0.9140 in DBF, and the slope of the estimated GPP to the flux tower GPP ranged from 0.6803 in DNF to 1.1677 in WET; additionally, the RMSE ranged from 0.6310 in OSH to 3.3179 gC m^{-2} day^{-1} in CRO. Comparisons of the GPP estimated by iBEPSd against the EC flux tower GPP for different PFTs indicated that the estimates in this party captured the magnitude and variability at most of the sites well. To deeply address the performances of the estimated GPP, I compared the time series of the estimates with that of the EC flux tower measurements at each site, as shown in Figure S15. The performances of the estimated GPP varied across sites, and the overall, maxima and minima, amplitude and seasonal variability of the flux tower GPP were very well captured by the estimates.

In terms of global distribution, the estimated GPP was highly consistent with the MODIS, MTE and VPM products (Table 4.4), which means the estimated GPP captured the spatial variations well. However, our estimated GPP was slightly higher than those of the three products, with an average slope of 1.0983, an R of 0.9302 and a low RMSE of 1.0489 g C m^{-2} day^{-1}. To further understand the differences in the estimated GPP against each product in each year, I also drew the scatterplots between the estimates and the products for each year, which are listed from Figure S17 to FigureS5.5. Numerous studies (Sjöström et al., 2013; Zhu et al., 2016; Anav et al., 2015; Chen et al., 2017b) have found that the MODIS and MTE GPP products are somewhat lower than the observed values. In addition, with respect to VPM, the overestimated GPP mainly occurred when the GPP was equal to or greater than 3000 g C m^{-2} $year^{-1}$, which was mainly the GPP of the EBF ecosystem. It has been reported (Zhang et al., 2017) that the VPM GPP for the EBF ecosystem used in this chapter may be underestimated by approximately 30 % compared with the flux tower measurements; however, according to Figure 4.5, the estimated GPP for the EBF ecosystem showed more agreement with the flux tower measurements. Therefore, as verified above, the GPP estimated in the present study could be used in subsequent analyses.

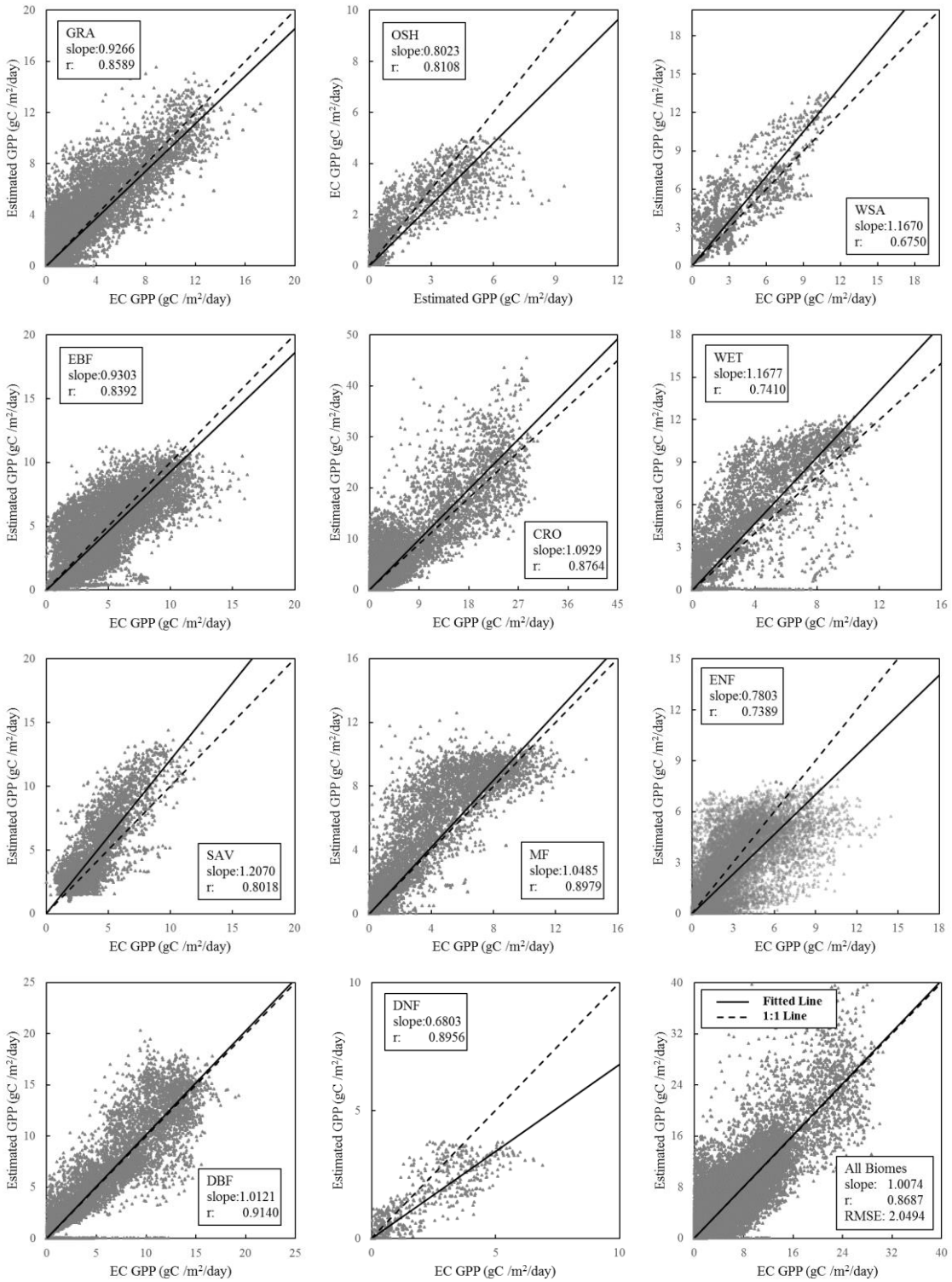

Figure 4.5 GPP validation against EC flux tower measurements for different PFTs.

Table 4.4 Slope, R, and RMSE of each GPP product during the study period. Statistics from the regression (Y=Slope·X) of the estimated GPP (as Y) on the GPP products (as X) (gC m^{-2} day^{-1}).

Year	MODIS			MTE-GL			MTE-MR			VPM		
	Slope	R	RMSE	Slope	R	RMSE	Slope	R	RMSE	Slope	R	RMSE
2000	1.1041	0.9292	0.9433	1.0147	0.9417	0.9916	1.0120	0.9404	0.9921	1.0030	0.9048	1.0685
2001	1.1384	0.9280	0.9797	1.0416	0.9425	0.9945	1.0368	0.9413	0.9943	1.0258	0.9045	1.0917
2002	1.1346	0.9261	0.9958	1.0513	0.9444	0.9844	1.0463	0.9432	0.9843	1.0199	0.9093	1.0797
2003	1.1395	0.9275	0.9940	1.0532	0.9433	0.9931	1.0481	0.9418	0.9942	1.0226	0.9100	1.0755
2004	1.1358	0.9259	1.0018	1.0437	0.9430	1.0073	1.0390	0.9413	1.0099	1.0125	0.9088	1.0837
2005	1.1777	0.9226	1.0427	1.0501	0.9419	1.0305	1.0443	0.9403	1.0321	1.0438	0.9097	1.0840
2006	1.1844	0.9247	1.0506	1.0673	0.9438	1.0150	1.0629	0.9422	1.0179	1.0408	0.9087	1.1052
2007	1.2098	0.9355	1.0094	1.0823	0.9471	1.0388	1.0780	0.9459	1.0393	1.0680	0.9045	1.1310
2008	1.2091	0.9394	0.9850	1.0852	0.9469	1.0375	1.0817	0.9455	1.0387	1.0734	0.9041	1.1331
2009	1.2183	0.9426	0.9889	1.1008	0.9480	1.0471	1.0967	0.9465	1.0496	1.0741	0.9111	1.1195
2010	1.2261	0.9394	1.0019	1.0886	0.9482	1.0437	1.0833	0.9466	1.0467	1.0777	0.9086	1.1206
2011	1.2545	0.9385	1.0499	1.1116	0.9481	1.0615	1.1080	0.9465	1.0656	1.1050	0.9033	1.1751
2012	1.2402	0.9375	1.0289	-	-	-	-	-	-	1.0980	0.9051	1.1495
2013	1.2644	0.9394	1.0624	-	-	-	-	-	-	1.1105	0.9045	1.1829
2014	1.2598	0.9370	1.0803	-	-	-	-	-	-	1.1009	0.9038	1.1913
2015	-	-	-	-	-	-	-	-	-	1.1080	0.9088	1.1715

4.3.1.2 The effect of CO_2 concentration on GPP

In this section, I analyzed the response of the GPP to increasing atmospheric CO_2 concentrations by comparing the estimated GPP with the other GPP products that did not consider the CO_2 fertilization modules; additionally, I analyzed the trend of the estimated GPP against $GPP_{2000}CO_2$, in which the CO_2 concentration is maintained to that recorded for the year 2000.

The patterns of the variation in the GPP of terrestrial ecosystems show large variability due to the interactions between the biological characteristics of plants and the external environmental factors (Beer et al., 2010; Anav et al., 2015). I used the same inputs, i.e., landcover, climatic dataset and soil water data, as the VPM model to drive the iBEPSd in this study to exclude the influences of the external environment. In addition, for MODIS and MTE, I also compared the driving climatic data of the models (i.e., GMAO for MODIS and CRU for MTE). The results (Figure 4.6) showed that, except for Ta in CRU that showed a very slightly positive trend of 0.0001°C ppm^{-1} and an R of 0.3116, most climatic factors showed a slightly negative correlation, and the overall relative relationship between the climatic datasets was almost unchanged during the study. Therefore, the trend of the changes in relative GPP were mainly caused by the changes in the CO_2 concentration. According to Figure 4.7, I found a strong linear positive correlation between the slope of the estimated GPP and the GPP products with the atmospheric CO_2 concentration; this relationship was most notable with the MODIS products (slope=0.0057, R=0.9743), followed by the MTE (slope=0.0037, R=0.9432 and 0.9423, for GL and MR, respectively) and the VPM products (slope=0.0037, R=0.9583). The ratios of the estimated GPP to GPP products were tightly consistent with the increases in the atmospheric CO_2 concentration. The above results could confirm the previous conjecture (Jung et al., 2010; Anav et al., 2015; Huang et al., 2015; De Kauwe et al., 2016; Chen et al., 2017)

that the underestimation observed in MODIS and MTE may originate from the exclusion of the CO_2 physiological effects on stomatal conductance in the algorithm.

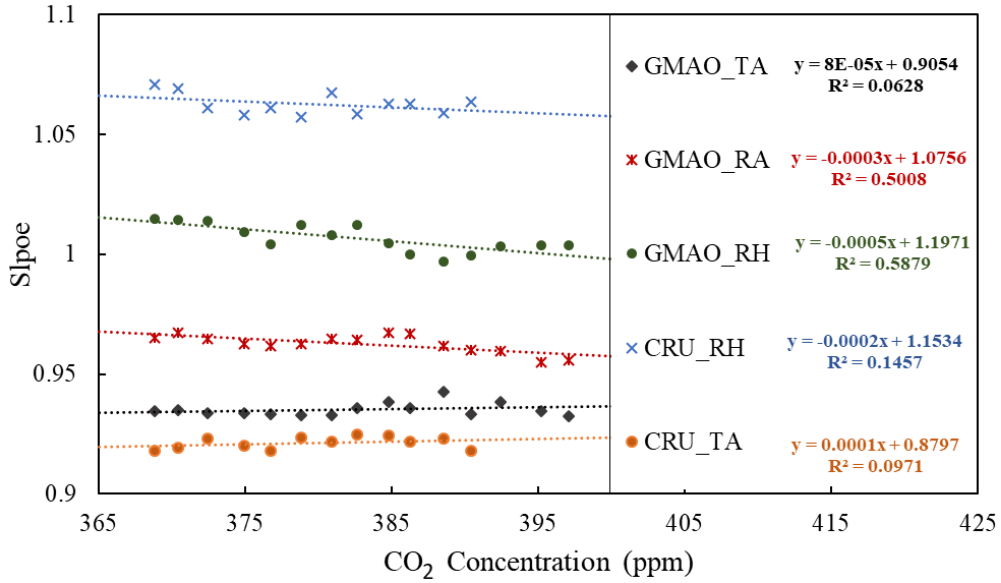

Figure 4.6 The correlation trends between rising CO_2 concentration and the ratio of the climate data used in this chapter to those used in MODIS and MTE products. NECP-DOE R2 were used in this part, CRU (Climatic Research Unit) were used in MTE and GMAO (Global Modeling and Assimilation Office) were used in MODIS. Slope were calculated by statistics from the regression (y=slope·x) of NECP-DOE R2 (as y) on CRU and GMAO (as x). TA, RH, RA donate the air temperature (°C), relative humidity (%) and radiation (W m^{-2}), respectively.

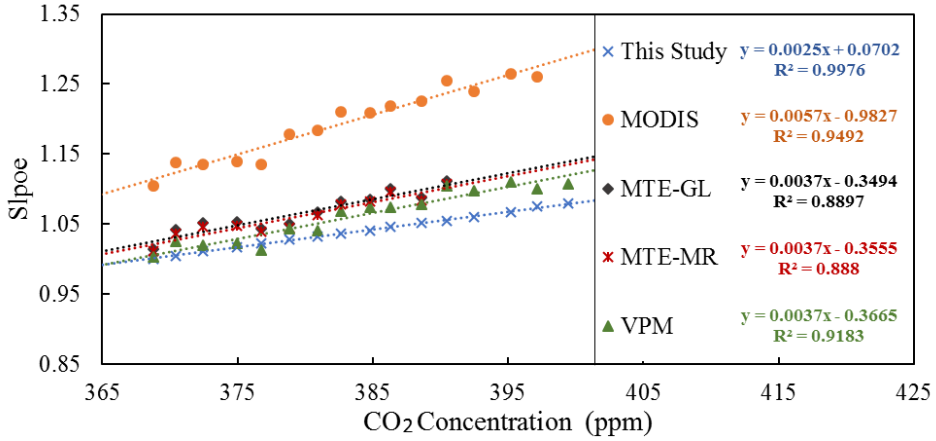

Figure 4.7 The correlation between the increasing atmospheric CO_2 concentration and the ratio of estimated GPP to other GPP products.

With respect to $GPP_{2000}CO_2$, the correlation was strongest with an R of 0.9988, and the lowest slope was 0.0025. The small trend of relative change was due to the different level of CO_2 fertilization effects rather than the exclusion of the CO_2 fertilization effect; furthermore, the other datasets used to drive the model were the same. Therefore, by comparing $GPP_{2000}CO_2$ with $GPP_{spa}CO_2$, I obtained the magnitude and spatial patterns of the effects of CO_2 concentration variability on GPP (Figure 4.8). Overall, the GPP in different regions had different levels of increase due to elevated atmospheric CO_2 concentrations, and the spatial distributions were highly consistent with previous research results (Sun et al., 2018; Chang et

al., 2016), which compared the GPP values of 2014 under different CO_2 levels. The effects of CO_2 concentration variability on GPP in Sub-Saharan Africa and in tropical rainforests (Chen et al., 2017b; Sun et al., 2018) were stronger than those in the middle and high latitudes, and the increment of GPP in the middle- and high-latitude areas of the Northern Hemisphere approximately averaged 0.2 gC m^{-2} day^{-1} from 2000 to 2015. In lower latitudes, there were abundant hydrothermal resources; additionally, in this study, I presumed the N limitation remained unchanged, which would reduce the positive effect in an environment with higher precipitation (Sowerby et al., 2008). Thus, the elevated atmospheric CO_2 concentrations could significantly enhance the photosynthetic rate (Long et al., 1991; Kirschbaum et al., 1994; Temme et al., 2015). This could also be reflected in the annual growth rate of the global GPP. The growth rate of the estimated GPP in this chapter was 0.6171 PgC $year^{-1}$, which is faster than those for the period of 2000-2010 in MODIS (0.01 PgC $year^{-1}$) and MTE
(0.25 PgC $year^{-1}$), which did not consider CO_2 fertilization. Conversely, this section did not reproduce the nitrogen limitation that would overestimate the CO_2 fertilization effect; thus, there was a higher-than-average trend for the models that considered the carbon fertilization effect that was limited by nitrogen levels. Chen et al. (2017b) selected 8 models from the ISIMIP2 to calculate the global GPP trends for 2000-2010, and the average trend of the models that included the nitrogen cycle module was 0.385 PgC $year^{-1}$, which was much smaller than our estimation; however, our results were almost equal to those of JULES (0.62 PgC $year^{-1}$) and the Hadley Center Global Environment Model version 2 - Earth System Modeling (HadGEM2-ES) (0.60 PgC $year^{-1}$), which both showed that not reproducing the nitrogen limitation might overestimate the GPP trends (Anav et al., 2015). In contrast, in middle and high latitudes, the vegetation is more limited by temperature, water and/or light (Nemani et al., 2003), and plants do not respond as robustly to the elevated atmospheric CO_2 concentration as those in low latitudes. The monthly positive effect of CO_2 concentration on GPP was reflected in each month (Figure 4.9) but varied based on the month and location; however, the effects were almost the same as the temporal-spatial patterns of GPP. The monthly GPP differences in our simulation also indicated that there were interactions between CO_2 effects and climate drivers (Liu et al., 2016). During winter in the middle and high latitudes of the Northern Hemisphere, the plants have not yet entered the growing season due to low temperatures and insufficient solar radiation; thus, there are no CO_2 fertilization effects. At the same time, since most of the terrestrial plants are located in the Northern Hemisphere and do not conduct photosynthesis, the atmospheric CO_2 concentration was the highest in winter across the whole year. This result may explain why, although the CO_2 fertilization effect was reflected every month in the tropics, the most significant performance was shown during the winter period of the Northern Hemisphere. After entering spring, the effects of CO_2 fertilization on GPP obviously appear, while from summer to autumn, the effects decrease as the subsolar point moves southward; furthermore, the variation in the monthly effects has an obvious seasonal characteristic in the Northern Hemisphere. During summer, the atmospheric CO_2 concentration reaches its lowest point throughout the year; thus, the weakest CO_2 fertilization effect should occur in summer, but plants grow more significantly. This may be because the higher atmospheric CO_2 concentration in spring ameliorates the photosynthetic process in plants to enable enhanced carbon fixation capacity, which would provide the essential resources for the rapid growth of plants in summer (Wu et al., 2015) as well as the interaction effect between the climate resources and the atmospheric CO_2 concentration on plant growth (Dijkstra et al., 2010; Nowak et al., 2004; Chang et al., 2016). During summer, there are abundant hydrothermal resources for plants growth. Based on the above results, considering the variability in the CO_2 concentration and incorporating the CO_2 fertilization module into the estimation should improve the GPP estimation.

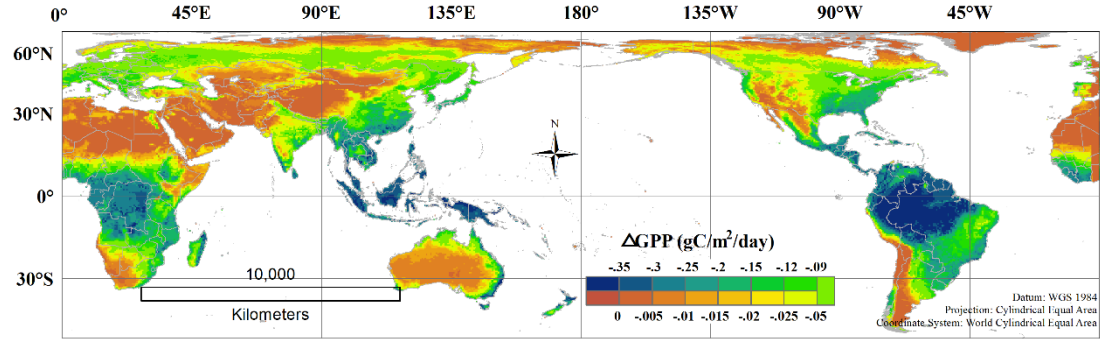

Figure 4.8 Comparison of the annual averaged GPP under dynamic and fixed atmospheric CO_2 concentrations from 2000 to 2015.

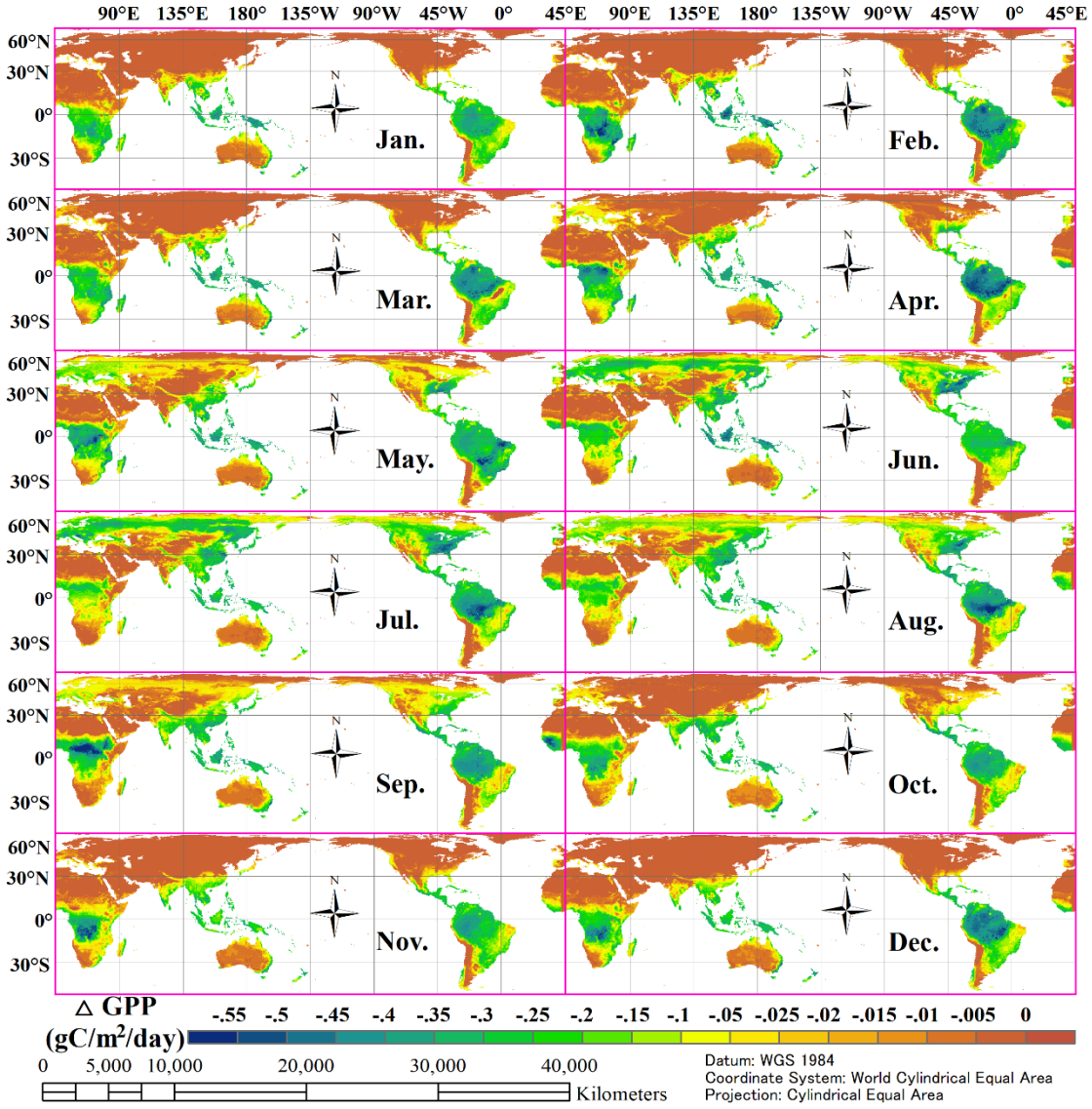

Figure 4.9 Comparison of the monthly averaged GPP under dynamic and fixed atmospheric CO_2 concentrations from 2000 to 2015.

4.3.1.3 The effect of CO_2 concentration distribution on GPP

In this section, I considered GPPspaCO_2 to be a nominally more accurate estimate than those obtained by inputting globally averaged values, and we used it as the standard value used to analyze the influences of the distribution of CO_2 concentration on the estimation of GPP. Except for the opposite positive and negative performances observed in Europe, Southeast Asia, southern North America and northern Brazil, the distribution of estimated biases in GPPannCO_2 and GPPmonCO_2 were almost identical in terms of the annual GPP estimates (Figure 4.10 and Figure 4.12). Both forms of data estimations underestimated the annual GPP in eastern Africa, northeastern North America and the Brazilian plateau; however, the estimation in the high latitudes of the Northern Hemisphere, central and western sub-Saharan Africa, Asian rainforests and most of Northeast Asia were overestimated. The maximum overestimation of GPPmonCO_2 was found in Northeast Asia, which presented a bias of approximately 1 gC m^{-2} $year^{-1}$; in contrast, the most underestimated values were found in Europe and Southeast Asia, where the calculated biases were over -1 gC m^{-2} $year^{-1}$. Regarding GPPannCO_2, the most underestimated GPP values were found in the Brazilian plateau, at approximately -10 gC m^{-2} $year^{-1}$; in contrast, the maximum overestimations were greater than 15 gC m^{-2} $year^{-1}$ in the African rainforests and the high latitudes of Eurasia. Both overestimated the annual GPP but had different magnitude of discrepancy; specifically, the biases of GPPannCO_2 (globally averaged 15-year mean bias was 1.6285 ± 3.0568 gC m^{-2} $year^{-1}$) were more significant than those of GPPmonCO_2 (0.0476 ± 0.2174 gC m^{-2} $year^{-1}$). This was because the GPPmonCO_2, in contrast with the GPPannCO_2, only reflected the impact of the distribution of the CO_2 concentration on the global GPP estimates, whereas the GPPannCO_2 was a comprehensive manifestation of the influences of the differences of seasonal variations and spatial distribution on the CO_2 concentration. The overestimation phenomenon could be explained from temporal and spatial dimensions: the rapid growth seasons for plants in the middle-high latitudes of the Northern and Southern Hemispheres occur in inverse periods; moreover, the atmospheric CO_2 concentration variations are similar, and the atmospheric CO_2 concentration during the vegetation growth season would decrease due to vegetation carbon fixation. In other words, most terrestrial ecosystems are located in the Northern Hemisphere, and photosynthesis in the Northern Hemisphere has the greatest contribution to the seasonal variation in the global carbon flux. Before the growing season (i.e., in early spring), under the higher CO_2 concentration conditions caused by accumulation during winter, plants would enhance the carbon fixation process to provide the essential conditions for plant growth in summer (Wu et al., 2015). In addition, during the growing periods, plants would conduct photosynthesis and absorb CO_2 from the atmosphere. Therefore, the atmospheric CO_2 concentration was lower than the annual mean value, and the estimates calculated from using the mean annual CO_2 concentration would be larger than the actual GPP; furthermore, the atmospheric CO_2 concentration in the Northern Hemisphere was lower than that in the Southern Hemisphere, and using globally averaged CO_2 concentrations results in the overestimation of GPP. This could be more easily explained by the distribution of the monthly biases of GPP (Figure 4.11 and Figure 4.13). The rapid growth period of vegetation in the Southern Hemisphere is approximately from November to March, when the atmospheric CO_2 concentration is high; however, it would decrease after neutralizing in the other months. Therefore, the estimated GPP would be an underestimation when the globally averaged value was used, and the differences of GPPmonCO_2 were much smaller than those of GPPannCO_2. Regarding tropical areas, the plants have strong photosynthetic capacity and fix atmospheric CO_2 with a low amplitude throughout the year; thus, during the same period, the atmospheric CO_2 concentration should be lower than the globally averaged CO_2 concentration; not considering the distribution of the atmospheric CO_2 concentration could lead to an overestimation of GPP. In tropical regions, the annual CO_2 concentration cycle has an anti-

phase relationship with the global averaged CO_2 cycle, and the estimates would be overestimated at the beginning and at the end of a year and underestimated in the middle of the year.

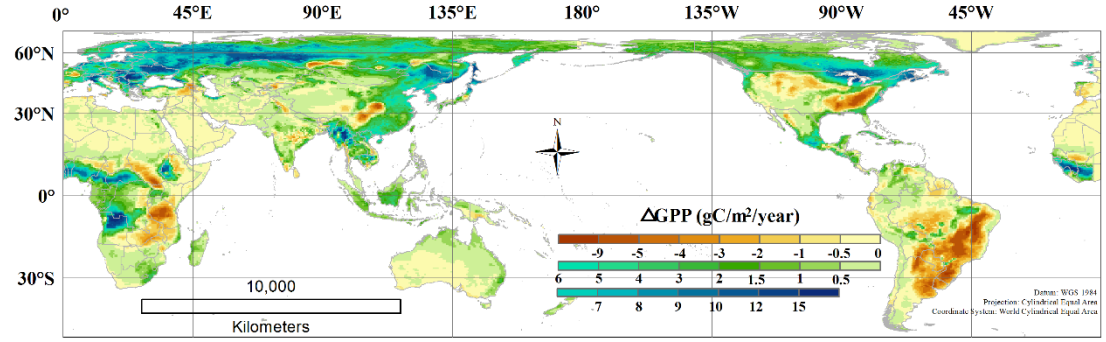

Figure 4.10 Comparison of the annual GPP estimates using different CO_2 data forms ($GPP_{ann}CO_2$ minus $GPP_{spa}CO_2$).

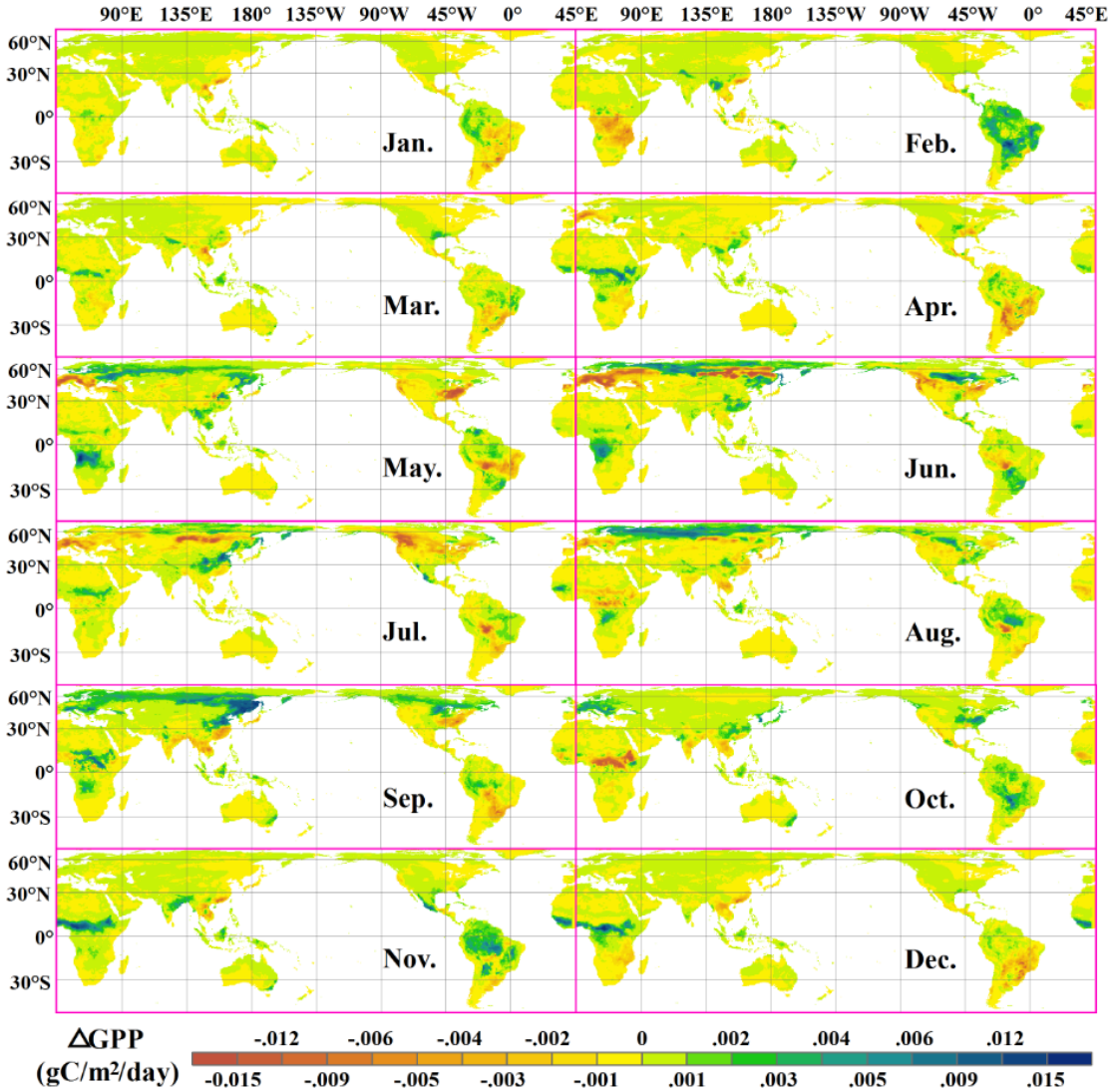

Figure 4.11 Comparison of the monthly GPP estimates using different CO_2 data forms ($GPP_{mon}CO_2$ minus $GPP_{spa}CO_2$).

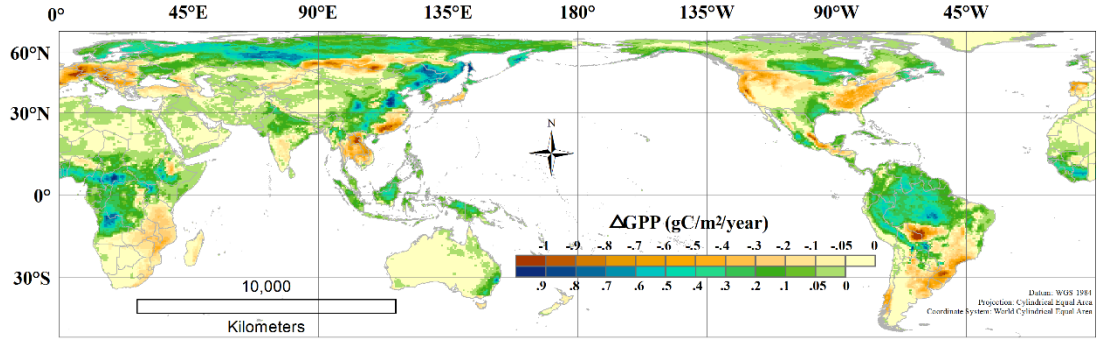

Figure 4.12 Comparison of the annual GPP estimates using different CO_2 data forms ($GPP_{mon}CO_2$ minus $GPP_{spa}CO_2$).

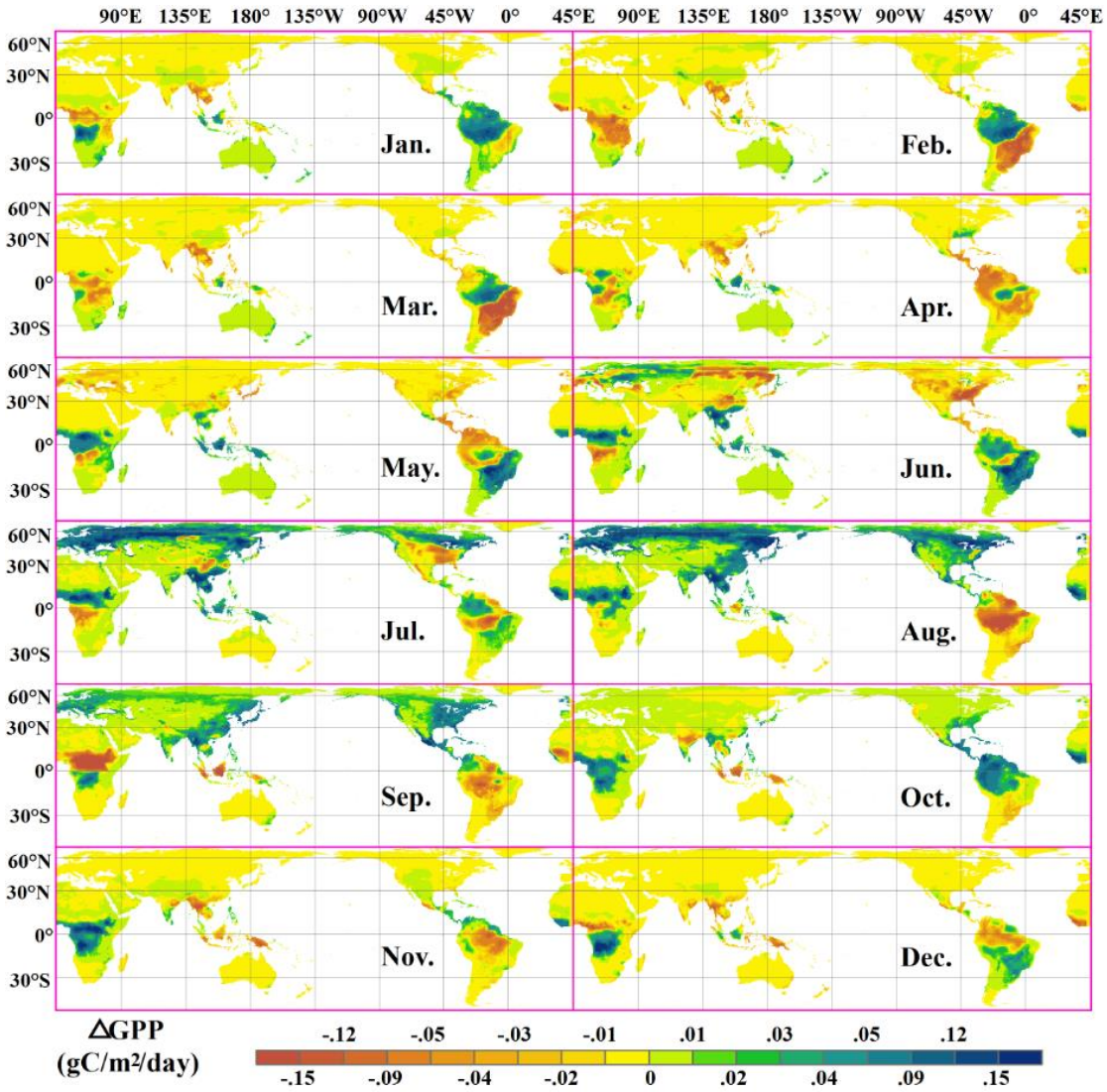

Figure 4.13 Comparison of the monthly GPP estimates using different CO_2 data forms ($GPP_{ann}CO_2$ minus $GPP_{spa}CO_2$).

Thus, not considering the temporal and spatial variations in the atmospheric CO_2 concentration would affect the estimation of the GPP; though the estimation would vary based on location and period, overall, there would be an overestimation effect.

4.3.2 New model estimation

4.3.2.1 GPP estimates

The estimated spatial distribution of the annual global GPP for 2014 is shown in Figure 4.14. This figure shows that the largest GPP is found in the tropics (e.g., the Amazon Rainforest, Congo Rainforest, and Indonesia), where the model estimates a value of more than 3000 gC m^{-2} $year^{-1}$. This is followed by values found for monsoonal subtropical regions (e.g., Southeastern Asia, Easternmost Australia), which present GPP values of approximately 1000 to 2300 gC m^{-2} $year^{-1}$, and temperate humid regions in Eastern North America and Western and Central Europe, which present GPP values of approximately 1400 gC m^{-2} $year^{-1}$. Low GPP values are typical of adverse environments, such as high-altitude regions (e.g., Tibetan Plateau), high latitude areas (e.g., Greenland, Northern Canada, Northern Russia) with short growing seasons and low temperatures, desert regions (e.g., Sahara, Taklamakan, Arabian) characterized by low levels of precipitation, and dry areas where water availability limits plant production (Avan et al., 2015).

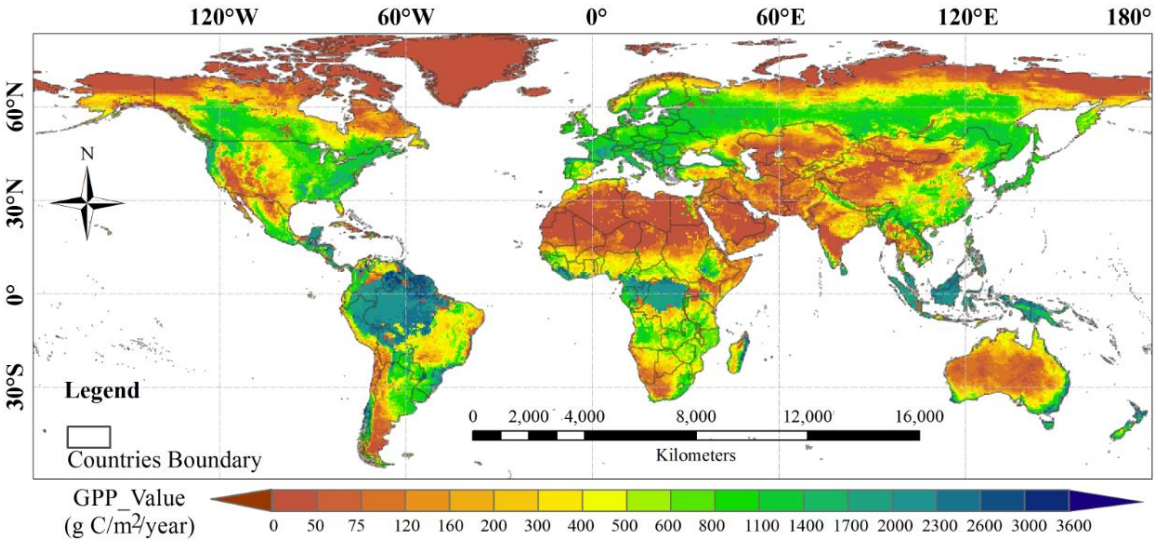

Figure 4.14 Global spatial distribution of the annual $GPP_{2014}^{\text{monthly spatial } CO_2}$.

At the global scale, Figure 4.15 shows the considerable seasonal variations, and the $GPP_{2014}^{\text{monthly spatial } CO_2}$ estimates are high during the northern hemispheric summer and low during the northern hemispheric winter. Although the GPP is seasonal in tropical and subtropical regions, seasonal variations in the global GPP appear to be largely influenced by the seasonal GPP in temperate and boreal regions. Figure 4.16 shows that the land components (ENF, DNF, DBF and MF) of temperate and boreal regions present a higher seasonal amplitude. In tropical and subtropical regions, the land cover classifications are mainly EBF, SAV, SHR and BAR with a lower seasonal amplitude. This may be attributable to the combined effects of a cold bias in the surface temperature and plant nitrogen limitations (Avan et al., 2015). Tropical EBF areas present high GPP levels throughout the year, with lower amplitudes corresponding to alternations between the wetter and drier seasons. Presenting relatively sufficient water, temperature, and light conditions, an estimated average monthly GPP of more than 150 gC m^{-2} $month^{-1}$ was found in tropical forests, which are the most productive on a monthly scale, and, thus, tropical forests are the world's most stable regions.

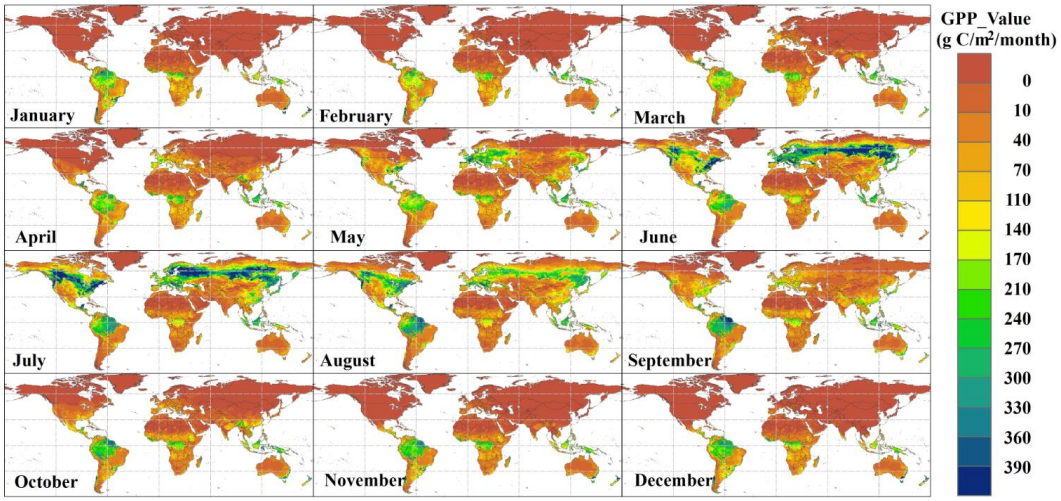

Figure 4.15 Global spatial distribution of estimated monthly GPPs.

However, the maximum monthly GPP in tropical forests is exceeded by that in forests in temperature zones in June and July, and this result is consistent with results from numerous studies (Wang et al., 2014; Avan et al., 2015). This result was found because the GPP of DBF, DNF, and MF can exceed that of EBF during the summer (Figure 4.16), and such areas are mainly distributed in temperate and boreal zones (Figure 4.15, 50°N ~ 70°N over the Eurasian continent and 45°N ~ 60°N over North America). Monthly latitudinal variations can be found at the global scale. Such variations, followed by solar insolation and temperature variations, such as light intensity, illumination time, and temperature, considerably affect photosynthesis, which is the direct source of the GPP. Figure 4.16 shows the monthly GPP for every land cover component as follows: woody savannah, savannah combined into SAV, open shrublands, and closed shrublands combined into SHR.

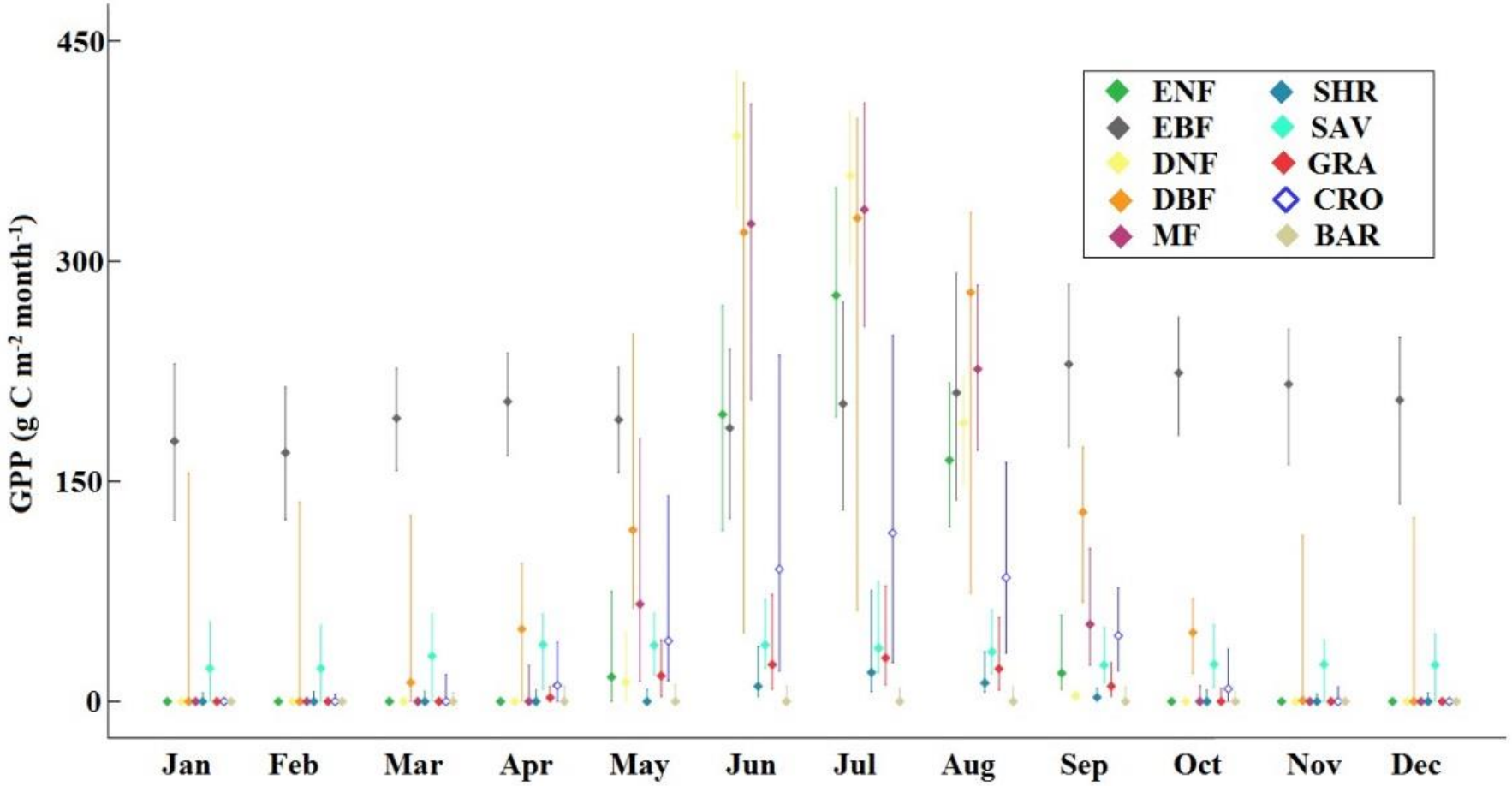

Figure 4.16 Median, upper quartile and lower quartile of the estimated monthly $GPP_{2014}^{monthly\ spatial\ CO_2}$ for all vegetated land cover types delineated using the MODIS land cover.

4.3.2.2 Accuracy assessment of GPP estimates

Figure 4.17 shows the comparison between $GPP_{2014}^{monthly\ spatial\ CO_2}$ and tower GPP. The Fluxnet 2015 dataset, which is based on EC technology, represents one of the only three types of datasets that appear capable of validating GPP estimates (Running et al., 2004). Therefore, it is meaningful and relevant to compare the estimated $GPP_{2014}^{monthly\ spatial\ CO_2}$ with tower GPP to test the estimation accuracy levels. Since the different spatial scales of $GPP_{2014}^{monthly\ spatial\ CO_2}$ and tower GPP increase the uncertainty, and the number of Fluxnet data in 2014 is a bit less, therefore, to better observe the relationship between $GPP_{2014}^{monthly\ spatial\ CO_2}$ and tower GPP, we utilized MODIS products as a "bridge" to establish a GPP vs. MODIS GPP Products space to test the accuracy of the estimates; the red dots denote the relationship between the MODIS GPP Products and the tower GPP (Table 4.6) from 2000 to 2014, and the green dots represent the relationship between the MODIS GPP Products in 2014 and the $GPP_{2014}^{monthly\ spatial\ CO_2}$. The same version of MODIS GPP was used to ensure consistency in the uncertainty and accuracy levels.

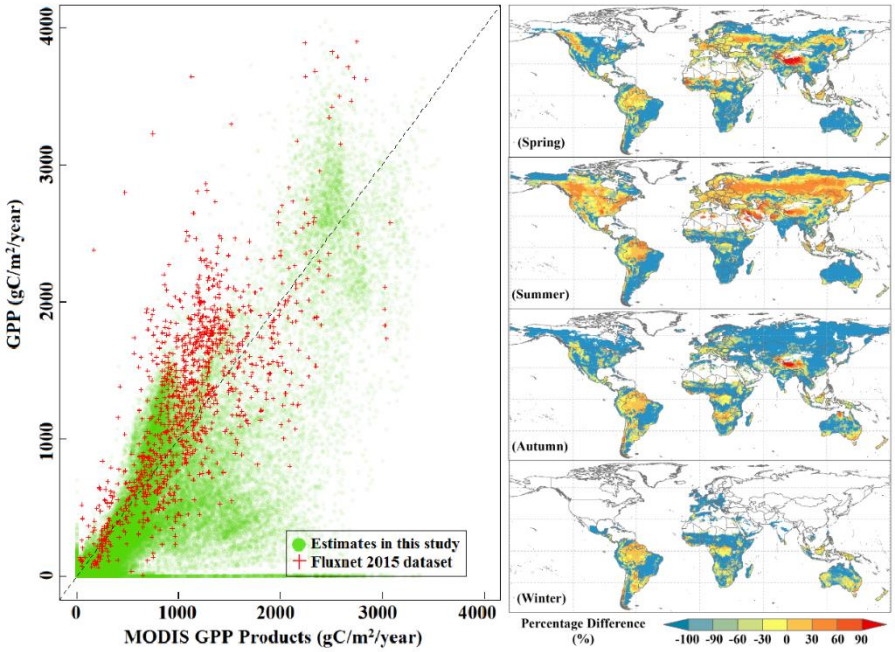

Figure 4.17 Accuracy assessment of GPPs (left: comparison between the estimated annual GPP in this study and the GPP from Flux tower sites; right: comparison between the estimated GPP in this study and MODIS product).

In addition, in order to evaluate the accuracy of the estimated GPPs relative to MODIS, at each Flux tower site the month-to-month difference between tower GPP and $GPP_{2014}^{monthly\ spatial\ CO_2}$ and difference between tower GPP and MODIS GPP were also compared and analyzed (Figure S13). Except for a very few sites (AU-Rob, US-Wcr, IT-Isp), the positive-negative characteristics of the differences between tower GPP and $GPP_{2014}^{monthly\ spatial\ CO_2}$ are in accordance with that of the difference between tower GPP and MODIS GPP, vice versa, simultaneously overestimated or underestimated. For every pixel, the air temperature is one of the important restrictive factors whether this method estimates GPP or not (if $T_{air} > 45°C$ or $T_{air} < 0°C$, GPP = 0 gC m^{-2} $year^{-1}$), however, for Fluxnet GPP dataset, the GPPs are estimated by carbon flux between ecosystem and atmosphere, which is calculated by using EC technology; and most of

the Flux tower sites are located in high latitudes with low winter temperature, therefore, in winter the estimated GPP are less than tower GPPs. Comparing $GPP_{2014}^{monthly\ spatial\ CO_2}$ with MODIS product, I found that the magnitude of the GPP which was lower than 2000 gC m^{-2} $year^{-1}$ is more concentrated, while that with values greater than 2000 gC m^{-2} $year^{-1}$ is relative more scattered. According to Figure 4.14, the locations with GPP greater than 2000 gC m^{-2} $year^{-1}$ are basically located within the scope of tropical, where the high cloud coverage are a major obstacle to optical remote sensing (Asner 2010). Furthermore, in the range of 1000 to 2000 gC m^{-2} $year^{-1}$ of MODIS GPP, we found that $GPP_{2014}^{monthly\ spatial\ CO_2}$ are significantly lower than MODIS product. These GPPs are mainly distributed in the Brazilian plateau, the African savanna, Eastern United States, almost the same with the distribution region of high C4 species fraction. In this research, we not only utilized the satellite-based LUE models relying on simple algorithms to estimate C4 species GPP (the theoretical basis of MODIS products), but also supplemented the restrictions of sucrose synthesis and Rubisco; accordingly, the $GPP_{2014}^{monthly\ spatial\ CO_2}$ would be lower than MODIS product. Moreover, besides high C4 species coverage areas, from the seasonal view $GPP_{2014}^{monthly\ spatial\ CO_2}$ are generally lower than MODIS product in the autumn, which is opposite to that in summer. By means of comparing MODIS product and $GPP_{2014}^{monthly\ spatial\ CO_2}$ at every flux tower site, the accuracy of MODIS product in autumn is higher than that of $GPP_{2014}^{monthly\ spatial\ CO_2}$ in more than half of observed months. On the other hand, in 62% of observed months in summer the accuracy of MODIS product is lower than that of $GPP_{2014}^{monthly\ spatial\ CO_2}$. Since the sites are mainly distributed with higher density in Europe and North America, but lower density in the Southern Hemisphere and low latitudes, we cannot conclude that the accuracy of $GPP_{2014}^{monthly\ spatial\ CO_2}$ is higher than MODIS product. In this section, the first objective was to attempt to utilize continuous spatial CO_2 concentration data obtained by satellite to estimate the terrestrial GPP; it can be observed from the results of the comparisons with tower GPP and MODIS product that the study has achieved this objective.

Table 4.6 A list of the Flux tower sites used in this study.

ID	Site	Latitude	Longitude	Country	PFT	Years
1	AR-SLu	-33.4648	-66.4598	Argentina	MF	2009-2011
2	AR-Vir	-28.2395	-56.1886	Argentina	ENF	2010-2012
3	AT-Neu	47.1167	11.3175	Austria	GRA	2002-2012
4	AU-Ade	-13.0769	131.1178	Australia	WSA	2007-2009
5	AU-ASM	-22.2830	133.2490	Australia	ENF	2010-2013
6	AU-Cpr	-34.0021	140.5891	Australia	SAV	2010-2013
7	AU-Cum	-33.6133	150.7225	Australia	EBF	2012-2013
8	AU-DaP	-14.0633	131.3181	Australia	GRA	2008-2013
9	AU-DaS	-14.1593	131.3881	Australia	SAV	2008-2013
10	AU-Dry	-15.2588	132.3706	Australia	SAV	2008-2013
11	AU-Emr	-23.8587	148.4746	Australia	GRA	2011-2013
12	AU-Fog	-12.5452	131.3072	Australia	WET	2006-2008
13	AU-Gin	-31.3764	115.7138	Australia	WSA	2000-2003
14	AU-GWW	-30.1913	120.6541	Australia	SAV	2013-2014
15	AU-How	-12.4943	131.1523	Australia	WSA	2001-2014
16	AU-Lox	-34.4704	140.6551	Australia	DBF	2008-2009
17	AU-RDF	-14.5636	132.4776	Australia	WSA	2011-2013
18	AU-Rig	-36.6499	145.5759	Australia	GRA	2011-2013
19	AU-Rob	-17.1175	145.6301	Australia	EBF	2014
20	AU-Stp	-17.1507	133.3502	Australia	GRA	2008-2014
21	AU-Tum	-35.6566	148.1517	Australia	EBF	2001-2013
22	AU-Wac	-37.4259	145.1878	Australia	EBF	2005-2008
23	AU-Whr	-36.6732	145.0294	Australia	EBF	2011-2013
24	AU-Wom	-37.4222	144.0944	Australia	EBF	2010-2011
25	AU-Ync	-34.9893	146.2907	Australia	GRA	2011-2013
26	BE-Bra	51.3092	4.5206	Belgium	MF	2000-2002, 2004-2013
27	BE-Lon	50.5516	4.7461	Belgium	CRO	2004-2014
28	BE-Vie	50.3051	5.9981	Belgium	MF	2000-2014
29	BR-Sa3	-3.0180	-54.9714	Brazil	EBF	2000-2004
30	CA-Man	55.8796	-98.4808	Canada	ENF	2000-2008
31	CA-NS1	55.8792	-98.4839	Canada	ENF	2002-2005
32	CA-NS2	55.9058	-98.5247	Canada	ENF	2001-2005
33	CA-NS3	55.9117	-98.3822	Canada	ENF	2001-2005
34	CA-NS4	55.9117	-98.3822	Canada	ENF	2002-2005
35	CA-NS5	55.8631	-98.4850	Canada	ENF	2001-2005
36	CA-NS6	55.9167	-98.9644	Canada	OSH	2001-2005
37	CA-NS7	56.6358	-99.9483	Canada	OSH	2002-2005
38	CA-Qfo	49.6925	-74.3421	Canada	ENF	2003-2010
39	CA-SF1	54.4850	-105.8176	Canada	ENF	2003-2006
40	CA-SF2	54.2539	-105.8775	Canada	ENF	2001-2005
41	CA-SF3	54.0916	-106.0053	Canada	OSH	2001-2006

42	CH-Cha	47.2102	8.4104	Switzerland	GRA	2006-2008, 2010-2012
43	CH-Dav	46.8153	9.8559	Switzerland	ENF	2000-2014
44	CH-Fru	47.1158	8.5378	Switzerland	GRA	2006-2008, 2010-2012
45	CH-Lae	47.4781	8.3650	Switzerland	MF	2004-2014
46	CH-Oe1	47.2858	7.7319	Switzerland	GRA	2002-2008
47	CH-Oe2	47.2863	7.7343	Switzerland	CRO	2004-2014
48	CN-Cha	42.4025	128.0958	China	MF	2003-2005
49	CN-Cng	44.5934	123.5092	China	GRA	2007-2010
50	CN-Dan	30.4978	91.0664	China	GRA	2004-2005
51	CN-Din	23.1733	112.5361	China	EBF	2003-2005
52	CN-Du2	42.0467	116.2836	China	GRA	2007-2008
53	CN-Ha2	37.6086	101.3269	China	WET	2003-2005
54	CN-HaM	37.3700	101.1800	China	GRA	2002-2004
55	CN-Qia	26.7414	115.0581	China	ENF	2003-2005
56	CN-Sw2	41.7902	111.8971	China	GRA	2010-2012
57	CZ-BK1	49.5047	18.5411	Czech Republic	ENF	2002-2012
58	CZ-BK2	49.4944	18.5429	Czech Republic	GRA	2002-2011
59	CZ-wet	49.0247	14.7704	Czech Republic	WET	2006-2014
60	DE-Geb	51.1001	10.9143	Germany	CRO	2001-2014
61	DE-Gri	50.9495	13.5125	Germany	GRA	2004-2014
62	DE-Hai	51.0792	10.4530	Germany	DBF	2000-2012
63	DE-Kli	50.8929	13.5225	Germany	CRO	2004-2014
64	DE-Lkb	49.0996	13.3047	Germany	ENF	2009-2013
65	DE-Obe	50.7836	13.7196	Germany	ENF	2008-2014
66	DE-RuR	50.6219	6.3041	Germany	GRA	2011-2014
67	DE-RuS	50.8657	6.4472	Germany	CRO	2011-2014
68	DE-Seh	50.8706	6.4497	Germany	CRO	2007-2010
69	DE-SfN	47.8064	11.3275	Germany	WET	2012-2014
70	DE-Spw	51.8923	14.0337	Germany	WET	2010-2014
71	DE-Tha	50.9636	13.5669	Germany	ENF	2000-2014
72	DK-Fou	56.4842	9.5872	Denmark	CRO	2005
73	DK-NuF	64.1308	-51.3861	Denmark	WET	2008-2014
74	DK-Sor	55.4859	11.6446	Denmark	DBF	2000-2012
75	DK-ZaF	74.4814	-20.5545	Denmark	WET	2008-2011
76	DK-ZaH	74.4732	-20.5503	Denmark	GRA	2000, 2002-2003, 2005-2008
77	ES-LgS	37.0979	-2.9658	Spain	OSH	2007-2009
78	FI-Hyy	61.8475	24.2950	Finland	ENF	2000-2014
79	FI-Jok	60.8986	23.5135	Finland	CRO	2000-2003
80	FI-Lom	67.9972	24.2092	Finland	WET	2007-2009
81	FI-Sod	67.3619	26.6378	Finland	ENF	2001-2014
82	FR-Fon	48.4764	2.7801	France	DBF	2005-2014

83	FR-Gri	48.8442	1.9519	France	CRO	2004-2014
84	FR-LBr	44.7171	-0.7693	France	ENF	2000-2008
85	FR-Pue	43.7414	3.5958	France	EBF	2000-2013
86	GF-Guy	5.2788	-52.9249	French Guyana	EBF	2004-2012
87	IT-BCi	40.5238	14.9574	Italy	CRO	2004-2014
88	IT-CA1	42.3804	12.0266	Italy	DBF	2011-2013
89	IT-CA2	42.3772	12.0260	Italy	CRO	2011-2013
90	IT-CA3	42.3800	12.0222	Italy	DBF	2011-2013
91	IT-Col	41.8494	13.5881	Italy	DBF	2000-2014
92	IT-Cp2	41.7043	12.3573	Italy	EBF	2012-2013
93	IT-Cpz	41.7052	12.3761	Italy	EBF	2000-2008
94	IT-Isp	45.8126	8.6336	Italy	DBF	2013-2014
95	IT-La2	45.9542	11.2853	Italy	ENF	2000-2002
96	IT-Lav	45.9562	11.2813	Italy	ENF	2003-2012
97	IT-MBo	46.0147	11.0458	Italy	GRA	2003-2013
98	IT-Noe	40.6061	8.1515	Italy	CSH	2004-2012
99	IT-PT1	45.2009	9.0610	Italy	DBF	2002-2004
100	IT-Ren	46.5869	11.4337	Italy	ENF	2000-2013
101	IT-Ro1	42.4081	11.9300	Italy	DBF	2000-2008
102	IT-Ro2	42.3903	11.9209	Italy	DBF	2002-2008, 2010-2012
103	IT-SR2	43.7320	10.2910	Italy	ENF	2013-2014
104	IT-SRo	43.7279	10.2844	Italy	ENF	2000-2014
105	IT-Tor	45.8444	7.5781	Italy	GRA	2008-2013
106	JP-MBF	44.3869	142.3186	Japan	DBF	2004-2005
107	MY-PSO	2.9730	102.3062	Malaysia	EBF	2003-2009
108	NL-Hor	52.2404	5.0713	Netherlands	GRA	2004-2011
109	NL-Loo	52.1666	5.7436	Netherlands	ENF	2000-2014
110	RU-Che	68.6130	161.3414	Russia	WET	2002-2005
111	RU-Cok	70.8291	147.4943	Russia	OSH	2003-2013
112	RU-Fyo	56.4615	32.9221	Russia	ENF	2000-2013
113	RU-Ha1	54.7252	90.0022	Russia	GRA	2002-2004
114	SD-Dem	13.2829	30.4783	Sudan	SAV	2005, 2007-2009
115	SN-Dhr	15.4028	-15.4322	Senegal	SAV	2010-2013
116	US-AR1	36.4267	-99.4200	USA	GRA	2009-2012
117	US-AR2	36.6358	-99.5975	USA	GRA	2009-2012
118	US-ARb	35.5497	-98.0402	USA	GRA	2005-2006
119	US-ARc	35.5465	-98.0400	USA	GRA	2005-2006
120	US-ARM	36.6058	-97.4888	USA	CRO	2003-2012
121	US-Blo	38.8953	-120.6328	USA	ENF	2000-2007
122	US-Cop	38.0900	-109.3900	USA	GRA	2001-2003, 2006-2007
123	US-GBT	41.3658	-106.2397	USA	ENF	2001-2003
124	US-GLE	41.3665	-106.2399	USA	ENF	2005-2014

125	US-Ha1	42.5378	-72.1715	USA	DBF	2000-2012
126	US-KS2	28.6086	-80.6715	USA	CSH	2003-2006
127	US-Los	46.0827	-89.9792	USA	WET	2000-2008, 2010, 2014
128	US-Me1	44.5794	-121.5000	USA	ENF	2004-2005
129	US-Me2	44.4523	-121.5574	USA	ENF	2002-2014
130	US-Me6	44.3233	-121.6078	USA	ENF	2010-2012
131	US-MMS	39.3232	-86.4131	USA	DBF	2000-2014
132	US-Myb	38.0498	-121.7651	USA	WET	2011-2014
133	US-Ne1	41.1651	-96.4766	USA	CRO	2001-2012
134	US-Ne2	41.1649	-96.4701	USA	CRO	2001-2013
135	US-Ne3	41.1797	-96.4397	USA	CRO	2001-2012
136	US-NR1	40.0329	-105.5464	USA	ENF	2000-2014
137	US-PFa	45.9459	-90.2723	USA	MF	2000-2014
138	US-Prr	65.1237	-147.4876	USA	ENF	2010-2012
139	US-SRG	31.7894	-110.8277	USA	GRA	2008-2014
140	US-SRM	31.8214	-110.8661	USA	WSA	2004-2014
141	US-Syv	46.2420	-89.3477	USA	MF	2001-2007, 2012-2014
142	US-Ton	38.4316	-120.9660	USA	WSA	2001-2014
143	US-Tw1	38.1074	-121.6469	USA	WET	2012-2014
144	US-Tw2	38.1047	-121.6433	USA	CRO	2012-2013
145	US-Tw3	38.1159	-121.6467	USA	CRO	2013-2014
146	US-Tw4	38.1030	-121.6414	USA	WET	2013-2014
147	US-Twt	38.1087	-121.6530	USA	CRO	2009-2014
148	US-UMB	45.5598	-84.7138	USA	DBF	2000-2014
149	US-UMd	45.5625	-84.6975	USA	DBF	2007-2014
150	US-Var	38.4133	-120.9507	USA	GRA	2000-2014
151	US-WCr	45.8059	-90.0799	USA	DBF	2000-2006, 2011-2014
152	US-Whs	31.7438	-110.0522	USA	OSH	2008-2014
153	US-Wi0	46.6188	-91.0814	USA	ENF	2002
154	US-Wi3	46.6347	-91.0987	USA	DBF	2002, 2004
155	US-Wi4	46.7393	-91.1663	USA	ENF	2002-2005
156	US-Wi6	46.6249	-91.2982	USA	OSH	2002-2003
157	US-Wi9	46.6188	-91.0814	USA	ENF	2004-2005
158	US-Wkg	31.7365	-109.9419	USA	GRA	2004-2014
159	ZA-Kru	-25.0197	31.4969	South Africa	SAV	2000-2005, 2007-2013
160	ZM-Mon	-15.4378	23.2528	Zambia	DBF	2007-2009

4.3.2.3 The effect of CO_2 concentration variability on GPP

In this section, I analyzed the response of the GPP to increasing atmospheric CO_2 concentrations using $GPP_{2014}^{\text{monthly mean global } CO_2}$ minus GPP_{2000} (Figure 4.18). Both $GPP_{2014}^{\text{monthly mean global } CO_2}$ and GPP_{2000} are estimated values using climate data in 2014 and the globally averaged monthly mean CO_2 concentration data, and the annual GPP is the sum of the monthly estimates. Overall, the global GPP has different levels of increases due to elevated atmospheric CO_2 concentrations. The effects of the CO_2 concentration variability on the GPP in middle and high latitudes are weaker than those in lower latitudes, and the increment of GPP in middle and high latitudes areas of the Northern Hemisphere are approximately 30 gC m^{-2}. The increment of the GPP in the rainforest is much higher than that in other areas around the world, particularly in the Amazon Rainforest, where the increase is up to 100 gC m^{-2} or more. This is followed by the increment of the GPP in humid temperate regions, which present increases of approximately 30 to 55 gC m^{-2}. Similar to the previous study (Ainsworth et al., 2004), the GPP increments in forests were greater than those in other PFTs; and, the increments in forests are ranked as EBF > DBF > MF > DNF > ENF, with average values of 54.96, 28.04, 14.36, 11.81 and 7.83 gC m^{-2}, respectively, calculated by the geostatistics method according to the MODIS land cover maps. Using the same geostatistics method, I found that the increments of GRA, SHR, SAV and GRO are approximately 3.18, 5.34, 10.41 and 10.47 gC m^{-2}, respectively. Most of the C4 species belong to herbs, and under natural atmospheric CO_2 concentration conditions, C4 species have been close to the CO_2 saturation point; thus, the increase in GRA is much smaller than that in the others. Broad-leaf forests are located in lower latitudes, where there are abundant hydrothermal resources; therefore, the elevated atmospheric CO_2 concentrations can significantly enhance the photosynthetic rate. In contrast, in middle and high latitudes, the plants, regardless of whether they are in a forest, are more limited by temperature and light; therefore, plants do not respond to the elevated atmospheric CO_2 concentrations as robustly as those in low latitudes.

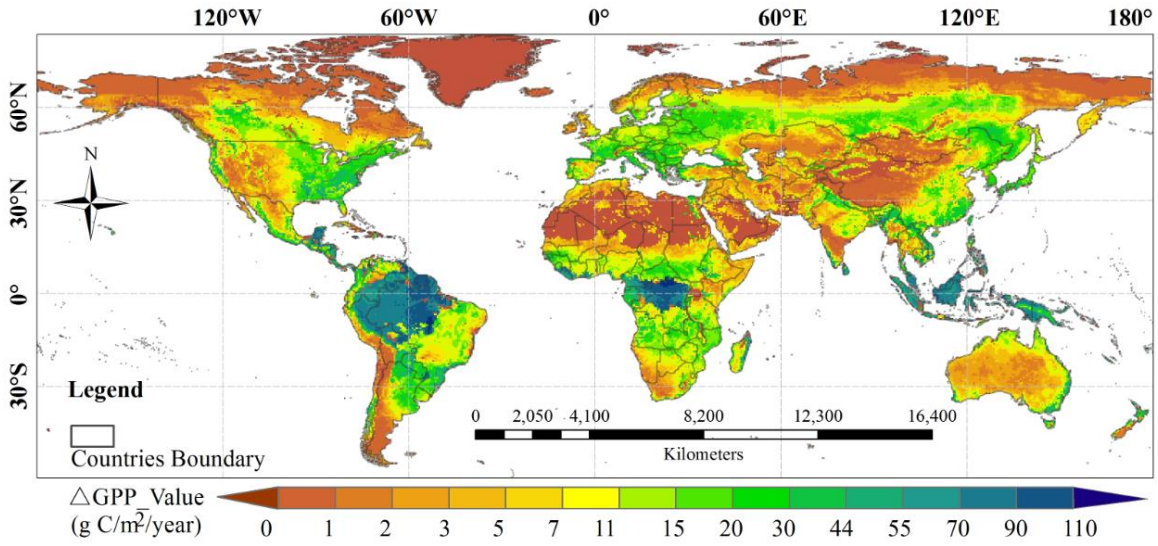

Figure 4.18 Comparison of the annual GPP under different atmospheric CO_2 concentrations (GPP_{2014} minus GPP_{2000}).

The annual GPP was the sum of the monthly GPP estimates, and the CO_2 concentrations in each month of 2014 were higher compared with the monthly CO_2 concentrations in 2000.

Figure 4.19 shows the differences in the monthly GPP estimates between 2014 and those in 2000 under the atmospheric CO_2 concentration conditions. The monthly GPP estimates increased each month, but the increases in the GPP varied based on the month and location; the differences between the months are relatively large, and the monthly maximum can reach more than 20 gC m^{-2}. In the Northern Hemisphere winter, because plants affected by temperature conditions almost stop growing, there are no signs of increasing GPP in middle and high latitudes. After entering the growth period, the GPP in middle and high latitudes in the Northern Hemisphere obviously respond to the elevated atmospheric CO_2 concentrations. Particularly in the summer, GPP increased most significantly under conditions in which there were abundant hydrothermal resources during the summer. There may be parts because that plants in the spring season, due to the higher CO_2 concentration, could improve the photosynthesis process to enable increased photosynthesis for carbon fixation, which provides the essential conditions for plant growth in the summer. From summer to autumn, the increment of the GPP decreased as a result of the subsolar point moving southward. The variation in the monthly GPP increment in the Northern Hemisphere has an obvious seasonal characteristic. The monthly GPP increments in ITCZ are almost consistent throughout the year as a result of perennial climate resources that are abundant and scarcely variant, and this is also the reason why the increment in the GPP in the Amazon rainforest is maximum. Under the same climate resource conditions of 2014, the global GPP estimates increase as the atmospheric CO_2 concentrations elevated from 2000 to 2014.

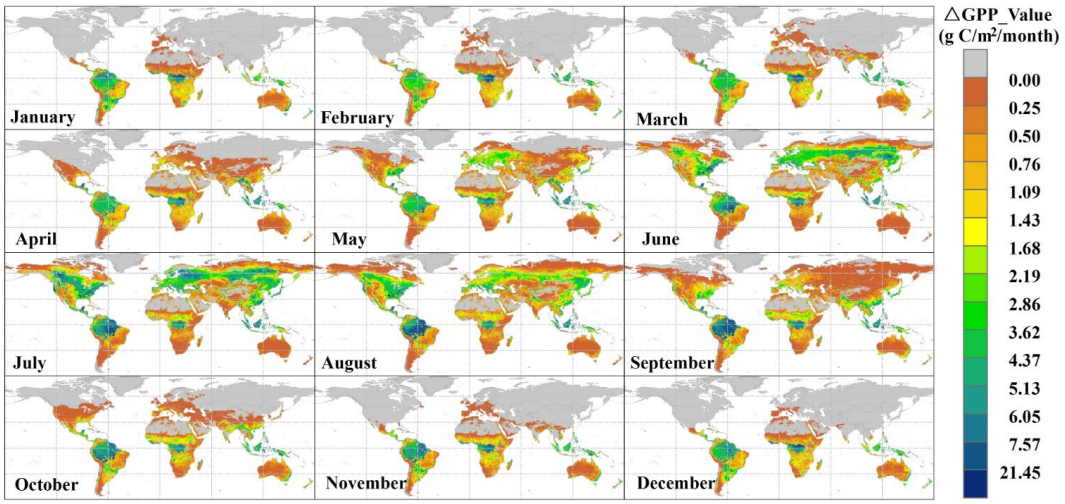

Figure 4.19 Comparison of the monthly GPP under different atmospheric CO_2 concentrations ($GPP_{2014}^{\text{monthly mean global } CO_2}$ minus GPP_{2000}).

4.3.2.4 The effect of CO_2 concentration distribution on GPP

Since $GPP_{2014}^{\text{monthly spatial } CO_2}$ has been verified using Fluxnet data in the *Section 4.3.2.3*, I consider $GPP_{2014}^{\text{monthly spatial } CO_2}$ a nominally relatively more accurate estimate than those inputting globally averaged values. I compared $GPP_{2014}^{\text{annual mean global } CO_2}$ and $GPP_{2014}^{\text{monthly mean global } CO_2}$ with $GPP_{2014}^{\text{monthly spatial } CO_2}$ and found that the estimated biases in the annual $GPP_{2014}^{\text{annual mean global } CO_2}$ and $GPP_{2014}^{\text{monthly mean global } CO_2}$ are nearly identical in terms of the annual GPP estimates; however, regarding the monthly GPP estimates, there were significant differences.

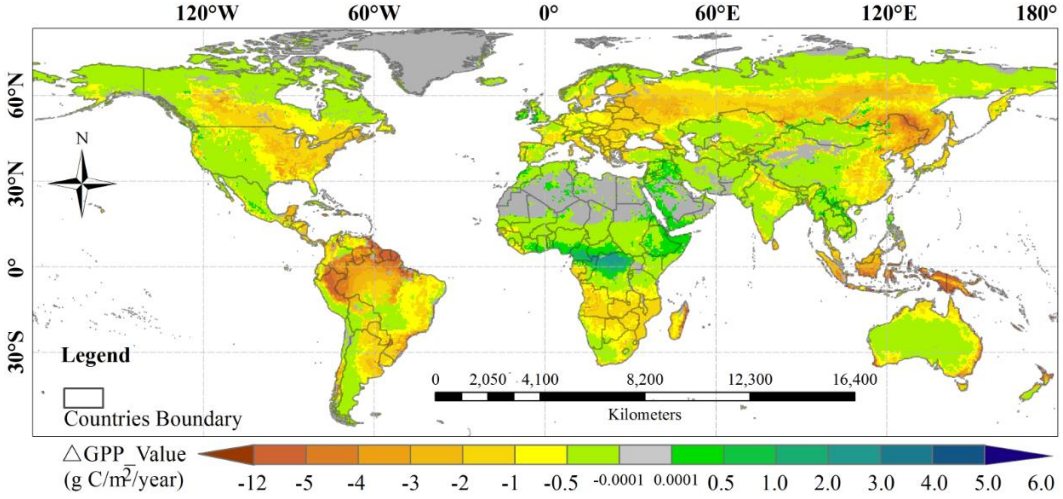

Figure 4.20 Comparison of the annual GPP estimates using different CO_2 data forms ($GPP_{2014}^{\text{monthly spatial } CO_2}$ minus $GPP_{2014}^{\text{annual mean global } CO_2}$).

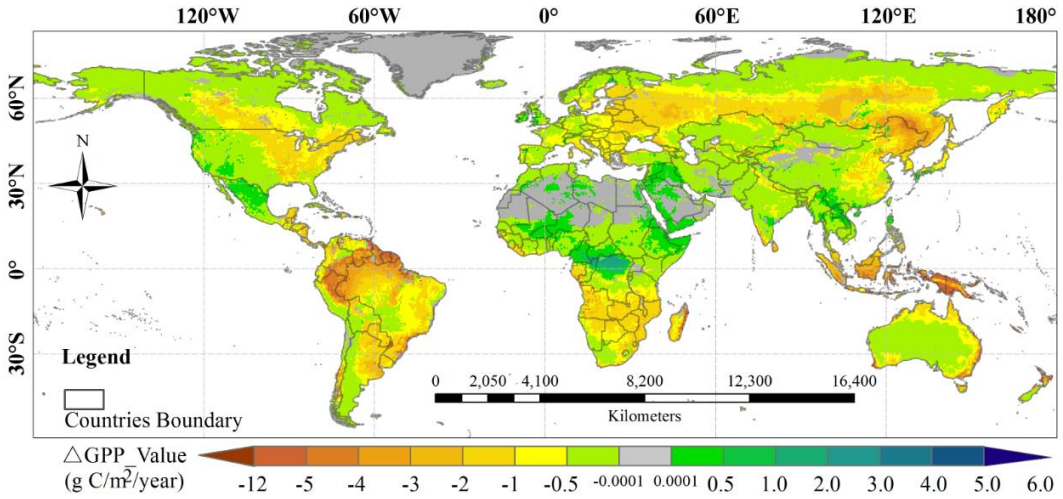

Figure 4.21 Comparison of annual GPP estimates using different CO_2 data forms ($GPP_{2014}^{\text{monthly spatial } CO_2}$ minus $GPP_{2014}^{\text{monthly mean global } CO_2}$).

The $GPP_{2014}^{\text{annual mean global } CO_2}$ estimates in high latitudes were slightly underestimated, whereas the estimates in middle latitude areas located in Europe, Eastern United States, and the Northeast part of East Asia were overestimated. In the lower latitudes, the GPP estimates are greater than $GPP_{2014}^{\text{monthly mean global } CO_2}$, except for those north of the sub-Saharan Africa and northwest of Southeast Asia, where the GPP were underestimated comparing with $GPP_{2014}^{monthly\ spatial\ CO_2}$ as shown in Figure 4.20 and Figure 4.21. The max positive biases are found in Northeast China, Indonesia and the Amazon rainforest, which present biases of over 12 gC m^{-2}, and the most underestimated estimates were found in the Congo Rainforest, where the calculated biases were approximately 6 gC m^{-2}. Although the spatial distributions of the biases in $GPP_{2014}^{\text{monthly mean global } CO_2}$ compared with that in $GPP_{2014}^{\text{annual mean global } CO_2}$ are near unanimous, the degrees of the discrepancies are different. The biases of $GPP_{2014}^{\text{annual mean global } CO_2}$ (globally averaged bias is approximately -0.74 gC m^{-2} with the standard deviation of approximately 1.10 gC m^{-2}) are more significant than those of $GPP_{2014}^{\text{monthly mean global } CO_2}$ (globally averaged bias is approximately -0.63 gC m^{-2} with a standard deviation of approximately 1.00 gC m^{-2}). This

result indicates that in comparison to using globally averaged annual mean CO_2 data to estimate the annual GPP, using globally averaged monthly mean CO_2 data to estimate the annual GPP is relatively more accurate.

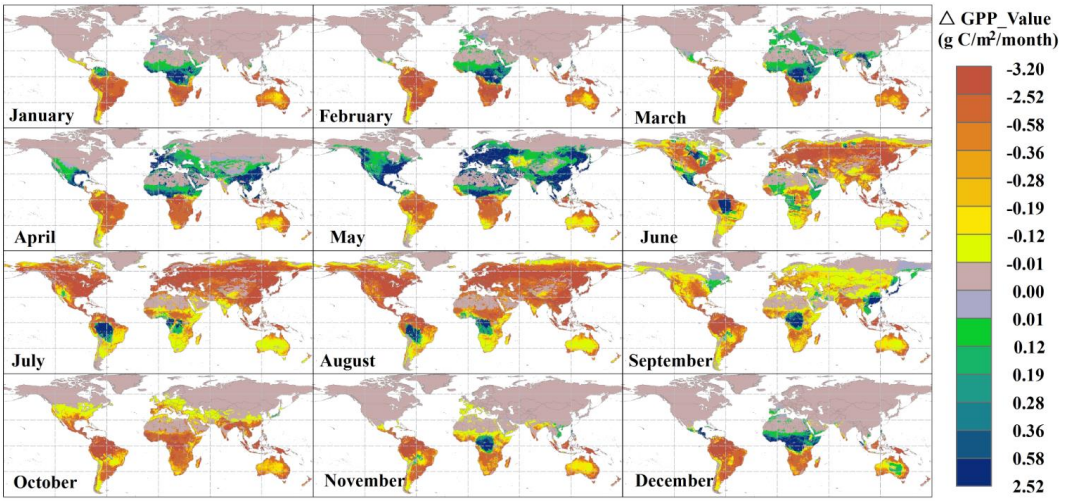

Figure 4.22 Comparison of monthly GPP estimates using different CO_2 data forms ($GPP_{2014}^{\text{monthly spatial } CO_2}$ minus $GPP_{2014}^{\text{annual mean global } CO_2}$).

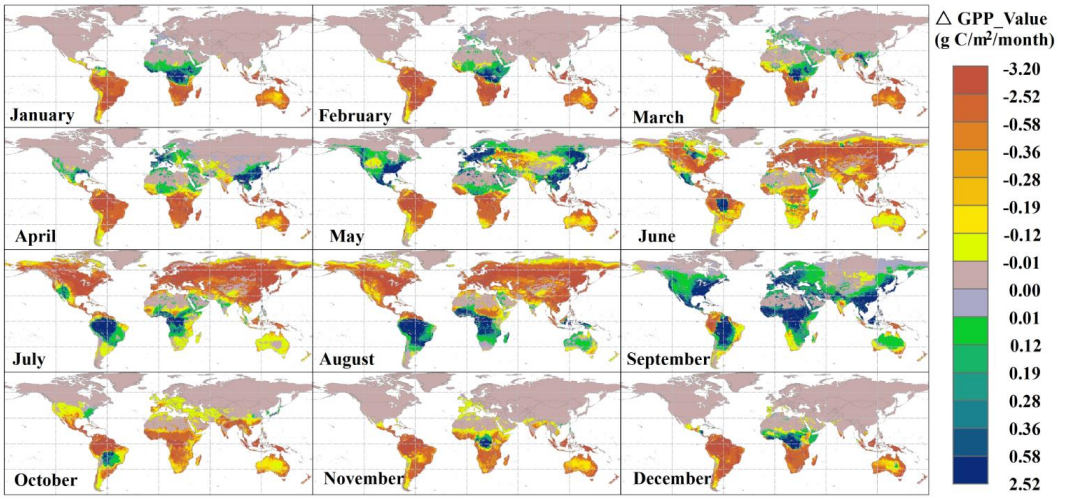

Figure 4.23 Comparison of monthly GPP estimates using different CO_2 data forms ($GPP_{2014}^{\text{monthly spatial } CO_2}$ minus $GPP_{2014}^{\text{monthly mean global } CO_2}$).

The monthly distributions of the GPP biases of $GPP_{2014}^{\text{annual mean global } CO_2}$ (Figure 4.22) are different from those of $GPP_{2014}^{\text{monthly mean global } CO_2}$ (Figure 4.23). Regarding $GPP_{2014}^{\text{annual mean global } CO_2}$ and using June as the turning point, it can be found that generally, before June the GPP in the North Hemisphere was underestimated, and after June, the GPP was overestimated because plants in the Northern Hemisphere during the summer grow quickly, the photosynthesis rate increases, the amount of the atmospheric CO_2 that is absorbed by plants increases, and the atmospheric CO_2 concentrations are lower than the annual mean. However, concentrated zones

of high CO_2 concentrations appeared in South America and Africa (maps of distributions of monthly global surface air CO_2 concentrations in 2014 are shown in Figure S14); therefore, in the corresponding area (e.g., Amazonis Planitia, Brazilian Highlands in South America, Congo Rainforest in Africa), the GPP estimates using the annual mean are lower. Overall, the CO_2 concentration distribution does not affect the GPP estimates in the Northern Hemisphere, except for during the growth period in which the GPP estimates were significantly overestimated (after June) or underestimated (before June). However, in most of the Southern Hemisphere, $GPP_{2014}^{\text{annual mean global } CO_2}$ are larger than $GPP_{2014}^{\text{monthly spatial } CO_2}$ for each month, which is mainly due to the globally averaged CO_2 concentrations being dominated by the vegetation in the Northern Hemisphere that grow seasonally, and the atmospheric CO_2 concentration in the Southern Hemisphere hardly affects the globally averaged value; moreover, in the Southern Hemisphere (except for in rainforest areas), the CO_2 concentration is low throughout the year; therefore, using the globally averaged annual CO_2 mean will overestimate the GPP.

Regarding $GPP_{2014}^{\text{monthly mean global } CO_2}$, in the Northern Hemisphere from June to August (i.e., summer), a large amount of atmospheric CO_2 is absorbed since vegetation grows rapidly; thus, atmospheric CO_2 concentration in the Northern Hemisphere is lower than the globally averaged CO_2 concentration, which is much lower than that in the Southern Hemisphere. Accordingly, during the summer, $GPP_{2014}^{\text{monthly mean global } CO_2}$ in the Northern Hemisphere were overestimated, and those in the Southern Hemisphere were underestimated. Nevertheless, in the spring (i.e., March, April, May), vegetation does not grow rapidly and does not absorb large amounts of CO_2 for photosynthesis; thus, due to the accumulation during the winter, the CO_2 concentration in the Northern Hemisphere reached the highest period, which is higher than the globally averaged CO_2 concentration. In contrast, the plants in the Southern Hemisphere grow normally and absorb atmospheric CO_2, and the CO_2 concentration in the Southern Hemisphere is lower than the globally averaged mean CO_2 concentration. Therefore, in the spring, by comparing $GPP_{2014}^{\text{monthly mean global } CO_2}$ with $GPP_{2014}^{\text{monthly spatial } CO_2}$, we can find that the Northern Hemisphere is obvious on the high side, and the Southern Hemisphere is on the low side.

Based on the above-mentioned results, the spatial distribution of CO_2 concentrations has a great influence on the estimation of the GPP, particularly for the monthly scale GPP estimates. Utilizing the globally averaged monthly mean CO_2 concentrations to estimate the GPP will cause seasonal estimation biases, which are opposite in the Northern and the Southern Hemispheres. Simultaneously, in the Southern Hemisphere, the GPP estimates in each month are overestimated, and the vegetation in the Northern Hemisphere during the growth periods before June will be overestimated, while that after June will be underestimated as a result of using globally averaged annual mean CO_2 concentration data to estimate GPP.

4.4 Conclusions

When estimating global GPP using RS-based methods, the effects of the temporal and spatial distribution of the atmospheric CO_2 concentration on GPP have rarely been incorporated. Here, I considered this effect when quantifying the global GPP. I used the iBEPSd model that incorporated RS variables and climatic factors to estimate the global GPP; furthermore, I compared the estimated GPP with the products of the models that did not consider the CO_2 fertilization module, and I compared the estimates obtained by inputting the CO_2 data without spatiotemporal characteristics to analyze the effects of the CO_2 concentration and its spatiotemporal influence on the estimation of GPP. The results showed that the estimated GPP values were able to capture the GPP variation and distribution when compared with the flux tower measurements and other GPP products. However, the relative relationship between the estimated GPP and the other GPP products exhibited a close relationship with the increasing CO_2 concentration, indicating that not considering the CO_2 fertilization effect would result in an underestimation of GPP. In addition, the estimations that do not consider the spatiotemporal distribution of the CO_2 concentration would cause an overall overestimated annual GPP, and these biases varied with location and period. This chapter suggested that the spatiotemporally varied CO_2 concentrations should be factored into GPP estimations when using an RS-based model for a long-term period and a large regional scale. And then, given the above-mentioned I attempted to use continuous spatial CO_2 concentration data obtained from GOSAT to estimate the GPP combined with the decoupling coefficients of PFTs to obtain the CO_2 concentration in canopy; then, according to climate data, I attempted to calculate the photosynthetic efficiency using the leaf- and canopy-level photosynthesis model and estimate the global monthly and annual GPP by scaling up to the whole ecosystem using the Big-leaf model. Finally, I applied this method, which was verified by the Fluxnet 2015 dataset and MODIS GPP products, to calculate the GPP estimates in 2000 and 2014 using input of globally averaged monthly CO_2 mean data to analyze the effects of the elevated atmospheric CO_2 concentration on the global GPP magnitude and distribution, and I also used globally averaged monthly and annual mean CO_2 data to estimate the global GPP and compared the two with that estimated by the continuous spatial CO_2 data to analyze the effects of atmospheric CO_2 concentration patterns on the estimation of the GPP. The following conclusions were made based on these steps:

a) Through using the Fluxnet 2015 dataset to assess the accuracy of the estimates, the GPP estimates are relatively consistent with tower GPP, indicating that the method proposed in this chapter, which introduces the continuous spatial CO_2 concentration data obtained by RS technology, is feasible.

b) From 2000 to 2014, the average atmospheric CO_2 concentration has increased by approximately 28 ppm, and this has increased the global GPP, with annual increment from over 50 gCm^{-2} in broad-leaf forests to 11.81 gCm^{-2} in coniferous forests, approximately 10.41 gCm^{-2} in SAV, 5.34 gCm^{-2} in SHR, and approximately 3.18 gCm^{-2} in GRA. Considering the spatial allocation, the increases in the lower latitudes are more significant than those in the middle and high latitudes; the increments in the GPP estimates in the middle and high latitudes in the Northern Hemisphere during the summer are greater than those during the other seasons, but in the Southern Hemisphere, the increments are almost the same throughout the year.

c) By comparing annual $GPP_{2014}^{\text{monthly spatial } CO_2}$ with $GPP_{2014}^{\text{annual mean global } CO_2}$ and $GPP_{2014}^{\text{monthly mean global } CO_2}$, the annual GPP, which was calculated according to globally averaged CO_2 concentrations, was overestimated, except for in zones located in the lower latitudes, such as

north of sub-Saharan Africa and northwest of Southeast Asia. The max biases occurred in Northeast China and the Amazon rainforest, which present annual overestimates of over 12 gC m^{-2}.

d) Regarding the monthly effects of CO_2 concentrations on the GPP estimates, without considering the temporal variability and global distribution of atmospheric CO_2 concentrations (i.e., $GPP_{2014}^{\text{annual mean global } CO_2}$), there are significant differences between the GPP estimates in the Northern Hemisphere during the first half and the second half of the year. The GPP estimates were underestimated before June and overestimated after June; moreover, the GPP in the Southern Hemisphere was overestimated all throughout the year. However, when considering temporal variability, but not considering the global distribution of atmospheric CO_2 concentrations (i.e., $GPP_{2014}^{\text{monthly mean global } CO_2}$) in the Northern Hemisphere or the vegetation growing periods, the GPP in the Northern Hemisphere was overestimated and that in the Southern Hemisphere was underestimated compared with $GPP_{2014}^{\text{monthly spatial } CO_2}$, while the results were opposite during the non-growing periods.

References

Agarwal, D.A.; Humphrey, M.; Beekwilder, N.F.; Jackson, K.R.; Goode, M.M.; van Ingen, C. A data-centered collaboration portal to support global carbon-flux analysis. *Concurr Comp-Pract E* **2010**, *22*, 2323-2334.

Ahongshangbam, J.; Patel, N.R.; Kushwaha, S.P.S.; Watham, T.; Dadhwal, V.K. Estimating Gross Primary Production of a Forest Plantation Area Using Eddy Covariance Data and Satellite Imagery. *Journal of the Indian Society of Remote Sensing* **2016**, *44*, 895-904.

Ainsworth, E.A.; Long, S.P. What have we learned from 15 years of free-air CO_2 enrichment (FACE)? A meta-analytic review of the responses of photosynthesis, canopy properties and plant production to rising CO_2. *New Phytologist* **2005**, *165*, 351-372.

Anav, A.; Friedlingstein, P.; Beer, C.; Ciais, P.; Harper, A.; Jones, C.; Murray-Tortarolo, G.; Papale, D.; Parazoo, N.C.; Peylin, P., et al. Spatiotemporal patterns of terrestrial gross primary production: A review. *Reviews of Geophysics* **2015**, *53*, 785-818.

Asner, G.P. Cloud cover in Landsat observations of the Brazilian Amazon. *International Journal of Remote Sensing* **2001**, *22*, 3855-3862.

Ballantyne, A.P.; Alden, C.B.; Miller, J.B.; Tans, P.P.; White, J.W. Increase in observed net carbon dioxide uptake by land and oceans during the past 50 years. *Nature* **2012**, *488*, 70-72.

Beck, P.S.; Goetz, S.J. Satellite observations of high northern latitude vegetation productivity changes between 1982 and 2008: ecological variability and regional differences. *Environmental Research Letters* **2011**, *6*, 045501.

Beer, C.; Reichstein, M.; Tomelleri, E.; Ciais, P.; Jung, M.; Carvalhais, N.; Rodenbeck, C.; Arain, M.A.; Baldocchi, D.; Bonan, G.B., et al. Terrestrial gross carbon dioxide uptake: global distribution and covariation with climate. *Science* **2010**, *329*, 834-838.

Bousquet, P.; Peylin, P.; Ciais, P.; Ramonet, M.; Monfray, P. Inverse modeling of annual atmospheric CO2 sources and sinks: 2. Sensitivity study. *Journal of Geophysical Research: Atmospheres* **1999**, *104*, 26179-26193.

Butz, A.; Guerlet, S.; Hasekamp, O.; Schepers, D.; Galli, A.; Aben, I.; Frankenberg, C.; Hartmann, J.M.; Tran, H.; Kuze, A., et al. Toward accurate CO_2 and CH_4 observations from GOSAT. *Geophysical Research Letters* **2011**, *38*.

Caemmerer, S.; Evans, J. Determination of the average partial pressure of CO_2 in chloroplasts from leaves of several C3 plants. *Functional Plant Biology* **1991**, *18*, 287-305.

Canadell, J.G.; Kirschbaum, M.U.; Kurz, W.A.; Sanz, M.-J.; Schlamadinger, B.; Yamagata, Y. Factoring out natural and indirect human effects on terrestrial carbon sources and sinks. *environmental science & policy* **2007**, *10*, 370-384.

Canadell, J.G.; Mooney, H.A.; Baldocchi, D.D.; Berry, J.A.; Ehleringer, J.R.; Field, C.B.; Gower, S.T.; Hollinger, D.Y.; Hunt, J.E.; Jackson, R.B., et al. Commentary: Carbon Metabolism of the Terrestrial Biosphere: A Multitechnique Approach for Improved Understanding. *Ecosystems* **2000**, *3*, 115-130.

Chang, J.; Ciais, P.; Viovy, N.; Vuichard, N.; Herrero, M.; Havlík, P.; Wang, X.; Sultan, B.; Soussana, J.F. Effect of climate change, CO_2 trends, nitrogen addition, and land-cover and management intensity changes on the carbon balance of European grasslands. *Global change biology* **2016**, *22*, 338-350.

Chapin III, F.S.; Matson, P.A.; Vitousek, P. Principles of terrestrial ecosystem ecology; Springer Science & Business Media: **2011**.

Chen, J.; Liu, J.; Cihlar, J.; Goulden, M. Daily canopy photosynthesis model through temporal and spatial scaling for remote sensing applications. *Ecological modelling* **1999**, *124*, 99-119.

Chen, J.M.; Mo, G.; Pisek, J.; Liu, J.; Deng, F.; Ishizawa, M.; Chan, D. Effects of foliage clumping on the estimation of global terrestrial gross primary productivity. *Global Biogeochemical Cycles* **2012**, *26*.

Chen, M.; Rafique, R.; Asrar, G.R.; Bond-Lamberty, B.; Ciais, P.; Zhao, F.; Reyer, C.P.; Ostberg, S.; Chang, J.; Ito, A. Regional contribution to variability and trends of global gross primary productivity. *Environmental Research Letters* **2017**, *12*, 105005.

Chen, Y.; Li, J.; Ju, W.; Ruan, H.; Qin, Z.; Huang, Y.; Jeelani, N.; Padarian, J.; Propastin, P. Quantitative assessments of water-use efficiency in Temperate Eurasian Steppe along an aridity gradient. *PloS one* **2017**, *12*, e0179875.

Ciais, P.; Janssens, I.; Shvidenko, A.; Wirth, C.; Malhi, Y.; Grace, J.; Schulze, E.-D.; Herman, M.; Phillips, O.; Dolman, H. The potential for rising CO_2 to account for the observed uptake of carbon by tropical, temperate, and boreal forest biomes. *The Carbon Balance of Forest Biomes* **2004**, 109-149.

Collatz, G.J.; Ball, J.T.; Grivet, C.; Berry, J.A. Physiological and Environmental-Regulation of Stomatal Conductance, Photosynthesis and Transpiration - a Model That Includes a Laminar Boundary-Layer. *Agricultural and Forest Meteorology* **1991**, *54*, 107-136.

Collatz, G.J.; Ribas-Carbo, M.; Berry, J. Coupled photosynthesis-stomatal conductance model for leaves of C4 plants. *Functional Plant Biology* **1992**, *19*, 519-538.

Cramer, W.; Kicklighter, D.W.; Bondeau, A.; Moore, B.; Churkina, G.; Nemry, B.; Ruimy, A.; Schloss, A.L.; Intercompariso, P.P.N.M. Comparing global models of terrestrial net primary productivity (NPP): overview and key results. *Global Change Biology* **1999**, *5*, 1-15.

Croft, H.; Chen, J.M.; Luo, X.; Bartlett, P.; Chen, B.; Staebler, R.M. Leaf chlorophyll content as a proxy for leaf photosynthetic capacity. *Global change biology* **2017**, *23*, 3513-3524.

Davis, K.J.; Bakwin, P.S.; Yi, C.; Berger, B.W.; Zhao, C.; Teclaw, R.M.; Isebrands, J. The annual cycles of CO_2 and H_2O exchange over a northern mixed forest as observed from a very tall tower. *Global Change Biology* **2003**, *9*, 1278-1293.

De Kauwe, M.G.; Keenan, T.F.; Medlyn, B.E.; Prentice, I.C.; Terrer, C. Satellite based estimates underestimate the effect of CO_2 fertilization on net primary productivity. *Nature Climate Change* **2016**, *6*, 892.

Deng, F.; Chen, J.M.; Plummer, S.; Chen, M.; Pisek, J. Algorithm for global leaf area index retrieval using satellite imagery. *IEEE Transactions on Geoscience and Remote Sensing* **2006**, *44*, 2219-2229.

Dentener, F.J. Global Maps of Atmospheric Nitrogen Deposition, 1860, 1993, and 2050. DAAC, O., Ed. Oak Ridge, Tennessee, USA, **2006**.

Dian, Y.Y.; Le, Y.; Fang, S.H.; Xu, Y.R.; Yao, C.H.; Liu, G. Influence of Spectral Bandwidth and Position on Chlorophyll Content Retrieval at Leaf and Canopy Levels. *Journal Of the Indian Society Of Remote Sensing* **2016**, *44*, 583-593.

Dijkstra, F.A.; Blumenthal, D.; Morgan, J.A.; Pendall, E.; Carrillo, Y.; Follett, R.F. Contrasting effects of elevated CO_2 and warming on nitrogen cycling in a semiarid grassland. *New Phytologist* **2010**, *187*, 426-437.

Donohue, R.J.; Roderick, M.L.; McVicar, T.R.; Farquhar, G.D. Impact of CO_2 fertilization on maximum foliage cover across the globe's warm, arid environments. *Geophysical Research Letters* **2013**, *40*, 3031-3035.

Duveiller, G.; Cescatti, A. Spatially downscaling sun-induced chlorophyll fluorescence leads to an improved temporal correlation with gross primary productivity. *Remote Sensing of Environment* **2016**, *182*, 72-89.

Eby, M.; Zickfeld, K.; Montenegro, A.; Archer, D.; Meissner, K.J.; Weaver, A.J. Lifetime of Anthropogenic Climate Change: Millennial Time Scales of Potential CO_2 and Surface Temperature Perturbations. *Journal of Climate* **2009**, *22*, 2501-2511.

Ed Dlugokencky, P.T. Trends in Atmospheric Carbon Dioxide. Availabe online: (accessed on 2017).

Erbs, D.G.; Klein, S.A.; Duffie, J.A. Estimation Of the Diffuse-Radiation Fraction for Hourly, Daily And Monthly-Average Global Radiation. *Sol Energy* **1982**, *28*, 293-302.

Farquhar, G.; Von Caemmerer, S. Modelling of photosynthetic response to environmental conditions. In *Physiological plant ecology II*, Springer: 1982; pp. 549-587.

Farquhar, G.D. Carbon dioxide and vegetation. *Science* **1997**, *278*, 1411-1411.

Farquhar, G.v.; von Caemmerer, S.v.; Berry, J. A biochemical model of photosynthetic CO_2 assimilation in leaves of C3 species. *Planta* **1980**, *149*, 78-90.

Frankenberg, C.; Fisher, J.B.; Worden, J.; Badgley, G.; Saatchi, S.S.; Lee, J.-E.; Toon, G.C.; Butz, A.; Jung, M.; Kuze, A., et al. New global observations of the terrestrial carbon cycle from GOSAT: Patterns of plant fluorescence with gross primary productivity. *Geophysical Research Letters* **2011**, *38*, n/a-n/a.

Friedl, M.A.; Sulla-Menashe, D.; Tan, B.; Schneider, A.; Ramankutty, N.; Sibley, A.; Huang, X. MODIS Collection 5 global land cover: Algorithm refinements and characterization of new datasets. *Remote sensing of Environment* **2010**, *114*, 168-182.

Frouin, R.; Pinker, R.T. Estimating photosynthetically active radiation (PAR) at the earth's surface from satellite observations. *Remote Sensing of Environment* **1995**, *51*, 98-107.

Gilmanov, T.G.; Verma, S.B.; Sims, P.L.; Meyers, T.P.; Bradford, J.A.; Burba, G.G.; Suyker, A.E. Gross primary production and light response parameters of four Southern Plains ecosystems estimated using long-term CO2-flux tower measurements. *Global Biogeochemical Cycles* **2003**, *17*, n/a-n/a.

Gitelson, A.A.; Vina, A.; Verma, S.B.; Rundquist, D.C.; Arkebauer, T.J.; Keydan, G.; Leavitt, B.; Ciganda, V.; Burba, G.G.; Suyker, A.E. Relationship between gross primary production and chlorophyll content in crops: Implications for the synoptic monitoring of vegetation productivity. *J Geophys Res-Atmos* **2006**, *111*.

Gower, S.; Krankina, O.; Olson, R.; Apps, M.; Linder, S.; Wang, C. Net primary production and carbon allocation patterns of boreal forest ecosystems. *Ecological applications* **2001**, *11*, 1395-1411.

Guanter, L.; Zhang, Y.; Jung, M.; Joiner, J.; Voigt, M.; Berry, J.A.; Frankenberg, C.; Huete, A.R.; Zarco-Tejada, P.; Lee, J.-E. Global and time-resolved monitoring of crop photosynthesis with chlorophyll fluorescence. *Proceedings of the National Academy of Sciences* **2014**, *111*, E1327-E1333.

Guo, M.; Wang, X.; Li, J.; Yi, K.; Zhong, G.; Tani, H. Assessment of global carbon dioxide concentration using MODIS and GOSAT data. *Sensors* **2012**, *12*, 16368-16389.

Hartmann, D.L.; Tank, A.M.K.; Rusticucci, M.; Alexander, L.V.; Brönnimann, S.; Charabi, Y.A.R.; Dentener, F.J.; Dlugokencky, E.J.; Easterling, D.R.; Kaplan, A. Observations: atmosphere and surface. In *Climate Change 2013 the Physical Science Basis: Working Group I Contribution to the Fifth Assessment Report of the Intergovernmental Panel on Climate Change*, Cambridge University Press: **2013**.

He, L.; Chen, J.M.; Liu, J.; Mo, G.; Bélair, S.; Zheng, T.; Wang, R.; Chen, B.; Croft, H.; Arain, M.A. Optimization of water uptake and photosynthetic parameters in an ecosystem model using tower flux data. *Ecological modelling* **2014**, *294*, 94-104.

Hilker, T.; Coops, N.C.; Wulder, M.A.; Black, T.A.; Guy, R.D. The use of remote sensing in light use efficiency based models of gross primary production: A review of current status and future requirements. *Science Of the Total Environment* **2008**, *404*, 411-423.

Houborg, R.; Cescatti, A.; Migliavacca, M.; Kustas, W. Satellite retrievals of leaf chlorophyll and photosynthetic capacity for improved modeling of GPP. *Agricultural and Forest Meteorology* **2013**, *177*, 10-23.

Houborg, R.; McCabe, M.F.; Cescatti, A.; Gitelson, A.A. Leaf chlorophyll constraint on model simulated gross primary productivity in agricultural systems. *International Journal of Applied Earth Observation and Geoinformation* **2015**, *43*, 160-176.

Howard Griffith, P.J. The Carbon Balance of Forest Biomes. *Taylor & Francis* **2005**, *57*, 232-233.

Huang, M.; Piao, S.; Sun, Y.; Ciais, P.; Cheng, L.; Mao, J.; Poulter, B.; Shi, X.; Zeng, Z.; Wang, Y. Change in terrestrial ecosystem water-use efficiency over the last three decades. *Global change biology* **2015**, *21*, 2366-2378.

Jarvis, P.G.; Mcnaughton, K.G. Stomatal Control of Transpiration - Scaling up from Leaf to Region. *Advances in Ecological Research* **1986**, *15*, 1-49.

Jin, M.L.; Dickinson, R.E. Land surface skin temperature climatology: benefitting from the strengths of satellite observations. *Environmental Research Letters* **2010**, *5*, 044004.

Joiner, J.; Yoshida, Y.; Vasilkov, A.P.; Yoshida, Y.; Corp, L.A.; Middleton, E.M. First observations of global and seasonal terrestrial chlorophyll fluorescence from space. *Biogeosciences* **2011**, *8*, 637-651.

Jones, H. G. Plants and Microclimate: A Quantitative Approach to Environmental Plant Physiology. Cambridge Univ. Press: **1992**.

Ju, W.; Chen, J.M.; Black, T.A.; Barr, A.G.; Liu, J.; Chen, B. Modelling multi-year coupled carbon and water fluxes in a boreal aspen forest. *Agricultural and Forest Meteorology* **2006**, *140*, 136-151.

Jung, M.; Reichstein, M.; Ciais, P.; Seneviratne, S.I.; Sheffield, J.; Goulden, M.L.; Bonan, G.; Cescatti, A.; Chen, J.; De Jeu, R. Recent decline in the global land evapotranspiration trend due to limited moisture supply. *Nature* **2010**, *467*, 951.

Jung, M.; Reichstein, M.; Margolis, H.A.; Cescatti, A.; Richardson, A.D.; Arain, M.A.; Arneth, A.; Bernhofer, C.; Bonal, D.; Chen, J. Global patterns of land-atmosphere fluxes of carbon dioxide, latent heat, and sensible heat derived from eddy covariance, satellite, and meteorological observations. *Journal of Geophysical Research: Biogeosciences* **2011**, *116*.

Kanamitsu, M.; Ebisuzaki, W.; Woollen, J.; Yang, S.-K.; Hnilo, J.; Fiorino, M.; Potter, G. Ncep–doe amip-ii reanalysis (r-2). *Bulletin of the American Meteorological Society* **2002**, *83*, 1631-1644.

Karl, T.R.; Hassol, S.J.; Miller, C.D.; Murray, W.L. Temperature trends in the lower atmosphere: Steps for understanding and reconciling differences. **2006**.

Kirschbaum, M.; King, D.; Comins, H.; McMurtrie, R.; Medlyn, B.; Pongracic, S.; Murty, D.; Keith, H.; Raison, R.; Khanna, P. Modelling forest response to increasing CO_2 concentration under nutrient-limited conditions. *Plant, cell & environment* **1994**, *17*, 1081-1099.

Kirschbaum, M.U.F.; Farquhar, G.D. Temperature-Dependence of Whole-Leaf Photosynthesis in Eucalyptus-Pauciflora Sieb Ex Spreng. *Aust J Plant Physiol* **1984**, *11*, 519-538.

Lasslop, G.; Reichstein, M.; Papale, D.; Richardson, A.D.; Arneth, A.; Barr, A.; Stoy, P.; Wohlfahrt, G. Separation of net ecosystem exchange into assimilation and respiration using a light response curve approach: critical issues and global evaluation. *Global Change Biology* **2010**, *16*, 187-208.

Le Quéré, C.; Andrew, R.; Friedlingstein, P.; Sitch, S.; Pongratz, J.; Manning, A.; Korsbakken, J.; Peters, G. Global carbon budget 2016 Earth System Science Data. **2016**.

Li, X.; Liang, S.; Yu, G.; Yuan, W.; Cheng, X.; Xia, J.; Zhao, T.; Feng, J.; Ma, Z.; Ma, M. Estimation of gross primary production over the terrestrial ecosystems in China. *Ecological Modelling* **2013**, *261*, 80-92.

Li, X.; Zhu, Z.; Zeng, H.; Piao, S. Estimation of gross primary production in China (1982–2010) with multiple ecosystem models. *Ecological modelling* **2016**, *324*, 33-44.

Liang, S.; Goldberg, M.D.; Xiong, X.; Butler, J.J.; Crawford, M.M.; Chen, J.M.; Shi, J.; Loboda, T.V.; Zheng, Q.; Walsh, S.J. *Comprehensive Remote Sensing: Atmosphere*; Elsevier: **2018**.

Liang, W.; Yang, Y.; Fan, D.; Guan, H.; Zhang, T.; Long, D.; Zhou, Y.; Bai, D. Analysis of spatial and temporal patterns of net primary production and their climate controls in China from 1982 to 2010. *Agricultural and Forest Meteorology* **2015**, *204*, 22-36.

Liu, J.; Chen, J.; Cihlar, J.; Park, W. A process-based boreal ecosystem productivity simulator using remote sensing inputs. *Remote sensing of environment* **1997**, *62*, 158-175.

Liu, J.; Chen, J.M.; Cihlar, J.; Chen, W. Net primary productivity distribution in the BOREAS region from a process model using satellite and surface data. *J Geophys Res-Atmos* **1999**, *104*, 27735-27754.

Liu, S.; Zhuang, Q.; He, Y.; Noormets, A.; Chen, J.; Gu, L. Evaluating atmospheric CO_2 effects on gross primary productivity and net ecosystem exchanges of terrestrial ecosystems in the conterminous United States using the AmeriFlux data and an artificial neural network approach. *Agricultural and forest meteorology* **2016**, *220*, 38-49.

Liu, Y.; Liu, R.; Chen, J.M. Retrospective retrieval of long-term consistent global leaf area index (1981–2011) from combined AVHRR and MODIS data. *Journal of Geophysical Research: Biogeosciences* **2012**, *117*.

Lloyd, S. Almost Any Quantum Logic Gate Is Universal. *Physical Review Letters* **1995**, *75*, 346-349.

Long, S.P. Modification of the response of photosynthetic productivity to rising temperature by atmospheric CO_2 concentrations: Has its importance been underestimated? *Plant, Cell and Environment* **1991**, *14*, 729-739.

Luo, Y.; Hui, D.; Zhang, D. Elevated CO_2 stimulates net accumulations of carbon and nitrogen in land ecosystems: a meta-analysis. *Ecology* **2006**, *87*, 53-63.

Luo, Y.; Su, B.; Currie, W.S.; Dukes, J.S.; Finzi, A.C.; Hartwig, U.; Hungate, B.; McMurtrie, R.E.; Oren, R.; Parton, W.J., et al. Progressive nitrogen limitation of ecosystem responses to rising atmospheric carbon dioxide. *Bioscience* **2004**, *54*, 731-739.

Ma, J.Y.; Yan, X.D.; Dong, W.J.; Chou, J.M. Gross primary production of global forest ecosystems has been overestimated. *Scientific reports* **2015**, *5*.

Masarie, K.A.; Tans, P.P. Extension and Integration of Atmospheric Carbon-Dioxide Data into a Globally Consistent Measurement Record. *J Geophys Res-Atmos* **1995**, *100*, 11593-11610.

Matsushita B, Y.C., Chen J, Wang Q, Kameyama S, Tamura M. Accurate Estimation of Net Primary Productivity of Terrestrial Ecosystem at a Regional Scale. *Acta Geographica Sinica* **2004**, *59*, 80-87.

McMurtrie, R.E.; Norby, R.J.; Medlyn, B.E.; Dewar, R.C.; Pepper, D.A.; Reich, P.B.; Barton, C.V. Why is plant-growth response to elevated CO_2 amplified when water is limiting, but reduced when nitrogen is limiting? A growth-optimisation hypothesis. *Functional Plant Biology* **2008**, *35*, 521-534.

Mildrexler, D.J.; Zhao, M.S.; Running, S.W. A global comparison between station air temperatures and MODIS land surface temperatures reveals the cooling role of forests. *J Geophys Res-Biogeo* **2011**, *116*.

Miles, N.L.; Richardson, S.J.; Davis, K.J.; Lauvaux, T.; Andrews, A.E.; West, T.O.; Bandaru, V.; Crosson, E.R. Large amplitude spatial and temporal gradients in atmospheric boundary layer CO_2mole fractions detected with a tower-based network in the US upper Midwest. *Journal of Geophysical Research: Biogeosciences* **2012**, *117*.

Monroe, R. Seasonal CO_2 Amplitude is Growing as More is Added to the Atmosphere. *https://scripps.ucsd.edu/news/13139* **2013**.

Monteith, J.L.; Moss, C. Climate and the efficiency of crop production in Britain [and discussion]. *Philosophical Transactions of the Royal Society of London B: Biological Sciences* **1977**, *281*, 277-294.

Morison, J.I.; Gifford, R.M. Stomatal sensitivity to carbon dioxide and humidity a comparison of two C3 and two C4 grass species. *Plant physiology* **1983**, *71*, 789-796.

Nemani, R.R.; Keeling, C.D.; Hashimoto, H.; Jolly, W.M.; Piper, S.C.; Tucker, C.J.; Myneni, R.B.; Running, S.W. Climate-driven increases in global terrestrial net primary production from 1982 to 1999. *Science* **2003**, *300*, 1560-1563.

Norby, R.J.; DeLucia, E.H.; Gielen, B.; Calfapietra, C.; Giardina, C.P.; King, J.S.; Ledford, J.; McCarthy, H.R.; Moore, D.J.; Ceulemans, R. Forest response to elevated CO_2 is conserved across a broad range of productivity. *Proceedings of the National Academy of Sciences of the United States of America* **2005**, *102*, 18052-18056.

Norby, R.J.; Sholtis, J.D.; Gunderson, C.A.; Jawdy, S.S. Leaf dynamics of a deciduous forest canopy: no response to elevated CO_2. *Oecologia* **2003**, *136*, 574-584.

Norman, J.M. Simulation of microclimates. Biometeorology in integrated pest management **1982**, 65-99.

Nowak, R.S.; Ellsworth, D.S.; Smith, S.D. Functional responses of plants to elevated atmospheric CO_2–do photosynthetic and productivity data from FACE experiments support early predictions? *New phytologist* **2004**, *162*, 253-280.

Oguma, H.; Morino, I.; Suto, H.; Yoshida, Y.; Eguchi, N.; Kuze, A.; Yokota, T. First observations of CO_2 absorption spectra recorded in 2005 using an airship-borne FTS (GOSAT TANSO-FTS BBM) in the SWIR spectral region. *International Journal Of Remote Sensing* **2011**, *32*, 9033-9049.

Peters, W.; Jacobson, A.R.; Sweeney, C.; Andrews, A.E.; Conway, T.J.; Masarie, K.; Miller, J.B.; Bruhwiler, L.M.; Petron, G.; Hirsch, A.I., et al. An atmospheric perspective on North American carbon dioxide exchange: CarbonTracker. *Proc Natl Acad Sci U S A* **2007**, *104*, 18925-18930.

Piao, S.; Fang, J.; Zhou, L.; Ciais, P.; Zhu, B. Variations in satellite-derived phenology in China's temperate vegetation. *Global change biology* **2006**, *12*, 672-685.

Poulter, B.; Frank, D.; Ciais, P.; Myneni, R.B.; Andela, N.; Bi, J.; Broquet, G.; Canadell, J.G.; Chevallier, F.; Liu, Y.Y., et al. Contribution of semi-arid ecosystems to interannual variability of the global carbon cycle. *Nature* **2014**, *509*, 600-603.

Pury, D.d.; Farquhar, G. Simple scaling of photosynthesis from leaves to canopies without the errors of big-leaf models. *Plant, cell & environment* **1997**, *20*, 537-557.

Raupach, M.; Canadell, J.; Quéré, C.L. Anthropogenic and biophysical contributions to increasing atmospheric CO_2 growth rate and airborne fraction. *Biogeosciences* **2008**, *5*, 1601-1613.

Reich, P.B.; Hobbie, S.E.; Lee, T.D. Plant growth enhancement by elevated CO_2 eliminated by joint water and nitrogen limitation. *Nature Geoscience* **2014**, *7*, 920.

Reichstein, M.; Tenhunen, J.; Roupsard, O.; Ourcival, J.M.; Rambal, S.; Miglietta, F.; Peressotti, A.; Pecchiari, M.; Tirone, G.; Valentini, R. Inverse modeling of seasonal drought effects on canopy CO_2/H_2O exchange in three Mediterranean ecosystems. *Journal of Geophysical Research: Atmospheres* **2003**, *108*.

Reuter, M.; Buchwitz, M.; Schneising, O.; Heymann, J.; Bovensmann, H.; Burrows, J. A method for improved SCIAMACHY CO_2 retrieval in the presence of optically thin clouds. *Atmospheric Measurement Techniques* **2010**, *3*, 209-232.

Ross, J.; Sulev, M. Sources of errors in measurements of PAR. *Agricultural and Forest Meteorology* **2000**, *100*, 103-125.

Running, S.W.; Nemani, R.R.; Heinsch, F.A.; Zhao, M.S.; Reeves, M.; Hashimoto, H. A continuous satellite-derived measure of global terrestrial primary production. *Bioscience* **2004**, *54*, 547-560.

Schaefer, K.; Schwalm, C.R.; Williams, C.; Arain, M.A.; Barr, A.; Chen, J.M.; Davis, K.J.; Dimitrov, D.; Hilton, T.W.; Hollinger, D.Y., et al. A model-data comparison of gross primary productivity: Results from the North American Carbon Program site synthesis. *J Geophys Res-Biogeo* **2012**, *117*.

Sellers, P.; Randall, D.; Collatz, G.; Berry, J.; Field, C.; Dazlich, D.; Zhang, C.; Collelo, G.; Bounoua, L. A revised land surface parameterization (SiB2) for atmospheric GCMs. Part I: Model formulation. *Journal of climate* **1996**, *9*, 676-705.

Sellers, P.J.; Tucker, C.J.; Collatz, G.J.; Los, S.O.; Justice, C.O.; Dazlich, D.A.; Randall, D.A. A revised land surface parameterization (SiB2) for atmospheric GCMs. Part II: The generation of global fields of terrestrial biophysical parameters from satellite data. *Journal of climate* **1996**, *9*, 706-737.

Sjostrom, M.; Zhao, M.; Archibald, S.; Arneth, A.; Cappelaere, B.; Falk, U.; de Grandcourt, A.; Hanan, N.; Kergoat, L.; Kutsch, W., et al. Evaluation of MODIS gross primary productivity for Africa using eddy covariance data. *Remote Sensing Of Environment* **2013**, *131*, 275-286.

Sowerby, A.; Emmett, B.A.; Tietema, A.; Beier, C. Contrasting effects of repeated summer drought on soil carbon efflux in hydric and mesic heathland soils. *Global Change Biology* **2008**, *14*, 2388-2404.

Still, C.; Berry, J.; Collatz, G.; DeFries, R.; Hall, F.; Meeson, B.; LOS, S.; Brown DE Colstoun, E.; Landis, D. ISLSCP II C4 vegetation percentage. *ORNL DAAC* **2009**.

Sun, Z.; Wang, X.; Tani, H.; Zhong, G.; Yin, S. Spatial Distribution of CO_2 Concentration over South America during ENSO Episodes by Using GOSAT Data. *American Journal of Climate Change* **2016**, *5*, 77.

Sun, Z.; Wang, X.; Yamamoto, H.; Tani, H.; Zhong, G.; Yin, S. An attempt to introduce atmospheric CO_2 concentration data to estimate the gross primary production by the terrestrial biosphere and analyze its effects. *Ecological Indicators* **2018**, *84*, 218-234.

Task, G.S.D. Global soil data products CD-ROM contents (IGBP-DIS). *ORNL DAAC* **2014**.

Temme, A.A.; Liu, J.C.; Cornwell, W.K.; Cornelissen, J.H.; Aerts, R. Winners always win: growth of a wide range of plant species from low to future high CO_2. *Ecology and evolution* **2015**, *5*, 4949-4961.

Tucker, C.J.; Pinzon, J.E.; Brown, M.E.; Slayback, D.A.; Pak, E.W.; Mahoney, R.; Vermote, E.F.; El Saleous, N. An extended AVHRR 8-km NDVI dataset compatible with MODIS and SPOT vegetation NDVI data. *International Journal of Remote Sensing* **2005**, *26*, 4485-4498.

Turner, D.P.; Ritts, W.D.; Cohen, W.B.; Gower, S.T.; Running, S.W.; Zhao, M.; Costa, M.H.; Kirschbaum, A.A.; Ham, J.M.; Saleska, S.R. Evaluation of MODIS NPP and GPP products across multiple biomes. *Remote Sensing of Environment* **2006**, *102*, 282-292.

van den Dool, H.; Huang, J.; Fan, Y. Performance and analysis of the constructed analogue method applied to US soil moisture over 1981-2001. *J Geophys Res-Atmos* **2003**, *108*.

Van Oijen, M.; Dreccer, M.; Firsching, K.-H.; Schnieders, B. Simple equations for dynamic models of the effects of CO_2 and O_3 on light-use efficiency and growth of crops. *Ecological Modelling* **2004**, *179*, 39-60.

Wan, Z.; Li, Z.-L. MODIS land surface temperature and emissivity. In *Land Remote Sensing and Global Environmental Change*, Springer: 2010; pp. 563-577.

Wang, H.; Prentice, I.C.; Davis, T.W. Biophsyical constraints on gross primary production by the terrestrial biosphere. *Biogeosciences* **2014**, *11*, 5987-6001.

Wei, Y.; Liu, S.; Huntzinger, D.N.; Michalak, A.M.; Viovy, N.; Post, W.M.; Schwalm, C.R.; Schaefer, K.; Jacobson, A.R.; Lu, C., et al. The North American Carbon Program Multi-scale Synthesis and Terrestrial Model Intercomparison Project – Part 2: Environmental driver data. *Geoscientific Model Development* **2014**, *7*, 2875-2893.

Welp, L.R.; Keeling, R.F.; Meijer, H.A.; Bollenbacher, A.F.; Piper, S.C.; Yoshimura, K.; Francey, R.J.; Allison, C.E.; Wahlen, M. Interannual variability in the oxygen isotopes of atmospheric CO_2 driven by El Nino. *Nature* **2011**, *477*, 579-582.

Wong, S.; Cowan, I.; Farquhar, G. Stomatal conductance correlates with photosynthetic capacity. *Nature* **1979**, *282*, 424-426.

Wu, C.; Wang, L.; Niu, Z.; Gao, S.; Wu, M. Nondestructive estimation of canopy chlorophyll content using Hyperion and Landsat/TM images. *International Journal of Remote Sensing* **2010**, *31*, 2159-2167.

Wu, D.; Zhao, X.; Liang, S.; Zhou, T.; Huang, K.; Tang, B.; Zhao, W. Time-lag effects of global vegetation responses to climate change. *Global change biology* **2015**, *21*, 3520-3531.

Yang, S.H.; Xu, J.Z.; Liu, X.Y.; Zhang, J.G.; Wang, Y.J. Variations of carbon dioxide exchange in paddy field ecosystem under water-saving irrigation in Southeast China. *Agricultural Water Management* **2016**, *166*, 42-52.

Yuan, W.; Cai, W.; Liu, S.; Dong, W.; Chen, J.; Arain, M.A.; Blanken, P.D.; Cescatti, A.; Wohlfahrt, G.; Georgiadis, T., et al. Vegetation-specific model parameters are not required for estimating gross primary production. *Ecological Modelling* **2014**, *292*, 1-10.

Yuan, W.; Cai, W.; Xia, J.; Chen, J.; Liu, S.; Dong, W.; Merbold, L.; Law, B.; Arain, A.; Beringer, J., et al. Global comparison of light use efficiency models for simulating terrestrial vegetation gross primary production based on the LaThuile database. *Agricultural and Forest Meteorology* **2014**, *192-193*, 108-120.

Yuan, W.P.; Liu, S.; Zhou, G.S.; Zhou, G.Y.; Tieszen, L.L.; Baldocchi, D.; Bernhofer, C.; Gholz, H.; Goldstein, A.H.; Goulden, M.L., et al. Deriving a light use efficiency model from eddy covariance flux data for predicting daily gross primary production across biomes. *Agricultural And Forest Meteorology* **2007**, *143*, 189-207.

Yueqin, Z.Y.X. The Climatic Estimation of photon flux density of direct solar radiation. *Acta Geographica Sinica* **1987**, *2*, 002.

Zhang, F.; Chen, J.M.; Chen, J.; Gough, C.M.; Martin, T.A.; Dragoni, D. Evaluating spatial and temporal patterns of MODIS GPP over the conterminous U.S. against flux measurements and a process model. *Remote Sensing of Environment* **2012**, *124*, 717-729.

Zhang, S.; Zhang, J.; Bai, Y.; Koju, U.A.; Igbawua, T.; Chang, Q.; Zhang, D.; Yao, F. Evaluation and improvement of the daily boreal ecosystem productivity simulator in simulating gross primary productivity at 41 flux sites across Europe. *Ecological Modelling* **2018**, *368*, 205-232.

Zhang, Y.; Xiao, X.M.; Wu, X.C.; Zhou, S.; Zhang, G.L.; Qin, Y.W.; Dong, J.W. Data Descriptor: A global moderate resolution dataset of gross primary production of vegetation for 2000-2016. *Scientific Data* **2017**, *4*.

Zhao, M.S.; Running, S.W. Drought-Induced Reduction in Global Terrestrial Net Primary Production from 2000 Through 2009. *Science* **2010**, *329*, 940-943.

Zheng, H.; Li, Y.; Chen, J.; Wang, T.; Huang, Q.; Huang, W.; Wang, L.; Li, S.; Yuan, W.; Zheng, X. A global carbon assimilation system based on a dual optimization method. *Biogeosciences* **2015**, *12*, 1131.

Zhu, H.; Lin, A.; Wang, L.; Xia, Y.; Zou, L. Evaluation of MODIS Gross Primary Production across Multiple Biomes in China Using Eddy Covariance Flux Data. *Remote Sensing* **2016**, *8*, 395.

Zhu, X.J.; Yu, G.R.; Wang, Q.F.; Gao, Y.N.; He, H.L.; Zheng, H.; Chen, Z.; Shi, P.L.; Zhao, L.; Li, Y.N., et al. Approaches of climate factors affecting the spatial variation of annual gross primary productivity among terrestrial ecosystems in China. *Ecological Indicators* **2016**, *62*, 174-181.

Zhu, Z.C.; Bi, J.; Pan, Y.Z.; Ganguly, S.; Anav, A.; Xu, L.; Samanta, A.; Piao, S.L.; Nemani, R.R.; Myneni, R.B. Global Data Sets of Vegetation Leaf Area Index (LAI)3g and Fraction of Photosynthetically Active Radiation (FPAR)3g Derived from Global Inventory Modeling and Mapping Studies (GIMMS) Normalized Difference Vegetation Index (NDVI3g) for the Period 1981 to 2011. *Remote Sensing* **2013**, *5*, 927-948.

Chapter 5 Discussion on sensitivity of GPP to external factors in RS models

RS-based models play a significant role in estimating and monitoring terrestrial ecosystem GPP. Several RS-based GPP models have been developed using different criteria, yet the sensitivities to environmental factors vary among models; thus, the comparison of model sensitivity is necessary for analyzing and interpreting results and for choosing suitable models. In this Chapter, I globally evaluated and compared the sensitivities of 12 RS-based models the same as used in Chapter 1, and benchmarked them against GPP responses to climatic factors measured at flux sites and to elevated CO_2 concentrations measured at FACE experiment sites. The results demonstrated that the models with relatively high sensitivity to increasing atmospheric CO_2 concentrations showed a higher increasing GPP trend. The fundamental difference in the CO_2 effect in the models' algorithm either considers the effect of CO_2 through changes in greenness indices (nine models) or introduces the influences on photosynthesis (three models). The overall effects of temperature and radiation, in terms of both magnitude and sign, vary among the models, while the models respond relatively consistently to variations in precipitation. Spatially, the larger differences among model sensitivity to climatic factors occur in the tropics; at high latitudes, models have a consistent and obvious positive response to variations in temperature and radiation, and precipitation significantly enhances the GPP in mid-latitudes. Compared with the results calculated by flux-site measurements, the model performance differed substantially among different sites. However, the sensitivities of most models are basically within the confidence interval of the flux-site results. In general, the comparison revealed that models differed substantially in the effect of environmental regulations, particularly CO_2 fertilization and water stress, on GPP, and none of the models showed performed consistently better across the different ecosystems and under the various external conditions.

5.1 Introduction

The prevalent algorithms requiring that RS data be inputted to estimate GPP could be categorized into the following groups (Song et al., 2013): (a) VI-based: empirical estimation from spectral vegetation indices (Li et al., 2013; Liu et al., 2014; Gitelson et al., 2006; Sims et al., 2008; Wu et al., 2010); (b) LUE-based: models that are based on LUE theory (Potter et al., 1993; Verstraeten et al., 1996 2006; Yuan et al., 2007; Running and Zhao 2015; Xiao et al., 2004); (c) process-based: models that are based on biophysical processes of plant photosynthesis (Ryu et al., 2011; Jiang et al., 2016; Liu et al., 1997; Zhang et al., 2018); and (d) ML-based: machine learning models that require RS data to train the model (Jung et al., 2011; Liu et al., 2016; Wei et al., 2017). VI-based models are conceptually related to GPP because they are generally developed based on the linkage between chlorophyll and the presence of photosynthetic biomass (Myneni et al., 1992; Wu et al., 2010; Rossini et al., 2012), which is essential for primary production (Hashimoto et al., 2012). Regarding GPP estimation, VI-based models can perform as well as complex physiological process models (Raczka et al., 2013). The most important point is the simple conceptual algorithm, which does not require the prior knowledge and is suitable for running at the global scale (Sellers et al., 1992; Wu et al., 2010). Compared with the VI-based algorithm, the LUE model has a more solid physical foundation, in which ecosystem GPP is determined by the APAR through LUE, which could be reduced by the environmental stresses that detract from the optimal condition (Yan et al., 2015; Alton et al., 2007; Zhang et al., 2015; Joiner et al., 2018; Yuan et al., 2014). The key linkage between terrestrial GPP and RS in the LUE-based model is the estimation of fAPAR using RS data (Wu et al., 2012; Xiao et al., 2004). Numerous LUE-based models have been developed and are

widely used to quantitatively estimate and analyze terrestrial GPP (Verstraeten et al., 1994 2006; Yuan et al., 2007 2014; Running and Zhao 2015; Xiao et al., 2004). In process-based models, RS data and/or products are usually the key model inputs used to assess the energy transfer, flux exchange, and physiological and biochemical processes and then to estimate the ecosystem GPP. Each node of the model involves the corresponding physical meaning and is expressed by several simplified mathematical functions. More recently, ML algorithms have been used to derive continental- and global-scale GPP from multiple RS products based on EC flux tower measurements with reasonable accuracy (Jung et al., 2011; Liu et al., 2016; Wei et al., 2017). The most widely known model is the MTE-GPP, in which gridded GPP data are derived from a statistical model based on the spatiotemporal interpolation of flux tower observations using the MTE regression trained by satellite fAPAR and gridded climate field predictors (Jung et al., 2011); this model has been used as a reference to validate and benchmark other the results of other models (Piao et al., 2013; Smith et al., 2016; Beer et al., 2010).

Regarding the aforementioned models, considerable and substantial efforts have been made to validate, regulate and contrast the models at flux tower sites (Yuan et al., 2014; Wang et al., 2012; Zhang et al., 2015; Wu et al., 2010), specific ecosystems (Wang et al., 2012; Lees et al., 2018; Souza et al., 2013; Meroni et al., 2015; Wu et al., 2010; Li et al., 2016; Hashimoto et al., 2012; Rossini et al., 2012) and regional scales (Yuan et al., 2014; Garbulsky et al., 2010; Yang et al., 2013, Ardö 2015; Zhang et al., 2015; Li et al., 2016). However, the optimal model that is suitable for estimating GPP across different ecosystems and a wide range of enviro-climatic conditions has not been identified and designed (Yuan et al., 2014; Ardö 2015; Zhang et al., 2015; Lees et al., 2018; Hashimoto et al., 2012; Garbulsky et al., 2010; Wang et al., 2012; Rossini et al., 2012), and the discrepancies associated with the spatial distributions of the environmental controls that influence the GPP variation simulated by different models are highly significant (Anav et al. 2015; Piao et al., 2013; Beer et al. 2010). Nonetheless, these studies have concluded that it is necessary and important to study and understand model sensitivity to indicators before designing and modifying GPP estimation models (Garbulsky et al., 2010; Wang et al., 2012; Yuan et al., 2014; Keenan et al., 2012; Yan et al., 2015; Schaefer et al., 2012; Zhang et al., 2016; Piao et al., 2013; Yang et al., 2013; Song et al., 2013). Almost no studies, however, have yet identified and compared the global discrepancy among model sensitivity to external enviro-climatic variability, and even fewer studies have analyzed the effect of CO_2 fertilization that is implied in RS models (De Kauwe et al., 2016; Smith et al., 2016; Sun et al., 2018ab; Liu et al., 2016; Verstraeten et al., 1994; Ryu et al., 2011; Jiang et al., 2016; Liu et al., 1997; Zhang et al., 2018), which is likely attributed to the fact that the effect from CO_2 in models is more concealed than are the influences from enviro-climatic factors (Sun et al., 2018a; Ahlstrom et al., 2015). VI-based models assume that CO_2 affects GPP solely through changes in the greenness index (Wylie et al., 2003; Piao et al., 2007; Thomas et al., 2016; Watham et al., 2017; Sun et al., 2018b); ML- and LUE-based models assume that CO_2 affects GPP solely through changes in the fAPAR (De Kauwe et al., 2016). However, both of the abovementioned indicators are closely related to leaf area (Cheng et al., 2017; Donohue et al., 2013), which is used as an input in process-based models; furthermore, process-based models incorporate some greenness indices and the modules that represent the photosynthetic rate that is affected by the CO_2 concentration (Jiang et al., 2016; Zhang et al., 2018). Models are typically developed based on specific assumptions, and they consider the different processes and complexities involved in the control of vegetation production (Garbulsky et al., 2010; Rossini et al., 2012; Yuan et al., 2014; Ardo et al., 2015); therefore, to make RS-based GPP estimations more robust, it is necessary to conduct a rigorous comparison using consistent validation datasets and driving variables (Wu et al., 2010 2017; Zhang et al., 2016).

In this chapter, twelve models belonging to four RS-based algorithms were tested regarding their abilities to estimate current global terrestrial GPP's apparent sensitivities to climatic variability and increasing atmospheric CO_2 concentration. The model ensemble used in this chapter is the same as that used in Chapter 1 including the AVM (Li et al., 2013, Liu et al., 2014), BESS (Ryu et al., 2011, Jiang et al., 2016), BEPS (Liu et al., 1997, Zhang et al., 2018), CASA (Potter et al., 1993), CFix (Verstraeten et al., 1994, 2006), EC-LUE (Yuan et al., 2007), GR (Gitelson et al., 2006), MODIS (Running and Zhao 2015), MTE (Jung et al., 2011), TG (Sims et al., 2008), VI (Wu et al., 2010, 2012) and VPM (Xiao et al., 2004). MODIS satellite data, MERRA-2 meteorological data (Rienecker et al., 2011), CT2016 CO_2 concentration data (Peters et al., 2007), CPC-SM (Global Soil Data Task, 2014) soil water content data, and other datasets were used to run the models at the global scale in this chapter, and the data from EC flux tower were used for site-scale estimations. The values calculated via the flux tower measurements and FACE experiments were used to test the sensitivity of the modeled GPP to individual changes in climatic variables and CO_2. Finally, I combined the results obtained from this chapter with the design concept, structure, and parameters of each model to comprehensively analyze individual sensitivity.

5.2 Materials and methods

5.2.1 Terrestrial GPP RS-based models

The models used in this chapter are detailed in Chapter 1. Based on the model's characteristics regarding its theoretical basis and core algorithm, each model was grouped into one of four categories, i.e., LUE-, VI-, process- and ML-based models, as shown in Figure 5.1. Among them, I directly used the MTE GPP product developed by Jung et al (2011). instead of re-estimating the MTE-GPP. All models belonged to the full or partial RS data-driven model, but the formulation and the number of limiting factors of the conceptual processes primarily responsible for estimating GPP differed among models. For the process-based models BEPS and BESS, two simulations—S1 and S2—were performed over the period (2000~2014), and one LUE-based model, CFix, was also used, which has a CO_2 fertilization effect item. In S1, the three models were forced with increasing atmospheric CO_2 concentration, while the environmental limiting factors were held constant (by recycling the environmental mean values and variability from the first three years of the study period, e.g., 2000-2002). For all models, S2 was performed, in which the models were forced with factors that all varied (using reconstructed historical environmental fields and increasing atmospheric CO_2 concentrations). All models used the same forcing datasets, shown in Table 5.1. Details of the datasets used and the variables computed in this study can be found in Chapter 1.

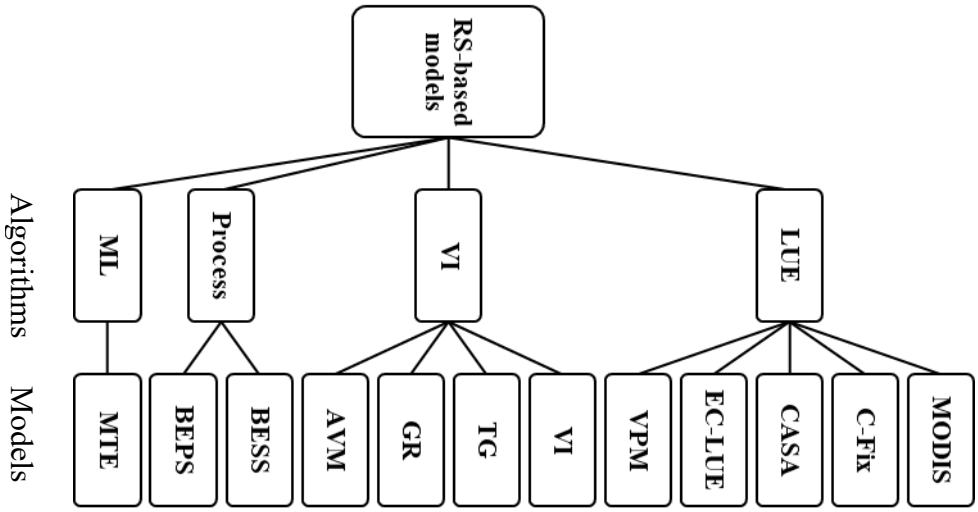

Figure 5.1 The classification of the RS-based GPP estimation models used in this chapter.

Table 5.1 Overview of the datasets used in this chapter.

Data[1]	Datasets / Products[2]	Period[3]	Resolution		Data source[4]	Application
			Spatial	Temporal		
Ca	CT2016	2000-2014	2° lat × 3° lon	Daily	NOAA ESRL	Sensitivity analysis Driving: BESS, BEPS, CFix
Meteorological measurements	FluxNet2015	Longer than 15 years	17 sites	Daily, Yearly	FluxNet	Sensitivity verification Driving all models
Flux_GPP		Longer than 12 years	33 sites	Daily		Verification of Estimation
SM	CPC-SM	2000-2014	0.5° × 0.5°	Monthly	NOAA ESRL	Driving: BEPS, CFix
WP & FC	Global Gridded Soil Characteristics	Static	1° × 1°	Static	IGBP-DIS	
LAI	GlobMap_V3	2000-2014	0.08° × 0.08°	8-day	Liu et al. (2012)	Driving: BEPS, BESS
CT	Koppen-Geiger climate classification	Static	0.5° × 0.5°	Static	Kottek et al. (2006)	
C4Fraction	ISLSCP II		1° × 1°		ORNL DAAC	
Ta	MERRA-2	2000-2014	0.5° lat × 0.625° lon	Daily	NASA GES DISC	Sensitivity analysis Driving: TG, VI, VPM, AVM, EC-LUE, CASA, CFix, BEPS, BESS
PAR						Sensitivity analysis Driving: VI, GR, VPM, EC-LUE, CASA, CFix, BEPS
SH						Calculating VPD for Driving: BEPS
LH						Driving: EC-LUE, CFix
H						
LST						Driving: TG, BESS
PS						Calculating VPD for Driving: BEPS, BESS
Pre						Sensitivity analysis
TD						Driving: BESS
WS						
PARDiff				Hourly		
PARDir						
NIRDiff						
NIRDir						
PET	MOD16A2	2001-2014	500m × 500m	8-days	LP DAAC	Driving: CASA
ET						
LCD	MCD12Q2			Yearly		Driving: VPM
LC Type	MCD12C1		0.05° × 0.05°			Driving all models Calculating CI
ALB_BSA_VIS	MCD43C3	2000-2014		Daily		Driving: BESS
ALB_WSA_VIS						
ALB_BSA_NIR						
ALB_WSA_NIR						
Red Band	MCD43C4					Calculating NDVI, EVI
NIR Band						Calculating NDVI, EVI, LSWI
Blue Band						Calculating EVI
SWIR Band						Calculating LSWI
*f*iso	MCD43C2					Calculating CI
*f*vol						
*f*geo						
NDVI	This study				This study	Driving: EC-LUE, CASA, CFix, BEPS
EVI						Driving: TG, VPM, GR, VI, AVM
CI				Yearly		Driving: BEPS, BESS
LSWI				Daily		Driving: VPM

[1] C_a : ambient CO_2 concentration; SM: soil moisture; WP: wilting point; FC: field capacity; LC type: Land Cover Type; CT: Climate Type; Ta: air temperature; PAR: Photosynthetically active radiation; SH: specific humidity; LH: latent heat flux; H: sensible heat flux; LST: land surface temperature; PARDiff: downwelling PAR diffuse flux; PARDir: downwelling PAR beam flux; NIRDiff: downwelling NIR diffuse flux; NIRDir: downwelling NIR beam flux; PS: surface pressure; WS: wind speed; TD: dew point temperature; Pre: total precipitation; PET: potential evapotranspiration; ET: evapotranspiration; NDVI: normalized difference vegetation index; EVI: enhanced vegetation index; CI: clumping index; LCD: land cover dynamic; LSWI: land surface water index; ALB_BSA_VIS: black sky albedo at visible range; ALB_WSA_VIS: white sky albedo at visible range; ALB_BSA_NIR: black sky albedo at NIR range; ALB_WSA_NIR: white sky albedo at NIR range; NIR: Near-infrared; SWIR: Short-wavelength infrared; *f*iso: isotropic coefficient; *f*vol: RossThick coefficient; *f*geo: LiSparseR coefficient.

[2] CT2016: Carbon Tracker 2016; CPC-SM: Climate Prediction Center Soil Moisture; MCD12C1: Land Cover Type Climate Modeling Grid product; ISLSCP II: The International Satellite Land Surface Climatology Project, Initiative II; MERRA-2: The Modern-Era Retrospective analysis for Research and Applications, Version 2; MOD16A2: MODIS/Terra Net Evapotranspiration 8-Day L4 Global 500 m SIN Grid V006; This study means the factor was calculated in this study; MCD12Q2: Land Cover Dynamics Yearly L3 Global 500 m SIN Grid; MCD43C3: MODIS/Terra and Aqua BRDF/Albedo (Bidirectional Reflectance Distribution Function and Albedo) Daily L3 Global 0.05Deg CMG V006; MCD43C4: MODIS/Terra and Aqua Nadir BRDF-Adjusted Reflectance Daily L3 Global 0.05Deg CMG V006; MCD43C2: MODIS/Terra and Aqua BRDF/Albedo Snow-free Parameters Daily L3 Global 0.05Deg CMG V006; GLAS: Geoscience Laser Altimeter System.

[3] The period of the data derived from MODIS is from 2000065 to 2014365, the data before 2000065 were replaced by the mean value of multi-years.

[4] NOAA ESRL: National Oceanic and Atmospheric Administration / Earth System Research Laboratory; IGBP-DIS: The International Geosphere-Biosphere Programme Data and Information System; LP DAAC: The Land Processes Distributed Active Archive Center; ORNL DAAC: Oak Ridge National Laboratory Distributed Active Archive Center; NASA GES DISC: Goddard Earth Sciences Data Information Services Center.

5.2.2 Analysis

5.2.2.1 Response of GPP to climate variations

Many methods can be used to investigate the sensitivities of GPP to climate variations (Nemani et al., 2003; Chang et al., 2016; Sun et al., 2018b; Piao et al., 2013; Schaefer et al., 2002; Friedlingstein et al., 2006; Bonan and Doney 2018; Bai et al., 2010); however, in this chapter, most of the models are not based on biochemical processes. Thus, the experiments of the control variables are not suitable. Therefore, I empirically estimated the response of GPP to climate variability (e.g., interannual mean annual temperature, radiation, and annual precipitation) over the last 15 years, referring to the multiple regression approach from Piao et al (2013):

$$y = \gamma^{int} x_T + \delta^{int} x_P + \eta^{int} x_R + \varepsilon \qquad \text{Eq-5.1}$$

where y is the detrended anomaly of GPP estimated by each model from S2, which considers rising atmospheric CO_2 concentration and climate change. The x_T is the detrended mean annual temperature anomaly, x_P is the detrended annual precipitation anomaly and x_R is the detrended mean annual radiation anomaly. The fitted regression coefficients γ^{int}, δ^{int} and η^{int} define the apparent GPP sensitivity to interannual variations in temperature, precipitation and radiation, respectively, and ε represents the residual error term. Note that in Eq-5.1, the γ^{int}, δ^{int} and η^{int} are not the true sensitivities of these GPPs; rather, these values are only the contributive effect of each factor's variation on GPP (Piao et al., 2013), given that temperature, precipitation and radiation are the three main factors that affect GPP (Nemani et al., 2003; Yu et al., 2013; Wu et al., 2017). That being said, there may be other environmental drivers (Chang et al., 2016; Bonan and Doney 2018) (e.g., wind speed, soil moisture) that have not been considered in Eq-5.1 but that also contribute to the variability of GPP; in addition, Eq-5.1 uses the annual scale temperature, precipitation and radiation, but these factors interact and co-vary over time. Based on the contributive method of GPP, I can obtain the spatial distributions of the sensitivities of GPP to the climatic variables. I also estimated the monthly response of GPP to climatic variations to obtain the seasonal characteristics of those responses; therefore, this method was used to calculate values for each month of an entire year (e.g., the monthly GPP estimates, as well as the monthly mean temperature, monthly mean radiation and monthly mean precipitation of all 15 Decembers, were inputted into Eq-5.1 to obtain the corresponding results for December).

5.2.2.2 Response of GPP to CO_2 trend

For all models including the ones that did not apparently contain the CO_2 fertilization effect module, I used a multiple regression approach, shown in Eq-5.2, that refers to the results of previous studies (Piao et al., 2013; Zhang et al., 2016; Wu et al., 2017; Smith et al., 2016) that estimated the response of GPP to CO_2 for each model based on the concept that this method attributes the time series of GPP to what I consider as the dominant drivers of change, i.e., temperature, precipitation, radiation and CO_2.

$$GPP = \beta CO_2 + a\mathrm{Tem} + b\mathrm{Pre} + c\mathrm{Rad} + d + \varepsilon \qquad \text{Eq-5.2}$$

where GPP is the estimated value of each model, and CO_2, Tem, Pre and Rad are the mean annual atmospheric CO_2 concentration (ppm), mean annual temperature (°C), annual precipitation (mm) and mean annual radiation (W m^{-2}), respectively. β, a, b, c and d are the regression coefficients, and ε is the residual error term. The regression coefficients indicate the

contributive effect of the CO_2, temperature, precipitation and radiation variations on the GPP variations. Similar to the assumption concept of Eq-5.1, other meteorological forcing elements, such as nitrogen deposition, wind speed, and soil moisture, might also influence GPP variations, and these would modulate the trend of the GPP time series in addition to the assumed CO_2 driver. In response to the above concerns, Piao et al (2013), the inventors of Eq-5.2, used 10 DGVMs to test the statistically estimated coefficients from Eq-5.1; the authors found that the coefficients calculated using the statistical method have a high consistency with the results computed using the process-based method (i.e., multiple simulations of control variables). For the monthly estimations, I inputted the monthly GPP estimates and the monthly mean temperature, radiation, atmospheric CO_2 concentration and total precipitation.

In this study, I also applied a control variable to estimate the value of β for BESS, BEPS and CFix who consider the CO_2 fertilization effect:

$$\beta = \Delta GPP / \Delta CO_2 \qquad \text{Eq-5.3}$$

where ΔGPP is equal to the difference between the average GPP estimates in the last 3 years and the first 3 years of S1, in which the models were forced with rising atmospheric CO_2 concentration while the environmental limiting factors were held constant. ΔCO_2 is the change in atmospheric CO_2 concentration during the corresponding period.

5.3 Results

5.3.1 Response of GPP to variations in enviro-climatic drivers

5.3.1.1 Response of GPP to CO_2 variations

Because Eq-5.3 is not appropriate for all models to calculate the CO_2 fertilization effect, the responses of the estimated GPP to rising atmospheric CO_2 concentration presented in this section were calculated by Eq-5.2, and the comparison between Eq-5.3 is further discussed in Section 5.4. At the global scale, the magnitude of β_{GPP}^{int} (i.e., the overall response of the estimated GPP to the effect of rising atmospheric CO_2 concentration) varied among models, but almost all of them showed a positive effect (Figure 5.2). The average of β_{GPP}^{int} from all models was 25.42 ± 15.28 Pg C year^{-1} 100 ppm^{-1}, and the minimum was MTE, which was close to zero, followed by MODIS (0.04), EC-LUE (15.26), GR (17.08), VPM (23.04), CASA (26.68), BESS (28.99), VI (29.44), CFix (37.33), TG (38.35), and AVM (43.41), and the most significant was BEPS (45.82, unit is Pg C year^{-1} 100 ppm^{-1}). Regarding the latitudinal distribution, all the models performed similar patterns, and the maximum of β_{GPP} appeared in the Tropics with high uncertainty (2.46 ± 1.79 gC m^{-2} yr^{-1} ppm^{-1}); the β_{GPP} in the Northern Hemisphere showed a positive effect and a relatively consistent distribution (1.29 ± 0.47 gC m^{-2} year^{-1} ppm^{-1}). In contrast, there was no uniform distribution feature in the Southern Hemisphere (0.24 ± 0.81 gC m^{-2} year^{-1} ppm^{-1}) and no tendency of variation with latitude (Figure 5.3). As the maps of the global distribution of the β_{GPP} (Figure 5.4) show, the rising atmospheric CO_2 concentration enhances GPP around almost the entire globe, except in some small sparse parts of Southern Africa, Midwestern Australia, Brazilian Plateau, and the longitudinal stripped areas distributed along the Kazakhstan-Mongolia direction. In addition, some models also showed a few unique distribution characteristics; the estimates from MODIS and VPM showed the negative response of GPP in some parts of the Amazon and Indonesian-Malay Rainforest to rising CO_2, while in these regions, the other models estimated the greatest CO_2 fertilization effect; additionally, MODIS and CASA showed that the β_{GPP} in large parts of southern Africa had opposite signs to those of the other models (Figure 5.4). Simultaneously, combined with the monthly cycle of β_{GPP} (Figure 5.5), it can be inferred that the individual differences among the models were mainly caused by the contributions of the negative effects during the boreal winter to the overall performance (i.e., VPM, MODIS and EC-LUE showed the slight overall negative feedback of GPP to rising CO_2 during the boreal winter, and during this period, the plants in the Northern Hemisphere basically stop photosynthesis, so the main contribution comes from the Tropics and the Southern Hemisphere, where there are large differences among models). Generally, the monthly β_{GPP} estimated by all models showed the same seasonal pattern as that of GPP, i.e., rising during spring, reaching a maximum in summer, falling during autumn and reaching a minimum in winter; this pattern was a consequence of the CO_2 fertilization effect enhancing the photosynthetic intensity in the northern continent during the growing season. In terms of the responses of each PFT to the rising CO_2 concentration (Figure 5.6), the most significant positive effect of CO_2 on GPP was in the EBF ecosystem (3.79 ± 1.78), except for MODIS and MTE, which estimated a slight negative response. This was followed by WSA (2.45 ± 1.29) and ENF (1.75 ± 0.59), and among PFTs, only CSH (-1.63 ± 2.30) slightly negatively responded to rising atmospheric CO_2 concentrations but had high uncertainty. For most models, the other PFTs had a positive β_{GPP} value (the unit is gC m^{-2} year^{-1} ppm^{-1}). In summary, the reflected carbon fertilization effect was quite different between models.

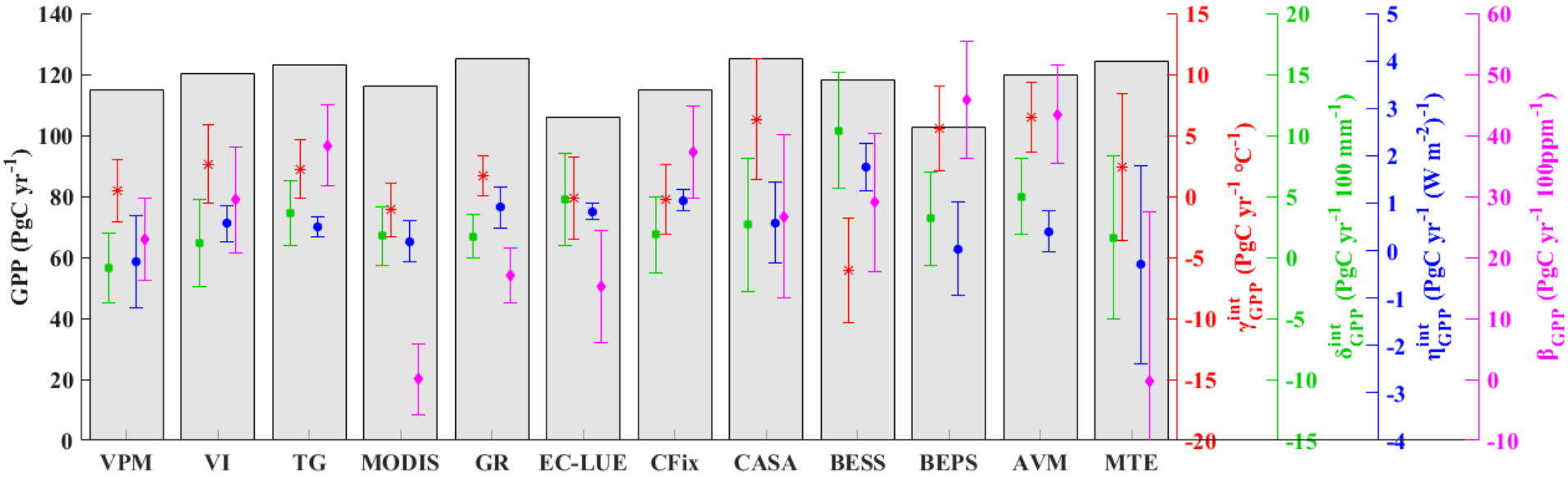

Figure 5.2 Annual globally averaged GPP and the sensitivities of interannual GPP variation to variations in environmental factors.

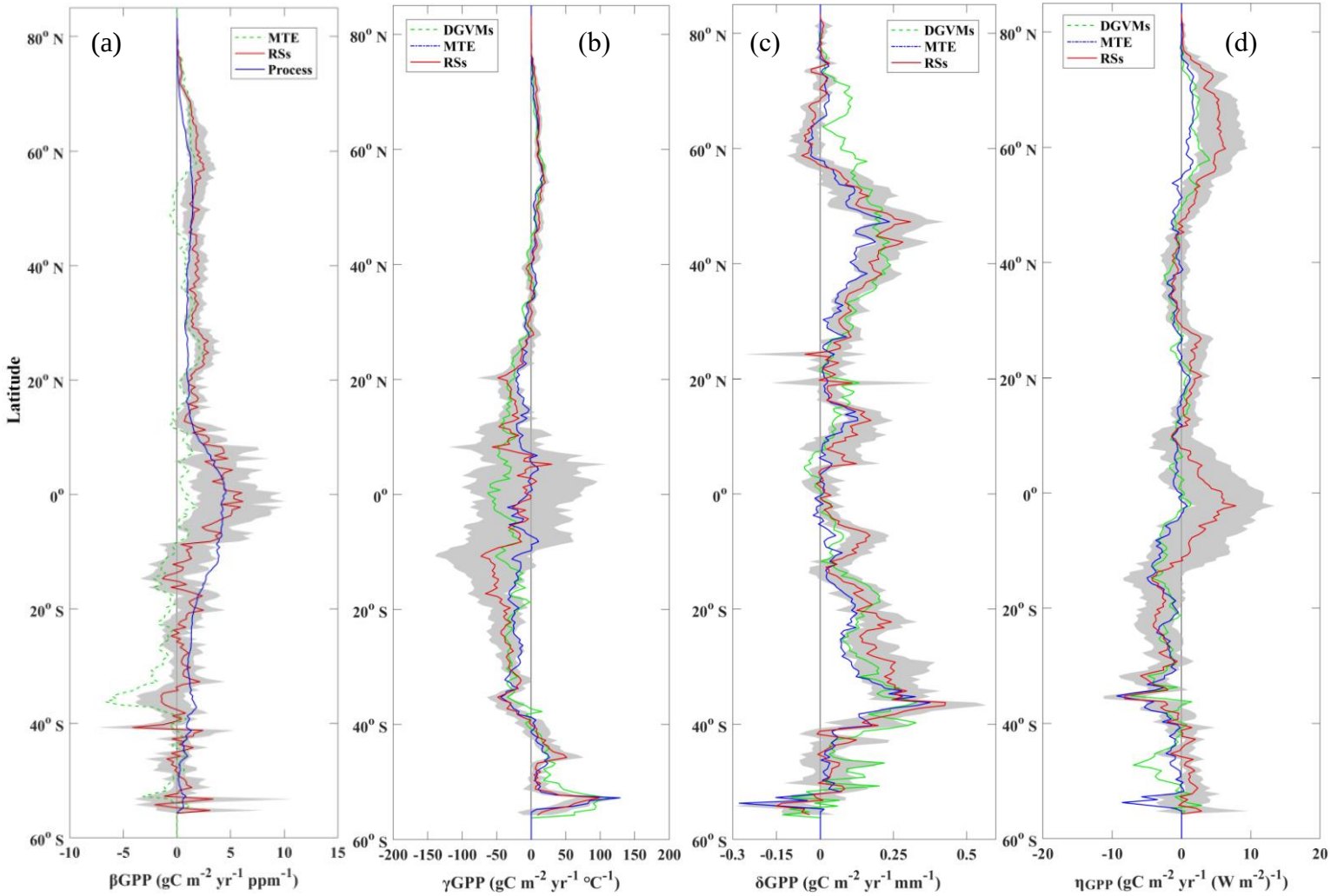

Figure 5.3 The latitudinal distribution of comparisons of the responses of GPP to changes in different factors (a) temperature, (b) precipitation, (c) radiation, and (d) atmospheric CO_2 concentration between DGVMs and RS-based models. Gray shadow is the s.d. of RS-based models.

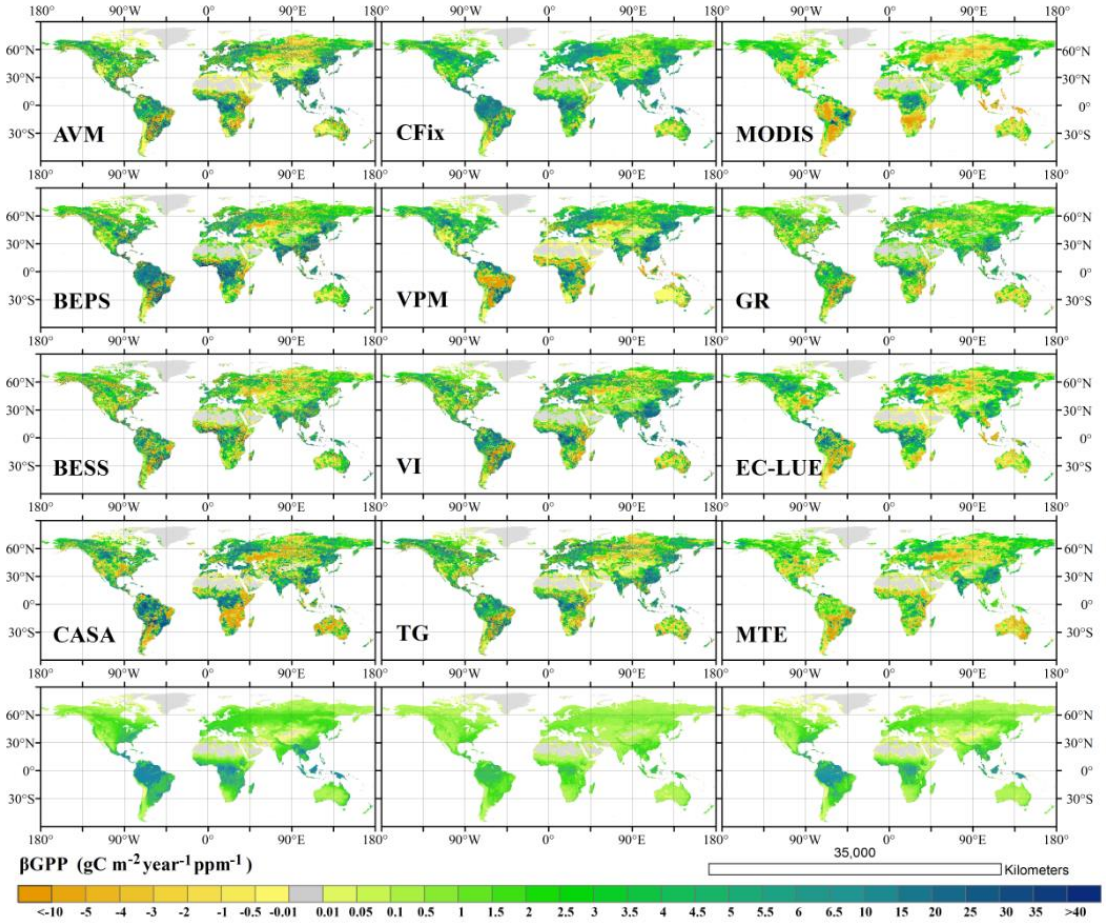

Figure 5.4 Global distribution of responses of GPP to rising atmospheric CO_2 concentration.

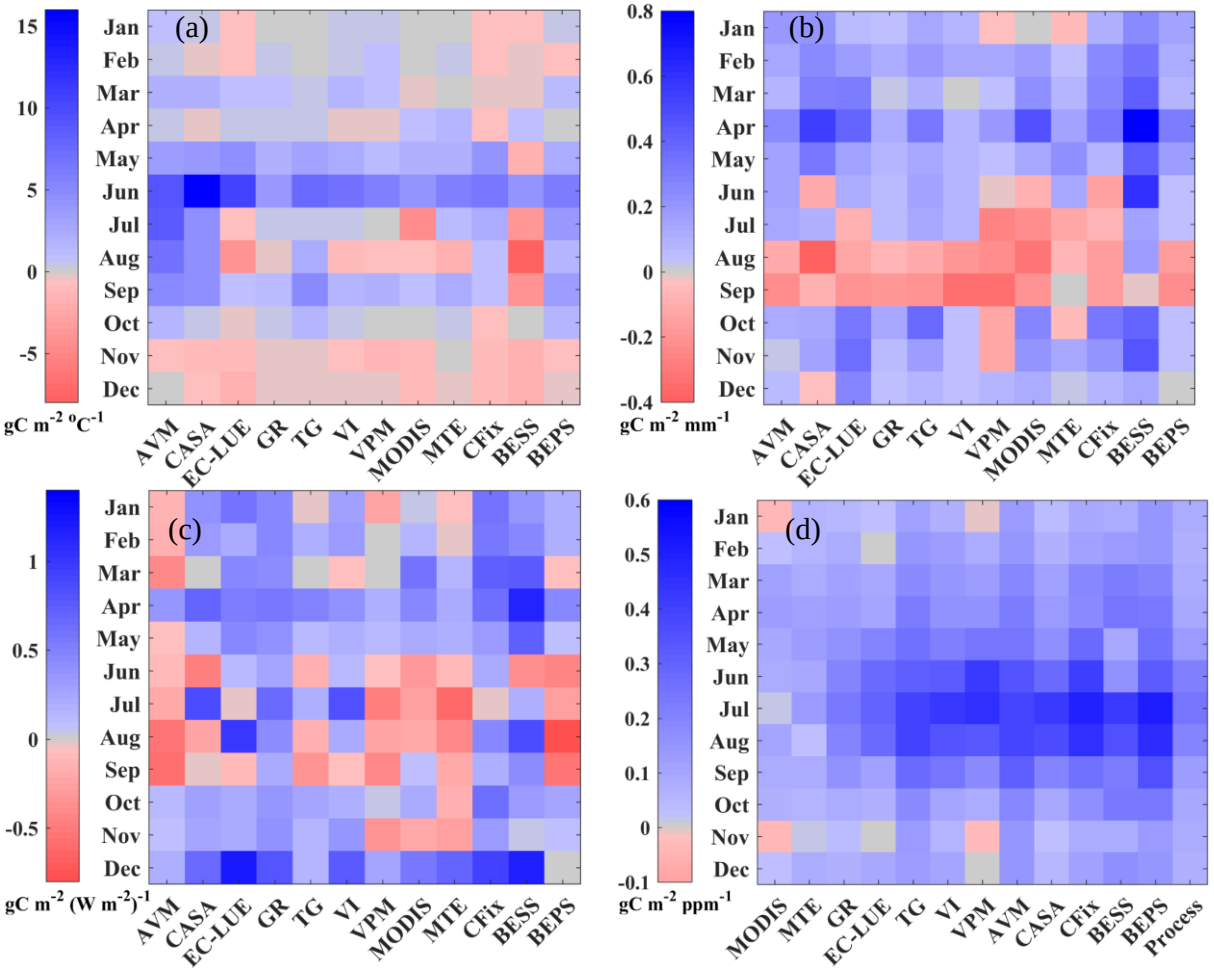

Figure 5.5 The monthly responses of GPP to variations in climate of each model, (a) to temperature change, (b) to precipitation change, (c) to radiation change and (d) to rising atmospheric CO_2 concentration.

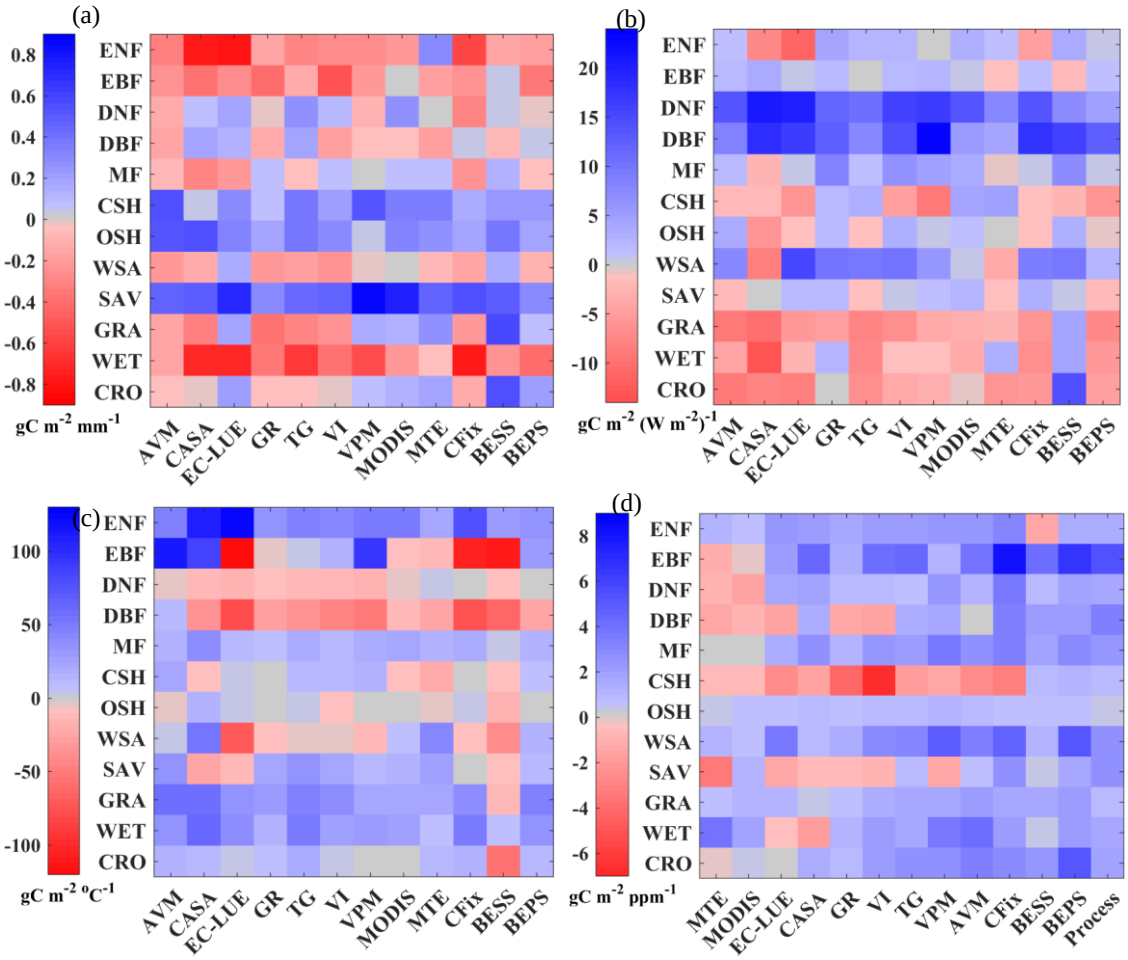

Figure 5.6 The responses of GPP to the variations in (a) precipitation, (b)radiation, (c) temperature and (d) rising CO_2 concentration across PFTs by each model.

5.3.1.2 Response of GPP to temperature variations

The influence of temperature on the interannual variation in global total GPP varied among models (all variables detrended), as seen from not only the differences in the magnitude (Figure 5.2) but also the spatial distribution of γ_{GPP} (Figure 5.7), especially in the tropical and subtropical regions (-28.99 ± 43.46 gC m^{-2} $°C^{-1}$). According to the spatial distribution of γ_{GPP}, the 12 models can be divided into two groups: in the first group, which includes AVM, MODIS, BEPS, VPM, GR, VI, CASA, TG and MTE, the estimated γ_{GPP} is negative only in South Asia, Latin America, northern Australia, Brazil Plateau, and southern and eastern Africa; in the second group, the productivity of almost all plants located between 30°N and 30°S declined with increasing temperature. All models showed high consistency in the mid-high latitudes in the Northern Hemisphere (6.56 ± 2.16 gCm^{-2} $°C^{-1}$) (Figure 5.3). The spatial distribution of the monthly γ_{GPP} indicated that all models estimated the significant seasonal pattern of the response of GPP to temperature in the northern continental region, with the greatest γ_{GPP} during June and the lowest γ_{GPP} during the boreal winter (Figure S17); additionally, the responses changed with the latitudinal gradient. In contrast, the γ_{GPP} in the low latitudes varied widely among models and did not have significant seasonal characteristics. As the monthly global overall γ_{GPP} shows (Figure 5.5), the effects of temperature on enhancing vegetation activities in spring and autumn were presented by all models, and CASA, AVM, TG, CFix and BEPS also presented the positive effect of temperature on GPP during summer, while the other models showed that temperature may inhibit plants that grow rapidly during summer. The negative effect of temperature on the

productivity of DBF was reflected in all models, and except for in AVM, the same inhibitory influence in DNF was also estimated by the other models (Figure 5.6). The most significant difference of γ_{GPP} among models was reflected in EBF. AVM, CASA and VPM estimated that the maximum was in EBF, but in EC-LUE, CFix and BESS, the temperature limited the GPP of EBF to the utmost extent. In addition, the sign of γ_{GPP} estimated by different models were also different in savannas and shrublands ecosystems. In general, for all other PFTs, the models estimated consistent results that supported that temperature promoted vegetation growth.

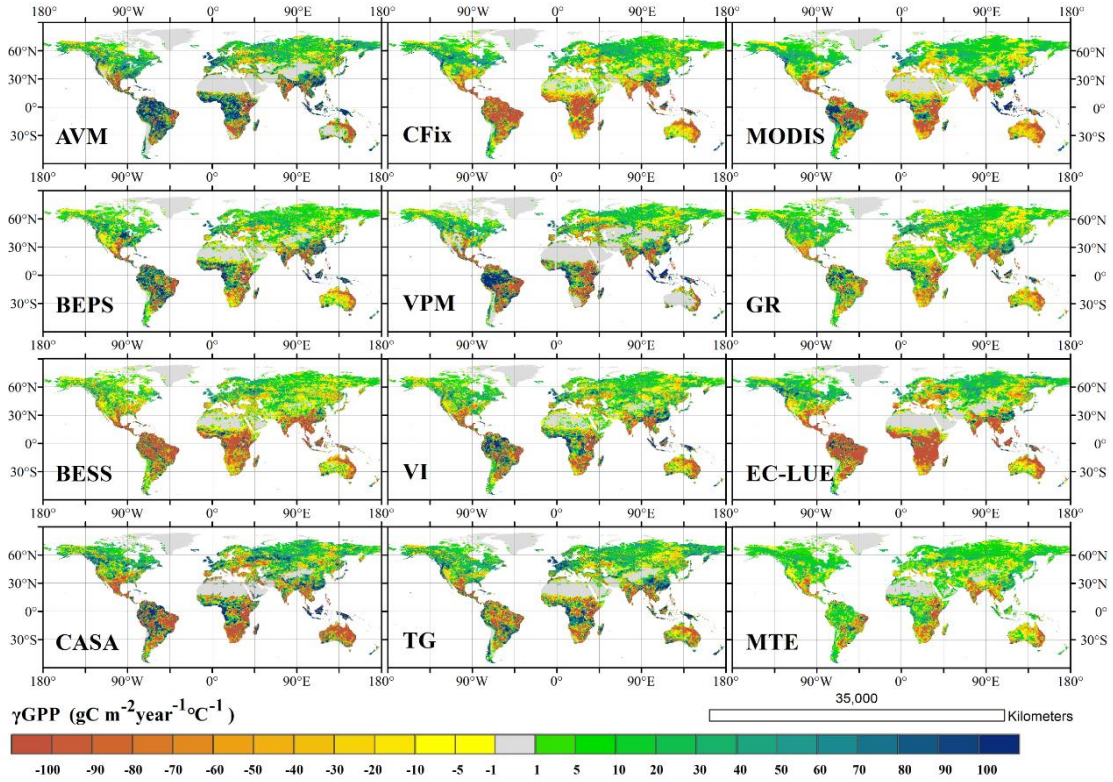

Figure 5.7 Global distribution of responses of GPP to variations in temperature.

5.3.1.3 Response of GPP to precipitation variations

No model used in this chapter needed to be driven by inputting precipitation data, but the models still showed a relatively consistent δ_{GPP}^{int} (Figure 5.2). The interannual variation of the modeled global total GPP was significantly and positively correlated with the precipitation variation in 11 of 12 models, with an average δ_{GPP}^{int} of 3.43 ± 2.65 PgC m^{-2} 100 mm^{-1}, except for VPM (-0.86 PgC m^{-2} 100 mm^{-1}). The latitudinal distribution of δ_{GPP} had an obvious bimodal distribution (Figure 5.3). The relatively larger positive responses of the modeled GPP to precipitation were found in the middle latitudes, with average values of 22 ± 7 and 13 ± 5 in the Southern Hemisphere and Northern Hemisphere, respectively, followed by the Tropics (7 ± 4) and high latitudes (2 ± 3), units in gC m^{-2} 100 mm^{-1}. This trend can also be seen from the spatial distribution of δ_{GPP} (Figure 5.8), and the response of the estimated GPP in the high latitudes of Eurasia to precipitation variation was mainly negative; in contrast, in the temperate regions of Eurasia and the American continent, especially in steppe ecosystems, precipitation significantly promoted vegetation growth. The spatial distribution of δ_{GPP} in the African continent was the most complex, and 11 of 12 models (EC-LUE showed a significant positive effect of precipitation except in the Congo Rainforest) did not estimate the same obvious spatial distribution characteristics. In addition, the models indicated that in most tropical rainforest

areas, the increase in precipitation was likely to limit GPP to some extent. As shown in Figure S18, which shows the monthly spatial distribution of δ_{GPP} during the period of boreal winter, the precipitation significantly enhanced the plants growing in the tropical savanna and forest-savanna mosaic of tropical Africa; however, during the period of boreal summer, the precipitation promoted productivity in the South Africa Plateau and in most parts of the Northern Hemisphere. Globally, although the monthly δ_{GPP} estimated by each model was not the same in terms of magnitude, the seasonal cycle was almost the same; during late summer and early autumn, the overall effect of precipitation variation on GPP variation was negative (Figure 5.5). In different PFTs, the modeled GPP had different responses to precipitation, and even the signs of δ_{GPP} were inconsistent (Figure 5.6). However, in savannas
(52 ± 17 PgC m^{-2} 100 mm^{-1}) and shrublands (29 ± 10 PgC m^{-2} 100 mm^{-1}), all the models estimated positive δ_{GPP} values, while the wetland ecosystem reflected the opposite situation to the above two ecosystems, with an average of -43 ± 24 PgC m^{-2} 100 mm^{-1}. The δ_{GPP} values estimated by CASA, EC-LUE and TG were positive in deciduous forest, while the δ_{GPP} values estimated by the other models were negative. Regarding grassland and cropland ecosystems, CASA, CFix and all VI-based models estimated negative effects of precipitation on GPP.

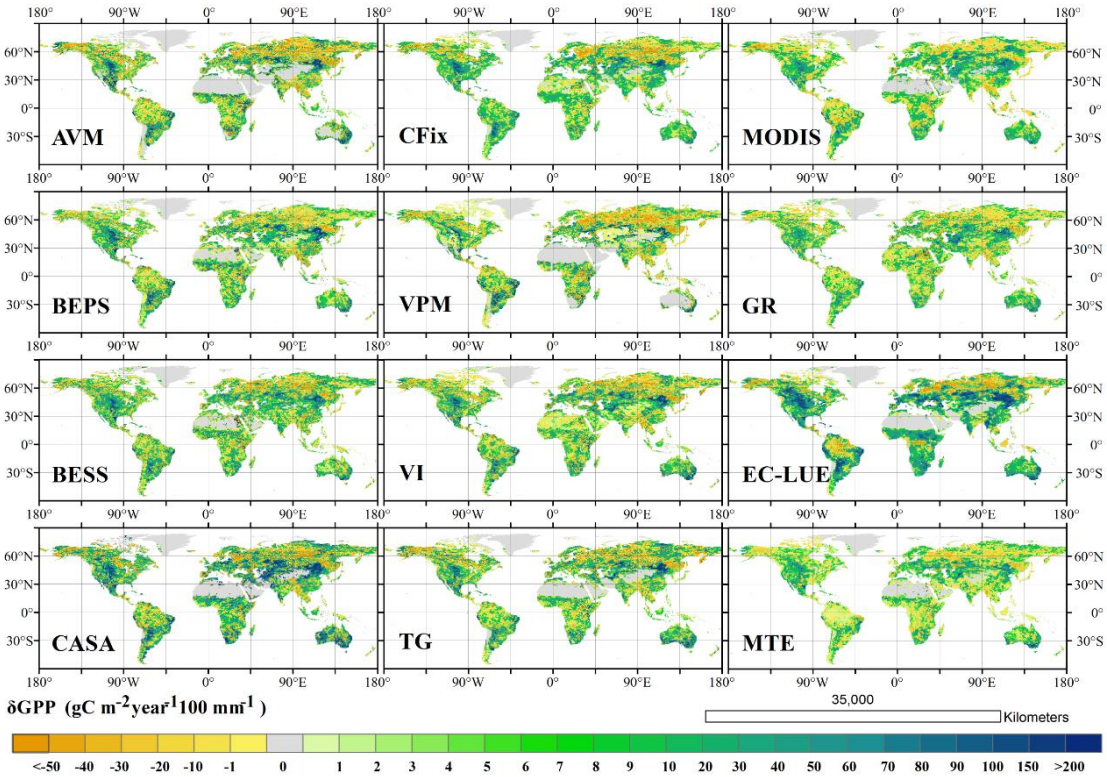

Figure 5.8 Global distribution of responses of GPP to variations in precipitation.

5.3.1.4 Response of GPP to radiation variations

At the global scale, the overall effect of radiation among the different models had differences in the magnitude and even in the sign of η_{GPP}^{int} (Figure 5.2), although the latitudinal distribution of η_{GPP}^{int} among the 12 models was similar (Figure 5.3). The sensitivity values were the highest in the high latitudes of the Northern Hemisphere (2.61 ± 1.37 gC $m^{-2}(W\ m^{-2})^{-1}$), followed by the Tropics (1.04 ± 3.47 gC $m^{-2}(W\ m^{-2})^{-1}$), and the temperate regions, which had negative responses (-0.67 ± 1.28 gC $m^{-2}(W\ m^{-2})^{-1}$). Five of the 12 models (i.e., CFix, GR, VI, EC-LUE and CASA) showed significant positive sensitivity in the Tropics, and all the models

showed a large spatially continuous positive sensitivity in the mid-high latitudes of the Northern Hemisphere (Figure 5.9). At the monthly scale, compared with γ_{GPP}^{int} and δ_{GPP}^{int}, the responses of models to radiation were not obvious, but all models basically reflected positive responses to radiation in the spring (March, April and May) and late autumn (October and November), likely because radiation affects the growth period of plants in the Northern Hemisphere. From the perspective of the monthly spatial distribution of sensitivity, the CASA, CFix, GR, EC-LUE, VI models showed a higher spatial consistency than did the other models. Regarding the sensitivity of PFTs to radiation variations, although the values were different, the relative magnitude of the responses among the various PFTs were basically consistent across models, with the greatest η_{GPP} occurring in deciduous forests (13.04 gC $m^{-2}(W\ m^{-2})^{-1}$) and the minimum value occurring in grassland (-5.20 gC $m^{-2}(W\ m^{-2})^{-1}$) (Figure 5.6).

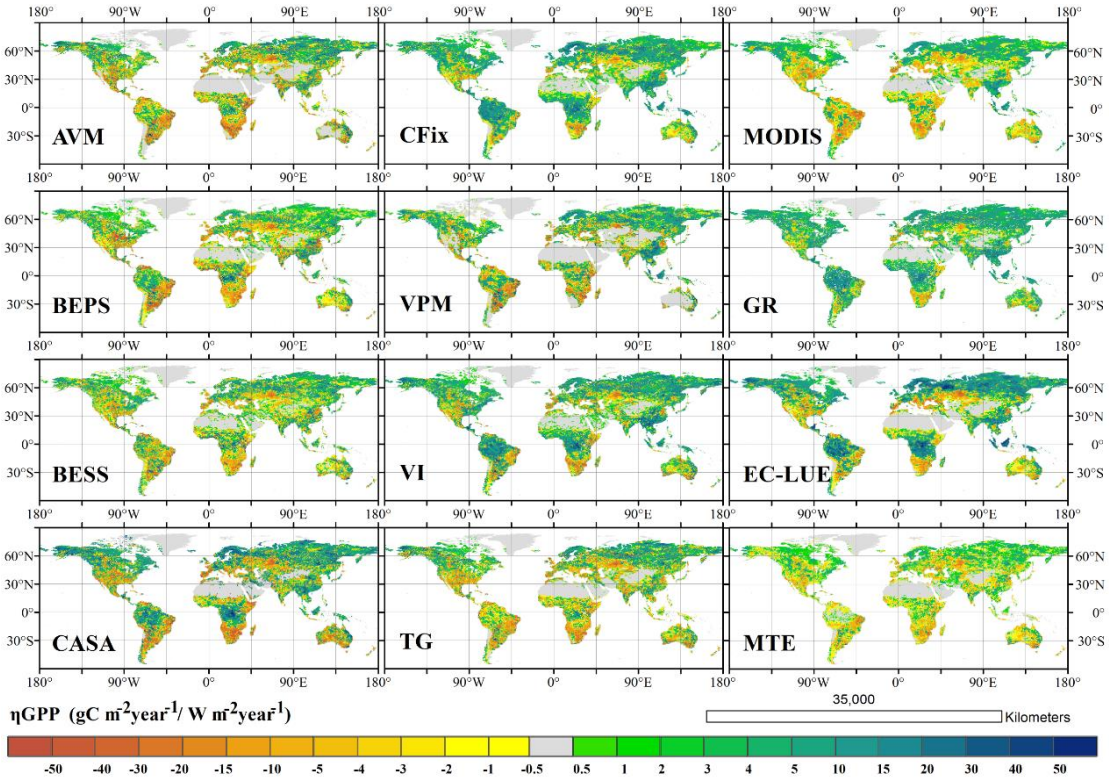

Figure 5.9 Global distribution of responses of GPP to variations in radiation.

5.3.2 Comparison with the *in-situ* results

The selected FluxNet sites with more than 15 years of available data were used as benchmark sites, and Figure 5.10 shows the comparisons between the modeled sensitivities and the sensitivity calculated by on-site measurements and the spatial distribution of $R\gamma_{GPP}^{int}$, $R\delta_{GPP}^{int}$ and $R\eta_{GPP}^{int}$ (the ratio of γ_{GPP}^{int}, δ_{GPP}^{int} and η_{GPP}^{int} to the 15-year average GPP of each model) averaged across the 12 models. No model obtained a corresponding value that was exactly consistent with the one calculated using the measurements at all sites; this trend included the sign of the sensitivities, but the estimations were basically located within the confidence interval of the calculated results, with only a few exceptions. However, the confidence intervals were wide, indicating that for a site and a given model, there were large factor-to-factor differences in estimation accuracy. Models behave and perform differently in response to each climatic factor and vary with site; furthermore, no model systematically overestimated (or underestimated) the sensitivity of GPP to climatic factors. Conversely, some sites existed where all models showed overestimation or underestimation.

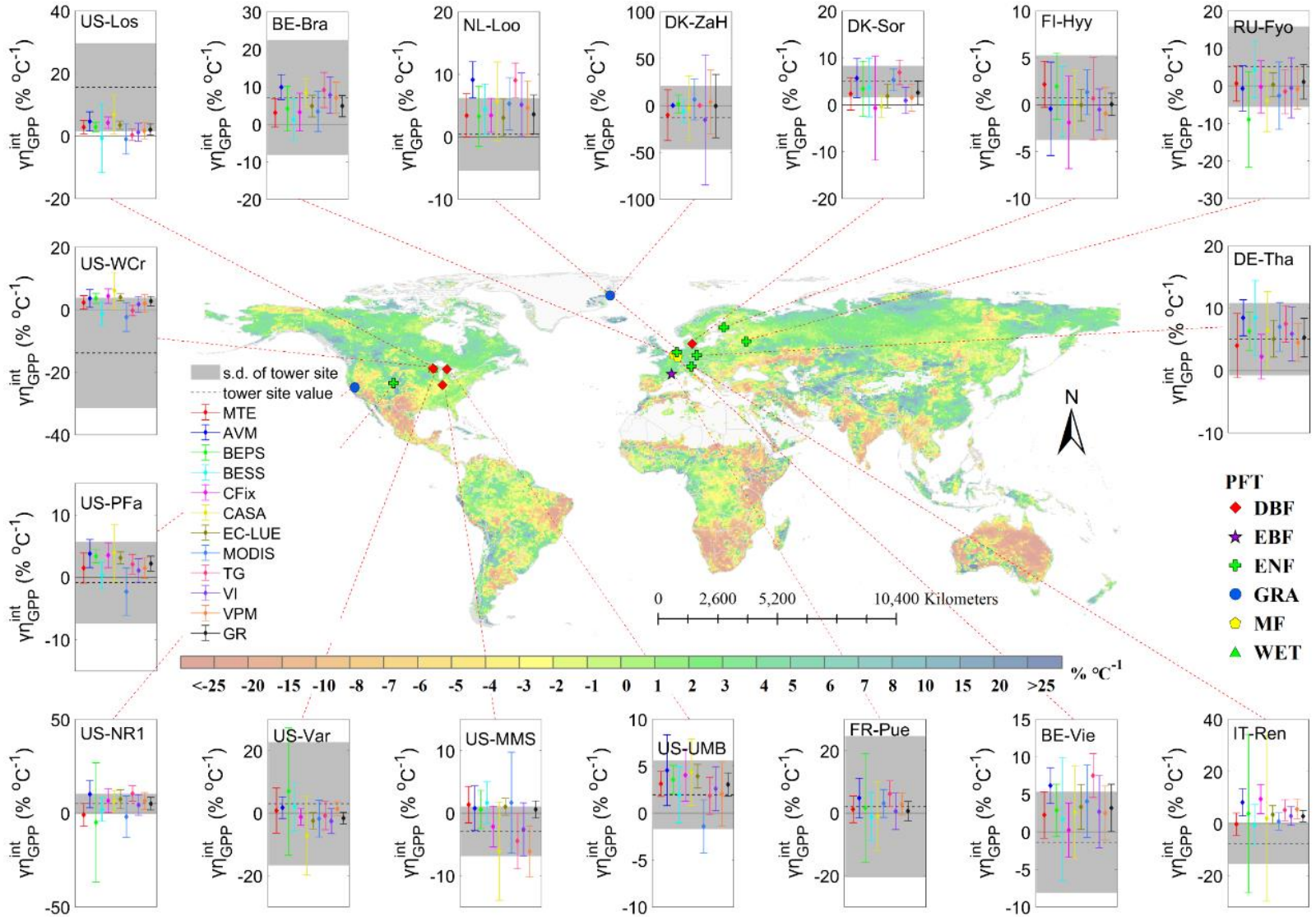

Figure 5.10 Comparisons of the observed relative response of GPP to temperature changes in EC flux towers (Table 5.3) and estimated relative response of GPP to interannual variation in temperature by 12 RS-based models for the period of 2000-2014.

For $R\gamma_{GPP}^{int}$ (Figure 5.10), the results from the sites showed that a step increase in temperature generally increased GPP across most sites, except at BE-Vie, DK-ZaH, IT-Ren, US-MMS, US-PFa and US-WCr, where almost all models overestimated the effect of temperature on GPP. Considering all 17 sites, the average RMSE (Table 5.2) of the model ensemble was 1.79 ± 0.20 %°C^{-1}, which ranged from 1.46 %°C^{-1} in MTE to 2.04 %°C^{-1} in BEPS. The maximum RMSEs of the models all occurred in the WET ecosystem (average of 13.21 ± 2.30), followed by the GRA (average of 5.92 ± 2.41), DBF (average of 4.19 ± 0.62), ENF (average of 2.48 ± 0.61), and MF (average of 2.20 ± 0.51); moreover, the $R\gamma_{GPP}^{int}$ values estimated by the models were closest to the value calculated using the on-site measurements in the EBF ecosystem (average of 1.91 ± 1.27). The GR only at GRA sites and that at all GRA sites estimated negative $R\gamma_{GPP}^{int}$; BEPS estimated a negative $R\gamma_{GPP}^{int}$ at only ENF sites; and the other models obtained a negative response of GPP to variations in temperature at more than one PFT. Ten of the 12 models (except CFix and MODIS) estimated the same trend of the GPP response to temperature as that at most sites as calculated using real measurements. The responses estimated by the 12 models were relatively consistent in the MF ecosystem (i.e., a positive effect of temperature on GPP except for MDOIS at US-PFa), while using measurements to estimate the influence resulted in negative values at two of the three MF tower sites. The sensitivity of GPP to temperature estimated by all models showed positive results in at least at 10 sites out of the 17 flux sites. The average $R\gamma_{GPP}^{int}$ for all sites of each model was larger than that of the site measurements. I utilized the natural break method to evaluate the performance of each model against the results calculated by the on-site measurements, and we divided the RMSE values into three groups, i.e., relatively good, medium and relatively poor, and combined the group with bias (model minus flux) to summarize the results (Table 5.2) as follows (similarly, we describe the results of $R\delta_{GPP}^{int}$ and $R\eta_{GPP}^{int}$): For all PFTs, MTE (+0.47, the unit of bias is % °C-1, + means overestimation, – means underestimation; and hereinafter the same and omitted) and BESS (+0.63) captured the relative optimal response of GPP to changes in temperature; VI (+2.21) and VPM (+2.04) were relatively better at MF sites; and at GRA sites, BESS (+3.06), CFix (-4.02), VI (-3.92) and MTE (+0.28) had estimates that were closest to the results for site $R\gamma_{GPP}^{int}$. Additionally, for ENF, MTE (+0.05), BESS (+1.70) and GR (+1.51) performed relatively well; and the estimations of AVM (-10.93), CFix (-11.31) and CASA (-8.69) were relatively better than those of the other models in WET. For DBF, BESS (+3.91), MODIS (+3.25) and TG (+3.45) belonged to the relatively good performing models; and with regard to EBF, BEPS (-0.41), MTE (-0.84), MODIS (+1.03) and VPM (+0.83) showed the optimal $R\gamma_{GPP}^{int}$.

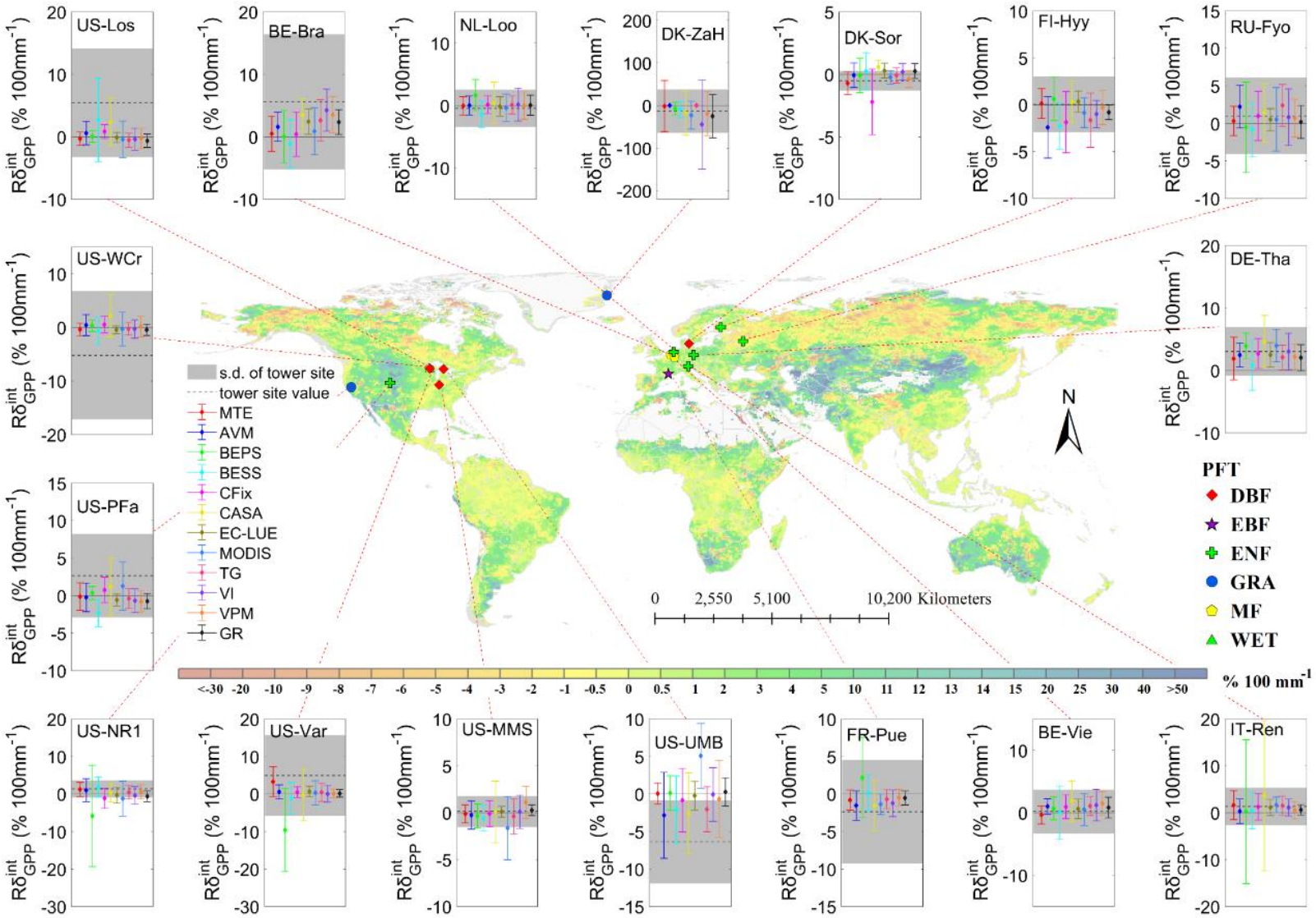

Figure 5.11 Comparisons of the observed relative response of GPP to changes in precipitation in EC flux towers (Table 5.3) and estimated relative responses of GPP to interannual variation in precipitation by 12 RS-based models for the period of 2000-2014.

Regarding $R\delta_{GPP}^{int}$(Figure 5.11), site $R\delta_{GPP}^{int}$ values were positive at 11 sites, and at the sites with negative $R\delta_{GPP}^{int}$ values, with the exception of DK-ZaH, the $R\delta_{GPP}^{int}$ values of the 12 models were all greater than that of the site $R\delta_{GPP}^{int}$ values, which was the same situation as that for the comparison of $R\gamma_{GPP}^{int}$. Considering all 17 sites, the average RMSE (Table 5.2) of the model ensemble was 1.02 ± 0.34 % 100 mm^{-1}, ranging from 0.72 % 100 mm^{-1} using CASA to 1.98 % 100 mm^{-1} using VI. All models received the lowest discrepancy against flux $R\delta_{GPP}^{int}$ in the ENF ecosystem (average of 0.51 ± 0.28), followed by MF (average of 1.68 ± 0.45), EBF (average of 1.78 ± 1.11), DBF (average of 2.02 ± 0.40), and WET (average of 5.11 ± 1.13); additionally, the greatest divergence of $R\delta_{GPP}^{int}$ against the flux results appeared in the GRA ecosystem (average of 6.27 ± 3.35). BESS, MTE, TG, VI and MODIS estimated the negative effect of precipitation on GPP at more than 9 of the 17 sites, and BEPS, CASA, EC-LUE and CFix obtained larger positive precipitation effects than those from the calculation using flux measurements at more sites. At most sites, the $R\delta_{GPP}^{int}$ estimated by all the models was in accordance with that calculated using measurements. For all PFTs, BESS (-0.77, the unit of bias is % 100 mm^{-1}), CASA (+0.12), EC-LUE (-0.38) and VPM (-0.56) captured the relative optimal response of GPP to changes in precipitation; furthermore, CASA (-0.63), EC-LUE (-1.99), TG (-1.71), VI (-1.22) and VPM (-1.40) performed relatively better at MF sites. At GRA sites, BESS (-1.12), CFix (-4.47), CASA (-5.22), EC-LUE (-4.28) and VPM (-5.50) estimated the closest results to those of sites $R\gamma_{GPP}^{int}$. For ENF, MTE (-0.19), EC-LUE (-0.38) and VPM (-0.44) performed relatively well; the estimations of BESS (-2.73) and CASA (-3.05) were relatively better than those of other models in WET. For DBF, BESS (+2.21), AVM (+2.30) and TG (+2.29) belonged to the relatively good performing models; and with regard to EBF, AVM (+0.82), CASA (+0.80) and MODIS (+0.99) showed the optimal $R\gamma_{GPP}^{int}$. At MF and WET sites, all models underestimated the sensitivity of GPP to precipitation; in contrast, in deciduous forest ecosystems, the $R\gamma_{GPP}^{int}$ value estimated by all models were larger than the value calculated by using the site measurements, and the $R\delta_{GPP}^{int}$ estimated by different models in GRA ecosystem varied widely. Finally, only CASA overestimated the $R\delta_{GPP}^{int}$ at ENF sites. In general, for all PFTs, all models underestimated the average effect of precipitation on GPP, except for MTE, AVM, CASA and TG.

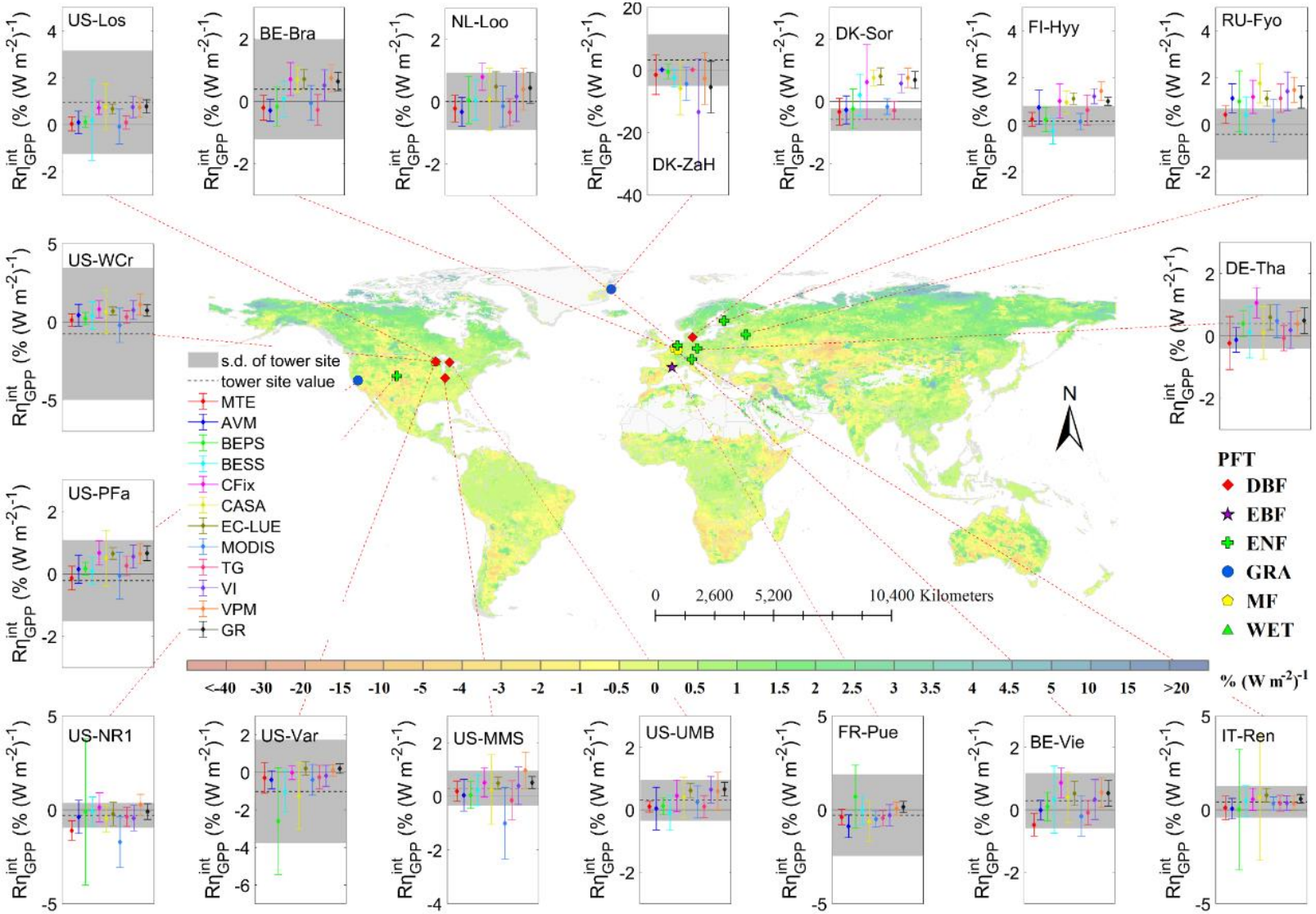

Figure 5.12 Comparisons of the observed relative response of GPP to radiation changes in EC flux towers (Table 5.3) and estimated relative response of GPP to interannual variation in radiation by 12 RS-based models for the period of 2000-2014.

In regard to $R\eta_{GPP}^{int}$ (Figure 5.12), the site results showed that increases in radiation would enhance the GPP at 10 of 17 sites, and except at the DK-ZaH site, the sign of $R\eta_{GPP}^{int}$ estimated by each model at any different site was consistent with that calculated by the corresponding site measurements. At more than 9 sites, MTE, AVM, MODIS and TG estimated negative response of GPP to radiation, but CFix, EC-LUE, VPM and GR obtained negative $R\eta_{GPP}^{int}$ at only one or two sites. Considering all 17 sites, the average RMSE (Table 5.2) of the model ensemble was 0.40 ± 0.22 % $(W\ m^{-2})^{-1}$, ranging from 0.21 % $(W\ m^{-2})^{-1}$ using CASA to 0.99 % $(W\ m^{-2})^{-1}$ using VI. In terms of the performance of models in each PFT: for MF, BESS (bias of 0.01 % $(W\ m^{-2})^{-1}$) had the strongest ability to capture the radiation effect; VI (-7.90) performed significantly worse at GRA sites; the estimations of BESS (+0.07), BEPS (0.21), MTE (-0.18) and MODIS (-0.17) were relatively better than those of other models at ENF sites; MTE (0.20) showed the optimal estimation at DBF sites; MODIS (-1.03) and MTE (-0.92) performed worst in WET; and for EBF, BEPS (+0.99) was the relatively poorest model for radiation sensitivity compared to the results calculated by using site measurements. For all the PFTs, we found VI (bias of -0.55 % $(W\ m^{-2})^{-1}$) showed the weakest performance for reflecting the sensitivity of GPP to variation in radiation. In addition, all models underestimated the effect of radiation on WET ecosystems; 5 of 12 models (i.e., MTE, AVM, BEPS, MODIS and TG) showed negative bias between the models' results and the flux results in the MF and DBF ecosystems. For GRA, only CFix and CASA overestimated the response of GPP to radiation changes; and in EBF ecosystems, apart from BEPS, BESS, VPM and GR, all models underestimated the $R\eta_{GPP}^{int}$.

Table 5.2 The RMSE of the sensitivity of GPP to climatic factors for each PFT (models' estimations vs. results calculated using flux measurements; Rγ, Rδ and $R\eta$ represent the sensitivity of GPP to temperature (% $°C^{-1}$), precipitation (% $100mm^{-1}$) and radiation (% $(W\ m^{-2})^{-1}$), respectively).

Model	Factor	All	MF	GRA	ENF	DBF	WET	EBF
MTE	γ	1.46[a]	1.98[b]	1.75[a]	1.84[a]	4.23[b]	12.79[b]	0.84[a]
	δ	0.97[b]	1.95[b]	5.84[b]	0.24[a]	2.01[b]	5.76[c]	1.56[b]
	η	0.31[a]	0.32[c]	2.41[b]	0.23[a]	0.24[a]	0.92[c]	0.10[a]
AVM	γ	1.95[c]	3.10[c]	6.53[b]	3.31[c]	4.50[b]	10.93[a]	2.78[c]
	δ	1.01[b]	1.67[b]	6.92[b]	0.51[b]	1.67[a]	4.84[b]	0.82[a]
	η	0.24[a]	0.28[b]	1.61[a]	0.30[b]	0.32[b]	0.86[b]	0.59[b]
BEPS	γ	2.04[c]	2.23[b]	7.60[c]	3.50[c]	4.48[b]	12.69[b]	0.41[a]
	δ	1.27[c]	2.01[b]	7.85[b]	1.31[c]	2.14[b]	5.39[c]	4.52[c]
	η	0.28[a]	0.23[b]	2.03[a]	0.24[a]	0.27[b]	0.84[b]	0.99[c]
BESS	γ	1.49[a]	2.27[b]	3.52[a]	1.57[a]	3.33[a]	16.33[b]	3.19[b]
	δ	0.81[a]	2.78[c]	3.59[a]	0.65[c]	1.58[a]	2.73[a]	2.51[b]
	η	0.36[b]	0.15[b]	2.86[b]	0.16[a]	0.37[b]	0.76[b]	0.25[a]
CFix	γ	1.99[c]	2.03[b]	4.21[a]	3.09[c]	4.79[c]	11.31[a]	
	δ	0.81[b]	1.86[b]	4.47[a]	0.54[b]	2.04[b]	4.60[b]	
	η	0.22[a]	0.37[c]	1.00[a]	0.35[c]	0.50[c]	0.23[a]	
CASA	γ	1.85[b]	2.11[b]	7.26[b]	2.39[b]	5.27[c]	8.69[a]	3.03[c]
	δ	0.73[a]	1.02[a]	3.69[a]	0.53[b]	2.09[b]	3.05[a]	0.80[a]
	η	0.57[b]	0.26[b]	4.56[b]	0.39[a]	0.49[c]	0.19[c]	0.33[b]
EC-	γ	1.79[b]	2.19[b]	5.42[b]	2.09[b]	4.64[c]	12.13[b]	
LUE	δ	0.77[a]	1.52[a]	4.28[a]	0.32[a]	1.95[b]	5.56[c]	
	η	0.21[a]	0.32[c]	1.23[a]	0.32[b]	0.51[c]	0.28[a]	
MODIS	γ	1.94[c]	2.25[b]	9.99[c]	2.39[b]	3.20[a]	16.58[c]	1.03[a]
	δ	1.09[b]	1.64[b]	5.41[b]	0.49[b]	3.15[c]	5.85[c]	0.99[a]
	η	0.48[b]	0.23[b]	3.85[b]	0.26[a]	0.37[c]	1.03[c]	0.21[a]
TG	γ	1.89[b]	3.19[c]	6.77[b]	2.96[c]	3.44[a]	15.23[c]	4.14[c]
	δ	1.02[b]	1.44[a]	6.93[b]	0.44[b]	1.65[a]	5.96[c]	1.68[b]
	η	0.24[a]	0.30[c]	1.62[a]	0.28[b]	0.31[b]	0.85[b]	0.16[a]
VI	γ	1.55[b]	1.52[a]	3.00[a]	2.15[b]	4.01[b]	14.39[b]	1.44[b]
	δ	1.98[c]	1.24[a]	15.89[c]	0.36[b]	2.00[b]	5.84[c]	1.13[b]
	η	1.00[c]	0.26[b]	8.33[c]	0.36[c]	0.48[c]	0.20[a]	0.00[a]
VPM	γ	1.86[b]	1.51[a]	8.39[c]	2.53[b]	4.11[b]	13.88[b]	0.83[a]
	δ	0.79[a]	1.41[a]	3.92[a]	0.26[a]	1.97[b]	5.66[c]	1.89[b]
	η	0.41[b]	0.32[c]	3.01[b]	0.40[c]	0.60[c]	0.21[a]	0.34[b]
GR	γ	1.69[b]	1.99[b]	6.59[b]	1.94[a]	4.28[b]	13.55[b]	1.42[b]
	δ	1.02[b]	1.58[b]	6.44[b]	0.45[b]	2.05[b]	6.08[c]	1.84[b]
	η	0.54[b]	0.31[c]	4.38[b]	0.31[b]	0.50[c]	0.18[a]	0.44[b]

Superscripts are the levels of model performance determined by natural break method:
[a:] relatively good
[b:] medium
[c:] relatively poor

Table 5.3 A list of the FluxNet sites used in Chapter 1 and this chapter.

ID	Name	PFT	Lat (°)	Lon (°)	Alt (m)	MAT (℃)	MAP (mm)	Period
1	AU-Tum	EBF	-35.66	148.15	1200	10.7	1159	2001-2013
2	BE-Bra	MF	51.31	4.52	16	9.8	750	2000-2014
3	BE-Vie	MF	50.31	6.00	493	7.8	1062	2000-2014
4	CA-Gro	MF	48.22	-82.16	340	1.3	831	2003-2014
5	CA-TP1	ENF	42.66	-80.56	265	8.0	1036	2003-2014
6	CA-TP3	ENF	42.71	-80.35	184	8.0	1036	2003-2014
7	DE-Hai	DBF	51.08	10.45	430	8.3	720	2000-2012
8	DE-Tha	ENF	50.96	13.57	380	7.7	820	2000-2014
9	DK-Sor	DBF	55.49	11.64	40	8.2	660	2000-2014
10	DK-ZaH	GRA	74.47	-20.55	38	-9	211	2000-2014
11	FI-Hyy	ENF	61.85	24.30	181	3.8	709	2000-2014
12	FR-Pue	EBF	43.74	3.60	270	13.5	883	2000-2014
13	IT-Lav	ENF	45.96	11.28	1353	7.8	1291	2003-2014
14	IT-Ren	ENF	46.59	11.43	1730	4.7	809	2000-2013
15	IT-SRo	ENF	43.73	10.28	6	14.2	920	2000-2012
16	NL-Loo	ENF	52.17	5.74	25	9.8	786	2000-2014
17	RU-Fyo	ENF	56.46	32.92	265	3.9	711	2000-2014
18	RU-Sam	GRA	72.37	126.50	-	-	-	2003-2014
19	US-ARM	CRO	36.61	-97.49	314	14.8	843	2001-2014
20	US-Ha1	DBF	42.54	-72.17	340	6.6	1071	2000-2012
21	US-Los	WET	46.08	-89.98	480	4.1	828	2000-2014
22	US-Me2	ENF	44.45	-121.56	1253	6.3	523	2003-2014
23	US-MMS	DBF	39.32	-86.41	275	10.9	1032	2000-2014
24	US-Ne1	CRO	41.17	-96.48	361	10.1	790	2002-2013
25	US-Ne2	CRO	41.16	-96.47	362	10.1	789	2002-2013
26	US-Ne3	CRO	41.18	-96.44	363	10.1	784	2001-2013
27	US-NR1	ENF	40.03	-105.55	3050	1.5	800	2000-2014
28	US-PFa	MF	45.95	-90.27	470	4.3	823	2000-2014
29	US-Ton	WSA	38.43	-120.97	177	15.8	559	2001-2014
30	US-UMB	DBF	45.56	-84.71	234	5.8	803	2000-2014
31	US-Var	GRA	38.41	-120.95	129	15.8	559	2000-2014
32	US-WCr	DBF	45.81	-90.08	520	4.0	787	2000-2014
33	ZA-Kru	SAV	-25.02	31.50	359	21.9	547	2000-2013

5.4 Discussions

5.4.1 The CO_2 fertilization effect in RS-based models

Three models, i.e., BESS, BEPS and CFix, require the atmospheric CO_2 concentration as an input to estimate GPP; therefore, Eq-5.3 (i.e., the control variable method) can be used to determine the pure effect of elevated CO_2 concentration on GPP. I found that the $\beta_{\mathrm{GPP}}^{int}$ values estimated using Eq-5.2 (hereafter represented by $\beta 1$) were larger than the β values estimated using Eq-5.3 (hereafter represented by $\beta 2$), which considered only the rising atmospheric CO_2 concentration. This result was consistent with the research conducted by Piao et al (2013), in which they used the 10 DGVMs from Trendy to calculate the β_{GPP} effect on global terrestrial GPP during the period of 1982-2010, which was longer than the period used in this study. The authors attributed this circumstance to $\beta 1$ in the Tropics, where the hydrothermal conditions are more suitable for vegetation growth, which contributes more to the overall effect; furthermore, the linear regression approach did not replicate the intricate nonlinear complexity of the carbon cycle (Piao et al., 2013). By contrast, in the present study, the more detailed latitudinal β distribution was used to compare the difference between the two methods, and I found that in the Tropics and in most parts of the Northern Hemisphere, $\beta 1$ was generally larger than $\beta 2$; however, the Southern Hemisphere had the opposite situation. Because the continental vegetation coverage is much larger in the Northern Hemisphere than that in the Southern Hemisphere, $\beta 2$ was lower than $\beta 1$. BESS and BEPS, belonging to RS-based process models, require the atmospheric CO_2 concentration to be input, as this value adjusts the photosynthesis rate by influencing stomatal conductance (Buckley 2017). Simultaneously, the two models also express another part of the CO_2 fertilization effect from VIs (Smith et al., 2015) or fAPAR (De Kauwe et al., 2016). LAI, which is closely related to fAPAR, was also the driving factor for running BESS and BEPS, and the rising atmospheric CO_2 concentration increased LAI, which had already been reported by scholars (Donohue et al., 2013; Devaraju et al., 2016). Therefore, in BESS and BEPS for the greener and greener Earth, $\beta 2$ is supposed to be lower than $\beta 1$. Generally, LUE models assume that CO_2 affects GPP solely through changes in the observed fAPAR (calculating fAPAR by the relationship with VIs) (Tucker et al., 1986); however, for CFix, one LUE model, it also introduces an individual CO_2 fertilization effect module that requires inputting the atmospheric CO_2 concentration and comparing the current CO_2 concentration level with the reference level to determine the degree of the CO_2 fertilization effect (Veroustraete et al., 1994). Therefore, CFix estimated that $\beta 2$ was lower than $\beta 1$ and had the highest $\beta 1$ value among the LUE models. From the monthly distribution of β_{GPP}, it was found that the amplitude of the intra-annual cycle of $\beta 2$ was gentler than that of $\beta 1$, especially when the vegetation in the Northern Hemisphere enters the summer growing season. This result can be partly explained by the fact that during boreal summer, the hydrothermal conditions for vegetation growing are adequate, and the interaction between the climatic factors and CO_2 will be more apparent than the single effect of CO_2 (Zhang et al., 2016; Sun et al., 2018a). It can be seen from the global distributions of R$\beta 1$ and R$\beta 2$ (Figure 7) that a significant discrepancy appeared in the arid areas, where R$\beta 1$ occasionally had negative values. It is hard to conclude that the negative value is not sound because $\beta 1$ represents the comprehensive response of GPP to the variation in CO_2, including its interaction with climatic factors. Hotter and dryer climatic conditions resulting from increasing atmospheric CO_2 concentrations are known to increase vegetation moisture stress and reduce productivity (Donohue et al., 2013; Poulter et al., 2014; Ahlstrom et al., 2015; Williams et al., 2013; Smith et al., 2016). Therefore, although theoretically an increasing atmospheric CO_2 concentration could drive an increase in water-use efficiency (Lawlor et al., 1991), the final effects of CO_2 on GPP could decrease or be negative if the negative effects of moisture stress are larger than the positive effects of CO_2 fertilization,

particularly in arid ecosystems (Smith et al., 2015; Zhang et al., 2016). This result has been proven in field experiments by Reich et al (2014), who showed that the positive effect of the increasing CO_2 concentration on productivity was apparent in wet years but not in years when moisture constraints were relatively strong. This result can also be seen in Figure 5.13; During the relatively dryer year in the semi-arid grassland, there was a negative GPP response to CO_2. This result was due to the positive effect of CO_2 on GPP being offset by the negative interaction among the environmental, meteorological and edaphic factors (Smith et al., 2015). The spatial distribution of the negative areas was consistent with the areas where the interactive effect was strongest (Zhang et al., 2016). In addition, the factor, the magnitude and the duration of the CO_2 fertilization effect on GPP are thought to be constrained by nutrient availability, specifically the availability of nitrogen (N) and phosphorus (P), which play critical roles in regulating plant photosynthesis and growth (Norby et al., 2010; Oren et al., 2001) and are represented by VIs (Song et al., 2013; Fisher et al., 2012) using Eq-5.2 but are missing in Eq-5.3. At the relatively humid two European sites, most models overestimated the response of GPP to CO_2 compared to the FACE results. One reason for this result is the mismatched footprint size (Pasetto et al., 2018); another reason is likely to be the saturating response to CO_2 (De Kauwe et al., 2016), which means that the $\beta 2$ was estimated by the RS models that ranged from a relatively low CO_2 concentration. This condition would result in more efficient and larger values than the β calculated from the higher CO_2 concentration ranges in the FACE experiments (Franks et al., 2013). Several scholars have suggested that the comparison of satellite and FACE estimates of CO_2 fertilization is invalid (De Kauwe et al., 2016), but due to the absence of true values of β, using the limited FACE experiments might be the next-best option for analyzing and comparing the β values of models. In addition, it should be noted that the β values at the FACE sites were calculated by physiological and ecological models driven by the inputs of the observed data because GPP cannot be measured or obtained directly (Ryan et al., 2017; Bachman et al., 2010; Schafer et al., 2003; Luo et al., 2001; Wittig et al., 2005; Gielen et al., 2005), and the sensitivity of each model to external factors seriously affects the accuracy. Furthermore, the nutrient constraints and the vegetation physiological response may represent a transient phenomenon that becomes more apparent with time due to the depletion of soil nutrients and the physiological adaptation (De Kauwe et al., 2016); therefore, the results obtained from a longer-running experimental site could be more convincing. Alternatively, when we accepted that GPP was approximately twice the magnitude as the value of NPP (Waring et al., 1998) that could be measured directly in field experiments, we found that the β value estimated by most models were basically within the range calculated at the two longest-running forest FACE sites, i.e., Oak Ridge (average of 17.7 %, ranging from 10.2 % to 34.6 % during 1998-2008) and Duke (average of 27.2 %, ranging from 7.7 % to 41.9 % during 1996-2007) (De Kauwe et al., 2016).

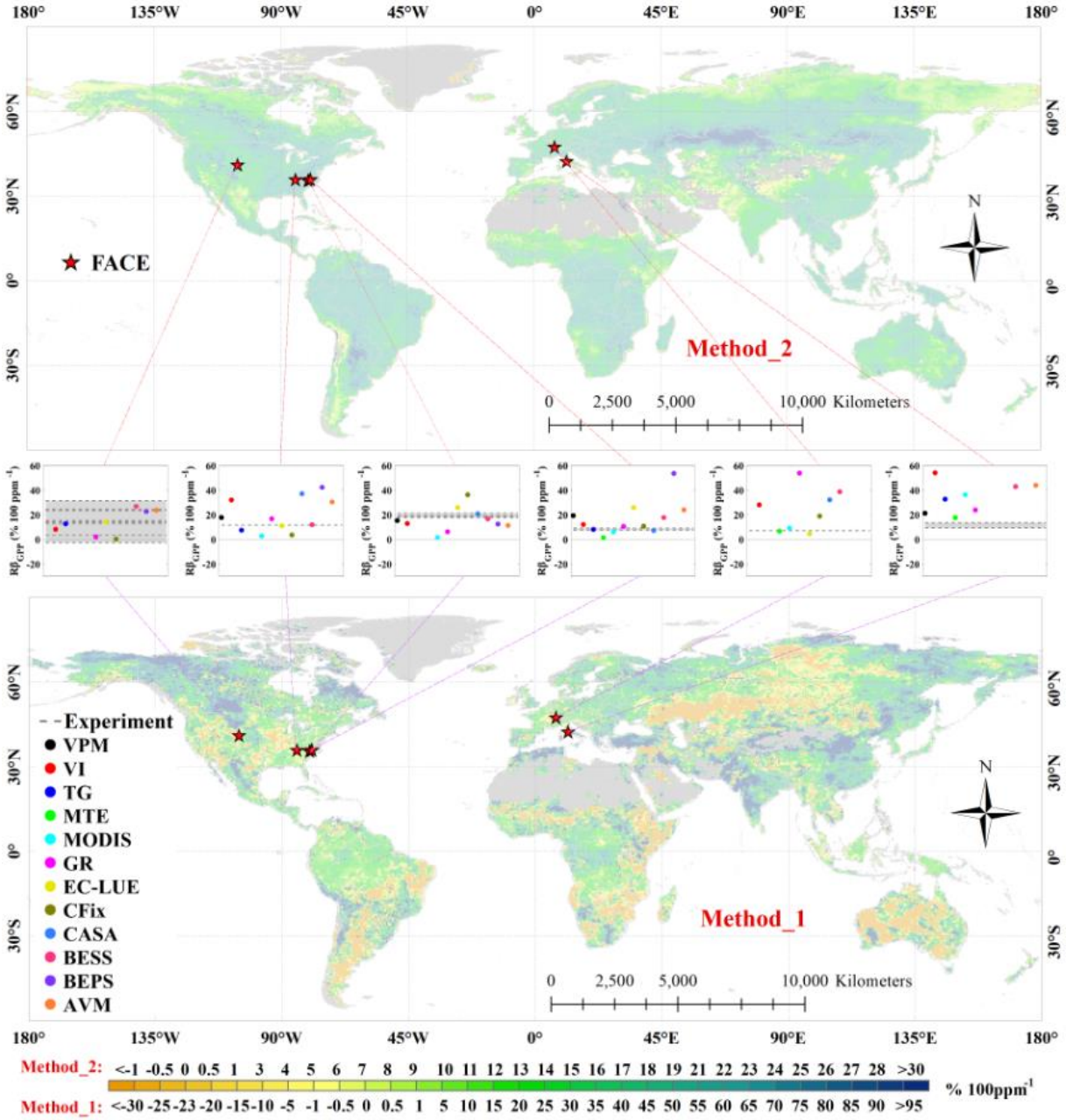

Figure 5.13 Comparisons of the observed relative response of GPP to rising atmospheric CO_2 concentration at the FACE experimental sites (Table 5.4) and the estimated relative response of GPP to rising atmospheric CO_2 by 12 RS-based models for the period of 2000-2014.

Table 5.4 The list of Free Air CO_2 enrichment experiments sites.

ID	1	2	3	4	5	6	7
LAT	42.37	41.14	35.58	35.97	35.9	35.9	47.47
LON	11.80	-104.82	-79.8	-79.08	-84.3	-79.1	7.5
Vegetation Type	Broadleaf Forest	Semi-arid Grassland	Needleleaf Forest	Needleleaf Forest	Broadleaf Forest	Needleleaf Forest	Mixed deciduous Forest
References	Wittig et al. (2005) Gielen et al. (2005)	Ryan et al. (2017) Bachman et al. (2010)	Luo et al. (2001)	Schäfer et al. (2003)	Wullschleger et al. (2002)	Hamilton et al. (2002)	Fatichi et al. (2013)

5.4.2 Comparison of models

Although satellite data are used by all models, the principles, parameters, structures and driving variables of VI-, LUE-, process- and ML-based models vary widely (Keenan et al., 2012; Song et al., 2013; Pasetto et al., 2018). It must be noted that some models may overly assume the meaning represented by VIs (Wang et al., 2012; Baret et al., 1991; Silleos et al., 2006; Yang et al., 2013; Watham et al., 2017). For example, AVM utilizes the enhanced vegetation index (EVI), the partial and indirect expression of water effects (Wu et al., 2010; Watham et al., 2017; Lees et al., 2018), as a moisture constraint combined with temperature to estimate GPP, which would hyper-respond to temperature, especially in areas with adequate thermal resources (Li et al., 2016) (e.g., rainforest); thus, this method would not be suitable for use at the global scale. Meanwhile, rainforests that have high temperatures throughout the year contribute most to the global GPP, and rainforests are significantly affected by the CO_2 fertilization effect; thus, β would be overestimated to a certain extent in AVM (Ryan et al., 2017). For a similar reason, apart from the models considering the CO_2 fertilization effect, using TG, which is based on EVI and land surface temperature (LST) (Sims et al., 2008), to estimate productivity is next only to AVM, followed by VI, in which the productivity is estimated using the multiplication of LUE and fAPAR (both of which are affected by CO_2) (Wu et al., 2010). GR, also a VI-based model, does not directly respond to temperature and only utilizes EVI as the proxy of the CO_2 effect (Yang et al., 2013); therefore, the sensitivity to CO_2 is lower than that in the other VI models. On the other hand, as the result of both the direct and the indirect radiation-influencing parameters that are introduced in GR (Gao et al., 2014), the effect of radiation on GPP would be relatively high, which is demonstrated by Figure 5.5. The sensitivity to radiation in GR is only lower than that in BESS, which also considers the effect of diffuse radiation, which is more effective than beam radiation on GPP, particularly during cloudy days (Ryu et al., 2011; Song et al., 2013; Jiang et al., 2016). For MODIS and MTE, studies have reported that these models are not suitable for interannual variation and trend benchmarking (Kelley 2013; Li et al., 2016), especially in terms of assessing the CO_2 fertilizer effects, because almost no apparent response to the rising atmospheric CO_2 concentration in the two models leads to an underestimated trend (Anav et al., 2015). Theoretically, the calculation of fAPAR is an expression of the effect from the CO_2 fertilization in the MODIS algorithm and MTE (Smith et al., 2016; De Kauwe et al., 2016). However, the calculation of fAPAR in MODIS is based on the LAI, which is estimated using different PFT-classifying schemes (Yan et al., 2016; Pasetto et al., 2018). There is a total of 29 variables in the MTE algorithm, most of which are environmental factors; additionally, there are complex linear and nonlinear coupled relationships among the various parameters (Beer et al., 2010; Jung et al., 2011). Finally, the weight of fAPAR cannot be determined and would be slight. What is more important is that the CO_2 data and fertilization effect were not used in the initial calibration of the model algorithms (Graven et al., 2013; Thomas et al., 2016; Prentice et al., 2017). For the models considering the CO_2 effect, i.e., BESS, CFix and BEPS, the β values of the latter two would be significantly higher than that in BESS; the empirical response function in CFix is based on the influences on the photosynthetic rate from the increasing CO_2 concentration (Veroustraete et al. 1994 2002) via the FvCB (Farquhar and von Caemmerer 1982) model measured at saturated light intensity (De Kauwe et al., 2016b); but in typical daytime field conditions the Rubisco-limited rate more steeply determines the photosynthetic rate than does the radiation-limited rate (Maire et al., 2012), as well as the β effect that is implied in fAPAR and calculated by the normalized difference vegetation index (NDVI); thus, CFix is over-sensitive to increasing CO_2 concentrations (Prentice et al., 2017). BEPS overestimates β because the influences of the CO_2 concentration on both stomatal conductance and fAPAR are considered in the algorithm, but double VIs, LAI and NDVI introduced in the model will cause the overlapping CO_2 effect on

fAPAR. Only VPM has a negative η_{GPP}^{int} effect (Figure 5.2), and it is easy to find that the negative responses in the Tropics and sub-tropics during the dry seasons (Figure 5.13) lead to a negative global overall effect. Studies (Poulter et al., 2009; Souza et al., 2013; Yang et al., 2013) have proven that during the dry season, due to influences from deep SM, GPP will reach its maximum. However, the LSWI is utilized in VPM to represent water stress and would be inconsistent with the EVI enhanced by deep SM (Poulter et al., 2009; Souza et al., 2013), which would lead to underestimating the GPP during the dry season. Furthermore, the wavelength bands selected to calculate the LSWI can hardly be absorbed by atmospheric vapor (Song et al., 2013; Zhang et al., 2015); thus, it cannot be utilized to assess the situation of atmospheric moisture (Lees et al., 2018) and can only represent the water content in the canopy, particularly in the leaves, which decreases during the dry season. In the Tropics, the sensitivity of the models to temperature varies widely (Yang et al., 2013; Zhang et al., 2016; Wu et al., 2017). First, RS data in the Tropics are inferior in quality, and the available rate does not reach half (Wu et al., 2017). Second, the non-periodic variation in VIs cause the relationship of GPP-VI to not be as obvious as that with temperate (Wu et al., 2010; Keenan et al., 2012); additionally, the corrections of all the models were conducted at flux tower sites that were concentrated in the mid-high latitudes of the Northern Hemisphere and rarely in the Tropics. These conditions may be uncertainties and disadvantages that result in the responsiveness of models in the Tropics to be insufficient (Wei et al., 2017; Tagesson et al., 2017; Prentice et al., 2017; Ito et al., 2017). The spatial continuity of sensitivity to precipitation is not significant (Yan et al., 2015), except in regions with high water stress (e.g., western North America, Australia, South Africa) and vary among models. One reason for this result is because precipitation data are not required to run the models, and second, the expression of moisture constraint varies among models (Yuan et al., 2014; Lees et al., 2018). The moisture constraint item in AVM, GR and VI is implied by the EVI (Wu et al., 2010; Song et al., 2013; Lees et al., 2018), which will represent leaf color changes caused by variations in moisture stress (Song et al., 2013). However, the EVI represents the greenness rather than the productivity, and the situation in which water conditions have caused photosynthesis but not yet caused EVI changes (Song et al., 2013; Lees et al., 2018) has insinuated that the EVI has insufficient emergency responses to short-term and rapid water stress changes (Yang et al., 2013; Joiner et al.., 2018). Additionally, in addition to VIs, introducing the non-universal indicators to reinforce the effect of water could also cause the over (or under)-estimation of δ_{GPP} to some extent (Li et al., 2013; Song et al., 2013; Zhang et al., 2015; Lees et al., 2018). For example, TG always overestimated δ_{GPP}. Because LST had low accuracy during cloudy days (Wan et al., 2008; Wu et al., 2010; Watham et al., 2017); but when the cloud coverage is low, the vegetation coverage will be lower (during the dry season (Vourlitis et al., 2008)), and LST could be seriously affected by the soil (Yang et al., 2013; Sun et al.,2016; Lees et al., 2018). MODIS, BESS and BEPS (Ryu et al., 2011; Jiang et al., 2016; Zhang et al., 2018) mainly rely on vapor pressure deficit (VPD) as an important variable to balance the atmospheric demand for water vapor (Hu et al., 2018) on GPP to express water stress (Leuning et al., 2005). However, the spatial distribution of VPD and the available water resources for plants are not consistent (Song et al., 2013; Lees et al., 2018) and are very sensitive to temperature variations (Nemani et al., 2002; Yuan et al., 2014). Therefore, as long as the model contains VPD, even if the external water resources are sufficient, there will be some degree of moisture pressure during summer (Hashimoto et al., 2013; Yan et al., 2015). For BESS, moreover, the considered VPD was calculated by the temperature that was estimated by considering the longwave radiation from the soil and atmosphere and the heat generated by photosynthesis (Ryu et al., 2011; Jiang et al., 2016); therefore, BESS is significantly sensitive to both temperature and water. From the perspective of demand theory (Churkina et al., 1999), the expressions of water stress in EC-LUE and CASA belong to the proxy of energy exchange (Garbulsky et al., 2010;Yan et al., 2015), reflecting the exchange of hydrothermal flux between

the soil and atmosphere (Yan et al., 2015). However, it is difficult to accurately estimate ET (Yuan et al., 2010; Mu et al., 2013; Yang et al., 2013; Hu et al., 2018), and in the CASA model, the water limitation is permanently greater than 0.5(Poulter et al., 2009; Wu et al., 2010; Souza et al., 2013; Song et al., 2013; Yuan et al., 2014; Zhang et al., 2016; Hu et al., 2018). Only CFix and BEPS introduce the SM, which is an important indicator used to assess the water stress on GPP. However, CFix considers the SM and atmospheric moisture circumstances to have an equal influence on photosynthesis (Veroustraete et al., 2002), which in reality not (Yuan et al., 2014; Zhang et al., 2016; Hu et al., 2018; Lees et al., 2018). The uncertainty in BEPS is relatively complex (Yang et al., 2013; Zhang et al., 2015): theoretically, the combination of the VPD and SM should produce a better estimation of GPP (Zhang et al., 2015; Lees et al., 2018); however, because the VIs are introduced in the algorithm, BEPS may be oversensitive to water stress (Li et al., 2013; Lees et al., 2018), and multiple factors may also neutralize the effect of one another. In general, most models do not consider SM or use VI as a proxy of SM (Prentice et al., 2017; Hu et al., 2018), and none of the models correctly indicate drought stress (Wu et al., 2010; Garbulsky et al., 2010; Schaefer et al., 2012; Yuan et al., 2014; Hu et al., 2018); the disadvantages and advantages of each model under different external conditions are different (Wang et al., 2012; Yang et al., 2013; Yuan et al., 2014), and the applicability of each is also inconsistent (Garbulsky et al., 2010; Yang et al., 2013).

5.4.3 Uncertainty analysis

The method used in this chapter is based on one assumption: sensitivity is more accurate when there is less interaction between variables. It has been demonstrated that the interaction is overall less than 7 % at the global level (Zhang et al., 2016), but in some regions, the interaction could be 35 % or larger (Wu et al., 2017; Zhang et al., 2016). Therefore, special attention is required in the interpretation of the spatial distribution of the sensitivity in the models.

From the original studies of the models, it is evident that GPP data measured using the EC technique at the limited number of sites (Schaefer et al., 2002; Wei et al., 2017) concentrated in the Northern hemisphere are required by nearly all models to accurately calibrate the conversion coefficient (m) (Li et al., 2013; Liu et al., 2014), light use efficiency (ε) (Yuan et al., 2014; Zhang et al., 2015) and the maximum rate of carboxylation (V_{max}) (Jiang et al., 2016; Zhang et al., 2018), which are the basis of GPP estimation via VI-, LUE- and Process-based methods, respectively. In natural ecosystems, V_{max}, m and ε are determined by a wide variety of biological, biophysical, and environmental parameters (Li et al. 2007), and the same ecosystem may have different values (Tagesson et al., 2017). Furthermore, the variable measured by the EC tower is NEE instead of GPP, and the latter is estimated by the simplified model of the real process involving numerous assumptions and judgments that will bring many hidden uncertainties to the model (Loescher et al., 2006).

Inputting the different climate datasets to run the same model will induce an overall global uncertainty of 9 % (Wu et al., 2017); if inputting combined climate variables from different datasets, the uncertainty can be larger than 30 %, which is even greater than the uncertainty of the model itself (Wu et al., 2017; Blyth et al., 2011; Zhao et al., 2006). All the meteorological data used in this study were obtained from MERRA-2, while the soil moisture data and other related data were derived from different datasets, which introduces some errors. I directly used the MET-GPP product developed by Jung et al (2011), which is based on the CRU dataset, so the uncertainty in the sensitivity analysis of MTE would be higher than that of the other models. All the RS data and products used in this study were from MODIS; thus, to some extent, the uncertainty caused by the different sensors should be reduced. However, RS data only represent the underlying surface state when the satellite passes, rather than the average for a certain period of time (Li et al., 2013; Yuan et al., 2014; Wu et al., 2010). The low quality of RS data will also introduce some uncertainties (Yang et al., 2013; Yuan et al., 2014; Li et al., 2016; Sun et al., 2016), particularly in terms of cloud contamination in the Tropics (Hilker et al., 2012), and the low solar angles and extended periods of darkness at high latitudes can affect the reflectance readings from the optical MODIS sensor (Beck et al., 2006).

Studies have shown that the qualitative analysis that compares the RS results with the site results is meaningful, while the spatial patterns and quantitative analysis are not sufficiently accurate (Pasetto et al., 2018). Therefore, the uncertainty introduced by the scale effect should be considered for the comparative evaluation of the sensitivity of the models at the site scale. In the preparatory stage of the spatial datasets, all the data should be resampled into the same spatial resolution and coordinate system, but different gap-filling methods, diversity and complex biophysical environments, mixed pixels and spatial heterogeneity may interactively affect model performance (Benz et al., 2004; Pasetto et al., 2018).

Finally, it should be noted that the main focus of this chapter was to compare and evaluate the differences in responses to climatic variability and increasing atmospheric CO_2 concentrations in the models, and the best performances of these models might be reached

through utilizing model-dependent parameter values and driving datasets from the original publications.

5.5 Conclusions

In this chapter, I evaluated and compared the sensitivity of GPP estimated by 12 RS-based GPP models and benchmarked these estimates against the GPP responses to climatic factors measured at flux tower sites and to elevated CO_2 concentrations measured at FACE experimental sites. The comparison among models and the comparison of models against observations helps document their strengths and weaknesses under current conditions and can also identify heuristic constraints about their applicable conditions and scopes. I report the following main conclusions: Regarding the GPP trend, the models with the relatively higher sensitivity to increasing atmospheric CO_2 concentrations (e.g., BEPS, AVM, TG, CFix and BESS) show more significant trends. Through the analysis of the response to increasing atmospheric CO_2 concentrations, considering only the effect of variation in CO_2 concentrations on photosynthesis without considering the CO_2 fertilization effect on the greenness index, LUE or fAPAR will underestimate the sensitivity of models to CO_2, and vice versa. Compared with the results from the FACE experiment, models will easily overestimate the CO_2 fertilization effect when the CO_2 saturation effect and environmental limitations, such as moisture, are not considered. At the global scale, the overall effects of temperature and radiation among different models have differences in magnitude and even in sign, while models were relatively consistent in their response to variations in precipitation, although the expressions of the water effect in different models were different. The spatial differences in response to climatic factors among models were mainly reflected in the Tropics where the highest uncertainty existed. At high latitudes, all models had a consistent and obvious positive response to temperature and radiation, while precipitation showed the most significant positive effect on GPP in the mid-latitudes. Although the models' estimations are basically within the confidence intervals of the sensitivities to climatic factors calculated by measurements at the flux sites, none of the models consistently reproduced the optimal ability to capture climatic stress across the different sites, indicating that for a site and a given model, there were large factor-to-factor differences in estimation accuracy.

Although there are various uncertainties, the optimal response model varies across ecosystems and affecting factors.

References

Ahlstrom, A.; Raupach, M.R.; Schurgers, G.; Smith, B.; Arneth, A.; Jung, M.; Reichstein, M.; Canadell, J.G.; Friedlingstein, P.; Jain, A.K., et al. The dominant role of semi-arid ecosystems in the trend and variability of the land CO_2 sink. *Science* **2015**, *348*, 895-899.

Alton, P.B.; Ellis, R.; Los, S.O.; North, P.R. Improved global simulations of gross primary product based on a separate and explicit treatment of diffuse and direct sunlight. *J Geophys Res-Atmos* **2007**, *112*.

Anav, A.; Friedlingstein, P.; Beer, C.; Ciais, P.; Harper, A.; Jones, C.; Murray-Tortarolo, G.; Papale, D.; Parazoo, N.C.; Peylin, P., et al. Spatiotemporal patterns of terrestrial gross primary production: A review. *Reviews of Geophysics* **2015**, *53*, 785-818.

Ardö, J. Comparison between remote sensing and a dynamic vegetation model for estimating terrestrial primary production of Africa. *Carbon balance and management* **2015**, *10*, 8.

Bachman, S.; Heisler-White, J.L.; Pendall, E.; Williams, D.G.; Morgan, J.A.; Newcomb, J. Elevated carbon dioxide alters impacts of precipitation pulses on ecosystem photosynthesis and respiration in a semi-arid grassland. *Oecologia* **2010**, *162*, 791-802.

Bachman, S.; Heisler-White, J.L.; Pendall, E.; Williams, D.G.; Morgan, J.A.; Newcomb, J. Elevated carbon dioxide alters impacts of precipitation pulses on ecosystem photosynthesis and respiration in a semi-arid grassland. *Oecologia* **2010**, *162*, 791-802.

Bai, W.; Wan, S.; Niu, S.; Liu, W.; Chen, Q.; Wang, Q.; Zhang, W.; Han, X.; Li, L. Increased temperature and precipitation interact to affect root production, mortality, and turnover in a temperate steppe: implications for ecosystem C cycling. *Global change biology* **2010**, *16*, 1306-1316.

Ballantyne, A.P.; Alden, C.B.; Miller, J.B.; Tans, P.P.; White, J.W.C. Increase in observed net carbon dioxide uptake by land and oceans during the past 50 years. *Nature* **2012**, *488*, 70.

Baret, F.; Guyot, G. Potentials And Limits Of Vegetation Indexes for Lai And Apar Assessment. *Remote Sensing Of Environment* **1991**, *35*, 161-173.

Beck, P.S.; Atzberger, C.; Høgda, K.A.; Johansen, B.; Skidmore, A.K. Improved monitoring of vegetation dynamics at very high latitudes: A new method using MODIS NDVI. *Remote sensing of Environment* **2006**, *100*, 321-334.

Beer, C.; Reichstein, M.; Tomelleri, E.; Ciais, P.; Jung, M.; Carvalhais, N.; Rodenbeck, C.; Arain, M.A.; Baldocchi, D.; Bonan, G.B., et al. Terrestrial gross carbon dioxide uptake: global distribution and covariation with climate. *Science* **2010**, *329*, 834-838.

Benz, U.C.; Hofmann, P.; Willhauck, G.; Lingenfelder, I.; Heynen, M. Multi-resolution, object-oriented fuzzy analysis of remote sensing data for GIS-ready information. *ISPRS Journal of photogrammetry and remote sensing* **2004**, *58*, 239-258.

Best, M.J.; Pryor, M.; Clark, D.B.; Rooney, G.G.; Essery, R.L.H.; Menard, C.B.; Edwards, J.M.; Hendry, M.A.; Porson, A.; Gedney, N., et al. The Joint UK Land Environment Simulator (JULES), model description - Part 1: Energy and water fluxes. *Geoscientific Model Development* **2011**, *4*, 677-699.

Blyth, E.; Clark, D.B.; Ellis, R.; Huntingford, C.; Los, S.; Pryor, M.; Best, M.; Sitch, S. A comprehensive set of benchmark tests for a land surface model of simultaneous fluxes of water and carbon at both the global and seasonal scale. *Geoscientific Model Development* **2011**, *4*, 255-269.

Bonan, G.B.; Doney, S.C. Climate, ecosystems, and planetary futures: The challenge to predict life in Earth system models. *Science* **2018**, *359*, eaam8328.

Bondeau, A.; Smith, P.C.; Zaehle, S.; Schaphoff, S.; Lucht, W.; Cramer, W.; Gerten, D.; Lotze-Campen, H.; Muller, C.; Reichstein, M., et al. Modelling the role of agriculture for the 20th century global terrestrial carbon balance. *Global Change Biology* **2007**, *13*, 679-706.

Buckley, T.N. Modeling stomatal conductance. *Plant physiology* **2017**, *174*, 572-582.

Chang, J.; Ciais, P.; Viovy, N.; Vuichard, N.; Herrero, M.; Havlík, P.; Wang, X.; Sultan, B.; Soussana, J.F. Effect of climate change, CO_2 trends, nitrogen addition, and land-cover and management intensity changes on the carbon balance of European grasslands. *Global change biology* **2016**, *22*, 338-350.

Chang, J.F.; Ciais, P.; Wang, X.H.; Piao, S.L.; Asrar, G.; Betts, R.; Chevallier, F.; Dury, M.; Francois, L.; Frieler, K., et al. Benchmarking carbon fluxes of the ISIMIP2a biome models. *Environmental Research Letters* **2017**, *12*.

Cheng, L.; Zhang, L.; Wang, Y.-P.; Canadell, J.G.; Chiew, F.H.; Beringer, J.; Li, L.; Miralles, D.G.; Piao, S.; Zhang, Y. Recent increases in terrestrial carbon uptake at little cost to the water cycle. *Nature communications* **2017**, *8*, 110.

Churkina, G.; Running, S.W.; Schloss, A.L.; Intercomparison, P.P.N.M. Comparing global models of terrestrial net primary productivity (NPP): the importance of water availability. *Global Change Biology* **1999**, *5*, 46-55.

Cramer, W.; Kicklighter, D.W.; Bondeau, A.; Moore, B.; Churkina, G.; Nemry, B.; Ruimy, A.; Schloss, A.L.; Intercompariso, P.P.N.M. Comparing global models of terrestrial net primary productivity (NPP): overview and key results. *Global Change Biology* **1999**, *5*, 1-15.

De Kauwe, M.G.; Keenan, T.F.; Medlyn, B.E.; Prentice, I.C.; Terrer, C. Satellite based estimates underestimate the effect of CO_2 fertilization on net primary productivity. *Nature Climate Change* **2016**, *6*, 892.

Devaraju, N.; Bala, G.; Caldeira, K.; Nemani, R. A model based investigation of the relative importance of CO_2-fertilization, climate warming, nitrogen deposition and land use change on the global terrestrial carbon uptake in the historical period. *Climate dynamics* **2016**, *47*, 173-190.

Donohue, R.J.; Roderick, M.L.; McVicar, T.R.; Farquhar, G.D. Impact of CO_2 fertilization on maximum foliage cover across the globe's warm, arid environments. *Geophysical Research Letters* **2013**, *40*, 3031-3035.

Dury, M.; Hambuckers, A.; Warnant, P.; Henrot, A.; Favre, E.; Ouberdous, M.; François, L. Responses of European forest ecosystems to 21 (st) century climate: assessing changes in interannual variability and fire intensity. *iForest: Biogeosciences and Forestry* **2011**, *4*, 82-99.

Farquhar, G.; Von Caemmerer, S. Modelling of photosynthetic response to environmental conditions. In *Physiological plant ecology II*, Springer: 1982; pp. 549-587.

Fatichi, S.; Leuzinger, S. Reconciling observations with modeling: The fate of water and carbon allocation in a mature deciduous forest exposed to elevated CO_2. *Agricultural And Forest Meteorology* **2013**, *174*, 144-157.

Fisher, J.B.; Badgley, G.; Blyth, E. Global nutrient limitation in terrestrial vegetation. *Global Biogeochemical Cycles* **2012**, *26*.

Franks, P.J.; Adams, M.A.; Amthor, J.S.; Barbour, M.M.; Berry, J.A.; Ellsworth, D.S.; Farquhar, G.D.; Ghannoum, O.; Lloyd, J.; McDowell, N., et al. Sensitivity of plants to changing atmospheric CO_2 concentration: from the geological past to the next century. *New Phytol* **2013**, *197*, 1077-1094.

Friedlingstein, P.; Cox, P.; Betts, R.; Bopp, L.; von Bloh, W.; Brovkin, V.; Cadule, P.; Doney, S.; Eby, M.; Fung, I. Climate–carbon cycle feedback analysis: results from the C4MIP model intercomparison. *Journal of climate* **2006**, *19*, 3337-3353.

Gao, Y.; Yu, G.; Yan, H.; Zhu, X.; Li, S.; Wang, Q.; Zhang, J.; Wang, Y.; Li, Y.; Zhao, L., et al. A MODIS-based Photosynthetic Capacity Model to estimate gross primary production in Northern China and the Tibetan Plateau. *Remote Sensing of Environment* **2014**, *148*, 108-118.

Garbulsky, M.F.; Peñuelas, J.; Papale, D.; Ardö, J.; Goulden, M.L.; Kiely, G.; Richardson, A.D.; Rotenberg, E.; Veenendaal, E.M.; Filella, I. Patterns and controls of the variability of radiation

use efficiency and primary productivity across terrestrial ecosystems. *Global Ecology and Biogeography* **2010**, *19*, 253-267.

Gielen, B.; Calfapietra, C.; Lukac, M.; Wittig, V.E.; De Angelis, P.; Janssens, I.A.; Moscatelli, M.C.; Grego, S.; Cotrufo, M.F.; Godbold, D.L., et al. Net carbon storage in a poplar plantation (POPFACE) after three years of free-air CO_2 enrichment. *Tree Physiology* **2005**, *25*, 1399-1408.

Gitelson, A.A.; Vina, A.; Verma, S.B.; Rundquist, D.C.; Arkebauer, T.J.; Keydan, G.; Leavitt, B.; Ciganda, V.; Burba, G.G.; Suyker, A.E. Relationship between gross primary production and chlorophyll content in crops: Implications for the synoptic monitoring of vegetation productivity. *J Geophys Res-Atmos* **2006**, *111*.

Graven, H.D.; Keeling, R.F.; Piper, S.C.; Patra, P.K.; Stephens, B.B.; Wofsy, S.C.; Welp, L.R.; Sweeney, C.; Tans, P.P.; Kelley, J.J., et al. Enhanced Seasonal Exchange of CO_2 by Northern Ecosystems Since 1960. *Science* **2013**, *341*, 1085-1089.

Hamilton, J.G.; DeLucia, E.H.; George, K.; Naidu, S.L.; Finzi, A.C.; Schlesinger, W.H. Forest carbon balance under elevated CO_2. *Oecologia* **2002**, *131*, 250-260.

Hashimoto, H.; Wang, W.; Milesi, C.; White, M.A.; Ganguly, S.; Gamo, M.; Hirata, R.; Myneni, R.B.; Nemani, R.R. Exploring simple algorithms for estimating gross primary production in forested areas from satellite data. *Remote Sensing* **2012**, *4*, 303-326.

Hashimoto, H.; Wang, W.; Milesi, C.; Xiong, J.; Ganguly, S.; Zhu, Z.; Nemani, R.R. Structural uncertainty in model-simulated trends of global gross primary production. *Remote Sensing* **2013**, *5*, 1258-1273.

Hilker, T.; Coops, N.C.; Wulder, M.A.; Black, T.A.; Guy, R.D. The use of remote sensing in light use efficiency based models of gross primary production: A review of current status and future requirements. *Science Of the Total Environment* **2008**, *404*, 411-423.

Hilker, T.; Lyapustin, A.I.; Tucker, C.J.; Sellers, P.J.; Hall, F.G.; Wang, Y.J. Remote sensing of tropical ecosystems: Atmospheric correction and cloud masking matter. *Remote Sensing Of Environment* **2012**, *127*, 370-384.

Hu, Z.M.; Shi, H.; Cheng, K.L.; Wang, Y.P.; Piao, S.L.; Li, Y.; Zhang, L.; Xia, J.Y.; Zhou, L.; Yuan, W.P., et al. Joint structural and physiological control on the interannual variation in productivity in a temperate grassland: A data-model comparison. *Global Change Biology* **2018**, *24*, 2965-2979.

Iain Colin Prentice, R.T. Development and validation of a global GPP/NPP model using MERIS and Sentinel-3 data (TerrA-P). *Study accomplished under the authority of ESA* **2017**.

Ito, A.; Nishina, K.; Reyer, C.P.O.; Francois, L.; Henrot, A.J.; Munhoven, G.; Jacquemin, I.; Tian, H.Q.; Yang, J.; Pan, S.F., et al. Photosynthetic productivity and its efficiencies in ISIMIP2a biome models: benchmarking for impact assessment studies. *Environmental Research Letters* **2017**, *12*, 085001.

Ito, A.; Oikawa, T. A simulation model of the carbon cycle in land ecosystems (Sim-CYCLE): a description based on dry-matter production theory and plot-scale validation. *Ecological Modelling* **2002**, *151*, 143-176.

Jiang, C.; Ryu, Y. Multi-scale evaluation of global gross primary productivity and evapotranspiration products derived from Breathing Earth System Simulator (BESS). *Remote Sensing of Environment* **2016**, *186*, 528-547.

Joiner, J.; Yoshida, Y.; Zhang, Y.; Duveiller, G.; Jung, M.; Lyapustin, A.; Wang, Y.; Tucker, C. Estimation of Terrestrial Global Gross Primary Production (GPP) with Satellite Data-Driven Models and Eddy Covariance Flux Data. *Remote Sensing* **2018**, *10*, 1346.

Jung, M.; Reichstein, M.; Margolis, H.A.; Cescatti, A.; Richardson, A.D.; Arain, M.A.; Arneth, A.; Bernhofer, C.; Bonal, D.; Chen, J.Q., et al. Global patterns of land-atmosphere fluxes of carbon dioxide, latent heat, and sensible heat derived from eddy covariance, satellite, and meteorological observations. *J Geophys Res-Biogeo* **2011**, *116*.

Keenan, T.F.; Baker, I.; Barr, A.; Ciais, P.; Davis, K.; Dietze, M.; Dragon, D.; Gough, C.M.; Grant, R.; Hollinger, D., et al. Terrestrial biosphere model performance for inter-annual variability of land-atmosphere CO_2 exchange. *Global Change Biology* **2012**, *18*, 1971-1987.

Keenan, T.F.; Prentice, I.C.; Canadell, J.G.; Williams, C.A.; Wang, H.; Raupach, M.; Collatz, G.J. Recent pause in the growth rate of atmospheric CO_2 due to enhanced terrestrial carbon uptake. *Nature communications* **2016**, *7*, 13428.

Kelley, D.I.; Colin Prentice, I.; Harrison, S.P.; Wang, H.; Simard, M.; Fisher, J.B.; Willis, K.O. A comprehensive benchmarking system for evaluating global vegetation models. *Biogeosciences Discussions* **2012**, *9*, 15723-15785.

Lawlor, D.W.; Mitchell, R.A.C. The Effects Of Increasing CO_2 on Crop Photosynthesis And Productivity - a Review Of Field Studies. *Plant Cell And Environment* **1991**, *14*, 807-818.

Lees, K.J.; Quaife, T.; Artz, R.R.E.; Khomik, M.; Clark, J.M. Potential for using remote sensing to estimate carbon fluxes across northern peatlands - A review. *Science Of the Total Environment* **2018**, *615*, 857-874.

Lentile, L.B.; Holden, Z.A.; Smith, A.M.; Falkowski, M.J.; Hudak, A.T.; Morgan, P.; Lewis, S.A.; Gessler, P.E.; Benson, N.C. Remote sensing techniques to assess active fire characteristics and post-fire effects. *International Journal of Wildland Fire* **2006**, *15*, 319-345.

Leuning, R.; Cleugh, H.A.; Zegelin, S.J.; Hughes, D. Carbon and water fluxes over a temperate Eucalyptus forest and a tropical wet/dry savanna in Australia: measurements and comparison with MODIS remote sensing estimates. *Agricultural and Forest Meteorology* **2005**, *129*, 151-173.

Li, F.; Wang, X.; Zhao, J.; Zhang, X.; Zhao, Q. A method for estimating the gross primary production of alpine meadows using MODIS and climate data in China. *International journal of remote sensing* **2013**, *34*, 8280-8300.

Li, X.; Liang, S.; Yu, G.; Yuan, W.; Cheng, X.; Xia, J.; Zhao, T.; Feng, J.; Ma, Z.; Ma, M. Estimation of gross primary production over the terrestrial ecosystems in China. *Ecological Modelling* **2013**, *261*, 80-92.

Li, X.; Zhu, Z.; Zeng, H.; Piao, S. Estimation of gross primary production in China (1982–2010) with multiple ecosystem models. *Ecological modelling* **2016**, *324*, 33-44.

Li, Z.; Yu, G.; Xiao, X.; Li, Y.; Zhao, X.; Ren, C.; Zhang, L.; Fu, Y. Modeling gross primary production of alpine ecosystems in the Tibetan Plateau using MODIS images and climate data. *Remote Sensing of Environment* **2007**, *107*, 510-519.

Liang, S.; Chen, J.M.; Xiong, X.; Butler, J.J.; Crawford, M.M.; Shi, J.; Loboda, T.V.; Goldberg, M.D.; Zheng, Q.; Walsh, S.J. *Comprehensive Remote Sensing: Terrestrial ecosystems*; Elsevier: 2018.

Liu, J.; Chen, J.; Cihlar, J.; Park, W. A process-based boreal ecosystem productivity simulator using remote sensing inputs. *Remote sensing of environment* **1997**, *62*, 158-175.

Liu, S.; Zhuang, Q.; He, Y.; Noormets, A.; Chen, J.; Gu, L. Evaluating atmospheric CO_2 effects on gross primary productivity and net ecosystem exchanges of terrestrial ecosystems in the conterminous United States using the AmeriFlux data and an artificial neural network approach. *Agricultural and forest meteorology* **2016**, *220*, 38-49.

Liu, Z.; Wang, L.; Wang, S. Comparison of different GPP models in China using MODIS image and ChinaFLUX data. *Remote Sensing* **2014**, *6*, 10215-10231.

Lobell, D.B.; Asner, G.P.; Ortiz-Monasterio, J.I.; Benning, T.L. Remote sensing of regional crop production in the Yaqui Valley, Mexico: estimates and uncertainties. *Agriculture, Ecosystems & Environment* **2003**, *94*, 205-220.

Loescher, H.W.; Law, B.E.; Mahrt, L.; Hollinger, D.Y.; Campbell, J.; Wofsy, S.C. Uncertainties in, and interpretation of, carbon flux estimates using the eddy covariance technique. *J Geophys Res-Atmos* **2006**, *111*.

Luo, Y.; Medlyn, B.; Hui, D.; Ellsworth, D.; Reynolds, J.; Katul, G. Gross primary productivity in duke forest: modeling synthesis of CO2 experiment and eddy–flux data. *Ecological Applications* **2001**, *11*, 239-252.

Ma, J.Y.; Yan, X.D.; Dong, W.J.; Chou, J.M. Gross primary production of global forest ecosystems has been overestimated. *Scientific reports* **2015**, *5*.

Maire, V.; Martre, P.; Kattge, J.; Gastal, F.; Esser, G.; Fontaine, S.; Soussana, J.F. The coordination of leaf photosynthesis links C and N fluxes in C3 plant species. *PLoS One* **2012**, *7*, e38345.

Meroni, M.; Rembold, F.; Migliavacca, M.; Ardö, J. Assimilation of satellite observations for the estimation of Savanna gross primary production. In Proceedings of Geoscience and Remote Sensing Symposium (IGARSS), 2015 IEEE International; pp. 3416-3418.

Mu, Q.; Zhao, M.; Kimball, J.S.; McDowell, N.G.; Running, S.W. A remotely sensed global terrestrial drought severity index. *Bulletin of the American Meteorological Society* **2013**, *94*, 83-98.

Myneni, R.B.; Ganapol, B.D.; Asrar, G. Remote-Sensing Of Vegetation Canopy Photosynthetic And Stomatal Conductance Efficiencies. *Remote Sensing Of Environment* **1992**, *42*, 217-238.

Nemani, R.; Hashimoto, H.; Votava, P.; Melton, F.; Wang, W.L.; Michaelis, A.; Mutch, L.; Milesi, C.; Hiatt, S.; White, M. Monitoring and forecasting ecosystem dynamics using the Terrestrial Observation and Prediction System (TOPS). *Remote Sensing Of Environment* **2009**, *113*, 1497-1509.

Nemani, R.R.; Keeling, C.D.; Hashimoto, H.; Jolly, W.M.; Piper, S.C.; Tucker, C.J.; Myneni, R.B.; Running, S.W. Climate-driven increases in global terrestrial net primary production from 1982 to 1999. *Science* **2003**, *300*, 1560-1563.

Norby, R.J.; Warren, J.M.; Iversen, C.M.; Medlyn, B.E.; McMurtrie, R.E. CO_2 enhancement of forest productivity constrained by limited nitrogen availability. *Proceedings of the National Academy of Sciences* **2010**, *107*, 19368-19373.

Ollinger, S.V.; Smith, M.-L. Net primary production and canopy nitrogen in a temperate forest landscape: an analysis using imaging spectroscopy, modeling and field data. *Ecosystems* **2005**, *8*, 760-778.

Oren, R.; Ellsworth, D.S.; Johnsen, K.H.; Phillips, N.; Ewers, B.E.; Maier, C.; Schäfer, K.V.; McCarthy, H.; Hendrey, G.; McNulty, S.G. Soil fertility limits carbon sequestration by forest ecosystems in a CO 2-enriched atmosphere. *Nature* **2001**, *411*, 469.

Pasetto, D.; Arenas-Castro, S.; Bustamante, J.; Casagrandi, R.; Chrysoulakis, N.; Cord, A.F.; Dittrich, A.; Domingo-Marimon, C.; Serafy, G.; Karnieli, A., et al. Integration of satellite remote sensing data in ecosystem modelling at local scales: Practices and trends. *Methods In Ecology And Evolution* **2018**, *9*, 1810-1821.

Peng, S.; Ciais, P.; Chevallier, F.; Peylin, P.; Cadule, P.; Sitch, S.; Piao, S.; Ahlström, A.; Huntingford, C.; Levy, P., et al. Benchmarking the seasonal cycle of CO_2fluxes simulated by terrestrial ecosystem models. *Global Biogeochemical Cycles* **2015**, *29*, 46-64.

Peters, W.; Jacobson, A.R.; Sweeney, C.; Andrews, A.E.; Conway, T.J.; Masarie, K.; Miller, J.B.; Bruhwiler, L.M.; Petron, G.; Hirsch, A.I., et al. An atmospheric perspective on North American carbon dioxide exchange: CarbonTracker. *Proc Natl Acad Sci USA* **2007**, *104*, 18925-18930.

Piao, S.; Ciais, P.; Friedlingstein, P.; de Noblet-Ducoudré, N.; Cadule, P.; Viovy, N.; Wang, T. Spatiotemporal patterns of terrestrial carbon cycle during the 20th century. *Global Biogeochemical Cycles* **2009**, *23*, n/a-n/a.

Piao, S.; Friedlingstein, P.; Ciais, P.; Viovy, N.; Demarty, J. Growing season extension and its impact on terrestrial carbon cycle in the Northern Hemisphere over the past 2 decades. *Global Biogeochemical Cycles* **2007**, *21*, n/a-n/a.

Piao, S.; Sitch, S.; Ciais, P.; Friedlingstein, P.; Peylin, P.; Wang, X.; Ahlstrom, A.; Anav, A.; Canadell, J.G.; Cong, N., et al. Evaluation of terrestrial carbon cycle models for their response to climate variability and to CO_2 trends. *Glob Chang Biol* **2013**, *19*, 2117-2132.

Potter, C.S.; Randerson, J.T.; Field, C.B.; Matson, P.A.; Vitousek, P.M.; Mooney, H.A.; Klooster, S.A. Terrestrial ecosystem production: a process model based on global satellite and surface data. *Global Biogeochemical Cycles* **1993**, *7*, 811-841.

Poulter, B.; Frank, D.; Ciais, P.; Myneni, R.B.; Andela, N.; Bi, J.; Broquet, G.; Canadell, J.G.; Chevallier, F.; Liu, Y.Y., et al. Contribution of semi-arid ecosystems to interannual variability of the global carbon cycle. *Nature* **2014**, *509*, 600-603.

Poulter, B.; Heyder, U.; Cramer, W. Modeling the sensitivity of the seasonal cycle of GPP to dynamic LAI and soil depths in tropical rainforests. *Ecosystems* **2009**, *12*, 517-533.

Raczka, B.M.; Davis, K.J.; Huntzinger, D.; Neilson, R.P.; Poulter, B.; Richardson, A.D.; Xiao, J.F.; Baker, I.; Ciais, P.; Keenan, T.F., et al. Evaluation of continental carbon cycle simulations with North American flux tower observations. *Ecol Monogr* **2013**, *83*, 531-556.

Rawlins, M.A.; McGuire, A.D.; Kimball, J.S.; Dass, P.; Lawrence, D.; Burke, E.; Chen, X.; Delire, C.; Koven, C.; MacDougall, A., et al. Assessment of model estimates of land-atmosphere CO_2 exchange across Northern Eurasia. *Biogeosciences* **2015**, *12*, 4385-4405.

Reich, P.B.; Hobbie, S.E.; Lee, T.; Ellsworth, D.S.; West, J.B.; Tilman, D.; Knops, J.M.; Naeem, S.; Trost, J. Nitrogen limitation constrains sustainability of ecosystem response to CO_2. *Nature* **2006**, *440*, 922.

Reich, P.B.; Hobbie, S.E.; Lee, T.D. Plant growth enhancement by elevated CO_2 eliminated by joint water and nitrogen limitation. *Nature Geoscience* **2014**, *7*, 920.

Rienecker, M.M.; Suarez, M.J.; Gelaro, R.; Todling, R.; Bacmeister, J.; Liu, E.; Bosilovich, M.G.; Schubert, S.D.; Takacs, L.; Kim, G.K., et al. MERRA: NASA's Modern-Era Retrospective Analysis for Research and Applications. *Journal Of Climate* **2011**, *24*, 3624-3648.

Rossini, M.; Cogliati, S.; Meroni, M.; Migliavacca, M.; Galvagno, M.; Busetto, L.; Cremonese, E.; Julitta, T.; Siniscalco, C.; Morra di Cella, U. Remote sensing-based estimation of gross primary production in a subalpine grassland. *Biogeosciences* **2012**, *9*, 2565-2584.

Running, S.W., and Maosheng Zhao. Daily GPP and annual NPP (MOD17A2/A3) products NASA Earth Observing System MODIS land algorithm. **2015**.

Ryan, E.M.; Ogle, K.; Peltier, D.; Walker, A.P.; De Kauwe, M.G.; Medlyn, B.E.; Williams, D.G.; Parton, W.; Asao, S.; Guenet, B. Gross primary production responses to warming, elevated CO_2, and irrigation: quantifying the drivers of ecosystem physiology in a semiarid grassland. *Global change biology* **2017**, *23*, 3092-3106.

Ryan, E.M.; Ogle, K.; Peltier, D.; Walker, A.P.; de Kauwe, M.G.; Medlyn, B.E.; Williams, D.G.; Parton, W.; Asao, S.; Guenet, B., et al. Gross primary production responses to warming, elevated CO_2, and irrigation: quantifying the drivers of ecosystem physiology in a semiarid grassland. *Global Change Biology* **2017**, *23*, 3092-3106.

Ryu, Y.; Baldocchi, D.D.; Kobayashi, H.; van Ingen, C.; Li, J.; Black, T.A.; Beringer, J.; Van Gorsel, E.; Knohl, A.; Law, B.E. Integration of MODIS land and atmosphere products with a coupled-process model to estimate gross primary productivity and evapotranspiration from 1 km to global scales. *Global Biogeochemical Cycles* **2011**, *25*.

Schaefer, K.; Denning, A.S.; Suits, N.; Kaduk, J.; Baker, I.; Los, S.; Prihodko, L. Effect of climate on interannual variability of terrestrial CO_2 fluxes. *Global Biogeochemical Cycles* **2002**, *16*.

Schaefer, K.; Schwalm, C.R.; Williams, C.; Arain, M.A.; Barr, A.; Chen, J.M.; Davis, K.J.; Dimitrov, D.; Hilton, T.W.; Hollinger, D.Y., et al. A model-data comparison of gross primary productivity: Results from the North American Carbon Program site synthesis. *J Geophys Res-Biogeo* **2012**, *117*.

Schäfer, K.V.; Oren, R.; Ellsworth, D.S.; Lai, C.T.; Herrick, J.D.; Finzi, A.C.; Richter, D.D.; Katul, G.G. Exposure to an enriched CO_2 atmosphere alters carbon assimilation and allocation in a pine forest ecosystem. *Global Change Biology* **2003**, *9*, 1378-1400.

Schafer, K.V.R.; Oren, R.; Ellsworth, D.S.; Lai, C.T.; Herrick, J.D.; Finzi, A.C.; Richter, D.D.; Katul, G.G. Exposure to an enriched CO_2 atmosphere alters carbon assimilation and allocation in a pine forest ecosystem. *Global Change Biology* **2003**, *9*, 1378-1400.

Sellers, P.; Berry, J.; Collatz, G.; Field, C.; Hall, F. Canopy reflectance, photosynthesis, and transpiration. III. A reanalysis using improved leaf models and a new canopy integration scheme. *Remote sensing of environment* **1992**, *42*, 187-216.

Silleos, N.G.; Alexandridis, T.K.; Gitas, I.Z.; Perakis, K. Vegetation indices: advances made in biomass estimation and vegetation monitoring in the last 30 years. *Geocarto International* **2006**, *21*, 21-28.

Sims, D.A.; Rahman, A.F.; Cordova, V.D.; El-Masri, B.Z.; Baldocchi, D.D.; Bolstad, P.V.; Flanagan, L.B.; Goldstein, A.H.; Hollinger, D.Y.; Misson, L., et al. A new model of gross primary productivity for North American ecosystems based solely on the enhanced vegetation index and land surface temperature from MODIS. *Remote Sensing Of Environment* **2008**, *112*, 1633-1646.

Smith, W.K.; Reed, S.C.; Cleveland, C.C.; Ballantyne, A.P.; Anderegg, W.R.; Wieder, W.R.; Liu, Y.Y.; Running, S.W. Large divergence of satellite and Earth system model estimates of global terrestrial CO_2 fertilization. *Nature Climate Change* **2016**, *6*, 306.

Song, C.; Dannenberg, M.P.; Hwang, T. Optical remote sensing of terrestrial ecosystem primary productivity. *Progress in Physical Geography* **2013**, *37*, 834-854.

Souza, M.C.; Biudes, M.S.; de Morais Danelichen, V.H.; Machado, N.G.; De Musis, C.R.; Vourlitis, G.L.; de Souza Nogueira, J. Estimation of gross primary production of the Amazon-Cerrado transitional forest by remote sensing techniques. *Revista Brasileira de Meteorologia* **2013**, *29*.

Sun, Y.; Piao, S.L.; Huang, M.T.; Ciais, P.; Zeng, Z.Z.; Cheng, L.; Li, X.R.; Zhang, X.P.; Mao, J.F.; Peng, S.S., et al. Global patterns and climate drivers of water-use efficiency in terrestrial ecosystems deduced from satellite-based datasets and carbon cycle models. *Global Ecology And Biogeography* **2016**, *25*, 311-323.

Sun, Z.; Wang, X.; Yamamoto, H.; Zhang, J.; Tani, H.; Zhong, G.; Yin, S. Extraction of rice-planting area and identification of chilling damage by remote sensing technology: a case study of the emerging rice production region in high latitude. *Paddy and Water Environment* **2017**, *15*, 181-191.

Sun, Z.Y.; Wang, X.F.; Yamamoto, H.; Tani, H.; Zhong, G.S.; Yin, S. An attempt to introduce atmospheric CO_2 concentration data to estimate the gross primary production by the terrestrial biosphere and analyze its effects. *Ecological Indicators* **2018**, *84*, 218-234.

Sun, Z.Y.; Wang, X.F.; Yamamoto, H.; Tani, H.; Zhong, G.S.; Yin, S.; Guo, E.L. Spatial pattern of GPP variations in terrestrial ecosystems and its drivers: Climatic factors, CO_2 concentration and land-cover change, 1982-2015. *Ecological Informatics* **2018**, *46*, 156-165.

Sun, Z.Y.; Zhang, J.Q.; Zhang, Q.; Hu, Y.; Yan, D.H.; Wang, C.Y. Integrated risk zoning of drought and waterlogging disasters based on fuzzy comprehensive evaluation in Anhui Province, China. *Natural Hazards* **2014**, *71*, 1639-1657.

Tagesson, T.; Ardö, J.; Cappelaere, B.; Kergoat, L.; Abdi, A.; Horion, S.; Fensholt, R. Modelling spatial and temporal dynamics of gross primary production in the Sahel from earth-observation-based photosynthetic capacity and quantum efficiency. *Biogeosciences* **2017**, *14*, 1333-1348.

Task, G.S.D. Global soil data products CD-ROM contents (IGBP-DIS). *ORNL DAAC* **2014**.

Thomas, R.T.; Prentice, L.C.; Graven, H.; Ciais, P.; Fisher, J.B.; Hayes, D.J.; Huang, M.Y.; Huntzinger, D.N.; Ito, A.; Jain, A., et al. Increased light-use efficiency in northern terrestrial ecosystems

indicated by CO_2 and greening observations. *Geophysical Research Letters* **2016**, *43*, 11339-11349.

Tian, H.; Chen, G.; Lu, C.; Xu, X.; Hayes, D.J.; Ren, W.; Pan, S.; Huntzinger, D.N.; Wofsy, S.C. North American terrestrial CO_2 uptake largely offset by CH_4 and N_2O emissions: toward a full accounting of the greenhouse gas budget. *Climatic Change* **2015**, *129*, 413-426.

Traore, A.K.; Ciais, P.; Vuichard, N.; Poulter, B.; Viovy, N.; Guimberteau, M.; Jung, M.; Myneni, R.; Fisher, J.B. Evaluation of the ORCHIDEE ecosystem model over Africa against 25 years of satellite-based water and carbon measurements. *Journal of Geophysical Research: Biogeosciences* **2014**, *119*, 1554-1575.

Veroustraete, F. On the use of a simple deciduous forest model for the interpretation of climate change effects at the level of carbon dynamics. *Ecological modelling* **1994**, *75*, 221-237.

Veroustraete, F.; Sabbe, H.; Eerens, H. Estimation of carbon mass fluxes over Europe using the C-Fix model and Euroflux data. *Remote Sensing of Environment* **2002**, *83*, 376-399.

Verstraeten, W.W.; Veroustraete, F.; Feyen, J. On temperature and water limitation of net ecosystem productivity: Implementation in the C-Fix model. *Ecological Modelling* **2006**, *199*, 4-22.

Vourlitis, G.L.; de Souza Nogueira, J.; de Almeida Lobo, F.; Sendall, K.M.; de Paulo, S.R.; Antunes Dias, C.A.; Pinto, O.B.; de Andrade, N.L.R. Energy balance and canopy conductance of a tropical semi-deciduous forest of the southern Amazon Basin. *Water Resources Research* **2008**, *44*.

Wan, Z. New refinements and validation of the MODIS land-surface temperature/emissivity products. *Remote sensing of Environment* **2008**, *112*, 59-74.

Wang, X.; Ma, M.; Li, X.; Song, Y.; Tan, J.; Huang, G.; Yu, W. Comparison of remote sensing based GPP models at an alpine meadow site. *J. Remote Sens* **2012**, *16*.

Waring, R.H.; Landsberg, J.J.; Williams, M. Net primary production of forests: a constant fraction of gross primary production? *Tree Physiology* **1998**, *18*, 129-134.

Wei, S.; Yi, C.; Fang, W.; Hendrey, G. A global study of GPP focusing on light-use efficiency in a random forest regression model. *Ecosphere* **2017**, *8*, e01724.

Williams, A.P.; Allen, C.D.; Macalady, A.K.; Griffin, D.; Woodhouse, C.A.; Meko, D.M.; Swetnam, T.W.; Rauscher, S.A.; Seager, R.; Grissino-Mayer, H.D., et al. Temperature as a potent driver of regional forest drought stress and tree mortality. *Nature Climate Change* **2013**, *3*, 292-297.

Wittig, V.E.; Bernacchi, C.J.; Zhu, X.G.; Calfapietra, C.; Ceulemans, R.; Deangelis, P.; Gielen, B.; Miglietta, F.; Morgan, P.B.; Long, S.P. Gross primary production is stimulated for three Populus species grown under free-air CO_2 enrichment from planting through canopy closure. *Global Change Biology* **2005**, *11*, 644-656.

Wittig, V.E.; Bernacchi, C.J.; Zhu, X.G.; Calfapietra, C.; Ceulemans, R.; Deangelis, P.; Gielen, B.; Miglietta, F.; Morgan, P.B.; Long, S.P. Gross primary production is stimulated for three Populus species grown under free-air CO_2 enrichment from planting through canopy closure. *Global Change Biology* **2005**, *11*, 644-656.

Wu, C.; Munger, J.W.; Niu, Z.; Kuang, D. Comparison of multiple models for estimating gross primary production using MODIS and eddy covariance data in Harvard Forest. *Remote Sensing of Environment* **2010**, *114*, 2925-2939.

Wu, C.Y.; Chen, J.M.; Desai, A.R.; Hollinger, D.Y.; Arain, M.A.; Margolis, H.A.; Gough, C.M.; Staebler, R.M. Remote sensing of canopy light use efficiency in temperate and boreal forests of North America using MODIS imagery. *Remote Sensing Of Environment* **2012**, *118*, 60-72.

Wu, Z.; Ahlström, A.; Smith, B.; Ardö, J.; Eklundh, L.; Fensholt, R.; Lehsten, V. Climate data induced uncertainty in model-based estimations of terrestrial primary productivity. *Environmental Research Letters* **2017**, *12*, 064013.

Wullschleger, S.D.; Gunderson, C.A.; Hanson, P.J.; Wilson, K.B.; Norby, R.J. Sensitivity of stomatal and canopy conductance to elevated CO_2 concentration - interacting variables and perspectives of scale. *New Phytologist* **2002**, *153*, 485-496.

Wylie, B.K.; Johnson, D.A.; Laca, E.; Saliendra, N.Z.; Gilmanov, T.G.; Reed, B.C.; Tieszen, L.L.; Worstell, B.B. Calibration of remotely sensed, coarse resolution NDVI to CO_2 fluxes in a sagebrush–steppe ecosystem. *Remote Sensing of Environment* **2003**, *85*, 243-255.

Xiao, X.; Zhang, Q.; Braswell, B.; Urbanski, S.; Boles, S.; Wofsy, S.; Moore, B.; Ojima, D. Modeling gross primary production of temperate deciduous broadleaf forest using satellite images and climate data. *Remote Sensing of Environment* **2004**, *91*, 256-270.

Yan, H.; Wang, S.Q.; Billesbach, D.; Oechel, W.; Bohrer, G.; Meyers, T.; Martin, T.A.; Matamala, R.; Phillips, R.P.; Rahman, F., et al. Improved global simulations of gross primary product based on a new definition of water stress factor and a separate treatment of C3 and C4 plants. *Ecological Modelling* **2015**, *297*, 42-59.

Yan, K.; Park, T.; Yan, G.; Chen, C.; Yang, B.; Liu, Z.; Nemani, R.R.; Knyazikhin, Y.; Myneni, R.B. Evaluation of MODIS LAI/FPAR product collection 6. Part 1: Consistency and improvements. *Remote Sensing* **2016**, *8*, 359.

Yang, Y.; Shang, S.; Guan, H.; Jiang, L. A novel algorithm to assess gross primary production for terrestrial ecosystems from MODIS imagery. *Journal of Geophysical Research: Biogeosciences* **2013**, *118*, 590-605.

Yu, G.R.; Zhu, X.J.; Fu, Y.L.; He, H.L.; Wang, Q.F.; Wen, X.F.; Li, X.R.; Zhang, L.M.; Zhang, L.; Su, W., et al. Spatial patterns and climate drivers of carbon fluxes in terrestrial ecosystems of China. *Glob Chang Biol* **2013**, *19*, 798-810.

Yuan, W.; Cai, W.; Xia, J.; Chen, J.; Liu, S.; Dong, W.; Merbold, L.; Law, B.; Arain, A.; Beringer, J., et al. Global comparison of light use efficiency models for simulating terrestrial vegetation gross primary production based on the LaThuile database. *Agricultural and Forest Meteorology* **2014**, *192-193*, 108-120.

Yuan, W.; Liu, S.; Yu, G.; Bonnefond, J.-M.; Chen, J.; Davis, K.; Desai, A.R.; Goldstein, A.H.; Gianelle, D.; Rossi, F., et al. Global estimates of evapotranspiration and gross primary production based on MODIS and global meteorology data. *Remote Sensing of Environment* **2010**, *114*, 1416-1431.

Yuan, W.P.; Liu, S.; Zhou, G.S.; Zhou, G.Y.; Tieszen, L.L.; Baldocchi, D.; Bernhofer, C.; Gholz, H.; Goldstein, A.H.; Goulden, M.L., et al. Deriving a light use efficiency model from eddy covariance flux data for predicting daily gross primary production across biomes. *Agricultural And Forest Meteorology* **2007**, *143*, 189-207.

Zeng, N.; Mariotti, A.; Wetzel, P. Terrestrial mechanisms of interannual CO_2 variability. *Global biogeochemical cycles* **2005**, *19*.

Zhang, L.-X.; Zhou, D.-C.; Fan, J.-W.; Hu, Z.-M. Comparison of four light use efficiency models for estimating terrestrial gross primary production. *Ecological modelling* **2015**, *300*, 30-39.

Zhang, S.; Zhang, J.; Bai, Y.; Koju, U.A.; Igbawua, T.; Chang, Q.; Zhang, D.; Yao, F. Evaluation and improvement of the daily boreal ecosystem productivity simulator in simulating gross primary productivity at 41 flux sites across Europe. *Ecological Modelling* **2018**, *368*, 205-232.

Zhang, X.; Rayner, P.J.; Wang, Y.P.; Silver, J.D.; Lu, X.; Pak, B.; Zheng, X. Linear and nonlinear effects of dominant drivers on the trends in global and regional land carbon uptake: 1959 to 2013. *Geophysical Research Letters* **2016**, *43*, 1607-1614.

Zhang, Y.; Xiao, X.; Wu, X.; Zhou, S.; Zhang, G.; Qin, Y.; Dong, J. A global moderate resolution dataset of gross primary production of vegetation for 2000–2016. *Scientific Data* **2017**, *4*, 170165.

Zhao, M.; Running, S.W.; Nemani, R.R. Sensitivity of Moderate Resolution Imaging Spectroradiometer (MODIS) terrestrial primary production to the accuracy of meteorological reanalyses. *J Geophys Res-Biogeo* **2006**, *111*.

Chapter 6 Summary and conclusions

6.1 Summary of present work

GPP plays a pivotal role in the global carbon balance and almost all ecosystem processes. Quantitative estimations of the GPP and its variations at spatial scales are important issues with future significance due to the increasing atmospheric CO_2 levels. It is significant to the study of terrestrial ecosystem that understand the response relationships between GPP and environmental changes. Since the influences and constraints of physical environments and biochemical processes, terrestrial GPP response to the environment varies with diverse spatial patterns. Aiming to derive spatiotemporal patterns of variation and distribution of terrestrial GPP using satellite remote sensing technique, to investigate the enviro-climatic effects on global terrestrial GPP, and to discuss the difference among RS-based GPP algorithms, four main tasks have been undertaken: (i) Estimation on GPP of the global terrestrial ecosystem using multi-model; (ii) Analysis on Long-term trends of variations in GPP and its attribution; (ii) Investigation on effect of CO_2 fertilization on GPP; (iv) Comparison of the sensitivity of GPP to external factors in RS-based models. The data used for these researches include remote sensing datasets, climate datasets, soil moisture and property, and the datasets from EC flux tower sites and FACE experimental sites. The data used are listed in Table 6.1.

6.2 Theoretical and practical innovations

This thesis focuses on utilizing RS-based models to research global terrestrial GPP, including spatial distribution changes, temporal trends, seasonal cycle, external factors influencing, CO_2 fertilization effect and other aspects. It has important theoretical and practical significance in multiple fields, such as terrestrial ecosystem carbon cycle, RS GPP algorithm, global climate change etc. And I summarized as the followings 5 major points:

(i) Comprehensively and systematically evaluating, comparing and analyzing the GPP estimations from RS-based model ensemble at the global scale;

(ii) Interpreting and benchmarking the prevalent RS-based model sensitivity to external factors on the basis of model structure, parameters, and hypothesis;

(iii) Utilizing RS-based GPP models to investigate the CO_2 fertilization effects, and discussed the effect in two aspects, physiological structure changes and photosynthetic rate enhancement;

(iv) Attempting to introduce the satellite-based atmospheric CO_2 concentration data into global terrestrial GPP estimating;

(v) According to the variations in global terrestrial GPP and its attributions, zoning and characterized analyzing the global terrestrial ecosystems.

Table 6.1 Overview of data used in this thesis.

Chapter	Data category	Short name	Time scale
Chapter 2	Satellite Data	MCD43C2, MCD43C3, MCD43C4,	2000–2014
		MCD12C1, MCD12Q2, MOD16A2	
		GLOBMAP LAI	
	In-situ Data	FluxNet 2015	
		FACE Experiments	
	Climate Data	MERRA-2	
	Soil Data	CPC-SM	
		IGBP-DIS GGSC	
	CO2 Data	CarbonTracker 2016	
	Others	ISLSCP II	
		Koppen-Geiger climate classification	
Chapter 3	Satellite Data	GIMMS-3g	1982-2015
		UMD LCC	1981-1994
		CCI-LC	1992-2015
	Climate Data	MERRA-2	1980-2015
	Soil Data	CPC-SM	
		IGBP-DIS GGSC	
	CO2 Data	CO2 records	1982-1999
		CarbonTracker 2016	2000-2015
Chapter 4	Satellite Data	MCD15A3, MOD17A2, MCD12C1,	2000-2015
		MCD12Q1	
		GOSAT-FTS L2	
		GLOBMAP LAI	
		GIMMS-3g	2014
	In-situ Data	FluxNet2015	
	Climate Data	MERRA-2	
		NCEP/DOE	
		MCDW	
	Soil Data	CPC-SM	
		IGBP-DIS GGSC	
	CO2 Data	GOSAT-FTS L2	
	Others	CarbonTracker2016	
		ISLSCP II	2014
Chapter 5	Satellite Data	MCD43C2, MCD43C3, MCD43C4,	2000–2014
		MCD12C1, MCD12Q2, MOD16A2	
		GLOBMAP LAI	
	In-situ Data	FluxNet 2015	
		FACE Experiments	
	Climate Data	MERRA-2	
	Soil Data	CPC-SM	
		IGBP-DIS GGSC	
	CO2 Data	CarbonTacker 2016	
	Others	ISLSCP II	
		Koppen-Geiger climate classification	

6.3 Limitation of this study

As mentioned before, there are so many advantages for remote sensing datasets, while, the disadvantages are also obvious, such as, same object with different spectra, different objects with same spectrum, mixed pixel, the quality difference etc., lead to remaining some limitations in this study. The limitations did not influence to achieve the objectives in each study. In the followings, I delineated the limitations that I think it is necessary and meaningful for our future study and other researches who want conduct similar researches.

First of all, the spatial scale conversion issues: the spatial resolution of final datasets used in this thesis was 0.5° × 0.5°, almost all the original data had to use superiority category methods, linear or nonlinear interpolation to obtain the consistently spatial resolution datasets. For example, the phenological dataset is at 1-km × 1-km spatial resolution, we had to select one typical value from more than 2500 pixels, but the complex underlying surface conditions do not allow me to get one value which can represent all the pixel especially in the plant functional types transition zone. More often than not, the interesting grid contained the plants from budburst to leaf full expansion. Simultaneously, when comparing the estimates with the measurement at sites, the mismatch footprint size also brought the limitations and uncertainty. Improving the spatial resolution is likely to be the optimal way to solve this limitation, but the improvement in spatial resolution would bring the geometric progression increase in the amount of data.

Second, although I used the consistent gap-filling scheme, priority space dimension, to make up the quality issues of RS data, some insurmountable problems still exist. For example, when calculating the Clumping Index, I used the median to represent the average situation throughout the year, only the grid with the high-quality flag would be used. However, in the Tropics, the proportion of high-quality grids appear during the dry season was much higher than that during rainy seasons. Unfortunately, during rainy seasons the tropics ecosystems always have the relatively higher productivity which contributes more to global and annual GPP, but using the dry seasons CI would reduce this contribution.

The representative issue of the data used in the thesis: the atmospheric CO_2 concentration data obtained from GOSAT is XCO_2 instead of the canopy CO_2 concentration which is important to photosynthesis. I used the decoupling coefficients and the pressure layer data to estimate the CO_2 concentration in the canopy, but the relationship of CO_2 concentration among different air pressure layers is not linear, and the influencing factors on decoupling coefficient are complex. Therefore, the method of getting the canopy CO_2 concentration should be further investigated to improve the special representativeness of satellite CO_2 concentration data. I mainly used two climate datasets, i.e. MERRA-2 and NECP-DOE, which is different from CRU that often as the driving dataset to run the ecosystem models. Because of the number of involving models and essential variables is relatively more, I mainly used two climate datasets, i.e. MERRA-2 and NECP-DOE, which is different from CRU that often as the driving dataset to run the ecosystem models. Therefore, it is not easy to compare our results with the results from others' researches. Although the study period for the long-term changing study meets the lowest requirement of climatology, the study period of the research on the sensitivity and accuracy of the RS-model ensemble limited by the availability of satellite data is only from 2000 to 2014. The study period is not long enough and leads to the weak persuasiveness of phenomenon.

In addition to the limitations of data, there are also some limitations to the methods used in this thesis. First of all, the selection of models, there are 12 models included in the model

ensemble used in this thesis including VI-, LUE-, process- and machine learning-based models. However, many other models that are also representative were not involved in the estimation and comparison. For VI models, the GPP estimation from SIF was considered in the study but I did not compare the long-term results with other estimates, because of the available temporal range of RS data; and due to the similar reason, some photochemical indexes (e.g., PRI (Photochemical Reflectance Index), MTCI (Merris Terrestrial Chlorophyll Index)) were also not discussed. Regarding LUE-based models, VPRM, CFlu etc. were also not considered in this thesis. I directly used the MTE GPP products instead of re-calculating it also became one of the limitations. Process-based models lack the dynamic constraint module between N and C; on one hand, because this constraint relationship is too complex; and on the other hand, because there is no spatiotemporal continuous sequence of N-deposition dataset could be used.

In Chapter 3, for the long-term GPP estimation and its attribution analysis I only selected the CFix model and verified the accuracy with MTE and MODIS GPP products. Choosing only the CFix model is also forced to no alternative since CFix is the only one considering CO_2 fertilization effect and with enough driving data. BESS and BEPS are more suitable for control variables and quantitative research, but there is no dataset meets the large requirement of driving variables. Therefore, the CFix model can only be selected secondly, which also led to a weaker stringency of conclusion by only one single model than by the model ensemble. In Chapter 4, for the study on the CO_2 fertilization effect, I firstly used BEPS models and then according to the photosynthesis principle proposed a RS-based model introducing GOSAT CO_2 data. Only used the BEPS model because it is the only one process model who considers the CO_2 fertilizer effect and also involves the soil moisture effect. The same as Chapter 3 only one model would reduce the stringency of study. The attempt which introduced the GOSAT CO_2 data lacks the direct constraints from soil moisture and nutrition. and since the GOSAT satellite data does not exist before 2009, I only compared the difference between 2000 and 2014, and only in 2014 we used the spatial continuous CO_2 concentration data; unless combined with DGVMs, this issue is not easily to solve.

Finally, it should be noted that in chapter 5 the main focus is to compare and evaluate the differences in response to the climatic variability and the rising atmospheric CO_2 concentration in the models, and the best performance of these models might be reached through utilizing model-dependent parameter values and driving datasets from the original publications.

6.4 Further study

Improve the proposed RS model and using the high spatiotemporal resolution RS data to drive models and benchmark it at EC flux sites and FACE experimental sites; Hoped that experts in the fields of ecosystem and climate change could publish a series of RS data to standardize the comparison among models, and to more clearly explain and discover the advantages and disadvantages and applicable conditions of each model. Combining with DGVMs and utilizing the respective advantages to discuss the effects of external factors on terrestrial ecosystems in detail, and trying to estimate more realistic and accurate global terrestrial GPP are necessary. Establishing and developing the full RS based GPP models by introducing the physiological vegetation indices (e.g., SIF, PRI, MTCI) and the more detailed CO_2 concentration data and etc is the next step. Hindcasting the history, inverting the present and deducing the future: utilize RS parameters or algorithms to adjust or correct the key parameters and process in the DGVMs, and make attempt to predict the spatiotemporal distribution of terrestrial GPP under the background of climate change.

6.5 Final conclusions

The main objectives of this study are investigating the spatiotemporal patterns of distribution and variations in global terrestrial GPP and comparing the prevailing RS-based models. Four research tasks (from Chapter 2 to Chapter 5) have been undertaken:

There is no model showing an isolated estimation in the spatial distribution, seasonal variation and interannual variation of GPP. However, The VI and LUE models, which are relatively simpler in form and have fewer parameters, also have comparable abilities of estimating GPP to those of complex process-based models.

The five factors considered in Chapter 3 resulted in an overall positive effect on the GPP trend but with different spatial patterns, magnitudes, and mechanisms. Globally, increases in GPP occurred in over 75% of the areas; the interactions between factors were positive, and the increases in atmospheric CO_2 concentration had the greatest contribution on global increasing GPP. However, regionally, the LCC and climatic factors appear play more important roles in GPP changes. Larger areas in the lower latitudes showed increases in the amplitude of the GPP annual cycle which dominated by shifts in water conditions; in contrast, in the middle latitudes GPP expressed not only the amplitude changes but also a lengthened rapid growth stage during the early period which were likely to be driven by increases in temperature and radiation; in large areas of the Southern Hemisphere, GPP increased in both the early and later period of the growing season, resulting in a lengthening growing season. However, at high altitudes, the changes in GPP were probably caused by the changes in the temperature and water conditions. The effect of nutrition cannot be quantified from this study since any resulting changes were implicit in the satellite-observed NDVI and were not explicitly modeled. In summary, Chapter 3 found a wide range of GPP trends, both spatially and seasonally. It appears that CO_2, LCC and climatic factors together played a role in global terrestrial GPP changes.

When estimating global GPP using RS-based methods, the effects of the temporal and spatial distribution of the atmospheric CO_2 concentration on GPP have rarely been incorporated. Chapter 4 considered this effect when quantifying the global GPP. First, I used process-based RS model, BEPS, to compared the estimated GPP with the products of the models that did not consider the CO_2 fertilization module, and I compared the estimates obtained by inputting the CO_2 data without spatiotemporal characteristics to analyze the effects of the CO_2 concentration and its spatiotemporal influence on the estimation of GPP. Second, I attempted to use continuous spatial CO_2 concentration data obtained from GOSAT to estimate the GPP combined with the decoupling coefficients of PFTs to obtain the CO_2 concentration in canopy; then, according to climate data, I attempted to calculate the photosynthetic efficiency using the leaf- and canopy-level photosynthesis model and estimate the global monthly and annual GPP by scaling up to the whole ecosystem using the big-leaf model. Through using the Fluxnet 2015 dataset to assess the accuracy of the estimates, the GPP estimates are relatively consistent with tower GPP, indicating that the method proposed in Chapter 4, which introduces the continuous spatial CO_2 concentration data obtained by RS technology, is feasible. The results showed that the relative relationship between the estimated GPP and the other GPP products exhibited a close relationship with the increasing CO_2 concentration, indicating that not considering the CO_2 fertilization effect would result in an underestimation of GPP. In addition, the estimations that do not consider the spatiotemporal distribution of the CO_2 concentration would cause an overall overestimated annual GPP, and these biases varied with location and period. In particular, the increases in the lower latitudes are more significant than those in the middle and high latitudes; the increments in the GPP estimates in the middle and high latitudes in the Northern Hemisphere during the summer are greater than those during the other seasons, but in the

Southern Hemisphere, the increments are almost the same throughout the year; without considering the spatiotemporal distribution of atmospheric CO_2 concentrations, the GPP estimates were underestimated before June and overestimated after June in the Northern Hemisphere; moreover, the GPP in the Southern Hemisphere was overestimated all throughout the year. Chapter 4 suggested that the spatiotemporally varied CO_2 concentrations should be factored into GPP estimations when using an RS-based model for a long-term period and a large regional scale.

In Chapter 5, I evaluated and compared the sensitivity of GPP estimated by 12 RS-based GPP models and benchmarked these estimates against the GPP responses to climatic factors measured at flux tower sites and to elevated CO_2 concentrations measured at FACE experimental sites. The comparison among models and the comparison of models against observations helps document their strengths and weaknesses under current conditions and can also identify heuristic constraints about their applicable conditions and scopes. I report the following main conclusions: through the analysis of the response to increasing atmospheric CO_2 concentrations, considering only the effect of variation in CO_2 concentrations on photosynthesis without considering the CO_2 fertilization effect on the greenness index, LUE or fAPAR, will underestimate the sensitivity of models to CO_2, and vice versa. Regarding the GPP trend, the models with the relatively higher sensitivity to increasing atmospheric CO_2 concentrations (e.g., BEPS, AVM, TG, CFix and BESS) show more significant trends. Compared with the results from the FACE experiment, models will easily overestimate the CO_2 fertilization effect when the CO_2 saturation effect and environmental limitations, such as moisture, are not considered. At the global scale, the overall effects of temperature and radiation among different models have differences in magnitude and even in sign, while models were relatively consistent in their response to variations in precipitation, although the expressions of the water effect in different models were different. The spatial differences in response to climatic factors among models were mainly reflected in the Tropics where the highest uncertainty existed. At high latitudes, all models had a consistent and obvious positive response to temperature and radiation, while precipitation showed the most significant positive effect on GPP in the mid-latitudes. Although the models' estimations are basically within the confidence intervals of the sensitivities to climatic factors calculated by measurements at the flux sites, none of the models consistently reproduced the optimal ability to capture climatic stress across the different sites, indicating that for a site and a given model, there were large factor-to-factor differences in estimation accuracy. Although there are various uncertainties, the optimal response model varies across ecosystems and affecting factors.

Acknowledgements

Doctoral life is fleeting, while I vaguely remember the first day, I entered Hokkaido University. Flowers bloom and fade year by year, fates come and go with the fleeting time. And the fate is so mysterious and beautiful. Hokkaido University has been in my life from the winter of 2014, and I wish it will be so in my remaining life. That was a short-stay exchange program, but also the turning point in my life. My deepest gratitude goes first and foremost to Wang Xiufeng, my supervisor, for her constant encouragement and guidance. I really appreciate it that without her consistent and illuminating instruction, this thesis could not have reached its present form even could not be finished. You are a famous educator in my heart, I am the student who studies following you; You are also a mother, I am treated as the son by you. I am a stupid student, thank you for encouraging me that my IQ could support me to complete my studies; I am a simple son, thank you for your understanding and persuasion about my various ignorance. Your attitude to life inspires me to be a strong man and teach me how to confront the difficulties and realities. Thank you very much for giving me an opportunity that let me be your student. Ten thousand taels of gold are easier to come by than an understanding heart.

I am also grateful to Associate Prof. Tani Hiroshi for the meaningful advices in seminars, intermediate presentations and also advices for my Ph.D. thesis. Many thanks to Prof. Sameshima Ryoji and Prof. Hirota Tomoyoshi. I am grateful to your critical comments and thoughtful suggestions.

I am greatly indebted to Assistant Prof. Zhijun Tong (Northeast Normal University, China) and Associate Prof. Tomomichi Kato whom I discussed with on my research and also got many useful advices from. I also sincerely thank Dr. Enliang Guo and Wei Cui for their encouragement, helpful suggestions throughout my study.

Thanks also go to my lab mates Zhong, Yin, Heri, Cat Tuong, Yamaya, Yoshiyama and Miura for their help and cooperation in making the laboratory atmosphere healthy. I will take the time we spent together and the wonderful memory as the most valuable treasure and bury them deeply in my heart. As an international student, the most difficult trouble I have to face is the cultural and linguistic differences and all of you always try your best to let me Integrate into foreign life and make me in a good mood. I feel very happy and relaxed with everyone. I also owe my sincere gratitude to my friends and my fellow classmates who gave me their help and time to find solutions to my problems during the difficult course of the thesis.

I also would like to thank CMIP5, ISIMIP, JAXA, ESA, WMO, NOAA and NASA for providing data for my study.

My Ph.D. Course was funded by Japanese Government Scholarship program. I am grateful to the Ministry of Education, Culture, Sports, Science and Technology, Japan. I sincerely thank them for giving me the financial supporting due to which I can put all my focus and heart in my doctoral research.

Finally, I would like to express my gratitude to my beloved family. Thanks to my parents for bringing me up, supporting me silently, understanding my dilemmas, and educating me to become a grateful person. Many thanks to my wife, FNU Wulan, who has always been helping me out of difficulties, making me a good mood, standing back of me without complaint.

Supplementary materials

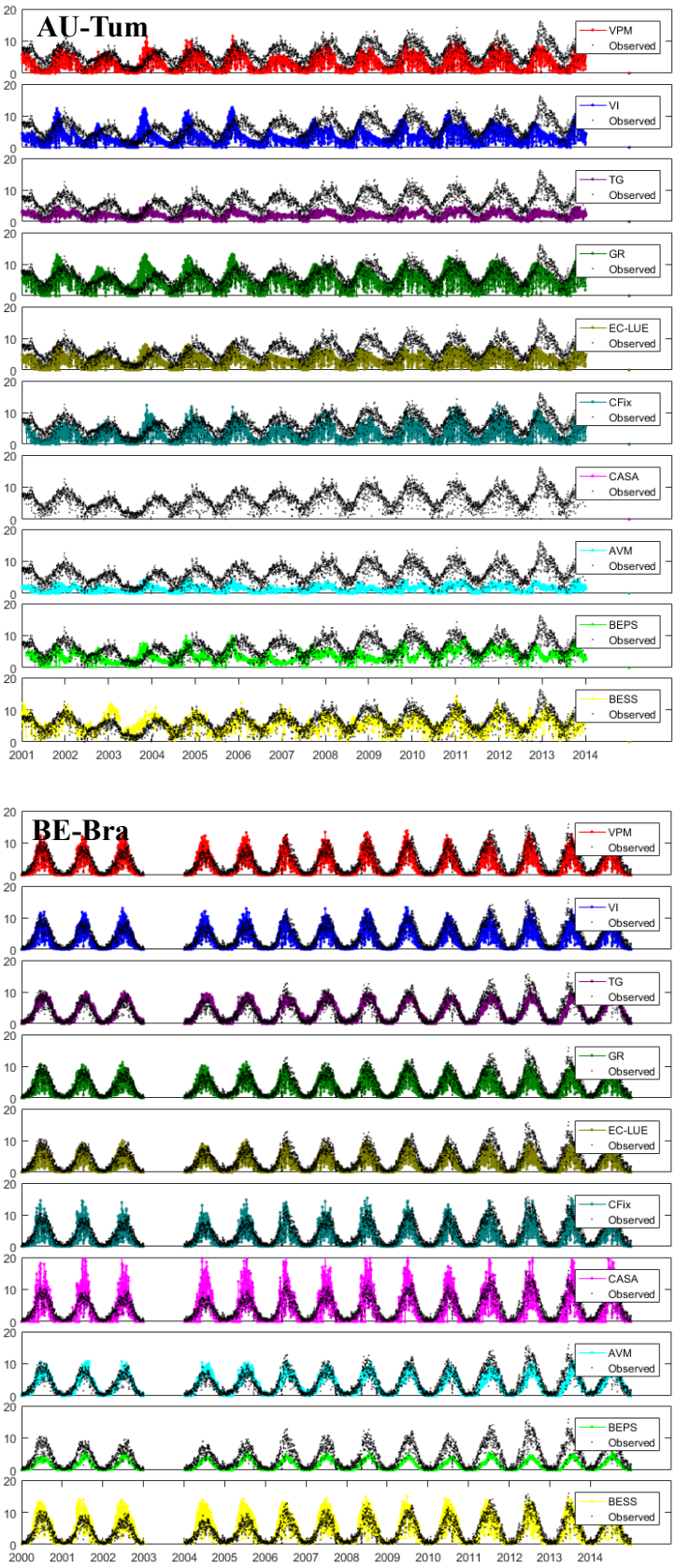

Figure S1-a Comparisons of flux GPP and estimated GPP of each site.

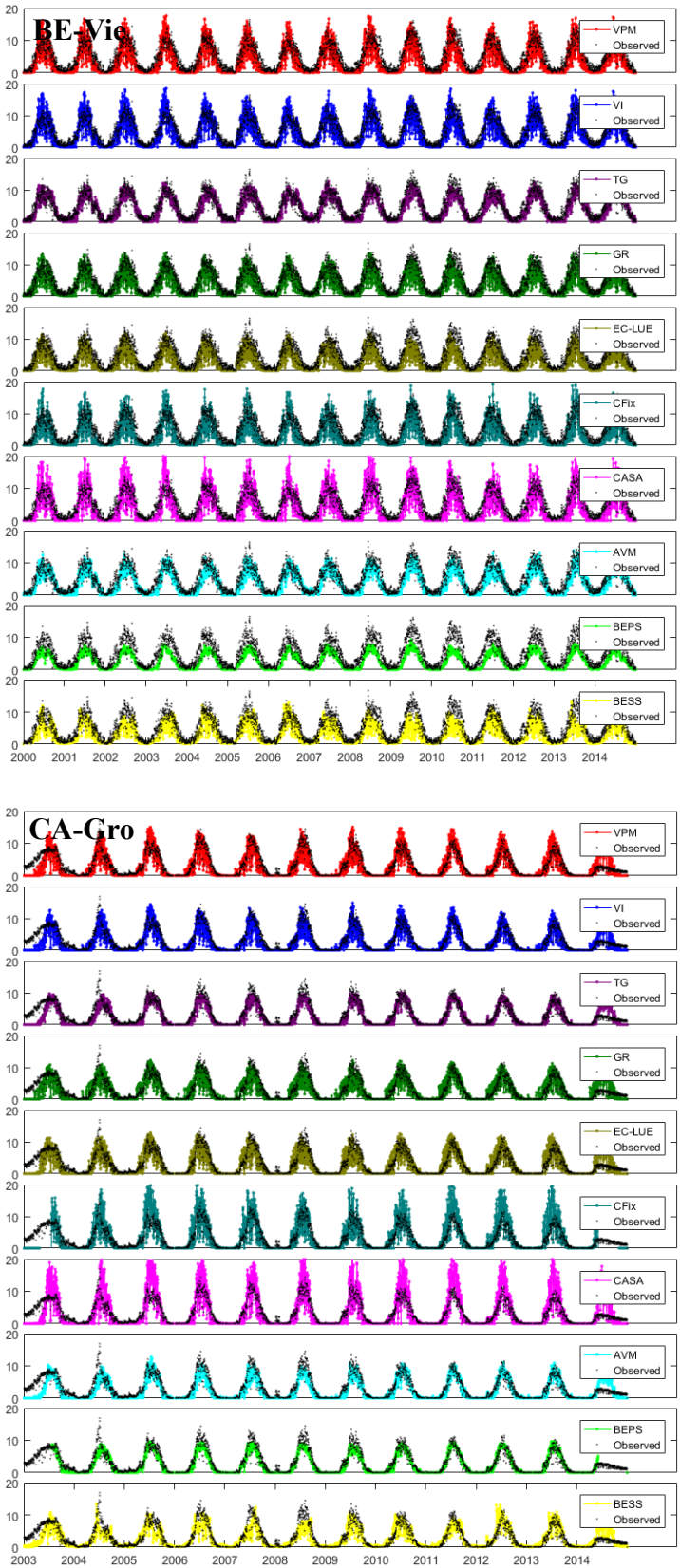

Figure S1-b Comparisons of flux GPP and estimated GPP of each site.

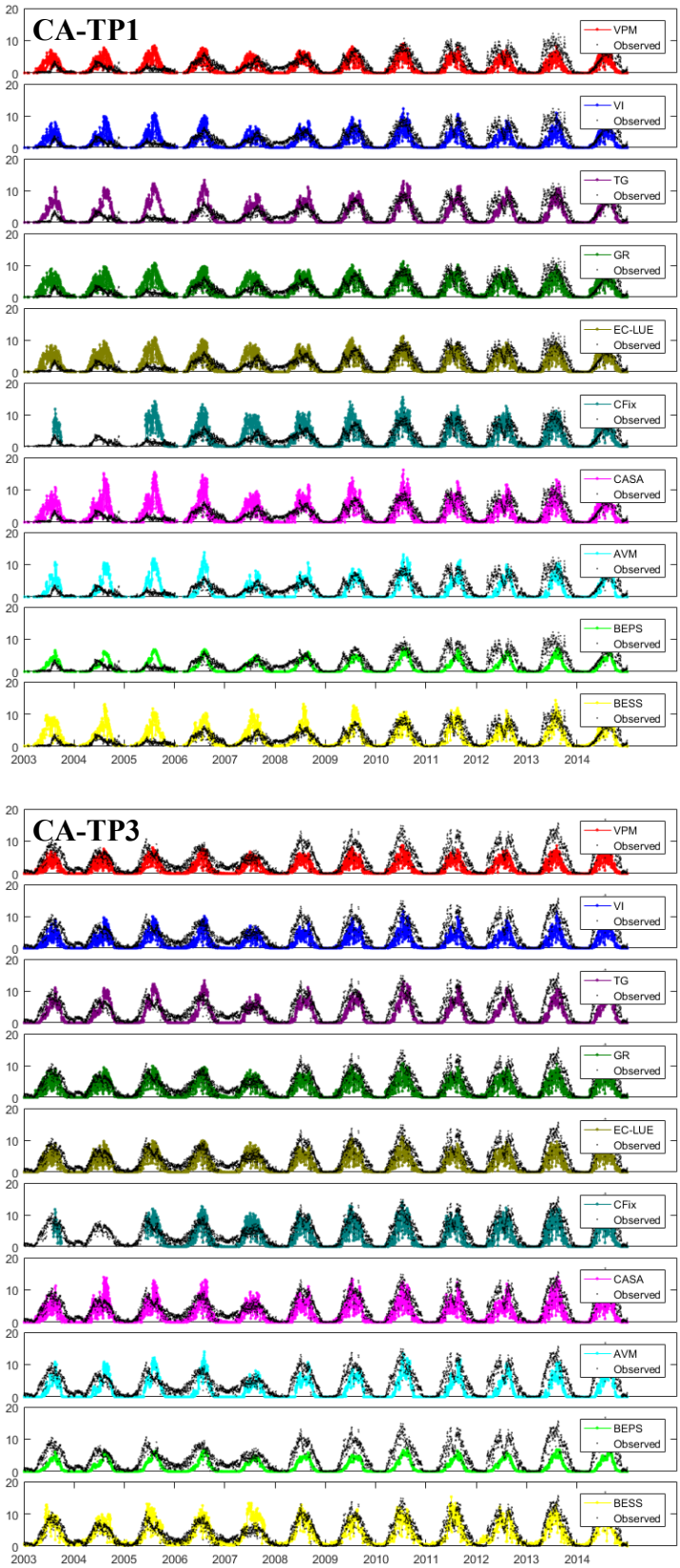

Figure S1-c Comparisons of flux GPP and estimated GPP of each site.

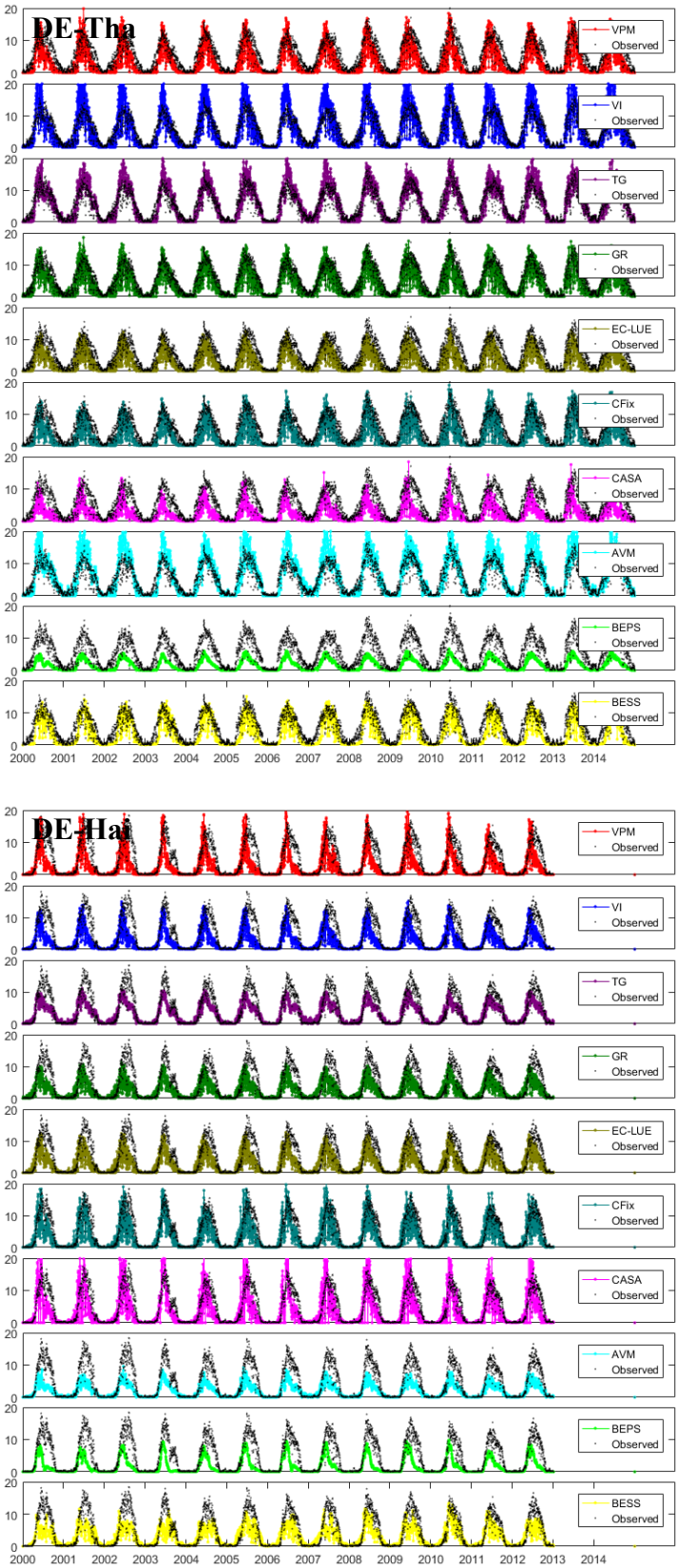

Figure S1-d Comparisons of flux GPP and estimated GPP of each site.

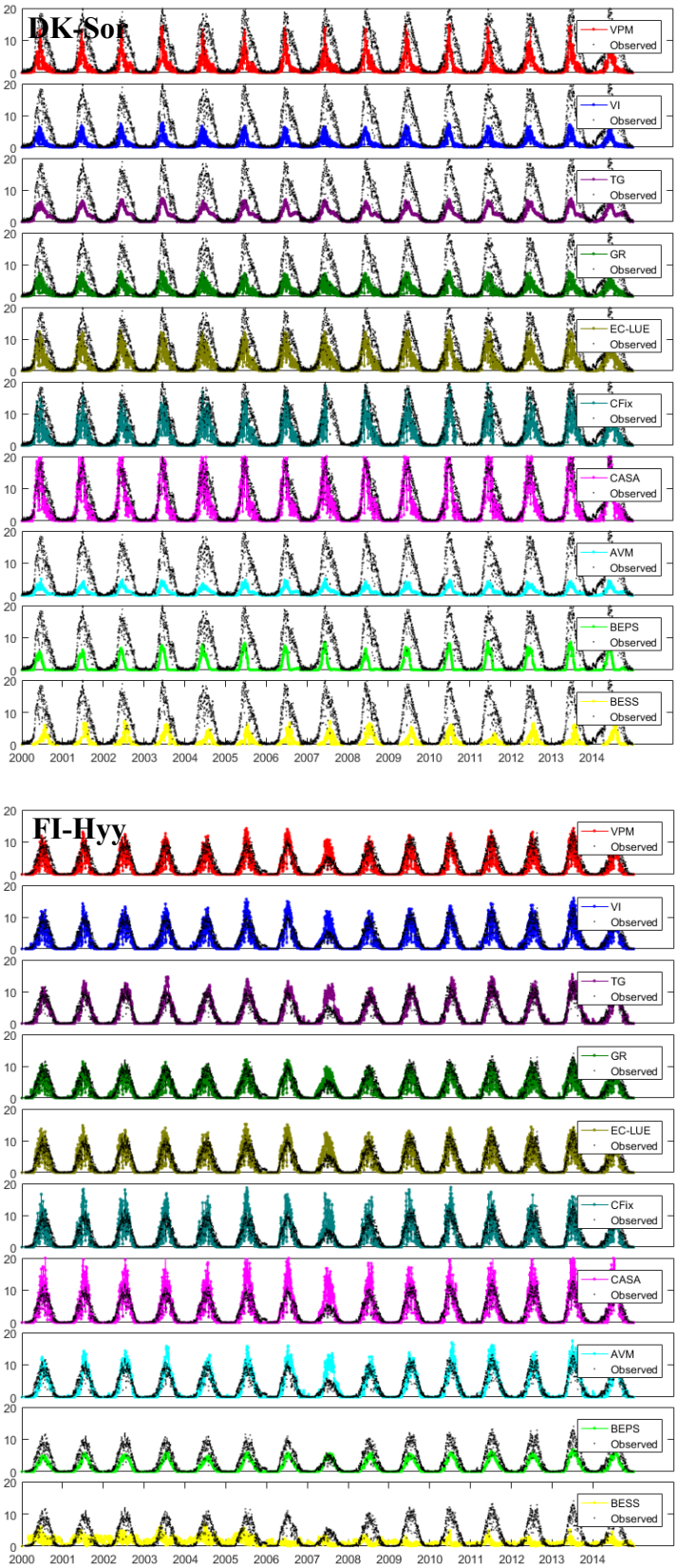

Figure S1-e Comparisons of flux GPP and estimated GPP of each site.

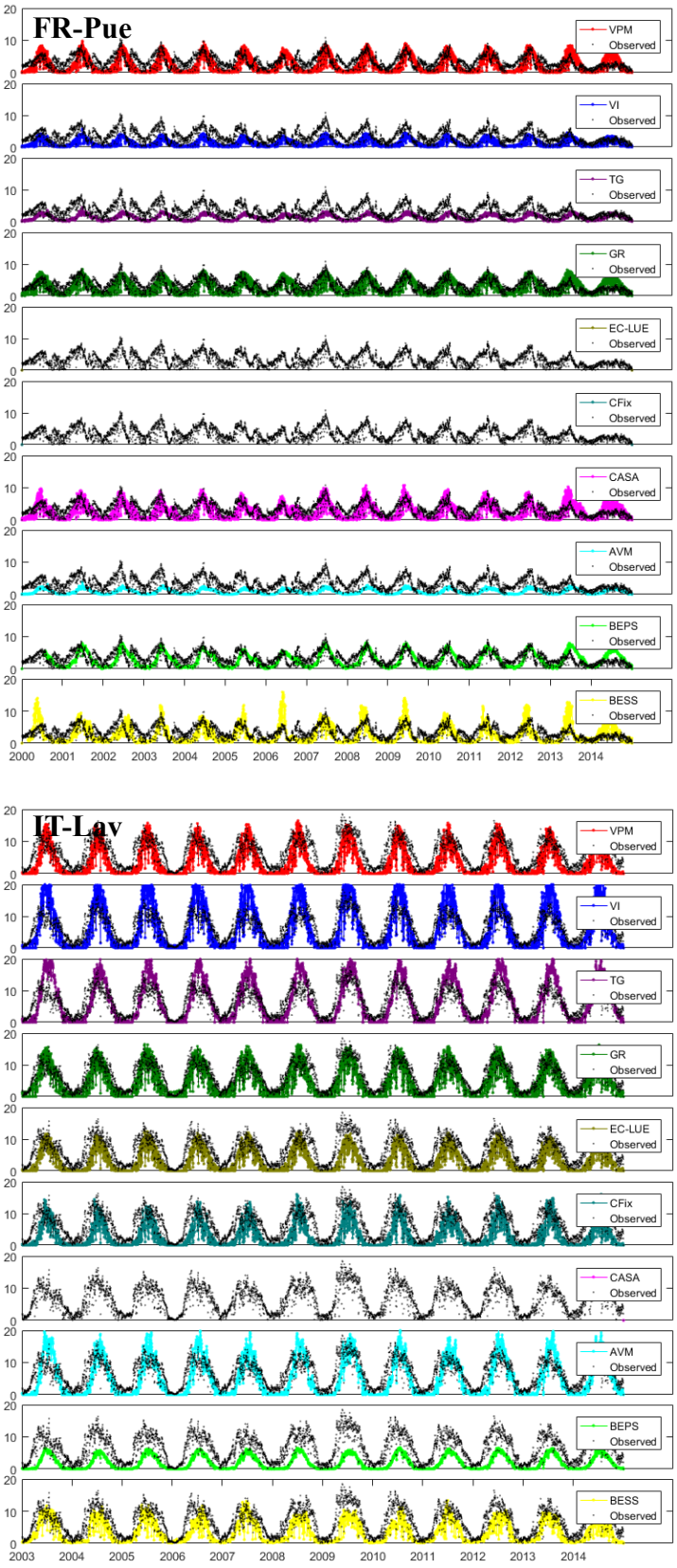

Figure S1-f Comparisons of flux GPP and estimated GPP of each site.

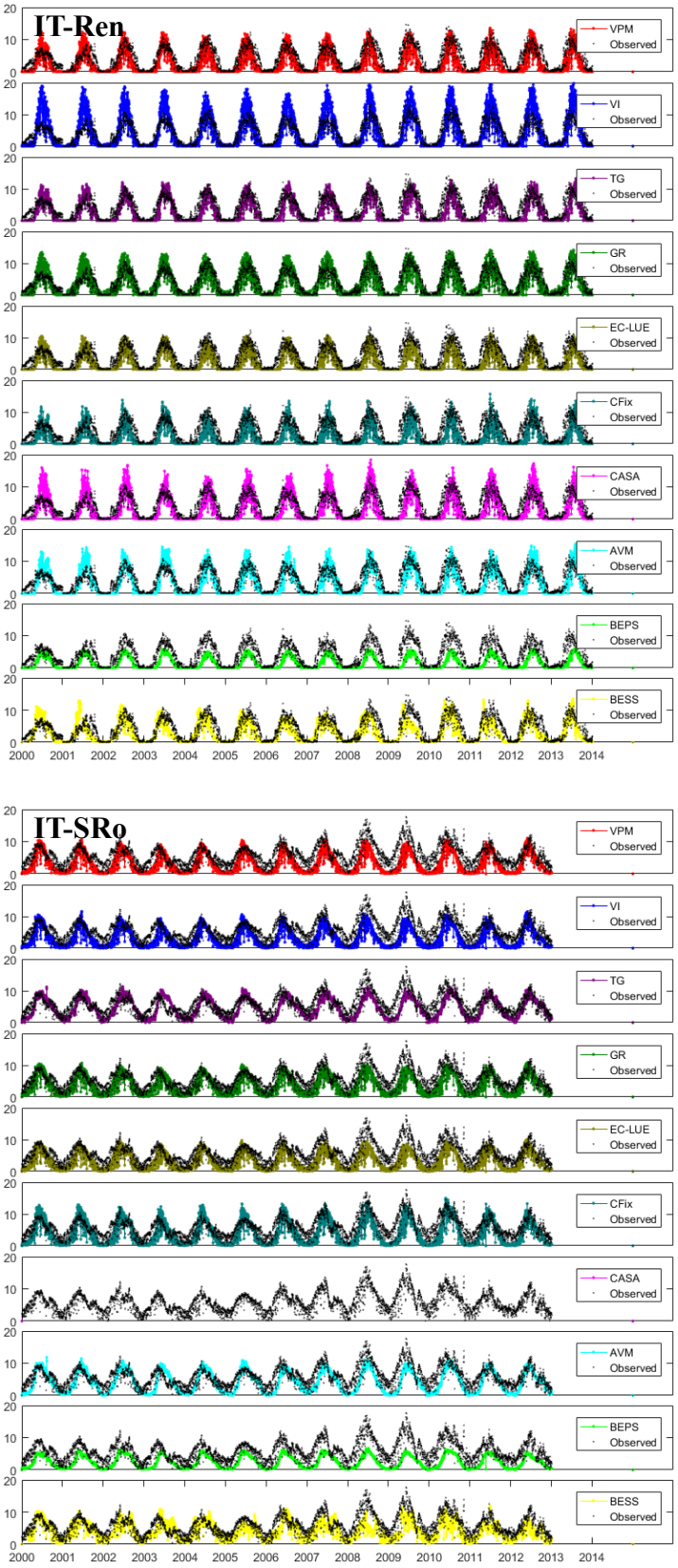

Figure S1-g Comparisons of flux GPP and estimated GPP of each site.

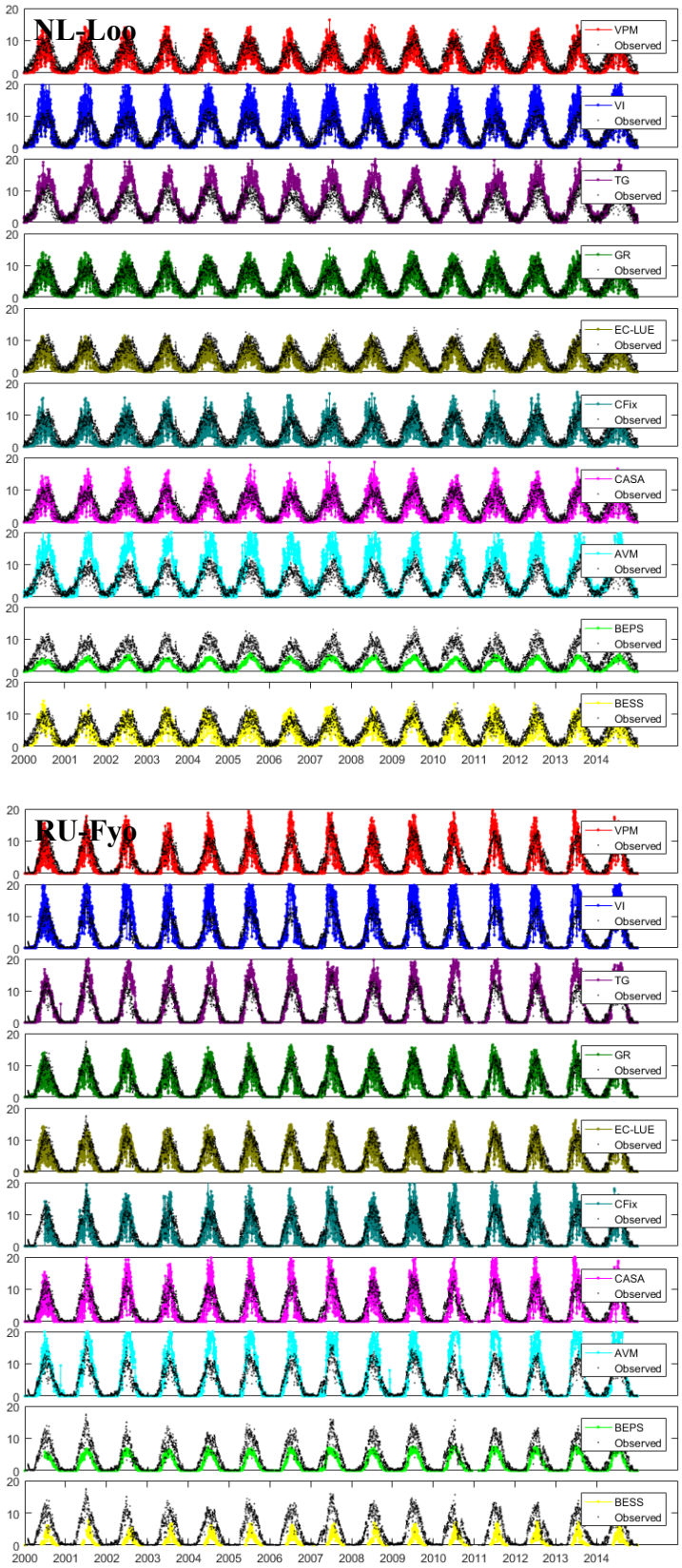

Figure S1-h Comparisons of flux GPP and estimated GPP of each site.

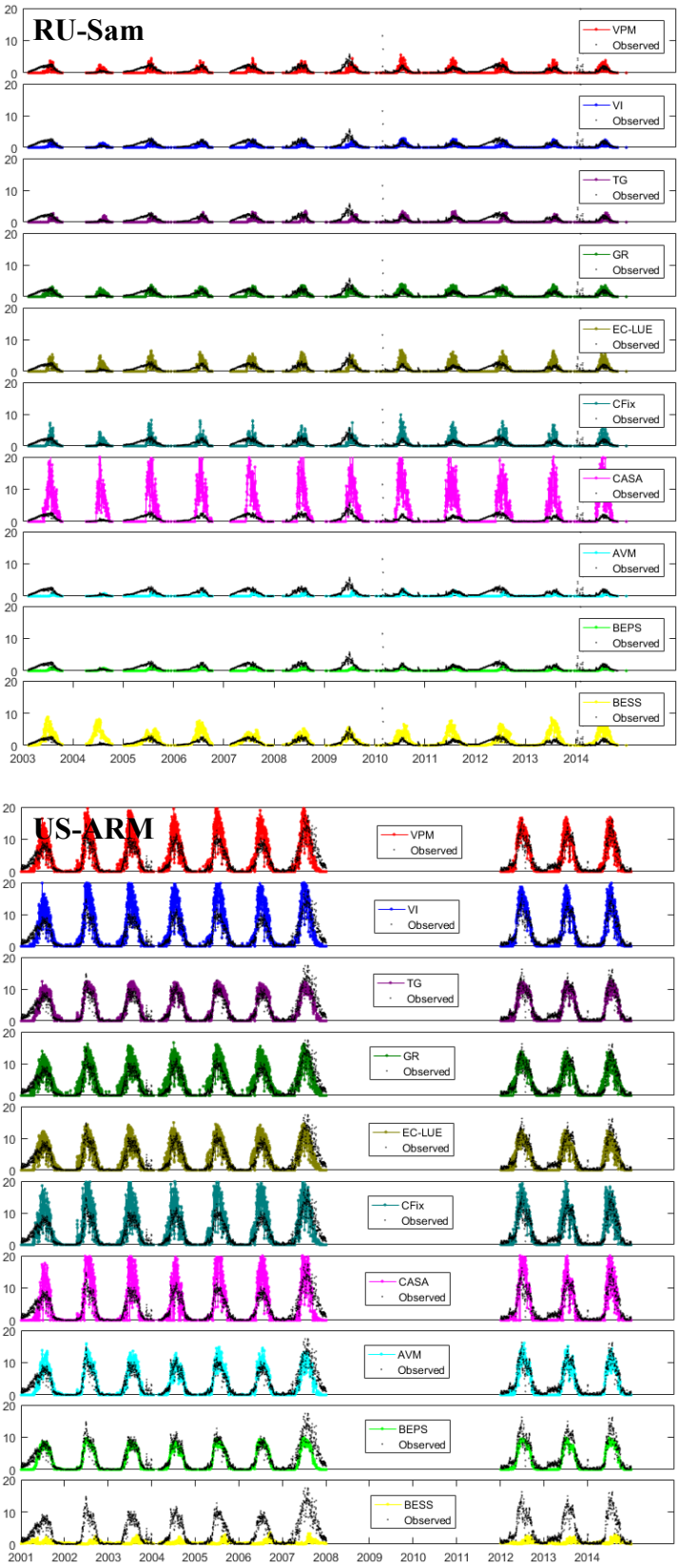

Figure S1-i Comparisons of flux GPP and estimated GPP of each site.

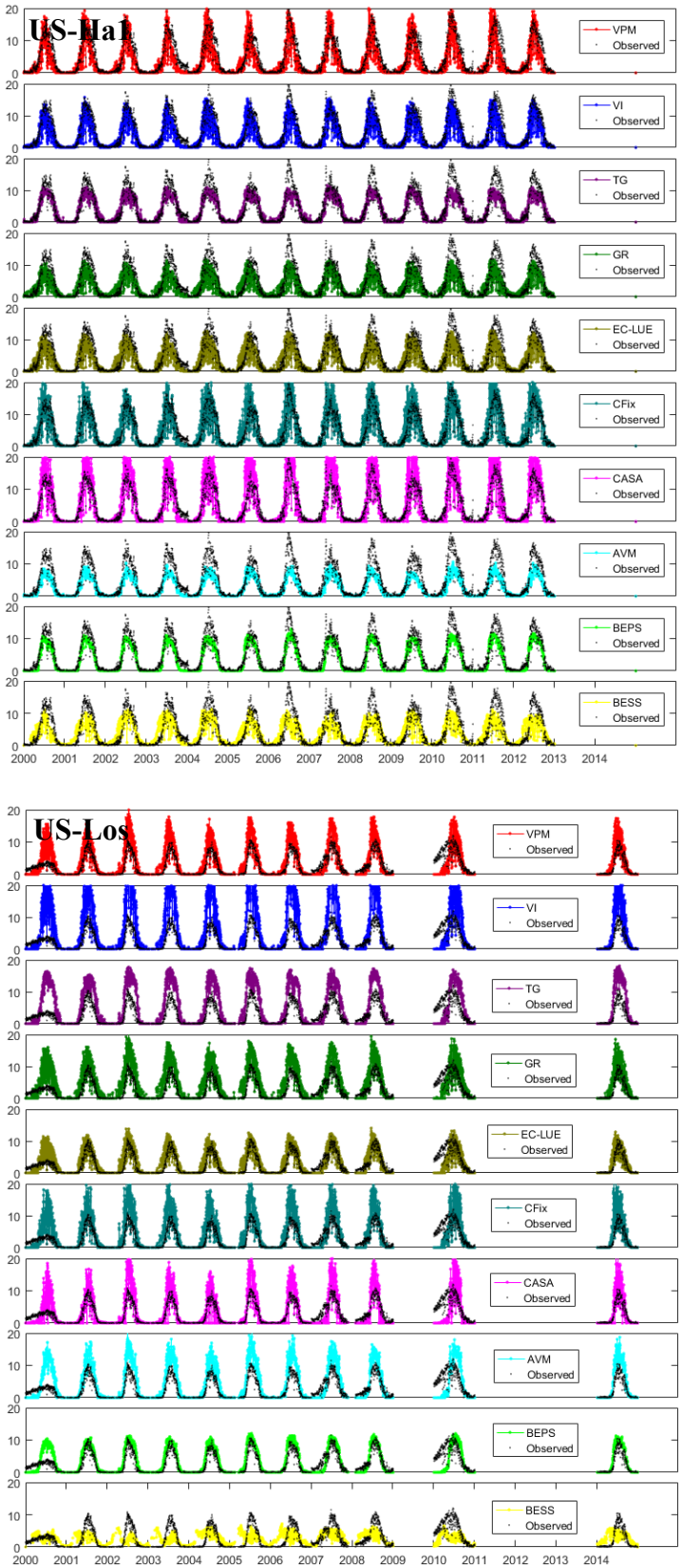

Figure S1-j Comparisons of flux GPP and estimated GPP of each site.

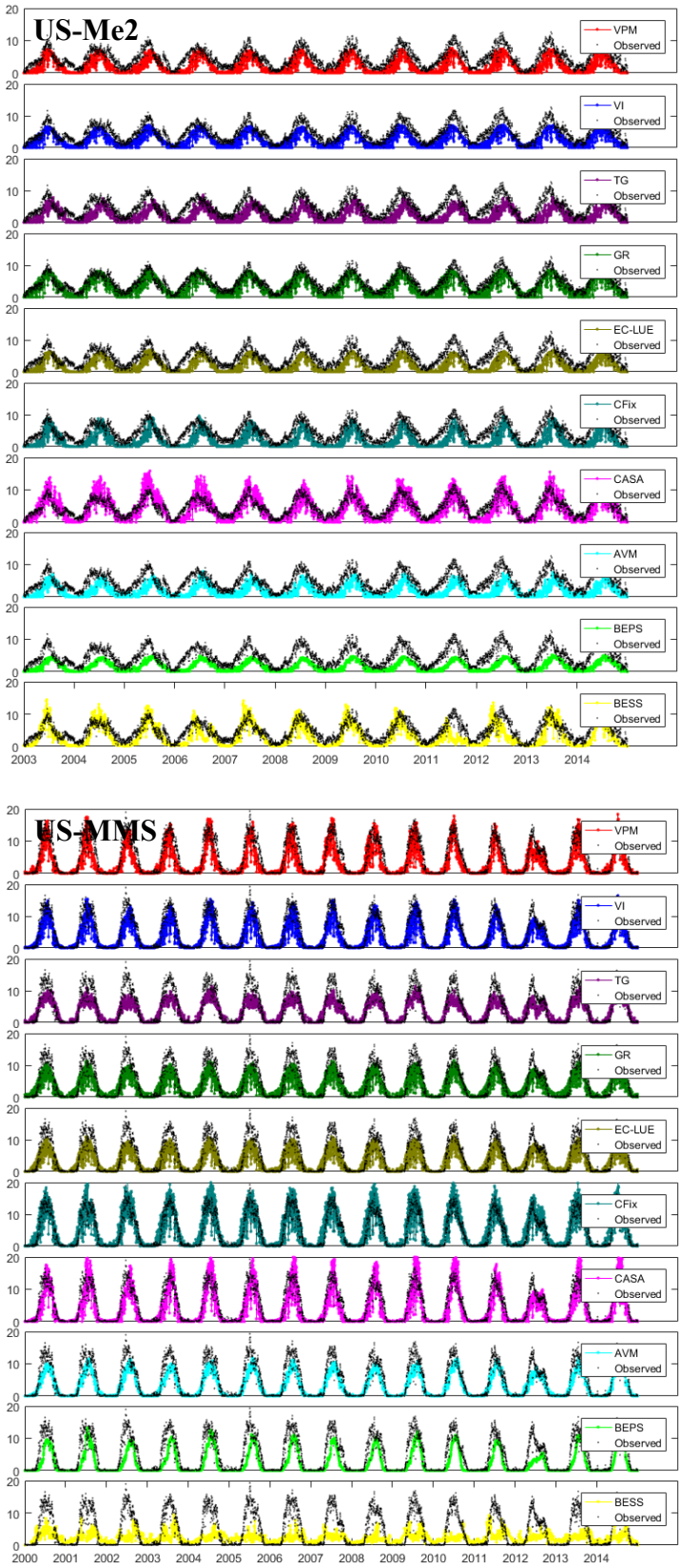

Figure S1-k Comparisons of flux GPP and estimated GPP of each site.

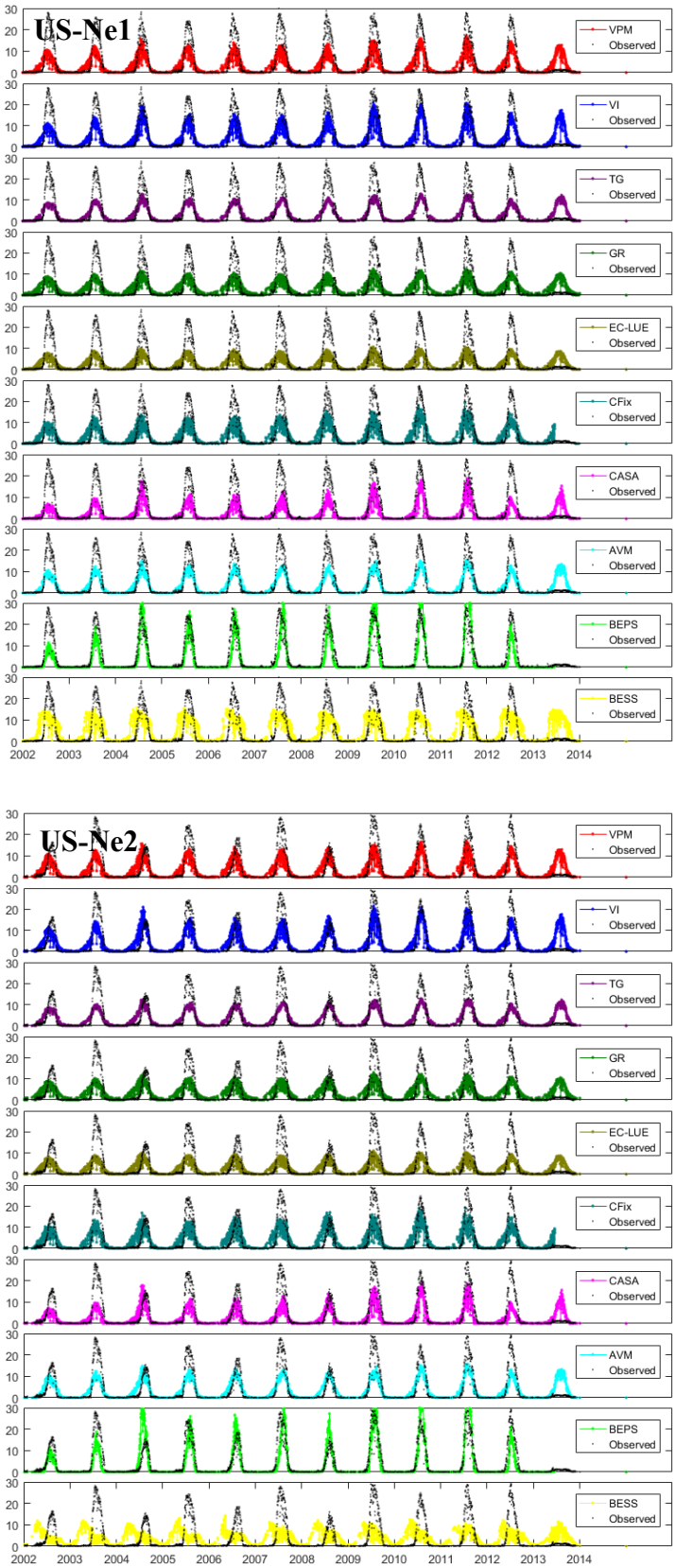

Figure S1-l Comparisons of flux GPP and estimated GPP of each site.

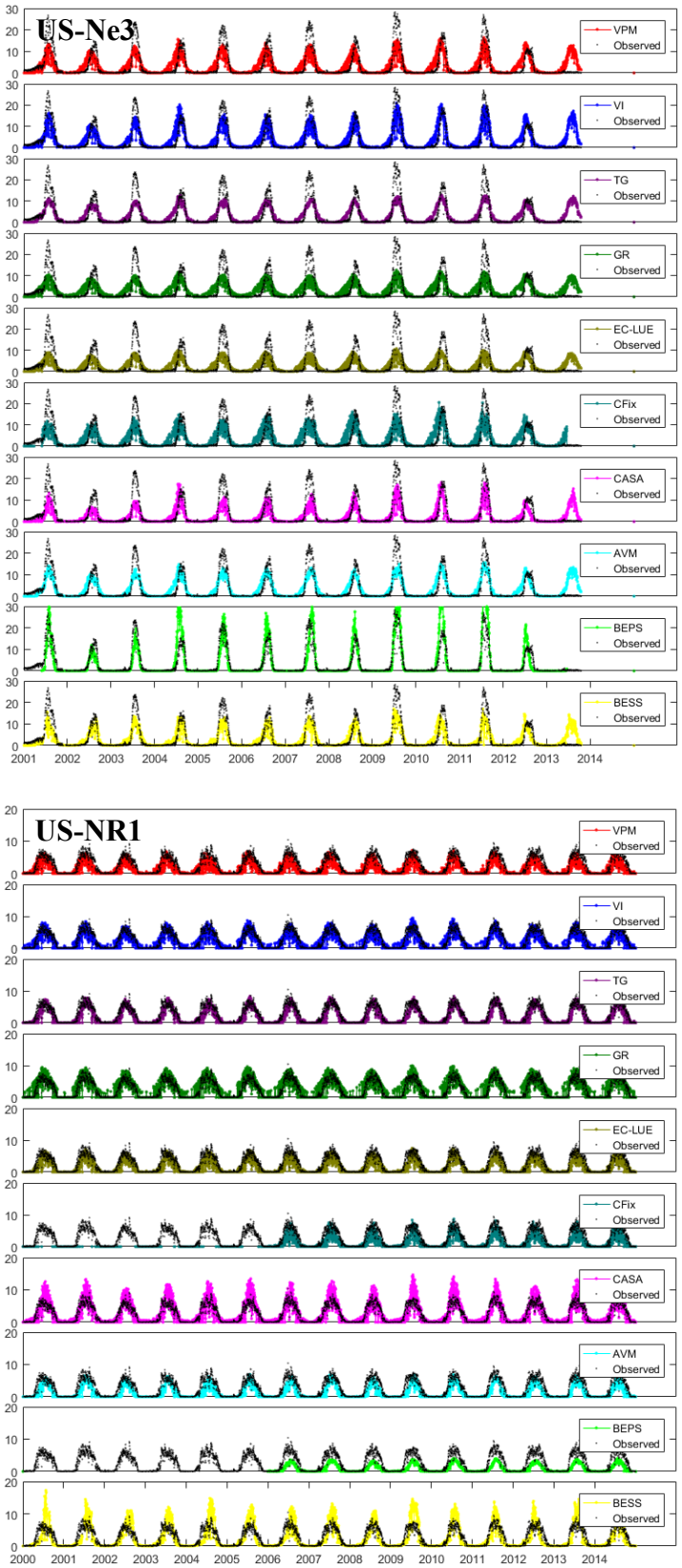

Figure S1-m Comparisons of flux GPP and estimated GPP of each site.

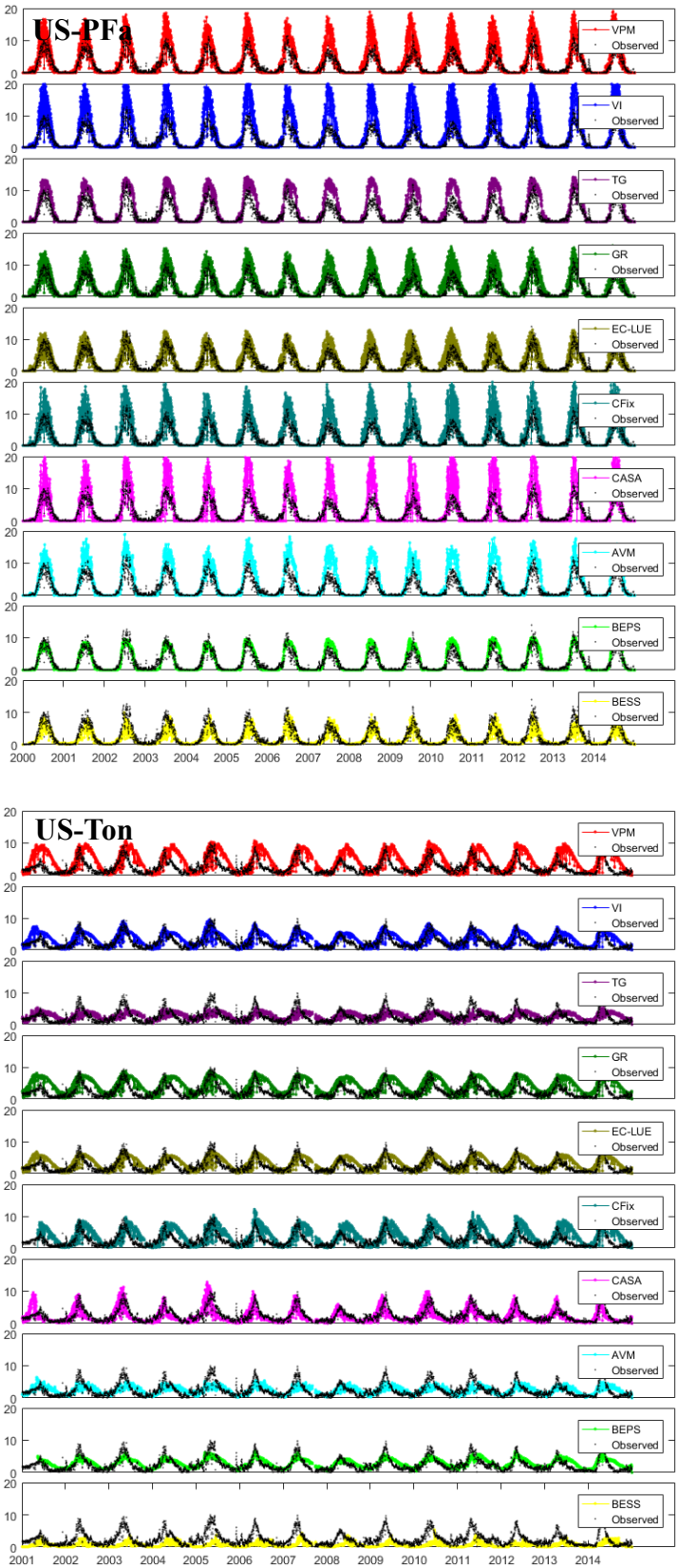

Figure S1-n Comparisons of flux GPP and estimated GPP of each site.

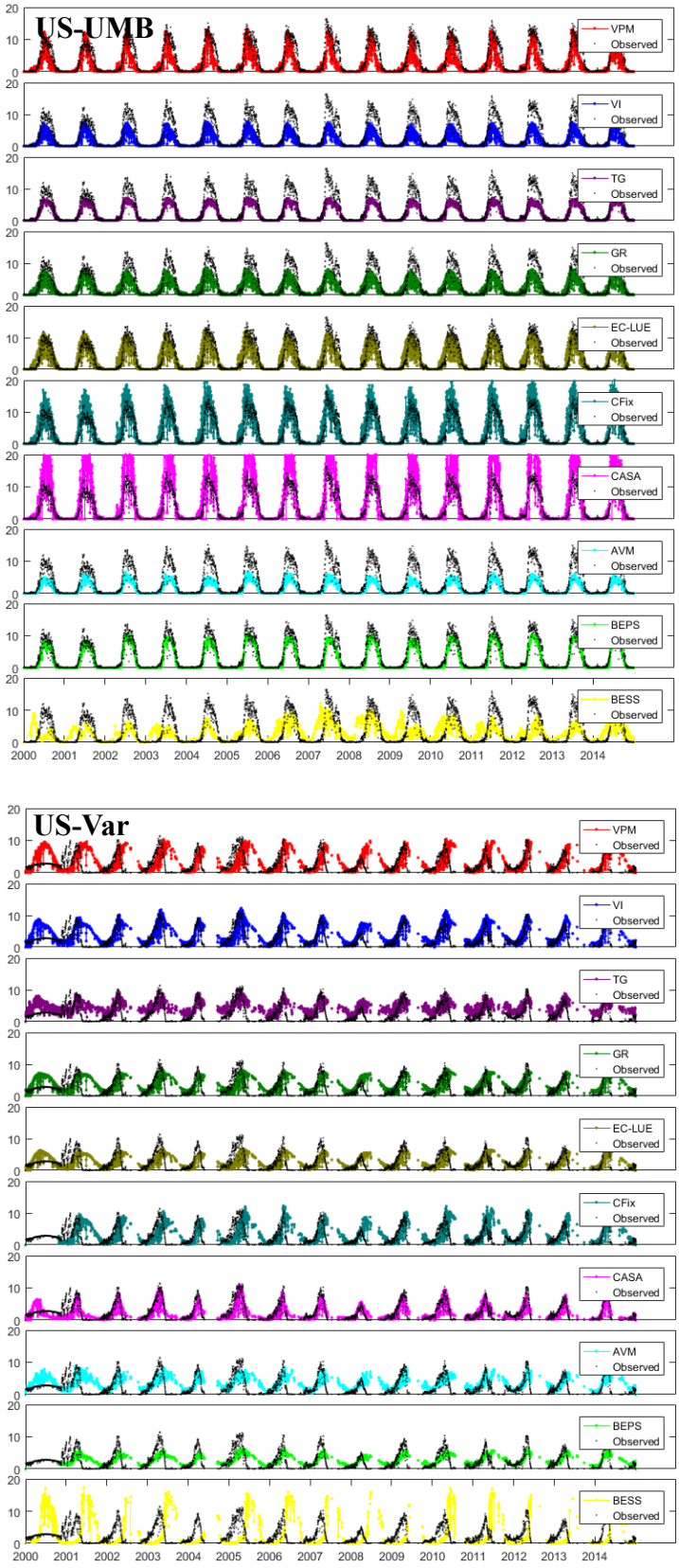

Figure S1-o Comparisons of flux GPP and estimated GPP of each site.

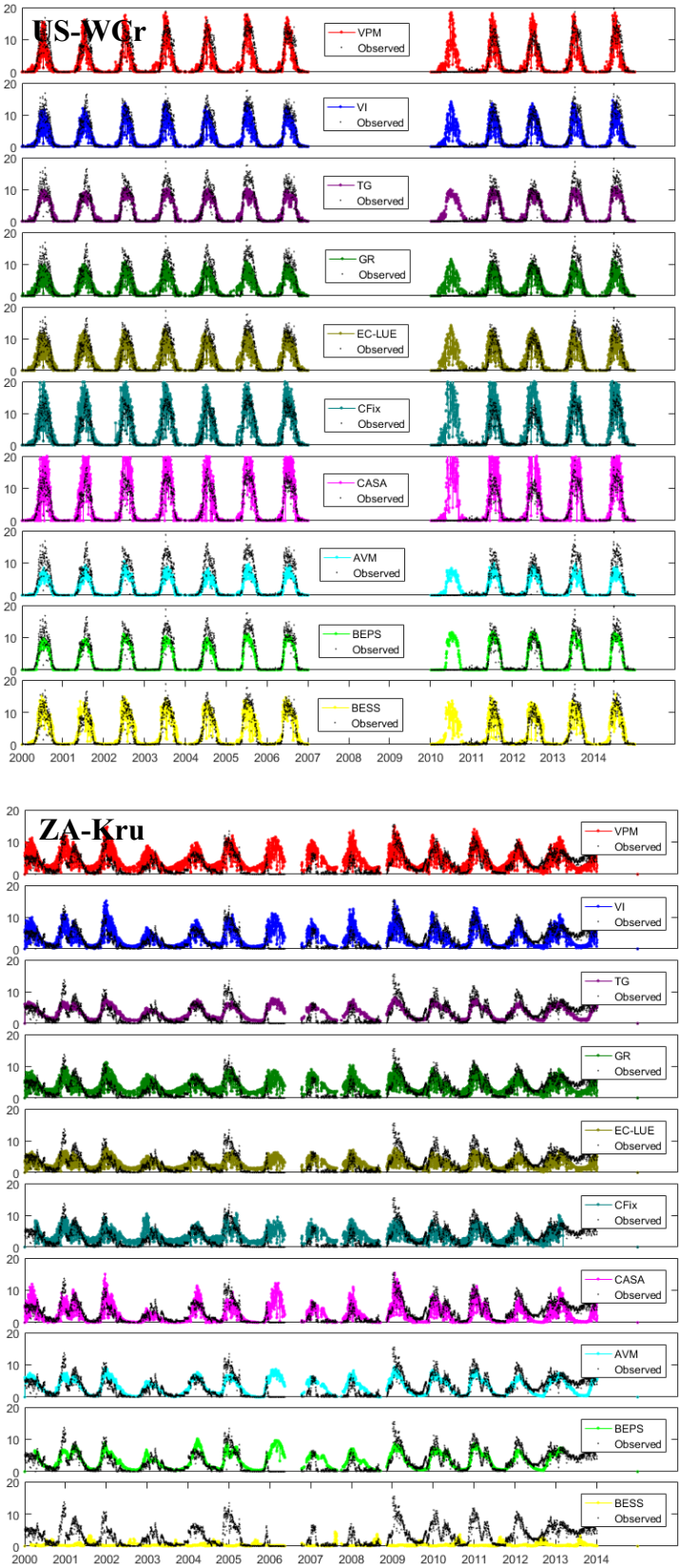

Figure S1-p Comparisons of flux GPP and estimated GPP of each site.

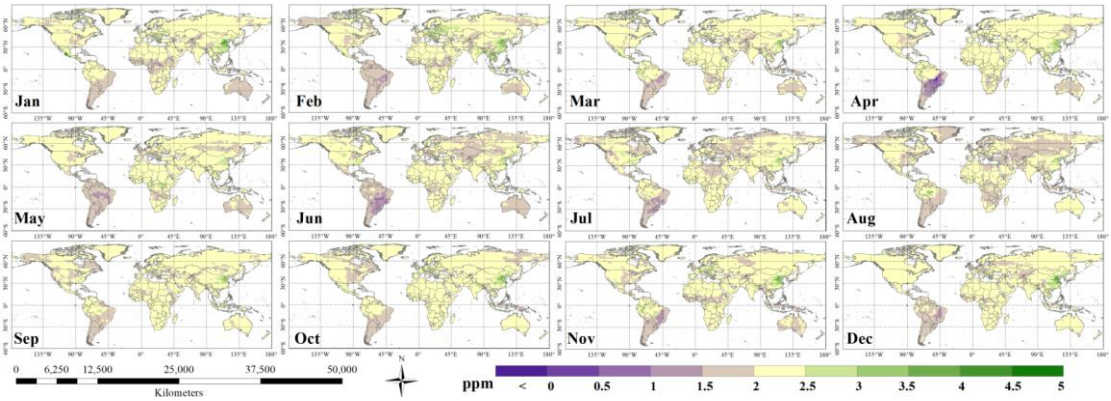

Figure S2 The monthly spatial distributions of linear trends in atmospheric CO_2 concentrations during the period 1982-2015.

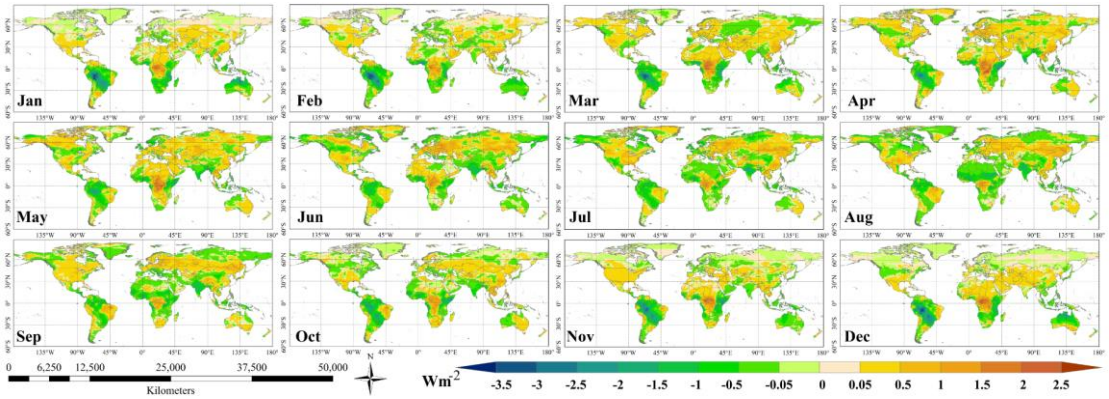

Figure S3 The monthly spatial distributions of linear trends in radiation during the period 1982-2015.

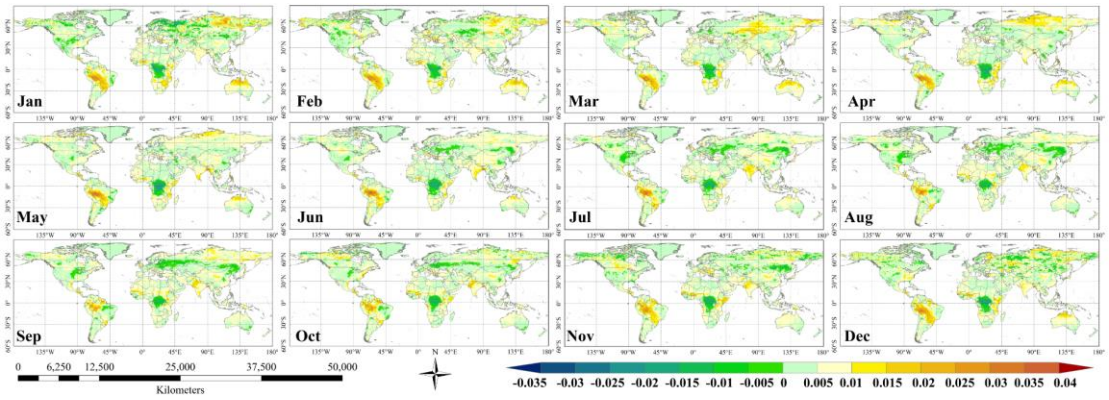

Figure S4 The monthly spatial distributions of linear trends in water conditions during the period 1982-2015.

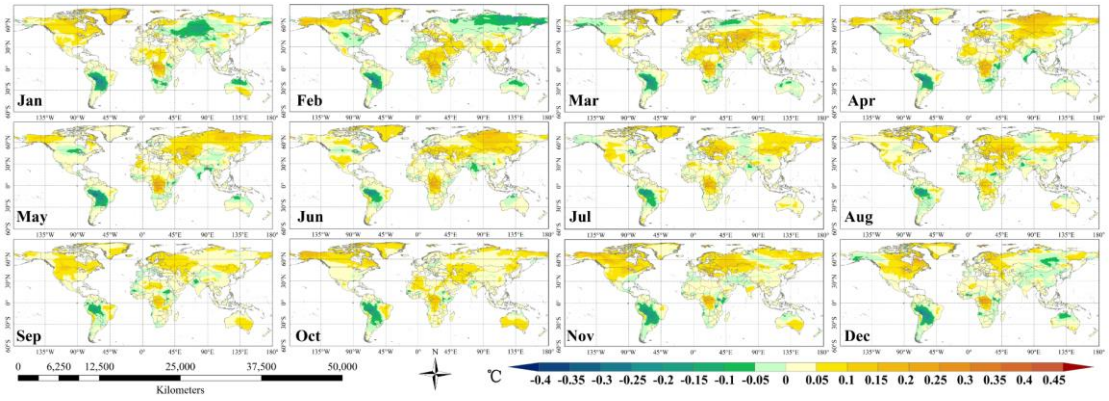

Figure S5 The monthly spatial distributions of linear trends in temperature during the period 1982-2015.

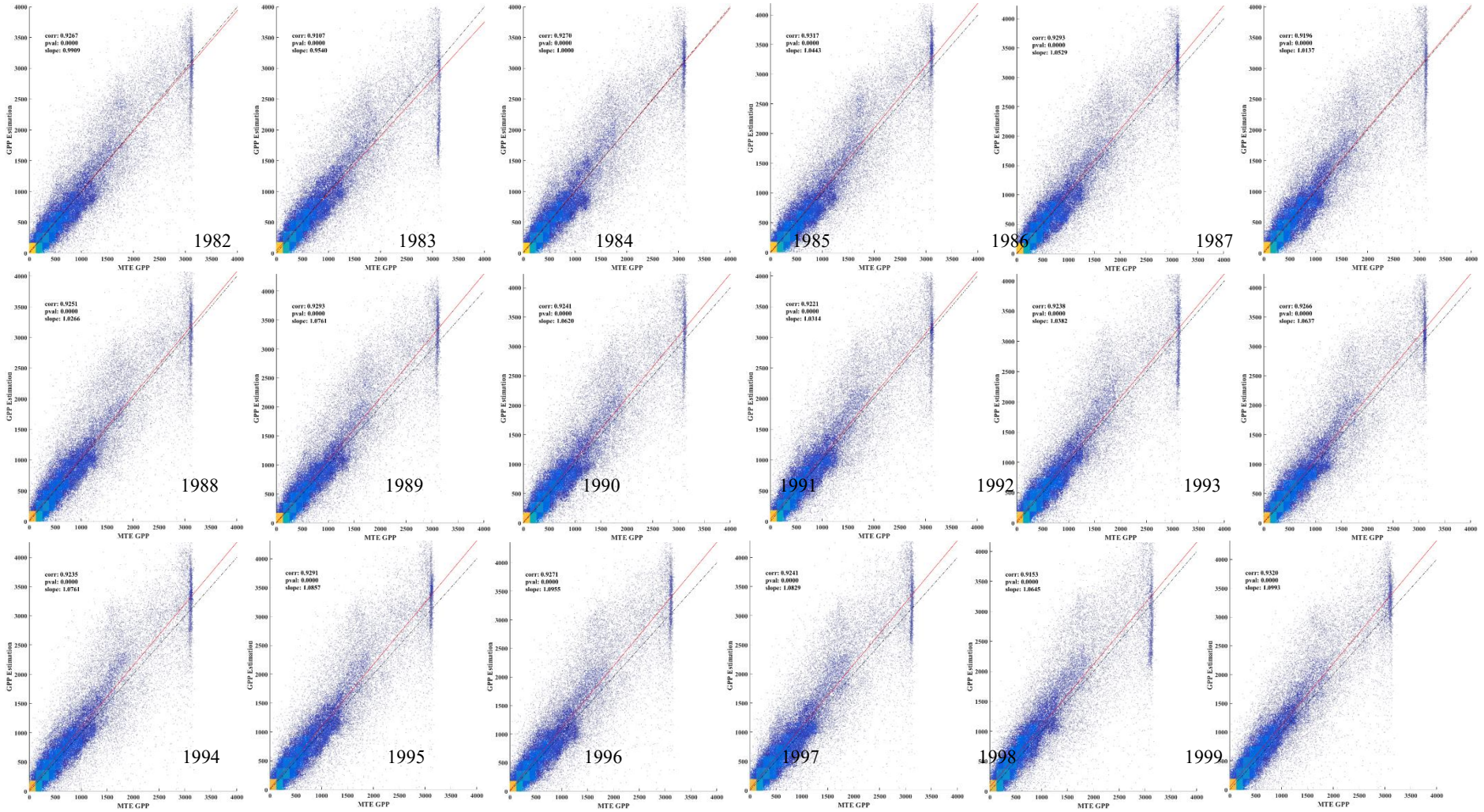

Figure S6-a Scatter plots of estimated GPP values (*y* axis) vs. MTE_GL GPP values (*x* axis) from 1982 to 2011. Only pixels over vegetated areas are shown. The parameters of the linear regression line in all panels are shown in Table 3.3.

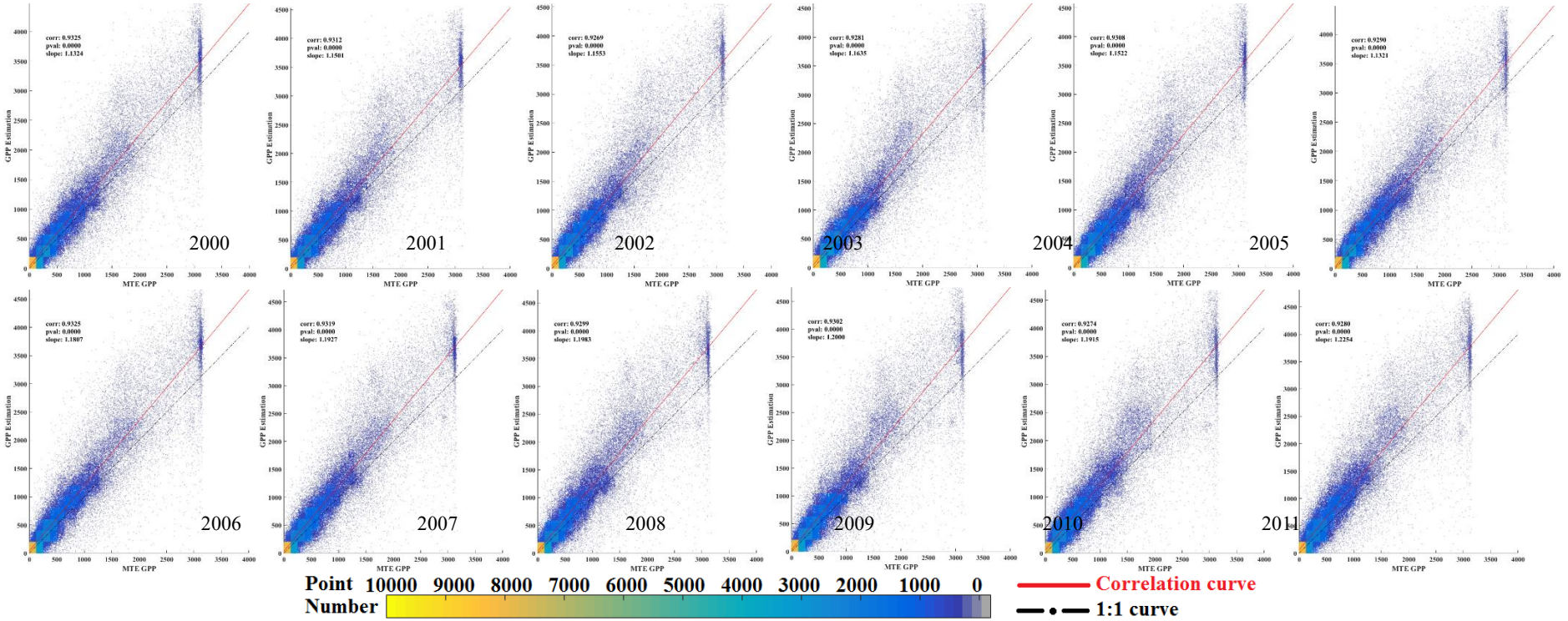

Figure S6-b Scatter plots of estimated GPP values (*y* axis) vs. MTE_GL GPP values (*x* axis) from 1982 to 2011. Only pixels over vegetated areas are shown. The parameters of the linear regression line in all panels are shown in Table 3.3.

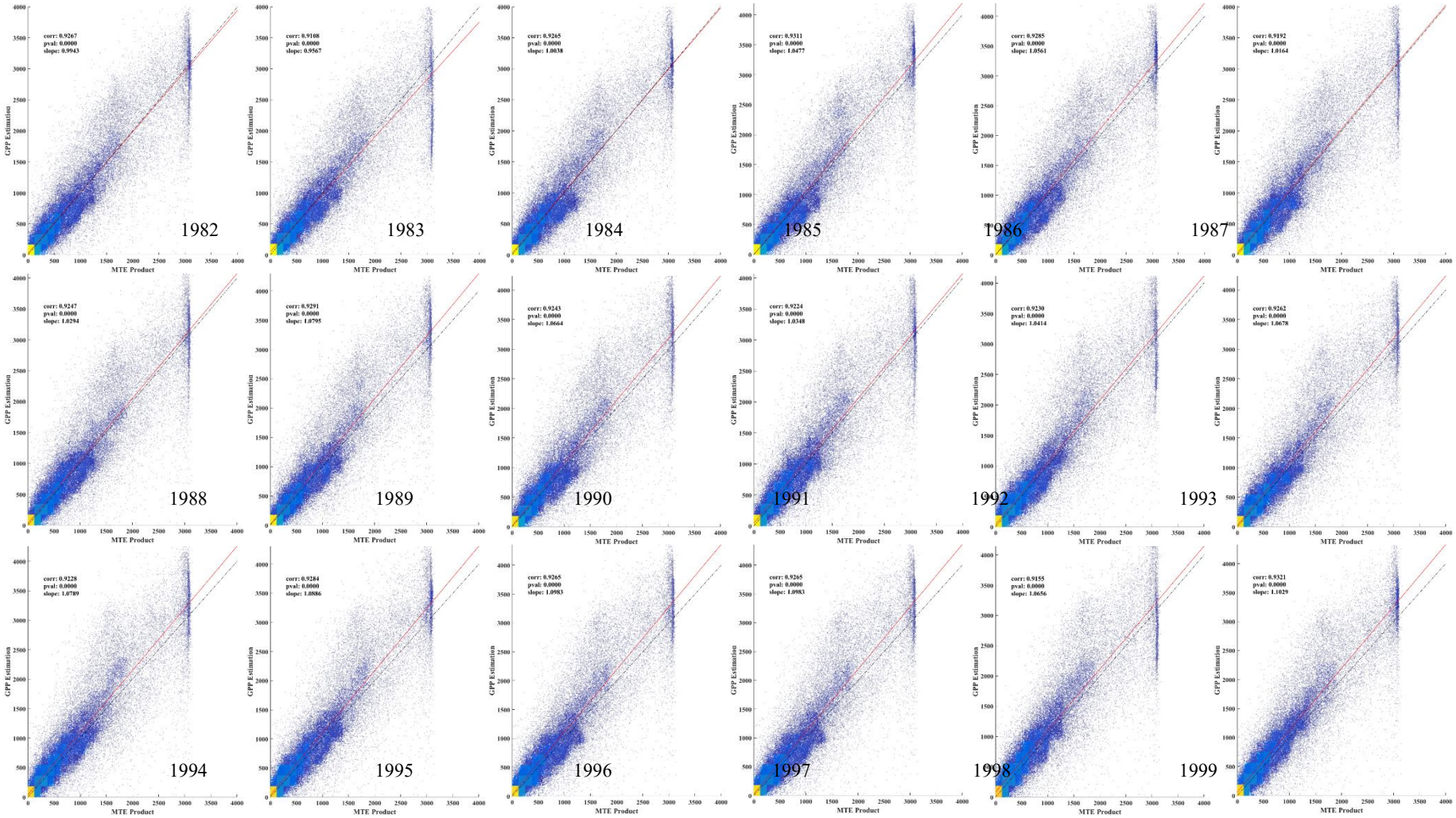

Figure S7-a Scatter plots of estimated GPP values (*y* axis) vs. MTE_MR GPP values (*x* axis) from 1982 to 2011. Only pixels over vegetated areas are shown. The parameters of the linear regression line in all panels are shown in Table 3.3.

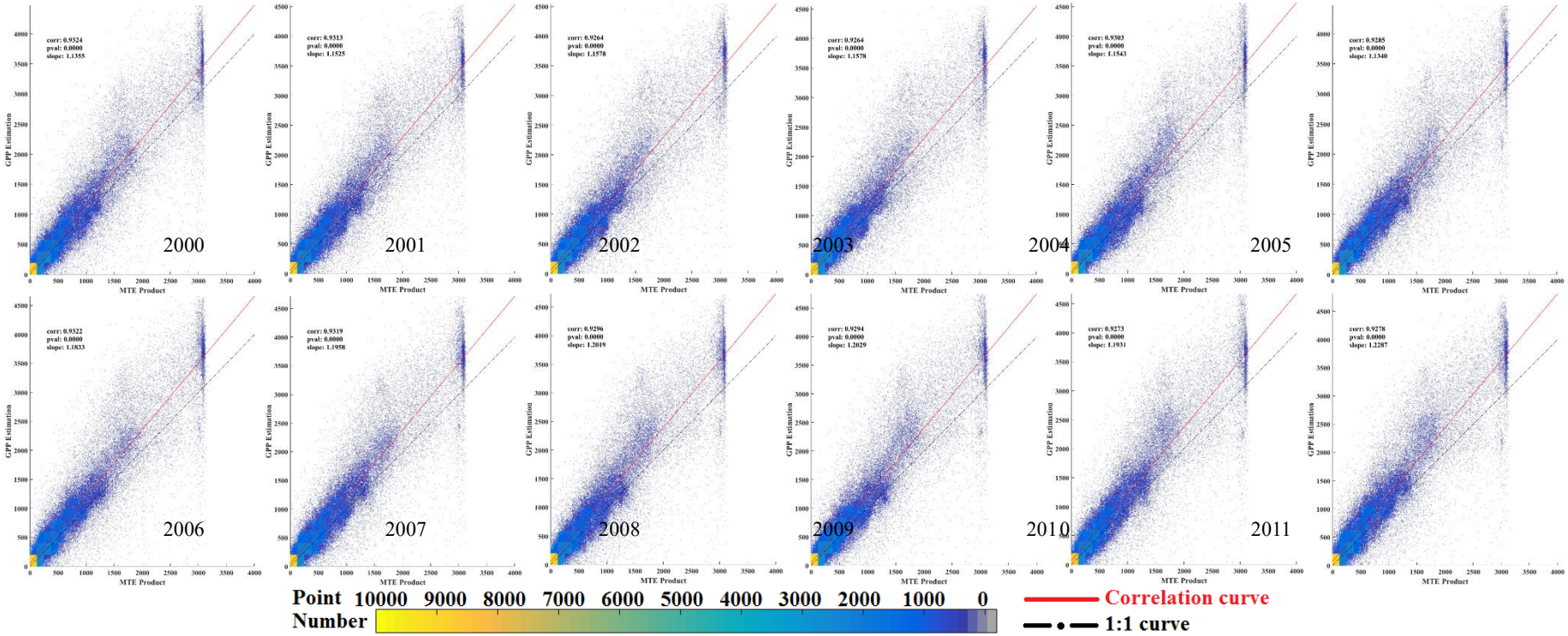

Figure S7-b Scatter plots of estimated GPP values (*y* axis) vs. MTE_MR GPP values (*x* axis) from 1982 to 2011. Only pixels over vegetated areas are shown. The parameters of the linear regression line in all panels are shown in Table 3.3.

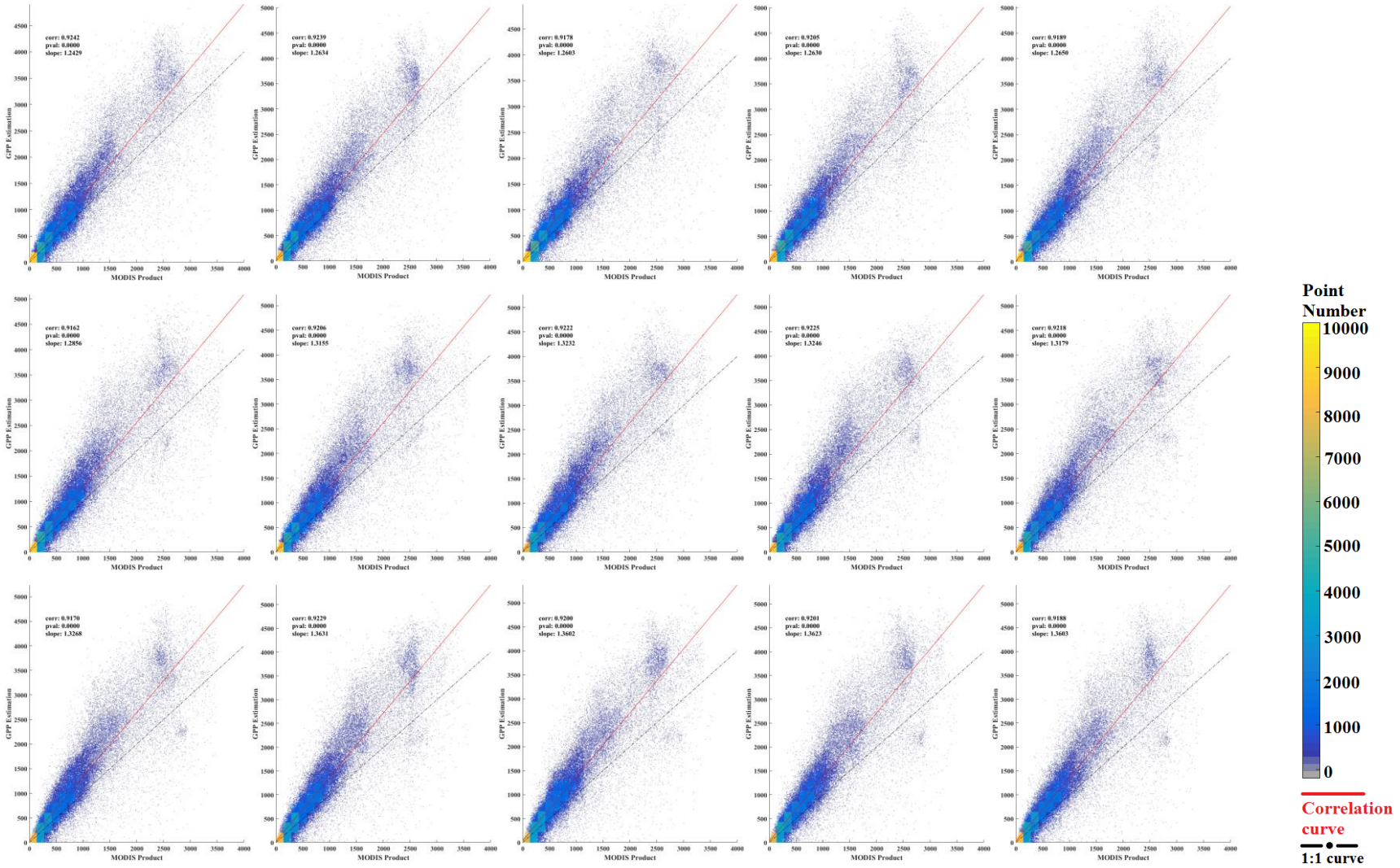

Figure S8 Scatter plots of estimated GPP values (y axis) vs. MODIS Product (x axis) from 1982 to 2011. Only pixels over vegetated areas are shown. The parameters of the linear regression line in all panels are shown in Table 3.3.

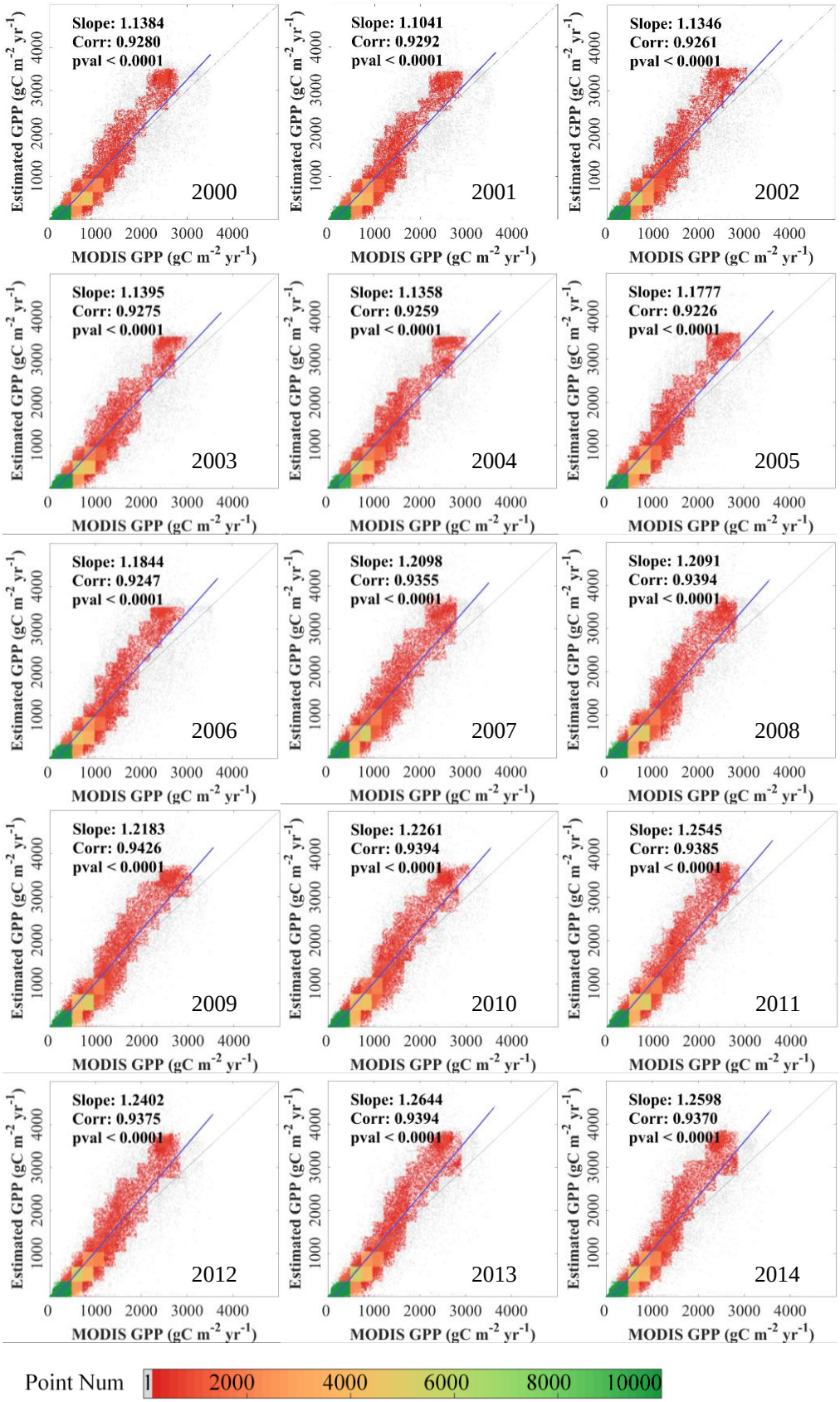

Figure S9 Comparisons of annual GPP estimated by the MODIS algorithm and the iBEPSd model.

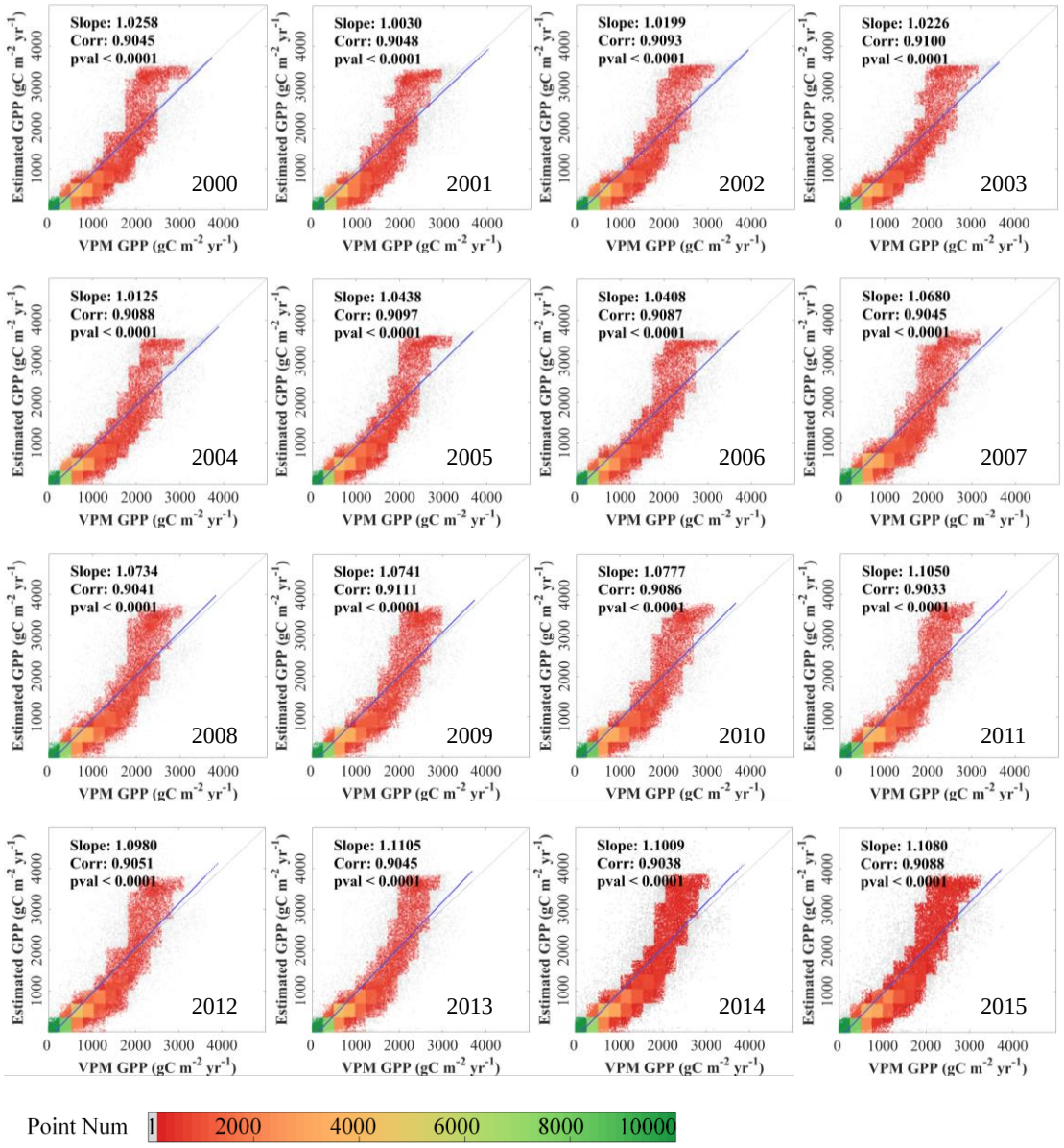

Figure S10 Comparisons of annual GPP estimated by the VPM algorithm and the iBEPSd model.

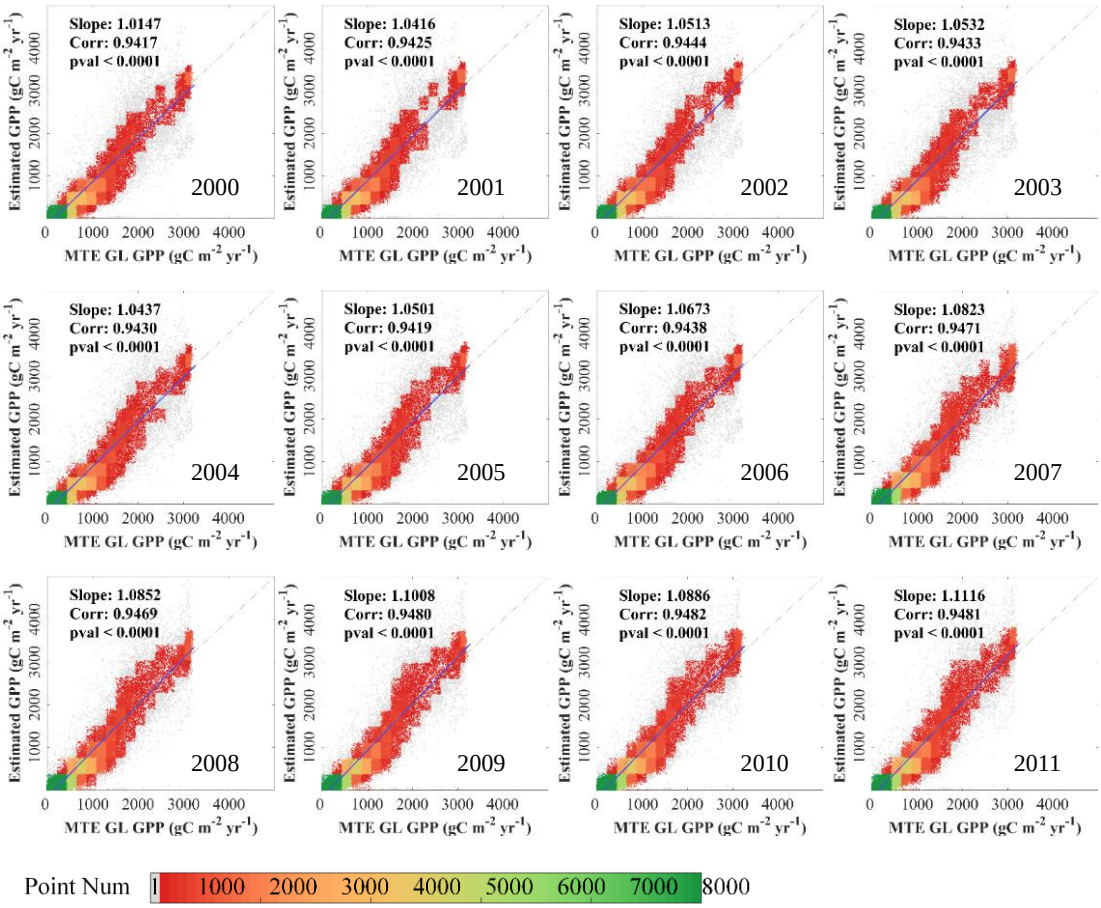

Figure S11 Comparisons of annual GPP estimated by the MTE-GL and the iBEPSd model.

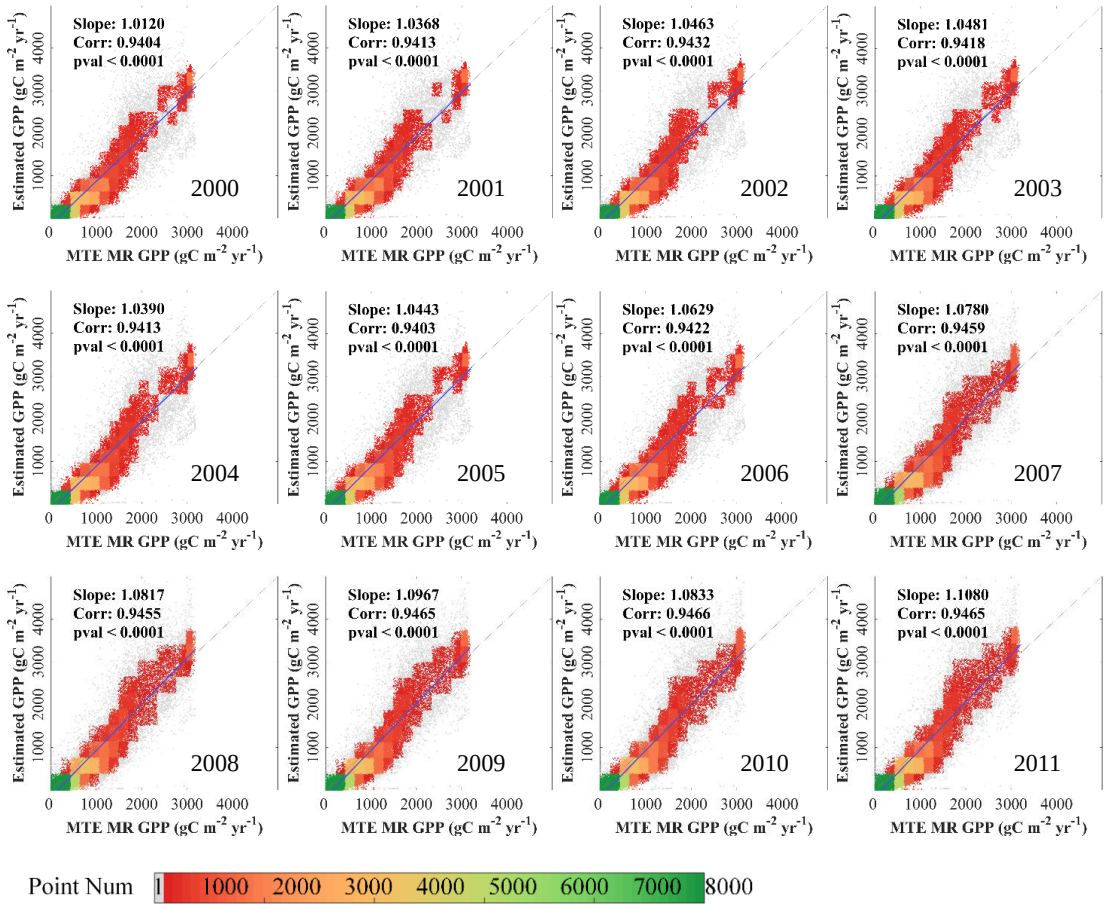

Figure S12 Comparisons of annual GPP estimated by the MTE-MR and the iBEPSd model.

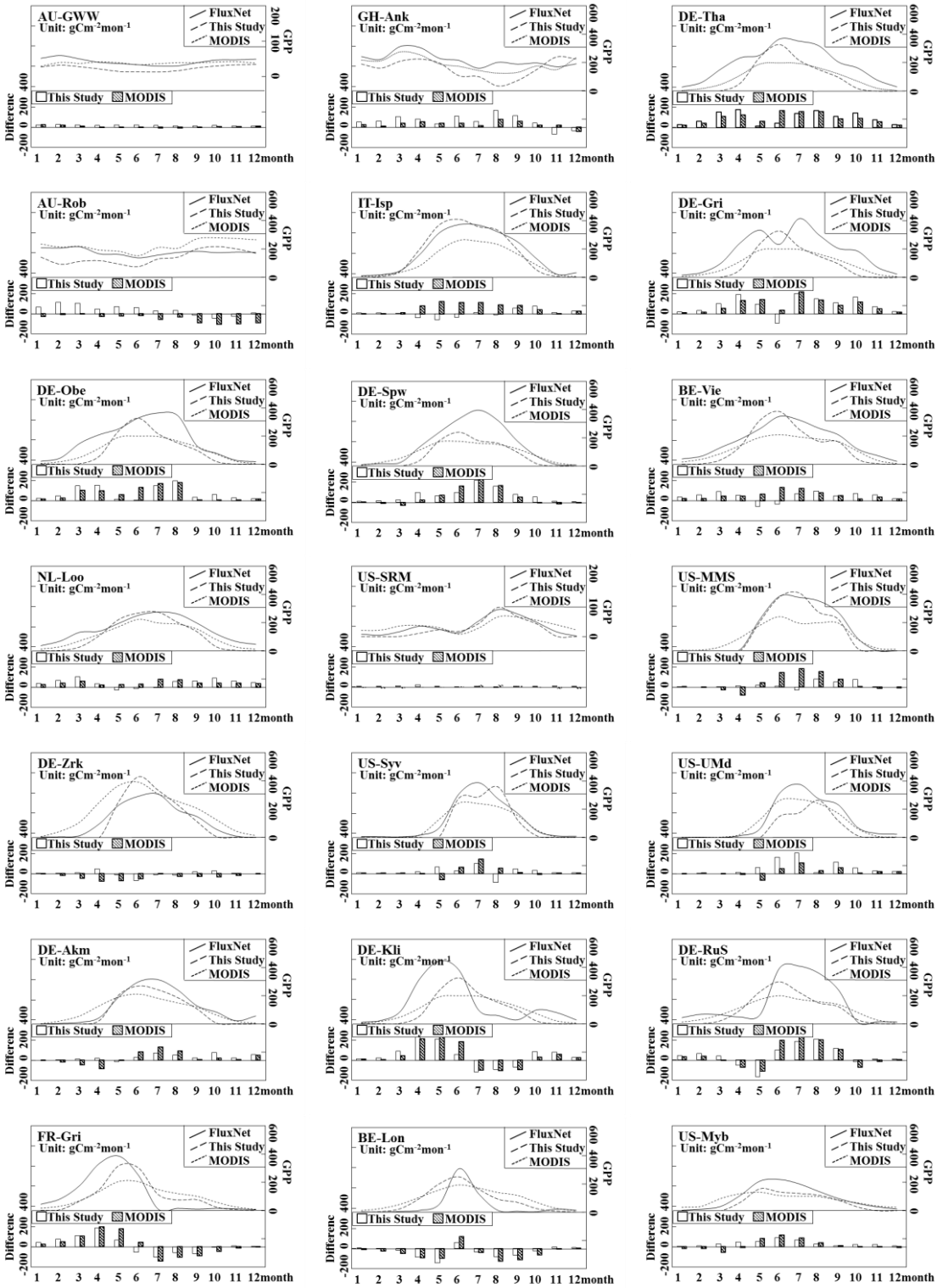

Figure S13-a Different GPP estimates at each flux tower site. (Above: Monthly distribution of GPP values of $GPP_{2014}^{monthly\ spatial\ CO_2}$, MODIS product and tower observations; Below: Difference between $GPP_{2014}^{monthly\ spatial\ CO_2}$ and tower GPP estimates, and difference between the MODIS GPP product and tower GPP estimates at each corresponding flux tower site.)

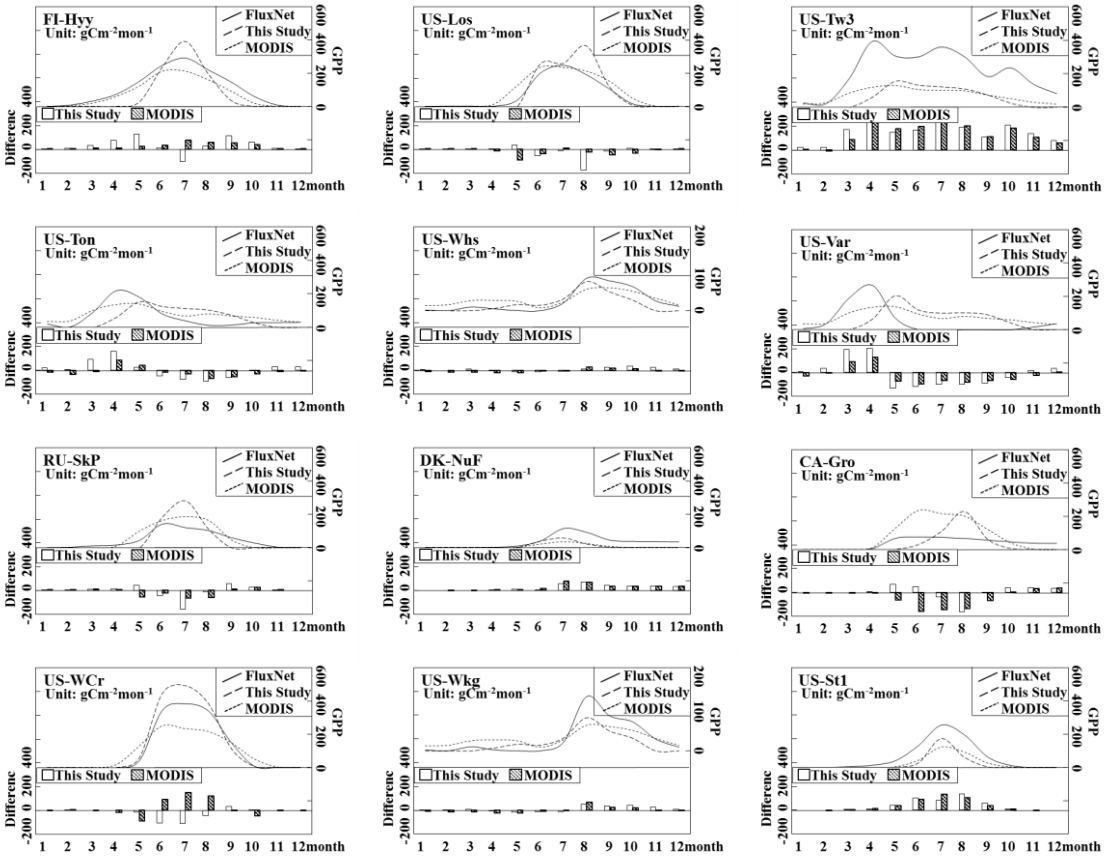

Figure S13-b Different GPP estimates at each flux tower site. (Above: Monthly distribution of GPP values of $GPP_{2014}^{monthly\ spatial\ CO_2}$, MODIS product and tower observations; Below: Difference between $GPP_{2014}^{monthly\ spatial\ CO_2}$ and tower GPP estimates, and difference between the MODIS GPP product and tower GPP estimates at each corresponding flux tower site.)

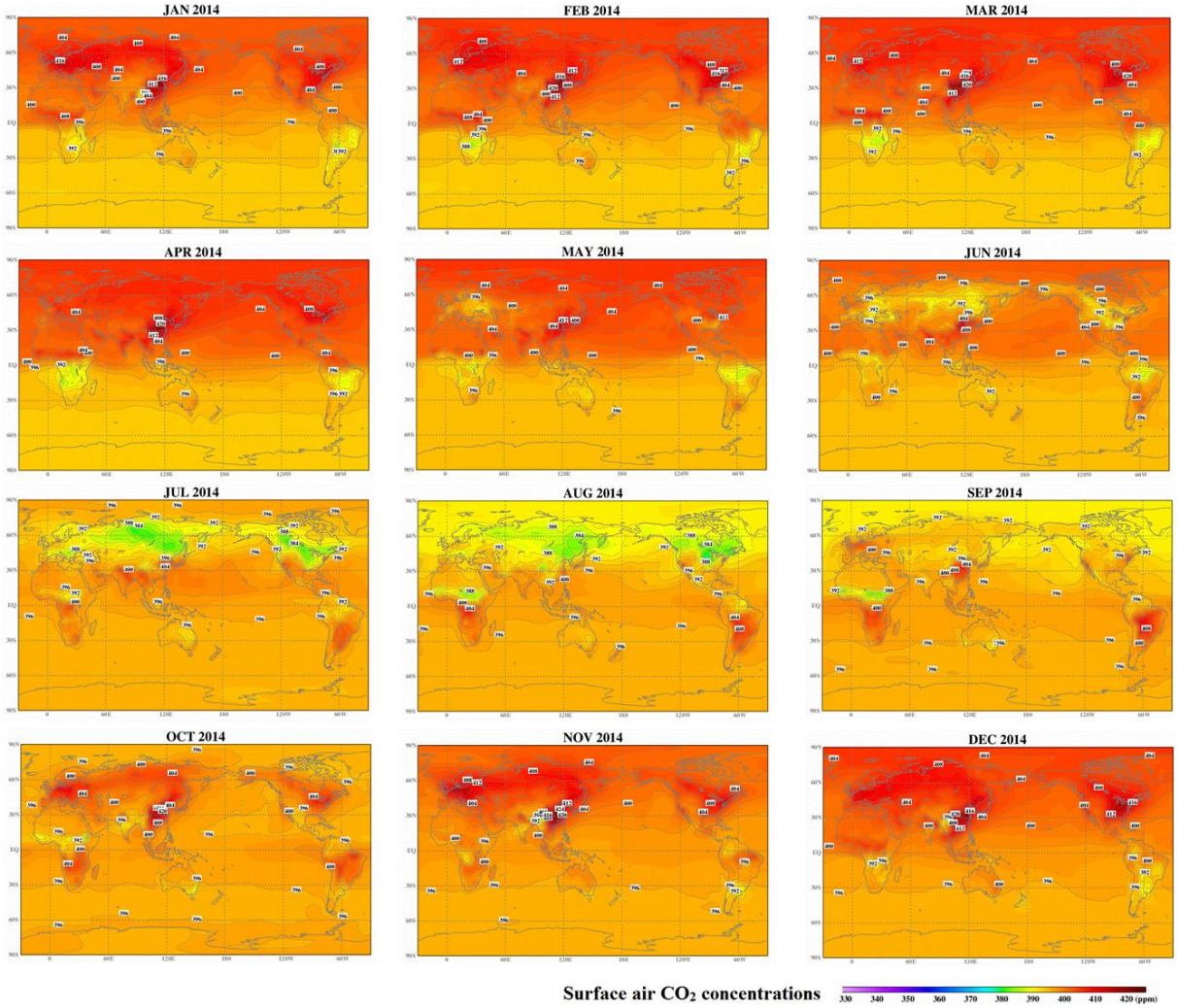

Figure S14 Monthly surface air CO_2 concentrations in 2014. Global maps of the monthly surface air CO_2 concentrations in 2014 obtained from the Japan Meteorological Agency (http://ds.data.jma.go.jp/ghg/kanshi/info_kanshi_e.html)

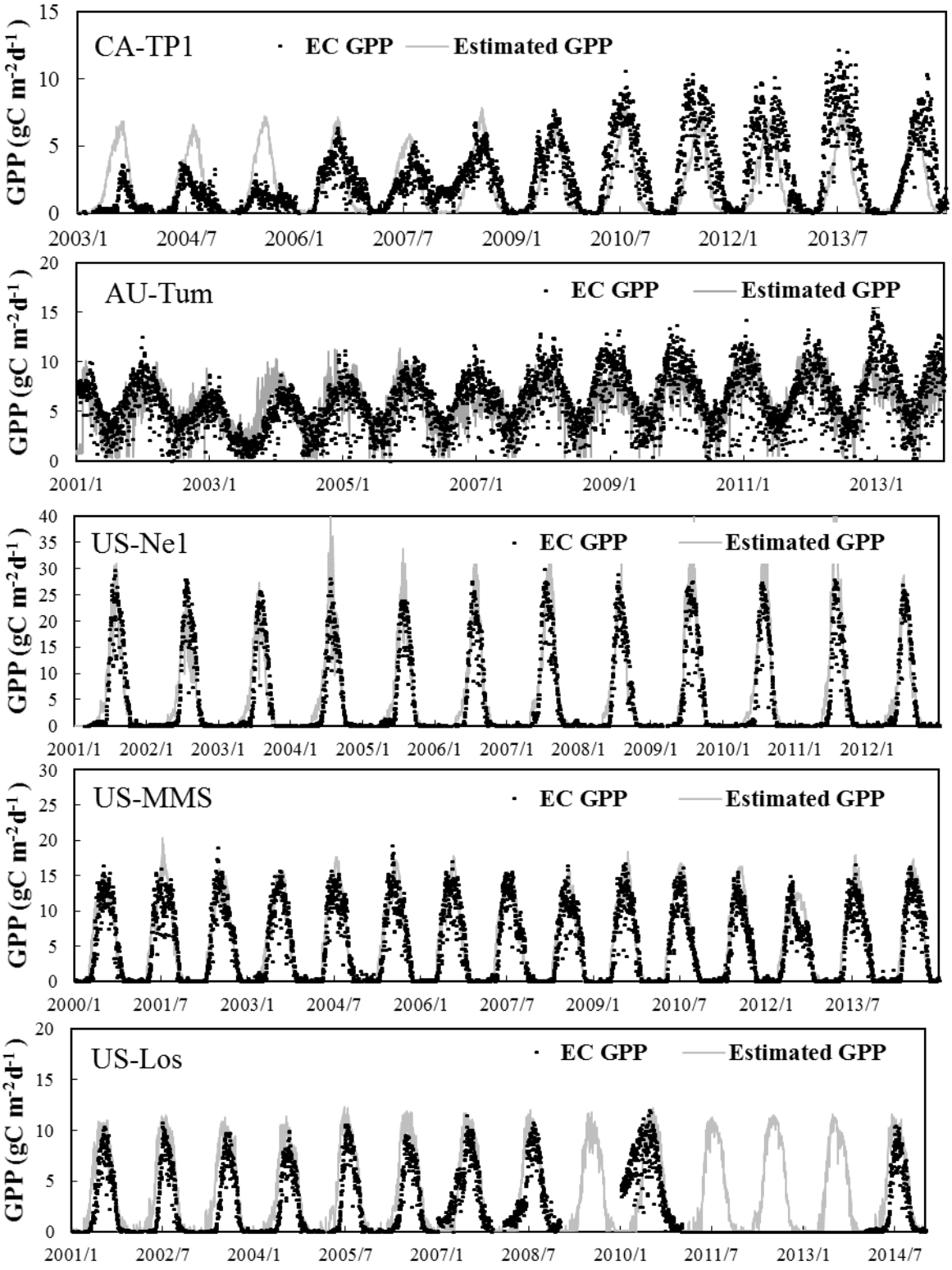

Figure S15-a Comparisons of flux GPP and the iBEPSd estimated GPP of each site.

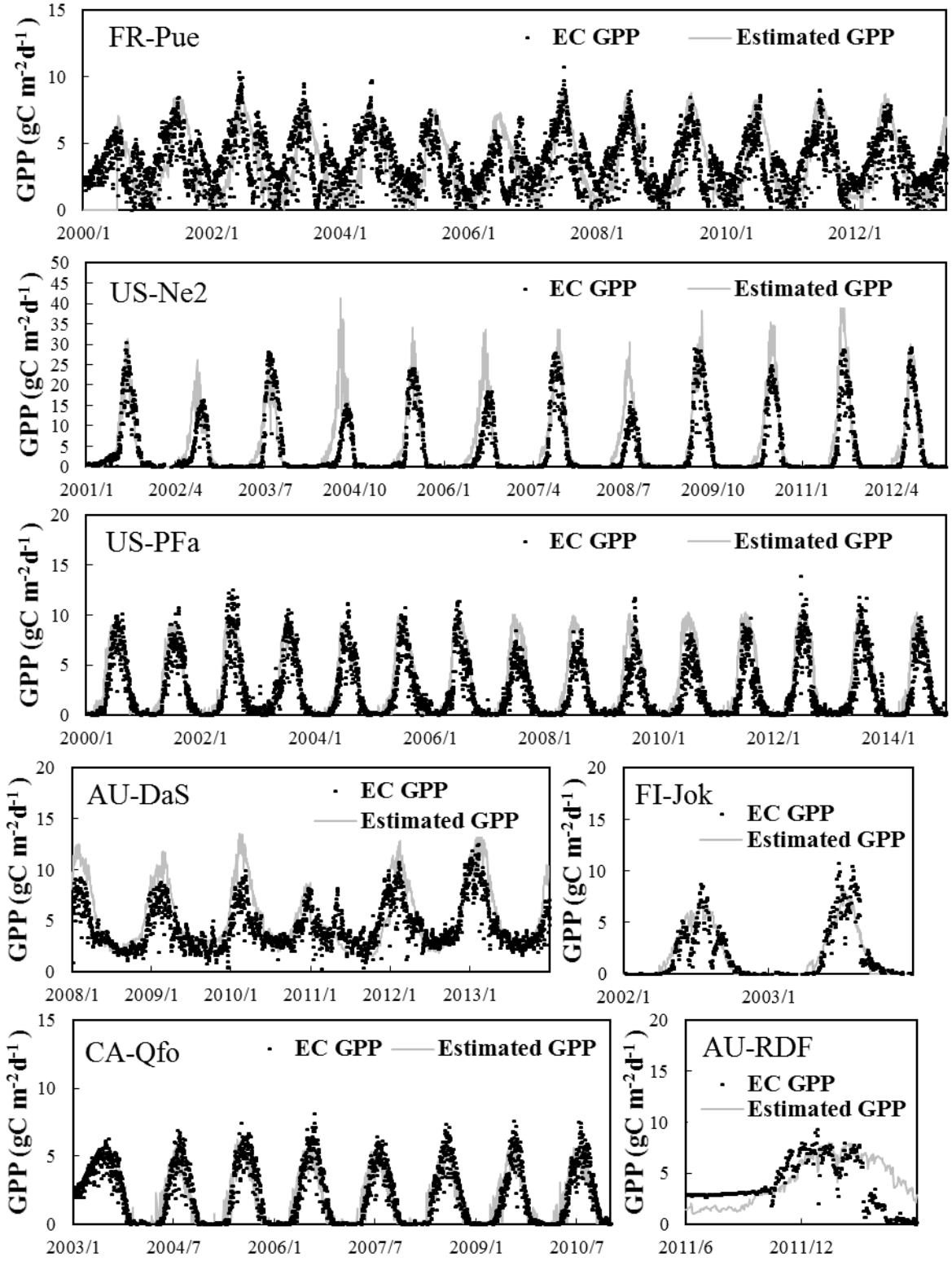

Figure S15-b Comparisons of flux GPP and the iBEPSd estimated GPP of each site.

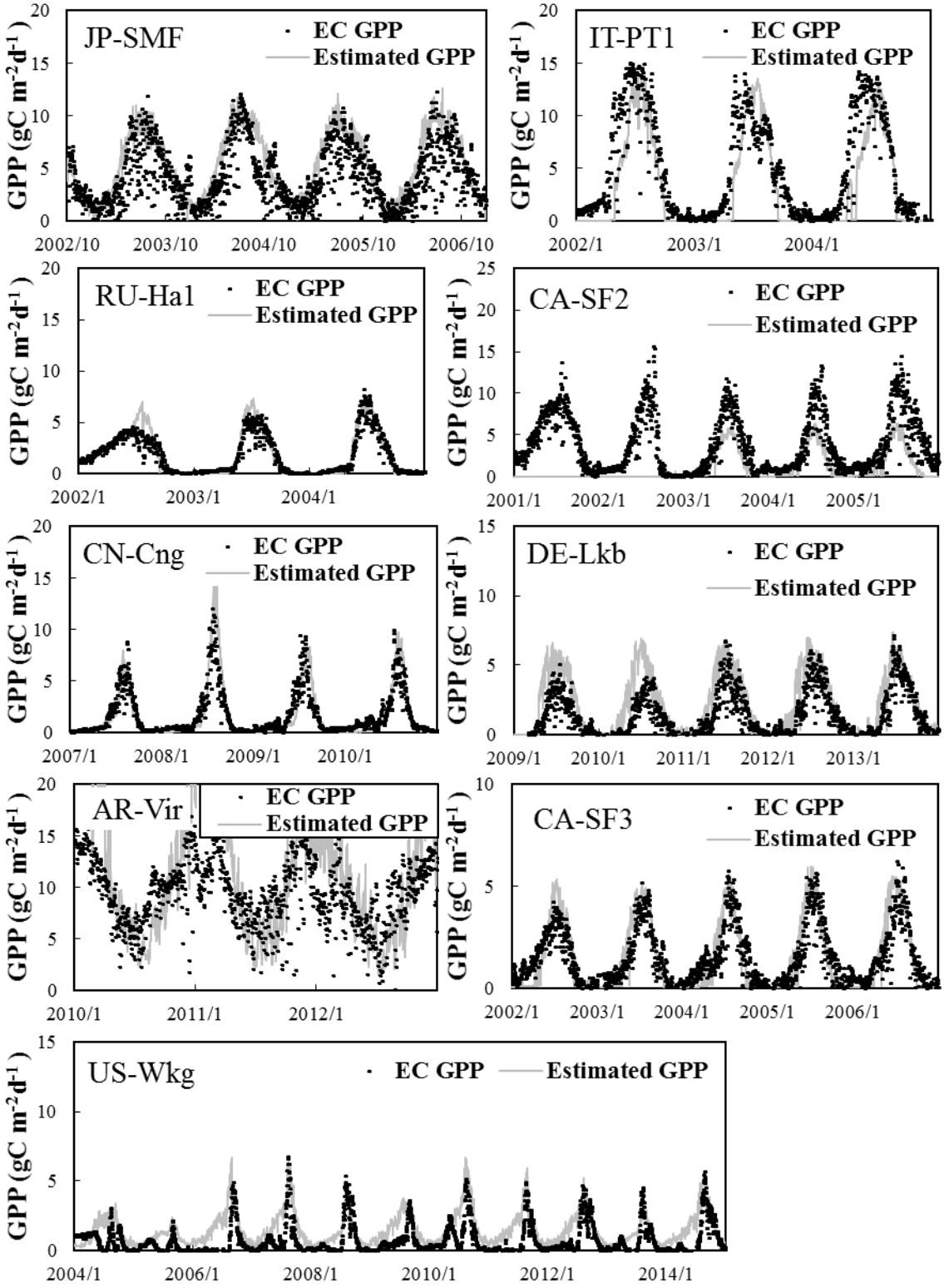

Figure S15-c Comparisons of flux GPP and the iBEPSd estimated GPP of each site.

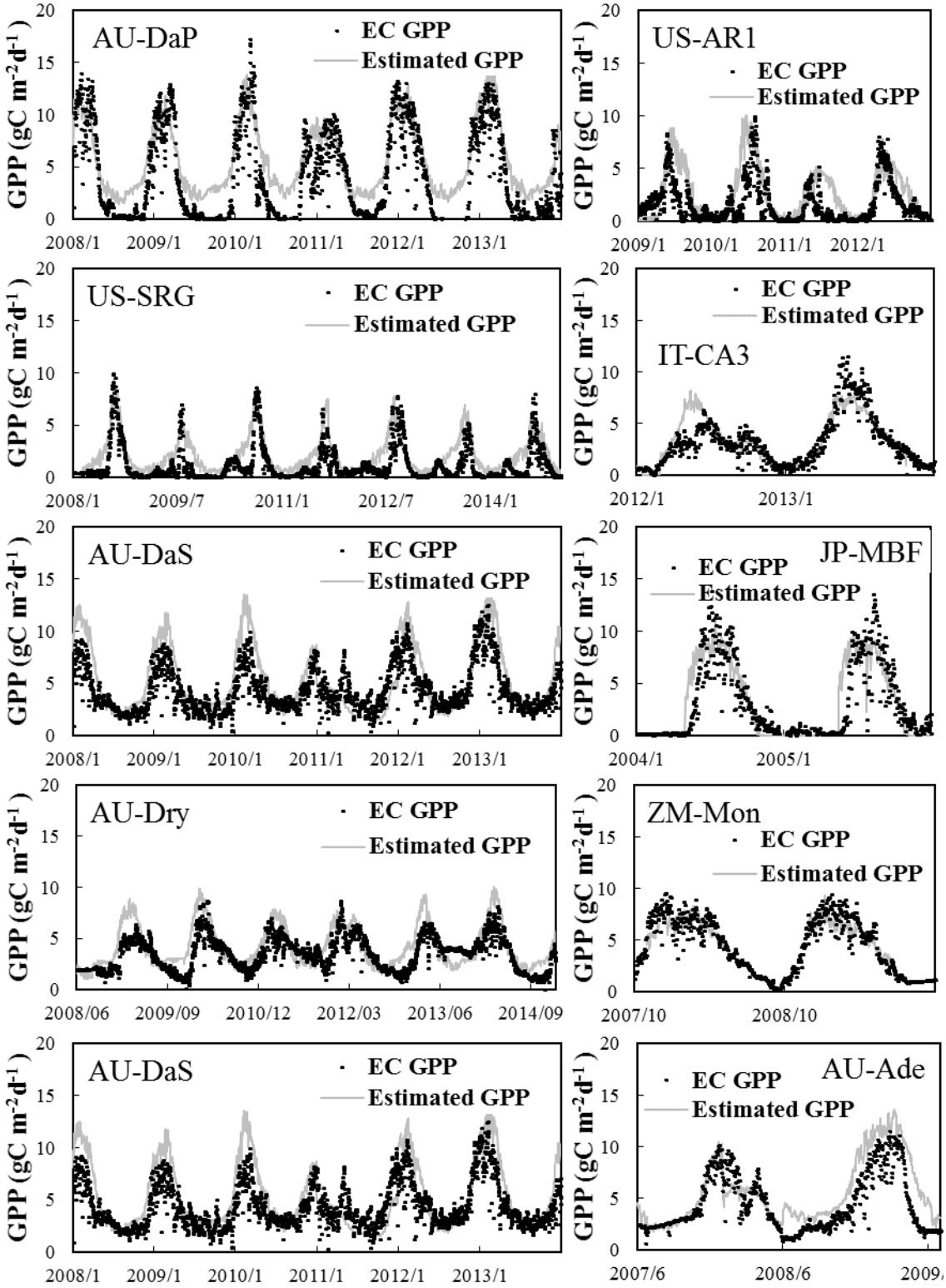

Figure S15-d Comparisons of flux GPP and the iBEPSd estimated GPP of each site.

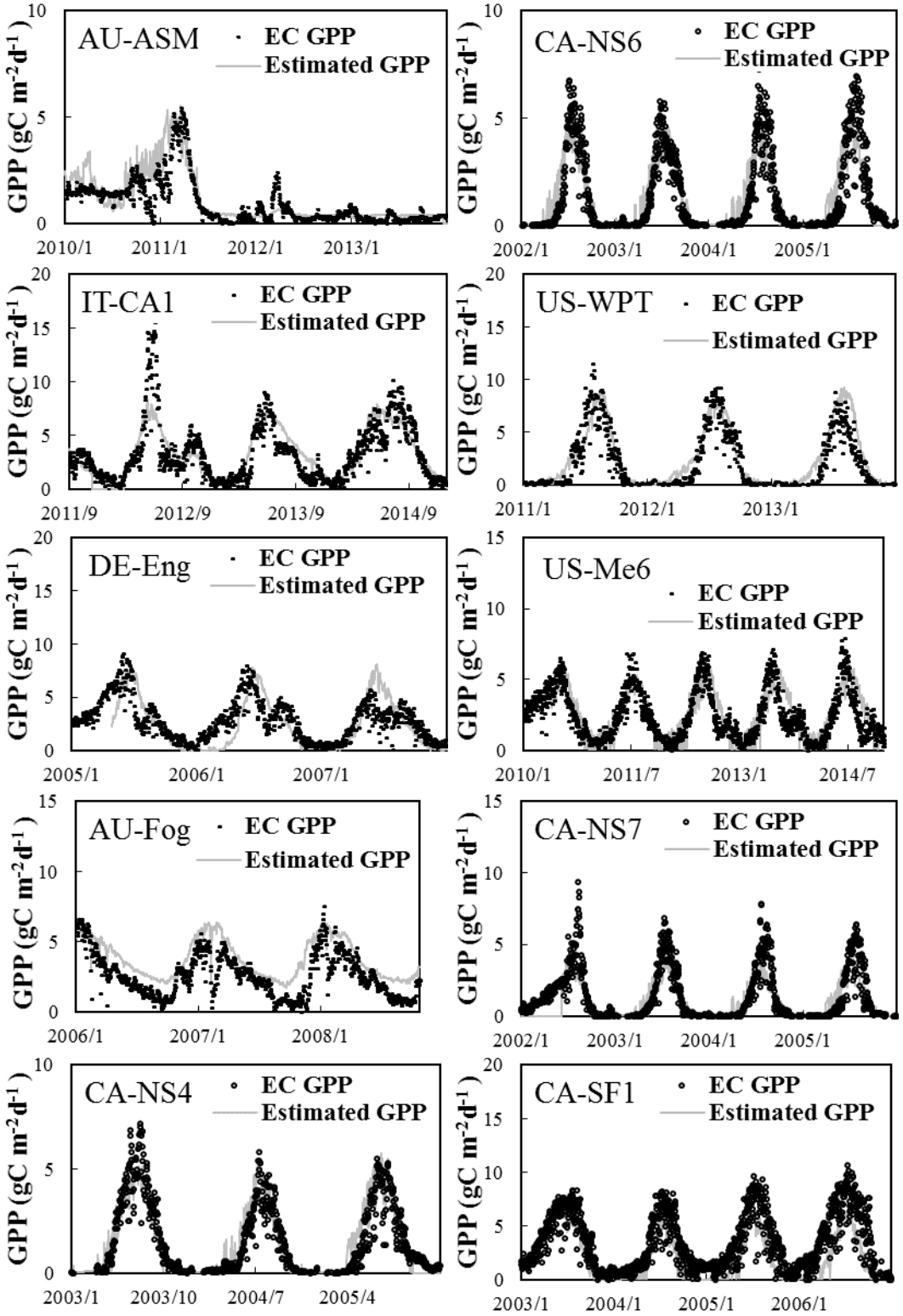

Figure S15-e Comparisons of flux GPP and the iBEPSd estimated GPP of each site.

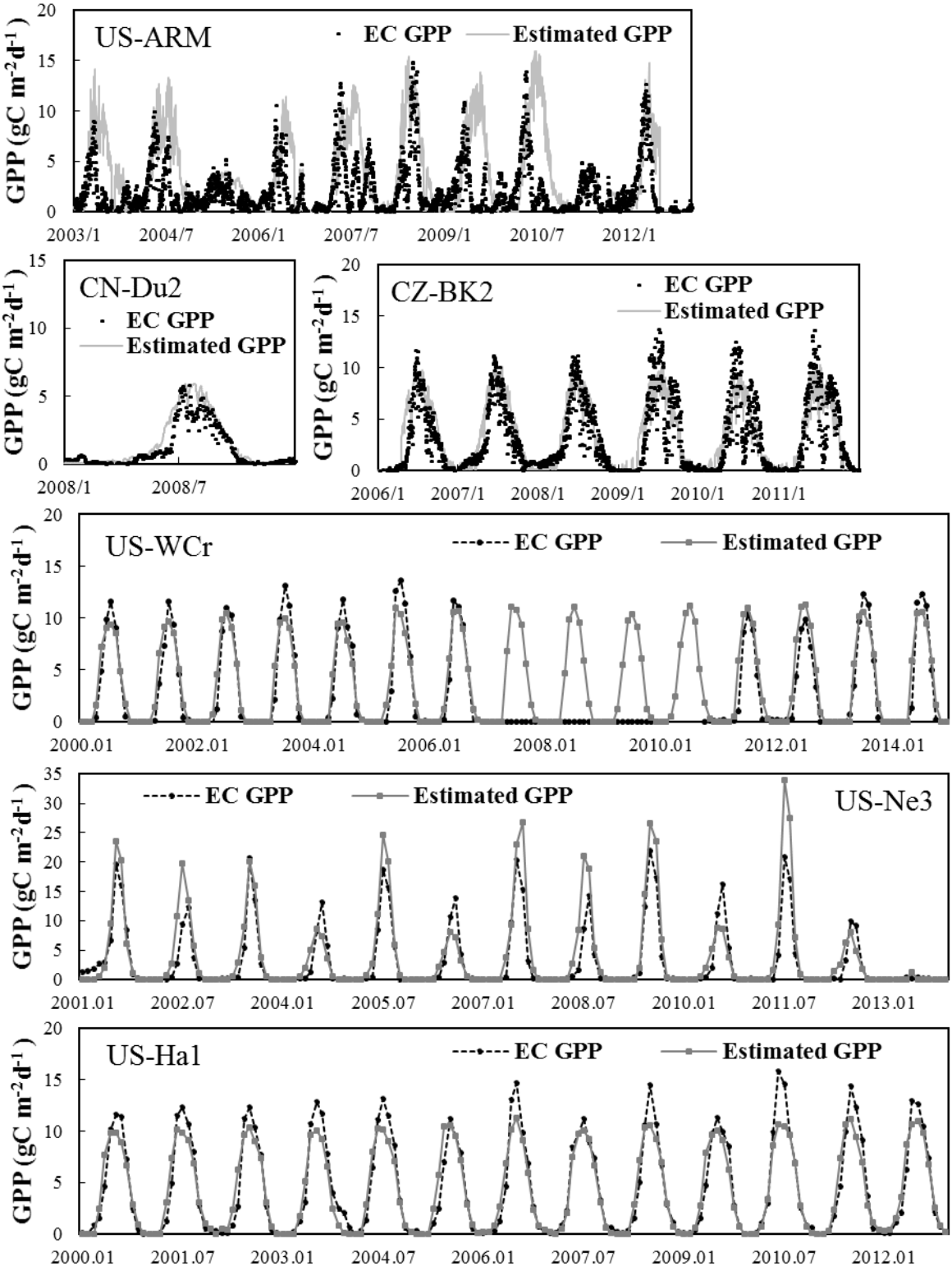

Figure S15-f Comparisons of flux GPP and the iBEPSd estimated GPP of each site.

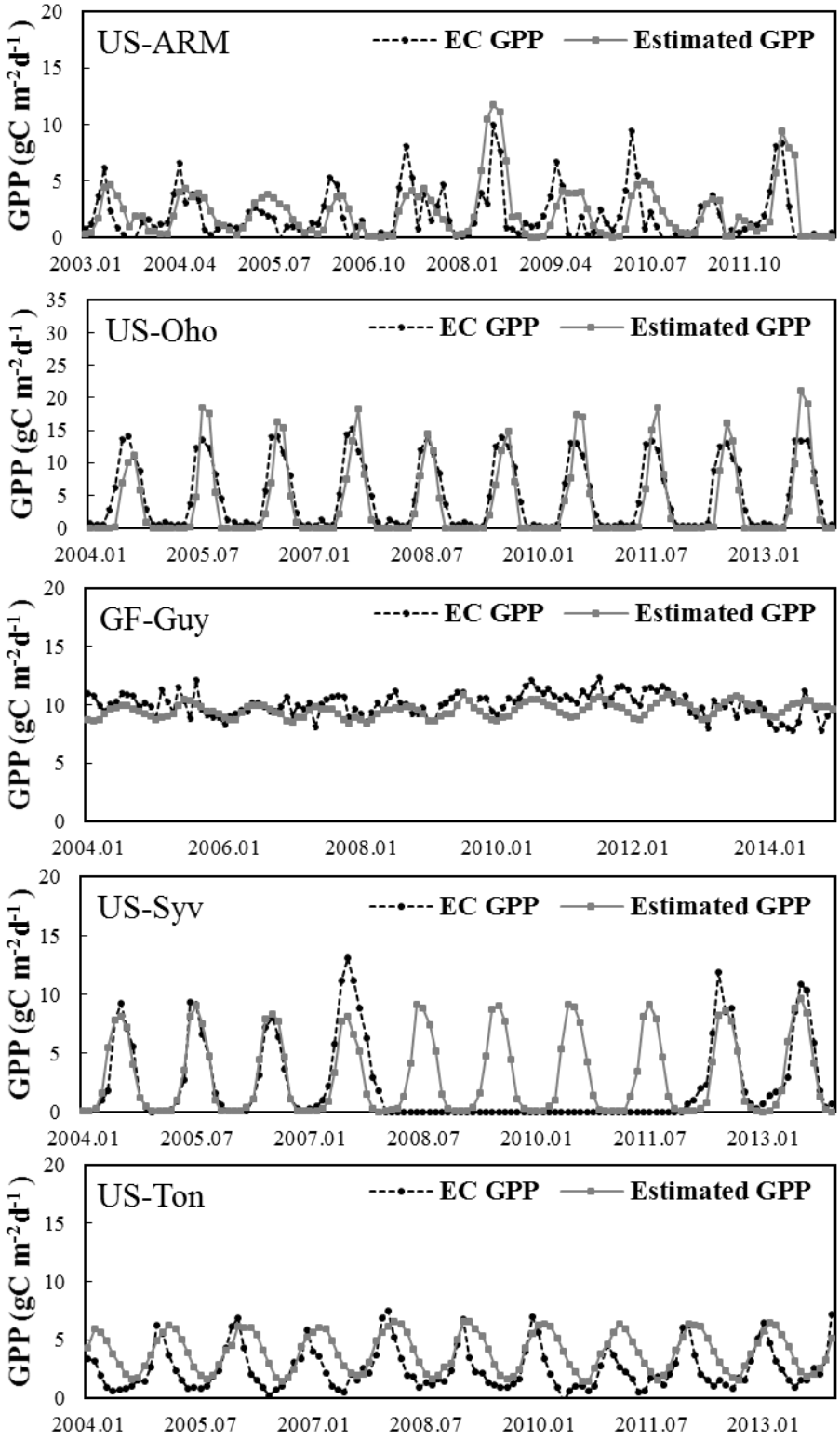

Figure S15-g Comparisons of flux GPP and the iBEPSd estimated GPP of each site.

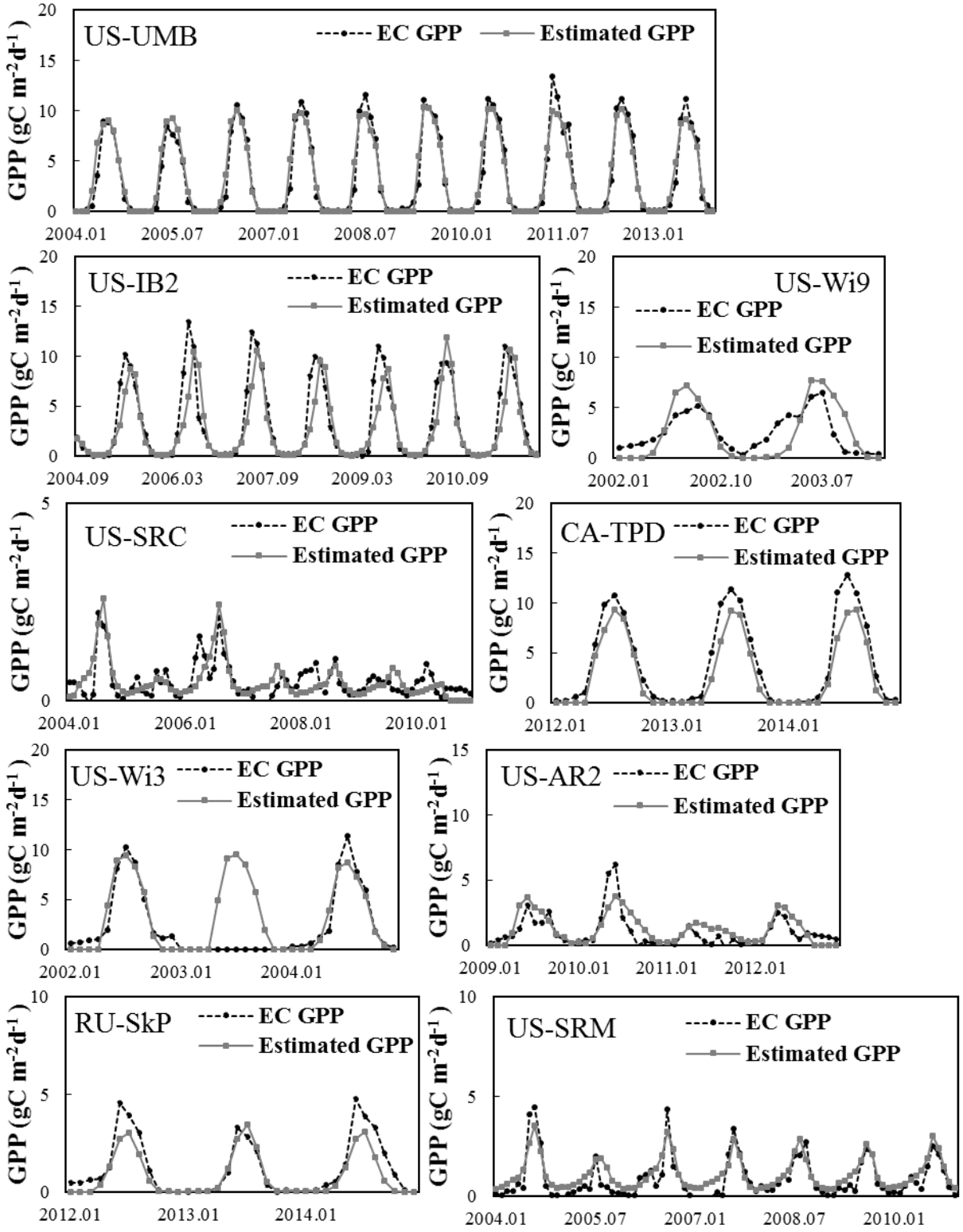

Figure S15-h Comparisons of flux GPP and the iBEPSd estimated GPP of each site.

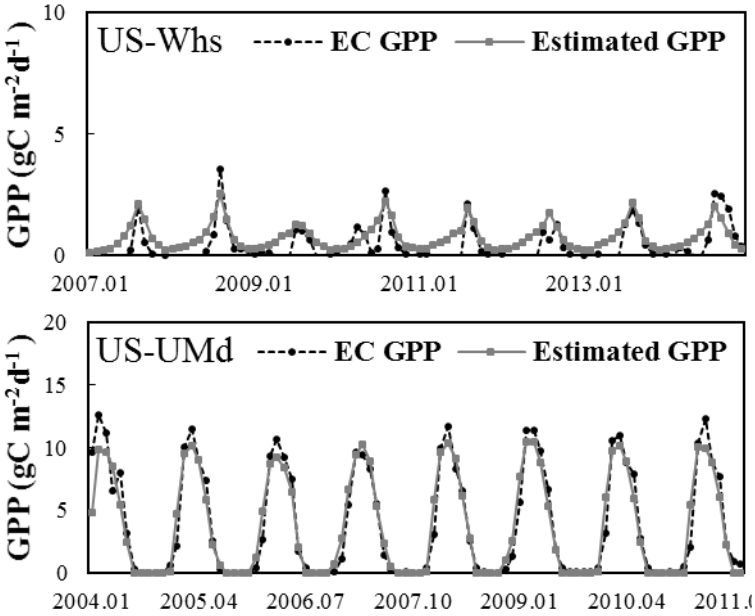

Figure S15-i Comparisons of flux GPP and the iBEPSd estimated GPP of each site.

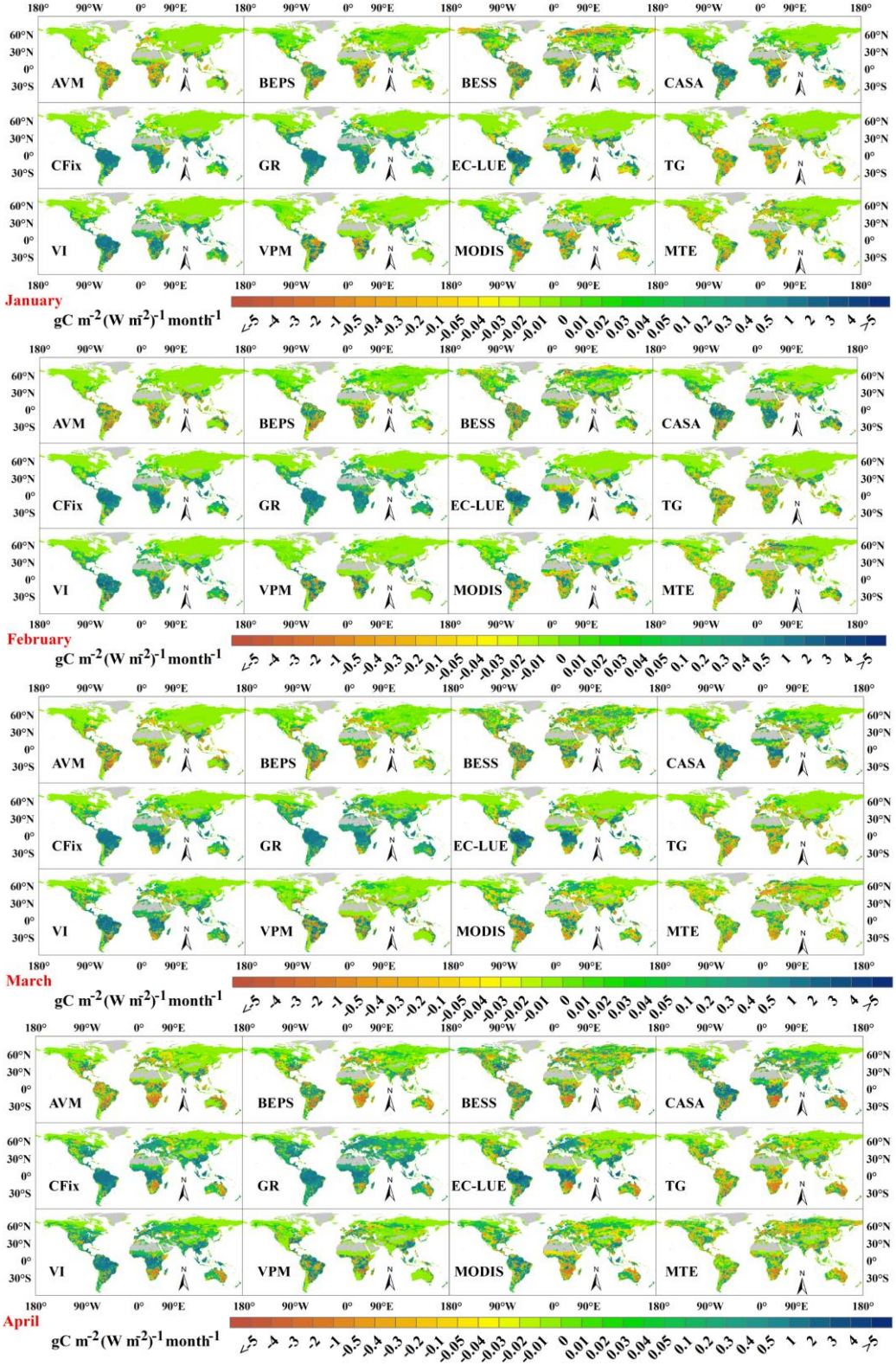

Figure S16-a Global distribution of the monthly responses of GPP to variation in radiation.

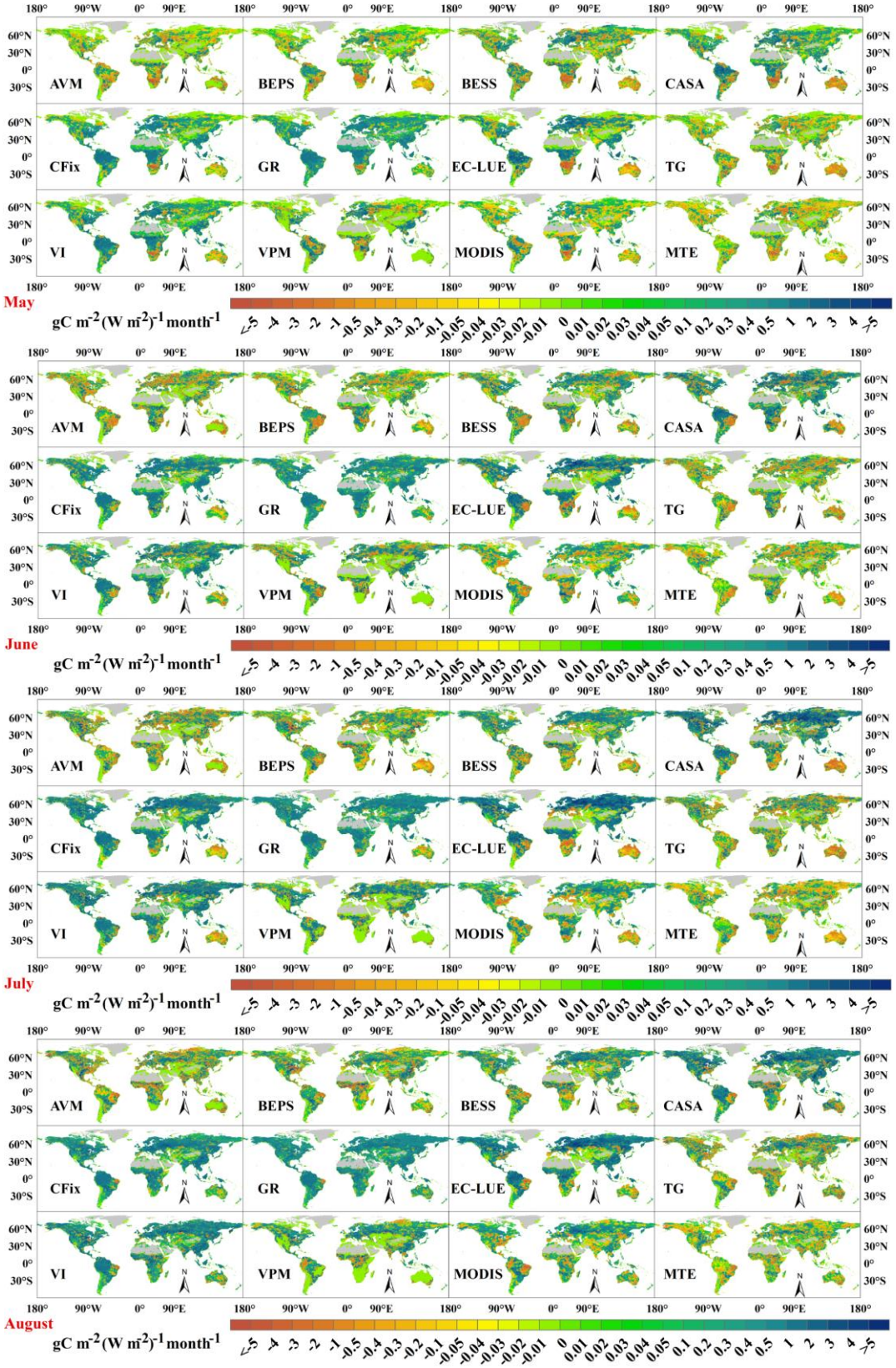

Figure S16-b Global distribution of the monthly responses of GPP to variation in radiation.

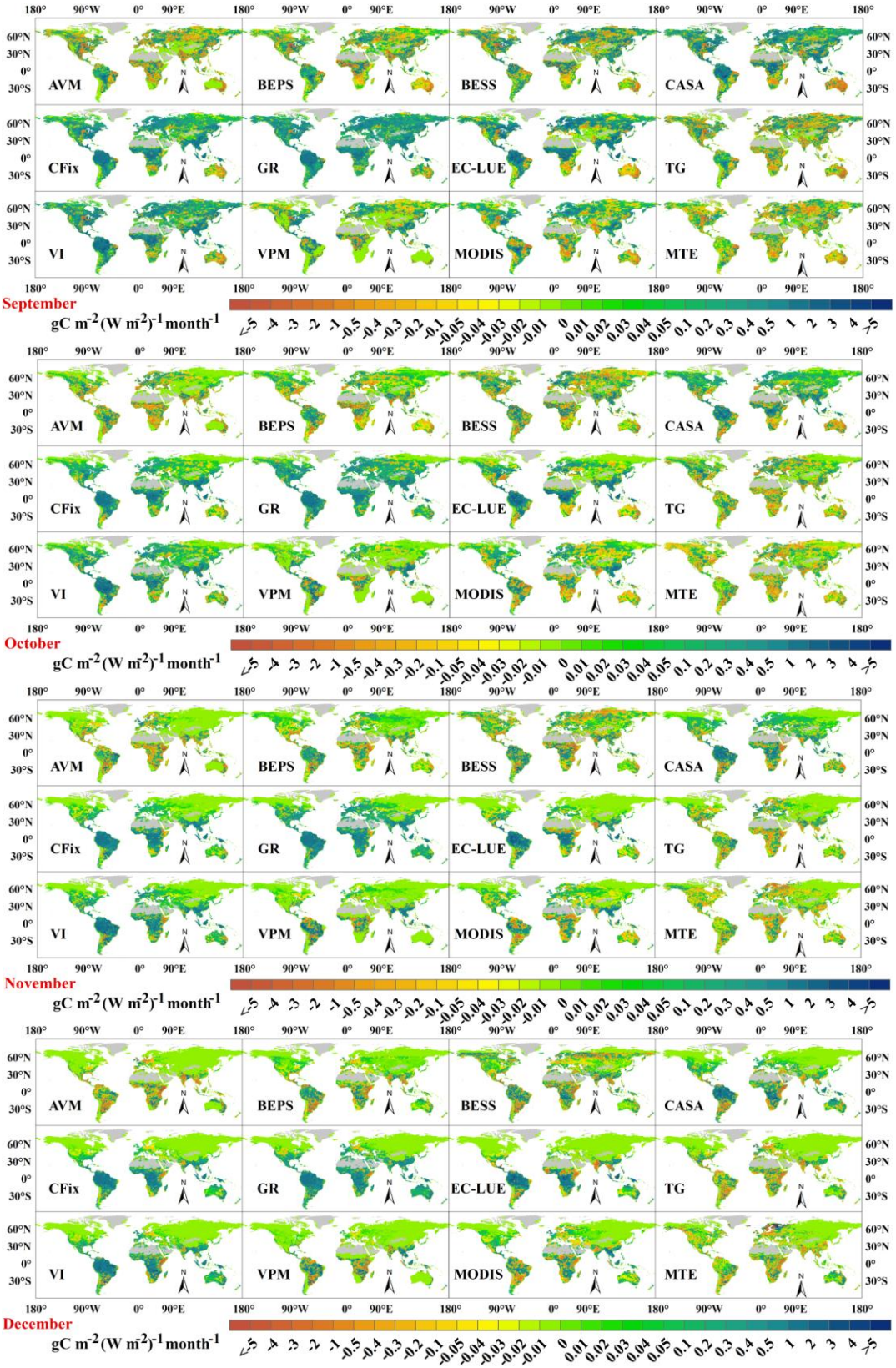

Figure S16-c Global distribution of the monthly responses of GPP to variation in radiation.

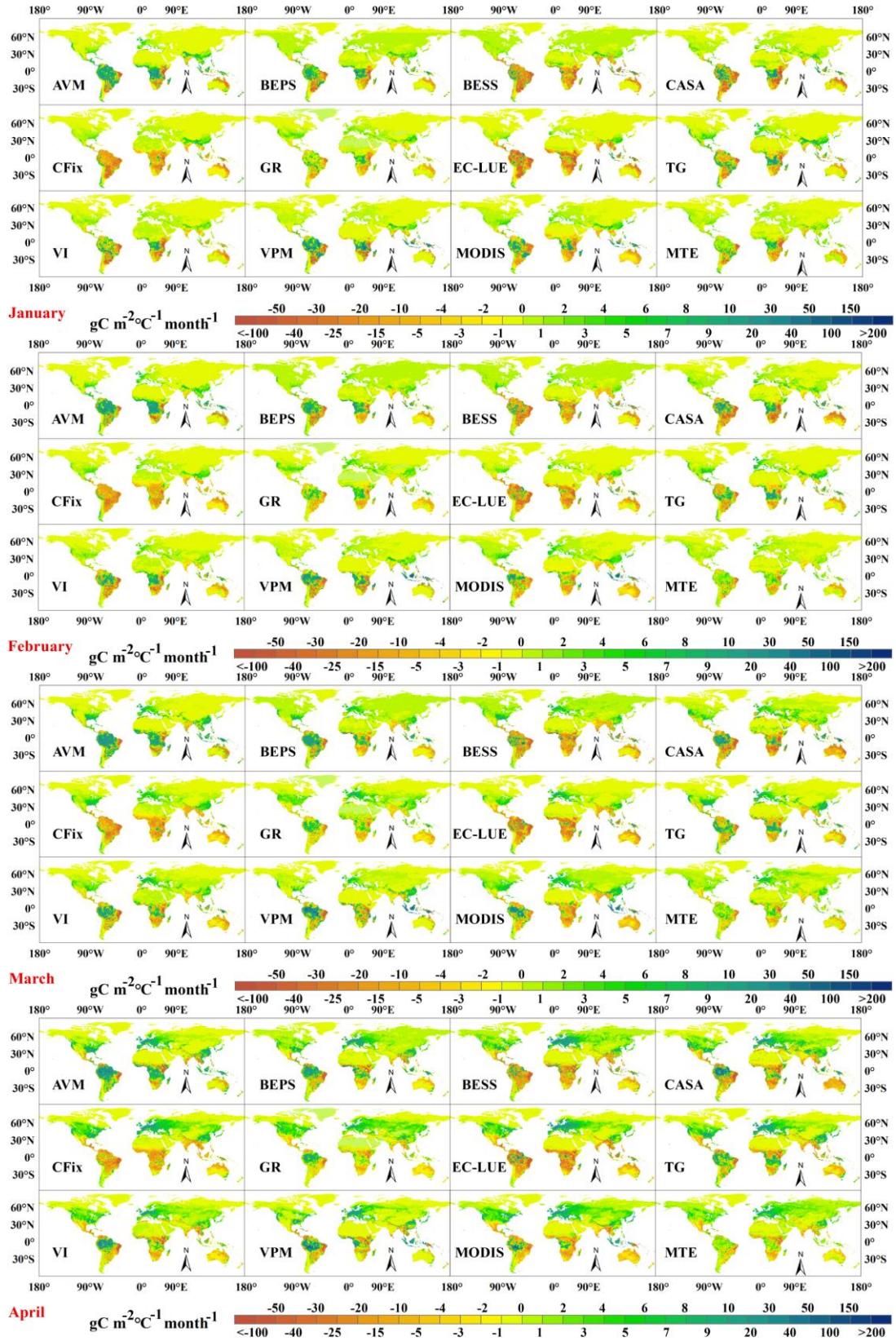

Figure S17-a Global distribution of the monthly responses of GPP to variation in Temperature.

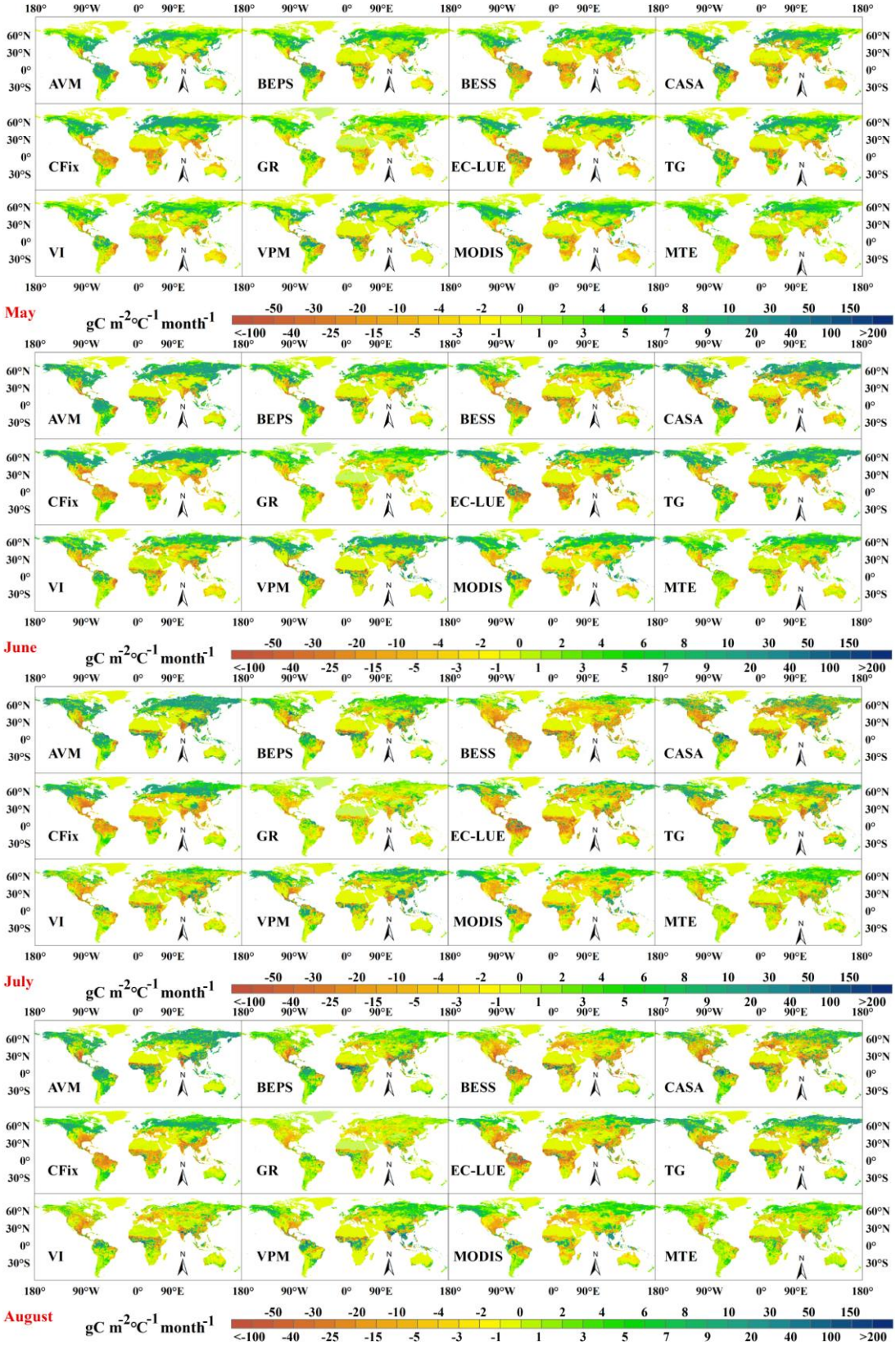

Figure S17-b Global distribution of the monthly responses of GPP to variation in Temperature.

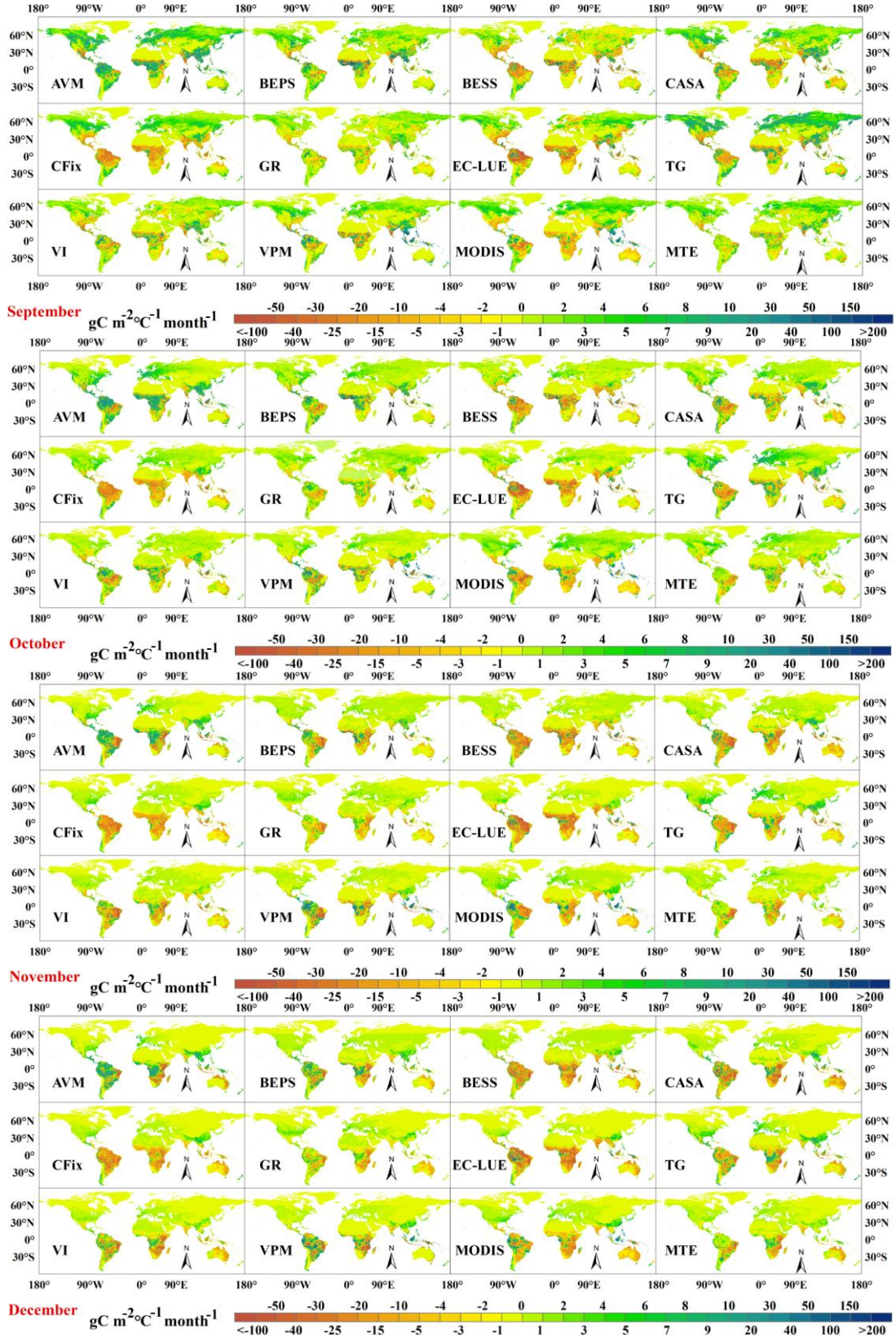

Figure S17-c Global distribution of the monthly responses of GPP to variation in Temperature.

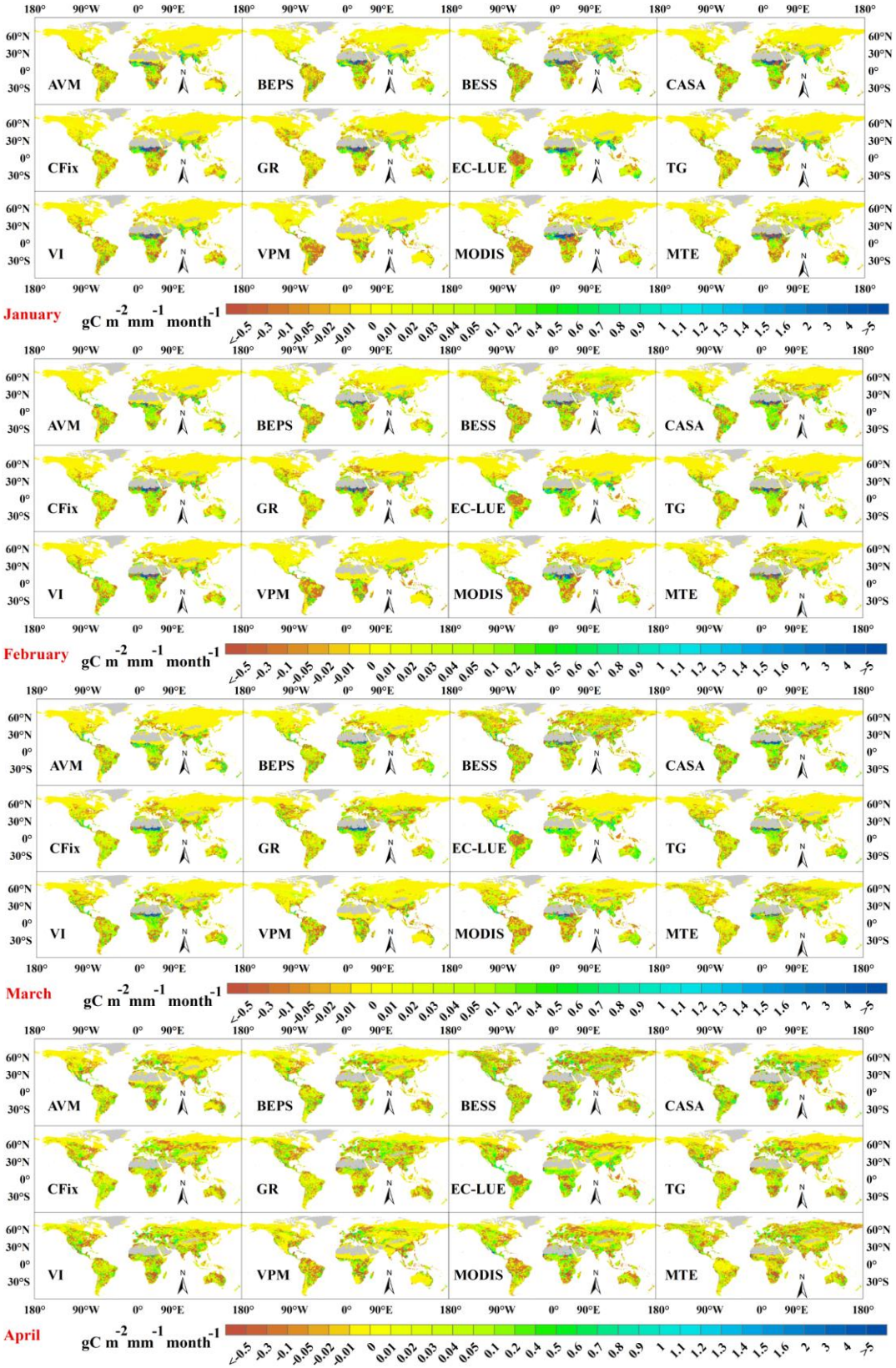

Figure S18-a Global distribution of the monthly responses of GPP to variation in precipitation.

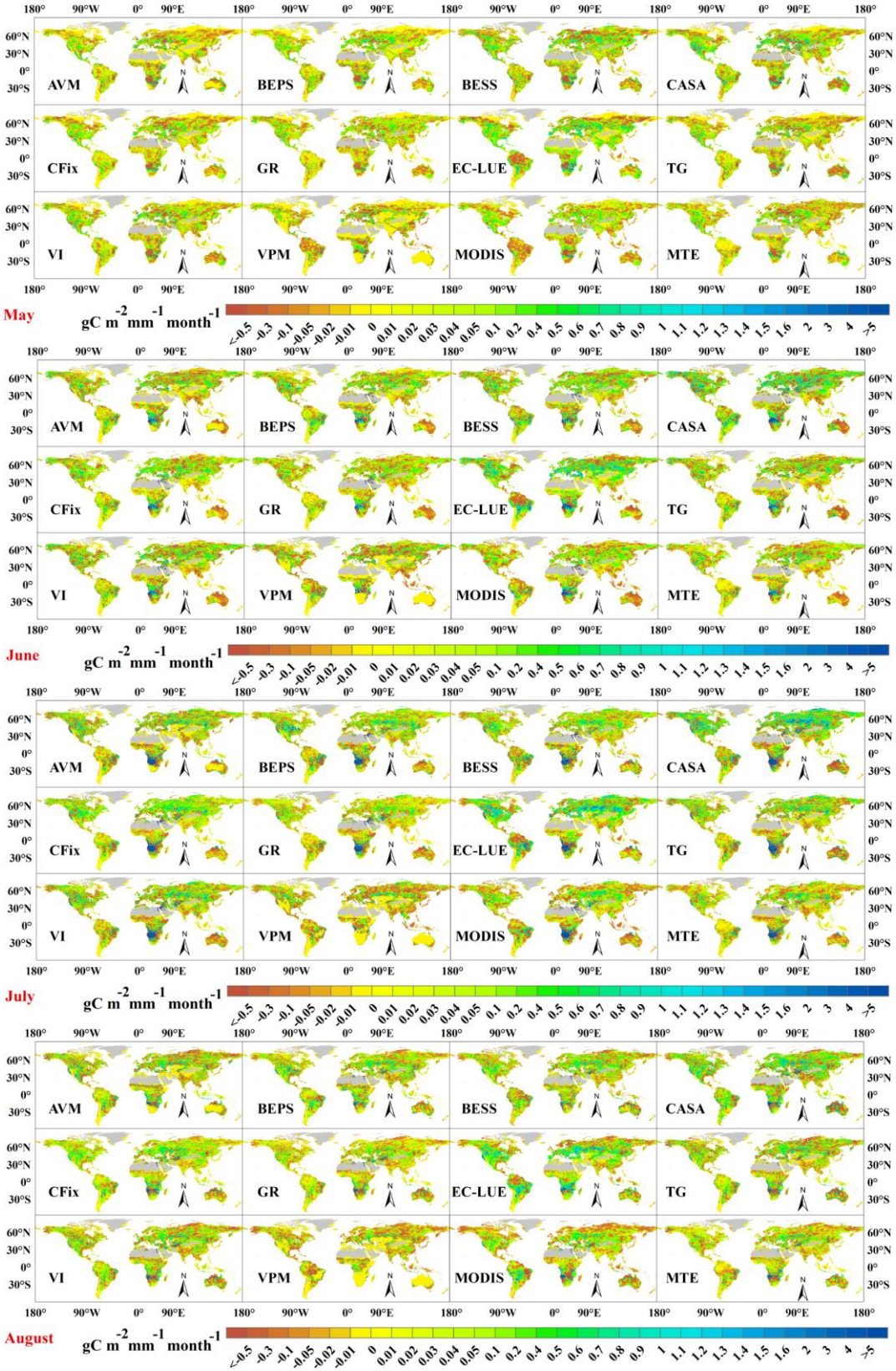

Figure S18-b Global distribution of the monthly responses of GPP to variation in precipitation.

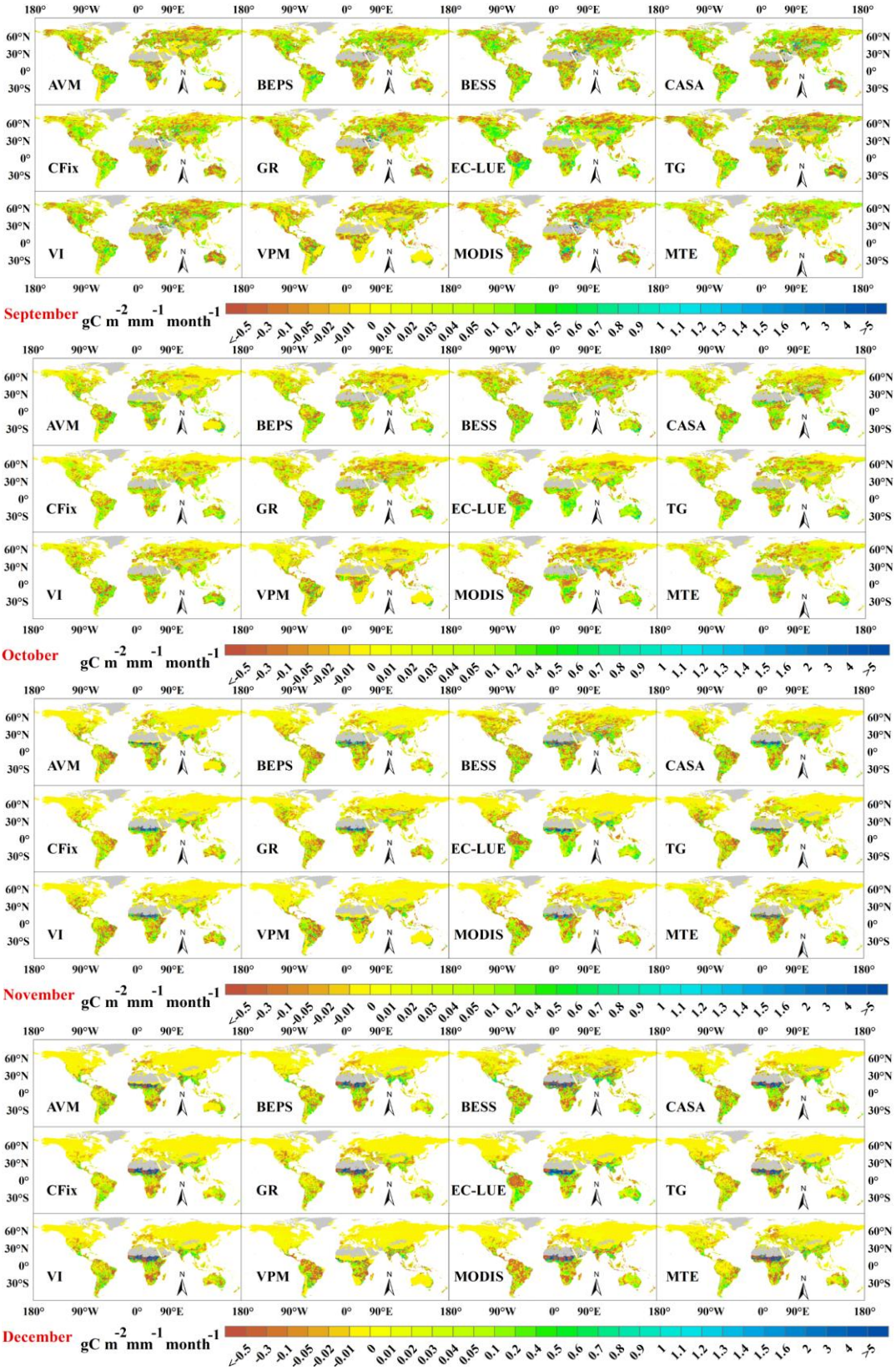

Figure S18-c Global distribution of the monthly responses of GPP to variation in precipitation.

Table S1 The comparisons of sensitivities of GPP to factors by RS-based models, DGVMs and ESMs at each Fluxnet site. The red squares represent the results from RS-based models including AVM, VPM, VI, BEPS, BESS, MODIS, MTE, CASA, CFix, GR, TG and EC-LUE; The green diamonds are the results calculated from DGVMs including VISIT, VEGAS, ORCHIDEE, LPJml, JULES, DLEM and CARAIB obtained from ISIMIP2; And the blue circles mean the results from ESMs got from CMIP5 including NorESM1_ME, MIROC_ESM_CHEM, MIROC_ESM, IPSL_CM5A_MR, IPSL_CM5A_LR, GISS_E2_R, GISS_E2_H, GFDL_ESM2M, GFDL_ESM2G.

	CO_2	Precipitation	Radiation	Temperature
US-Var	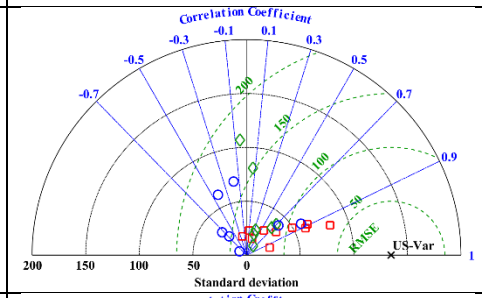	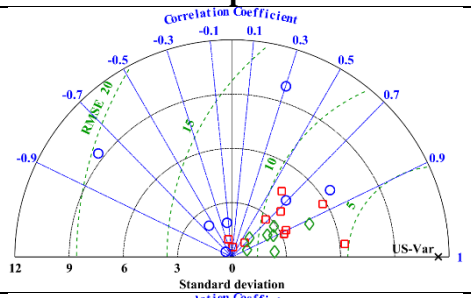	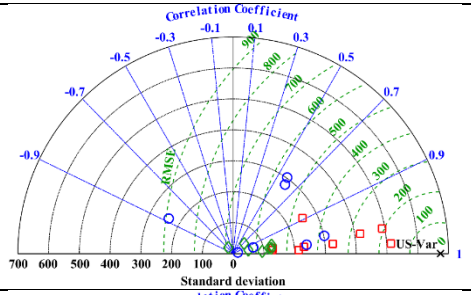	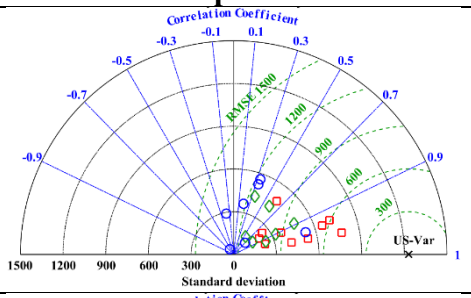
US-UMB	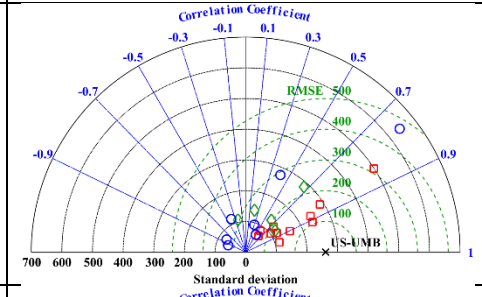	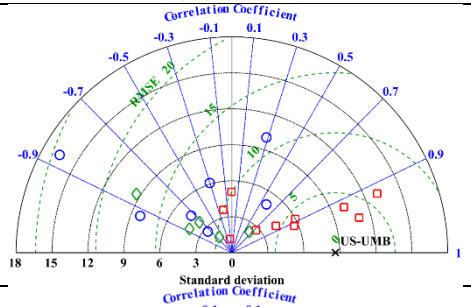	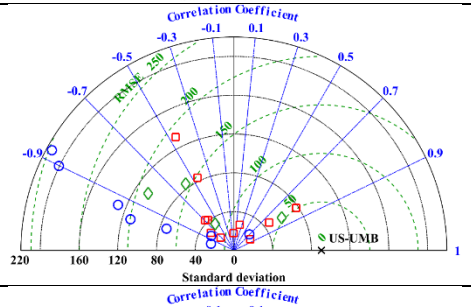	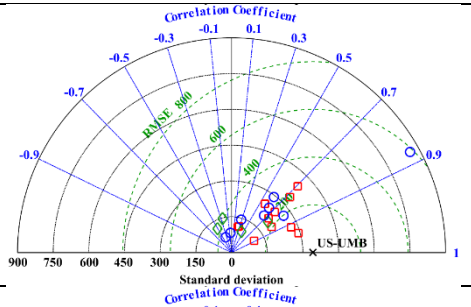
US-PFa	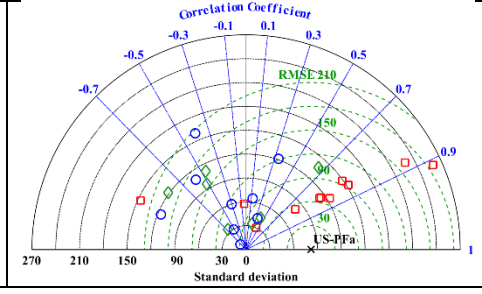	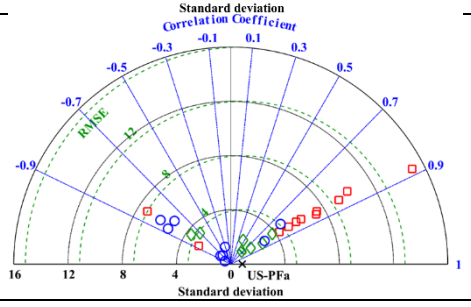	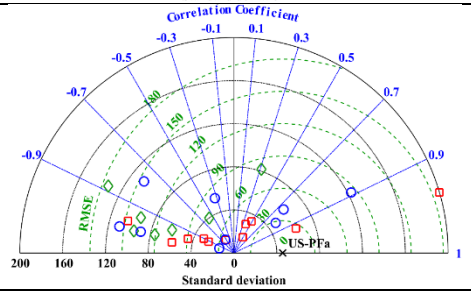	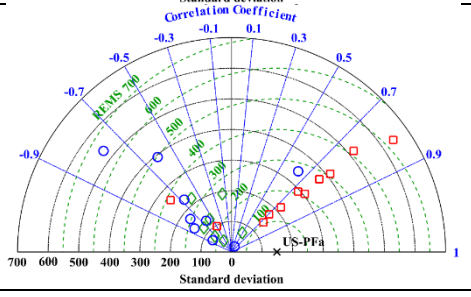

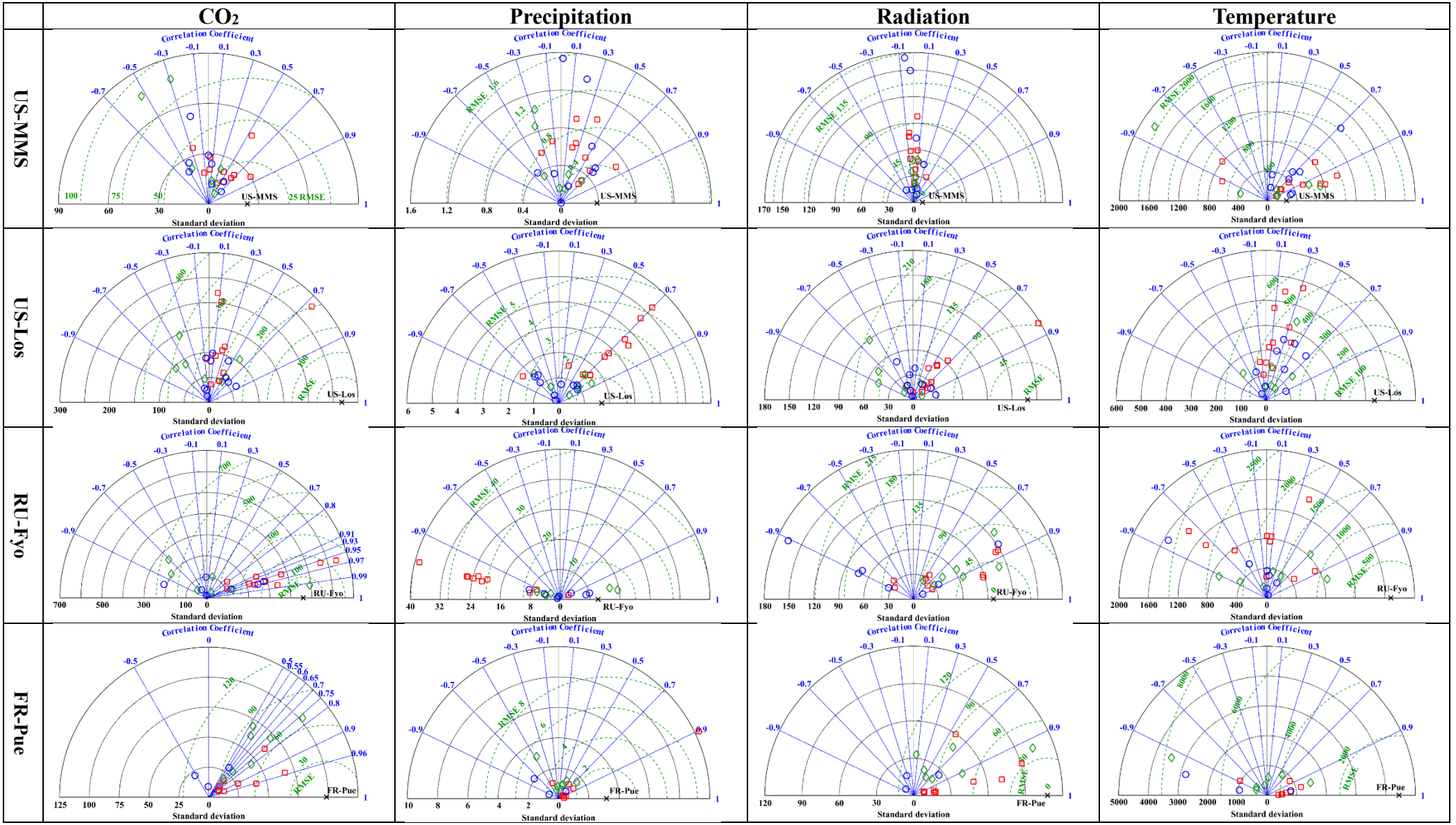
CO2
Precipitation
Radiation
Temperature
US-MMS
US-Los
RU-Fyo
FR-Pue
Correlation Coefficient
Standard deviation
RMSE
US-MMS
US-Los
RU-Fyo
FR-Pue

	CO_2	Precipitation	Radiation	Temperature
NL-Loo	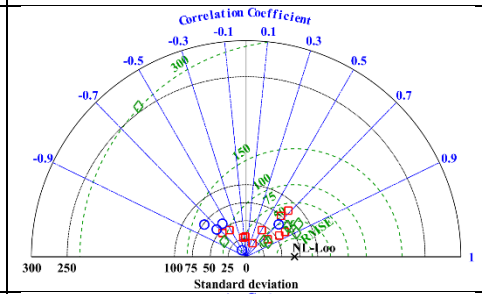	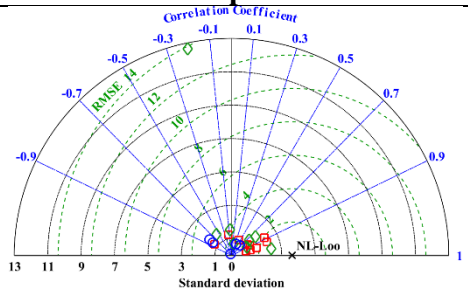	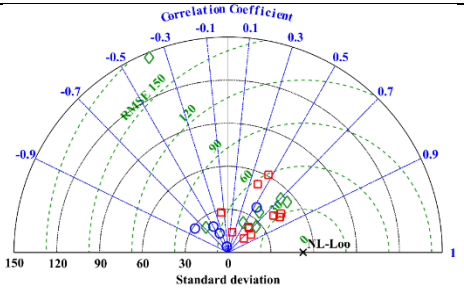	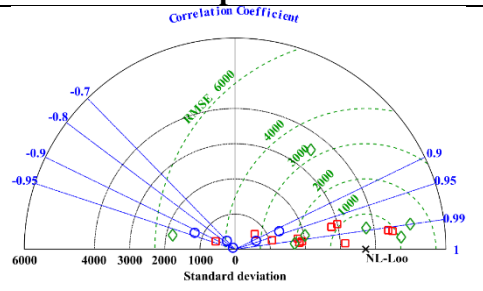
IT-Ren	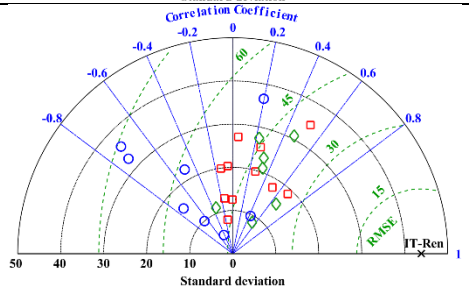	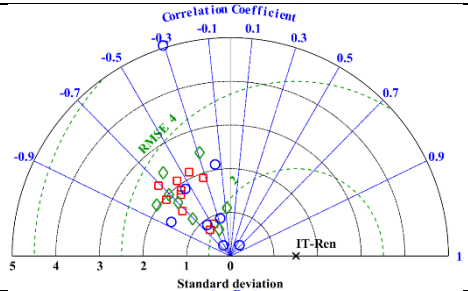	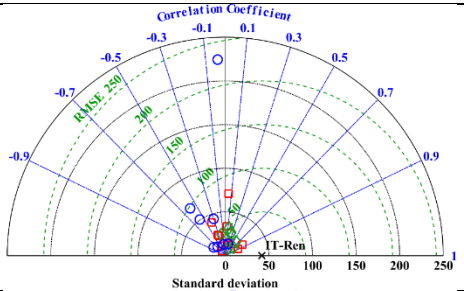	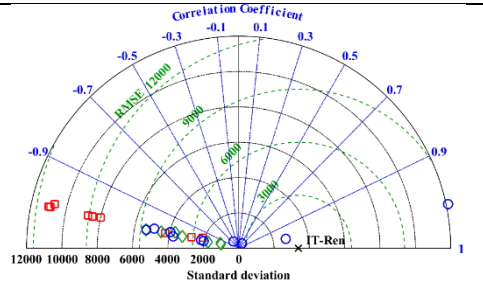
FI-Hyy	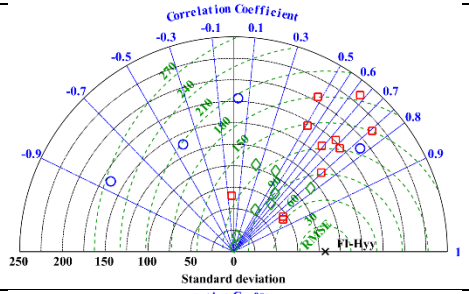	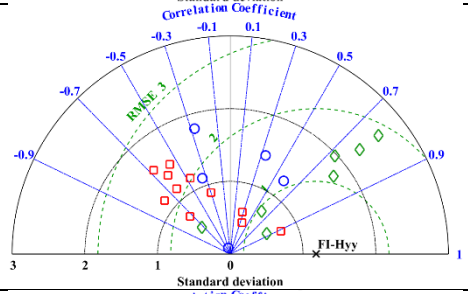	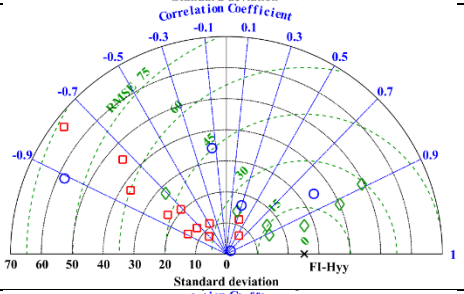	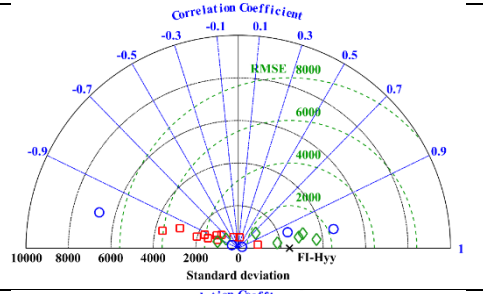
DK-ZaH	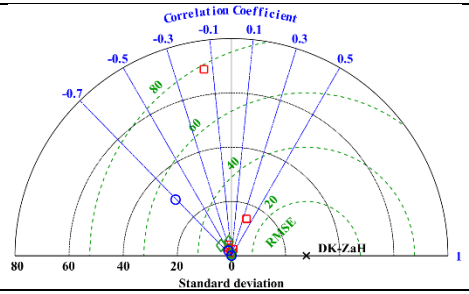	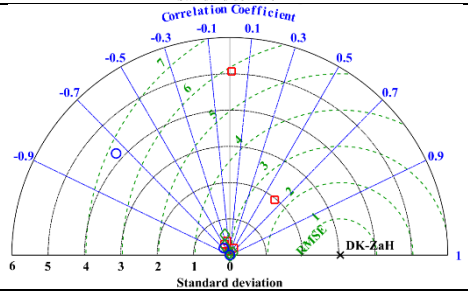	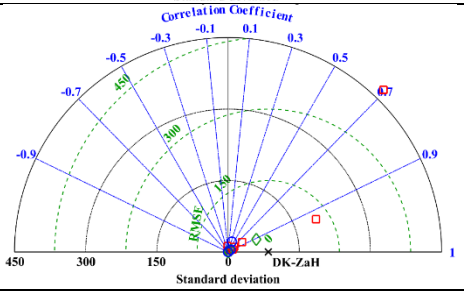	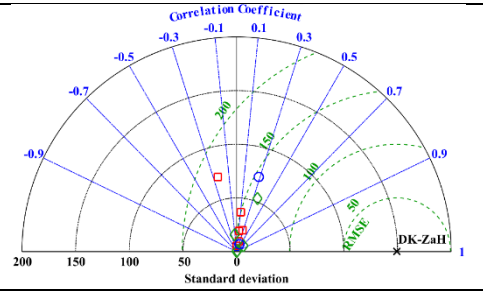

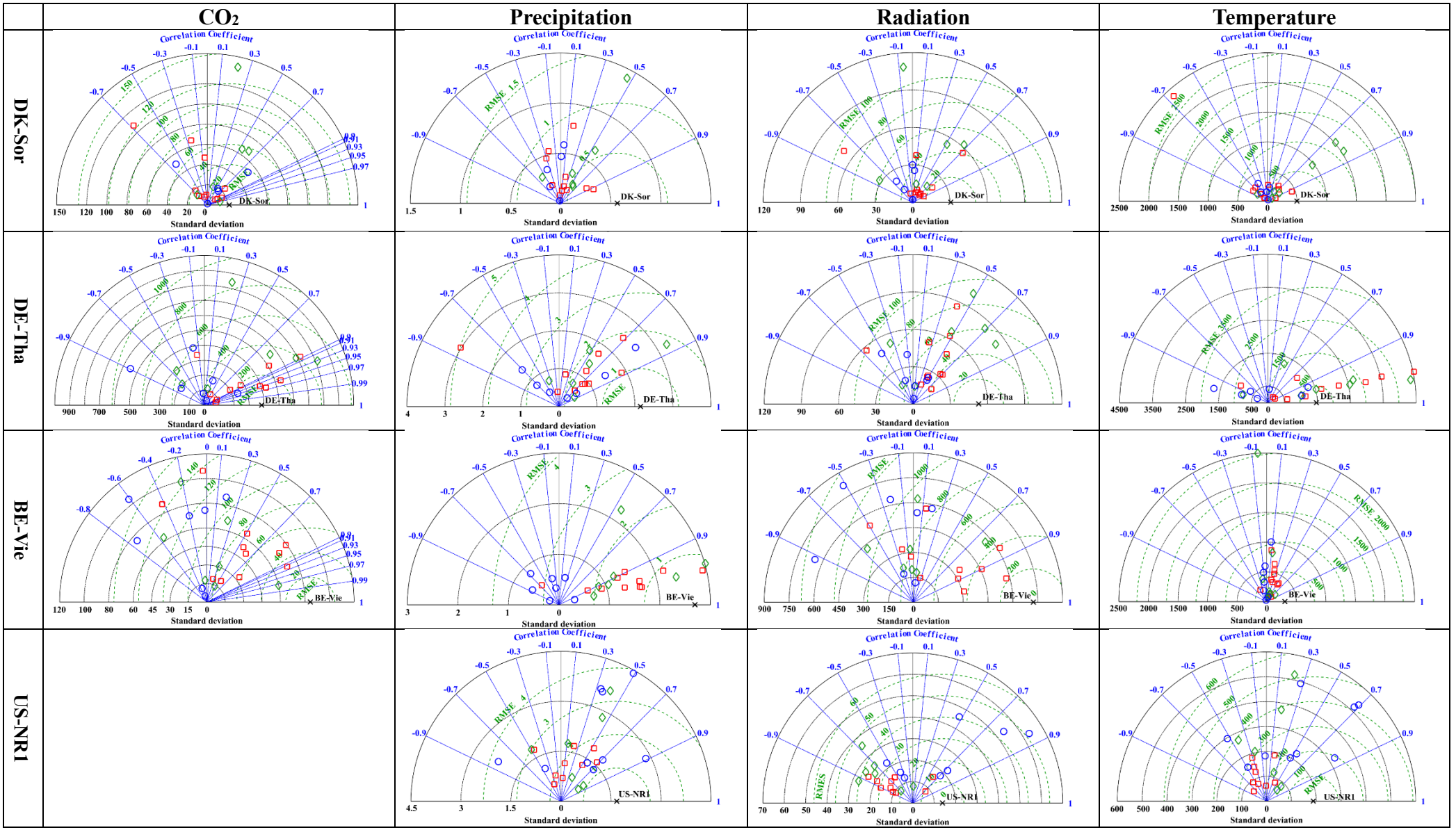
CO2
Precipitation
Radiation
Temperature
DK-Sor
DE-Tha
BE-Vie
US-NR1
Correlation Coefficient
Standard deviation
RMSE

	CO_2	Precipitation	Radiation	Temperature
BE-Bra	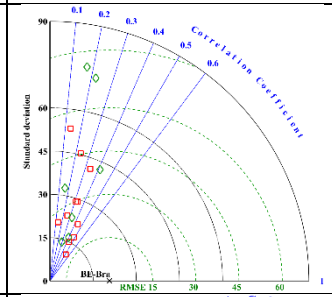	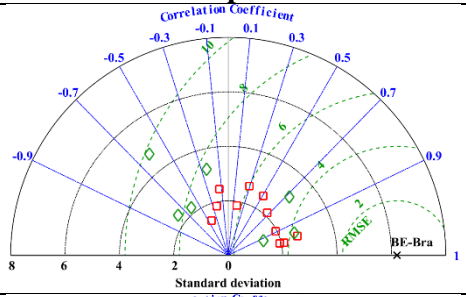	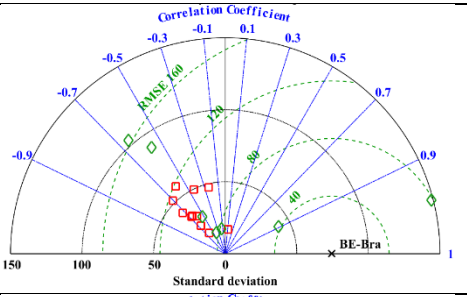	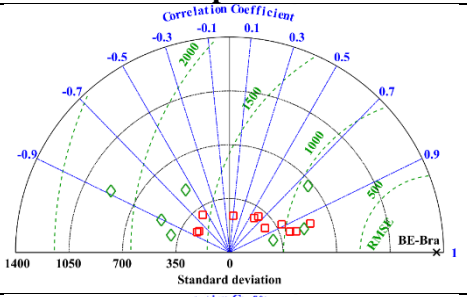
US-WCr	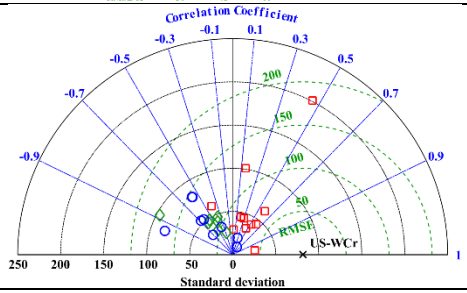	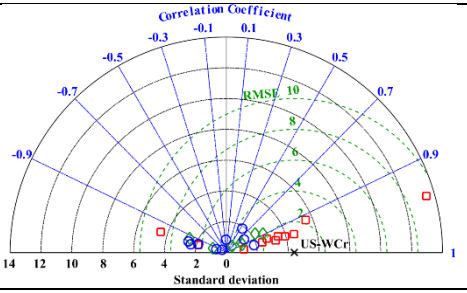	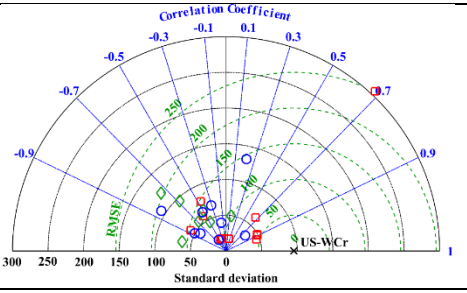	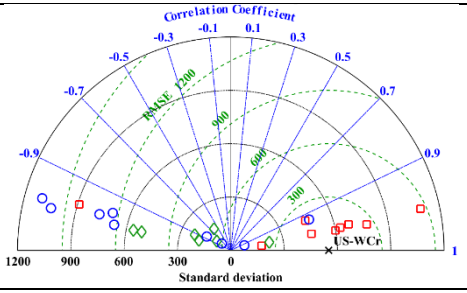

Abbreviations

GPP	Gross primary production / Gross primary productivity
ρNIR	Spectral reflectance in near infrared
$[O_2]$	Atmospheric O_2 concentration
$\tilde{a}$	Leaf absorbance
A_{canopy}	Total assimilation rate of canopy
ALB_BSA_NIR	Black sky albedo at NIR range
ALB_BSA_VIS	Black sky albedo at visible range
ALB_WSA_NIR	White sky albedo at NIR range
ALB_WSA_VIS	White sky albedo at visible range
APAR	Absorbed photosynthetically active radiation
AVHRR	Advanced very high-resolution radiometer
AVM	Alpine Vegetation Model
BEPS	Boreal Ecosystem Productivity Simulator
BESS	Breathing Earth System Simulator
BRDF	Bidirectional reflectance distribution function
C_a	Ambient CO_2 concentration
CARAIB	CARbon Assimilation In the Biosphere
CASA	Carnegie-Ames-Stanford Approach
CCI	Climate Change Initiative
CFix	Carbon Fixation
C_i	Leaf-internal CO_2 concentration
CI/Ω	Clumping index
CO_2	Carbon dioxide
CPC	Climate Prediction Center
CRO	Croplands
CRU	Climatic Research Unit
CSH	Closed shrublands

CT	Carbon Tracker / Climate Type
DBF	Deciduous broadleaf forest
DGVM	Dynamic global vegetation model
DIS	Data and Information System
DISC	Data and Information Services Center
DLEM	Dynamic Land Ecosystem Model
DNF	Deciduous needleleaf forest
DOE	Department of Energy
EBF	Evergreen broadleaf forest
EC	Eddy covariance
EC-LUE	Eddy Covariance Light Use Efficiency model
EF	Evaporative fraction
E_{KC}	Activation energy for K_O
E_{KO}	Activation energy for K_C
ENF	Evergreen needleleaf forest
ESA	European Space Agency
ESRL	Earth System Research Laboratory
ET	Evapotranspiration
EVI	Enhanced vegetation index
ε_{max}	Potential light use efficiency without environmental limitation
ε_{wl}	LUE with water stress
FACE	Free-Air CO_2 enrichment
fAPAR	Fractional absorbed photosynthetically active radiation
FC/$Soil_{cap}$	Field water holding capacity
$f$geo	LiSparseR coefficient
$f$iso	Isotropic coefficient
f_{KcKo}	Ratio of turnover of oxygenase and carboxylase
FTS	Fourier Transform Spectrometer

FvCB	Farquhar, von Caemmerer and Berry published a biochemical model for C3 photosynthetic rates
*f*vol	RossThick coefficient
GEOS	Goddard Earth Observing System Data Assimilation System
GES	Goddard Earth Sciences
GIMMS	Global Inventory Modelling and Mapping Studies
GLCF	Global Land Cover Facility
GMAO	Global Modeling and Assimilation Office
GOME	The Global Ozone Monitoring Experiment
GOSAT	Greenhouse Gases Observing Satellite
$GPP_{2000}CO_2$	The daily value of the spatial continuous atmospheric CO_2 concentration in the year 2000 was simply employed for every year of the inputted data.
$GPPannCO_2$	Estimated GPP using the globally averaged annual mean CO_2 concentrations
$GPPmonCO_2$	Estimated GPP using the globally averaged monthly mean CO_2 concentrations
$GPPspaCO_2$	Estimated GPP under the daily spatial continuous atmospheric CO_2 concentration
GR	Greenness-Radiation
GRA	Grasslands
g_s	Stomatal conductance
g_{smax}	Maximum stomatal conductance
H	Sensible heat flux
HadGEM2-ES	Hadley Center Global Environment Model version 2 - Earth System Modeling
iBEPSd	Improved BEPS daily
IGBP	The International Geosphere-Biosphere Programme
IPCC	Intergovernmental Panel on Climate Change
ISIMIP	Inter-Sectoral Impact Model Intercomparison Project
ISLSCP	International Satellite Land Surface Climatology Project
ITCZ	Intertropical Convergence Zone

JAXA	Japan Aerospace Exploration Agency
J_c	Rubisco-limiting
J_e	Light-limiting
JMA	Japan Meteorological Agency
J_{max}	Light-saturated rate of electron
J_s	Sucrose synthesis-limiting
JULES	The Joint UK Land Environment Simulator
k	Light extinction coefficient
K_C	Michaelis-Menten Constant for CO_2
$K_{C,25}$	Michaelis-Menten constant for CO_2 at 25℃
K_O	Inhibition constant of O_2
$K_{O,25}$	Inhibition Constant of O_2 at 25℃
LAI	Leaf area index
LC	Land cover
LCC	Land-cover change
LCCS	Land cover classification system
LH/λH	Latent heat flux
LP DAAC	The Land Processes Distributed Active Archive Center
LPJml	Lund-Potsdam-Jena managed Land
LST	Land surface temperature
LSWI	Land surface water index
LUE	Light use efficiency
LUT	Look-up table
LWP	Leaf water potential
MCD12C1	Land Cover Type Climate Modeling Grid product
MCD12Q2	Land Cover Dynamics Yearly L3 Global 500 m SIN Grid
MCD43C2	MODIS/Terra and Aqua BRDF/Albedo Snow-free Parameters Daily L3 Global 0.05Deg CMG V006

MCD43C3	MODIS/Terra and Aqua BRDF/Albedo (Bidirectional Reflectance Distribution Function and Albedo) Daily L3 Global 0.05Deg CMG V006
MCD43C4	MODIS/Terra and Aqua Nadir BRDF-Adjusted Reflectance Daily L3 Global 0.05Deg CMG V006
MCI	Mid Continent Intensive
MERRA	Modern-Era Retrospective analysis for Research and Applications
MF	Mixed forest
ML	Machine-learning
MOD16A2	MODIS/Terra Net Evapotranspiration 8-Day L4 Global 500 m SIN Grid V006
MODIS	Moderate Resolution Imaging Spectroradiometer
MTE	Multi-Tree Ensemble
MVC	Maximum value composite
N	Nitrogen
NACP	North American Carbon Program
NASA	National Aeronautics and Space Administration
NCEP	National Centers for Environmental Prediction
NDHD	Normalized difference between hotspot and darkspot
NDVI	Normalized difference vegetation index
$NDVI_{max}$	95% percentile of the NDVI time series at one pixel
NEE	Net ecosystem exchange
NIR	Near infrared
NIR_{Diff}	Downwelling NIR diffuse flux
NIR_{Dir}	Downwelling NIR beam flux
N_m	Maximum nitrogen content
NOAA	National Oceanic and Atmospheric Administration
NPP	Net primary production
N_{ratio}	Nitrogen constrain factor
ORCHIDEE	Organising Carbon and Hydrology In Dynamic Ecosystems

ORNL DAAC	Oak Ridge National Laboratory Distributed Active Archive Center
OSH	Open shrublands
PAR	Photosynthetically active radiation
PAR_{Diff}	Downwelling PAR diffuse flux
PAR_{Dir}	Downwelling PAR beam flux
P_{area}	Photosynthetic area
PET	Potential evapotranspiration
PFT	Plant functional type
P_{period}	Photosynthetic period
PPFD	Photosynthesis photon flux density
$PPFD_{cof}$	Coefficient in a relationship between g_s and PPFD
P_{rate}	Photosynthetic rate of canopy leaf
Pre/P	Precipitation
PS	Surface pressure
P_{scaled}	Scalar for the effect of partitioning of leaf morphology
PSD	Physical sciences division
R	Correlation coefficient
R_{gas}	Molar gar constant
RGS	Rapid growth stage
RH	Relative humidity
RMSE	Root mean square error
R_n	Net radiation
RS	Remote sensing
S_0	Solar constant
SAA	South Atlantic anomaly
SAV	Savannas
SCIAMACHY	SCanning Imaging Absorption SpectroMeter for Atmospheric CHartographY

S_{CO2}	Carbon fertilization factor due to the rising atmospheric CO_2 concentration levels
SDAT	Spatial data access tool
S_{dif}	Diffuse radiation above the canopy
$S_{dif,under}$	Diffuse radiation under the plant canopy
S_{dir}	Direct radiation above the canopy
SDS	Soil data system
S_g	Total solar radiation
SH	Specific humidity
SIF	Sun-induced chlorophyll fluorescence
SM/$Soil_{water}$	Soil moisture
SR	Simple ratio
SWIR	Short wavelength infrared
Ta	Air temperature
TD	Dew point temperature
TEM	Terrestrial ecosystem model
TG	Temperature-Greenness
T_{max}	Maximum temperature
T_{min}	Minimum temperature
$Tmin_{max}$	Maximum daily lowest temperature
$Tmin_{min}$	Minimum daily lowest temperature
T_{opt}	Optimal temperature
T_s	Temperature dependency factor
T_{scaled}	Down-regulation scalars for the effect of temperature on LUE
VEGAS	Vegetation-global atmosphere-soil model
VI	Vegetation indices
vis	Visible bands
VISIT	Vegetation integrative simulator for trace gases
V_m	Maximum carboxylation rate

$V_{m,25}$	Maximum carboxylation rate at 25 ℃
VPD	Vapor pressure deficit
VPM	Vegetation photosynthesis model
WET	Wetlands
WP	Wilting point
WS	Wind speed
WSA	Woody savanna
W_{SLSWL}	Scalar for the effect of water limitation
W_{ssm}	Downward-regulation scalar for the effect of soil moisture
$W_{\mathrm{VPDscaled}}$	Downward-scalar that reduces the potential LUE by VPD
XCO_2	Atmospheric Column CO_2 concentration
x_P	Detrended annual precipitation anomaly
x_R	Detrended mean annual radiation anomaly
x_T	Detrended mean annual temperature anomaly
β	CO_2 fertilization effect
$\beta 1$	Estimated CO_2 fertilization effect using statistical model
$\beta 2$	Estimated CO2 fertilization effect using process-based model
Γ*	CO_2 compensation point
γ^{int}	Apparent GPP sensitivity to interannual variations in temperature
δ^{int}	Apparent GPP sensitivity to interannual variations in precipitation
δ_{NIR}	Leaf scattering coefficient for NIR
δ_{PAR}	Leaf scattering coefficient for PAR
η^{int}	Apparent GPP sensitivity to interannual variations in radiation
θ	Solar zenith angle
θ_{noon}	Solar zenith angle at noon
ρsN	Soil reflectance for NIR
ρsP	Soil reflectance for PAR
ρSWIR	Spectral reflectance in short-wavelength infrared range
φ_0	Intrinsic quantum efficiency of photosynthesis

$GPP_{2014}^{\text{monthly mean global } CO_2}$	Estimated GPPs in 2014 using globally averaged monthly mean CO_2 data
$GPP_{2014}^{\text{annual mean global } CO_2}$	Estimated GPPs in 2014 using globally averaged annual mean CO_2 data
$GPP_{2014}^{\text{monthly spatial } CO_2}$	Estimated GPPs in 2014 using continuous spatial monthly CO_2 data
β_{GPP}^{int}	Overall response of the estimated GPP to the effect of rising atmospheric CO_2 concentration
γ_{GPP}^{int}	Overall response of the estimated GPP to the effect of variations in temperature
δ_{GPP}^{int}	Overall response of the estimated GPP to the effect of variations in precipitation
η_{GPP}^{int}	Overall response of the estimated GPP to the effect of variations in radiation
$R\beta_{GPP}^{int}$	Ratio of β_{GPP}^{int} to the 15-year average GPP of each model
$R\gamma_{GPP}^{int}$	Ratio of γ_{GPP}^{int} to the 15-year average GPP of each model
$R\delta_{GPP}^{int}$	Ratio of δ_{GPP}^{int} to the 15-year average GPP of each model
$R\eta_{GPP}^{int}$	Ratio of η_{GPP}^{int} to the 15-year average GPP of each model